



**HAL**  
open science

# New spin-crossover compounds including polymorphism for a multiscale approach towards high T(LIESST)

Wenbin Guo

► **To cite this version:**

Wenbin Guo. New spin-crossover compounds including polymorphism for a multiscale approach towards high T(LIESST). Material chemistry. Université de Bordeaux, 2021. English. NNT : 2021BORD0015 . tel-03937008

**HAL Id: tel-03937008**

**<https://theses.hal.science/tel-03937008>**

Submitted on 13 Jan 2023

**HAL** is a multi-disciplinary open access archive for the deposit and dissemination of scientific research documents, whether they are published or not. The documents may come from teaching and research institutions in France or abroad, or from public or private research centers.

L'archive ouverte pluridisciplinaire **HAL**, est destinée au dépôt et à la diffusion de documents scientifiques de niveau recherche, publiés ou non, émanant des établissements d'enseignement et de recherche français ou étrangers, des laboratoires publics ou privés.

THÈSE PRÉSENTÉE POUR OBTENIR LE GRADE DE  
**DOCTEUR DE L'UNIVERSITÉ DE BORDEAUX**

ÉCOLE DOCTORALE DES SCIENCES CHIMIQUES (SC)

SPÉCIALITÉ : Physico-chimie de la matière condensée

Par Wenbin GUO

---

**New spin-crossover compounds including  
polymorphism for a multiscale approach towards high  
T(LIESST)**

---

Sous la direction de M. Guillaume CHASTANET  
Philippe GUIONNEAU

En vue d'une soutenance le 12 Janvier 2021

Membres du jury :

M. Mario MAGLIONE	Directeur de recherche CNRS	Examineur
M. Smail TRIKI	Professeur, Université de Bretagne	Rapporteur
M. Guillem AROMI	Professeur, Université de Barcelone, Espagne	Rapporteur
M. Yann GARCIA	Professeur, Université Catholique de Louvain, Belgique	Examineur
M. Guillaume CHASTANET	Chargé de Recherche CNRS	Directeur de thèse
M. Philippe GUIONNEAU	Professeur, Université de Bordeaux	Directeur de thèse



## *Acknowledgements*

### *Acknowledgements*

During these three years, I was lucky to meet, collaborate and communicate with wonderful people on scientific and personal levels. Without their help, support and guidance, this thesis work wouldn't be completed, thus I would like to thank all of them.

First of all, I would like to express my heartfelt thanks to my supervisors Guillaume CHASTANET and Philippe GUIONNEAU for their continuous support, guidance, encouragement and trust.

During these three years, they taught and trained me this project and provided me a tremendous amount of advices in every scientific aspect of this thesis work. Their dynamic and optimistic attitude, passion for research, research ethics, patience and motivation make them role models for every young scientist. I thank them for offering me confidence to face the troubles and encouraging me to solve the problems. Espically during the third year, they did really encourage and prompt me to go ahead when I was pessimistic and negative during the confinement owing to the COVID-19. Without them, I couldn't have finished my thesis writing. Their cautious attitude and scientific spirit will accompany with me forever.

I would like to express many thanks to the members of the jury Mario MAGLIONE, Prof. Smail TRIKI, Prof. Yann GARCIA and Prof. Guillem AROMI for agreeing to read this manuscript in great detail.

I would like to express many thanks to Mathieu MARCHIVIE, Dr. Sébastien PILLET and Dr. El-Eulmi BENDEIF for their great contribution to this thesis work. They were very kind and warm to help me and gave me many advices on my thesis. Mathieu trained me how to use Fullprof and Jana2006 to analyze the x-ray diffraction data. I went to Nancy to work with Sébastien and El-Eulmi two times. Their deep knowledge and research passion infect me a lot. Their enthusiasm on crystallography will influence me forever.

I would like to express many thanks also to Dr. Mathieu GONIDEC, Prof. Corine MATHONIERE, Dr. Patrick ROSA, Dr. Cédric DESPLANCHES, Dr. Baptiste VIGNOLLE and Dr. Elizabeth HILLARD. Thanks to Mathieu for the NMR measurements. He has great

## *Acknowledgements*

patient to explain me the results because I know almost nothing about NMR. As an expert on photomagnetism, I learned many things on Corine's classes. Patrick was also very kind to help and train me for the VSM and CHNF measurements. He can operate almost all the instruments in the lab.

I would like to thank many people who also participated on my thesis project. I would like to express many thanks also to Dr. Nathalie DARO and Dr. Elodie TAILLEUR for their kind training on experiments and synthesis during the first year of the PhD.

I would like to express many thanks also to Eric LEBRAUD, Dr. Stanislav PECHEV and Dr. Brice KAUFFMANN for their kind help of the X-ray diffraction measurements. I would like to express many thanks also to Dr. Dominnique DENUX for his help on DSC measurements.

I would like to express many thanks also to Xinghui, Marlène, Thi Thiet, Liza, Margaux, and Juan, Anaïs, Lorenzo, Ram, and Luc. During these years, we had good times staying together. Thank you all!

Now many thanks are oriented to my good friends inside and outside the laboratory, who stay with me all the time during these three years: Junjie, Chenghao, Wencan, Dianming, Zhengyan, Hongwei, Yuechao, Fenghuan, Suji, Rizaic, and Peizhao.

Last but not least, I owe many thanks to my family, Xiaohong and Hongyu, and my girlfriend, Yingying, for their immense support, trust, patience and encouragement throughout all my life.

***Merci à tous!***

*Wenbin GUO  
Pessac, Octobre 2020*

## Table of contents

<b>GENERAL INTRODUCTION</b> .....	1
<b>PART I -</b> .....	7
<b>STATE OF THE ART ON LIGHT-INDUCED EXCITED SPIN-STATE TRAPPING (LIESST)</b> .....	7
<b>I.1. Generalities on the spin crossover phenomenon</b> .....	9
I.1.1. Introduction .....	9
I.1.2. Multiscale view of SCO: from the coordination sphere to the crystal scale .....	15
<b>I.2. The Light-Induced Excited Spin State Trapping effect</b> .....	23
I.2.1. The photoswitching process .....	23
I.2.2. The lifetime of the photo-induced state .....	25
I.2.3. $T(\text{LIESST})$ : a tool to compare compounds .....	28
I.2.4. How to increase $T(\text{LIESST})$ ? .....	32
<b>I.3. Motivation of the PhD work</b> .....	36
<b>Bibliography</b> .....	41
<b>PART II – PROMOTING DISTORTION OF THE COORDINATION POLYHEDRON BY STERIC STRAIN: FLUORINE SUBSTITUTION OF PM-ZFA FAMILY</b> .....	49
<b>II.1. Introduction</b> .....	51
<b>II.2. Synthesis of the fluorine-substituted ligands and of the <math>[\text{Fe}(\text{PM-zFA})_2(\text{NCS})_2]</math> complexes</b> .....	52
II.2.1. Synthesis of the fluorine-substituted ligands .....	52
II.2.2. Synthesis of the $[\text{Fe}(\text{PM-zFA})_2(\text{NCS})_2]$ complexes .....	55
<b>II.3. Characterizations of the <math>[\text{Fe}(\text{PM-zFA})_2(\text{NCS})_2]</math> complexes</b> .....	57
II.3.1. $[\text{Fe}(\text{PM-oFA})_2(\text{NCS})_2]$ ( <i>I-oFA</i> ) .....	57
II.3.2. $[\text{Fe}(\text{PM-mFA})_2(\text{NCS})_2]$ ( <i>I-mFA</i> ) .....	58
II.3.3. $[\text{Fe}(\text{PM-pFA})_2(\text{NCS})_2] \cdot n\text{CHCl}_3$ ( <i>I-pFA</i> ) .....	70
<b>II.4. Discussion on the structure-properties relationship of <math>[\text{Fe}(\text{PM-zFA})_2(\text{NCS})_2]</math></b> .....	82
<b>Bibliography</b> .....	86

## *Table of contents*

<b>PART III – PROMOTING DISTORTION OF THE COORDINATION POLYHEDRON USING POLYMORPHISM: BROMINE SUBSTITUTION OF PM-ZBRA FAMILY .....</b>	<b>89</b>
<b>III.1. Introduction .....</b>	<b>91</b>
<b>III.2. Synthesis of the substituted ligands and the [Fe(PM-zBrA)<sub>2</sub>(NCS)<sub>2</sub>] (z = o, m, p) complexes .....</b>	<b>92</b>
III.2.1. Synthesis of the PM-zBrA ligands.....	92
III.2.2. Synthesis of the [Fe(PM-zBrA) <sub>2</sub> (NCS) <sub>2</sub> ] (z = o, m, p) complexes .....	95
<b>III.3. Characterizations of the [Fe(PM-zBrA)<sub>2</sub>(NCS)<sub>2</sub>] complexes (z = m, o) .....</b>	<b>98</b>
III.3.1. [Fe(PM-oBrA) <sub>2</sub> (NCS) <sub>2</sub> ] (I-oBrA).....	98
III.3.2. Polymorph [Fe(PM-mBrA) <sub>2</sub> (NCS) <sub>2</sub> ]-I: I-mBrA.....	99
III.3.3. Polymorph [Fe(PM-mBrA) <sub>2</sub> (NCS) <sub>2</sub> ]-II: II-mBrA .....	107
III.3.4. Discussions on I-mBrA and II-mBrA .....	114
<b>III.4. Characterizations of four [Fe(PM-pBrA)<sub>2</sub>(NCS)<sub>2</sub>] polymorphs.....</b>	<b>117</b>
III.4.1. Polymorph [Fe(PM-pBrA) <sub>2</sub> (NCS) <sub>2</sub> ]-I: I-pBrA.....	117
III.4.2. Polymorph [Fe(PM-pBrA) <sub>2</sub> (NCS) <sub>2</sub> ]-II: II-pBrA .....	145
III.4.3. Polymorph [Fe(PM-pBrA) <sub>2</sub> (NCS) <sub>2</sub> ]-III: III-pBrA .....	157
III.4.4. Polymorph [Fe(PM-pBrA) <sub>2</sub> (NCS) <sub>2</sub> ]-IV: IV-pBrA.....	172
III.4.5. Discussions on the four pBrA polymorphs.....	179
<b>III.5. Conclusion .....</b>	<b>188</b>
<b>Bibliography .....</b>	<b>190</b>
<b>PART IV – T(LIESST): A CLOSE AND COMPREHENSIVE VIEW .....</b>	<b>195</b>
<b>IV.1. Introduction.....</b>	<b>197</b>
<b>IV.2. T(LIESST) and the coordination sphere .....</b>	<b>198</b>
IV.2.1. Comparison of the [Fe(PM-zXA) <sub>2</sub> (NCS) <sub>2</sub> ] compounds.....	198
IV.2.2. Comparison with the whole PM-L family.....	202
IV.2.3. New solvatomorphs based on [Fe(PM-pFA) <sub>2</sub> (NCE) <sub>2</sub> ] and [Fe(PM-pBrA) <sub>2</sub> (NCE) <sub>2</sub> ] .....	205
IV.2.4. Comparison with SCO complexes based on bidentate ligands .....	211
<b>IV.3. Lifetime of the metastable HS* state – a multiscale view .....</b>	<b>216</b>
<b>Bibliography .....</b>	<b>223</b>
<b>GENERAL CONCLUSIONS AND PERSPECTIVES.....</b>	<b>227</b>
<b>APPENDIX 1 - HIRSHFELD SURFACE AND FINGERPRINT .....</b>	<b>237</b>

## *Table of contents*

APPENDIX 2 - SINGLE-CRYSTAL AND POWDER X-RAY DIFFRACTION EXPERIMENTS. ....	239
APPENDIX 3 - MAGNETIC AND PHOTO-MAGNETIC MEASUREMENTS .....	241
APPENDIX 4 - ELEMENTAL ANALYSIS AND DIFFERENTIAL SCANNING CALORIMETRY MEASUREMENTS .....	242
APPENDIX 5 - CRYSTALLOGRAPHIC DATA FOR POLYMORPHS [FE(PM-PBRA) <sub>2</sub> (NCS) <sub>2</sub> ]. ....	244
APPENDIX 6 - SYNTHESIS AND CRYSTALLOGRAPHIC DATA FOR [FE(PM-PFA) <sub>2</sub> (NCS) <sub>2</sub> ].S .....	247
APPENDIX 7 - SYNTHESIS AND CRYSTALLOGRAPHIC DATA FOR [FE(PM-PBRA) <sub>2</sub> (NCE) <sub>2</sub> ].S .....	255
APPENDIX 8 - LIST OF PUBLICATIONS .....	259

## *Table of contents*

# **General Introduction**

## *General Introduction*

Nowadays, Material Science is growing very fast, driven by technical and engineering demands. The research and development of new materials with desired properties become more and more significant and urgent. Among these fields, spin crossover (SCO) materials have attracted great interest owing to applications in molecular electronics, as data treatment unit, sensor, actuators and/or smart pigments. Thermal, pressure, magnetic- and electric-fields, light, chemical controls can be used as *stimuli* to induce the spin state switching in SCO materials.

Light is a crucial tool to promote the spin switching in materials as it can operate at ultrafast timescale (femtosecond). Light might be used to promote a photo-reaction on the ligand that will affect the ligand field and the spin state. This can be achieved through Ligand-Driven Light-Induced Spin Change (LD-LISC) and Light-Driven Coordination-Induced Spin-State Switching (LD-CISS). Light can also be used to bring energy and heat the sample, called the photothermal effect. Light can be tuned to excite and populate states involving the metal center according to the Light-Induced Excited Spin-State Trapping effect (LIESST). Through the population of excited states, a metastable state ( $h\nu$ -HS\*) can be trapped at low temperature.

In order to use SCO devices operating at ambient conditions, the spin switching of materials should be effective around room temperature. Dozens of SCO materials have been reported with the thermal spin transition temperature ( $T_{1/2}$ ) around or above ambient conditions. However, the relaxation temperature ( $h\nu$ -HS\*  $\rightarrow$  LS) that measures the limit temperature at which the photo-induced state is erased within few minutes, named  $T(\text{LIESST})$ , is usually below 50 K, which is severely restricted its application. It is still a great challenge to establish the structure-properties relationships corresponding to the LIESST process, though this approach is crucial to discover SCO materials with a high relaxation temperature  $T(\text{LIESST})$ . The fundamental understanding of the LIESST effect must be yet deeply completed prior to any rational design of any efficient material.

To understand the relationship of relaxation temperature between thermal and light-induced SCO, the database of  $T(\text{LIESST})$  vs  $T_{1/2}$  was created and developed by my host group. It was evidenced a linear relationship between these values as  $T(\text{LIESST}) = T_0 - 0.3 T_{1/2}$ . In order to enhance the  $T(\text{LIESST})$ ,  $T_0$  should increase. It was proposed that this could be achieved through the increase of the distortion of the coordination polyhedron. The crucial role of variation of trigonal distortion ( $\Delta\theta$ ) on  $T(\text{LIESST})$  was confirmed in complexes with bidentate ligands. Later, based on photocrystallographic studies of two polymorphs of  $[\text{Fe}(\text{PM-BiA})_2(\text{NCS})_2]$  complex (PM-BiA = N-2'-pyridylmethylene)-4-(aminobiphenyl)), both the variation of angle

distortion ( $\Delta\Sigma$ ) and bond distortion ( $\Delta\zeta$ ) play a crucial role on  $T(\text{LIESST})$ . The role of the coordination sphere distortion on the lifetime of the  $h\nu\text{-HS}^*$  implies that three-dimensional potential wells must be used, to describe the anisotropic breathing of the coordination sphere.

Guided by these valuable works,  $T(\text{LIESST})$  can be enhanced by increasing the distortion of the coordination sphere. We focus this work on the synthesis of new compounds with ligands designed to promote strong distortion of the coordination sphere. The first strategy is to promote the steric strain close to the coordination sphere by halogen substitution from *para*, *meta*, to *ortho* position at the molecular scale based on the bidentate ligand. The second one is related to the subtle change of the intermolecular interactions in polymorphism or solvatomorphism.

**Part I** displays some fundamental knowledge on SCO and LIESST effect. In **Part II**, the synthesis, crystallography and (photo)magnetic studies of new molecular compounds with fluorine from *para*, *meta*, to *ortho* position are presented. In **Part III**, polymorphs are characterized and the intermolecular interactions are analyzed. The deep examination of the relevant parameters to high  $T(\text{LIESST})$  as discussed in **Part IV** brings new perspectives on  $T(\text{LIESST})$ .

***Abbreviations***

SCO	Spin CrossOver
HS	High Spin
LS	Low Spin
HS*	High Spin Metastable state
<i>h<math>\nu</math></i> -HS*	Light-Induced High Spin Metastable State
Q-HS*	Thermal Quenching High Spin Metastable State
SCXRD	Single-Crystal X-Ray Diffraction
PXRD	Powder X-Ray Diffraction
MLCT	Metal-Ligand Charge Transfer
LIESST	Light-Induced Excited Spin State Trapping
TIESST	Thermally-Induced Excited Spin-State Trapping
<i>T</i> (LIESST)	Relaxation temperature of the <i>h<math>\nu</math></i> -HS*
<i>T</i> (TIESST)	Relaxation temperature of the Q-HS*
DSC	Differential Scanning Calorimetry
SQUID	Superconducting Quantum Interference Device
RMSD	Root Mean Square Deviation
$\Theta$	trigonal distortion
$\Sigma$	angle distortion
$\zeta$	length distortion
<i>S</i>	Shape factor
<i>o</i>	Ortho position
<i>m</i>	Meta position
<i>p</i>	Para position
PM	N-(2' -Pyridylmethylene)
AzA	4-(Phenylazo)aniline
BiA	4-(Aminobiphenyl)aniline,
DiyA	4-(Phenylbutadiyne)aniline
PeA	4-(Phenylethynyl)aniline,
TeA	4-(Aminoterphenyl)aniline
TheA	4-(Thienylethynyl)aniline
NEA	4-(naphthalene-1-ethynyl)aniline
FIA	4-(2-amino)aniline
bt	2,2'-bi-2-thiazoline
bpym	2,2'-bipyrimidine
phen	1,10-phenanthroline
ptz	1-propyl-1H-tetrazole,
1-bpp	2,6-bis(pyrazol-1-yl)pyridine
3-bpp	2,6-bis (pyrazol-3-yl) pyridine,
abpt	4-amino-3,5-bis(pyridin-2-yl)-1,2,4-triazole

## *Abbreviations*

**Part I -  
State of the Art on Light-Induced Excited Spin-State  
Trapping (LIESST)**

<b>I.1. Generalities on the spin crossover phenomenon.....</b>	<b>9</b>
I.1.1. Introduction .....	9
I.1.2. Multiscale view of SCO: from the coordination sphere to the crystal scale .....	15
<b>I.2. The Light-Induced Excited Spin State Trapping effect .....</b>	<b>23</b>
I.2.1. The photoswitching process .....	23
I.2.2. The lifetime of the photo-induced state.....	25
I.2.3. $T(LIESST)$ : a tool to compare compounds .....	28
I.2.4. How to increase $T(LIESST)$ ? .....	32
<b>I.3. Motivation of the PhD work .....</b>	<b>36</b>
<b>Bibliography .....</b>	<b>41</b>

## I.1. Generalities on the spin crossover phenomenon

### I.1.1. Introduction

The spin crossover (SCO) phenomenon has been discovered more than 90 years ago<sup>1-2</sup> and is increasingly envisioned to take part in devices in molecular electronics, as data treatment unit, sensor, actuators and/or smart pigments.<sup>3-11</sup> This has led to a huge interest of the scientific community in coordination chemistry, materials science and physical chemistry aspects of SCO during the last 40 years. In this part, however, we will only present some basic concepts of SCO.

- *What drives the occurrence of SCO?*

In perfectly octahedral ligand field, the five  $d$  orbitals of a transition metal ion are split into two subsets of orbitals,  $t_{2g}$  (made of  $d_{xy}$ ,  $d_{yz}$  and  $d_{zx}$ ) and  $e_g$  (made of  $d_{z^2}$  and  $d_{x^2-y^2}$ ). The  $t_{2g}$  orbitals are basically non-bonding and are therefore at lower energy than the anti-bonding  $e_g$  orbitals. The splitting between the two sets is referred to as ligand field splitting,  $10Dq$ . This ligand field strength depends on both the particular set of ligands and the given metal ion. The population of these two sublevels by electrons is driven by the difference between ligand field splitting energy ( $\Delta = 10Dq$ ) and the interelectronic repulsion energy ( $\Pi$ ). Metals with electronic configurations  $d^4$  to  $d^7$  can adopt either high-spin (HS, when  $\Delta$  is weaker than  $\Pi$ ) or low-spin (LS, when  $\Delta$  is greater than  $\Pi$ ) electronic ground states. Under certain circumstances, when the energy difference between the HS and LS states becomes comparable with the thermal energy  $k_B T$ , a switching from one configuration to the other may occur, leading to the spin crossover (SCO) phenomenon. **Figure I.1** shows the HS and LS electronic configurations of a  $Fe^{2+}$  ion in octahedral geometry, where the six electrons adopt a spin singlet state  $^1A_1 (t_{2g}^6 e_g^0)$  in LS or a spin quintet state  $^5T_2 (t_{2g}^4 e_g^2)$  in HS state.

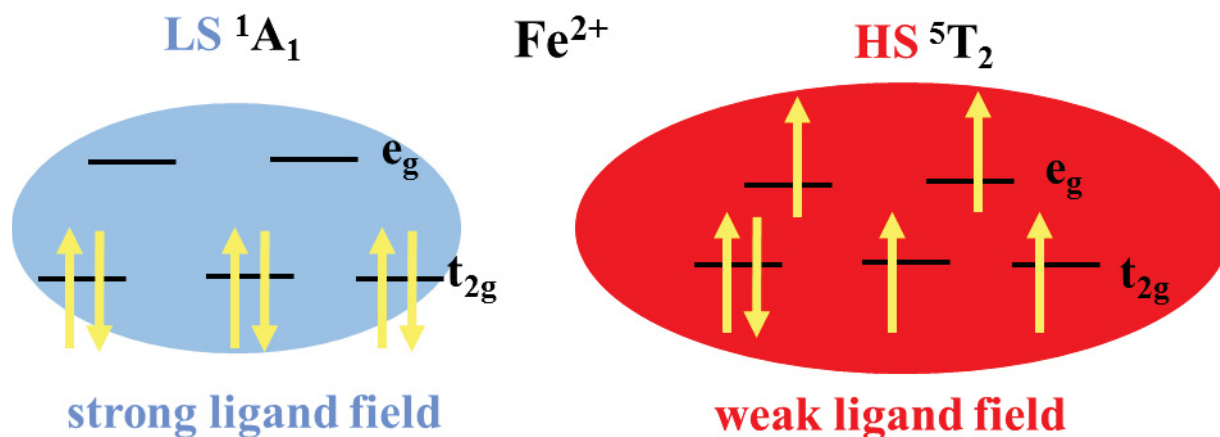


Figure I.1. Schematic picture of low spin and high spin states in octahedral Fe<sup>2+</sup> ions under strong and weak ligand fields.

As a result of the SCO, there are several changes of physical properties arising from the change of electronic configuration. The most obvious modifications concern the metal spin state, the metal-ligand bond lengths and the magneto-optical properties, together with variations in vibration (molecules and network) and thermodynamic characteristics. Notably, the LS ion forms bond-lengths typically 10% shorter than those of the HS ion, bond vibrations differ in both spin states and LS give more coloured and less “magnetic” samples than HS. All these changes can be used to probe the SCO which opens up the use of a very wide range of characterisation techniques<sup>12</sup>, as detailed below.

- *What perturbation can induce SCO?*

Temperature is the most straightforward perturbation used to promote SCO. Temperature, in a schematic way, brings energy to the electrons to populate the e<sub>g</sub> level leading to a LS to HS switch upon warming. The entropy in HS state is higher than that in LS state due to the large spin multiplicity at HS state. The change in spin state, can also be promoted by the magnetic field that favors the HS state.<sup>13</sup> However, it requires very high magnetic field (20-100 T), which makes this stimulus rarely used and barely investigated.<sup>13</sup> Typical Fe-N bond lengths in FeN<sub>6</sub> environments are around 2.0 Å and 2.2 Å in the LS and HS states, respectively, providing a noticeable change upon SCO corresponding to an increase of the metal coordination sphere volume from LS to HS.<sup>14</sup> Applying pressure is therefore another important stimulus that favors the state of lower volume that is the LS state.<sup>15-17</sup>

Light represents also a crucial tool to promote the spin switching through different means.<sup>18</sup> First, light might be used to promote a photo-reaction on the ligand that will affect the ligand field and the spin state. This can be achieved through Ligand-Driven Light-Induced Spin Change (LD-LISC)<sup>19-20</sup> and Light-Driven Coordination-Induced Spin-State Switching (LD-CISSS)<sup>21</sup>. Second, light can also be tuned to excite and populate states involving the metal center. Through the population of excited states, a metastable state can be trapped at low temperature. This is the case of the Light-Induced Excited Spin-State Trapping effect (LIESST)<sup>22</sup> that will be detailed in the following section **1.2**. Finally, light can be used to bring energy and heat the sample, promoting photothermal effect.<sup>23-25</sup> While LD-LISC and photothermal effects might be achieved at room temperature, obtaining LIESST at such temperature is strongly challenging.

Though the most intensively studied, temperature is therefore far to be the only route to induce the SCO in a compound. With in view applications using SCO devices running at ambient conditions, the use of high-pressure, magnetic-fields or light-irradiation as *stimuli* are to be envisaged, though with unequal perspectives. Note also that getting ambient conditions SCO can also take the road of electric or chemical controls.<sup>26</sup>

- *Which techniques to record SCO?*

At SCO, the magnetic moment changes between two different spin states that can be easily discriminated using magnetic measurements. In the particular case of Fe<sup>2+</sup> based compounds, SCO occurs between a diamagnetic (LS) and a paramagnetic (HS) states, providing an important magnetic contrast. Hence, the measurement of the magnetic susceptibility as a function of temperature,  $\chi(T)$ , becomes a technique of the first choice to characterize the occurrence of SCO. The *magnetic susceptibility* is indeed dependent on the value of spin state, expressed as  $\chi T = Cg^2S(S+1)$  with  $C = N_A\beta^2/3k_B$ ,  $N_A$ ,  $\beta$ ,  $k_B$ ,  $g$  being the Avogadro number, the Bohr magneton, the Boltzmann constant, and the Lande factor, respectively. Comprehensive surveys of the techniques and computational methods used in magnetochemistry were given by Palacio<sup>27</sup> and Kahn<sup>28</sup>. Another usual method to determine the spin state, as well as the oxidation state of iron-based compounds is <sup>57</sup>Fe *Mössbauer spectroscopy*.<sup>29-30</sup> The latter is actually the true method to obtain the absolute HS/LS ratio within a compound since the electron density at the nucleus strongly differ in HS and LS. Isomer shift  $\sigma$  and the quadrupole splitting  $\Delta E_Q$ <sup>30</sup>, are consequently different for the HS and LS states, and increase from the LS to HS switch.

Along SCO, the population/depopulation of the antibonding HS as function of the temperature, leads to strong differences in bond lengths and bond vibrational characteristics. Therefore, vibrational spectroscopic techniques are very useful, such as *infrared*<sup>31</sup> or *Raman spectroscopies*<sup>32</sup>. The impressive variation of bond lengths can be accurately probed using diffraction technics, preferentially using *Single-crystal X-ray diffraction* (SCXRD)<sup>14,33</sup> instead of *Powder X-ray diffraction* (PXRD)<sup>14</sup>, through at least the crystal structure determination in both LS and HS states and with the possibility to explore the full phase diagrams. For instance, structural “movies”, determined by variable temperature SCXRD, provide many information from atomic to material scales, including variations of geometry and volume of the coordination sphere, changes of ligand conformation, modification of intermolecular interactions, rearrangement of molecular packing, symmetry breaking and so on.<sup>14,34,35</sup>

The change of electronic configuration at the SCO also affects the absorption properties, leading to color change upon switching. Therefore, *absorption spectroscopies* and *optical reflectivity* are important to trigger thermo-, piezo- and photo-chromism of the SCO materials.<sup>36-37</sup>

Extended X-ray Absorption Fine Structure (EXAFS) and X-ray Absorption Near Edge Structure (XANES) provide information essentially about geometry and oxidation states, which have been used to study the structural and electronic changes occurring during SCO.<sup>38-39</sup> These methods become relevant to get information notably when the SCO sample is not available in the crystalline state.

In the solid state, the thermodynamic rules the behavior of the materials. The LS state is enthalpically favored whereas the HS state is entropically favored. Therefore, *calorimetric measurements* are crucial to determine the enthalpy and entropy changes. The enthalpy change  $\Delta H = H_{HS} - H_{LS}$  is typically around 10 to 20 kJ mol<sup>-1</sup>, and the entropy change  $\Delta S = S_{HS} - S_{LS}$  is of the order of 50 to 80 J mol<sup>-1</sup> K<sup>-1</sup>.<sup>40</sup> It is important to highlight that the SCO process is entropy-driven. In fact, only around 25 % of the entropy gain from LS to HS change arises from the change in spin multiplicity,  $\Delta S_{spin} = R \ln((2S_{HS}+1)/(2S_{LS}+1))$  (13.38 J mol<sup>-1</sup> K<sup>-1</sup> for Fe<sup>2+</sup>) while 75% comes from vibrations (molecules, phonons).<sup>41</sup>

It is interesting to note that, in the last decades, if the large panel of approaches to probe the spin crossover allowed a deep investigation and therefore a significant step forward in the understanding of the SCO phenomenon, conversely, the requirements of the investigation of the SCO phenomenon allowed to push the fontiers of some characterization technics. It is for example the case of High-Pressure or Low Temperature SCXRD.<sup>34,42-43</sup>

- *What are the spin crossover features?*

Temperature is the main perturbation used to induce the SCO. The feature of the SCO gives information on how the SCO-active centers interact with each others. Indeed, the organization of molecules in a crystal lattice and the supramolecular interactions between them play a key role in the overall behavior of the solid. In fact, the volume change associated with the spin-state switch - change which is actually anisotropic - propagates in the solid *via* intermolecular interactions. These interactions, between the molecules in the crystal lattice, can be schematized, in a first approach, by springs (Figure I.2). The strength of these springs determines the cooperativity of the solid, that is to say how collective the propagation of the anisotropic volume change of the coordination sphere up to macroscopic scales is.<sup>44-46</sup>

In a simple view, the smaller the intermolecular distances, the higher the spring force, the higher the cooperativity. Cooperativity, when it is strong, then looks like a domino effect (ferroelasticity): the spin change of a metallic center propagates to the neighboring centers. It is still not clear which kinds of intermolecular interactions contribute to strong cooperativity, however, covalent bonds in polymeric system, hydrogen bonding, and  $\pi$ --- $\pi$  contacts seem to be essential. It should be noted that the intermolecular interactions are not isotropic in the three directions of the crystal lattice, this being able to generate competitions of elastic interactions and give rise to antiferroelasticity. The multi-scale view of SCO (as seen in the following section I.1.2) is therefore important to understand the propagation of the variation in volume from the coordination sphere to the macroscopic solid and to explain the observed behaviors. The spin crossover in the solid state is therefore strongly influenced by cooperativity. Figure I.2 shows schematically the temperature evolution of the HS fraction for different levels of cooperativity. The switching temperature, denoted  $T_{1/2}$ , is defined as the temperature at which half of the metal centers has switched. To date, several very different SCO shapes have been observed in the solid state, as listed below.

*Gradual SCO* (Figure I.2a) are characteristic of weakly cooperative compounds. Such SCO is characterized by the evolution of the HS fraction that covers a wide temperature range, often up to 100 K. It is similar to the features observed in solution with a Boltzmann distribution of the spin state. For example, structural analysis from 120 K to 430 K of  $[\text{FeL}(\text{ClO}_4)_2]$  (L = 1,4,7-tri(1-amionophenyl)-1,4,7-triaza cyclononane) that exhibits a gradual SCO, suggests the continuous variation of average bond lengths and distortion within the  $\text{FeN}_6$  polyhedron and

the absence of direct short contacts between adjacent  $[\text{FeL}]^{2+}$  ions.<sup>47</sup> It is however crucial to note that one given bond length can adopt only two values, the one of the HS state and the one of the LS state. The observation of continuous feature modifications, thus the determination of intermediate bond length values, only reflects an average of the bond lengths at the macroscopic sample scale. This is by the way efficiently used to determine the HS/LS ratio from Fe-N bond lengths.<sup>48-49</sup>

*Abrupt and hysteretic SCO* (Figures **I.2b** and **I.2c**) can be observed in cooperative compounds leading to a switching event occurring in a complete mode within few Kelvin (< 10K). A hysteresis may appear as shown in Figure **I.2c** for very strongly cooperative systems. Such strong cooperativity might be associated with structural phase transition. This lead to the saillant concept of bistability. Bistability refers to the ability of a system to be observed in two different electronic states at the same condition for a given external perturbation, depending on the history of the compound.<sup>50-51</sup> This aspect has driven many research with the aim to use SCO materials as memory elements.<sup>7-11,15</sup>

*Stepped SCO* (Figure **I.2d** and **I.2e**) is associated with the appearance of an intermediate situation with a partial conversion of the metal centers, some remaining HS at low temperature for example. Usually, it occurs when different SCO-active sites are present in the network, either before the occurrence of the spin switch or during the SCO through the appearance of symmetry breaking. Stepped SCO have been reported in a vast variety of SCO materials made of  $\text{Fe}^{2+}$ <sup>52-53</sup>,  $\text{Fe}^{3+}$ ,<sup>54</sup>  $\text{Co}^{2+}$ <sup>55</sup>, or  $\text{Mn}^{3+}$ <sup>56</sup> ions. Real *et al.* firstly suggested the presence of “negative cooperativity” to explain the stepped behavior of the dinuclear compound  $[\text{Fe}(\text{bt})(\text{NCS})_2]_2\text{bpym}$  (bt = 2,2'-bi-2-thiazoline and bpym = 2,2'-bipyrimidine).<sup>57</sup> Symmetry breaking is mainly explained as the result of competing ferro-elastic and antiferro-elastic interactions.<sup>58-59</sup> As already mentioned, the coordination sphere volume change is not isotropic, nor the network of intermolecular interactions. This might lead to elastic competition promoting and ordering of intermediate phases with HS-LS periodic orders, in different ratio, on each step. This can end up with very peculiar cases such as Devil’s staircase (Figure **I.2e**), one of the exotic multi-stepped SCO, explained by the formation of modulated commensurate and incommensurate structures in crystals.<sup>60-61</sup>

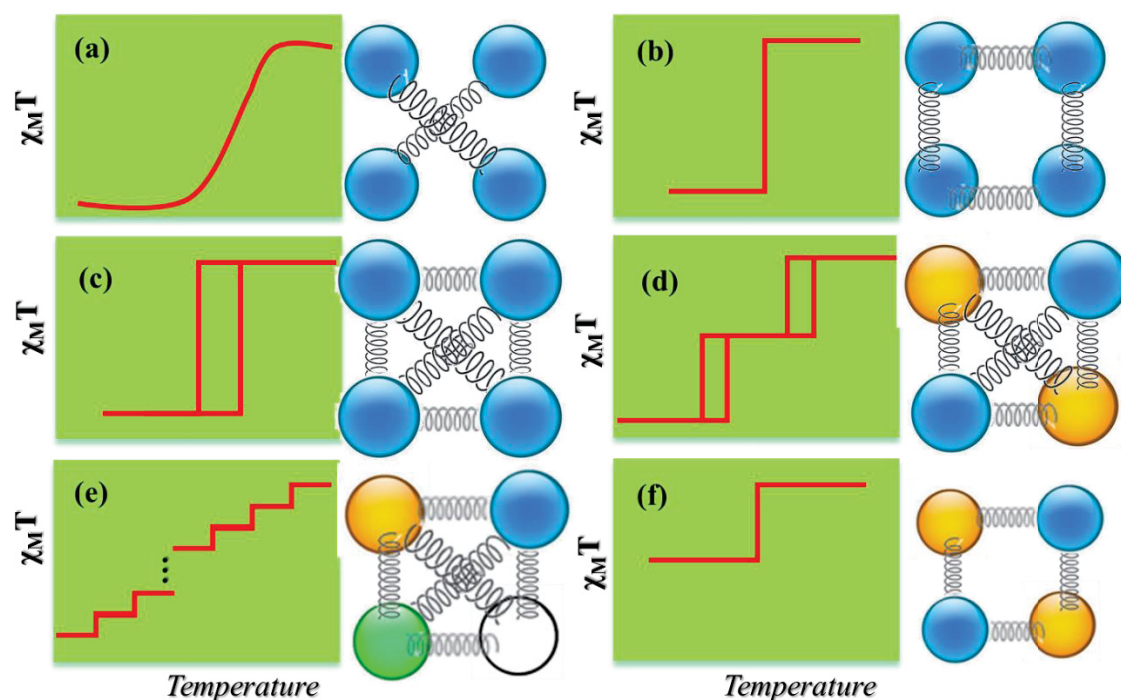


**Figure 1.2.** Schematic spin crossover curves as function of temperature. The springs represent the interactions that can reflect the cooperativity. The color of spheres represents the independent crystallography sites.

*Incomplete SCO* (Figure 1.2f) means some of the metal sites being SCO-inactive, either from the beginning, or during the occurrence of symmetry breaking. It can also occur in compound with one metal site, the partial conversion is then due to a perturbation from the crystal packing and comes down to consider the remaining HS site as a disorder on the LS sites.<sup>62</sup> The interesting point for this kind of SCO is the possible presence of hidden hysteresis. For example, photoinduced hidden hysteresis was reported in Hofmann-like spin-crossover metal–organic frameworks<sup>63</sup> and molecular complexes<sup>64</sup>.

### 1.1.2. Multiscale view of SCO: from the coordination sphere to the crystal scale

From the structural point of view, the most obvious modification accompanying the spin crossover concerns the reversible shortening of the metal-ligand bond lengths from HS to LS states. The latter was noticed and thoroughly studied in the early stage of the SCO phenomenon.<sup>65-67</sup> It has been shown that this internal modification of the coordination sphere has repercussions to all larger physical scales, up to the macroscopic one.<sup>34,68</sup> Consequently, in order to understand how the SCO induces structural changes and, conversely, how structural

properties can influence the SCO properties, one needs to adopt a multiscale view of the SCO.<sup>14,34-35</sup> In other words, determining the bond lengths variations at the SCO is mandatory but largely insufficient to describe the mechanism of the SCO occurring in the crystalline materials. Indeed, the interplay between SCO and structural properties appears so complex that it is still under investigation. Since we aim to draw structure-properties relationships in this work, in particular to penetrate the crucial parameters that govern the light-induced SCO, the structural description will tend to encompass a multiscale view. The latter means that all physical scales must be described: the geometry of metal-ligand coordination sphere, the conformation of molecules, the topology of intermolecular interactions, the rearrangement of molecular packing including phase transition, the coherent domain scale though the microstructure of crystals (or polycrystals) and, when possible, the macroscopic description of the crystal itself. By the last two decades, the SCO community has sometimes attempted to propose a full description of the structure-properties relationships.<sup>68</sup> This very rich field has given rise to the definition of numerous structural parameters nowadays used as daily tools such as the distortion and the volume of the coordination sphere<sup>14,69-70</sup> as well as some crystal packing or phase diagram features<sup>35,71</sup>. This race to the ultimate multiscale understanding of SCO was yet on course at the time this work started. Many structural features regarding the multiscale view had been reported, as very briefly recall below with the choice to underline those that will be determined and used along this work.

*The coordination sphere* modifications at the SCO include, from LS to HS, an increase of the metal-ligand bond lengths by an average value of 0.2 Å in the case of the Fe<sup>2+</sup>N<sub>6</sub> surrounding (on which this work is focusing, as already stated) and an increase of the deviation from the ideal octahedron, meaning an increase of the distortion. The whole results in an increase of the volume of the coordination sphere ( $\Delta V_p$ ) by around 25% for Fe<sup>2+</sup>N<sub>6</sub>.<sup>34</sup> It is interesting to note that this volume variation appears always of the same amplitude, whatever the SCO complex involved. It is much more intricate to propose a unique tendency for the distortion since it strongly depends on which type of distortion it is referred to (see below); to some extent the distortion of the coordination sphere may appear crucial for the SCO features and at the same time typical for a given compound. The amplitude of the average bond-lengths variation at the SCO is very similar from one compound to another – note that this is true if one pays attention to separate pure thermal effects from SCO effects – and therefore it is hardly a discriminating parameter to account for various SCO features.<sup>48</sup> In addition, the bond-lengths variations are

strongly anisotropic which makes the isotropic description (average bond-lengths and volume) rather insufficient.

The reflection on the distortion feature is tricky to drive since it strongly depends on the way the distortion is defined. Across the investigation of the distortion of the coordination sphere in SCO compounds, four parameters were finally selected<sup>14</sup>, among many others in the fields of possibilities<sup>70</sup>.

These parameters all account for a different but complementary point of view. The **angle distortion**  $\Sigma$  is defined by the sum of the deviations to 90° of the 12 *cis* ligand-metal-ligand angles<sup>72,70</sup> (Figure I.3, Eq I.1).

The **trigonal distortion**  $\Theta$  is defined as the sum of the deviations from 60° of the 24 possible  $\theta$  angles, where  $\theta$  is defined as the ligand-metal-ligand angle measured on the projection of the two triangular faces of the octahedron projected along its pseudo-threefold axes on the medium plane containing the metal ion<sup>73</sup> (Figure I.3, Eq I.2). The  $\Theta$  value indicates the deviation in the coordination polyhedron geometry from a perfect octahedron ( $O_h$ ) to a trigonal prismatic structure ( $D_{3h}$ ).

The **length distortion**  $\zeta$  means the sum of the deviations from the average metal-ligand bond length (Eq I.3), which carries a mixture of distortion and elongation information.<sup>74</sup>

The value of the **shape parameter**,  $S$ , is another way to quantify the deviation from the ideal octahedron ( $O_h$ ) and takes part of a global description of symmetries.<sup>75</sup> The values of  $\zeta$ ,  $\Theta$ ,  $\Sigma$  and  $S$  are zero for a perfect octahedron. These values can be calculated using the software *OctaDist*<sup>76</sup> (<https://octadist.github.io>) based on development made in the “Switchable Molecules and Materials” group at ICMCB and  $S$  can be calculated by the *shape* software.<sup>77</sup> These parameters have HS and LS values that, in fact, are different from one compound to another. Consequently, these parameters appear essentially a relevant feature for a given compound and are therefore eligible for drawing structure-properties relationships. As it will be described in the next part of this chapter, the trigonal distortion,  $\Theta$ , has been directly correlated to some SCO features and is now an integrated tool within the study of the SCO phenomenon.<sup>73,78-82</sup> These four parameters will be used and commented when relevant in this work; it is worth mentioning already that their discussion requires an accurate determination of the crystal structures at least in both HS and LS states, or better at many temperatures. As a general comment, it is clear that the structure-properties interplay should be always, when

possible, envisaged through variable temperature investigation as recently demonstrated<sup>48</sup>, this remark is valid for all physical scales, listed below.

$$\Sigma = \sum_{i=1-12} |90 - \alpha_i| / ^\circ \quad \text{Eq I.1}$$

$$\Theta = \sum_{i=1-24} |60 - \theta_i| / ^\circ \quad \text{Eq I.2}$$

$$\zeta = \sum_{i=1-6} |(Fe-L_i) - \langle Fe-L \rangle| / \text{Å} \quad \text{Eq I.3}$$

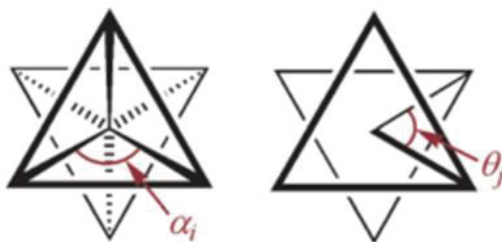


**Figure I.3.** Definitions of the angles used to calculate the distortion parameters  $\Sigma$  and  $\Theta$  for a six-coordinated metal site. Adapted from ref. 78.

The molecules, of course, are affected by the modifications of the coordination sphere at the SCO. If the latter are relatively easy to quantify and classify since the events (elongation, distortion) are the same in nature even though different in amplitude, on the other hand the effects of the SCO at the scale of the molecular complex are almost impossible to rationalize because they appear rather different from one compound to another. The response of the molecule to the coordination sphere modification goes from a simple “absorption” of the volume change to a strong molecular deformation involving ligand significant movement. The most spectacular effects, reported so far, are conformational modifications and even reversible bond breaks.<sup>83</sup> For example, the deformation of ligands suggests the conformational change as *cis-trans*<sup>20-21</sup>, *anti-gauche*<sup>84</sup>, and angular *Jahn–Teller* distortion in bpp family<sup>77</sup>. By extension, it can be included at this scale the order-disorder of molecules together with anions or solvent entities also. For example, the order–disorder transitions of anion leading to cooperative SCO were found in  $[\text{Fe}(\text{DAPP})(\text{abpt})][\text{ClO}_4]_2$  (DAPP = bis(3-aminopropyl)(2-pyridyl-methyl)amine, abpt = 4-amino-3,5-bis(pyridin-2-yl)-1,2,4-triazole)<sup>85</sup>,  $[\text{Fe}\{3\text{-bpp-(5-C}_6\text{H}_3\text{OH)}_2\}_2][\text{ClO}_4]_2 \cdot \text{H}_2\text{O} \cdot 2\text{acetone}$  (3-bpp-(5-C<sub>6</sub>H<sub>3</sub>OH)<sub>2</sub> = 2,6-bis[5-(2'-phenol)pyrazol-3-yl]-pyridine)<sup>86</sup> and  $[\text{Fe}(\text{picpzpz})_2][\text{BF}_4]_2 \cdot \text{MeOH}$  (picpzpz = 3-(2-pyrazinyl)-1-[(2-pyridyl)methyl]pyrazole)<sup>87</sup>. Modifications of the conformation of the ligands, anion, and even solvent appear quite common in SCO compounds and may be linked to some specific behaviours. For example, the hysteretic SCO behaviour is driven by the modification of the conformation of the triflimide from a *syn*

conformation to an intermediate conformation in  $[\text{Fe}(\text{qsal-I})_2]\text{NTf}_2$  (qsal-I = (*N*-8-quinoly1)-5-*I*-salicylaldiminate).<sup>88</sup> Elsewhere, the conformational changes of the flexible alkyl chains at the SCO impact the magnetic response in  $[\text{Fe}(\text{C}_{10}\text{-pbh})_2]$  ( $\text{C}_{10}\text{-pbh}$  = (1*Z*, *N'* *E*)-4-(decyloxy)-*N'*-(pyridin-2-ylmethylene)-benzo-hydrazone).<sup>84</sup> Actually, the subtle relationships between the molecule geometry and the SCO features represents one of the possible way for the rational design of the SCO complexes.

It is worth noting that the molecular shape can inhibit the SCO in some cases. As suggested by Halcrow “if the difference in shape between the high and low spin forms of a material is too large, it will freeze the compound in its high spin state”.<sup>78</sup> This is because a solid lattice cannot accommodate the structural rearrangement that would be required for the transition to proceed.<sup>68</sup> The typical example is the HS compound  $[\text{Fe}(\text{bpp})_2](\text{PF}_6)_2$ .<sup>78</sup>

*The intermolecular interactions* can be significantly affected by the SCO and, conversely, the topology of the interactions between metallic centers may strongly influence the SCO features.<sup>14,68</sup> As a general tendency, strong intermolecular interactions favor an abrupt SCO and large hysteresis. The whole difficulty lies in the characterization of what is a “strong” interaction and accounting for all interactions. In essence, many different kind of intermolecular interactions can be found in SCO molecular crystals including hydrogen bonding,  $\pi$ - $\pi$  contacts, chalcogen bonding, halogen bonding and even atom-atom contacts (as hydrogen-hydrogen ones). This diversity and the huge amount of interactions develop intricate topologies and make very difficult to describe and therefore rationalize the link between SCO features and intermolecular interactions. By the way, the description of intermolecular interactions constitutes in itself, a research field in molecular materials. Many attempts over the years were made to propose a general view of intermolecular interactions in SCO compounds<sup>67,70</sup>, but it is probably the new description proposed by the Hirshfeld surfaces through fingerprints representations<sup>89</sup> that provides the better tool so far to summarize the intermolecular interactions, notably in SCO compounds as recently shown.<sup>90</sup> The description of intermolecular interactions is indeed crucial since they can be viewed as sources of cooperativity.<sup>42-44</sup> Therefore, to account for that, their discussions through fingerprints will be used, when possible, in this work. The details on the Hirshfeld surfaces and fingerprints calculation process can be seen in [Appendix I](#).

To illustrate the complexity of the interplay between intermolecular interactions and SCO features, it can be noted that SCO can be prohibited when the intermolecular environment is

too congested, though intermolecular interactions are too dense<sup>91-92</sup> or, on the contrary, when the intermolecular interactions are too weak<sup>93-94</sup>.

*The molecular packing* scale is of course very important in the description of a crystalline compound. As for intermolecular interactions, the features of the crystal packing can drastically, or only smoothly change in parallel to the SCO. When discussing crystal packing in view of correlating to SCO features, many doors suddenly open.<sup>93</sup> One is polymorphism, *i.e.* the possibility for the same molecule to crystallize within different crystal packings including different symmetries. Largely encountered in the SCO literature, one of our goal in this work will be to use this property to discuss structure-properties relationships. This physical scale also accounts for phase transitions and it has been demonstrated how the phase diagrams can be tricky in SCO compounds<sup>34</sup>. The literature on this subject is very dense reporting for instance symmetry breaking associated to spin crossover.<sup>55,95</sup> The unit-cell dimensions and symmetry can summarize part of the information of the crystal packing. Unit-cell modifications associated to SCO is one of the crucial parameters, probably the first one, to determine when studying SCO compounds. It has been done since the early stage.<sup>64-66</sup> If the absolute value of the unit-cell has a poor meaning in the objective of rationalizing the SCO features, the relative variation from HS to LS is clearly meaningful. When this work started, the relative unit-cell volume decrease from HS to LS was known to lay between 1 and 10 % based on the existing literature.<sup>14,34</sup> However, it has already been quoted a long time ago that a fine description must focus on the unit-cell parameters that reflects the anisotropy of the unit-cell modifications, rather than the volume.<sup>68</sup> It has been shown that the anisotropy of the unit-cell modifications is a common feature as illustrated, for instance, in triazole based SCO compounds where one parameter can be modified by more than 10% while others are scarcely changed.<sup>96</sup> It is worth noting that a fine unit-cell description, when talking about thermal SCO must be obtained from more than the sole HS and LS unit-cells, respectively, at high and low temperature but from a variable temperature study, including many temperature points on both sides of the SCO.<sup>68,71</sup> This will be done in this work, when possible, and will allow to separate pure thermal from pure SCO effects.

*The microstructure scale in a crystal* means the scale of the coherent domain, *i.e.* the smallest part that indeed is formed by a monodomain in which the unit-cell only repeat by translation, without break of any kind (**Figure I.4**). Ideally, a single-crystal is one monodomain but, in practice, this is never the case. A real monocrystal is made by a huge number of coherent domains slightly misaligned like fragments in a regular mosaic.<sup>97</sup> When the coherent domains

are seriously misaligned and rotated then the sample is a polycrystal, in other words a powder. Though it must be handled with care, the size and morphology of coherent domains can be extracted from the Bragg peaks morphologies both in single-crystal and in powders. In the former, the degree of mosaicity is estimated through a number denoted as the mosaicity of the crystal and in the latter the average size and morphology of the domains, then called crystallites, are estimated. Of crucial importance in other fields like metallurgy, the investigation of microstructural parameters in SCO materials is still in its infancy. In some specific cases, it has however been clearly demonstrated that the microstructure is strongly affected by the SCO; the coherent domain volume following the unit-cell deep modifications<sup>98</sup> and some tentative to correlate SCO features to microstructure have been attempted<sup>99</sup>. Overall, the determination of microstructural properties offers probably one of the best ways to investigate the mechanical fatigability of the SCO materials, *i.e.* the resilience of the SCO phenomenon to a large number of events. This approach has already shown that in some cases there is a significant mechanical fatigability both in powder<sup>98</sup> and in single-crystals<sup>100</sup>. However, this field is to be explored yet and a metallurgical approach of SCO material represents one of the present roads to follow. Of course, this approach challenges also the huge field of nanocrystals. Again, even though the literature of nanomaterials in SCO is very dense<sup>101</sup> and will not be discussed here since out of range, it is clear that structural information on nanocrystals are rare and constitute one of the challenges included in the microstructure global one.

The upper and ultimate scale is the *macroscopic* one, *i.e.* the *crystal scale*. It is less in the field of competence of the structural description but, anyway, it is clear that this scale is affected by the SCO through the modification of the colour, the sample volume, the facets and surface aspects and the mechanical parameters. All the lower scale transformation translates up to the volume expansion of the macroscopic sample, due to the elastic interactions between its constituent molecules<sup>14</sup>, which sometimes may lead to irreversible cracks of the samples. Conversely, the shape of the macroscopic sample may strongly affect the way the SCO starts and propagates along the sample as shown by microscopic early studies.<sup>102</sup> The links between the macroscopic scale, such as the morphology of the crystal, and the SCO features is currently under investigation.<sup>42,103-105</sup>

Above is a very brief account of the multiscale view of the SCO consequences and interplay with the structural features. In this work, since structure-properties relationships are targeted mainly at the scales going from the metal coordination sphere to the crystal packing, the microscopic and macroscopic scales will not be commented much anymore and the focus is

therefore made on the information coming from the X-ray diffraction investigation, *i.e.* the crystal structures and the panel of included informations.

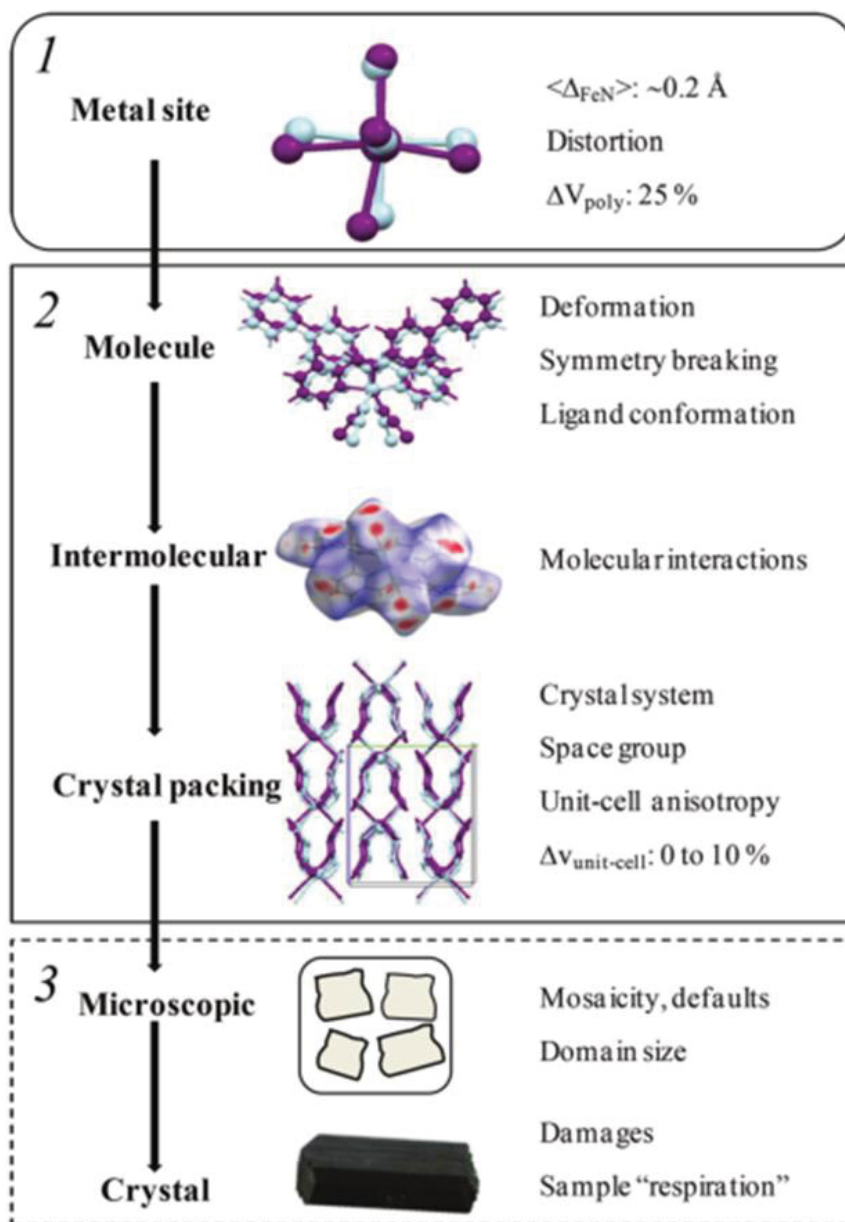


Figure I.4. Scheme of the multiscale view of the structural modifications from the polyhedron to crystal along the spin crossover process. Adapted from ref. 34.

## **I.2. The Light-Induced Excited Spin State Trapping effect**

### **I.2.1. The photoswitching process**

Among the various ways of using light to induce a spin crossover, the Light-Induced Excited Spin-State Trapping (LIESST) effect is probably the most studied. This effect is reversible, occurs in the solid state and allows the trapping of a metastable state using light irradiation within few femtoseconds. The lifetime of the photo-induced state is strongly temperature dependent and is easily observed at cryogenic temperatures (below 50 K). The current work of this thesis is focused on this lifetime and more details on this phenomenon are given below.

The LIESST effect has been first reported for the solid state in 1984 on the  $[\text{Fe}(\text{ptz})_6](\text{BF}_4)_2$  (ptz = 1-propyl-1H-tetrazole) SCO compound.<sup>106</sup> Later, Hauser *et al.* evidenced the reversibility of this phenomenon, called reverse-LIESST.<sup>107</sup> This photoswitching effect is based on the excitation by light of metallic *d-d* or metal-ligand charge transfer (MLCT) transitions. Hauser *et al.* deeply studied this effect using absorption spectroscopy as summarized in **Figures I.5a** and **I.5b** that report the evolution of the absorption spectra as a function of light irradiation at 20 K and the corresponding Jablonski-Perrin scheme.<sup>108</sup> At 20 K, the ground state is the LS state ( $^1A_1$ ). Irradiation into the  $^1T_1$ ,  $^1T_2$  transitions at 514 nm allows the population of excited states. From these excited states, two inter-system crossings involving the triplet  $^3T_1$  state, lead to the population of the metastable  $h\nu$ -HS\* state  $^5T_2$ . An irradiation at 820 nm, into the  $^5T_2 \rightarrow ^5E_1$  transition of the  $h\nu$ -HS\*, leads to the reverse-LIESST and allows to erase the  $h\nu$ -HS\* state and recover the LS state.

Many studies have been devoted to the understanding of the photoswitching process.<sup>109-114</sup> Tribollet *et al.* have shown, for the compound  $[\text{Fe}(\text{phen})_3](\text{BF}_4)_2$  (phen = 1,10-phenanthroline) in solution, that the LIESST process involves a cascade of excited states including the MLCT charge transfer bands.<sup>113</sup> Thus, the population of the  $^1\text{MLCT}$  state is followed by a first non-radiative relaxation  $^1\text{MLCT} \rightarrow ^3\text{MLCT}$  in less than 100 fs. The second non-radiative relaxation to state  $^5T_2$  involves two processes. The first one concerns the intersystem transition between the triplet state and the quintuplet state in about 200 fs. The second process is the de-excitation of the quintuplet state, *via* a cascade of vibrational levels, to the lowest level (vibrational cooling). This step is completed in less than 9 ps (**Figure I.5c**) and is effective thanks to the electron-phonon coupling.

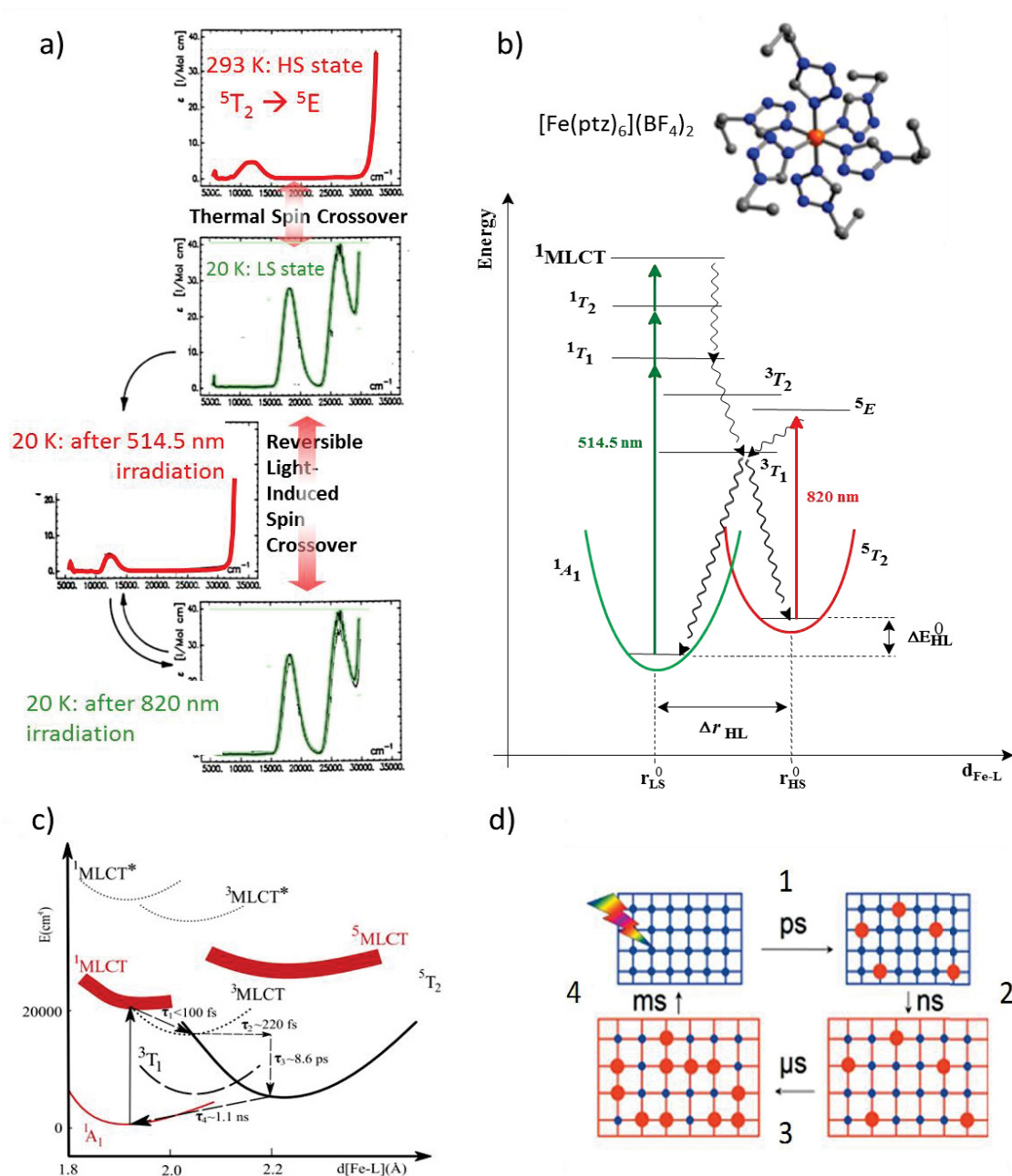


**Figure 1.5.** Single-crystal UV-Vis spectra (a) and vibrational potential wells for LIESST and reverse-LIESST processes in  $[\text{Fe}(\text{ptz})_6](\text{BF}_4)_2$  (b); Adapted from ref. 108. Energy levels and non-radiative relaxations path identified for the complex  $[\text{Fe}(\text{phen})_3]^{2+}$  (c); Adapted from ref. 113. Schematic drawing of the photoswitching dynamics in the solid state: HS molecules (red circles) generated within 1 ps by laser pulse in the cold lattice with mainly LS molecules (blue circles) (d); Adapted from ref. 115.

Recently, time-resolved photocrystallography studies have been carried out by the team of Collet *et al.*<sup>115-118</sup> These authors also confirmed the presence of several steps during photo-switching (Figure 1.5d). Based on the structural changes, they first observed the excitation of  $\text{Fe}^{2+}$  ions at constant unit-cell volume. This conversion is done in few ps (1). Then, an expansion

of the crystal lattice is observed, over a period of few ns (2). This expansion of the lattice, along with the heat generated by the light pulse, causes other molecules to switch into the  $h\nu$ -HS\* state. This increase in the HS fraction occurs in few  $\mu$ s (3). Therefore, the LIESST process involves an elastic step that drives the expansion or not of the lattice. This expansion depends on the elastic strength and also the size of the particles and can drive the occurrence of non-linear effects.<sup>117</sup> Therefore, the elastic interactions are of importance in the photoswitching process. Finally, the  $h\nu$ -HS\* state reached being metastable, the latter will relax towards the stable LS state in few ms (4). The population of state  $h\nu$ -HS\* therefore involves non-equilibrium processes and thermal effects, leading to non-linear effects. Indeed, ultrafast crystallography showed that a single photon can transform more than 7 molecules.<sup>117,119</sup> Let us mention that the reverse-LIESST process has also been elucidated using time-resolved spectroscopy.<sup>120</sup>

### **I.2.2. The lifetime of the photo-induced state**

Much work has been devoted to the study of relaxation processes from the metastable HS\* state to the LS state, independently on how this HS\* is reached (by light irradiation or thermal quenching). The mechanism explaining the relaxation process involves the non-adiabatic multiphonon theory between the two spin states.<sup>121</sup> Each spin state is represented by a harmonic potential well. The horizontal separation between these two wells,  $\Delta Q_{HL}$ , is linked to the variation of the metal-ligand bond length during the SCO. The vertical arrangement of the two wells corresponds to the zero point energy difference  $\Delta E_{HL}^0$  separating the lowest vibrational energy levels of the LS and HS\* states. The value of  $\Delta E_{HL}^0$  is assimilated to the enthalpy change,  $\Delta H$ , associated with the spin crossover at zero temperature (Figure I.6a). The HS\*  $\rightarrow$  LS relaxation is therefore a function of the overlap between the different wavefunctions of the vibrational levels of the HS\* and LS states. Two regions of relaxation were determined as a function of temperature and population of these vibrational levels<sup>121-122</sup> (Figure I.6):

- A region governed by the tunnelling effect, at low temperature, where the relaxation process is independent on temperature;
- A region where the relaxation is thermally activated, at higher temperature, where the relaxation process is temperature dependent. The relaxation constant then follows an Arrhenius type law.

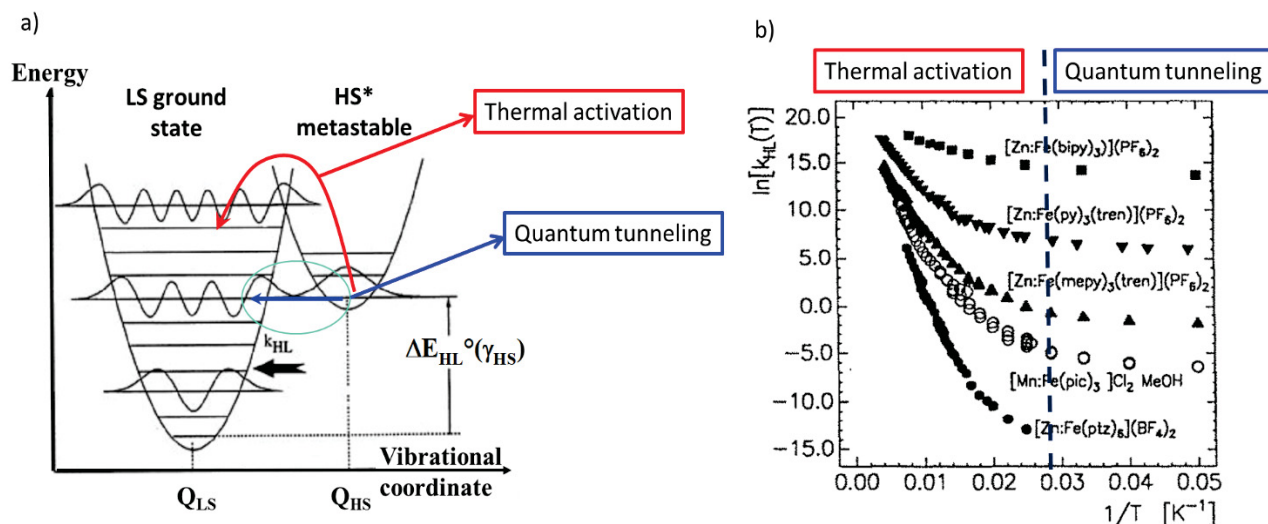


**Figure I.6.** Simplified two-dimensional potential-energy diagram of HS\* and LS states (a) and Arrhenius plots for various compounds of the isothermal  $h\nu$ -HS\*  $\rightarrow$  LS relaxations at different temperatures (b). Adapted from ref. 108.

In order to build the Arrhenius plot and to extract the activation energy parameter, the knowledge of isothermal HS\*  $\rightarrow$  LS relaxations at different temperatures is needed. A complete kinetic study therefore consists in recording the evolution of the HS fraction,  $\gamma_{HS}$ , as a function of time at different temperatures. The modeling of the experimental behaviors obtained then makes it possible to determine the relaxation rate constant,  $k_{HL}(T)$ , at each temperature. The thermal dependence of this rate constant is then plotted in a so-called Arrhenius graph,  $\ln k_{HL}$  vs  $1/T$ , in order to determine the activation energy,  $E_a$ , and the pre-exponential factor  $k_{HL}(T \rightarrow \infty)$ . The curves in **Figure I.6b** show the "tunnel region" where  $\ln k_{HL}$  is constant, while it increases in the thermally activated part.<sup>108,123</sup> The role of cooperativity on the lifetime of the photoinduced state has also been identified.

In noncooperative systems (solution, gradual SCO), the relaxation kinetics follow an exponential decay (**Figure I.7a**) that can be modelled by the **equation I.4** where  $k_0$  is the relaxation rate in the tunneling regime.<sup>124-125</sup> However, it often happens that the experimental behavior cannot be described by a simple exponential, but rather by a distribution of exponential laws. This is the case, for example, with diluted systems for which the presence of defects due to dilution causes a stretching of the relaxation curve. This deviation can also come from local inhomogeneities of the coordination sphere. To deal with this type of behavior in "stretched exponential", Hauser introduced a Gaussian distribution  $\sigma$  of the activation energy,  $E_a$ .<sup>124</sup>

$$\gamma_{HS} = \exp[-k_{HL}(T) \cdot t] \text{ with } k_{HL}(T) = k_0 + k_{HL}(T \rightarrow \infty) * \exp\left[\frac{-E_a}{k_B T}\right] \quad \text{Eq I.4}$$

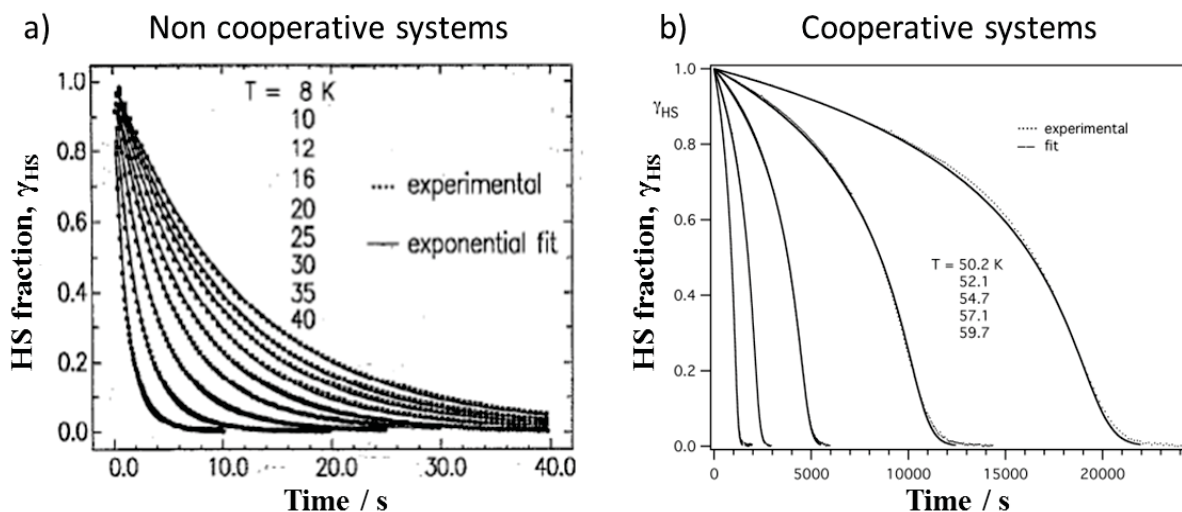


**Figure I.7.** Isothermal  $h\nu$ -HS\*  $\rightarrow$  LS relaxations at different temperatures in the non-cooperative compound  $[\text{Zn}_{1-x}\text{Fe}_x(\text{mepY})_3(\text{tren})](\text{PF}_6)_2$  (a) and in the cooperative  $[\text{Fe}(\text{ptz})_6](\text{BF}_4)_2$  (b); Adapted from ref. 124 and 126, respectively.

In the case of cooperative materials, we have mentioned that the presence of strong intermolecular interactions generates non-linear phenomena in particular responsible for the abrupt nature of the transitions. This "domino" effect due to cooperativity also impacts the  $h\nu$ -HS\*  $\rightarrow$  LS relaxations as illustrated in [Figure I.7b](#). At short timescale, relaxation is slowed down compared to a simple exponential while it is accelerated at longer times. The explanation put forward for this sigmoidal behavior of relaxation curves is that, initially, the energy cost to grow LS germs into a HS network is not favorable. As these germs appear, the "domino" effect sets in as a reflect of the internal pressure exerted by the LS sub-network on the HS network.<sup>126</sup> Relaxation is therefore self-accelerated. In general, the more the internal pressure increases, the more the  $h\nu$ -HS\*  $\rightarrow$  LS relaxation accelerates.

To account for this sigmoidal behavior, Hauser evidenced that the zero point energy difference  $\Delta E_{HL}^0$  varies depending on the HS fraction.<sup>126</sup> This behavior results in a change in the activation energy during relaxation. Cooperative interactions tend to stabilize the HS state. At the onset of relaxation, therefore, the activation energy is maximum. During relaxation, the LS state population destabilizes the HS state by internal pressure resulting in a decrease in activation energy. This can be described by [equations I.5-7](#) where  $\alpha(T)$  is the self-acceleration factor.

$$\frac{d\gamma_{HS}}{dt} = -k_{HL}(T, \gamma_{HS}) \cdot \gamma_{HS} \quad \text{Eq I.5}$$

$$k_{HL}(T, \gamma_{HS}) = k_{HL}(T) \cdot \exp[\alpha(T) \cdot (1 - \gamma_{HS})] \quad \text{Eq I.6}$$

$$\alpha(T) = \left[ \frac{E_a^*}{k_B T} \right] \text{ and } k_{HL}(T) = k_0 + k_{HL}(T \rightarrow \infty) \exp \left[ \frac{E_a}{k_B T} \right] \quad \text{Eq I.7}$$

Unlike a simple exponential behavior, the relaxation constant depends not only on the temperature, but also on the LS fraction present in the material at time  $t$ . The parameter characterizing the cooperativity in this type of equation is the additional activation energy  $E_a^*$  linked to the self-acceleration term  $\alpha(T)$  (Eq I.7). The activation energy  $E_a$  therefore decreases as the LS fraction increases. The dependence of  $E_a$  on  $\gamma_{LS}$  or  $\gamma_{HS}$  varies according to equations I.8 and I.9.<sup>124</sup>

$$E_a(\gamma_{LS}) = E_a(\gamma_{LS} = 0) - E_a^* \cdot \gamma_{LS} \quad \text{Eq I.8}$$

$$E_a(\gamma_{HS}) = E_a(\gamma_{HS} = 1) - E_a^* \cdot (1 - \gamma_{HS}) \quad \text{Eq I.9}$$

### I.2.3. $T(\text{LIESST})$ : a tool to compare compounds

Since the LIESST effect occurs in the solid state at the femtosecond timescale, in a reversible way, there is a strong need to increase the lifetime of the photoinduced state in order to achieve the photoswitching at room temperature. The first attempt at correlating the photoinduced properties of spin crossover compounds was proposed by Herber *et al.* from the monitoring of NCS<sup>-</sup> vibrations using IR spectroscopy.<sup>127</sup> However, it was actually Hauser *et al.* who proposed the first relationship.<sup>124</sup> In 1991, on the basis of a set of measurements of relaxation constants in the tunneling region,  $k_{HL}(T \rightarrow 0 \text{ K})$ , Hauser observed a direct correlation of relaxation at  $T \rightarrow 0 \text{ K}$  with the equilibrium temperature  $T_{1/2}$ . This relationship is known today as the "inverse energy gap law". Since  $\Delta E_{HL}^0$  is related to  $T_{1/2}$ , the higher  $T_{1/2}$ , the higher  $\Delta E_{HL}^0$ , the lower  $E_a$ , the faster the relaxation. Hauser *et al.* also evidenced that an increase in the bond-lengths variations upon SCO can increase the activation energy.<sup>108</sup> The main drawback of this study is that Hauser was only interested in diluted systems, without studying the effects of cooperativity. Moreover, this work was based on the determination of the relaxation constants of the tunnel region, without taking into account the thermally activated zone. This is why in 1998, Létard *et al.* introduced the  $T(\text{LIESST})$  experiment.<sup>128</sup>

This experiment measures the limit temperature for photo-inscription,  $T(\text{LIESST})$ , as an element of comparison. One of the advantages of this approach is that it takes into account all the relaxation processes (tunnel effect, thermally activated regime), whatever the kind of compound (cooperative or not). To this aim, a measurement of the variation in magnetic response is carried out using the SQUID magnetometry, in a relatively modest time scale (a few hours). The experiment consists in measuring the thermo-induced spin crossover down to 10 K. At this temperature, an appropriate irradiation is switched on until photo-saturation of the magnetic signal (meaning it does not evolve anymore upon further irradiation). The irradiation is then switched off and the temperature is slowly increased at 0.3 K/min. When reaching the thermally activated region of the relaxation, the photo-induced  $h\nu\text{-HS}^*$  state relaxes to the LS state and the magnetic  $h\nu\text{-HS}^*$  is erased and the LS state is recovered (Figure I.8). The  $T(\text{LIESST})$  temperature is defined as the inflexion point of this curve recorded in the dark and is determined by the minimum of the  $\partial(\chi_M T)/\partial T$  curve. Far to be an absolute meaningful value, the  $T(\text{LIESST})$  temperature is a simple and quick way to compare compounds in regards to their interest for light-induced SCO.

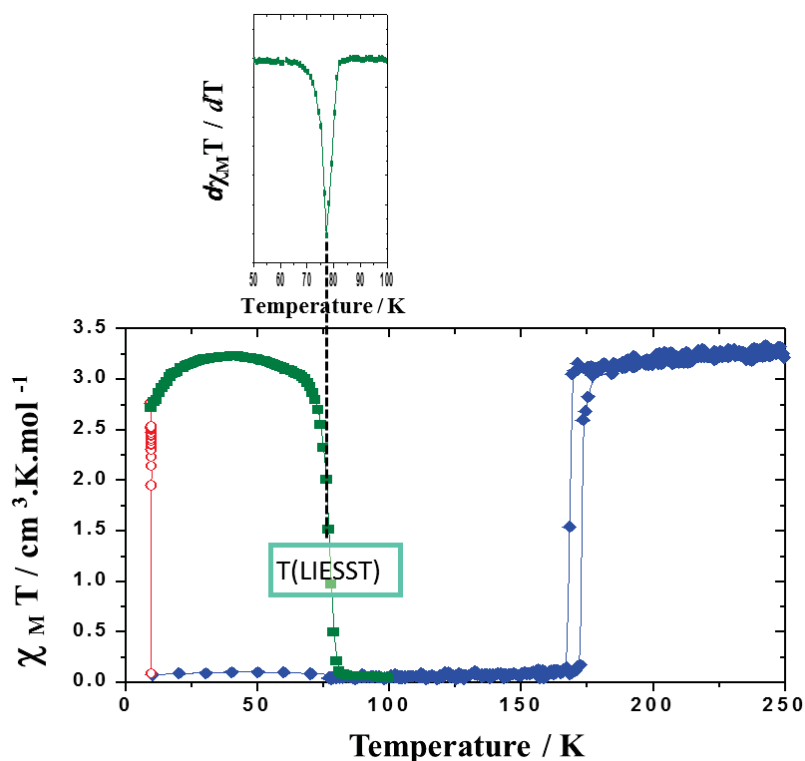
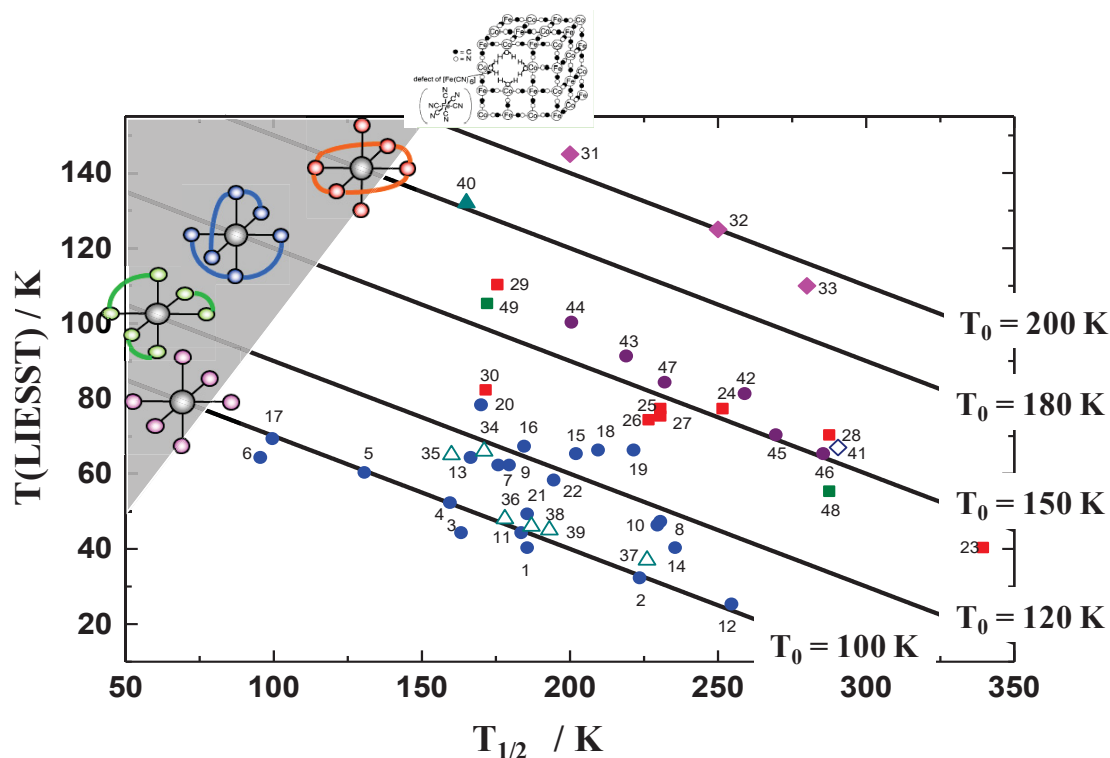


Figure I.8. The schematic picture of the relaxation temperature measurement  $T(\text{LIESST})$ . Insert up: the defined  $T(\text{LIESST})$  temperature as the minimum of the  $\partial(\chi_M T)/\partial T$  curve. Adapted from ref. 128.

As this limit temperature is dependent on relaxation, the measurement speed was set at 0.3 K/min and is kept constant for all compounds in order to obtain a rigorous comparison between the different materials studied.<sup>18,129-132</sup> Typically, a measurement in a SQUID magnetometer takes a dozen hours of recording to estimate the  $T(\text{LIESST})$ , the time resolution of the device being of the order of a minute.

By performing this measurement on a large number of samples, around twenty pairs [ $T_{1/2}$ ,  $T(\text{LIESST})$ ] were initially plotted on a  $T(\text{LIESST})$  as a function of  $T_{1/2}$  graph (Figure I.9). Despite the large scattering of points observed, the authors noted that the physical properties of the complexes followed a general trend. In fact, most of the complexes studied belonged to the  $[\text{FeL}_2(\text{NCE})_2]$  family<sup>67</sup> L being a bidentate aromatic unit and  $\text{NCE}^-$  a thiocyanato (E = S) or a selenocyanato (E = Se) as anionic co-ligand. By comparing the complexes having the same ligand L, but differentiated by the co-ligand  $\text{NCE}^-$  several couples (S and Se) then followed the same trend (samples 1-2, 7-8, 9-10, 11-12, 13 -14 in Figure I.9). Two virtual lines have thus been proposed with the general equation  $T(\text{LIESST}) = T_0 - 0.3 T_{1/2}$ .<sup>129</sup> Extrapolated values of  $T_0$  when  $T_{1/2} \rightarrow 0$  K were respectively 100 K and 120 K. This relationship was subsequently confirmed on a family of compounds  $[\text{Fe}(\text{3-bpp})_2]\text{X}_2 \cdot n\text{H}_2\text{O}$  (with 3-bpp = 2,6-bis (pyrazol-3-yl) pyridine, X =  $\text{NCS}^-$ ,  $\text{Br}^-$ ,  $\text{NCSe}^-$ ,  $\text{BF}_4^-$ ,  $\text{PF}_6^-$ ,  $\text{I}^-$ ) whose coordination sphere was unchanged. These ten compounds aligned on a new line defined by  $T_0 = 150$  K. Subsequently, together with [ $T_{1/2}$ ,  $T(\text{LIESST})$ ] couples of data, different lines were added to this database. More than 150 compounds have been investigated to provide a  $T(\text{LIESST})$  value. With regard to the linear relationship between  $T(\text{LIESST})$  and  $T_{1/2}$ , we immediately notice that the lower the equilibrium temperature  $T_{1/2}$ , the higher the value of  $T(\text{LIESST})$ . This observation of crucial importance for the design of functional light-induced SCO switches is in good agreement with the "inverse energy gap law" issued by Hauser<sup>126</sup>.



**Figure I.9.**  $T(\text{LIESST})$  vs  $T_{1/2}$  database in spin crossover complexes with the different types of ligands. The region in gray corresponds to a  $T(\text{LIESST})$  temperature inferior or at least equal to  $T_{1/2}$  that might lead to hidden phases; Adapted from ref. 129.

As we can see from such database, most of compounds exhibits  $T(\text{LIESST})$  lower than 100 K. Up to now, the “bpp family” based on the tridentate ligands 3-bpp = 2,6-bis(pyrazol-3-yl)pyridine and 1-bpp = 2,6-bis(pyrazol-1-yl)pyridine is providing  $T(\text{LIESST})$  frequently above 100 K.<sup>133-135</sup> This is illustrated by a recent report of a  $T(\text{LIESST})$  of 120 K in this family.<sup>136</sup> Another high  $T(\text{LIESST})$  value at 108 K related to the photo isomerization of  $\text{NCS}^-$  into  $\text{SCN}^-$  was reported in a polymorph of  $\text{trans}-[\text{Fe}(\text{abpt})_2(\text{NCS})_2]$  (abpt = 4-amino-3,5-bis(pyridin-2-yl)-1,2,4-triazole).<sup>137</sup> To the best of our knowledge, the highest  $T(\text{LIESST})$  known so far is 135 K in the molecular complex  $[\text{Fe}(\text{L})(\text{CN})_2] \cdot \text{H}_2\text{O}$  (L = 2,13-dimethyl-6,9-dioxa-3,12,18-triazabicyclo[12.3.1]octadeca-1(18),2,12,14,16-pentaene).<sup>138</sup> This compound presents a modification of the metal coordination number upon spin crossover, going from 7 in the HS state to 6 in the LS state, with the coordination/decoordination of a Fe-O bond and a change of the ligand conformation.<sup>83</sup> Let us notice that the relaxation temperature in systems involving concomitantly spin transition and electron transfer can be much higher than in purely SCO systems. For example, Li *et al.* evidenced a relaxation temperature of 250 K in the  $\{\text{Fe}(\mu\text{-CN})_3\text{Co}\}_4$  octanuclear complex driven by thermally and photoinduced intramolecular electron transfer.<sup>139</sup>

It is of huge interest to evidenced which factors are influencing the  $T(\text{LIESST})$  in order to find levers to increase it. Based on detailed crystallographic studies and especially photocrystallography, meaningful clues were proposed, as discussed in the following section.

### **I.2.4. How to increase $T(\text{LIESST})$ ?**

There is a first obvious tool to play on  $T(\text{LIESST})$  that is  $T_{1/2}$ . According to the “inverse energy gap law” already mentioned, increasing  $T_{1/2}$  decreases  $T(\text{LIESST})$ . This consists in moving the vibrational potential wells vertically in [Figure I.6](#). Playing on the counter-ion or the number of solvated molecules for example, the switching temperature can be tuned, consequently affecting  $T(\text{LIESST})$ . This allows to move along one given  $T_0$  line, for a given molecule. However, this does not allow to move from one  $T_0$  line to another. To go from one line to the other at constant  $T_{1/2}$ , so to increase  $T_0$ , the denticity of the ligand seems to be a crucial parameter. This vertical displacement in the diagram seems to be linked to the rigidity of the ligands and to the deformation of the coordination sphere at the transition. Thus, compounds based on monodentate ligands are lying on  $T_0 = 100$  K while many of the bidentate ligands based complexes sit on  $T_0 = 120$  K, and tridentate ligands based complexes sit on  $T_0 = 150$  K; the highest value being attributed to macrocyclic complexes ( $T_0 = 180$  K).

Photocrystallography allowed to go beyond this vision based on the denticity of the ligands. The first crystal structure of a sample in the  $h\nu\text{-HS}^*$  state was obtained on the prototype compound  $[\text{Fe}(\text{phen})_2(\text{NCS})_2]$  in 2001<sup>140</sup>, followed by many others. One of the first hypothesis was that  $T(\text{LIESST})$  was strongly correlated to the bond length change associated to SCO. Indeed, increasing this bond length change consists in separating the vibrational potential wells horizontally (in [Figure I.6](#)). However, this one-parameter description suffers from experimental evidences that other parameters than the bond length variation had to be taken into account. Indeed, studies using phosphorus ligand-based complexes that present larger metal-ligand bond-length variations<sup>141-142</sup>, have shown some photoswitching effects without any clear improvement compared to nitrogen-based ligands.<sup>143</sup>

The most promising parameter that would favor long-lived metastable states is suspected to be the distortion of the coordination sphere. This follows from the non-isotropic bond-length variation upon the spin crossover (*cf.* multiscale view of SCO).<sup>34,35</sup> From structure-properties relationships, it appeared that  $T(\text{LIESST})$  increases with the distortion of the coordination sphere.<sup>73</sup> A screening of some  $\text{Fe}^{2+}$  SCO complexes clearly demonstrated that, provided similar

bond lengths and crystal packings, the trigonal distortion of the coordination polyhedrons linearly varies with  $T(\text{LIESST})$  (Figure I.10). For this family of compounds, this structure-properties relationships incidentally anticipated that the highest  $T(\text{LIESST})$  should be around 125 K with  $\Delta\theta = 145^\circ$ .<sup>73</sup> This empirical relationship has been confirmed so far, and the highest  $T(\text{LIESST})$  for an  $\text{Fe}^{2+}$  molecular complex corresponds indeed to the largest observed polyhedron trigonal distortion  $\Delta\theta$ .<sup>73</sup> Moreover, Hayami *et al.* suggested large molecular distortions around metal ions with the bending mode play an important role in increasing energy barrier.<sup>144</sup> They also suggested both stretching and bending modes must be considered when designing molecular compounds with high  $T(\text{LIESST})$ . Interestingly, theoretical calculation on the trigonal distortion latter confirmed the crystallography observation and notably the crucial role of  $\theta$  on  $T(\text{LIESST})$ .<sup>74,145</sup> The above results give a clear guideline for the design of SCO materials and reciprocally it validates the relevance of the  $T(\text{LIESST})$  measurement.

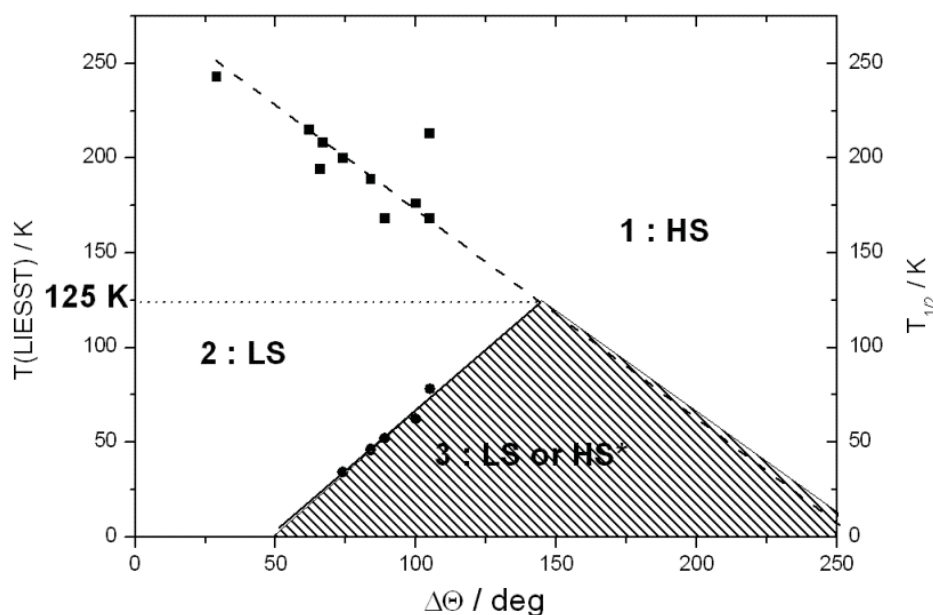


**Figure I.10.** The modification of the trigonal distortion from HS to LS, denoted  $\Delta\theta$  for  $\text{Fe}^{2+}$  complexes belonging to the same family  $[\text{Fe}(\text{L})_2(\text{NCE})_2]$  with L a bidentate ligand and X = S or Se, is compared to their  $T(\text{LIESST})$  (circle) and  $T_{1/2}$  (square) values. The zone where a LIESST effect may be observed is thus delimited (zone 3). This correlation is made feasible since all the compounds have similar metal ligand bond lengths and relatively close crystal packings. Adapted from ref 73.

One of the most speaking example that illustrates the role of the coordination sphere distortion on the  $T(\text{LIESST})$  is the study of the two polymorphs of the mononuclear  $[\text{Fe}(\text{PM-BiA})_2(\text{NCS})_2]$  complex (PM-BiA = N-2'-pyridylmethylene)-4-(aminobiphenyl)).<sup>74,94,146</sup> Polymorph **I-S-BiA** (S referring to the NCS co-ligand) exhibits a  $T(\text{LIESST})$  at 78 K, the highest for bidentate ligand based compounds, lying on the  $T_0 = 120$  K line. Polymorph **II-S-BiA** presents a  $T(\text{LIESST})$  of 34 K, lying on the  $T_0 = 100$  K line. Polymorph **I-S-BiA** crystallizes in orthorhombic system with space group  $Pccn$  while polymorph **II-S-BiA** crystallizes in monoclinic system with space group  $P2_1/c$ . Polymorph **II-S-BiA** shows a gradual SCO with  $T_{1/2} = 205$  K, while polymorph **I-S-BiA** shows an abrupt and hysteretic SCO with  $T_{1/2}\uparrow = 173$  K and  $T_{1/2}\downarrow = 168$  K (**Figure I.11**). The multiscale description of the thermal SCO of these two polymorphs suggests that the different behaviors are related to differences in intermolecular interactions, deformation of molecules, intermolecular interactions, crystal packings and distortion of coordination spheres.

Photocrystallographic studies have been performed on these two polymorphs. As seen in **Figure I.11c**, if only the average metal-ligand bond length  $\langle\text{Fe-N}\rangle$  is considered, the variation of  $\langle\text{Fe-N}\rangle$  in polymorph **I-S-BiA** and **II-S-BiA** is almost similar. In the isotropic elongation view, the different values of  $T(\text{LIESST})$  can not be explained. If the anisotropic elongation ( $\zeta$ ) or the angular distortion ( $\Sigma$ ) is considered, one can clearly see the huge differences between the polymorphs. For example, the variation of  $\zeta$  from LS to  $h\nu\text{-HS}^*$  at 20 K in polymorph **I-S-BiA** and **II-S-BiA** are 0.5 Å and 0.3 Å, respectively. For a given  $\Delta r_{HL}$ , the increase of  $\Delta\zeta$  results in an increase of the energy barrier. As a consequence, the photoinduced  $h\nu\text{-HS}^*$  can be better stabilized at high temperature in polymorph **I-S-BiA** than in polymorph **II-S-BiA**, since the thermal energy needed to overcome the energy barrier during the relaxation from  $h\nu\text{-HS}^*$  to LS is higher.<sup>74</sup>

The role of the coordination sphere distortion in the lifetime of the  $h\nu\text{-HS}^*$  implies that the single configurational coordinate with two simple two-dimensional potential wells (**Figures I.5 and I.6**) is no more valid. Therefore, a three-dimensional view must be used, going from isotropic breathing of the coordination sphere towards anisotropic breathing (**Figure I.12**). At this stage, the most relevant distortion parameter among the above parameters has not been clarified, if any.

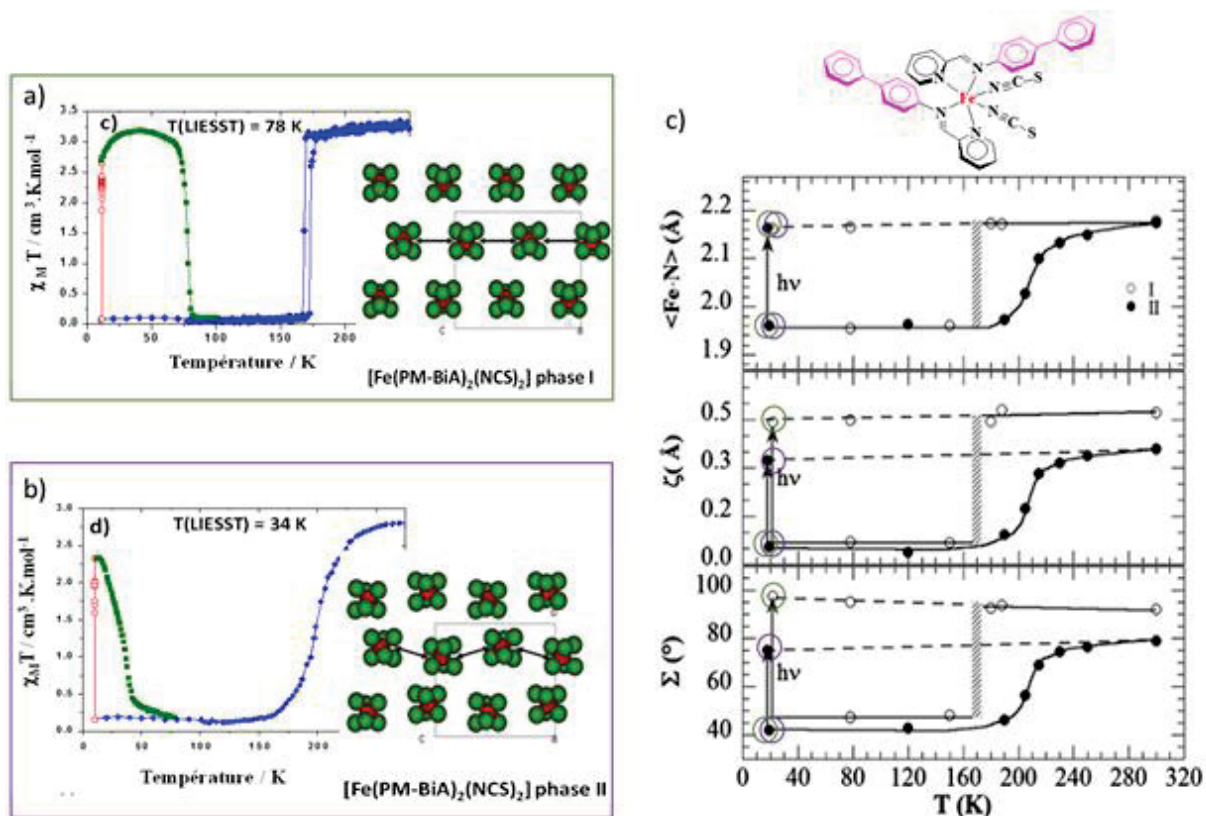


Figure I.11. The magnetic and photomagnetic curves of polymorphs I-S-BiA (a) and II-S-BiA (b) and selected distortion parameters of the coordination sphere of the two polymorphs (c). Insert (a) and (b): the packing of polyhedra in the two polymorphs. Insert (c) up: the molecular structure of [Fe(PM-BiA)<sub>2</sub>(NCS)<sub>2</sub>]. Adapted from ref 74 and 94.

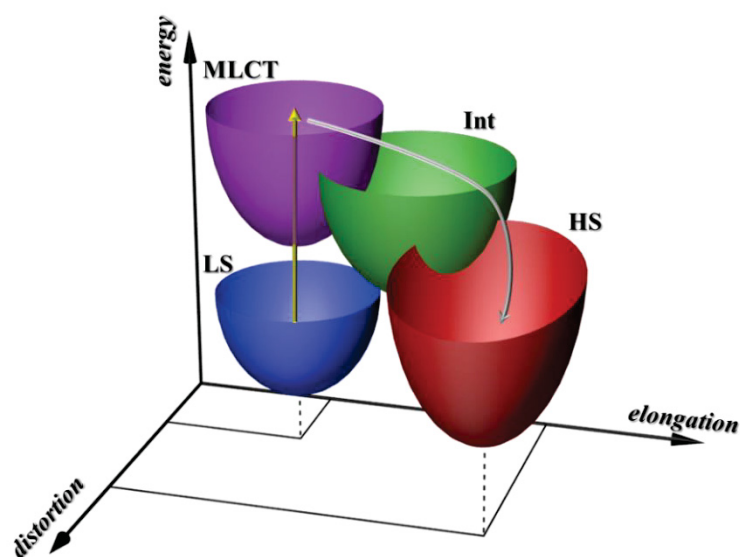
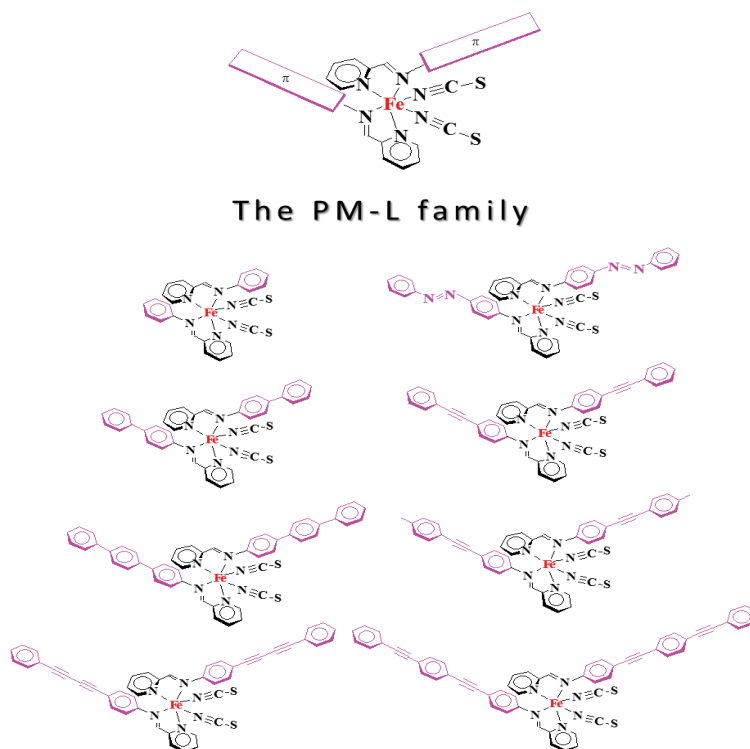


Figure I.12. Sketch of the LS (blue) and HS (red) potential wells in the anisotropic breathing model, *i.e.* the elongation and distortion. Adapted from ref 111 and 18.

### I.3. Motivation of the PhD work

From the quick overview reported above on the parameters influencing the lifetime of the photoinduced state, it appears clearly that one has to work on the distortion of the coordination sphere. To this aim, a path that comes directly to mind is to use synthetic chemistry in order to introduce some steric strains close to the coordination sphere. In addition, as related above, polymorphism has clearly demonstrated that the crystal packing can influence the coordination sphere distortion and cooperative interactions can stabilize the  $h\nu$ -HS\*. Therefore, our first chosen strategy was to synthesize new ligands to promote either steric strain close to the coordination sphere. And the other strategy was to regulate the intermolecular interactions by using polymorphs and solvatomorphs. To do so, we focused our attention on the  $[\text{Fe}(\text{PM-L})_2(\text{NCE})_2]$  family that has been synthesized first more than 20 years ago in the group.<sup>69</sup> (Figure I.13). Over 16 compounds are reported in literature (Table I.1) with  $\text{NCS}^-$  or  $\text{NCSe}^-$  counter-anions, leading to various SCO features and  $T(\text{LIESST})$  values.



**Figure I.13.** Examples of compounds belonging to  $[\text{Fe}(\text{PM-L})_2(\text{NCE})_2]$  family. PM = N-(2' - Pyridylmethylene), AzA = 4-(Phenylazo)aniline, BiA = 4-(Aminobiphenyl)aniline, DiyA 4-(Phenylbutadiyne)aniline, PEA = 4-(naphthalene-1-ethynyl)aniline, FIA = 4-(2-amino)aniline, FIA = 4-(2-amino)aniline, NEA = 4-(Aminoterphenyl)aniline and TheA = 4-(Thienylethynyl)aniline. Adapted from ref 69.

**Table I.1.** The summary of the SCO characteristics of the reported compounds in the family of  $[\text{Fe}(\text{PM-L})_2(\text{NCE})_2]$  (E = S and Se) when this work starts.

Compound	Kind of SCO	$T_{1/2\downarrow}$ / K	$T_{1/2\uparrow}$ / K	$\Delta T$ / K	$T(\text{LIESST})$ / K	Ref.
$[\text{Fe}(\text{PM-HA})_2(\text{NCS})_2]$	No SCO, HS					68
<i>I</i> - $[\text{Fe}(\text{PM-BiA})_2(\text{NCS})_2]$	Hysteretic	168	173	5	78	69,94
<i>II</i> - $[\text{Fe}(\text{PM-BiA})_2(\text{NCS})_2]$	Gradual	190			34	69,94
$[\text{Fe}(\text{PM-NEA})_2(\text{NCS})_2]$	Gradual	210			58	149
$[\text{Fe}(\text{PM-TeA})_2(\text{NCS})_2] \cdot 0.5\text{CH}_3\text{OH}$	Incomplete	125				69
<i>I</i> - $[\text{Fe}(\text{PM-TheA})_2(\text{NCS})_2]$	Gradual	208			no	69
$[\text{Fe}(\text{PM-PEA})_2(\text{NCS})_2]$	Hysteresis *	188	228	40	64	150
<i>I</i> - $[\text{Fe}(\text{PM-PEA})_2(\text{NCSe})_2]$	Hysteresis *	266	307	41	no	90
<i>II</i> - $[\text{Fe}(\text{PM-PEA})_2(\text{NCSe})_2]$	Gradual	245			no	149
$[\text{Fe}(\text{PM-DiyA})_2(\text{NCS})_2]$	No SCO, HS					68
$[\text{Fe}(\text{PM-AzA})_2(\text{NCS})_2]$	Gradual	189			46	48,69
$[\text{Fe}(\text{PM-FIA})_2(\text{NCS})_2]$	Gradual	165			64	150
$[\text{Fe}(\text{PM-FIA})_2(\text{NCSe})_2]$	Gradual	236			35	150
$[\text{Fe}(\text{L}_\text{H}^{\text{iPr}})_2(\text{NCS})_2]$	Abrupt	154	167	13	Not reported	151
$[\text{Fe}(\text{L}_\text{H}^{\text{C6}})_2(\text{NCS})_2]$	Gradual	117			Not reported	152
$[\text{Fe}(\text{L}_\text{H}^{\text{C16}})_2(\text{NCS})_2]$	Gradual	176			Not reported	152

\* SCO hysteresis associated with a structural phase transition.

This family of ligands was initially designed to promote  $\pi$ - $\pi$  interactions between the aromatic plateaus. However, additionally to these desired interaction, strong S---H and H---H interactions are also present, building a dense network of intermolecular interactions and leading to a wide range of cooperativity and polymorphism (Figure I.14).<sup>34</sup> Polymorphism is the possibility for the same chemical entity to crystallise by adopting different crystal structures. Polymorphs have strictly the same chemical formula but are distinguished by their crystal packing and therefore, potentially, by their physical properties. From the chemical point, polymorphs may be prepared by changing the reactions conditions, including the temperature, solvent, and pressure. The two polymorphs of  $[\text{Fe}(\text{PM-BiA})_2(\text{NCS})_2]$  discussed above (Figure I.11) also belong to this family. More recently it has been shown that polymorphism can also be found in  $[\text{Fe}(\text{PM-PeA})_2(\text{NCSe})_2]$ , where polymorph **I-Se-PEA** (Se referring to the NCSe co-ligand) shows abrupt SCO with a large hysteresis associated with a structural phase transition<sup>90</sup>, while polymorph **II-Se-PEA** displays a gradual SCO<sup>147</sup>. In addition to polymorphism, structural phase transitions with change of crystal symmetry can also occur in this family. Notably, the latter occurs in a non classical way in  $[\text{Fe}(\text{PM-PEA})_2(\text{NCS})_2]$ <sup>148</sup> and in polymorph **I-Se-PEA** of  $[\text{Fe}(\text{PM-PeA})_2(\text{NCSe})_2]$ <sup>90</sup> since there is an increase of symmetry when lowering the

temperature from  $P2_1/c$  in the HS state to  $Pccn$  in the LS state. Not fully explained so far, this unusual feature in the whole field of molecular crystals illustrates the diversity and the complexity of behaviors that can be encountered in this SCO family.

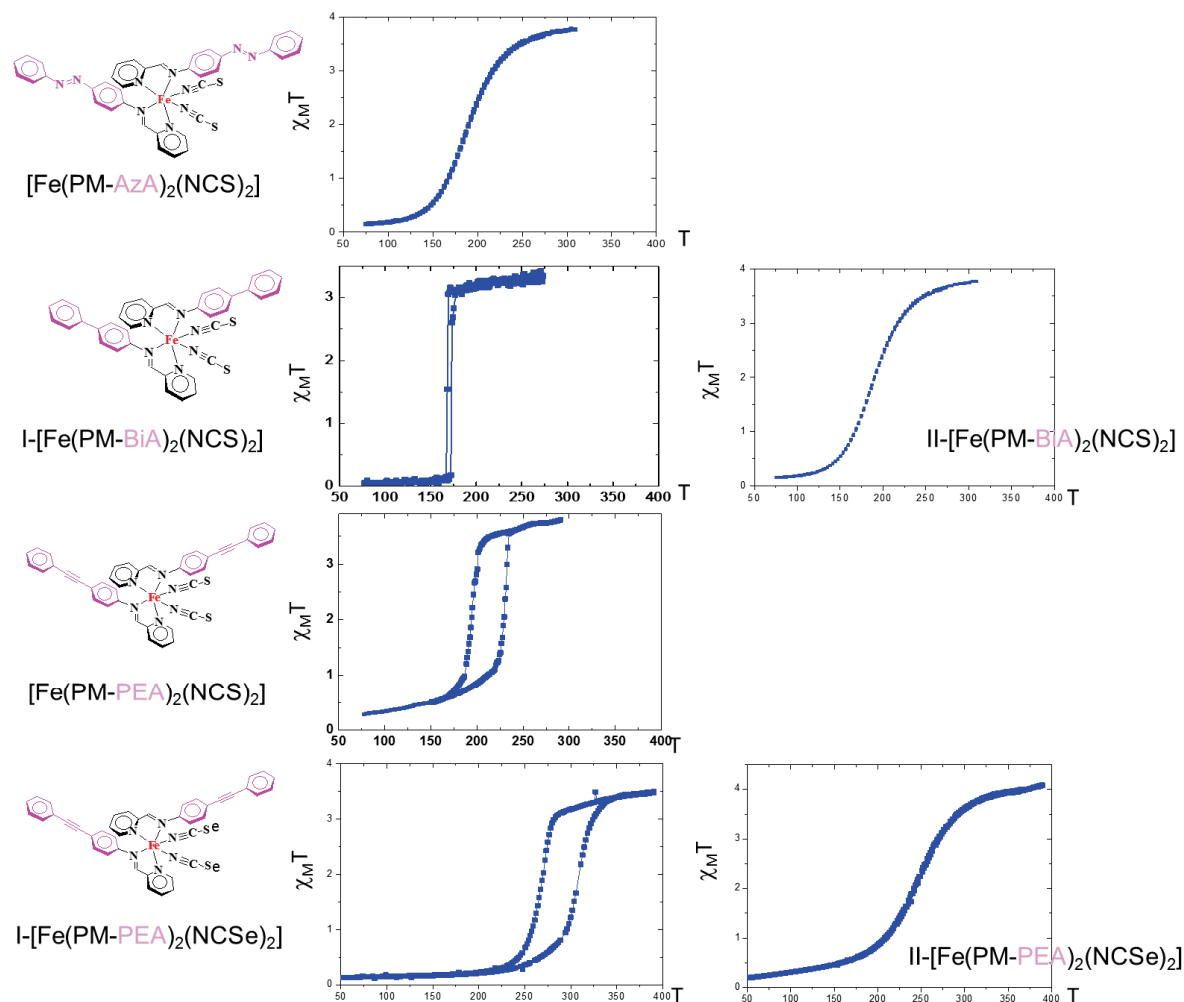


Figure I.14. Molecular structure and magnetic results of the selected compounds belonging to  $[\text{Fe}(\text{PM-L})_2(\text{NCE})_2]$  family. Adapted from ref 69, 90, 149-150.

The present work takes part to a larger project aiming at the design of SCO compounds with high  $T(\text{LIESST})$  values. *Our main goal is to focus on a deep and comprehensive understanding of the relevant parameter(s) that can allow to reach high  $T(\text{LIESST})$ . The general idea is to synthesize and carefully study new compounds presenting high distortion of the coordination sphere.* Our playground is the above  $[\text{Fe}(\text{PM-L})_2(\text{NCE})_2]$  family since taking advantage of the well documented existing structure-properties relationships and the diversity of behaviors that it exhibits we will try to design new and optimized compounds.

This family has been shown to be extremely rich in terms of behaviors and in terms of possible functionalization (Figures I.13 and I.14). It will be used as a platform to promote high distortion of the coordination sphere through the substitution in *ortho* position of the imine part (Figure I.15). Since the steric strain can prevent the coordination to occur, halogen substituent of various atomic radius will be studied. Finally, different positions of the substitution will be explored to relax progressively the steric strain. We expect that the shorter distance of Fe---X will favor a stronger distortion of coordination sphere.

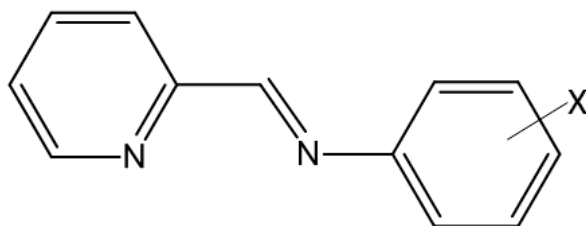


Figure I.15. Schematic picture of the designed PM-*z*XA ( $z = o, m, p$ ;  $X = F, Cl, Br, I$ ) ligands.

To follow this strategy we have decided to work with halogen functionalization, especially from the small atomic radius of the Fluor atom to the large one of Bromine atom. We have thus played on three different levers. First, by moving the halogen group from *para*, to *meta* and *ortho* positions, the steric strain should induce a significant increase of the distortion of the coordination sphere, which can favor a long lifetime of the photoinduced state. Second, the delicate influence of intermolecular interactions on the distortion of polyhedron can be explored when polymorphism appears in one of these complexes. In addition, the introduction of different halogen groups is expected to strongly affect the intermolecular interactions due to the difference in electronegativity.

Halogen atoms have already been introduced in several families of SCO complexes. For example, Luo *et al.* found that the spin transition temperatures  $T_{1/2}$  and the width of thermal hysteresis loops show a positive correlation with the electronegativity of the halogen atoms in complexes  $[\text{Fe}(4\text{-X-L})_3](\text{BF}_4)_2$  ( $\text{L} = \text{N-benzyl-4-amino-1, 2, 4-triazole}$  and  $\text{X} = \text{H, F, Cl, Br}$  and  $\text{I}$ ).<sup>153</sup> Damrauer *et al.* reported the stabilization of the HS state of terpyridine based complexes introducing steric strain with halogens. It has been shown that the position of the halogen can influence the lifetime of photo-excited states in MLCT based compounds of  $[\text{Fe}(\text{dftpy})_2]^{2+}$ ,  $[\text{Fe}(\text{dctpy})_2]^{2+}$  and  $[\text{Fe}(\text{dbtpy})_2]^{2+}$ , where dbtpy, dctpy and dftpy are the di-bromo, di-chloro and di-fluoro substituted tripyridine ligands in *ortho* positions.<sup>154-155</sup> Halogen-Halogen

interactions might also promote cooperative transition, like in the  $[\text{Fe}(\text{qsal})_2][(\text{C}_6\text{F}_3\text{I}_3)\text{X}]$  compounds.<sup>156-157</sup>

In this manuscript, we will describe the synthesis, crystallographic and (photo)magnetic studies of new compounds of the studied family based on *ortho*, *meta* and *para* fluoro and bromo substituted PM-zXA ligands.

In **Part II**, synthesis, structure, magnetic and photomagnetic properties of new complexes with fluorine substitution at *ortho*, *meta*, and *para* position will be described. The structural properties from the scale of the coordination sphere to crystalline stacking will be displayed.

In **Part III**, new compounds with bromo-substituted ligands showing polymorphism will be described and compared. Especially, high  $T(\text{LIESST})$  and unique unit-cell volume change in one polymorph will be shown and the photo-crystallography of this compound will be also explored via PXRD at low temperature, giving rise to the structure-properties relationship. The structural analysis in a multiscale approach will be discussed and compared in all polymorphs to draw structure-properties relationships.

Finally, the deep examination of the relevant parameters to high  $T(\text{LIESST})$  on all compounds with bidentate ligands will be discussed in **Part IV**, giving rise to new perspectives of the relaxation temperature  $T(\text{LIESST})$ .

## Bibliography

- [1] L Cambi, L Szegö, Ber Deutsch Chem Ges., 1931, **64**, 167.
- [2] L Cambi, L Malatesta, Ber Deutsch Chem Ges., 1937, **70**, 2067.
- [3] P. Gütllich, A. B. Gaspar, Y. Garcia, 2013, **9**, 342.
- [4] *Spin-Crossover Materials Properties and Applications*, ed. M. A. Halcrow, John Wiley & Sons, 2013.
- [5] *Spin Crossover in Transition Metal Compounds I–III*, ed. P. Gütllich, H. A. Goodwin, *Top. Curr. Chem.*, 2004, vol. 233–235.
- [6] K. S. Kumar, M. Ruben, *Coord. Chem. Rev.*, 2017, **346**, 176.
- [7] K. Ridier, A. C. Bas, Y. Zhang, L. Routaboul, L. Salmon, G. Molnár, C. Bergaud, A. Bousseksou, *Nat. Commun.*, 2020, **11**, 3611.
- [8] T. Mallah, M. Cavallini, *C. R. Chim.*, 2018, **21**, 1270.
- [9] A. Bousseksou, G. Molnár, L. Salmon, W. Nicolazzi, *Chem Soc Rev.*, 2011, **40**, 3313-35.
- [10] J. Linares, E. Coddjovi, Y. Garcia, *Sensors*, 2012, **12**, 4479.
- [11] G. Aromí, L. A. Barrios, O. Roubeau, P. Gamez, *Coord. Chem. Rev.*, 2011, **255**, 485-546.
- [12] S. Brooker, *Chem. Soc. Rev.*, 2015, **44**, 2880.
- [13] A. Bousseksou, F. Varret, M. Goiran, K. Boukheddaden, J. P. Tuchagues, *In: Spin Crossover in Transition Metal Compounds III. Top. Curr. Chem.*, Springer, Berlin, Heidelberg. 2004, **235**. 65.
- [14] E. Collet, P. Guionneau, *C. R. Chim.*, 2018, **21**, 1133.
- [15] P. Gütllich, V. Ksenofontov, A. B. Gaspar, *Coord. Chem. Rev.*, 2005, **249**, 1811.
- [16] V. Ksenofontov, A. B. Gaspar, J. A. Real, P. Gütllich, *J. Phys. Chem. B*, 2001, **105**, 12266.
- [17] A. B. Gaspar, G. Molnar, A. Rotáru, H. J. Shepherd, *C. R. Chim.*, 2018, **21**, 1095.
- [18] G. Chastanet, M. Lorenc, R. Bertoni, C. Desplanches, *C. R. Chim.*, 2018, **21**, 1075.
- [19] M. L. Boillot, J. Zarembowitch, A. Sour, *Top. Curr. Chem.*, 2004, **234**, 261.
- [20] B. Rosner, M. Milek, A. Witt, B. Gobaut, P. Torelli, R. H. Fink, M. M. Khusniyarov, *Angew. Chem. Int. Ed.*, 2015, **54**, 12976.
- [21] S. Venkataramani, U. Jana, M. Dommaschk, F. D. Sonnichsen, F. Tuzek, R. Herges, *Science*, 2011, **331**, 445.
- [22] S. Decurtins, P. Gütllich, C. P. Kohler, H. Spiering, A. Hauser, *Chem. Phys. Lett.*, 1984, **105**, 1.
- [23] E. Freysz, S. Montant, S. Létard, J. L. Létard, *Chem. Phys. Lett.*, 2004, **394**, 318.

- [24] S. Bonhommeau, G. Molnar, A. Galet, A. Zwick, J. A. Real, J. J. McGarvey, A. Bousseksou, *Angew. Chem. Int. Ed.*, 2005, **44**, 4069-4073.
- [25] M. Palluel, N. M. Tran, N. Daro, S. Buffière, S. Mornet, É. Freysz, G. Chastanet, *Adv. Fun. Mater.*, 2020, **30**, 2000447.
- [26] M. M. Khusniyarov, *Chem. Eur. J.*, 2016 **22**, 15178.
- [27] *Localized and itinerant molecular magnetism. From molecular assemblies to the devices*, F. Palacio, Kluwer Academic, NATO ASI Series C, 1996, 321:5.
- [28] *Molecular magnetism*, O Kahn, 1993, VCH, New York Heidelberg.
- [29] Y. Garcia., G. Bravic, C. Gieck, D. Chasseau, W. Tremel, P. Gütllich, *Inorg. Chem.*, 2005, **44**, 9723.
- [30] P. Gütllich, R. Link, A. X. Trautwein, *Mössbauer spectroscopy and transition metal chemistry. Inorganic Chemistry Concepts Series*, 1978, Springer, Berlin Heidelberg New York.
- [31] D. C. Figg, R. H. Herber, *Inorg Chem.*, 1990, **29**, 2170.
- [32] J. A. Wolny, V. Schünemann, Z. Németh, G. Vanko, *C. R. Chim.*, 2018, **21**, 1152.
- [33] *Elements of Modern X-ray Physics*, J. Als-Nielsen, D. McMorrow, Wiley, New York, 2001
- [34] P. Guionneau. *Dalton. Trans.*, 2014, **14**, 382.
- [35] P. Guionneau, M. Marchivie, G. Chastanet, *Chem. Eur. J.*, 10.1002/chem.202002699.
- [36] F. Varret, K. Boukheddaden, E. Codjovi, C. Enachescu, J. Linares, *In: Spin Crossover in Transition Metal Compounds II. Top. Curr. Chem. Springer, Berlin, Heidelberg*, 2004, 199.
- [37] C. Chong, A. Slimani, F. Varret, K. Boukheddaden, E. Collet, J. C. Ameline, R. Bronisz, A. Hauser, *Chem. Phys. Lett.*, 2011, **504**, 29.
- [38] J. J. Lee, H.S. Sheu, C. R. Lee, J. M. Chen, J. F. Lee, C. C. Wang, C. H. Huang, Y. Wang, *J. Am. Chem. Soc.*, 2000, **122**, 5742.
- [39] R. Boca, M. Vrbova, R. Werner, W. Haase, *Chem. Phys. Lett.*, 2000, **328**, 188.
- [40]. E. König, *In: Complex Chemistry. Structure and Bonding*, Springer, Berlin, Heidelberg, 1991, 51.
- [41] W. Nicolazzi, A. Bousseksou, *C. R. Chim.*, 2018, **21**, 1170.
- [42] P. Guionneau, E. Collet, *in: Spin-Crossover Materials*, John Wiley & Sons Ltd, 2013, 507.
- [43] A. E. Goeta, J. A. K. Howard, A. K. Hughes, D. O'Hare, R. C. B. Copley, *J. Mater. Chem.*, 2007, **17**, 485.
- [44] H Spiering, *In: Spin Crossover in Transition Metal Compounds III. Top. Curr. Chem.*, Springer, Berlin, Heidelberg, 2004, 171-195.
- [45] K. S. Murray, C.J. Kepert, *Top. Curr. Chem.*, 2004, **233**, Springer, Berlin, Heidelberg.

- [46] P. Gütllich, Y. Garcia, H. A. Goodwin, *Chem Soc Rev.*, 2000, **29**, 419.
- [47] H. J. Shepherd, P. Rosa, I. A. Fallisc, P. Guionneau, J. A. K. Howard, A. E. Goeta, *J Phys Chem Solids*, 2012, **73**, 193.
- [48] S. Lakhouloufi, M. H. Lemee-Cailleau, G. Chastanet, P. Rosa, N. Daro, P. Guionneau, *Phys. Chem. Chem. Phys.*, 2016, **18**, 28307.
- [49] J. F. Létard, S. Asthana, H. J. Shepherd, P. Guionneau, A. E. Goeta, N. Suemura, R. Ishikawa, S. Kaizaki, *Chem. Eur. J.*, 2012, **18**, 5924.
- [50] O. Kahn, J. P. Launay, *Chemtronics*, 1988, **3**, 140.
- [51] O. Kahn, C. J. Martinez, *Science*, 1998, **279**, 44.
- [52] D. Chernyshov, M Hostettler, K. W. Törnroos, H. B. Bürgi, *Angew Chem Int Ed.*, 2003, **18**, 3825.
- [53] N. Bréfuel, H. Watanabe, L. Toupet, J. Come, N. Matsumoto, E. Collet, K. Tanaka, J. P. Tuchagues, *Angew. Chem. Int. Ed.*, 2009, **48**, 9304.
- [54] M. Griffin, S. Shakespeare, H. J. Shepherd, C. J. Harding, J. F. Létard, C. Desplanches, A. E. Goeta, J. A. Howard, A. K. Powell, V. Mereacre, Y. Garcia, A. D. Naik, H. Müller-Bunz, G. G. Morgan, *Angew. Chem. Int. Ed.*, 2011 **24**, 896.
- [55] M. G. Cowan, J. Olguín, S. Narayanaswamy, J. L. Tallon, S. Brooker, *J. Am. Chem. Soc.*, 2012, **15**, 2892.
- [56] A. J. Fitzpatrick, E. Trzop, H. Müller-Bunz, M. M. Dîrtu, Y. Garcia, E. Collet, G. G. Morgan, *Chem. Commun.*, 2015, **25**, 17540.
- [57] J. A. Real, H. Bolvin, A. Bousseksou, A. Dworkin, O. Kahn, F. Varret, J. Zarembowitch, *J. Am. Chem. Soc.*, 1992, **114**, 4650.
- [58] M. Paez-Espejo, M. Sy, K. Boukheddaden. *J Am Chem Soc.*, 2016 **138**, 3202.
- [59] D. Chernyshov, H.-B. Burgi, M. Hostettler, K. W. Törnroos, *Phys. Rev. B*, 2004, **70**, 094116.
- [60] H. Watanabe, K. Tanaka, N. Brefuel, H. Cailleau, J.-F. Letard, S. Ravy, P. Fertey, M. Nishino, S. Miyashita, E. Collet, *Phys. Rev. B*, 2016, **93**, 014419.
- [61] E. Trzop, D. Zhang, L. Piñeiro-Lopez, F. J. Valverde-Muñoz, M. Carmen Muñoz, L. Palatinus, L. Guerin, H. Cailleau, J. A Real, E. Collet, *Angew. Chem. Int. Ed.*, 2016, **55**, 8675.
- [62] P. Guionneau, C. Brigouleix, Y. Barrans, A. E. Goeta, J. F. Létard, J. A. K. Howard, J. Gaultier, D. Chasseau, *C. R. Acad. Sci. Paris, Chem.*, 2001, **4**, 161.
- [63] E. Milin, V. Patinec, S. Triki, E. Bendeif, S. Pillet, M. Marchivie, G. Chastanet, K Boukheddaden, *Inorg. Chem.*, 2016, **55**, 11652.

- [64] T. Boonprab, S. J. Lee, S. G. Telfer, K. S. Murray, W. Phonsri, G. Chastanet, E. Collet, E. Trzop, G. N. L. Jameson, P. Harding, D. J. Harding, *Angew. Chem. Int. Ed.*, 2019, **58**, 11811.
- [65] E. König, *Prog. Inorg. Chem.*, 1987, **35**, 527.
- [66] E. König, G. Ritter, S. H. Kulshreshtha, *Chem. Rev.*, 1985, **85**, 219.
- [67] P. Gütllich, *In: Metal Complexes. Structure and Bonding*, Springer, Berlin, Heidelberg, 1981, **44**, 83.
- [68] P. Guionneau, M. Marchivie, G. Bravic, J.-F. Létard, D. Chasseau, *Top. Curr. Chem.*, 2004, **234**, 97.
- [69] P. Guionneau, J. F. Létard, D. S. Yufit, D. Chasseau, G. Bravic, A. E. Goeta, J. A. K. Howard, O. Kahn, *J. Mater. Chem.*, 1999, **9**, 985.
- [70] P. Guionneau, M. Marchivie, G. Bravic, J. F. Létard, D. Chasseau, *J. Mater. Chem.*, 2002, **12**, 2546.
- [71] T. A. Pfaffeneder, S. Thallmair, W. Bauer and B. Weber, *New J. Chem.*, 2011, **35**, 691.
- [72] J. K. McCusker, A. L. Rheingold, D.N. Hendrickson, *Inorg. Chem.*, 1996, **35**, 2100.
- [73] M. Marchivie, P. Guionneau, J. F. Létard, D. Chasseau, *Acta Cryst.*, 2005, **B61**, 25.
- [74] M. Buron-Le Cointe, J. Hébert, C. Baldé, N. Moisan, L. Toupet, P. Guionneau, J. F. Létard, E. Freysz, H. Cailleau, E. Collet, *Phys. Rev. B.*, 2012, **85**, 064114.
- [75] S. Alvarez, *J. Am. Chem. Soc.*, 2003, **125**, 6795.
- [76] R. Ketkaew, Y. Tantirungrotechai, P. Harding, G. Chastanet, P. Guionneau, M. Marchivie, D. J. Harding, *under review*.
- [77] M. Llunell, D. Casanova, J. Cirera, M. Alemany, S. Alvarez, SHAPE, v2.0, University of Barcelona, Barcelona, Spain, 2010.
- [78] M. A. Halcrow, *Chem. Soc. Rev.*, 2011, **40**, 4119.
- [79] R. J. Wei, J. Tao, R. B. Huang, L. S. Zheng, *Eur. J. Inorg. Chem.*, 2013, 916.
- [80] C. Kohler, E. Rentschler, *Eur. J. Inorg. Chem.*, 2016, 1955.
- [81] K. Takahashi, K. Kawamukai, M. Okai, T. Mochida, T. Sakurai, H. Ohta, T. Yamamoto, Y. Einaga, Y. Shiota, K. Yoshizawa, *Chem. Eur. J.*, 2016, **22**, 1253.
- [82] Q. Yang, X. Cheng, C. Gao, B. W. Wang, Z. M. Wang, S. Gao, *Cryst. Growth Des.*, 2015, **15**, 2565.
- [83] P. Guionneau, F. Le Gac, A. Kaiba, J. S. Costa, D. Chasseau, J. F. Létard, *Chem Commun.*, 2007, **28**, 3723.
- [84] D. Rosario-Amorin, P. Dechambenoit, A. Bentaleb, M. Rouzières, C. Mathonière, R. Clérac, *J. Am. Chem. Soc.*, 2018, **140**, 98.

- [85] G. S. Matouzenko, A. Bousseksou, S. A. Borshch, M. Perrin, S. Zein, L. Salmon, G. Molnar, S. Lecocq, *Inorg. Chem.*, 2004, **43**, 227.
- [86] G. A. Craig, J. S. Costa, O. Roubeau, S. J. Teat, G. Aromí, *Chem. Eur. J.*, 2011, **17**, 3120.
- [87] B. A. Leita, S. M. Neville, G. J. Halder, B. Moubaraki, C. J. Kepert, J. F. Létard, K. S. Murray, *Inorg. Chem.*, 2007, **46**, 8784.
- [88] N. Phukkaphan, D. L. Cruickshank, K. S. Murray, W. Phonsri, P. Harding, D. J. Harding, *Chem. Commun.*, 2017, **53**, 9801.
- [89] M. A. Spackman, D. Jayatilaka, *Cryst. Eng. Comm.*, 2009, **11**, 19.
- [90] E. Tailleur, M. Marchivie, N. Daro, G. Chastanet, P. Guionneau, *Chem. Commun.*, 2017, **53**, 4763.
- [91] G. S. Matouzenko, A. Bousseksou, S. Lecocq, P. J. van Koningsbruggen, M. Perrin, O. Kahn, A. Collet, *Inorg. Chem.*, 1997, **36**, 5869.
- [92] S. Zein, G. S. Matouzenko, S. A. Borshch, *J. Phys. Chem. A*, 2005, **109**, 8568.
- [93] M. Marchivie, P. Guionneau, J. F. Létard, D. Chasseau, *Acta Crystallogr.*, 2003, **59**, 479.
- [94] J. F. Létard, G. Chastanet, O. Nguyen, S. Marcen, M. Marchivie, P. Guionneau, D. Chasseau, P. Gütllich, *Monatsh. Chem.*, 2003, **134**, 165.
- [95] M. Shatruk, H. Phan, B. A. Chrisostomo, A. Suleimenova, *Coord. Chem. Rev.*, 2015, **289**, 62.
- [96] A. Grosjean, P. Négrier, P. Bordet, C. Etrillard, D. Mondieig, S. Pechev, E. Lebraud, J. F. Létard, P. Guionneau, *Eur. J. Inorg. Chem.*, 2013, 796.
- [97] C. G. Darwin, *Philos. Mag.*, 1922, **43**, 800.
- [98] A. Grosjean, N. Daro, S. Pechev, L. Moulet, C. Etrillard, G. Chastanet, P. Guionneau, *Eur. J. Inorg. Chem.*, 2016, **13-14**, 1961.
- [99] T. Forestier, A. Kaiba, S. Pechev, D. Denux, P. Guionneau, C. Etrillard, N. Daro, E. Freysz, J.-F. Létard, *Chem. Eur. J.*, 2009, **15**, 6122.
- [100] P. Guionneau, S. Lakhlof, M. H. Lemée-Cailleau, G. Chastanet, P. Rosa, C. Mauriac, J. F. Létard, *Chem. Phys. Lett.*, 2012, **542**, 52.
- [101] L. Salmon, L. Catala, *C. R. Chim*, 2018, **21**, 211230.
- [102] K. Boukheddaden, M. Sy, *Curr. Inorg. Chem.*, 2016, **6**, 40.
- [103] A. Slimani, F. Varret, K. Boukheddaden, C. Chong, H. Mishra, J. Haasnoot, S. Pillet, *Phys. Rev. B*, 2011, **84**, 094442.
- [104] G. Molnár, A. Bousseksou, A. Zwick, J.J. McGarvey, *Chem. Phys. Lett.*, 2003, **367**, 593.
- [105] S. Bedoui, G. Molnár, S. Bonnet, C. Quintero, H.J. Shepherd, W. Nicolazzi, L. Salmon, A. Bousseksou, *Chem. Phys. Lett.*, 2010, **499**, 94.

- [106] S. Decurtins, P. Gutlich, C. P. Kohler, H. Spiering, A. Hauser, *Chem. Phys. Lett.*, 1984, **105**, 1.
- [107] A. Hauser, *Chem. Phys. Lett.*, 1986, **124**, 543.
- [108] A. Hauser, *Coord. Chem. Rev.*, 1991, **111**, 275.
- [109] C. Bressler, C. Milne, V. T. Pham, A. ElNahas, R. M. van der Veen, W. Gawelda, S. Johnson, P. Beaud, D. Grolimund, M. Kaiser, C. N. Borca, G. Ingold, R. Abela, M. Chergui, *Science*, 2009, **323**, 489.
- [110] A. Cannizzo, C. J. Milne, C. Consani, W. Gawelda, Ch. Bressler, F. van Mourik, M. Chergui, *Coord. Chem. Rev.*, 2010, **254**, 2677.
- [111] R. Bertoni, M. Cammarata, M. Lorenc, S. F. Matar, J. F. Létard, H. T. Lemke, E. Collet, *Acc. Chem. Res.*, 2015, **48**, 774.
- [112] M. Khalil, M. A. Marcus, A. L. Smeigh, J. K. McCusker, H. H. Chong, R. W. Schoenlein, *J. Phys. Chem. A*, 2006, **110**, 38.
- [113] J. Tribollet, G. Galle, G. Jonusauskas, D. Deldicque, M. Tondusson, J. F. Létard, E. Freysz, *Chem. Phys. Lett.*, 2011, **513**, 42.
- [114] M. A. Naumova, A. Kalinko, J. W. L. Wong, M. Abdellah, H. Geng, E. Domenichini, J. Meng, S. A. Gutierrez, P.-A. Mante, W. Lin, P. Zalden, A. Galler, F. Lima, K. Kubicek, M. Biednov, A. Britz, S. Checchia, V. Kabanova, M. Wulff, J. Zimara, D. Schwarzer, S. Demeshko, V. Murzin, D. Gosztola, M. Jarenmark, J. Zhang, M. Bauer, M. L. L. Daku, W. Gawelda, D. Khakhulin, C. Bressler, F. Meyer, K. Zheng, S. E. Canton, *J. Phys. Chem. Lett.*, 2020, **11**, 2133.
- [115] M. Lorenc, J. Hébert, N. Moisan, E. Trzop, M. Servol, M. Buron-Le Cointe, H. Cailleau, M.L. Boillot, E. Pontecorvo, M. Wulff, S. Koshihara, E. Collet, *Phys. Rev. Lett.*, 2009, **103**, 028301.
- [116] E. Collet, N. Moisan, C. Baldé, R. Bertoni, E. Trzop, C. Laulhé, M. Lorenc, M. Servol, H. Cailleau, A. Tissot, M.-L. Boillot, T. Graber, R. Henning, P. Coppens, M. Buron-Le Cointe, *Phys. Chem. Chem. Phys.*, 2012, **14**, 6192.
- [117] R. Bertoni, M. Lorenc, H. Cailleau, A. Tissot, J. Laisney, M.-L. Boillot, L. Stoleriu, A. Stancu, C. Enachescu, E. Collet, *Nat. Mater.*, 2016, **15**, 606.
- [118] M. Chergui, E. Collet, *Chem. Rev.*, 2017, **117**, 11025.
- [119] R. Bertoni, M. Lorenc, T. Graber, R. Henning, K. Moffat, J. F. Létard, E. Collet, *Cryst. Eng. Comm.*, 2016, **18**, 7269.
- [120] A. Marino, P. Chakraborty, M. Servol, M. Lorenc, E. Collet, A. Hauser, *Angew. Chem. Int. Ed.*, 2014, **53**, 3863.

- [121] E. Buhks, G. Navon, M. Bixon, J. Jortner, *J. Am. Chem. Soc.*, 1980, **102**, 2918.
- [122] C. L. Xie, N. D. Hendrickson, *J. Am. Chem. Soc.*, 1987, **109**, 6981.
- [123] A. Hauser, C. Enachescu, M. L. Daku, A. Vargas, N. Amstutz, *Coord. Chem. Rev.*, 2006, **250**, 1642.
- [124] A. Hauser, A. Vef, P. Adler, *J. Chem. Phys.*, 1991, **95**, 8710.
- [125] A. Hauser, J. P. Alder, P. Gütllich, *Chem. Phys. Lett.*, 1988, **152**, 468.
- [126] A. Hauser, *Chem. Phys. Lett.*, 1992, **192**, 65.
- [127] R. H. Herber, L. M. Casson, *Inorg. Chem.*, 1986, **25**, 847.
- [128] J. F. Létard, P. Guionneau, L. Rabardel, J. A. Howard, A. E. Goeta, D. Chasseau, O. Kahn, *Inorg. Chem.*, 1998, **37**, 4432.
- [129] J. F. Létard, *J. Mater. Chem.*, 2006, **16**, 2550.
- [130] N. Paradis, G. Chastanet, T. Palamarcu, P. Rosa, F. Varret, K. Boukheddaden, J. F. Létard, *J. Phys. Chem. C*, 2015, **119**, 20039.
- [131] G. Chastanet, C. Desplanches, C. Baldé, P. Rosa, M. Marchivie, P. Guionneau, *Chem. Sq.*, 2018, **2**, 2.
- [132] J. F. Létard, P. Guionneau, O. Nguyen, J. S. Costa, S. Marcén, G. Chastanet, M. Marchivie, L. G. Capes, *Chem. Eur. J.*, 2005, **11**, 4582.
- [133] S. Marcén, L. Lecren, L. Capes, H. A. Goodwin, J. F. Létard, *Chem. Phys. Lett.*, 2002, **358**, 87.
- [134] M. A. Halcrow, *Coord. Chem. Rev.*, 2009, **253**, 2493.
- [135] G. A. Craig, O. Roubeau, G. Aromi, *Coord. Chem. Rev.*, 2014, **269**, 13.
- [136] V. Garcia-Lopez, M. Palacios-Corella, S. Cardona-Serra, M. Clemente-Leon, E. Coronado, *Chem. Commun.*, 2019, **55**, 12227.
- [137] C. F. Sheu, C. H. Shih, K. Sugimoto, B. M. Cheng, M. Takata, Y. Wang, *Chem. Commun.*, 2012, **48**, 5715.
- [138] S. Hayami, Z. Z. Gu, Y. Einaga, Y. Kobayashi, Y. Ishikawa, Y. Yamada, A. Fujishima, O. Sato, *Inorg. Chem.*, 2001, **40**, 3240.
- [139] D. F. Li, R. Clérac, O. Roubeau, E. Harté, C. Mathonière, R. Le Bris, S. M. Holmes, *J. Am. Chem. Soc.*, 2008, **130**, 252.
- [140] M. Marchivie, P. Guionneau, J. A. Howard, G. Chastanet, J. F. Létard, A. E. Goeta, D. Chasseau, *J. Am. Chem. Soc.*, 2002, **124**, 194.
- [141] C. C. Wu, J. Jung, P. K. Gantzel, P. Gütllich, D. N. Hendrickson, *Inorg. Chem.*, 1997, **36**, 5339.

- [142] F. Cecconi, M. Di Vaira, S. Midollini, A. Orlandini, L. Sacconi, *Inorg. Chem.*, 1981, **20**, 3423.
- [143] P. Rosa, A. Debay, L. Capes, G. Chastanet, A. Bousskesou, P. Le Floch, J. F. Letard, *Eur. J. Inorg. Chem.*, 2004, 3017.
- [144] S. Hayami, K. Hiki, T. Kawahara, Y. Maeda, D. Urakami, K. Inoue, M. Ohama, S. Kawata, O. Sato, *Chem. Eur. J.*, 2009, **15**, 3497.
- [145] N. Suaud, M. Bonnet, C. Boilleau, P. Labèguerie, N. Guihéry, *J. Am. Chem. Soc.*, 2009, **131**, 715.
- [146] K. Ichiyangi, J. Hebert, L. Toupet, H. Cailleau, P. Guionneau, J. F. Létard, E. Collet *Phys. Rev B*, 2006, **73**, 060408.
- [147] E. Tailleur, M. Marchivie, P. Negrier, D. Denux, S. Massip, Denise Mondieig, G. Chastanet, P. Guionneau, *Cryst. Eng. Comm.*, 2019, **21**, 6246.
- [148] J. F. Létard, P. Guionneau, E. Codjovi, O. Lavastre, G. Bravic, D. Chasseau, O. Kahn, *J. Am. Chem. Soc.*, 1997, **119**, 10861.
- [149] J. F. Létard, J. M. Kollmansberger, C. Carbonera, M. Marchivie, P. Guionneau, *C. R. Chim.*, 2008, **11**, 1155.
- [150] L. Capes, J. F. Létard, O. Kahn, *Chem. Eur. J.*, 2000, **6**, 2246.
- [151] N. Mochida, A. Kimura, T. Ishida, *Magnetochemistry*, 2015, **1**, 17.
- [152] Y. Oso, T. Ishida, *Chem. Lett.*, 2009, **38**, 604.
- [153] Y. H. Luo, Y. Sun, Q. L. Liu, L. J. Yang, G. J. Wen, M. X. Wang, B. W. Sun, *ChemistrySelect*, 2016, **1**, 3879.
- [154] S. M. Fatur, S. G. Shepard, R. F. Higgins, M. P. Shores, N. H. Damrauer. *J. Am. Chem. Soc.*, 2017, **139**, 4493.
- [155] S. G. Shepard, S. M. Fatur, A. K. Rappé, N.H. Damrauer. *J. Am. Chem. Soc.*, 2016, **138**, 2949.
- [156] I. R. Jeon, C. Mathonière, R. Clérac, M. Rouzières, O. Jeannin, E. Trzop, E. Collet, M. Fourmigué, *Chem. Commun.*, 2017, **53**, 10283.
- [157] I. R. Jeon, O. Jeannin, R. Clérac, M. Rouzières, M. Fourmigué, *Chem. Commun.*, 2017, **53**, 4989.

**Part II – Promoting Distortion of the Coordination  
Polyhedron by Steric Strain: Fluorine Substitution of PM-  
zFA Family**

<b>II.1. Introduction</b> .....	51
<b>II.2. Synthesis of the fluorine-substituted ligands and of the [Fe(PM-zFA)<sub>2</sub>(NCS)<sub>2</sub>] complexes</b> .....	52
II.2.1. Synthesis of the fluorine-substituted ligands .....	52
II.2.2. Synthesis of the [Fe(PM-zFA) <sub>2</sub> (NCS) <sub>2</sub> ] complexes.....	55
<b>II.3. Characterizations of the [Fe(PM-zFA)<sub>2</sub>(NCS)<sub>2</sub>] complexes.....</b>	57
II.3.1. [Fe(PM- <i>o</i> FA) <sub>2</sub> (NCS) <sub>2</sub> ] ( <i>I-o</i> FA) .....	57
II.3.2. [Fe(PM- <i>m</i> FA) <sub>2</sub> (NCS) <sub>2</sub> ] ( <i>I-m</i> FA).....	58
II.3.3 [Fe(PM- <i>p</i> FA) <sub>2</sub> (NCS) <sub>2</sub> ]·nCHCl <sub>3</sub> ( <i>I-p</i> FA) .....	70
<b>II.4. Discussion on the structure-properties relationship of [Fe(PM-zFA)<sub>2</sub>(NCS)<sub>2</sub>] .....</b>	82
<b>Bibliography</b> .....	86

## **II.1. Introduction**

SCO materials belonging to the  $[\text{Fe}(\text{PM-L})_2(\text{NCE})_2]$  family ( $E = \text{S}$  and  $\text{Se}$ ) display rich structural (polymorphism and symmetry breaking), magnetic and photomagnetic behaviours, providing interesting clues for structural-properties relationship in SCO.<sup>1-6</sup> More than 16 compounds have been reported so far in this family. Since we strongly suspect the relaxation temperature  $T(\text{LIESST})$  to be greatly related to the distortion of the coordination sphere<sup>7</sup>, our target is to chemically promote such distortion and see if it increases the relaxation temperature  $T(\text{LIESST})$ . The PM-zXA ( $z = o, m, p$ ; X = halogen atoms) ligands have been designed for that purpose by introducing the halogen group on a phenyl ring.

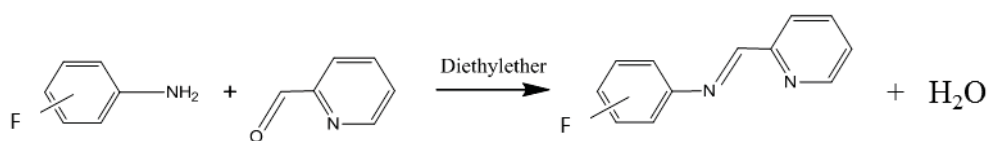
In this part, we will describe the synthesis of the fluorine-substituted ligands PM-zFA and the related  $[\text{Fe}(\text{PM-zFA})_2(\text{NCS})_2]$  complexes. Fluorine functionalization was first explored due to its small size. Indeed, Fluor is one of the smallest atoms of the periodic table. Therefore, a substitution using this atom might promote strain close to the coordination sphere without preventing this coordination, especially with a functionalization in *ortho* position of the aniline ring. Moreover, Fluor possesses a large electronegativity which may provide F---H hydrogen bonding in the solid, which could help to bring cooperativity in the materials.

Targeting the above expectations, three ligands with different mono-substituted fluoro-aniline groups were first synthesized and then three corresponding iron complexes were crystallized and studied. Their magnetic properties as well as their crystal structures, when accessible, are described, using the multiscale approach described in [Part I.1.2](#).

## II.2. Synthesis of the fluorine-substituted ligands and of the [Fe(PM-*z*FA)<sub>2</sub>(NCS)<sub>2</sub>] complexes

### II.2.1. Synthesis of the fluorine-substituted ligands

The Schiff base ligands (PM-*z*FA) (*z* = *o*, *m*, *p*) were synthesized from the condensation of the 2-pyridine-carbaldehyde with the corresponding fluorine substituted aniline (Scheme II.1) according to the literature procedure.<sup>8</sup>



Scheme II.1. Reaction scheme of the *N*-(2'-pyridylmethylene)-*n*-fluoroaniline ligands (*n* = 2, 3, 4).

- *Synthesis of N*-(2'-pyridylmethylene)-4-fluoroaniline (PM-*p*FA)

A solution of 4-fluoroaniline (0.94 ml, 10 mmol) in diethylether (50 ml), was added to pyridine-2-carbaldehyde (0.95 ml, 10 mmol) in diethylether (50 ml). Then magnesium sulfate (5g, MgSO<sub>4</sub>) was added in order to absorb the reaction water and the yellow solution was stirred overnight under argon atmosphere. The solution was filtered and the magnesium sulfate washed with CH<sub>2</sub>Cl<sub>2</sub> (5 ml), in order to remove all the products. The solvent was removed under vacuum by rotary evaporator. The ligand was recrystallized in a mixture of CH<sub>2</sub>Cl<sub>2</sub> (10 ml) and petroleum ether (30 ml). After one day at -25 °C the bulk-yellow crystal was filtrated and recrystallized one more time.

The crystals obtained upon recrystallization were good enough to record single-crystal X-ray diffraction (SCXRD) data and to determine the crystal structure of PM-*p*FA ligand. At 300 K, the PM-*p*FA ligand crystallizes in the monoclinic system with space group *P*2<sub>1</sub>/*m* (Table II.1). All atoms site on the general Wyckoff position (4f) except for C13, C16, C18, C21 and F2 (2e). The special Wyckoff position (2e) leads to only a half molecule **B** in the asymmetric unit. Then, there are one and a half molecules in the asymmetric unit, where C15, C17, N3 and N4 atoms are disordered and half occupied in molecule **B** (Figure II.1). The dihedral angles between the phenyl and pyridine rings are only 5.54° and 0.73°, respectively, leading to the

nearly planar geometry of the two molecules. In both molecules, the intraligand H---H distances are less than 2.2 Å (Figure II.1a and b). It is worth to mention that the intermolecular hydrogen bonding N---H (2.834 Å for N1---H11 and 2.895 Å for N2---H20 Å) and F---H contacts (2.488 Å for F2---H13 and 2.747 Å for F1---H2) play an important role in the layer by layer packing of molecules in the mode **B/AA/B** along the *b* axis (Figure II.1c). The comparison between the experimental powder X-ray diffraction (PXRD) pattern and the simulated PXRD pattern from the SCXRD data shows strong differences (Figure II.2). This indicates that the main phase of the crystalline powder has a different crystal structure from the single-crystal used to determine the crystal structure. This may be due to the possible polymorphism in ligand.

**Table II.1.** Crystal data and structure refinement data for **PM-*p*FA** ligand at 300 K.

Empirical formula	C <sub>12</sub> H <sub>9</sub> FN <sub>2</sub>
Formula weight / g mol <sup>-1</sup>	200.21
Temperature / K	300
Radiation MoKα / Å	λ = 0.71073
Crystal size / mm <sup>3</sup>	0.28 × 0.24 × 0.20
Crystal system	monoclinic
Space group	P2 <sub>1</sub> /m
<i>a</i> / Å	4.720(2)
<i>b</i> / Å	31.460(14)
<i>c</i> / Å	9.939(5)
α / °	90
β / °	91.582(17)
γ / °	90
Volume / Å <sup>3</sup>	1 475.3(12)
Z-formula	6
ρ <sub>calc</sub> / g cm <sup>-3</sup>	1.352
μ / mm <sup>-1</sup>	0.095
F(000)	624.0
2θ range for data collection / °	2.59 - 52.728
Index ranges	-5 ≤ h ≤ 5, -38 ≤ k ≤ 39, -12 ≤ l ≤ 12
Reflections collected	17490
Independent reflections	3062 [R <sub>int</sub> = 0.0510, R <sub>sigma</sub> = 0.0488]
Data/restraints/parameters	3062/0/233
Goodness-of-fit on F <sup>2</sup>	1.136
Final R indexes [I ≥ 2σ (I)]	R <sub>1</sub> = 0.0647, wR <sub>2</sub> = 0.1701
Final R indexes [all data]	R <sub>1</sub> = 0.1265, wR <sub>2</sub> = 0.1953
Largest diff. peak/hole / e Å <sup>-3</sup>	0.19/-0.19

$$R_1 = \frac{\sum ||F_0| - |F_c||}{\sum |F_0|}, wR_2 = \left[ \frac{\sum w(F_0^2 - F_c^2)^2}{\sum w(F_0^2)^2} \right]^{1/2}$$

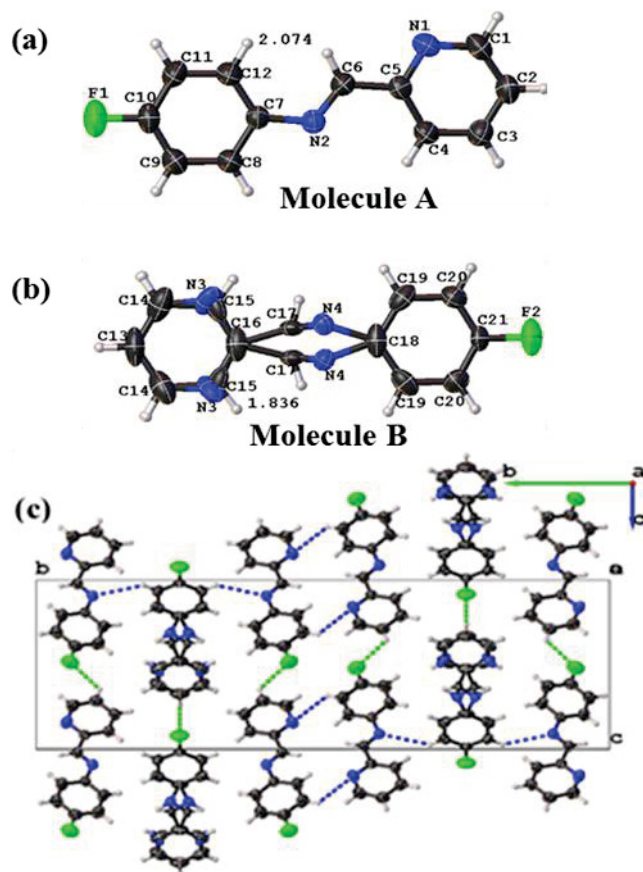


Figure II.1. Molecule A (a), molecule B (b), and the crystal packing (c) in the **PM-pFA** ligand at 300 K. The N---H and F---H hydrogen bonding are represented by the blue and green dashed line, respectively. Thermal ellipsoids are depicted at the 50 % probability level.

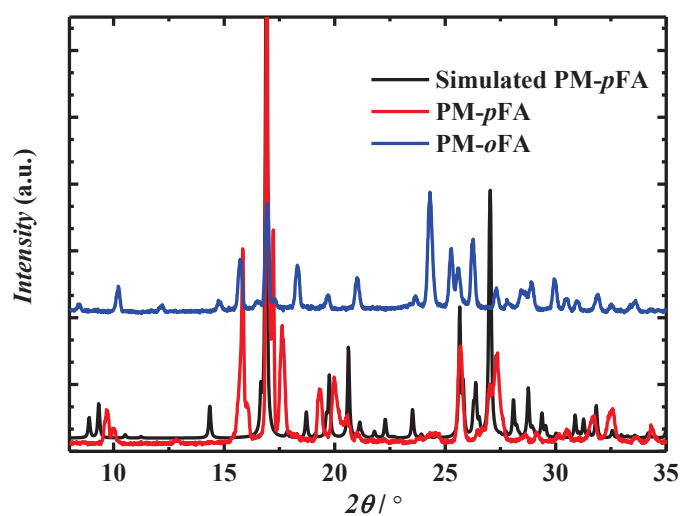


Figure II.2. Experimental and simulated X-ray powder diffraction patterns of **PM-pFA** ligand (red and black) and **PM-oFA** ligand (blue) at 300 K. The simulation is done from the experimental single-crystal XRD data.

- *Synthesis of N-(2'-pyridylmethylene)-3-fluoroaniline (PM-mFA)*

Using the same procedure, ligand PM-mFA was synthesized using 3-fluoroaniline. After evaporation of diethylether, only light yellow oil was formed. Different solvents were used for crystallization, however nor single-crystals nor powder were obtained.

- *Synthesis of N-(2'-pyridylmethylene)-2-fluoroaniline (PM-oFA)*

Using the same procedure, the ligand PM-oFA was synthesized using 2-fluoroaniline. The ligand was recrystallized in a mixture of diethyl ether (10 ml) and petroleum ether (30 ml). After one day at -25 °C, the colorless solid was filtrated and recrystallized one more time. The quality of the crystals was not good enough to record data and determine the crystal structure. The powder X-ray diffractogram (Figure II.2) strongly differs from the PM-pFA one, suggesting a different crystal structure.

### **II.2.2. Synthesis of the $[\text{Fe}(\text{PM-zFA})_2(\text{NCS})_2]$ complexes**

All the solvents were treated in order to remove the oxygen in solution before use. Methanol was distilled while diethylether, acetonitrile and dichloromethane were frozen and unfrozen in liquid nitrogen three times. The reactions and crystallizations were performed under argon atmosphere.

A first step consisted in preparing the  $\text{Fe}(\text{NCS})_2$  reactant. 1 mmol of  $\text{FeSO}_4 \cdot 7\text{H}_2\text{O}$  and 2 mmol of KNCS were dissolved in 20 ml of methanol each, in presence of few ascorbic acid. After stirring 2 hours, the resulting solution is filtered under nitrogen atmosphere to remove the  $\text{K}_2\text{SO}_4$  formed during the reaction.

As a common method for the synthesis of complexes, we used the layering technique for crystallization, where two solvents containing ligand and metal salt, respectively, diffuse and crystallize slowly at the intermediate layer.

- *Synthesis of  $[\text{Fe}(\text{PM-oFA})_2(\text{NCS})_2]$*

Owing to the very soluble nature of PM-oFA, different solvents were tried for crystallization, including diethylether, dichloromethane, methanol, and chloroform. However, no crystals were formed. After evaporating the solvents (diethylether and methanol), dark solids were obtained, named as **I-oFA** hereafter. Elemental analysis gives: C: 48.66, H: 3.31, N: 12.63 smaller than

*Part II – Promoting Distortion of the Coordination Polyhedron by Steric Strain: Fluorine Substitution of PM-zFA Family*

the theoretical values C: 54.55, H: 3.17, N: 14.68, calculated based on the formula  $[\text{Fe}(\text{PM-}o\text{FA})_2(\text{NCS})_2]$  (Appendix 4).

- *Synthesis of  $[\text{Fe}(\text{PM-}m\text{FA})_2(\text{NCS})_2]$*

In this case, 2 ml of diethylether containing 0.2 mmol of ligand (the oily ligand being taken using a syringe) is layered on top of 2 ml of the  $\text{Fe}(\text{NCS})_2$  methanol solution (0.05mmol/ml) and blue needle crystals were formed in a dark blue solution at 25 °C after one week, later referred to as **I-*m*FA** hereafter.

- *Synthesis of  $[\text{Fe}(\text{PM-}p\text{FA})_2(\text{NCS})_2] \cdot n\text{CHCl}_3$*

When 2 ml of the freshly prepared  $\text{Fe}(\text{NCS})_2$  solution (0.05mmol/ml) is layered on top of 2 ml of chloroform containing 0.2 mmol of ligand, dark block crystals are formed in a dark blue solution at 25 °C after two days, later referred to as **I-*p*FA** hereafter. Elemental analysis gives: C: 52.37, H: 3.08, N: 13.42 close to the theoretical values C: 50.62, H: 2.96, N: 13.38, calculated based on the formula  $[\text{Fe}(\text{PM-}o\text{FA})_2(\text{NCS})_2] \cdot 0.47\text{CHCl}_3$  (Appendix 4).

## II.3. Characterizations of the $[\text{Fe}(\text{PM-zFA})_2(\text{NCS})_2]$ complexes

### II.3.1. $[\text{Fe}(\text{PM-oFA})_2(\text{NCS})_2]$ (**I-oFA**)

Although the crystal structure remains unknown, magnetic measurements of **I-oFA** were performed on a powder sample, using a SQUID magnetometer (see Appendix 3). Figure II.3 shows the thermal evolution of the  $\chi_M T$  product ( $\chi_M$  being the molar magnetic susceptibility and  $T$  the temperature). The  $\chi_M T$  value at 320 K of  $3.37 \text{ cm}^3 \text{ K mol}^{-1}$  as expected for a HS  $\text{Fe}^{2+}$ . Upon cooling, the  $\chi_M T$  product gradually decreases to reach a value close to  $0.51 \text{ cm}^3 \text{ K mol}^{-1}$  below 70 K, suggesting a LS state with the presence of some paramagnetic impurity or some HS residue. So complex **I-oFA** shows a gradual and slightly incomplete SCO and a thermal switching temperature around 215 K. Since the crystal structure is missing, we suppose that there is no solvent in powder samples and the formula weight of  $572.43 \text{ g/mol}$  is adopted for the data treatment.

An irradiation at 830 nm was applied for 1h at 10 K, leading to about 20 % of photoswitching. The  $T(\text{LIESST})$  measurement performed after this photo-excitation leads to a  $T(\text{LIESST})$  value of 55 K.

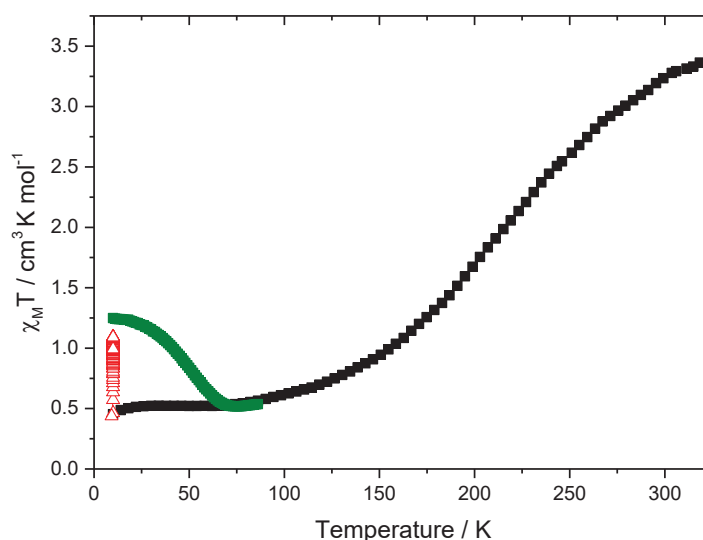
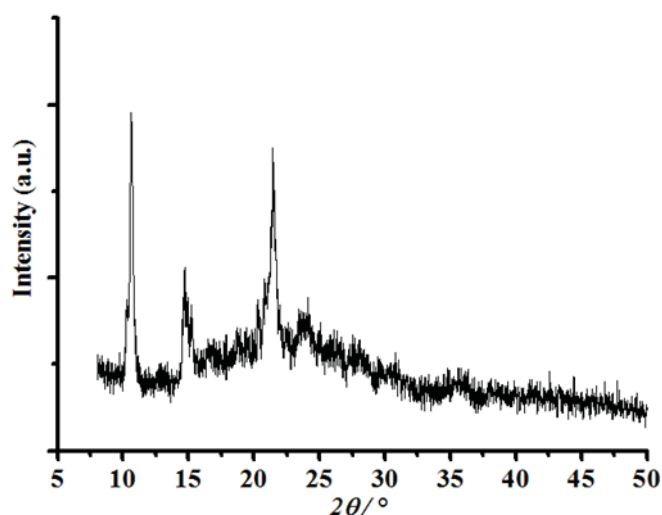


Figure II.3 Thermal dependence of the  $\chi_M T$  product of **I-oFA** recorded at 0.4 K/min (in settle mode) under 20 kOe of applied magnetic field, before irradiation (■), under irradiation (Δ) and after irradiation in the dark (■).

Unfortunately, the absence of single crystals for this compound does not allow the crystal structure determination, which makes, of course, any attempt of structure-properties relationships impossible. Only PXRD diffraction could have been done as reported in [Figure II.4](#) showing the poor crystallinity of the compound that, by the way, prevents from any *ab initio* PXRD crystal structure determination.



[Figure II.4](#). Experimental X-ray powder diffraction pattern of complex **I-oFA**.

### II.3.2. [Fe(PM-*m*FA)<sub>2</sub>(NCS)<sub>2</sub>] (**I-mFA**)

- *Magnetic properties of I-mFA*

Magnetic measurements were performed on a polycrystalline sample, using a SQUID magnetometer (see [Appendix 3](#)). [Figure II.5](#) shows the thermal evolution of the  $\chi_{MT}$  product. The  $\chi_{MT}$  value at 300 K of  $3.45 \text{ cm}^3 \text{ K mol}^{-1}$ , agrees well with a HS  $\text{Fe}^{2+}$  ion ( $g = 2.14$ ). Upon cooling, the  $\chi_{MT}$  product gradually decreases to reach a value close to  $1.91 \text{ cm}^3 \text{ K mol}^{-1}$  at 150 K, showing a large plateau between 30 K and 150 K. The decreasing value of  $\chi_{MT}$  corresponds to  $\sim 50\%$  of  $\chi_{MT}$  value at 300 K. The slight decrease of  $\chi_{MT}$  below 20 K may be due to the zero-field splitting. So complex **I-mFA** shows an incomplete SCO of about 50 % of the compound and the thermal switching temperature is around 215 K. The partial SCO might come from different  $\text{Fe}^{2+}$  sites in the structure, 50% of them being SCO-active. Of course some paramagnetic impurities cannot be excluded and crystallography might help to elucidate this observation of the plateau.

An irradiation at 830 nm was applied for 1h at 10 K, leading to less than 10 % of photoswitching. The  $T(\text{LIESST})$  measurement performed after this photo-excitation leads to a  $T(\text{LIESST})$  value of around 32 K.

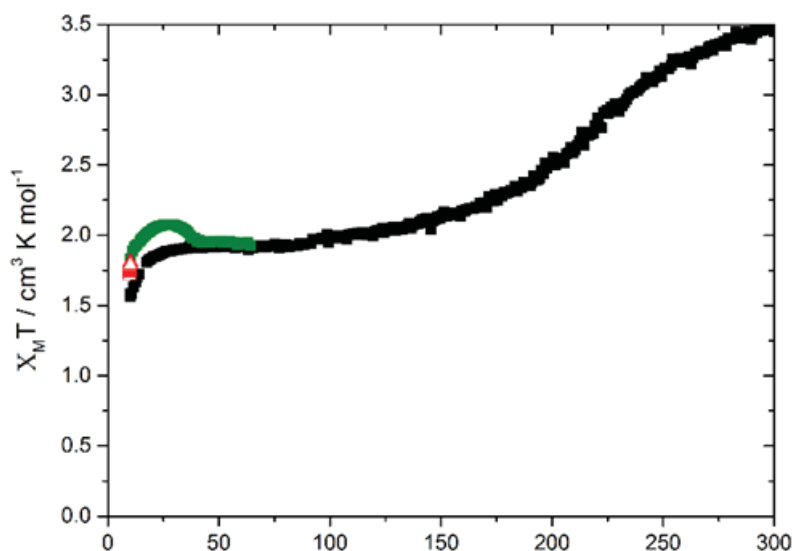


Figure II.5. Thermal dependence of the  $\chi_M T$  product of **I-mFA** recorded at 0.4 K/min (in settle mode) under 20 kOe of applied magnetic field, before irradiation (■), under irradiation (Δ) and after irradiation in the dark (■).

- *Crystallographic investigation of I-mFA*

SCXRD data were recorded at 100 K, 200 K and 300 K and the crystal structure determination and refinements were performed using the *Olex2* software<sup>9</sup>. The detailed experimental and structural data are shown in [Table II.2](#).

At 300 K, the complex **I-mFA** crystallizes in a monoclinic system with *C2/c* space group. The *a* parameter of 50.7003(10) Å is unusually large for  $\text{Fe}^{2+}$  molecular complexes and even in the general context of small molecule based crystals. This gives rise to a huge unit-cell volume of 10444.1(3) Å<sup>3</sup> ([Table II.2](#)). There are two independent crystallographic  $\text{Fe}^{2+}$  ions in the asymmetric unit with all atoms on the general Wyckoff position (8f), labelled hereafter Fe1 and Fe2. In both molecules, the thiocyanate groups adopt a *cis* configuration with two additional bidentate ligands coordinated to the  $\text{Fe}^{2+}$ . As seen in [Figure II.6a and 6b](#), the bond lengths for Fe-N (N from thiocyanate groups) are almost the same in both  $\text{FeN}_6$  octahedra while the other Fe-N distances in  $\text{Fe1N}_6$  are slightly longer than that in  $\text{Fe2N}_6$ . Hence the average value of Fe-N distances are 2.180(5) Å and 2.160(5) Å for Fe1 and Fe2 species, respectively, which are the typical values for HS  $\text{Fe}^{2+}$  ion, agreeing well with the magnetic measurement.

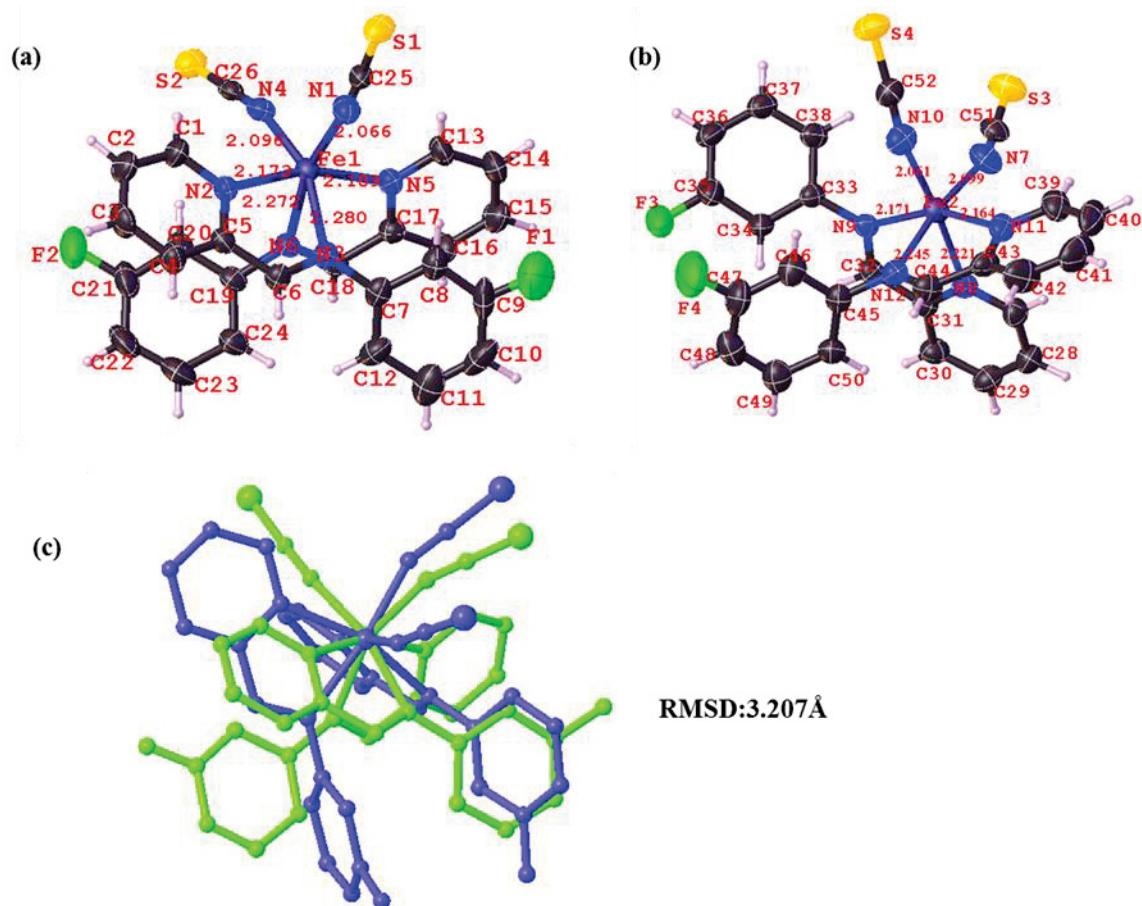


Figure II.6. Fe1 (a), Fe2 (b) in the asymmetric unit and their overlay with RMSD value (c) of the complex **I-mFA** at 300 K.

There are huge differences in the ligand conformation between the two molecules. As seen in Figure II.6a, the two pyridines in Fe1 are in *trans* conformation and the two fluoro-phenyl rings are away from each other with a long F1---F2 distance of 10.53 Å. In Fe2, the pyridines are in *cis* conformation and the two fluoro-phenyl rings are adjacent and point towards the same direction, with a short F3---F4 (3.75 Å) distance (Figure II.6b). Note that it is the first time that a *cis* conformation is observed among the [Fe(PM-L)<sub>2</sub>(NCS)<sub>2</sub>] compounds.<sup>1</sup> This difference is illustrated by the overlay Figure II.6c and the colossal value of the root mean square deviation (RMSD = 3.207 Å), thus almost meaningless.

Table II.2. Crystal data and structure refinement data for complex **I-mFA**.

Empirical formula	C <sub>26</sub> H <sub>18</sub> F <sub>2</sub> FeN <sub>6</sub> S <sub>2</sub>		
Formula weight / g mol <sup>-1</sup>	572.43		
Temperature / K	300	200	100
Radiation MoK $\alpha$ / Å	$\lambda = 0.71073$		
Crystal size / mm <sup>3</sup>	0.24×0.06×0.04		
Crystal system	monoclinic		
Space group	C2/c		
<i>a</i> / Å	50.7003(10)	49.936(2)	49.534(5)
<i>b</i> / Å	9.45650(10)	9.3384(4)	9.2969(9)
<i>c</i> / Å	21.8685(4)	21.7673(9)	21.725(2)
$\alpha$ / °	90		
$\beta$ / °	95.0490(10)	94.5107(12)	94.624(3)
$\gamma$ / °	90		
Volume / Å <sup>3</sup>	10 444.1(3)	10 119.1(7)	9 972.1(17)
Z-formula	16		
$\rho_{\text{calc}}$ / g cm <sup>-3</sup>	1.456	1.503	1.525
$\mu$ / mm <sup>-1</sup>	0.779	0.804	0.816
F(000)	4 672.0	4672.0	4 672.0
$2\theta$ range for data collection / °	3.226 - 51.362	3.754 - 52.744	3.762 - 52.742
Index ranges	-61 ≤ <i>h</i> ≤ 61, -11 ≤ <i>k</i> ≤ 11, -26 ≤ <i>l</i> ≤ 26	-62 ≤ <i>h</i> ≤ 62, -11 ≤ <i>k</i> ≤ 11, -27 ≤ <i>l</i> ≤ 27	-61 ≤ <i>h</i> ≤ 61, -11 ≤ <i>k</i> ≤ 11, -27 ≤ <i>l</i> ≤ 27
Reflections collected	38 172	99 655	97 200
Independent reflections	9 936 [R <sub>int</sub> = 0.0975, R <sub>sigma</sub> = 0.0758]	10 341 [R <sub>int</sub> = 0.1094, R <sub>sigma</sub> = 0.0694]	10 212 [R <sub>int</sub> = 0.1053, R <sub>sigma</sub> = 0.0637]
Data/restraints/parameters	9936/0/667	10341/0/655	10212/0/655
Goodness-of-fit on F <sup>2</sup>	1.014	1.083	1.022
Final R indexes [ <i>I</i> ≥ 2 $\sigma$ ( <i>I</i> )]	R <sub>1</sub> = 0.0689, wR <sub>2</sub> = 0.2068	R <sub>1</sub> = 0.0614, wR <sub>2</sub> = 0.1578	R <sub>1</sub> = 0.0607, wR <sub>2</sub> = 0.1373
Final R indexes [all data]	R <sub>1</sub> = 0.1479, wR <sub>2</sub> = 0.2794	R <sub>1</sub> = 0.1146, wR <sub>2</sub> = 0.1825	R <sub>1</sub> = 0.0991, wR <sub>2</sub> = 0.1556
Largest diff. peak/hole / e Å <sup>-3</sup>	1.27/-1.29	1.94/-0.72	3.52/-0.92

$$R_1 = \frac{\sum ||F_0| - |F_C||}{\sum |F_0|}, wR_2 = [\frac{\sum w(F_0^2 - F_C^2)^2}{\sum w(F_0^2)^2}]^{1/2}$$

Upon slow cooling to 100 K, the crystal-packing of **I-mFA** remains in the same C2/c space group. Compared to 300 K, all the unit-cell parameters become smaller (Table II.2). There are also two molecules in the asymmetric unit with all atoms on the general Wyckoff position (8f). As seen in Figures II.7a and 7b, the Fe-N bond distances in Fe1N<sub>6</sub> are longer than that in Fe2N<sub>6</sub>. The average value of Fe-N distances (<Fe-N>) are 2.171(4) Å and 1.960(4) Å for Fe1 and Fe2, respectively, which are the typical values for HS and LS Fe<sup>2+</sup> ions, respectively. This means a mixture of HS-LS motifs in the crystal packing at 100 K with a 50% ratio.

By the superposition of the structurally independent molecules at 100 K and 300 K (Figures II.7c and 7d), the RMSD value is only 0.071 Å for Fe1 in agreement with the absence of SCO on this site. Regarding Fe2, the RMSD value is 0.233 Å, owing to the atomic displacements of NCS<sup>-</sup> groups, corresponding to the SCO activity of this site. The crystal structure was also determined at 200 K to further examine the plateau seen on the magnetic curve. The average value of Fe-N distances are then 2.171(5) Å and 1.983(5) Å for Fe1 and Fe2 molecules, respectively, which also indicates the fully HS state of Fe1 and ~ 90% LS of Fe2 at 200 K leading to a crystal with roughly 55% HS and 45% LS entities.

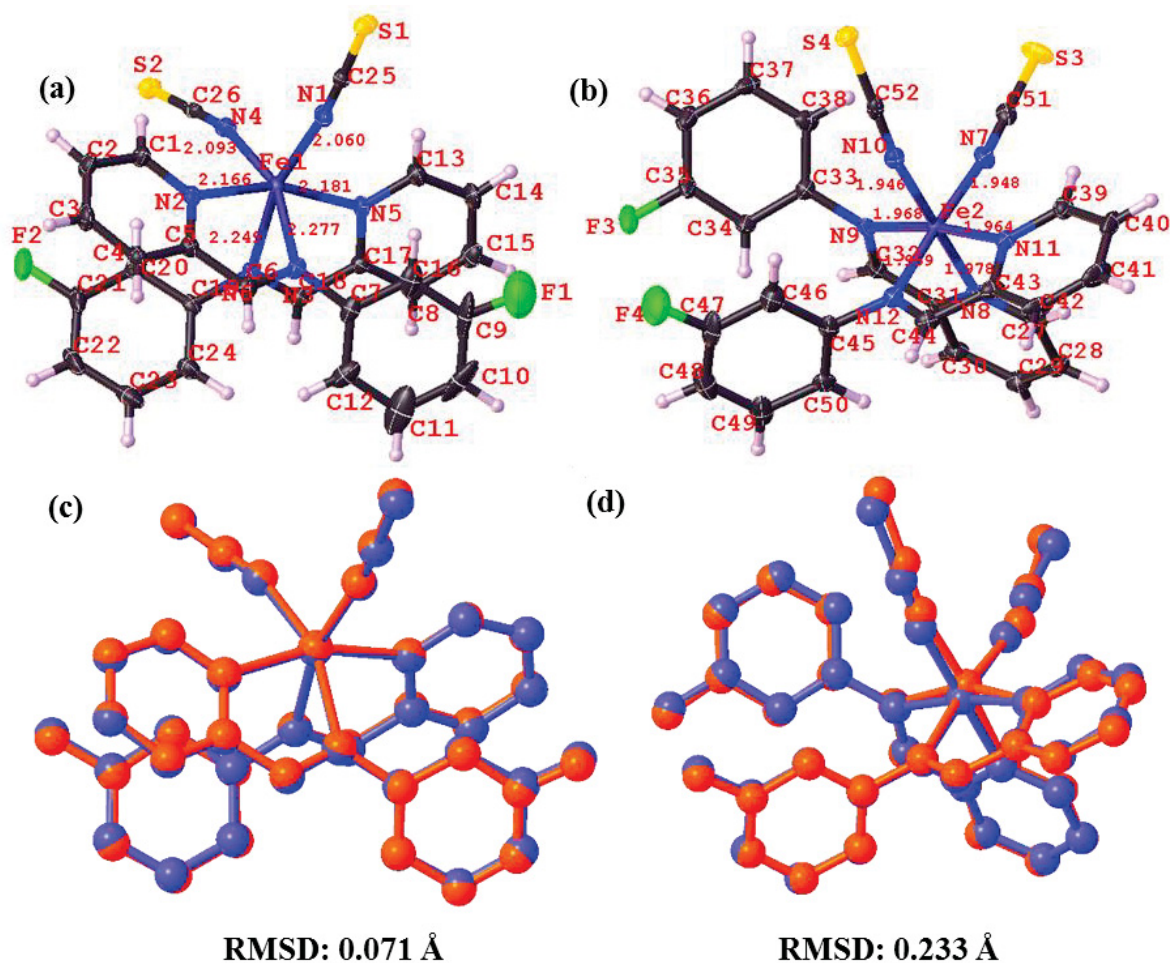
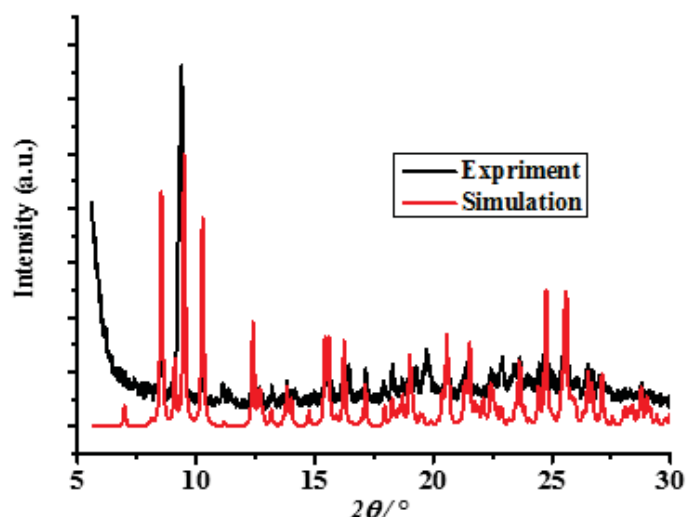


Figure II.7. Fe1 (a) and Fe2 (b) molecules in the asymmetric unit at 100 K, and the overlay of Fe1 (c) and Fe2 (d) between 300 K (red) and 100 K (blue) with the corresponding RMSD (Å) values (b) of the complex **I-mFA**.

These observations explain the broad plateau from 30 K to 150 K in the  $\chi_M T$  vs  $T$  (Figure II.5) with a mixture of HS-LS motifs in the crystal packing. Moreover, the polycrystalline sample recorded on the SQUID presents a similar PXRD pattern to the one simulated from SCXRD data (Figure II.8). It therefore agrees with a compound with two different Fe<sup>2+</sup> sites, one being SCO-active, the other one being not.



**Figure II.8.** Experimental and simulated X-ray powder diffraction patterns of complexes **I-mFA**. The simulation pattern (red) comes from the experimental single-crystal XRD data at 300 K.

**Table II.3** reports the calculated distortion parameters for  $\text{FeN}_6$  polyhedra and some selected N-Fe-N angles. At 300 K, the bond distortion ( $\zeta$ ), angular distortion ( $\Sigma$ ), trigonal distortion ( $\Theta$ ) and shape values in  $\text{Fe1N}_6$  are larger than in  $\text{Fe2N}_6$ . Especially, the value of the trigonal distortion angles in  $\text{Fe1N}_6$  ( $\Theta = 231^\circ$ ) is much larger than that in  $\text{Fe2N}_6$  ( $\Theta = 199^\circ$ ). This might be due to the differences in the ligands conformation and might explain why Fe1 does not experience spin crossover, in agreement with the fact that strong distortion favors the HS state. The Fe-NC-S angles are  $170.13^\circ$  and  $161.96^\circ$  in Fe1 molecule, and  $156.97^\circ$  and  $160.96^\circ$  in Fe2 molecule describing less linear  $\text{NCS}^-$  groups in Fe2. However, they are bending towards each other leading to a shorter S3---S4 (6.058 Å) distance in Fe2 compare to S1---S2 (7.859 Å) in Fe1 motif. In order to describe the N-Fe-N angles, here,  $\sigma_1$  is defined with nitrogen coming from imine groups, and  $\sigma_2$  with nitrogen coming from pyridine. In addition  $\sigma_3$  is defined as the dihedral angle between the phenyl and pyridine rings of one ligand, in order to show its possible change in planarity. These definitions of  $\sigma_1$ ,  $\sigma_2$  and  $\sigma_3$  apply in all the thesis. The deviation of  $\sigma_1$  and (SC)N-Fe-N(CS) angles from the expected  $90^\circ$  in a perfect octahedron clearly shows that Fe1 is much more distorted than Fe2. On the other hand, the difference in  $\sigma_2$  values translates the *cis* conformation of the ligand in Fe2 compare to the *trans* one in Fe1. In the *trans* stereoisomer Fe1, the planarity of the ligands described by  $\sigma_3$  is higher than in Fe2 to avoid short atom-atom contacts. Moreover, in Fe2, one ligand presents a  $\sigma_3$  of  $89.12^\circ$  illustrating the orthogonality between the fluoro-phenyl and pyridine rings. Apparently, this high bending of  $\text{NCS}^-$  does not favor the inactive of SCO. The ligand filed is depending not only on the bending

of NCS<sup>-</sup> but also on the conformation of PM-*m*FA ligands. Here, the small value of  $\sigma_3$  in Fe1 site indicates that planarity of the ligands favors the weak ligand field.

**Table II.3.** The coordination sphere parameters in complex **I-*m*FA**.

Compound	<b>I-<i>m</i>FA</b>			
	300	300	100	100
Temperature / K	300	300	100	100
Fe <sup>2+</sup> site	Fe1	Fe2	Fe1	Fe2
<Fe-N> / Å	2.180(5)	2.160(5)	2.171(4)	1.960(4)
$\zeta$ / Å	0.405	0.32	0.388	0.058
$\Sigma$ / °	92	71	91	41
$\Theta$ / °	231	199	237	133
Shape <sup>b</sup>	1.529	0.977	1.596	0.387
(SC)N-Fe-N(CS) / °	100.2	92.8	100.12	88.59
$\sigma_1$ / °	76.98	88.58	77.15	93.52
$\sigma_2$ / °	162.09	90.51*	162.10	92.93*
$\sigma_3$ / °	49.76 / 45.59	49.84 / 89.12	49.38 / 46.23	54.72 / 86.35

\*pyridine in *cis*. <sup>a</sup> values obtained using the OctaDist program (<https://octadist.github.io>). <sup>b</sup> values obtained using the SHAPE program (ref.10)

At 100 K, the average Fe1-N distance (<Fe1-N) becomes 2.171(4) Å, which slightly decreases compared to 2.180(5) Å at 300 K. The distortion parameters  $\zeta$  and  $\Sigma$  decrease a little while  $\Theta$  and shape increase a little from 300 K to 100 K. The tiny variation of distortion parameters result from the small variation in  $\sigma_1$ ,  $\sigma_2$  and  $\sigma_3$ , which agrees well with the observed small RMSD value. Concerning Fe2, all distortion parameters ( $\zeta$ ,  $\Sigma$ ,  $\Theta$ , shape) are smaller at 100 K than at 300 K, owing to SCO. Indeed, the  $\Theta$  value is 133° at 100 K, leading to the variation of trigonal distortion angles ( $\Delta\Theta$ ) of 66°. This variation is mainly due to the decrease of (SC)N-Fe-N(CS) angle, which corresponds to the motion of NCS<sup>-</sup> groups (Figure II.7b).

All these motions have necessary an impact on the intermolecular interactions. Figures II.9a and b, show the fingerprints and Hirshfeld surfaces<sup>11</sup> calculated by the CrystalExplorer software<sup>12</sup>. There are huge differences in the fingerprint shapes of the two molecules within the packing. At 300K, the ratio of F---H in Fe1 molecules (13.3%) is much higher than in Fe2 (8.6 %), meaning stronger F---H hydrogen bonding around Fe1 molecules (Figure II.9c). An important contribution to the intermolecular interactions comes from the S---H bonding, with rather similar contributions around both molecules (25.5% for Fe1 and 22.0% for Fe2). The ratio of the C---C distances, that usually corresponds to the  $\pi$ --- $\pi$  interaction, are similar and around 3.4 Å in both molecules. Moreover, no F---F and F---S short contacts can be evidenced in the fingerprints.

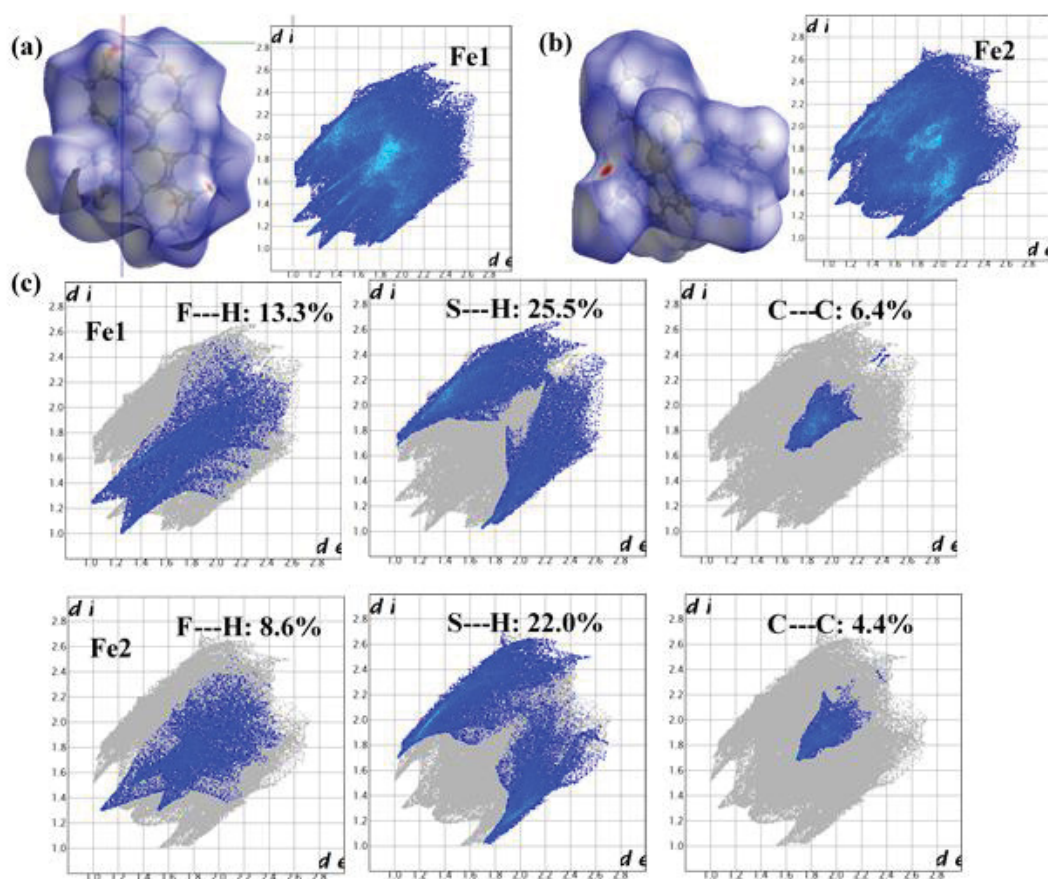


Figure II.9. The fingerprints and Hirshfeld surface for Fe1 (a) and Fe2 (b) molecules and selected contacts in fingerprints around both sites (c) of the complex **I-mFA** at 300K.

Guided by Hirshfeld surfaces, the hydrogen bonding around Fe1 and Fe2 at 300 K are shown in Figures II.10a and b, respectively. Adjacent Fe1 and Fe2 are linked by S2---H32 (2.917 Å) and  $\pi$ --- $\pi$  interactions along *a* direction or by F3---H5 (2.486 Å) around [10-1] (Figure II.10a). The  $\pi$ --- $\pi$  interactions can be demonstrated by the shape index of Hirshfeld surface<sup>11</sup> (Figure II.10c). The maps of shape index on the Hirshfeld surface can be used to identify complementary hollows (red) and bumps (blue) where two molecular surfaces touch one another. These patterns of red and blue triangles on the shape index surface are diagnostic for close C/C interplanar contacts. More details of Hirshfeld surfaces can be seen in Appendix 1. Two S4---H44 (2.896 Å) connect adjacent Fe2 with an inversion center and S4---H40 (3.113 Å) connects adjacent Fe2 with a two-fold axis parallel to the *b* axis (Figure II.10d). Fe1 molecules are connected through S1---H4 (2.881 Å) along the *b* axis, giving rise to a two-fold axis (Figure II.10d). Along the *c* axis, Fe1 connect through the F1---H1 (2.360 Å) bonding.

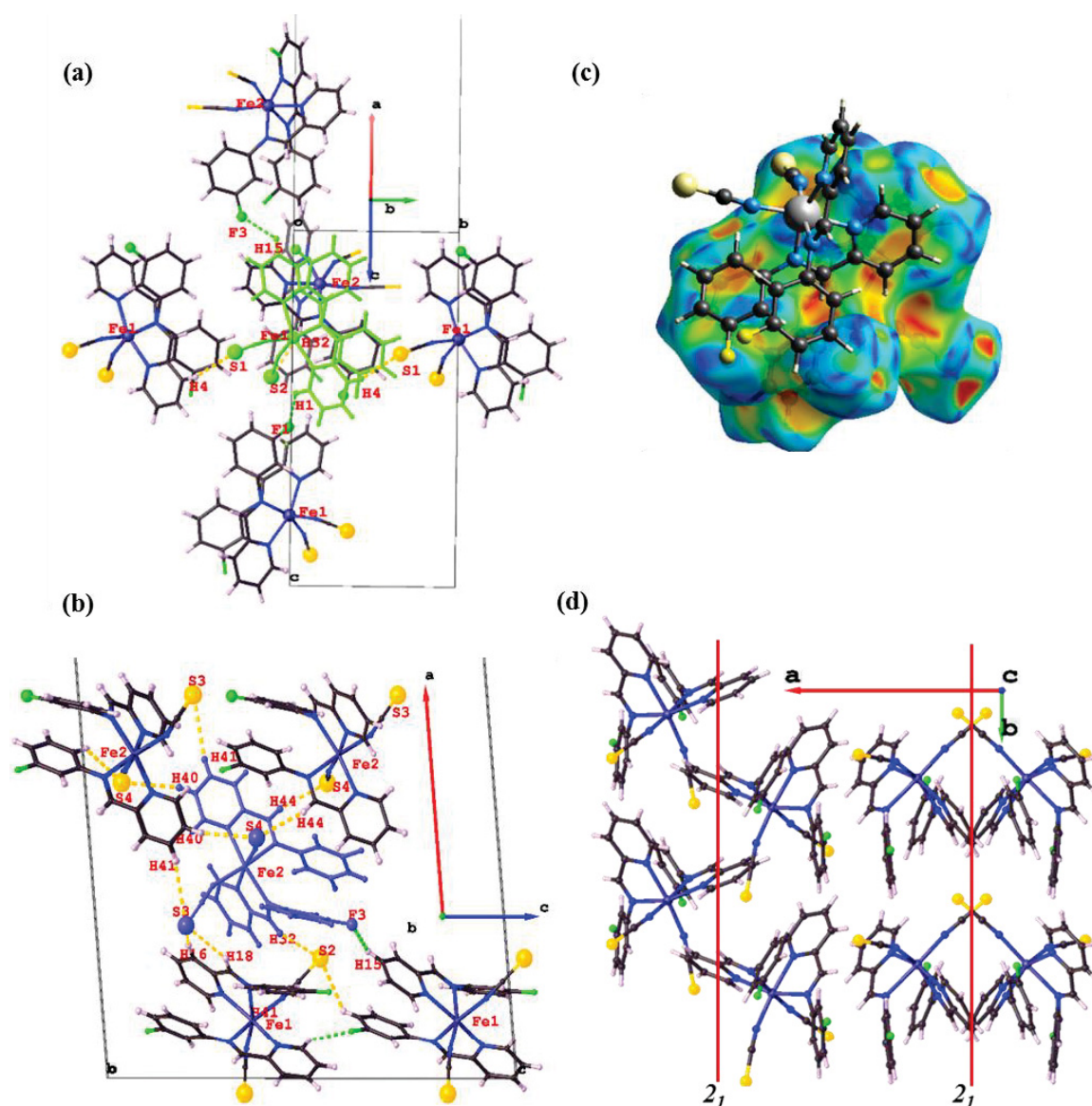


Figure II.10. Pictures of the hydrogen bonding around Fe1 (a), Fe2 (b) molecules, the weak  $\pi$ - $\pi$  interaction (c) between Fe1 and Fe2 evidenced by the shape index of Hirshfeld surface<sup>11</sup>, and the crystal packing (d) of the complex **I-mFA** at 300 K.

The molecular 3D packing is shown in Figure II.11a with symmetry elements. Along the *a* axis, double layers of Fe1 or Fe2 arrange alternately, leading to eight molecules along the *a* direction of the unit cell. This can explain the observed large value of the *a* parameter as mentioned above (Table II.2) that is quite uncommon for this family of molecular complexes.

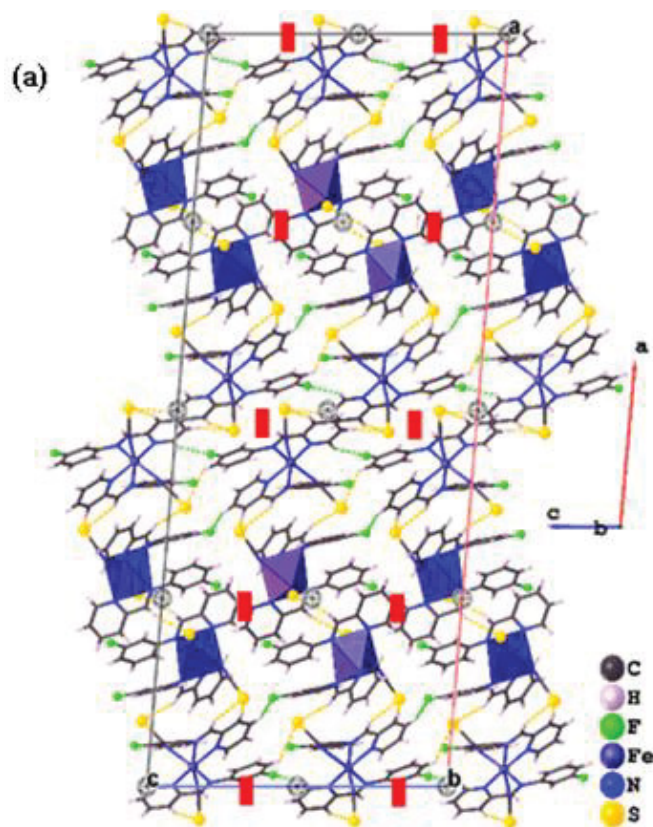


Figure II.11. Pictures of the crystal packing the complex **I-mFA** at 300 K. Black sphere and red bold line means the inversion center and  $2_1$  axis, respectively.  $\text{Fe}_2\text{N}_6$  polyhedra are in blue.

At 100 K, the fingerprints of the two molecules shown in Figures II.12a and b are very different for the two molecules, but rather similar compare to the 300 K plots. The important contribution to the intermolecular interactions comes from S---H bonding, with rather similar contributions around both molecules (Figures II.12c and d). The ratio of the selected S---H, F---H and C---C distances in Fe1 are higher than in Fe2. Compared with fingerprints at 300 K, the variation of S---H in Fe1 fingerprint decrease by 1.1% while it increases by 0.9% in Fe2, which might be due to the motion of the  $\text{NCS}^-$  groups in Fe2 at SCO. The ratio of F---H in the fingerprints slightly decrease from 13.3% to 12.9% for Fe1 and from 8.6% to 8.1% for Fe2.

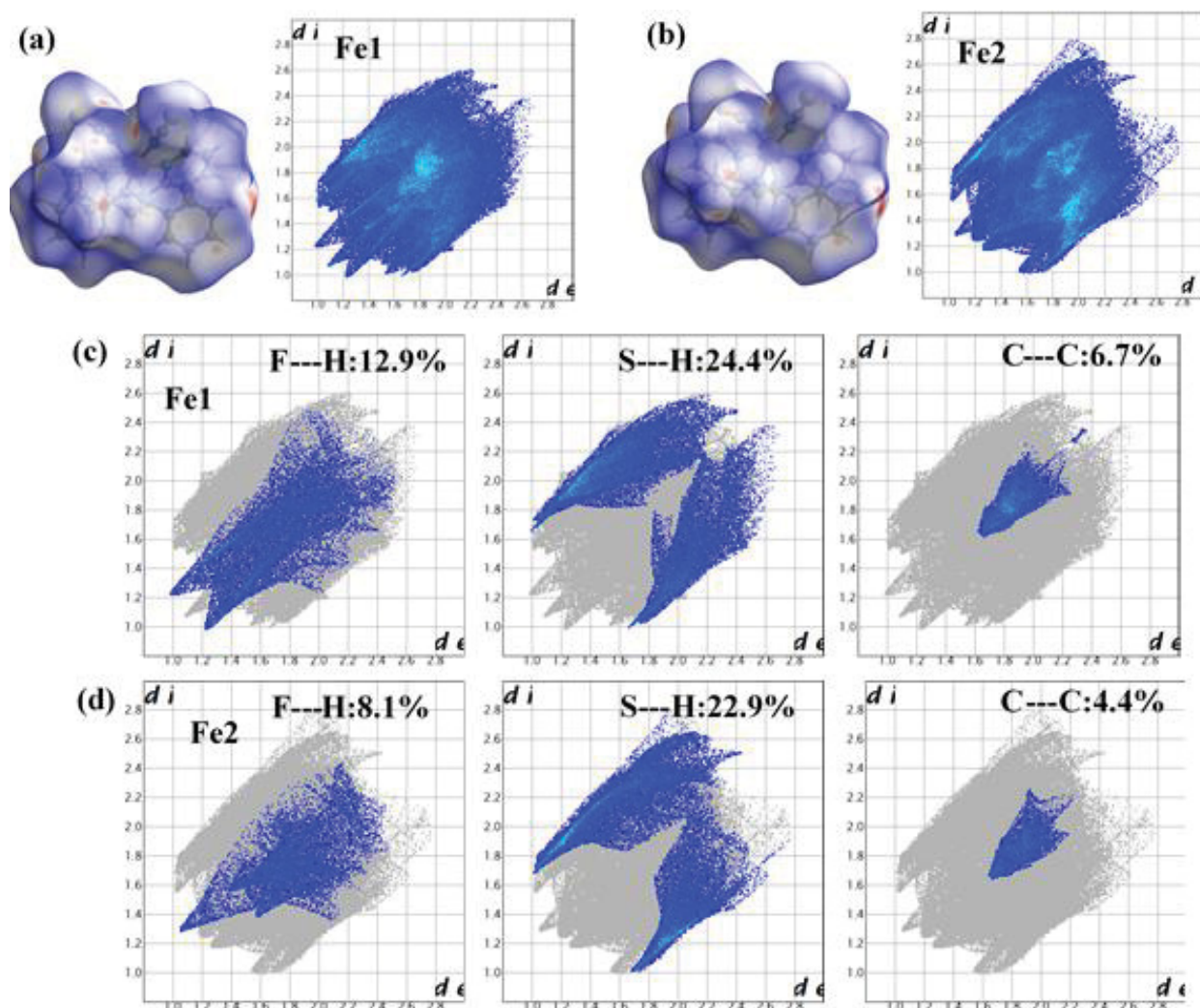


Figure II.12. The fingerprints and Hirshfeld surface for Fe1 (a) and Fe2 (b) and the selected contacts in fingerprints Fe1 (c) and Fe2 (d) of the complex **I-mFA** at 100K.

Guided by Hirshfeld surfaces, the hydrogen bonding around Fe1 and Fe2 at 100 K are detailed in Figure II.13a and b, respectively. Adjacent Fe1 and Fe2 are linked by S2---H32 (2.875 Å) and  $\pi$ --- $\pi$  interactions along *a* direction or by F3---H15 (2.440 Å) around [10-1] (Figure II.13a). Two S4---H44 (2.839 Å) connect adjacent Fe2 with an inversion center and S4---H40 (2.871 Å) connect adjacent Fe2 with a two-fold axis parallel to the *b* axis (Figure II.13d). Fe1 molecules are connected through S1---H4 (2.789 Å) along the *b* axis, giving rise to a two-fold axis (Figure II.13d). Along the *c* axis, Fe1 molecules connect through F1---H1 (2.298 Å). The resulting molecular packing is shown in Figure II.13a with symmetry elements and blue octahedral Fe2N<sub>6</sub>, which is quite similar to 300 K. Along the *a* axis, there is a long-range ordering of HS-HS-LS-LS motif.

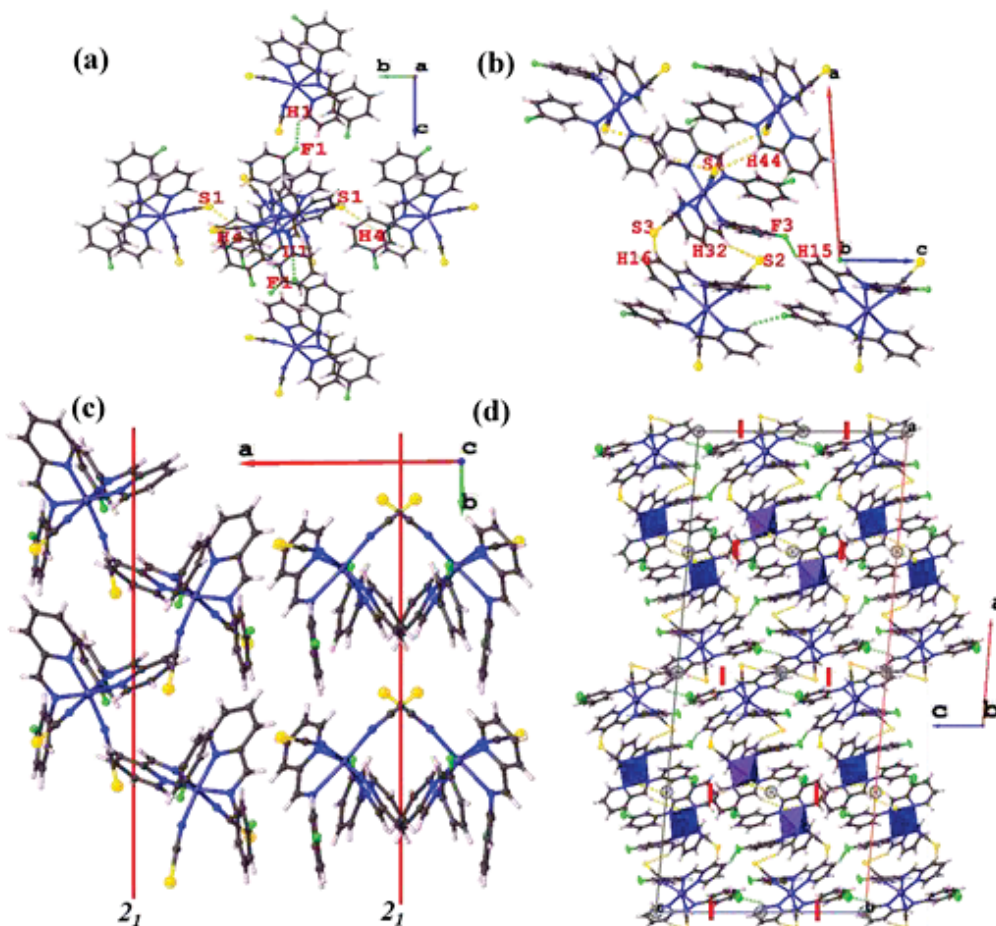


Figure II.13. The interactions around Fe1 (a) and Fe2 (b), molecular packing at  $ab$  plane (c), and 3D packing (d) of the complex **I-mFA** at 100K. The molecules with blue octahedral are Fe2.

- *Structure-properties relationship of I-mFA*

Two crystallographically independent molecules are present in complex **I-mFA**, with totally different ligand conformations. Indeed, one of the peculiar point of this compound, from the structural point of view, is the half-half mixture of *cis* and *trans* molecular complexes within the crystal packing. This feature is quite rare in  $\text{Fe}^{2+}$  SCO compounds. Upon thermal treatment: Fe1(*trans*) is spin crossover inactive while Fe2(*cis*) shows a complete SCO. The fact that Fe1 does not undergo a SCO can be linked to the huge distortion of the  $\text{Fe1N}_6$  coordination sphere at 300 K. The whole results in an incomplete SCO, as confirmed by magnetic measurements, with a switching temperature  $T_{1/2}$  of 215 K. Moreover, a weak LIESST effect (<10%) was recorded leading to a  $T(\text{LIESST})$  value around 32 K. This places this compound on the  $T_0 = 100$  K line of the  $T(\text{LIESST})$  vs  $T_{1/2}$  database (Figure I.9 in Part I), as most of the PM-L compounds, except **I-S-BiA**.<sup>1,3</sup>

### II.3.3. $[\text{Fe}(\text{PM-}p\text{FA})_2(\text{NCS})_2] \cdot n\text{CHCl}_3$ (**I-}p\text{FA}**)

- *Magnetic properties of I-}p\text{FA}*

Magnetic measurements were performed on polycrystalline samples, using a SQUID magnetometer (Appendix 3). Figure II.14 reports the thermal evolution of the  $\chi_M T$  product of **I-}p\text{FA}**. The  $\chi_M T$  value at 300 K of  $3.31 \text{ cm}^3 \text{ K mol}^{-1}$  agrees well with a HS  $\text{Fe}^{2+}$  ion ( $g = 2.10$ ). Upon cooling, the  $\chi_M T$  product decreases to reach a value of  $0.31 \text{ cm}^3 \text{ K mol}^{-1}$  at 10 K, indicating a gradual and almost complete SCO, without any hysteretic behavior. In the differentiate curve (Figure II.14), the presence of two maxima indicates a two-step character of the spin crossover, with switching temperatures close to 140 K and 100 K. This behavior is reproducible.

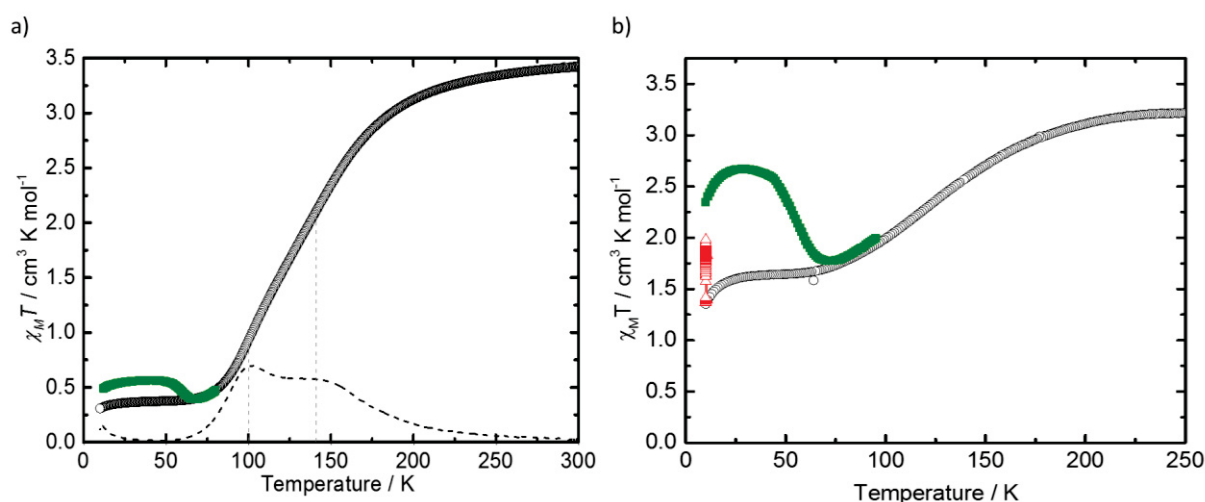


Figure II.14. Thermal dependence of the  $\chi_M T$  product of **I-}p\text{FA}** recorded at 0.4 K/min (in settle mode) under 10 kOe of applied magnetic field. The dotted curve in (a) is the derivative of the SCO curve, whose maxima indicate the switching temperatures. The green curve stands for the  $T(\text{TIESST})$  (a) and  $T(\text{LIESST})$  (b) measurements described in the text.

When a sample is quickly cooled at 10 K in the SQUID (several tens of seconds), the HS\* state may be quenched totally or partially. It is called the Thermal-Induced Excited Spin-State Trapping, in analogy to the LIESST process. A  $T(\text{TIESST})$  curve can be recorded then afterward, following the same protocol as for the  $T(\text{LIESST})$  measurement, leading to the determination of the  $T(\text{TIESST})$  relaxation temperature. Let us note that the Q-HS\* obtained by thermal quenching and the  $h\nu$ -HS\* obtained by light irradiation might be different in some cases<sup>14-15</sup>. The green curve presented in Figure II.14 corresponds to the  $T(\text{TIESST})$  curve for this compound. Only a few percent of the quenched HS can be trapped, leading to a  $T(\text{TIESST})$  value of 57 K.

When the sample was prepared for photomagnetic measurement, the full SCO was not recovered, even after several tries. [Figure II.14b](#) reports the incomplete SCO curve recorded in the SQUID indicating that the sample has evolved, probably due to a loss of solvent. Light irradiation at 830 nm and 10 K was applied anyway and the  $T(\text{LIESST})$  was recorded giving a value of 55 K, close to the  $T(\text{TIESST})$  value recorded.

- *Crystallographic investigation of I-pFA*

The structure of **I-pFA** was determined by SCXRD at 300 K and 100 K. Due to the large unit-cell volume and the weak intensity of SCXRD peaks, the final structural refinement is good but not excellent as shown by relatively high values of  $wR_2$ . As seen in [Table II.4](#), complex **I-pFA** crystallizes in the trigonal system with space group  $R\bar{3}$  at 300 K. All atoms site on the general Wyckoff position (18f). One can notice the huge unit cell with a volume of 30177(9) Å<sup>3</sup>, which already makes this compound as quite peculiar in this family of SCO complexes and, as a general matter, in Fe<sup>2+</sup> SCO complexes.

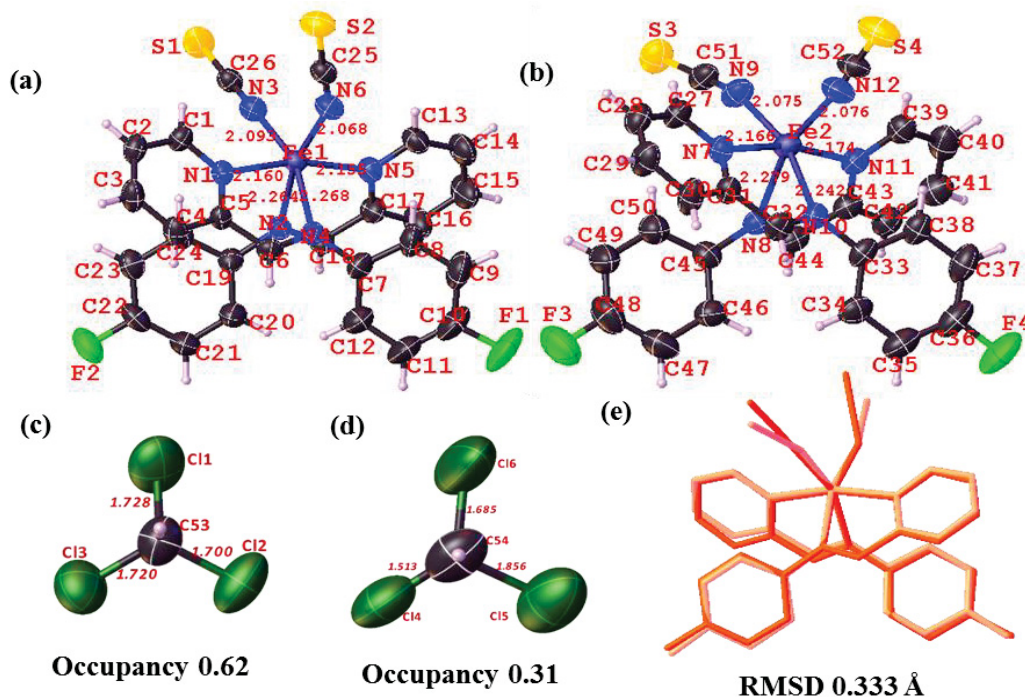
At 300 K, there are two independent Fe<sup>2+</sup> complexes and two chloroform molecules in the asymmetric unit ([Figure II.15](#)). The two Fe<sup>2+</sup> molecular complexes are labelled Fe1 and Fe2 hereafter. Both molecules are made of two thiocyanate groups adopting a *cis* configuration with two other bidentate ligands coordinated to the Fe<sup>2+</sup> ions. These two ligands adopt a conformation with the pyridine groups in *trans* position, similar to the Fe1 site in complex **I-mFA**. The NCS<sup>-</sup> groups are bent in Fe1 and Fe2, with S1-NC-Fe1, S2-NC-Fe1, S3-NC-Fe2 and S4-NC-Fe2 angles of 150.25°, 177.37°, 161.29°, and 158.84°, respectively. The average Fe-N bond lengths ( $\langle\text{Fe-N}\rangle$ ) are 2.164(5) Å and 2.165(6) Å for Fe1 and Fe2 ([Figure II.15](#) and [Table II.5](#)), respectively, which are typical for Fe<sup>2+</sup> in HS state, agreeing with the magnetic measurement. Moreover, the RMSD value resulting from the overlay of Fe1 and Fe2 molecules is high (0.333 Å), the main difference originates from the bending and orientation of NCS<sup>-</sup> groups. In the asymmetric unit, the two chloroform are partially occupied with crystallographic occupancies of 0.62 and 0.31, respectively. Since all atoms site on the general Wyckoff position, the average value of solvent per molecular complex is 0.47, which is the average value of 0.62 and 0.31 for the two sites. So the final experimental formula is [Fe(PM-*p*FA)<sub>2</sub>(NCS)<sub>2</sub>].0.47CHCl<sub>3</sub> at 300 K.

Table II.4. Crystal data and structure refinement data for complex I-pFA.

Empirical formula	C <sub>26.47</sub> H <sub>18.47</sub> Cl <sub>1.39</sub> F <sub>2</sub> FeN <sub>6</sub> S <sub>2</sub> n = 0.47	C <sub>26.32</sub> H <sub>18.32</sub> Cl <sub>0.97</sub> F <sub>2</sub> FeN <sub>6</sub> S <sub>2</sub> n = 0.32
Formula weight / g mol <sup>-1</sup>	627.82	611.09
Temperature / K	300	100
Radiation MoK $\alpha$ / Å		$\lambda = 0.71073$
Crystal size / mm <sup>3</sup>	0.26×0.10×0.08	0.24×0.20×0.10
Crystal system		Trigonal
Space group		R-3
<i>a</i> = <i>b</i> / Å	29.096(3)	28.395(3)
<i>c</i> / Å	41.160(8)	40.729(5)
Volume / Å <sup>3</sup>	30 177(9)	28 439(8)
Z-formula	36	36
$\rho_{\text{calc}}$ / g cm <sup>-3</sup>	1.244	1.285
$\mu$ / mm <sup>-1</sup>	0.720	0.728
F(000)	11 481.0	11 188.0
2 $\theta$ range for data collection / °	1.894 - 55.284	2.596 - 51.67
Index ranges	-35 ≤ <i>h</i> ≤ 35, -33 ≤ <i>k</i> ≤ 35, -50 ≤ <i>l</i> ≤ 35	-34 ≤ <i>h</i> ≤ 32, -34 ≤ <i>k</i> ≤ 34, -49 ≤ <i>l</i> ≤ 49
Reflections collected	44 249	81 001
Independent reflections	14 640 [R <sub>int</sub> = 0.0346, R <sub>sigma</sub> = 0.0456]	12 112 [R <sub>int</sub> = 0.1333, R <sub>sigma</sub> = 0.1118]
Data/restraints/parameters	14 640/0/739	12 112/2/723
Goodness-of-fit on F <sup>2</sup>	1.166	1.075
Final R indexes [ <i>I</i> ≥ 2 $\sigma$ ( <i>I</i> )]	R <sub>1</sub> = 0.0935, wR <sub>2</sub> = 0.2627	R <sub>1</sub> = 0.0862, wR <sub>2</sub> = 0.2317
Final R indexes [all data]	R <sub>1</sub> = 0.1618, wR <sub>2</sub> = 0.3405	R <sub>1</sub> = 0.1735, wR <sub>2</sub> = 0.2942
Largest diff. peak/hole / e Å <sup>-3</sup>	1.74/-0.66	1.77/-0.58

$$R_1 = \frac{\sum ||F_0| - |F_c||}{\sum |F_0|}, wR_2 = \left[ \frac{\sum w(F_0^2 - F_c^2)^2}{\sum w(F_0^2)^2} \right]^{1/2}$$

Part II – Promoting Distortion of the Coordination Polyhedron by Steric Strain: Fluorine Substitution of PM-*z*FA Family



**Figure II.15.** The Fe1 (a), Fe2 (a) and two chloroform molecules (c, d) in the asymmetric unit, and the overlay of two Fe<sup>2+</sup> complexes (e) in complex **I-pFA** at 300 K. The red and pink represent Fe1 and Fe2 molecules, respectively.

Upon cooling at 100 K, complex **I-pFA** remains in the same *R*-3 space group with smaller unit-cell parameters compared to the ones at 300 K (Table II.4). There are still two Fe<sup>2+</sup> complexes with similar conformations of the complexes as the ones at 300 K and two partially occupied chloroform molecule sites in the asymmetric unit, with one chloroform refined without anisotropy. As seen in Figure II.16a and Table II.5, the average values of Fe-N distances are 2.032(6) Å and 1.970(6) Å for Fe1 and Fe2 molecules, respectively, which suggests a partial HS to LS conversion for Fe1 (~65% LS) and a fully LS state for Fe2. This is reasonably consistent with the  $\chi_M T$  value (0.85 cm<sup>3</sup> K mol<sup>-1</sup>) that suggest 25% HS from magnetic measurement.

From the superposition of molecules at 100 K and 300 K (Figure II.16b), the RMSD values are 0.156 Å for Fe1, and 0.205 Å for Fe2, respectively. The contribution to the RMSD mainly comes from the atomic displacement of NCS<sup>-</sup> groups. The smaller RMSD value for Fe1 compared to Fe2 is due to the incomplete SCO. Two chloroform molecules in the asymmetric unit are disordered with crystallographic occupancies of 0.48 and 0.17, respectively. Since all atoms site on the general Wyckoff position, this leads to  $n = 0.32$  in the formula. The later value is the average value of 0.48 and 0.17 corresponding to the two crystallographically independent chloroform sites. So the final experimental formula is [Fe(PM-*p*FA)<sub>2</sub>(NCS)<sub>2</sub>]·0.32CHCl<sub>3</sub> at 100 K.

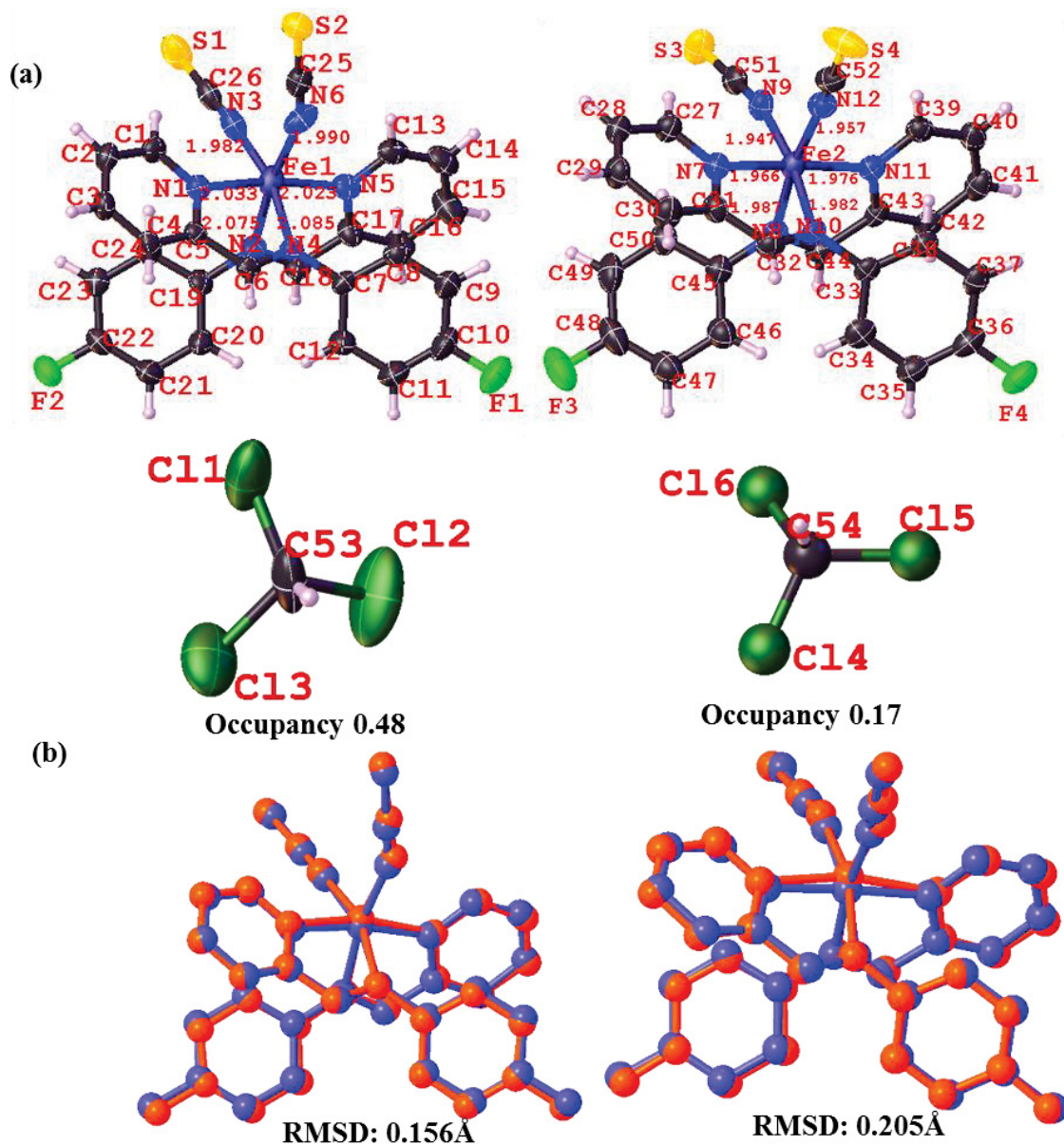


Figure II.16. Fe1, Fe2 and two chloroform molecules in the asymmetric unit at 100 K (a), and the superposition of Fe1 (left), Fe2 (right) molecules between 300 K (red) and 100 K (blue) with RMSD values (b) for complex **I-pFA**.

The smaller amount of solvent molecule at low temperature compared to room temperature might come from the high volatility of the chloroform that could have been removed by the cooling nitrogen flux as well as by the time to perform the two experiments.

From the structure obtained from SCXRD, we can simulate the PXRD pattern of this compound and compare it to the experimental one (Figure II.17). The relatively low crystallinity of the powder does not allow to definitively state that powder and single-crystal own the same crystal structure. However, all observed peaks (excepted one that is at the limit

of observation) on the powder pattern coincide with expected ones. The PXRD patterns could be different because the use of crystals can induce orientation effects and then differences in peak intensities. Therefore, though many expected peaks are not observed, it is highly probable that powder and single-crystals are very close in nature; as it is confirmed by the similitude between magnetic (powder based) SCO features and structural features (single-crystal based).

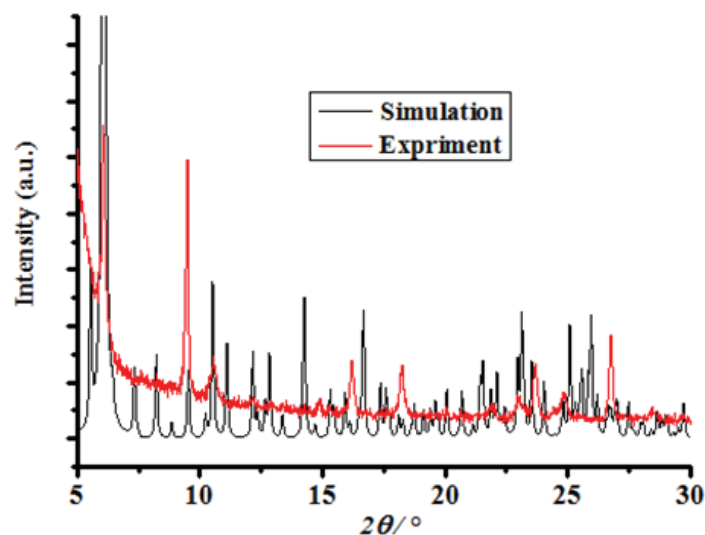


Figure II.17. Experimental and simulated X-ray powder diffraction patterns of complex **I-pFA**. The simulation pattern (black) comes from the experimental single-crystal XRD data.

Table II.5. The coordination sphere parameters of complex **I-pFA**.

Compound	<b>I-pFA.</b>			
Temperature / K	300	300	100	100
Fe <sup>2+</sup> site	Fe1	Fe2	Fe1	Fe2
<Fe-N> / Å	2.164	2.165	2.032	1.970
ζ / Å	0.379	0.409	0.198	0.074
Σ / °	85	84	64	57
Θ / °	237	234	180	172
Shape <sup>b</sup>	1.473	1.284	0.830	0.607
(SC)N-Fe-N(CS) / °	98.43	103.34	93.78	95.77
σ <sub>1</sub> / °	78.22	78.73	82.88	84.72
σ <sub>2</sub> / °	166.52	167.48	171.40	176.81
σ <sub>3</sub> / °	46.81 /	52.49 /	50.96 /	60.19 /
	38.28	45.22	42.09	48.99

σ<sub>1</sub>: N-Fe-N with N from imine; σ<sub>2</sub>: N-Fe-N with N from pyridine; σ<sub>3</sub>: dihedral angle of phenyl and pyridine in one ligand. <sup>a</sup> values obtained using the OctaDist program (<https://octadist.github.io>). <sup>b</sup> values obtained using the SHAPE program (ref.10).

**Table II.5** reports the calculated distortion parameters for FeN<sub>6</sub> polyhedra at 300 K and 100 K. At 300 K, the angular ( $\Sigma$ ) and trigonal ( $\Theta$ ) distortions for both Fe1 and Fe2 are around 85° and 237°, respectively. There are no huge differences in the bond distortion ( $\zeta$ ) and shape values of Fe1N<sub>6</sub> and Fe2N<sub>6</sub>. At 100 K,  $\Sigma$  and  $\Theta$  are 64° and 180° for Fe1, and 57° and 172° for Fe2, respectively, which corresponds to the fully LS state for Fe2 and incomplete LS state for Fe1. The variation of  $\zeta$ ,  $\Sigma$ , and  $\Theta$  are very close for both Fe<sup>2+</sup> sites, but different enough to delay the SCO of Fe1 compare to Fe2.

As show in **Figures II.18a** and **b**, there are no huge differences in the shape of fingerprints of the two Fe molecules. In the Hirshfeld surfaces, the short contacts (red spots) are mainly around NCS<sup>-</sup> groups and pyridine ring, which agrees well with the high ratio of S---H interactions in fingerprints, above 20 % (**Figure II.18e**). Another short contact is the F---H interactions that contribute to around 15 % to the fingerprints. The ratio of C---C interactions, which usually corresponds to  $\pi$ --- $\pi$  interaction, are very similar for both molecules and around 6 %, The sharp stripe around 1.0 Å suggests possible H---H contacts with H coming from pyridine. Compared to the shape of fingerprint of complex **I-mFA**, the contacts appear at longer distances, even above 2.8 Å ( $d_i$  and  $d_e$ ) in fingerprints, which results from the S---H and F---H with H coming from the solvent. It means the the solvent tends to separate the Fe<sup>2+</sup> sites with Fe---Fe distances of 13.197 Å (Fe1---Fe1) and 12.305 Å (Fe2---Fe2) in **I-pFA** compared to 10.935 Å (Fe1---Fe1) and 11.355 Å (Fe2---Fe2) in **I-mFA**.

Concerning the solvent sites, there are huge differences in the fingerprints of the two chloroform molecules (**Figures II.18c** and **d**). The shortest contact for C(53)HCl<sub>3</sub> is S4---H53 (2.813 Å) while the shortest one for C(54)HCl<sub>3</sub> is Cl5---Cl6 (2.139 Å). Three C(54)HCl<sub>3</sub> solvents linked together, form a crown ring. The ratio of Cl---H contact is near 50% in both solvent.

The calculated Hirshfeld surfaces and fingerprints of the sample cooled at 100 K are shown in **Figure II.19**. Compared with 300 K, there are no huge differences in the shape of fingerprints for Fe1, Fe2 and solvent molecules. The shortest contacts of Cl5---Cl6 and S4---H53 are 1.913 Å and 2.432 Å, respectively, shorter than at 300 K. The ratio of F---H and S---H interactions are almost the same as that at 300 K, however, the shape of S---H is different in Fe1. The ratio of C---C slightly decreases. The sharp stripe below 1.0 Å suggests the possible H---H contacts, where hydrogen atoms come from pyridine rings.

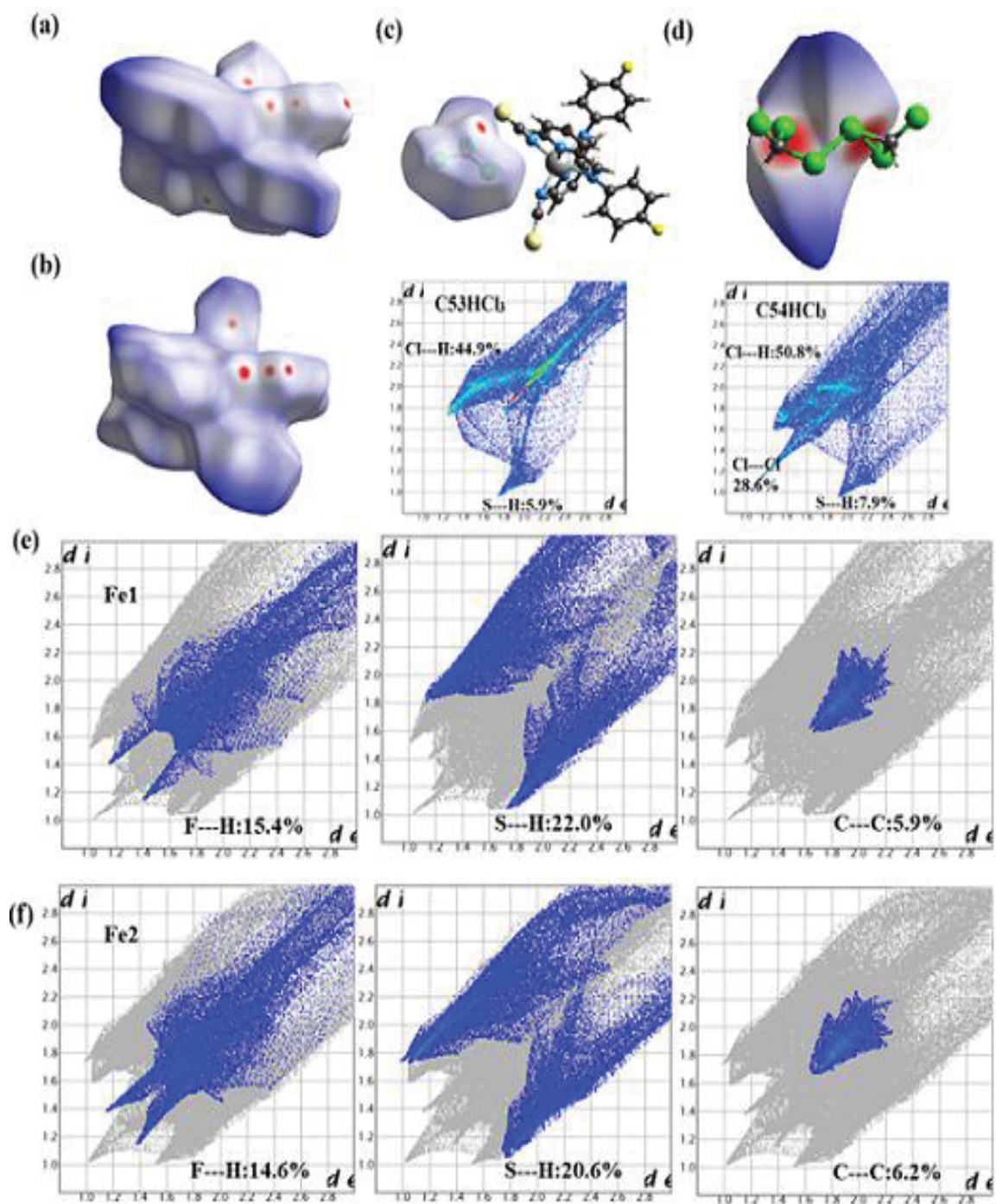


Figure II.18. The fingerprints and Hirshfeld surfaces for Fe1 (a), Fe2 (b), the C(53)HCl<sub>3</sub> (c), the C(54)HCl<sub>3</sub> solvents (d), and selected contacts in fingerprints of Fe1 (e) and Fe2 (f) the complex **I-pFA** at 300 K.

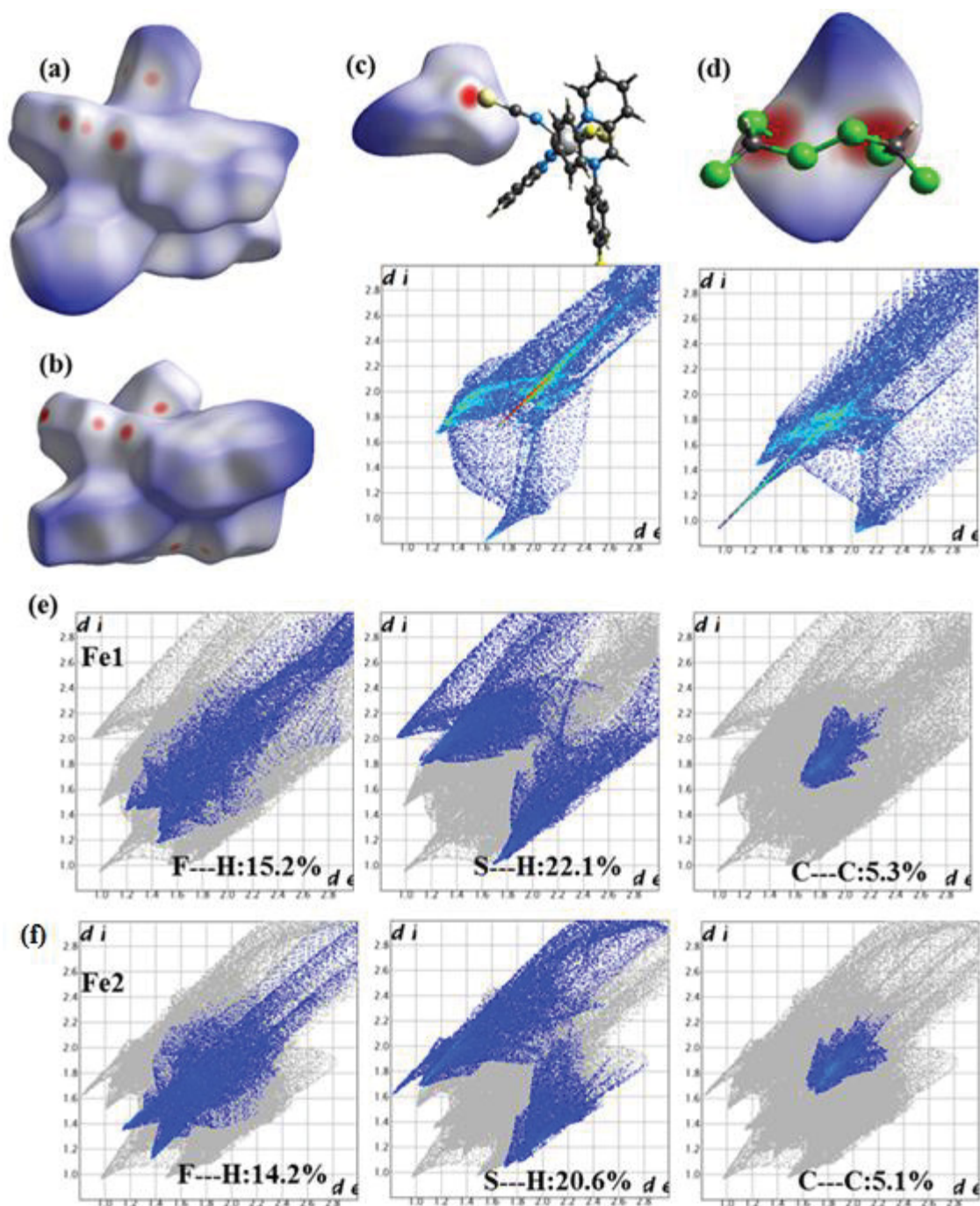


Figure II.19. The fingerprints and Hirshfeld surfaces for Fe1 (a), Fe2 (b), C(53)HCl<sub>3</sub> (c), C(54)HCl<sub>3</sub> solvent (d) and selected contacts in fingerprints of Fe1 (e) and Fe2 (f) of the complex I-*p*FA at 100 K.

As shown in Figure II.20a, six Fe2 are connected to each other by S4---H50 (2.983 Å) and S4---H49 (3.002 Å), forming a hole with diameter around 12 Å in *ab* plane. Sulfur and fluorine atoms are inside and outside the hole, respectively. Six C(53)HCl<sub>3</sub> solvents are located in the hole with S4---H53 (2.813 Å) and S3---H53 (2.940 Å) hydrogen bonds. Also, in the *ab* plane, another hole with a 3-fold axis symmetry is built from by six Fe2 and three C(54)HCl<sub>3</sub> solvents

(Figure II.20b). Fluorine atoms are inside and sulfur atoms are outside the hole, respectively, in the opposite way compare to the other hole. The adjacent Fe2---Fe2 distance is 12.305 Å and the diameter of the hole is around 10 Å. The crown of three C(54)HCl<sub>3</sub> also connects three Fe1 by S1---H54 (2.962 Å) bonding. Hence, six Fe1 also form a hole with two crowns up and down (Figure II.20c). The diameter of the hole is around 10 Å. Except for the interactions between Fe<sup>2+</sup> and CHCl<sub>3</sub> molecules, Fe1 and Fe2 are connected by S4---H18(2.934 Å) along the *c* axis. In the *ab* plane, F1---H21 links two Fe1 together and F---H bondings (F4---H46: 2.683 Å; F4---H44: 2.784 Å) connect two Fe2 (Figure II.20d).

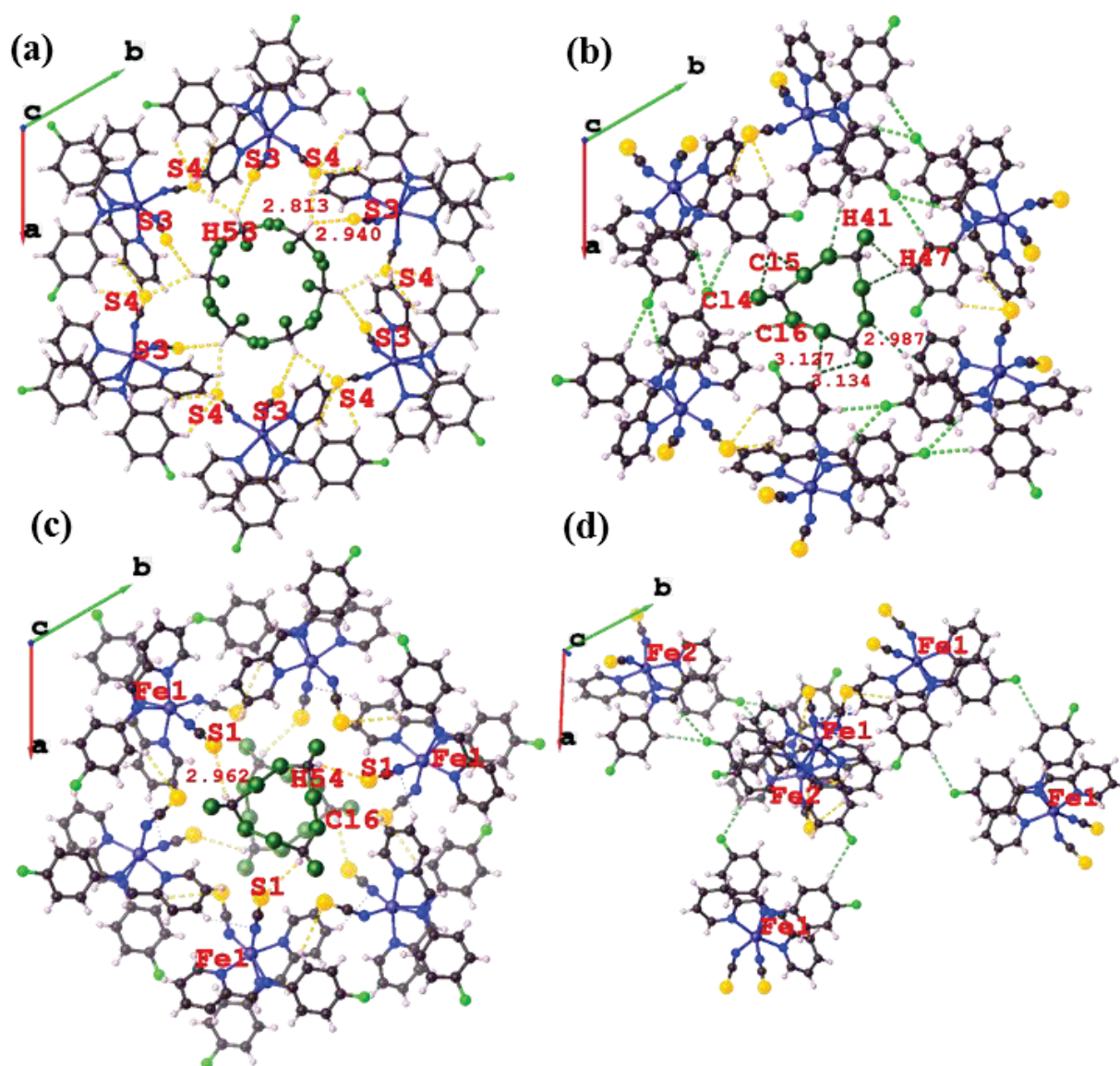
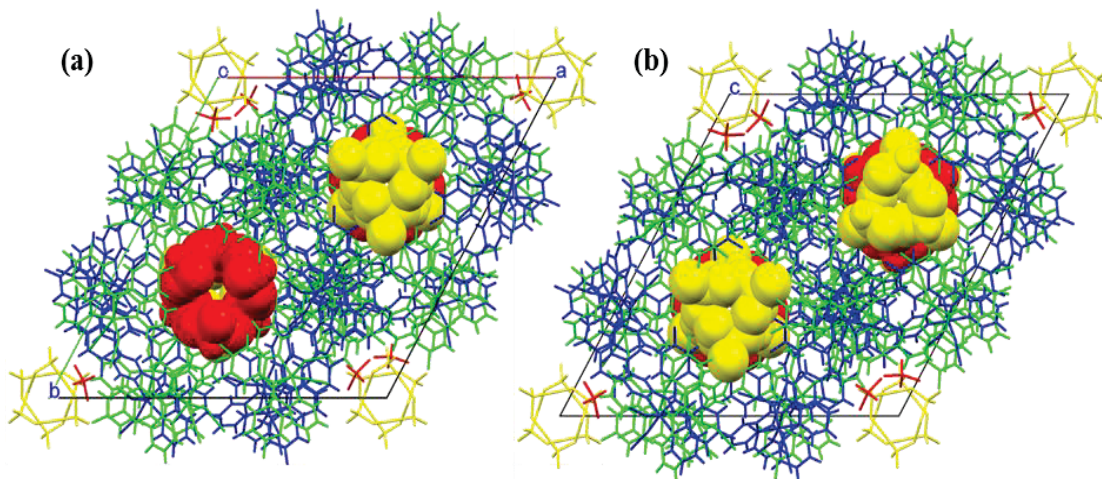


Figure II.20. View of the crystal packing enhancing the solvent position along *c* axis. Six-number rings of Fe2 with six C(53)HCl<sub>3</sub> (a), six-number rings of Fe2 with three C(54)HCl<sub>3</sub> (b), six-number rings of Fe1 with six C(54)HCl<sub>3</sub> (c), and the linkage of Fe<sup>2+</sup> molecules arrangement (d) of the complex **I-pFA** at 300 K.

So the 3D structure can be viewed as Fe1 and Fe2 layers alternately arranged along the  $c$  axis, where two types of disordered chloroform are located in the nanopore (Figure II.21). The molecular packing at 100 K is very similar to that at 300 K. Due to this 1D nano-channel along  $c$  axis, the density of single crystal at 300 K ( $1.244 \text{ g cm}^{-3}$ ) is smaller than **I-mFA** with the density of  $1.456 \text{ g cm}^{-3}$ . The gradual SCO may be related to the small density even though the short contacts of Cl---Cl exists between solvents. The observed density of **I-mFA** at 300 K is the smallest value in the  $[\text{Fe}(\text{PM-L})_2(\text{NCE})_2]$  ( $E = \text{S, Se}$ ) family.<sup>1-6</sup>



**Figure II.21.** The 3D packing model containing 1D channel with chloroform located of the complex **I-pFA** at 300 K (a) and 100 K (b). The yellow and the red spheres represent for the solvents. The green and blue sticks represent the Fe1 and Fe2, respectively.

- *Structure-properties relationship of I-pFA*

Compound **I-pFA** exhibits a two-step spin crossover that is consistent with the presence of two  $\text{Fe}^{2+}$  crystallographic sites within the crystal packing. The global feature of the SCO curve is gradual with steps at 100 K and 140 K. Since a partial HS to LS conversion for Fe1 (~65% LS) and a fully LS state for Fe2 at 100 K, the two steps character of the curve could have its origin in the different interaction networks adopted by each  $\text{Fe}^{2+}$  site, the solvent molecules being suspected to play an important role here. The two disordered chloroform molecules present in the asymmetric unit develop rather different connections within the crystal packing. The C(53)HCl<sub>3</sub> one only connects with Fe2 while the crown-shaped C(54)HCl<sub>3</sub> is linked to both Fe1 and Fe2 *via* S---H and Cl---H, respectively. When decreasing the temperature, Fe2 is more likely to experience the spin crossover first with a huge modification of S4---H53 distance. After that, Fe1 starts to switch upon further cooling, accompanied with the modification of Cl15---Cl16 and Cl16---H41. However, the gradual character of both steps, does not provide such clear picture of the steps.

*Part II – Promoting Distortion of the Coordination Polyhedron by Steric Strain: Fluorine Substitution of PM-zFA Family*

From 300 K to 100 K, the solvent is partially lost from 0.47 to 0.32 occupancy per iron within the crystal. This loss may be related to the experimental condition. Indeed, the possible loss of solvent at 300 K during the measurement as well as the nitrogen flow that cool the crystal during collecting data at 100 K might be responsible of this loss of solvent. It is therefore hard, if not imprudent to draw any conclusions from that loss. The incomplete SCO observed during the  $T(\text{LIESST})$  measurement (Figure II.14b) could have its origin in a partial loss of solvent upon time.

Regarding the the metastable HS\* state, it can be partially observed by thermal quenching and by LIESST effect, leading to  $T(\text{TIESST})$  and  $T(\text{LIESST})$  values of 57 and 55 K, respectively. No clear steps in the  $T(\text{TIESST})$  or  $T(\text{LIESST})$  curves could be observed as a reflect of the two-step character of the thermal SCO. This places this compound on the  $T_0 = 100$  K line of the  $T(\text{LIESST})$  vs  $T_{1/2}$  database (Figure I.9 in Part I), as most of the PM-L compounds, except **I-S-BiA**.

## II.4. Discussion on the structure-properties relationship of [Fe(PM-zFA)<sub>2</sub>(NCS)<sub>2</sub>]

Table II.6 summarizes the magnetic and structural features of the three fluorinated PM-L based complexes **I-oFA**, **I-mFA** and **I-pFA**. The structure of **I-oFA** is unknown due to the absence of single-crystal samples. Complexes **I-mFA** and **I-pFA** crystallize in different space groups with rather distinct unit-cell parameters, both exhibiting large unit-cell volume compared to usual ones for this family of compounds and both having a crystal packing based on two structurally independent iron sites. **I-mFA** shows an incomplete SCO around 215 K involving only one of the iron sites (Fe2), the other one remaining HS even at low temperature. Complex **I-pFA** displays a gradual two-step SCO with switching temperatures around 140 K and 100 K, one site being fully LS and one only partially at 100 K.

As mentioned before, in complex **I-mFA**, the pyridine rings are in *cis* configuration in Fe2 site and in *trans* configuration in Fe1 site. Let us notice that this is the first observation of a *cis* conformation of the pyridine units in this PM-L family. This *cis* ion displays a spin crossover. The other site exhibiting a usual *trans* conformation of the pyridine rings remains HS at low temperature. A closer look at the coordination sphere of these two sites shows that all the distortion parameters of the SCO active site in HS are smaller than the inactive site. This corroborates again the impact of very high distortion on the stabilization of the HS state. Since the conformation of the ligands are strongly different in both sites, one can wonder about the influence of the fluorine group on this distortion. For the SCO inactive site Fe1, the fluorine groups are at 5.654 Å and 5.650 Å from the Fe<sup>2+</sup> center. For the SCO active Fe2 site, the fluorine groups are at 6.526 Å and 6.273 Å from the Fe<sup>2+</sup> center, almost 1 Å farther than in Fe1. Therefore, even in *meta* position the fluorine atoms may exert a steric strain on the coordination, in that case preventing the SCO to occur.

Table II.6 Selected relevant structural and magnetic data of **I-oFA**, **I-mFA** and **I-pFA**.

Compound	<i>I-oFA</i>	<i>I-mFA</i>				<i>I-pFA</i>			
<i>SCO type</i>	Gradual	Gradual and incomplete				Gradual and two steps			
$T_{1/2} / K$	215	215				140/100			
$T(\text{LIESST}) / K$	55	32				55			
$T(\text{TIESST}) / K$	no	no				57			
<i>Space group</i>		<i>C2/c</i>				<i>R-3</i>			
<i>Temperature / K</i>	no single crystal by SCXRD	300		100		300		100	
$\text{Fe}^{2+}$ site		Fe1	Fe2	Fe1	Fe2	Fe1	Fe2	Fe1	Fe2
<i>Conformation of pyridine</i>		<i>trans</i>	<i>cis</i>	<i>trans</i>	<i>cis</i>	<i>trans</i>	<i>trans</i>	<i>trans</i>	<i>trans</i>
<i>Spin state</i>		HS	HS	HS	LS	HS	HS	65%LS	100%LS
$\langle \text{Fe-N} \rangle / \text{\AA}$		2.180	2.160	2.171	1.960	2.164	2.165	2.032	1.970
$\zeta / \text{\AA}$		0.405	0.32	0.388	0.058	0.379	0.409	0.198	0.074
$\Delta\zeta / \text{\AA}$		Fe1 : 0.017, Fe2 : 0.262				Fe1 : 0.181		Fe2 : 0.335	
$\Sigma / ^\circ$		92	71	91	41	85	84	64	57
$\Delta\Sigma / ^\circ$		Fe1 : 1, Fe2 : 30				Fe1 : 21		Fe2 : 27	
$\Theta / ^\circ$		231	199	237	133	237	234	180	172
$\Delta\Theta / ^\circ$		Fe1 : -6, Fe2 : 66				Fe1 : 57		Fe2 : 62	
<i>Shape (S)</i>		1.529	0.977	1.596	0.387	1.473	1.284	0.830	0.607
$\Delta S$		Fe1 : -0.067, Fe2 : 0.590				Fe1 : 0.643		Fe2 : 0.677	
$F\text{---}Fe / \text{\AA}$ (300 K)		F1-Fe1: 5.654, F2-Fe1: 5.650, F3-Fe2: 6.526, F4-Fe2: 6.273				F1-Fe1: 7.059 F3-Fe2: 7.052 F2-Fe1: 7.031 F4-Fe2: 6.945			

This gives some clues on the conformation of the ligands in complex **I-oFA**. If we only look at the spin crossover temperatures, we expect an increase with a weakening of the coordination sphere distortion. Since complex **I-oFA** show the same switching temperature than complex **I-mFA**, at first sight, the distortion should be the same in both. However, if we look at the position of these compounds on the  $T(\text{LIESST})$  vs  $T_{1/2}$  database, we mentioned that complex **I-oFA** lies on the  $T_0 = 120$  K line while complexes **I-mFA** and **I-pFA** lay on  $T_0 = 100$  K line. If the hypothesis of the increase of  $T_0$  related to an increase of  $\Delta\Theta$  is true, therefore one may expect a higher variation of the trigonal distortion in **I-oFA** than in the other compounds. It could mean that the strategy of promoting the steric strain by adding substituents close to the coordination sphere is successful. However, without crystal structure we cannot be sure. Moreover, we cannot exclude ligand rotation to increase Fe---F distance in **I-oFA** to minimize the steric strain. A 2,6-fluorophenyl group might have prevent such rotation.

In complex **I-pFA**, the pyridine rings are in *trans* conformation in both Fe<sup>2+</sup> sites. If we compare with the Fe1 site of complex **I-mFA** that presents also a *trans* conformation of the pyridine groups, the distortion parameters are not changed. It means that this conformation allows the fluorine groups to be far enough from the coordination sphere to do not affect the distortion and the switching properties. The differences in behavior might come first from the incomplete SCO observed in complex **I-mFA** and the different crystal packings, especially because of the presence of chloroform solvent molecules in complex **I-pFA**. It is important to notice that spin-crossover compounds with high symmetry of *R*-3 are not common. For example, the molecular complexes [Fe(ptz)<sub>6</sub>(BF<sub>4</sub>)<sub>2</sub>] (ptz = 1- propyl-tetrazole)<sup>15</sup> and [Fe(btzb)<sub>3</sub>](PF<sub>6</sub>)<sub>2</sub>·solv (btzb = 1,4-bis(tetrazol-1-yl)butane; solv = 0.5 MeOH or H<sub>2</sub>O)<sup>16</sup> crystallize in the trigonal system.

Moreover, complex **I-pFA** can be viewed as a nanoporous molecular materials since the 1D pore along the *c* axis is larger than 10 Å. Nanoporous materials are usual found in the metal–organic frameworks or covalent–organic frameworks. Actually, the SCO affected by the solvent have already been reported in many framework compounds.<sup>17-24</sup> For example, the abrupt SCO of complex [Fe(bpp)(H<sub>2</sub>L)](ClO<sub>4</sub>)<sub>2</sub>·1.5C<sub>3</sub>H<sub>6</sub>O (bpp = 2,6-bis(pyrazol-3-yl)pyridine, H<sub>2</sub>L = 2,6-bis(5-(2-methoxyphenyl)pyrazol-3-yl)pyridine) turns into fully HS when losing one-third of acetone. The new [Fe(bpp)(H<sub>2</sub>L)](ClO<sub>4</sub>)<sub>2</sub>·C<sub>3</sub>H<sub>6</sub>O complex can replace acetone by MeOH and H<sub>2</sub>O to form [Fe(bpp)(H<sub>2</sub>L)](ClO<sub>4</sub>)<sub>2</sub>·1.25MeOH·0.5H<sub>2</sub>O through a single crystal-to-single crystal process.<sup>18</sup> Another example is related to the reversibility of single crystal-to-single crystal transformation by reabsorption of MeOH in complex {Fe(3-CNpy)<sub>2</sub>(CH<sub>3</sub>OH)<sub>2/3</sub>[Au(CN)<sub>2</sub>]<sub>2</sub>} (3-CNpy = 3-CNpyridine), where the hysteresis loop disappears when absorbing the MeOH molecules.<sup>19</sup> Another famous example is observed in {Fe(pz)[Pt(CN)<sub>4</sub>]}, a 3D metal–organic framework upon water adsorption. Paesani *et al.* demonstrates the pore expansion owing to the water adsorption results in a progressive stabilization of the HS state by the analysis of the structural and dynamical properties of the framework, with a consequent decrease of *T*<sub>1/2</sub>.<sup>20</sup> The nanoporous metal-organic framework [Fe<sub>2</sub>(azpy)<sub>4</sub>(NCS)<sub>4</sub>] (guest) (azpy is *trans*-4,4-azopyridine) displays the reversible uptake and release of guest molecules, causing substantial changes in the local geometry of the iron(II) centers.<sup>24</sup>

Nanoporous molecular materials have been reported in some organic molecules, where only weak non-covalent interactions exist instead of the directional covalent or coordination bonds.<sup>25-29</sup> It is very interesting that complex **I-pFA** display SCO with the nanoporosity and

high symmetry. This sample also shows large holes within the crystal packing. While these pores are here filled by the chloroform molecules, it however opens interesting perspectives in the context of the scarcity of molecular complexes combining nanoporosity and SCO. This is especially true since, as shown here, chloroform may be quite easy to remove. So, one study in perspective of this work concerns the remove of the solvent or its exchange in a single crystal-to-single crystal way. This could bring interesting features in the context of mixing SCO and MOF properties.

In summary, three complexes were synthesized and characterized in the  $[\text{Fe}(\text{PM-zFA})_2(\text{NCS})_2]$  system ( $z = o, m, p$ ). From the structural analysis of complexes **I-pFA** and **I-mFA**, the angle distortion of the coordination sphere do really enhance from **I-pFA** to **I-mFA**. Especially, in complex **I-mFA** with an incomplete SCO, the nearer F---Fe distance in Fe1 leads to a stronger distortion that favors the HS state compare to the farer F---Fe distance in Fe2 that leads to a weaker distortion that favors the occurrence of SCO. Moreover, complex **I-pFA** provides a rare example of nanoporous structure with the high symmetry ( $R-3$ ). Unfortunately, the structure of complex **I-oFA** is unknown due to the absence of single crystal sample even if we can suspect a higher variation of the distortion parameters in this compound compared to the other ones.

Two interesting and unprecedented phenomena occur here. Firstly, the coexistence of *cis* and *trans* conformations of the pyridine groups in two different  $\text{Fe}^{2+}$  sites in complex **I-mFA**. Secondly, an unusual high symmetry is observed in complex **I-pFA** together with nanoporosity. These two structural aspects never appeared yet in  $[\text{Fe}(\text{PM-L})_2(\text{NCE})_2]$  family, not even in the larger  $\text{Fe}^{2+}$  family based on bidentate ligands.

## Bibliography

- [1] P. Guionneau, M. Marchivie, G. Bravic, J. F. Létard, D. Chasseau, *Top. Curr. Chem.*, 2004, **234**, 97.
- [2] E. Tailleur, M. Marchivie, N. Daro, G. Chastanet, P. Guionneau, *Chem. Commun.*, 2017, **53**, 4763.
- [3] J. F. Létard, G. Chastanet, O. Nguyen, S. Marcén, M. Marchivie, P. Guionneau, D. Chasseau, P. Gütllich, *Monatsh. Chem.*, 2003, **134**, 165.
- [4] P. Guionneau, M. Marchivie, G. Bravic, J. F. Létard, D. Chasseau, *J. Mater. Chem.*, 2002, **12**, 2546.
- [5] J. F. Létard, P. Guionneau, E. Codjovi, O. Lavastre, G. Bravic, D. Chasseau, O. Kahn, *J. Am. Chem. Soc.*, 1997, **119**, 10861.
- [6] P. Guionneau. *Dalton. Trans.*, 2014, **14**, 382.
- [7] M. Marchivie, P. Guionneau, J. F. Létard, D. Chasseau, *Acta Cryst.*, 2005, **B61**, 25.
- [8] P. Harding, D. J. Harding, N. Soponrat, K. Tinpun, S. Samuadnuan, H. Adams, *Aust. J. Chem.*, 2010, **63**, 75.
- [9] O. V. Dolomanov, L. J. Bourhis, R. J. Gildea, J. A. K. Howard, H. Puschmann, *J. Appl. Crystallogr.*, 2009, **42**, 339.
- [10] M. Llunell, D. Casanova, J. Cirera, M. Alemany, S. Alvarez, SHAPE, v. 2.0, University of Barcelona, Barcelona, Spain, 2010.
- [11] M. A. Spackman, D. Jayatilaka, *Cryst. Eng. Comm.*, 2009, **11**, 19.
- [12] D. Jayatilaka, S. K. Wolff, D. J. Grimwood, J. J. McKinnon, M. A. Spackman, *Acta Cryst.*, 2006. **A62**, s90.
- [13] N. Bréfuel, E. Collet, H. Watanabe, M. Kojima, N. Matsumoto, L. Toupet, K. Tanaka, J. P. Tuchagues, *Chem. Eur. J.*, 2010, **16**, 14060.
- [14] G. A. Craig, J. S. Costa, S. J. Teat, O. Roubeau, D. S. Yufit, J. A. Howard, G. Aromí, *Inorg. Chem.*, 52, 7203.
- [15] S. Lakhroufi, P. Guionneau, M. H. Lemée-Cailleau, P. Rosa, J.-F. Létard, *Phys. Rev. B*, 2010, **82**, 132104.
- [16] C. M. Grunert, J. Schweifer, P. Weinberger, W. Linert, *Inorg. Chem.*, 2004, **43**, 155-165.
- [17] J. Cirera, *Rev. Inorg. Chem.*, 2014, **34**, 199.
- [18] J. S. Costa, S. Rodríguez-Jiménez, G. A. Craig, B. Barth, C. M. Beavers, S. J. Teat, G. Aromí, *J. Am. Chem. Soc.*, 2014, **136**, 3869.

*Part II – Promoting Distortion of the Coordination Polyhedron by Steric Strain: Fluorine Substitution of PM-zFA Family*

- [19] W. Huang, F. Shen, M. Zhang, D. Wu, F. Pan, O. Sato, *Dalton Trans.*, 2016, **45**, 14911.
- [20] C. Huy Pham, J. Cirera, F. Paesani, *J. Am. Chem. Soc.*, 2016, **138**, 6123.
- [21] A. Galet, M. C. Munoz, J. A. Real, *Chem. Commun.*, 2006, **41**, 4321.
- [22] N. N. Adarsh, M. M. Dîrtu, P. Guionneau, E. Devlin, Y. Sanakis, J. A. K. Howard, B. Chattopadhyay, Y. Garcia, *Eur. J. Inorg. Chem.*, 2019, 585.
- [23] M. Quesada, V. A. de la Peña-O'Shea, G. Aromí, S. Geremia, C. Massera, O. Roubeau, P. Gamez, J. Reedijk, *Adv. Mater.*, 2007, **19**, 1397.
- [24] G. J. Halder, C. J. Kepert, B. Moubaraki, K. S. Murray, J. D. Cashion, *Science*, 2002, **298**, 1762.
- [25] J. Tian, P. K. Thallapally, B. P. McGrail, *Cryst. Eng. Comm.*, 2012, **14**, 1909.
- [26] S. J. Dalgarno, P. K. Thallapally, L. J. Barbour, J. L. Atwood, *Chem. Soc. Rev.*, 2007, **36**, 236.
- [27] G. Couderc, J. Hulliger, *Chem. Soc. Rev.*, 2010, **39**, 1545.
- [28] N. B. McKeown, *J. Mater. Chem.*, 2010, **20**, 10588.
- [29] J. R. Holst, A. Trewin, A. I. Cooper, *Nat. Chem.*, 2010, **2**, 944.

*Part II – Promoting Distortion of the Coordination Polyhedron by Steric Strain: Fluorine Substitution of PM-zFA Family*

**Part III – Promoting Distortion of the Coordination  
Polyhedron Using Polymorphism: Bromine Substitution of  
PM-zBrA Family**

<b>III.1. Introduction</b> .....	91
<b>III.2. Synthesis of the substituted ligands and the [Fe(PM-<i>z</i>BrA)<sub>2</sub>(NCS)<sub>2</sub>] (<i>z</i> = <i>o</i>, <i>m</i>, <i>p</i>) complexes</b> .....	92
III.2.1. Synthesis of the PM- <i>z</i> BrA ligands.....	92
III.2.2. Synthesis of the [Fe(PM- <i>z</i> BrA) <sub>2</sub> (NCS) <sub>2</sub> ] ( <i>z</i> = <i>o</i> , <i>m</i> , <i>p</i> ) complexes .....	95
<b>III.3. Characterizations of the [Fe(PM-<i>z</i>BrA)<sub>2</sub>(NCS)<sub>2</sub>] complexes (<i>z</i> = <i>m</i>, <i>o</i>)</b> .....	98
III.3.1. [Fe(PM- <i>o</i> BrA) <sub>2</sub> (NCS) <sub>2</sub> ] (I- <i>o</i> BrA).....	98
III.3.2. Polymorph [Fe(PM- <i>m</i> BrA) <sub>2</sub> (NCS) <sub>2</sub> ]-I: I- <i>m</i> BrA.....	99
III.3.3. Polymorph [Fe(PM- <i>m</i> BrA) <sub>2</sub> (NCS) <sub>2</sub> ]-II: II- <i>m</i> BrA .....	107
III.3.4. Discussions on I- <i>m</i> BrA and II- <i>m</i> BrA .....	114
<b>III.4. Characterizations of four [Fe(PM-<i>p</i>BrA)<sub>2</sub>(NCS)<sub>2</sub>] polymorphs</b> .....	117
III.4.1. Polymorph [Fe(PM- <i>p</i> BrA) <sub>2</sub> (NCS) <sub>2</sub> ]-I: I- <i>p</i> BrA.....	117
III.4.2. Polymorph [Fe(PM- <i>p</i> BrA) <sub>2</sub> (NCS) <sub>2</sub> ]-II: II- <i>p</i> BrA .....	145
III.4.3. Polymorph [Fe(PM- <i>p</i> BrA) <sub>2</sub> (NCS) <sub>2</sub> ]-III: III- <i>p</i> BrA .....	157
III.4.4. Polymorph [Fe(PM- <i>p</i> BrA) <sub>2</sub> (NCS) <sub>2</sub> ]-IV: IV- <i>p</i> BrA.....	172
III.4.5. Discussions on the four <i>p</i> BrA polymorphs.....	179
<b>III.5. Conclusion</b> .....	188
<b>Bibliography</b> .....	190

### **III.1. Introduction**

As shown in [Part. II](#), the distortion of the coordination sphere can be promoted by changing the position of fluorine atom from *para* to *ortho* position in complexes **I-*p*FA** and **I-*m*FA**. Since the atomic radius of fluorine is the smallest in the halogen serie, bigger halogen atoms, such as Cl, Br and I, could be used to explore the steric strain effect. Since the chlorine substituted PM-*z*ClA ( $z = o, m, p$ ) ligands are explored by our collaborators, Prof. Anuj K Sharma from the University of Rajasthan (Rajasthan, India), we haven't focus on it. In addition, the atomic radius of iodine may be too large to coordinate with  $\text{Fe}^{2+}$  ions, especially for PM-*o*IA. So, here we selected the bromine substitution PM-*z*BrA ( $z = o, m, p$ ) ligands to study the steric strain effect. Rich polymorphism appears in these systems, where the distortion of the coordination sphere are subtly regulated by the intra- and inter molecular interactions.

In this part, the synthesis of the PM-*z*BrA ( $z = o, m, p$ ) ligands and the crystallization of the  $[\text{Fe}(\text{PM-}z\text{BrA})_2(\text{NCS})_2]$  complexes are firstly introduced. Then the characterizations of seven new compounds are described which includes the two polymorphs of  $[\text{Fe}(\text{PM-}m\text{BrA})_2(\text{NCS})_2]$  and four polymorphs of  $[\text{Fe}(\text{PM-}p\text{BrA})_2(\text{NCS})_2]$ .

## III.2. Synthesis of the substituted ligands and the [Fe(PM-*z*BrA)<sub>2</sub>(NCS)<sub>2</sub>] (*z* = *o*, *m*, *p*) complexes

### III.2.1. Synthesis of the PM-*z*BrA ligands

The Schiff base ligands (PM-*z*BrA) were synthesized from the condensation of the 2-pyridine-carbaldehyde with the corresponding bromine substituted aniline (Scheme III.1) adapting the literature procedure.<sup>1</sup>



Scheme III.1. Reaction scheme of the N-(2'-pyridylmethylene)-*n*-bromoaniline synthesis (*n* = 2,3,4).

- *Synthesis of N-(2'-pyridylmethylene)-4-bromoaniline (PM-*p*BrA)*

A solution of 4-bromoaniline (1.72 g, 10 mmol) in diethylether (50 ml), was added to pyridine-2-carboxaldehyde (0.9512 ml, 10 mmol) in diethylether (50 ml). Then magnesium sulfate (5g, MgSO<sub>4</sub>) was also added in order to absorb the reaction water. After that, the yellow solution was stirred overnight under argon atmosphere. The solution was filtered and the magnesium sulfate washed with CH<sub>2</sub>Cl<sub>2</sub> (5 ml), in order to remove all the products. The solvent was removed under vacuum on rotary evaporator. The ligand was recrystallized in a mixture of CH<sub>2</sub>Cl<sub>2</sub> (10 ml) and petroleum ether (30 ml). After one day at -25 °C, the pale-yellow crystals were filtrated and recrystallized one more time.

The crystals obtained upon recrystallization were good enough to record SCXRD data and to determine the crystal structure of the ligand (Table III.1 and Figure III.1). At 300 K, the PM-*p*BrA crystallizes in the monoclinic system with space group *P*2<sub>1</sub>/*a*, which agrees with the recently reported result.<sup>2</sup> The synthesis protocol in this literature is different from the method described above, where the ethanol solution containing reactants was refluxed at 60 °C for 6 hours and crystals were grown through a slow evaporation of an ethanol solution at 25 °C. The dihedral angle between phenyl ring and pyridine ring is only 17.94° within the ligand. This

*Part III – Promoting Distortion of the Coordination Polyhedron Using Polymorphism:  
Bromine Substitution of PM-zBrA Family*

leads to the nearly planar geometry of ligand, leading to a short intraligand H6---H8 contact (2.074 Å). It is worth to mention that the intermolecular Br---Br contacts (3.576 Å) play an important role in the molecular packing. The comparison between the experimental X-ray diffraction patterns and the simulated one by single-crystal structure (Figure III.2) indicates that the polycrystalline compound is homogenous and identical to the single-crystal one.

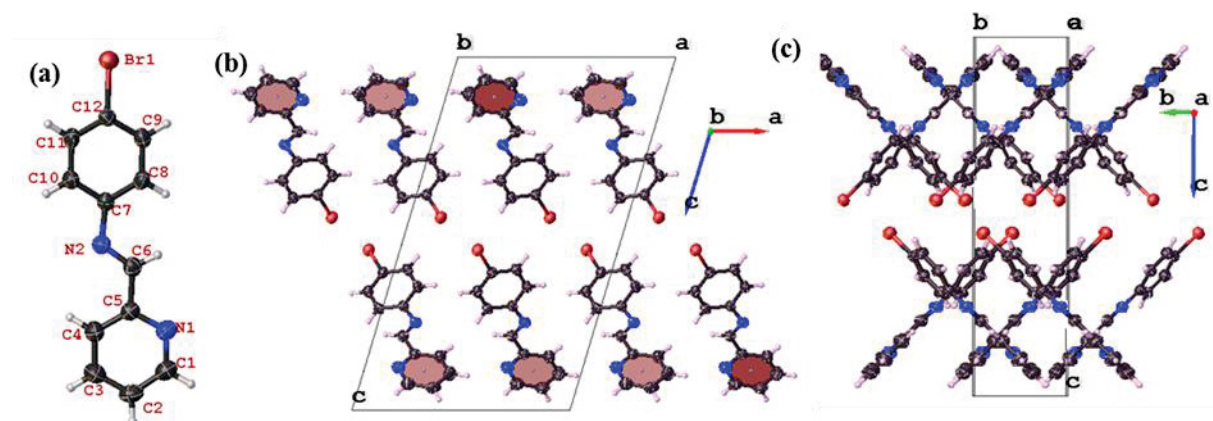


**Figure III.1.** Crystal structure of the PM-*p*BrA ligand at 298 K with the molecule in the asymmetric unit (a), the crystal packing along the *b* axis (b), and the crystal packing along the *c* axis (c). Thermal ellipsoids are depicted at the 50 % probability level.

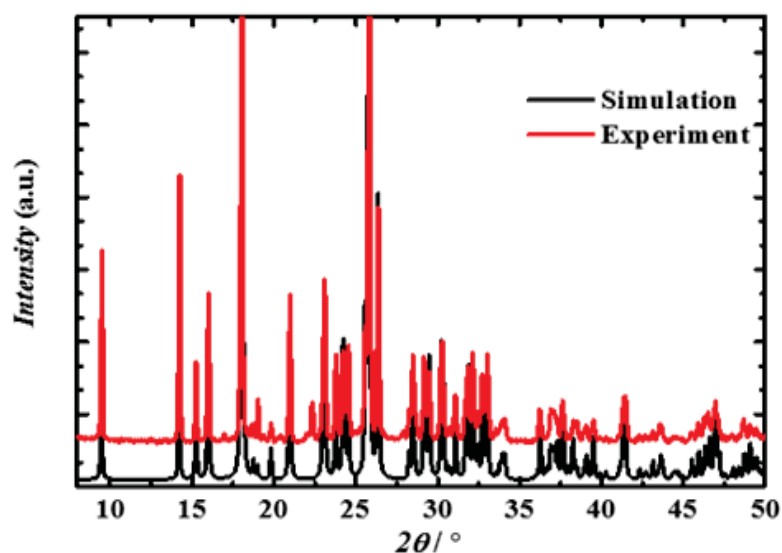


**Figure III.2.** The experimental powder diffraction pattern and simulated one from the single-crystal data of PM-*p*BrA ligand at 300 K.

Table III.1. Crystal data and structure refinement data for **PM-pBrA** ligand.

Empirical formula	C <sub>12</sub> H <sub>9</sub> BrN <sub>2</sub>
Formula weight / g mol <sup>-1</sup>	261.12
Temperature / K	298
Radiation MoK $\alpha$ / Å	0.71073
Crystal size / mm <sup>3</sup>	0.08 × 0.24 × 0.12
Crystal system	monoclinic
Space group	P2 <sub>1</sub> /a
<i>a</i> / Å	11.6167(5)
<i>b</i> / Å	4.8924(4)
<i>c</i> / Å	19.5165(3)
$\alpha$ / °	90
$\beta$ / °	106.7795(5)
$\gamma$ / °	90
Volume / Å <sup>3</sup>	1061.97(10)
Z-formula	4
$\rho_{\text{calc}}$ / g cm <sup>-3</sup>	1.633
$\mu$ / mm <sup>-1</sup>	3.835
F(000)	520.0
2 $\theta$ range for data collection / °	6.542 - 54.982
Index ranges	-15 ≤ <i>h</i> ≤ 14, -6 ≤ <i>k</i> ≤ 6, -25 ≤ <i>l</i> ≤ 25
Reflections collected	18180
Independent reflections	2 439 [R <sub>int</sub> = 0.0412, R <sub>sigma</sub> = 0.0249]
Data/restraints/parameters	2439/0/136
Goodness-of-fit on F <sup>2</sup>	1.136
Final R indexes [ <i>I</i> ≥ 2 $\sigma$ ( <i>I</i> )]	R <sub>1</sub> = 0.0382, wR <sub>2</sub> = 0.1252
Final R indexes [all data]	R <sub>1</sub> = 0.0528, wR <sub>2</sub> = 0.1446
Largest diff. peak/hole/e Å <sup>-3</sup>	0.44/-0.37

$$R_1 = \frac{\sum ||F_0| - |F_c||}{\sum |F_0|}, wR_2 = \left[ \frac{\sum w(F_0^2 - F_c^2)^2}{\sum w(F_0^2)^2} \right]^{1/2}$$

- *Synthesis of N-(2'-pyridylmethylene)-3-bromoaniline (PM-mBrA)*

Using the same procedure, ligand PM-*m*BrA was synthesized. Only petroleum ether was used for recrystallization because the ligand is very soluble in polar solvents. The crystals are colorless flakes. It is difficult to perform the SCXRD because the crystal can slowly dissolve in the oil used for mounting the crystals. Actually, the crystals of PM-*m*BrA can only be stable at low temperature. After removing the ligand from the fridge, it will quickly turn into liquid at room temperature.

- *Synthesis of N-(2'-pyridylmethylene)-2-bromoaniline (PM-oBrA)*

Using the same procedure, ligand PM-*o*BrA was synthesized. However, it leads to a yellow oil whatever the crystallization method used.

### **III.2.2. Synthesis of the $[\text{Fe}(\text{PM-zBrA})_2(\text{NCS})_2]$ ( $z = o, m, p$ ) complexes**

All the solvent were treated in order to remove the oxygen in solution before use. Methanol was distilled while diethylether and dichloromethane were frozen and unfrozen in liquid nitrogen three times. The reactions and crystallizations were performed under argon atmosphere.

A first step, common to all the complexation reactions, consisted in preparing the  $\text{Fe}(\text{NCS})_2$  reactant 1 mmol of  $\text{FeSO}_4 \cdot 7\text{H}_2\text{O}$  and 2 mmol of KNCS were dissolved in 20 ml of methanol each, in presence of few ascorbic acid. After stirring 2 hours at 25 °C, the resulting solution is filtered to remove the  $\text{K}_2\text{SO}_4$  formed during the reaction.

As a common method for the synthesis of the various complexes, the layer by layer technique is often used for crystallization, where two solvents containing ligand and metal salt, respectively, diffuse and crystallize slowly at the intermediate layer. Details for each compound (-o, -m, -p ones) are given hereafter.

- *Synthesis of  $[\text{Fe}(\text{PM-oBrA})_2(\text{NCS})_2]$*

Owing to the very soluble nature of PM-oBrA, different solvents were used for the layering technique, including diethylether, dichloromethane, methanol, and chloroform. However, no crystals were formed and the color of solution went dark blue. Upon slow evaporation of these solutions, a powder is obtained, related to compound **I-oBrA**. Elemental analysis gives: C: 52.32, H: 2.93, N: 13.14 larger than the theoretical values C: 44.98, H: 2.61, N: 12.11. As seen in [Appendix 4](#), the results of elements were different at two measurements. It was not obvious to obtain something relevant, maybe because of the presence of Br that are influencing the measurements and datatratements.

- *Synthesis of  $[\text{Fe}(\text{PM-mBrA})_2(\text{NCS})_2]$ : polymorphs **I-mBrA** and **II-mBrA***

Depending on the reaction conditions, two polymorphs were obtained separately when reacting the PM-mBrA ligand to a solution of  $\text{Fe}(\text{NCS})_2$ , later referred to as **I-mBrA** and **II-mBrA**.

If 2 ml of diethylether containing 0.2 mmol of ligand, are slowly dropped into 2 ml of the  $\text{Fe}(\text{NCS})_2$  methanol solution (0.05mmol/ml), blue needle crystals are formed in a dark blue solution at 25 °C after one week, leading to polymorph **I-mBrA**. Elemental analysis gives: C: 44.49, H: 2.48, N: 11.46 close to the theoretical values C: 44.98, H: 2.61, N: 12.11 ([Appendix 4](#)).

*Part III – Promoting Distortion of the Coordination Polyhedron Using Polymorphism:  
Bromine Substitution of PM-zBrA Family*

If 2 ml of the freshly prepared  $\text{Fe}(\text{NCS})_2$  solution (0.05mmol/ml) are slowly dropped into 2 ml of dichloromethane containing 0.2 mmol of ligand, dark block crystals are formed in a dark blue solution at 25 °C after two days, leading to polymorph **II-mBrA**. Elemental analysis gives: C: 0.11, H: 1.63, N: 0.63, which does not correspond to the theoretical values C: 44.98, H: 2.61, N: 12.11 ([Appendix 4](#)). The values are very small at two measurements and it is not clear why it is so low value in this complex.

- *Synthesis of  $[\text{Fe}(\text{PM-pBrA})_2(\text{NCS})_2]$ : polymorphs **I-pBrA**, **II-pBrA**, **III-pBrA** and **IV-pBrA***

Depending on the reaction conditions, single crystals of four polymorphs can be obtained when reacting the PM-pBrA ligand to a solution of  $\text{Fe}(\text{NCS})_2$ , later referred to as **I-pBrA**, **II-pBrA**, **III-pBrA** and **IV-pBrA**.

When 2 ml methanol containing 0.2 mmol ligand are added dropwise into 2 ml of  $\text{Fe}(\text{NCS})_2$  methanolic solution (0.05mmol/ml), blue needle crystals are formed after one week at 25 °C, leading to **I-pBrA**. Elemental analysis gives: C: 44.93, H: 2.57, N: 11.79 close to the theoretical values C: 44.98, H: 2.61, N: 12.11 ([Appendix 4](#)).

The dropwise addition of 2 ml of  $\text{Fe}(\text{NCS})_2$  methanolic solution (0.05mmol/ml) into 2 ml of dichloromethane containing 0.2 mmol of ligand, followed by the addition of 6 ml of diethylether, leads to a mixture of dark block and needle crystals after one week at 25 °C. This mixture corresponds to **I-pBrA** and **II-pBrA**. Polymorph **II-pBrA** has never been obtained without polymorph **I-pBrA**.

When 2 ml of acetonitrile containing 0.2 mmol ligand are slowly dropped into 2 ml of  $\text{Fe}(\text{NCS})_2$  methanolic solution (0.05mmol/ml) at let for one week at 60 °C, a mixture of dark blue crystals of **I-pBrA** and **III-pBrA** are obtained. Polymorph **III-pBrA** has never been obtained without concomitance of polymorph **I-pBrA**. Moreover, it was obtained in very small quantities preventing any CHNS or SQUID measurements.

When 2 ml of  $\text{Fe}(\text{NCS})_2$  methanolic solution are added dropwise (0.1mmol/ml) into 2 ml of acetonitrile containing 0.4 mmol of ligand, the dark block crystals of **IV-pBrA** are formed after one week at 25 °C. Elemental analysis gives: C: 44.94, H: 2.58, N: 11.79 close to the theoretical values C: 44.98, H: 2.61, N: 12.11 ([Appendix 4](#)).

*Part III – Promoting Distortion of the Coordination Polyhedron Using Polymorphism:  
Bromine Substitution of PM-zBrA Family*

The powder of polymorphs **I-pBrA** and **II-pBrA** can also be prepared in the following procedures. When 5ml CH<sub>3</sub>CN containing 1mmol ligand are added quickly into 15 ml of Fe(NCS)<sub>2</sub> methanolic solution (0.05 mmol/ml) during stirring under argon. After reaction one night at 25 °C, the solid were flitrated and washed by the cool diethylether, naturally drying in the hood. The products is polymorph **I-pBrA**.

When 10ml CH<sub>3</sub>OH containing 1 mmol ligand are added quickly into 10 ml of Fe(NCS)<sub>2</sub> methanolic solution (0.05 mmol/ml) during stirring under argon. The methanol solution containing reactants was refluxed at 25 °C for 2 hours, then 5ml diethylether were added after cooling down to room temperature. The solid were flitrated and washed by the cool diethylether. The products is polymorph **II-pBrA**. Elemental analysis gives: C: 44.97, H: 2.45, N: 11.85 close to the theoretical values C: 44.98, H: 2.61, N: 12.11 ([Appendix 4](#)).

### III.3. Characterizations of the $[\text{Fe}(\text{PM-}z\text{BrA})_2(\text{NCS})_2]$ complexes ( $z = m, o$ )

#### III.3.1. $[\text{Fe}(\text{PM-}o\text{BrA})_2(\text{NCS})_2]$ (**I-*o*BrA**)

The magnetic measurements were performed on a powder sample, using a SQUID magnetometer (see Appendix 3). Figure III.3 shows the thermal evolution of the  $\chi_{MT}$  product. The  $\chi_{MT}$  value at 300 K of  $3.75 \text{ cm}^3 \text{ K mol}^{-1}$ , indicating the fully HS state. Upon cooling, the  $\chi_{MT}$  product gradually decreases to reach a value close to  $0.48 \text{ cm}^3 \text{ K mol}^{-1}$  below 50 K, suggesting a LS state. No thermal quenching could have been observed. This compound exhibits a gradual and almost complete SCO, with a switching temperature around 220 K. An irradiation at 830 nm was applied for 1h at 10 K, leading to less than 30 % of photoswitching. The  $T(\text{LIESST})$  measurement performed after this photo-excitation gives a  $T(\text{LIESST})$  value of 50 K. Both  $T_{1/2}$  and  $T(\text{LIESST})$  are very similar to the ones observed in **I-*o*FA**. Since the crystal structure is missing, we suppose that there is no solvent in **I-*o*BrA** and the formula weight of 694.25 g/mol is adopted for the data treatment.

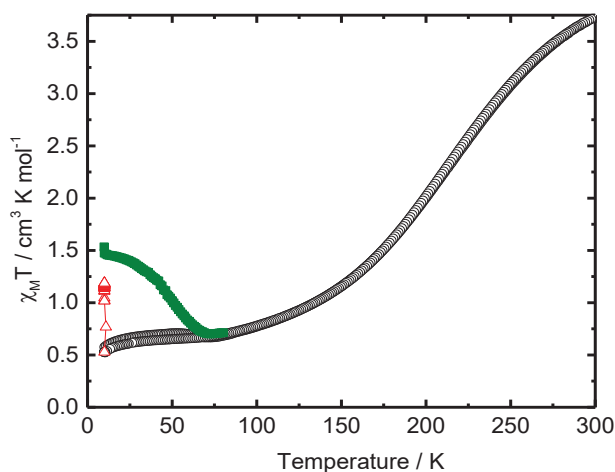


Figure III.3. Thermal dependence of the  $\chi_{MT}$  product of **I-*o*BrA** recorded at 0.4 K/min (in settle mode) under 20 kOe of applied magnetic field, before irradiation (■), under irradiation (Δ) and after irradiation in the dark (■).

Since no crystals were obtained, only PXRD was performed leading to a diffractogram showing the poor crystallinity of the sample (Figure III.4). This diffractogram fits well with the one obtained for **I-*o*FA** (Figure II.4). We can therefore assume that both **I-*o*BrA** and **I-*o*FA**

are isomorphous which can explain the very similar magnetic behaviors recorded for these two compounds.

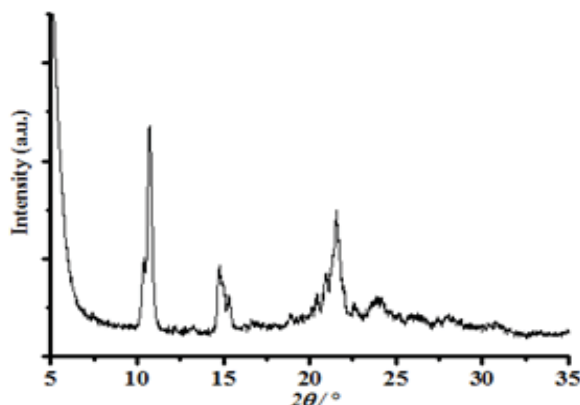


Figure III.4. Experimental powder X-ray diffraction pattern of complex **I-oBrA**.

### III.3.2. Polymorph $[\text{Fe}(\text{PM-}m\text{BrA})_2(\text{NCS})_2]\text{-I}$ : **I-mBrA**

- *Magnetic properties of I-mBrA*

The magnetic measurements were performed on crystals, using a SQUID magnetometer (see Appendix 3). Figure III.5 shows the thermal evolution of the  $\chi_M T$  product. The  $\chi_M T$  value at 300 K of  $3.87 \text{ cm}^3 \text{ K mol}^{-1}$ , indicates a fully HS state. Upon cooling, the  $\chi_M T$  product does not evolve down to 30 K, temperature below which the signal decreases most probably due to the zero-field splitting. So polymorph **I-mBrA** does not display SCO and remains HS in the whole temperature range. This absence of SCO might come from a high distortion of the coordination sphere and crystallographic investigations will allow to shine light on this aspect.

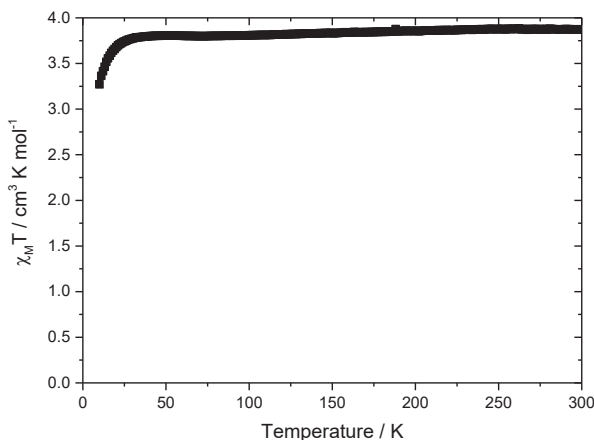


Figure III.5. Thermal dependence of the  $\chi_M T$  product of polymorph **I-mBrA** recorded at 0.4 K/min (in settle mode) under 10 kOe of applied magnetic field.

- Crystallographic investigation of **I-mBrA**

Data were recorded and the crystal structure determined at 80 K and 300 K by SCXRD. At 300 K, polymorph **I-mBrA** crystallizes in the monoclinic crystal-system with *C2/c* space group (Table III.2).

Table III.2. Crystal data and structure refinement data for polymorph **I-mBrA**.

Empirical formula	C <sub>26</sub> H <sub>18</sub> Br <sub>2</sub> FeN <sub>6</sub> S <sub>2</sub>	
Formula weight / g mol <sup>-1</sup>	694.25	80
Temperature / K	300	80
Radiation MoK $\alpha$ / Å	$\lambda = 0.71073$	
Crystal size / mm <sup>3</sup>	0.22 × 0.04 × 0.04	
Crystal system	monoclinic	
Space group	<i>C2/c</i>	<i>P2<sub>1</sub>/c</i>
<i>a</i> / Å	19.7976(10)	19.3712(17)
<i>b</i> / Å	22.3712(10)	22.2718(19)
<i>c</i> / Å	20.4026(9)	23.6667(15)
$\alpha$ / °		90
$\beta$ / °	107.600(3)	125.435(5)
$\gamma$ / °		90
Volume / Å <sup>3</sup>	8 613.2(7)	8 319.3(12)
Z-formula	12	
$\rho_{\text{calc}}$ / g cm <sup>-3</sup>	1.606	1.663
$\mu$ / mm <sup>-1</sup>	3.480	3.603
F(000)	4128.0	4128.0
2 $\theta$ range for data collection / °	3.884 - 37.418	2.58 - 52.744
Index ranges	-17 ≤ <i>h</i> ≤ 17, -20 ≤ <i>k</i> ≤ 20, -18 ≤ <i>l</i> ≤ 18	-24 ≤ <i>h</i> ≤ 24, -27 ≤ <i>k</i> ≤ 27, -29 ≤ <i>l</i> ≤ 23
Reflections collected	47114	143473
Independent reflections	3182 [R <sub>int</sub> = 0.1929, R <sub>sigma</sub> = 0.1001]	17010 [R <sub>int</sub> = 0.1270, R <sub>sigma</sub> = 0.0928]
Data/restraints/parameters	3 182/1/489	17 010/0/1000
Goodness-of-fit on F <sup>2</sup>	0.913	0.972
Final R indexes [I ≥ 2 $\sigma$ (I)]	R <sub>1</sub> = 0.0460, wR <sub>2</sub> = 0.1022	R <sub>1</sub> = 0.0464, wR <sub>2</sub> = 0.0789
Final R indexes [all data]	R <sub>1</sub> = 0.1084, wR <sub>2</sub> = 0.1245	R <sub>1</sub> = 0.1131, wR <sub>2</sub> = 0.0967
Largest diff. peak/hole / e Å <sup>-3</sup>	0.53/-0.79	1.83/-1.08

$$R_1 = \frac{\sum ||F_0| - |F_c||}{\sum |F_0|}, wR_2 = \left[ \frac{\sum w(F_0^2 - F_c^2)^2}{\sum w(F_0^2)^2} \right]^{1/2}$$

There are one and a half molecules in the asymmetric unit, where Fe2 atom sits on the special Wyckoff position (4e) while Fe1 sits on the general Wyckoff position (8f). For

Part III – Promoting Distortion of the Coordination Polyhedron Using Polymorphism:  
Bromine Substitution of PM-zBrA Family

simplicity, Fe1 and Fe2 based complexes are labelled Fe1 and Fe2, hereafter. As seen in Figure III.6 the thiocyanate groups are in a *cis* configuration and PM-*m*BrA are also in *cis*, where two the pyridine rings are in *trans* conformation. By the superposition of Fe1 and Fe2, one can notice the difference in ligand orientation. Indeed, the two equivalent Br3 atoms point toward the NCS(3)<sup>-</sup> with the Br3---S3 distance of 5.670 Å in Fe2. In Fe1, the Br1 atom is pointing away from the NCS(2)<sup>-</sup> while the Br2 atom is pointing toward the NCS(1)<sup>-</sup> leading to a long Br1---S2 distance of 9.039 Å and a short Br2---S1 distance of 5.219 Å.

The average value of Fe-N distances in both molecules are 2.164(2) Å and 2.156(5) Å, respectively, which are the typical value for HS Fe<sup>2+</sup> ion. The thiocyanate groups are not linear with angles of 158.70° (Fe2-NC-S3), 157.44° (Fe1-NC-S2), and 158.74° (Fe1-NC-S1). The bending of NCS<sup>-</sup> groups gives rise to the large value of N1-Fe1-N6 (105.96°), and N7-Fe2-N7 (104.24°).

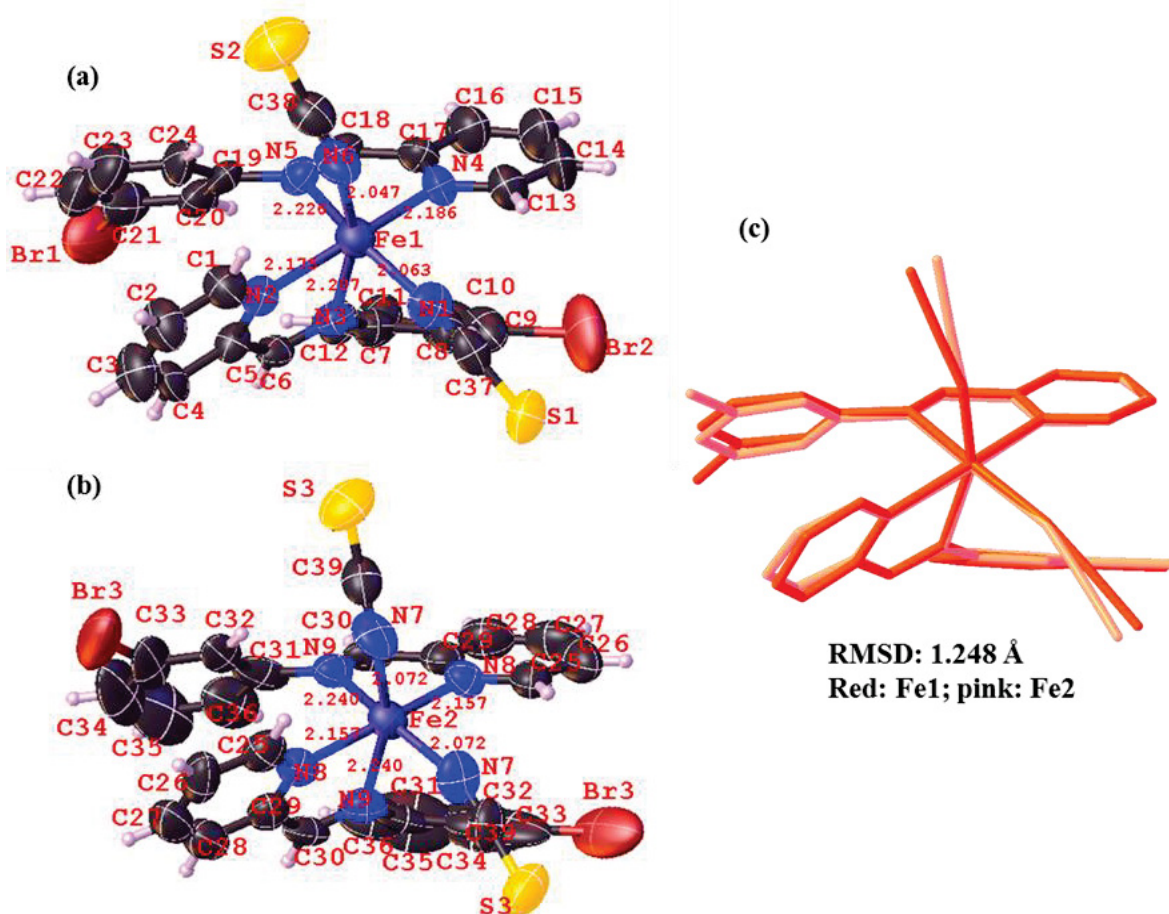


Figure III.6. The two crystallographically independent Fe1 (a) and Fe2 (b) molecules and their superposition of Fe1 (red) and Fe2 (yellow) (c) in polymorph I-*m*BrA at 300 K. The unit of the Fe-N distances is in angstrom.

As shown in Figure III.7, the molecules connect to each other to form quasi-one-dimensional chain through S---H hydrogen bonding (S1---H6, 2.914 Å and S3---H18, 2.985 Å) and weak  $\pi_{\text{phenyl}}\text{---}\pi_{\text{phenyl}}$  and  $\pi_{\text{pyridine}}\text{---}\pi_{\text{pyridine}}$  interactions, with a  $\{\text{Fe1Fe1Fe2}\}_{\infty}$  sequence along the  $a$  axis. The  $\pi_{\text{phenyl}}\text{---}\pi_{\text{phenyl}}$  and  $\pi_{\text{pyridine}}\text{---}\pi_{\text{pyridine}}$  distances are 3.724 Å, 3.704 Å, 3.692 Å, 3.839 Å, and 3.794 Å. The shortest Fe---Fe distances are 7.354 Å (Fe1---Fe2) and 7.386 Å (Fe1---Fe1) along the  $a$  axis. Moreover, these short  $\pi\text{---}\pi$  interactions can be demonstrated by the shape index in Hirshfeld surface (Figure III.7). The maps of shape index on the Hirshfeld surface can be used to identify complementary hollows (red) and bumps (blue) where two molecular surfaces touch one another.<sup>3-5</sup> More details of Hirshfeld surface are given in Appendix 1. Further, the chains are linked by S---H and Br---H hydrogen bonds to form a 2D layer at the  $ab$  plane (Figure III.8a). Then a three-dimensional network can be viewed as the layers interconnected by hydrogen bondings (Figure III. 8b), where the Fe---Fe distances are 9.556 Å and 9.188 Å (Fe1---Fe2) between the chains (Figure III.8c). In the  $ab$  plane, the same Fe1---Fe1 distances (14.937 Å) along the diagonal (the blue line in Figure III.8a), suggests Fe1 is in the face center, which corresponds to the observed monoclinic face-center lattice.

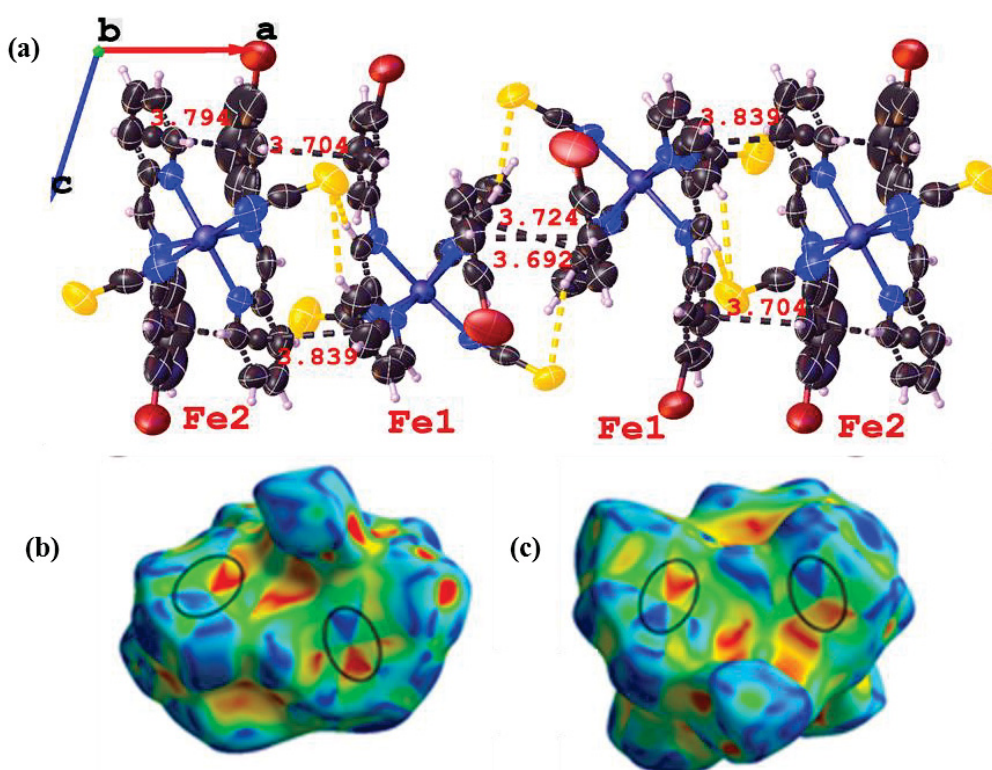


Figure III.7. The Fe1 and Fe2 packings along  $a$  direction (a), the shape index in Hirshfeld surface for  $\pi\text{---}\pi$  interactions between Fe1 and Fe2 (b) and between Fe1 and Fe1 (c) in *I*-*m*BrA at 300 K. The black circles stand for the position of  $\pi\text{---}\pi$  contact.



Part III – Promoting Distortion of the Coordination Polyhedron Using Polymorphism:  
Bromine Substitution of PM-zBrA Family

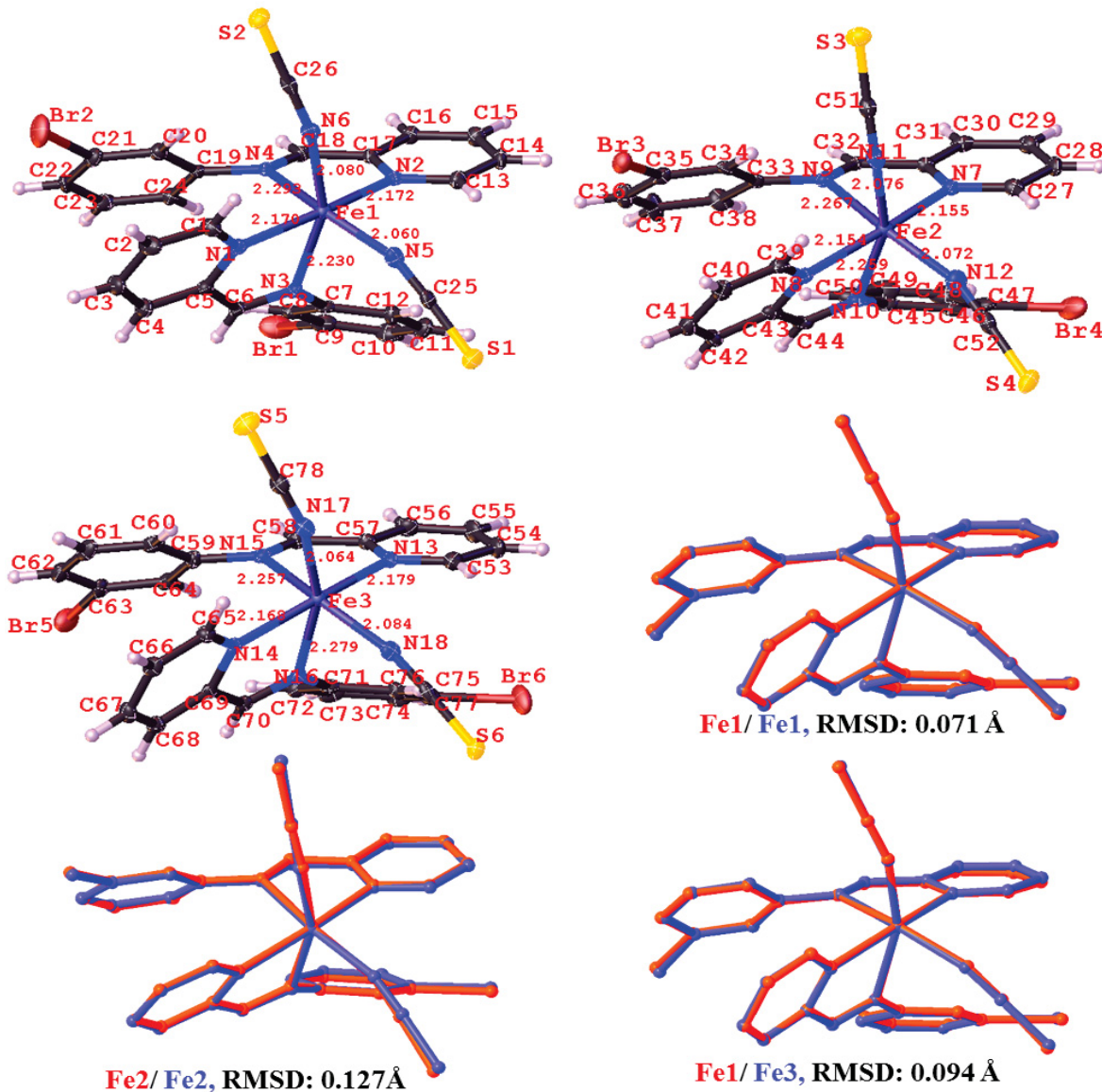


Figure III.9. Fe1, Fe2 and Fe3 molecules in the asymmetric unit at 80 K and their overlay between 300 K and 80 K of polymorph **I-mBrA**. The hydrogen atoms are omitted for clarity and the red and blue stand for molecules at 300 K and 80 K, respectively.

The symmetry breaking also reflects itself in the Fe---Fe distances, even if the crystal packing at 80 K is similar to the one at 300 K. The pseudo-one-dimensional chain  $\{\text{Fe1Fe2Fe3}\}_\infty$  along the *a* axis, is formed by S---H bonding and  $\pi_{\text{phenyl}}\text{---}\pi_{\text{phenyl}}$  and  $\pi_{\text{pyridine}}\text{---}\pi_{\text{pyridine}}$  intermolecular interactions, similarly to the 300 K structure (Figure III.10a). The Fe---Fe distances are 7.428 Å (Fe1---Fe2), 7.286 Å (Fe1---Fe3), and 7.067 Å (Fe2---Fe3) along the *a* axis at 80 K. Another change in the Fe---Fe distances is the inter-chain distance along *b* direction, where Fe1---Fe2 distance (9.188 Å at 300 K) changes into 9.279 Å (Fe1---Fe3) and 8.995 Å (Fe1---Fe2) at 80 K due to the reduced symmetry (Figure III.10c).

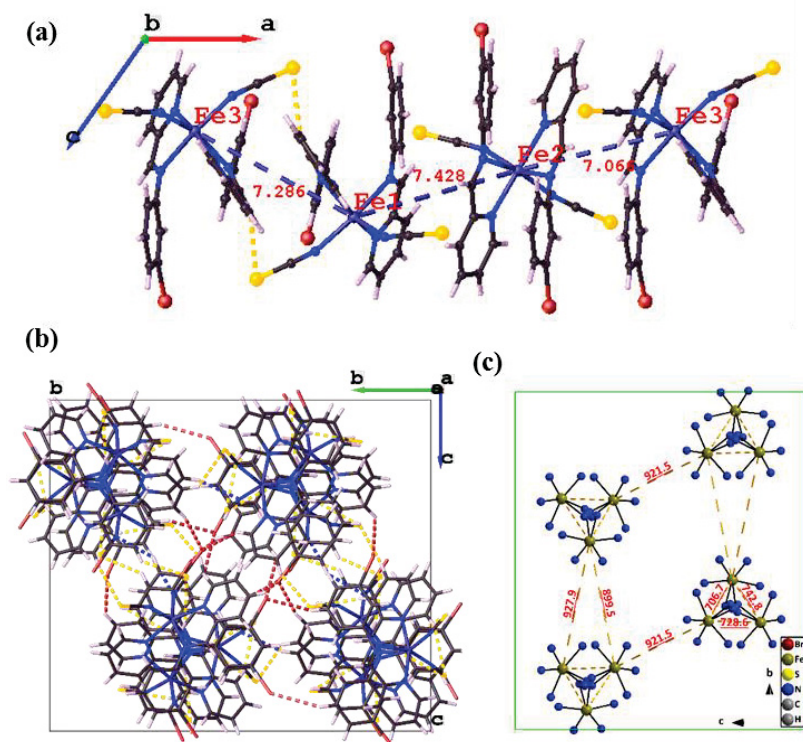


Figure III.10. Molecular packing at  $ab$  plane (a), the crystal packing projecting along the  $a$  axis (b) and the Fe---Fe distances at the  $ac$  plane (b) for polymorph **I-mBrA** at 80 K.

As seen in Table III.3, the angular distortions ( $\Sigma$ ) are larger than  $90^\circ$  and the trigonal distortions ( $\theta$ ) are around  $250^\circ$ , which indicates clearly the strong distortion of the coordination sphere. Another thing need to be noticed is that the value of  $\theta$  and  $\Sigma$  in Fe2 at 300 K and 80 K is smaller than others, which may result from the less bent NCS<sup>-</sup> groups.

Table III.3. The coordination sphere parameters of polymorph **I-mBrA**.

Compound	<b>I-mBrA</b>					
	Temp. / K	300	300	80	80	80
Fe <sup>2+</sup> site	Fe1	Fe2	Fe1	Fe2	Fe3	
<Fe-N> / Å	2.164	2.156	2.168	2.164	2.172	
$\zeta$ / Å	0.436	0.337	0.391	0.395	0.399	
$\Sigma$ / °	94.2	90.4	94.68	90.10	94.77	
$\theta$ / °	254	239	251	232	248	
(SC)N-Fe-N(CS) / °	105.96	104.32	105.27	103.74	105.60	
Shape	1.764	1.596	1.765	1.539	1.739	
$\sigma_1$ / °	76.11	76.51	75.76	75.96	75.24	
$\sigma_2$ / °	163.41	163.95	164.24	163.27	163.36	
$\sigma_3$ / °	48.01 /	43.99 /	48.62 /	44.80 /	50.08 /	
	42.75	43.99	39.78	40.82	38.08	

$\sigma_1$ :N-Fe-N with N from imine;  $\sigma_2$ :N-Fe-N with N from pyridine;  $\sigma_3$ ,dihedral angle of phenyl and pyridine in one ligand. <sup>a</sup> values obtained using the OctaDist program (<https://octadist.github.io>). <sup>b</sup> values obtained using the SHAPE program (ref.6).

SCXRD data allow to simulate to PXRD pattern at 300 K to compare with the experimental one (Figure III.11). One can clearly see the good agreement observed between both diffractograms indicating that the phase characterized by magnetic measurements corresponds to the crystalline phase studied in SCXRD. Therefore, this compound does not show any SCO down to 10 K, while it presents a symmetry breaking upon cooling.

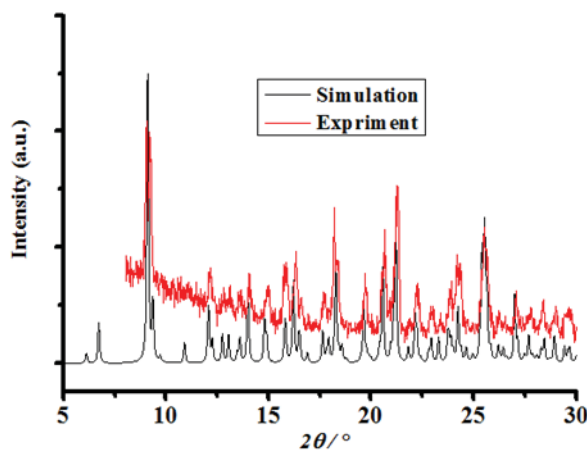


Figure III.11. Experimental (red) and simulated (black) powder X-ray diffraction patterns of complex **I-mBrA**.

In many cases, when structural phase transition and SCO occur, both event are concomitant.<sup>7-9</sup> However, they can also occur at different temperatures. For example, the spin crossover and the structural order–disorder phase transition from *R*-3 to *P*-1 are in fact two distinct phenomena in  $[\text{Fe}(\text{ptz})_6](\text{BF}_4)_2$ .<sup>10</sup> In complex  $[\{\text{Fe}(3\text{-bpp})(\text{NCS})_2\}_2(4,4'\text{-bypiridine})] \cdot 2\text{CH}_3\text{OH}$ , a symmetry breaking occurs around 161 K in the HS region.<sup>11</sup>

In polymorph **I-mBrA**, the symmetry breaking therefore drives the compound from a *C*2/*c* space group with two crystallographically independent  $\text{Fe}^{2+}$  sites at 300 K to a *P*2<sub>1</sub>/*c* space group with three independent molecules at 80 K, without any spin state changes. This indicates the structural phase transition here is probably a pure thermal effect for this compound. The high distortion of the coordination sphere is probably responsible for the absence of SCO in this polymorph. The structural transition weakly affects the packing and has almost no effect on the coordination sphere distortion, keeping it locked in HS.

If we compare this compound with complex **I-mFA**, there are huge differences regarding first the ligand conformation. In complex **I-mFA** the pyridine groups are either in *cis* conformation in Fe2 or in *trans* conformation in Fe1 whereas in polymorph **I-mBrA** both  $\text{Fe}^{2+}$  sites have their pyridine groups in *trans*. In complex **I-mFA**, “*trans*-Fe1” does not experience

any spin crossover so as “*trans*-Fe1” and “*trans*-Fe2” sites in polymorph **I-mBrA**. It looks therefore consistent. The bromine groups in polymorph **I-mBrA** are between 5.95 Å and 6.99 Å away from the Fe<sup>2+</sup> center which is farer than in complex **I-mFA** where the fluorine are at 5.65 Å from the “*trans*-Fe1” center. This might be explained by the bigger size of the bromine compare to the fluorine.

### III.3.3. Polymorph [Fe(PM-*m*BrA)<sub>2</sub>(NCS)<sub>2</sub>]-II: **II-mBrA**

- *Magnetic properties of II-mBrA*

Magnetic measurements were performed on a polycrystalline sample, using a SQUID magnetometer (see Appendix 3). Figure III.12 reports the thermal evolution of the  $\chi_M T$  product. The  $\chi_M T$  value at 300 K of 3.64 cm<sup>3</sup> K mol<sup>-1</sup> agrees well with a HS Fe<sup>2+</sup> ion ( $g = 2.22$ ). Upon cooling, the  $\chi_M T$  product gradually decreases to reach a value close to 0 cm<sup>3</sup> K mol<sup>-1</sup> below 100 K (0.03 cm<sup>3</sup> K mol<sup>-1</sup> exactly), indicating a gradual and complete spin crossover, without any hysteretic behaviour. The transition temperature is about  $T_{1/2} = 163$  K. The occurrence of a SCO on this sample is strongly different from what was observed on polymorph **I-mBrA**.

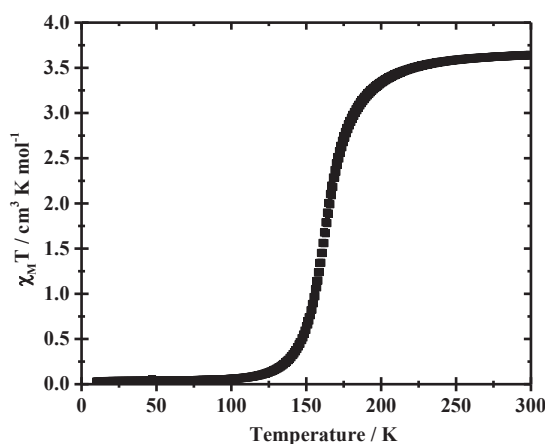


Figure III.12. Thermal dependence of the  $\chi_M T$  product of polymorph **II-mBrA** recorded at 0.4 K/min (in settle mode) under 10 kOe of applied magnetic field.

The HS\* state cannot be thermally quenched in the SQUID magnetometer. Regarding the LIESST effect, it looks very efficient while irradiating at 650 nm but as soon as the light is switched off, the system relaxes in few seconds to the LS state. Therefore no  $T(\text{LIESST})$  measurement was possible. Crystallographic investigations were then performed to understand the origin of the difference with the polymorph **I-mBrA** and the absence of long-lived HS\*

state. It could be due to the small energy barrier between  $hv$ -HS\* and LS, associated with the weak modification of the polyhedron distortion (Table III.5).

- *Crystallographic investigation of II-mBrA*

Data were recorded and the crystal structures were determined at 150 K and 300 K by SCXRD. As seen in Table III.4, polymorph II-mBrA crystallizes in the same C2/c space group at 300 K and 150 K.

Table III.4. Crystal data and structure refinement data for polymorph II-mBrA.

Empirical formula	C <sub>26</sub> H <sub>18</sub> Br <sub>2</sub> FeN <sub>6</sub> S <sub>2</sub>	
Formula weight / g mol <sup>-1</sup>	694.25	
Temperature / K	300	150
Radiation MoK $\alpha$ / Å	$\lambda = 0.71073$	
Crystal size / mm <sup>3</sup>	0.28 × 0.22 × 0.16	
Crystal system	monoclinic	
Space group	C2/c	
<i>a</i> / Å	11.9502(6)	11.6370(10)
<i>b</i> / Å	15.4615(7)	15.2426(12)
<i>c</i> / Å	16.4078(10)	15.9001(13)
$\alpha$ / °	90	90
$\beta$ / °	100.622(3)	98.492(4)
$\gamma$ / °	90	90
Volume / Å <sup>3</sup>	2 979.7(3)	2 789.4(4)
Z-formula	4	
$\rho_{\text{calc}}$ / g cm <sup>-3</sup>	1.548	1.653
$\mu$ / mm <sup>-1</sup>	3.354	3.582
F(000)	1376.0	1376.0
2 $\theta$ range for data collection / °	5.844 - 52.744	5.94 - 48.806
Index ranges	-14 ≤ <i>h</i> ≤ 14, -19 ≤ <i>k</i> ≤ 19, -20 ≤ <i>l</i> ≤ 16	-12 ≤ <i>h</i> ≤ 12, -17 ≤ <i>k</i> ≤ 17, -18 ≤ <i>l</i> ≤ 18
Reflections collected	7868	4137
Independent reflections	3033 [R <sub>int</sub> = 0.0477, R <sub>sigma</sub> = 0.0408]	2205 [R <sub>int</sub> = 0.0204, R <sub>sigma</sub> = 0.0292]
Data/restraints/parameters	3033/0/168	2205/0/168
Goodness-of-fit on F <sup>2</sup>	1.089	1.083
Final R indexes [ <i>I</i> ≥ 2 $\sigma$ ( <i>I</i> )]	R <sub>1</sub> = 0.0735, wR <sub>2</sub> = 0.2370	R <sub>1</sub> = 0.0620, wR <sub>2</sub> = 0.1660
Final R indexes [all data]	R <sub>1</sub> = 0.0969, wR <sub>2</sub> = 0.2561	R <sub>1</sub> = 0.0794, wR <sub>2</sub> = 0.1784
Largest diff. peak/hole / e Å <sup>-3</sup>	2.09/-0.61	1.83/-0.59

$$R_1 = \frac{\sum ||F_0| - |F_C||}{\sum |F_0|}, wR_2 = \left[ \frac{\sum w(F_0^2 - F_C^2)^2}{\sum w(F_0^2)^2} \right]^{1/2}$$

Part III – Promoting Distortion of the Coordination Polyhedron Using Polymorphism:  
Bromine Substitution of PM-zBrA Family

All atoms sit on the general Wyckoff position (8f) except Fe<sup>2+</sup> (4e position), so there is only half a molecule in the asymmetric unit. The thiocyanate group and PM-*m*BrA are in a *cis* configuration, where the two pyridine rings are in *trans* conformation (Figure III.13). The ligand conformation is similar to Fe2 in polymorph I-*m*BrA with the Br atoms pointing toward the S with S1---Br1 of 6.893 Å (at 300 K). The Fe-NC-S angle is 145.5° and the (SC)N-Fe-N(CS) angle is 97.86°. The bending of NCS<sup>-</sup> groups gives rise to the large S1---S1 distance of 7.767 Å. The average Fe-N bond length (<Fe-N>) is 2.154(5) Å at 300 K (Figure III.13), which is the typical for and Fe<sup>2+</sup> in its HS state, agreeing with the magnetic measurement.

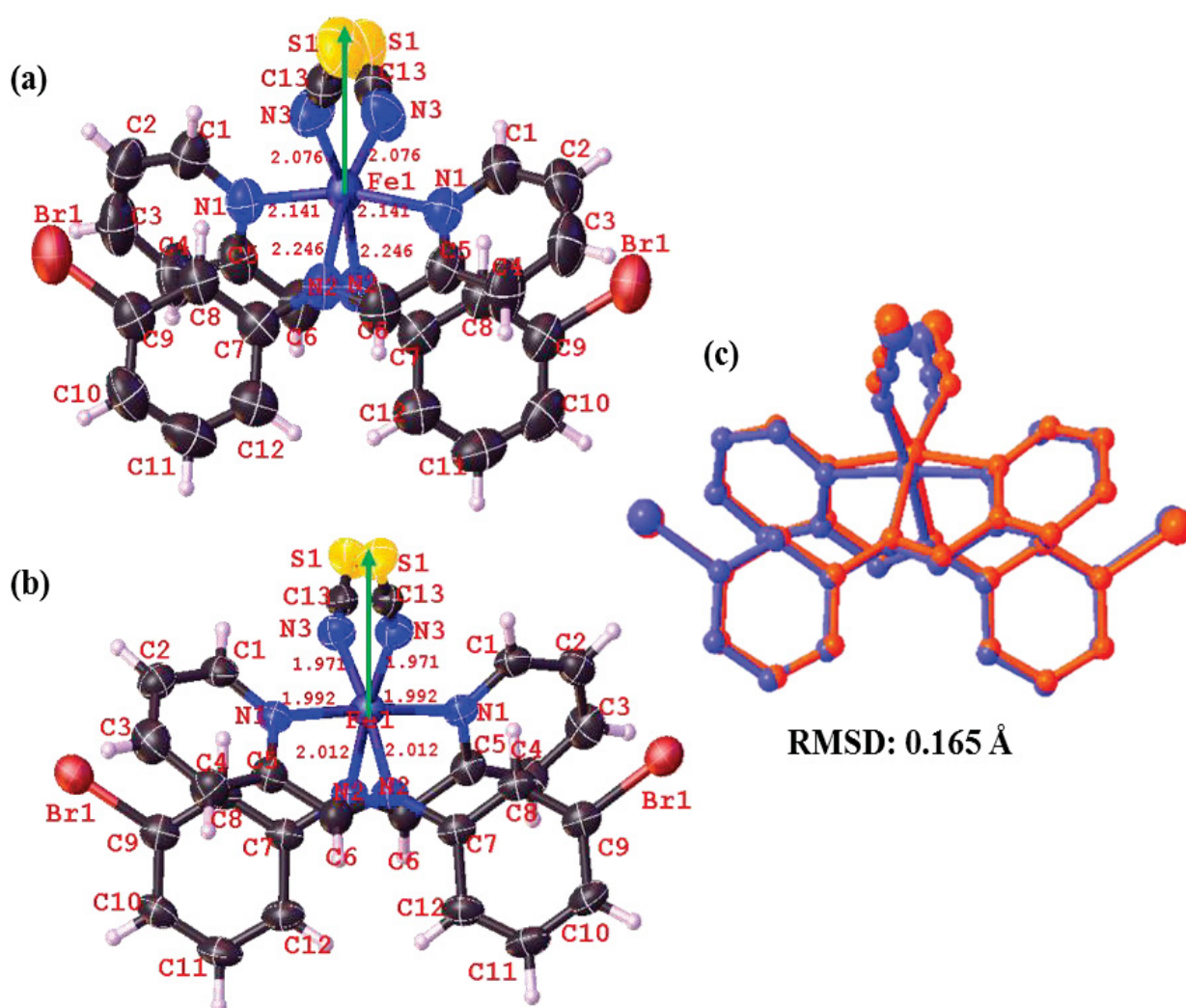


Figure III.13. One full iron molecule in polymorph II-*m*BrA at 300 K (a), 150 K (b) and the superposition of the molecular structures (c). The hydrogen atoms are omitted for clarity and the red and blue stand for 300 K and 150 K, respectively.

Upon cooling to 150 K, the ligand conformation is similar to that at 300 K with Br1---S1 distance of 6.751 Å. The Fe-NC-S angle is 151.8° and the (SC)N-Fe-N(CS) angle is 93.71°, leading to a smaller S1---S1 (7.617 Å). The <Fe-N> value is 1.993(4) Å, which is slightly higher than the typical value 1.96 Å expected for LS state. It represents a HS residue of about 15 %, in agreement with the magnetic properties, where the  $\chi_{MT}$  value of 0.53 cm<sup>3</sup> K mol<sup>-1</sup> at 150 K corresponds to 14% HS residue. By the superposition of the molecules between HS and LS, the atomic displacement of NCS<sup>-</sup> and motion of PM-*m*BrA ligands can be observed (Figure III.13c). The small RMSD value of 0.165 Å suggests the modifications at SCO are rather limited.

SCXRD data allow to simulate to PXRD pattern at 300 K to compare with the experimental one (Figure III.14). One can clearly see the good agreement observed between both diffractograms indicating that the phase characterized by magnetic measurements corresponds to the crystalline phase studied in SCXRD. This opens the possibility of structure-properties relationship.

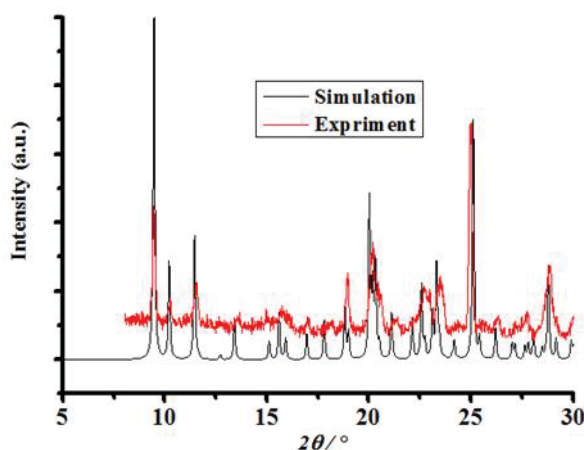


Figure III.14. Experimental (red) and simulated (black) from SCXRD data powder X-ray diffraction patterns of complex **II-*m*BrA**.

As seen in Table III.5, the angular ( $\Sigma$ ) and trigonal ( $\Theta$ ) distortions at 300 K are small ( $\Sigma = 74^\circ$  and  $\Theta = 196^\circ$ ) and vary weakly upon spin crossover ( $\Sigma = 54^\circ$  and  $\Theta = 156^\circ$  at 150 K) leading to weak  $\Delta\Sigma$  (20°) and  $\Delta\Theta$  (40°) from 300 K to 150 K. This weak modification of the distortion might be at the origin of the very fast relaxation of the  $h\nu$ -HS\* state.

Table III.5. The coordination sphere parameters in polymorph II-*m*BrA.

Compound	II- <i>m</i> BrA	
Temp. / K	300	150
Fe <sup>2+</sup> site	Fe1	Fe1
<Fe-N> / Å	2.154	1.993
ζ / Å	0.359	0.083
Σ / °	74.25	54.0
Θ / °	196	156
(SC)N-Fe-N(CS) / °	97.86	93.71
Shape	0.943	0.481
σ1 / °	81.80	86.61
σ2 / °	165.94	174.34
σ3 / °	42.00	46.05

σ1: N-Fe-N with N from imine; σ2: N-Fe-N with N from pyridine; σ3: dihedral angle of phenyl and pyridine in one ligand. <sup>a</sup> values obtained using the OctaDist program (<https://octadist.github.io>).  
<sup>b</sup> values obtained using the SHAPE program (ref.6).

The intermolecular interactions were explored with the fingerprints and the Hirshfeld surfaces. The main short contact is H2---π (2.725 Å at 300 K and 2.781 Å at 150 K) with π bond coming from thiocyanate group, as shown in the red spots in Hirshfeld surface (Figures III.15a and b). From 300 K to 150 K, the ratio of S---H remains almost the same while Br---H decreases of 4.5% (Figures III.15c and d). Another short contact can be noticed as π<sub>phenyl</sub>---π<sub>phenyl</sub> (3.947 Å at 300 K and 3.955 Å at 150 K), as seen in the shape index of Hirshfeld surface (Figure III.15e).

At 300 K, the molecules are connected along the *c* direction by H2---π bonding (Figure III.16). Along the *a* direction, the adjacent molecules are connected by π<sub>phenyl</sub>---π<sub>phenyl</sub> and Br1---H6 (3.023 Å) interactions with an inversion center. Br1---H1 (3.124 Å) bonding also links two molecules with an inversion center along the *b* direction. At *bc* plane, the molecules are packed with two-fold axis along *b* direction. So the molecular packing can be viewed as hydrogen bonded chains interacting through weak π<sub>phenyl</sub>---π<sub>phenyl</sub> interaction (Figure III.16). The structure at 150 K is very similar to that at 300 K. The variation of Fe---Fe distance along *c* and [110] directions are only 0.02 Å and 0.16 Å. The weak intermolecular interaction network appears consistent with the gradual SCO feature.

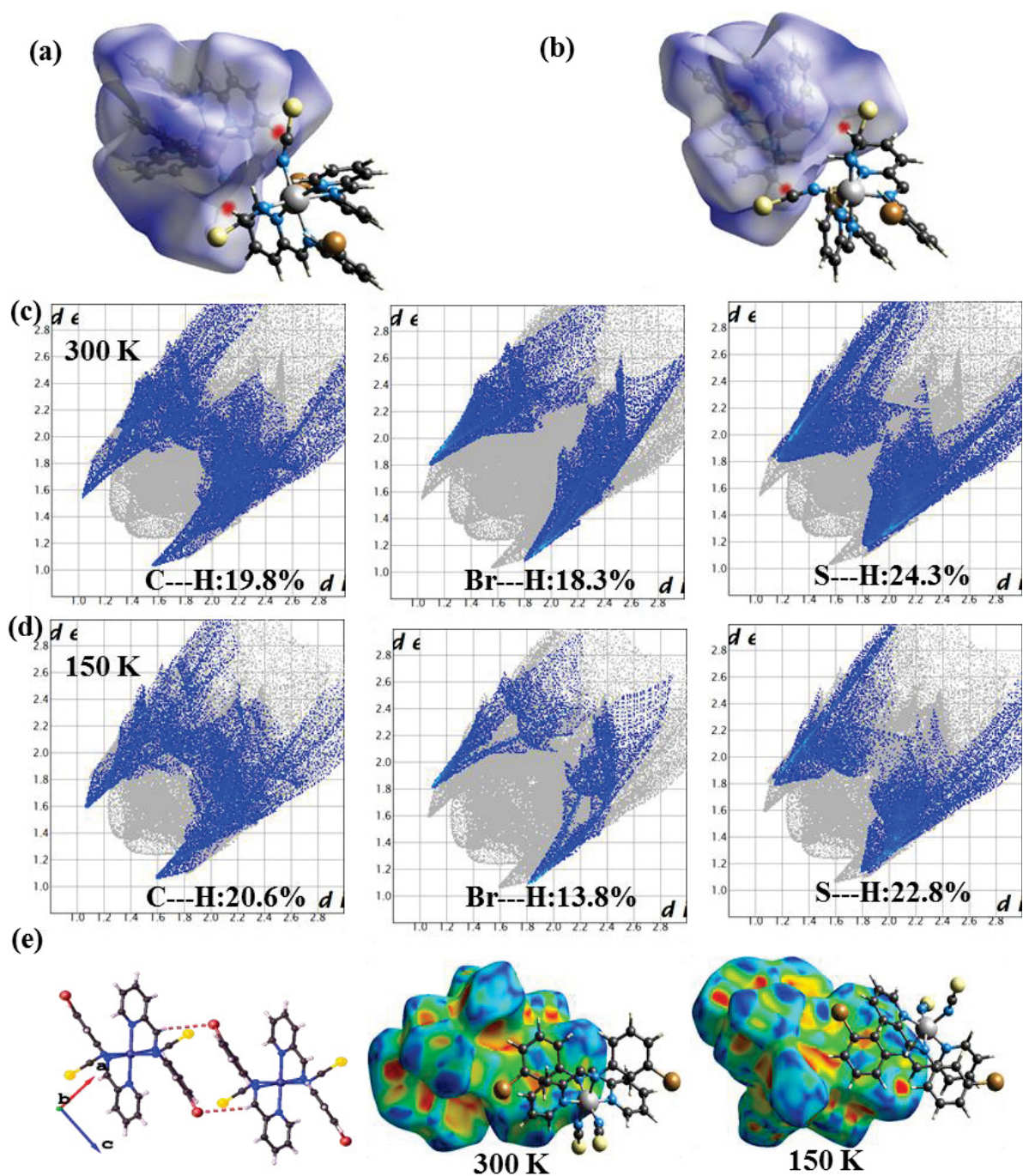
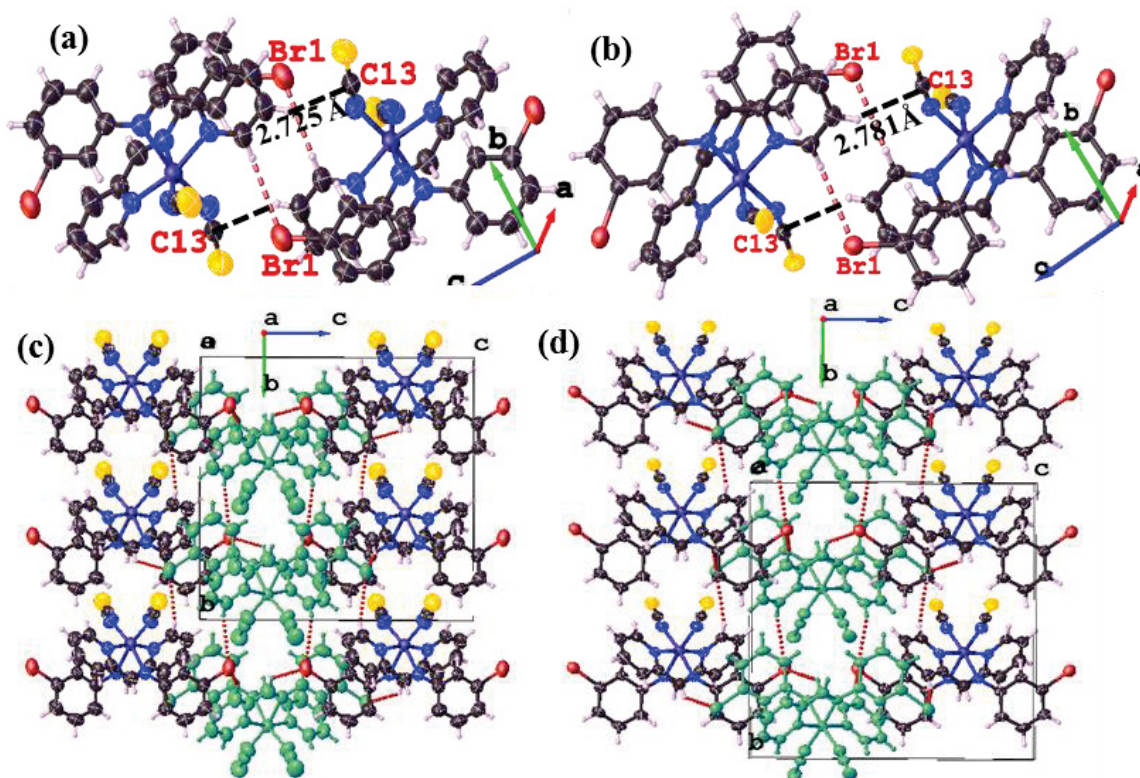


Figure III.15. The calculated Hirshfeld surfaces of Fe1 at 300 K (a) and 100 K (b), and selected hydrogen bonding in fingerprints at 300 K (c) and 100 K (d), and the  $\pi_{\text{phenyl}} \cdots \pi_{\text{phenyl}}$  interaction (e) of II-mBrA.



**Figure III.16.** The H--- $\pi$  contacts at 300 K (a) and 150 K (b), and three-dimensional packings at  $bc$  plane at 300 K (c) and 150 K (d) in polymorph **II-mBrA**. The molecules in green stand for the  $2_1$  axis along  $b$  direction.

- **Structure-properties relationship of II-mBrA**

From the structure described above, polymorph **II-mBrA** crystallizes in the same space group  $C2/c$  in HS and LS with a half  $Fe^{2+}$  molecule in the asymmetric unit. It exhibits a gradual spin crossover at  $T_{1/2} = 163$  K. This spin crossover is associated to very small modifications of the coordination sphere since the angular and trigonal distortions vary only of  $20^\circ$  and  $40^\circ$ , respectively. This might be at the origin of the impossibility to record a long-lived HS\* induced by light or thermal quenching.

Regarding the intermolecular interactions, the S---H ones are not obvious, compared with the other compounds, even if they contribute to around 24 % in fingerprints, the shortest S---H contacts are larger than 3.0 Å. The Br---H and  $\pi_{\text{phenyl}}\text{---}\pi_{\text{phenyl}}$  contacts are much weaker than H--- $\pi$  interactions. The weak modification of interactions at SCO results in the gradual SCO. In this respect, this polymorph adopts a fairly widespread behavior in  $Fe^{2+}$  complexes with a structure-properties relationship based on smooth structural modifications leading to a gradual SCO.<sup>12-13</sup>

### III.3.4. Discussions on I-*m*BrA and II-*m*BrA

As described above, the two polymorphs crystallize in the same space group  $C2/c$  at 300 K. However, complex **I-*m*BrA** does not exhibit any SCO while it is experiencing a structural transition upon cooling with a symmetry breaking that leads the compounds into a  $P2_1/c$  space group. On the contrary, complex **II-*m*BrA** is SCO active and down 150 K it does not exhibit any structural phase transition.

At 300 K, there are two crystallographically independent molecules with different ligand conformations in complex **I-*m*BrA**, one with Br next to S atom (Fe2) and the other one with Br far from S atom (Fe1). In complex **II-*m*BrA** there is only one Fe site that is rather similar to the Fe2 site in complex **I-*m*BrA**. Despite this similarity, there are huge differences between the corresponding molecular geometries at 300 K as revealed by the overlay (**Figure III.17**). Firstly, the distortion of the coordination sphere in polymorph **I-*m*BrA** is much stronger than that in **II-*m*BrA**, in agreement with the stabilization of the HS state and the absence of SCO event in complex **I-*m*BrA**. Secondly, the bending of  $\text{NCS}^-$  groups lead to a large angle of (SC)N-Fe-N-(CS) in both polymorphs (around  $105^\circ$  in **I-*m*BrA** and  $97^\circ$  in **II-*m*BrA**) at 300 K (**Tables III.3 and 5**) but show a clear difference between them. The higher bending in complex **I-*m*BrA** can be correlated with the higher distortion in this polymorph.

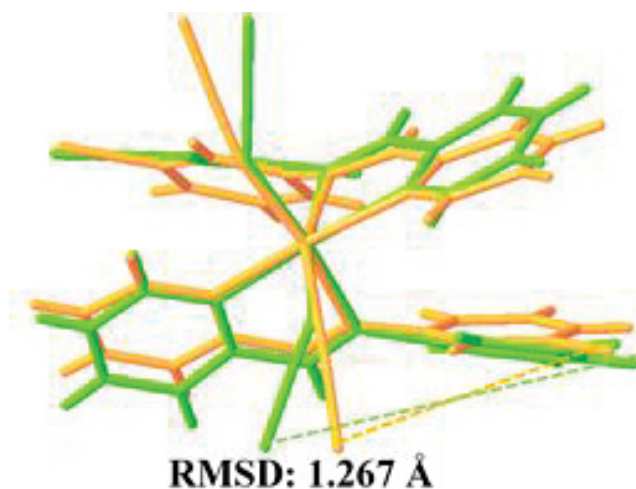


**Figure III.17.** Superposition of the molecular complex corresponding to the Fe2 site in polymorph **I-*m*BrA** (orange) and the molecular complex in polymorph **II-*m*BrA** (green) at 300K.

*Part III – Promoting Distortion of the Coordination Polyhedron Using Polymorphism:  
Bromine Substitution of PM-zBrA Family*

Based on the literature survey of analogous *trans*-[Fe(Rdpt)<sub>2</sub>(NCE)<sub>2</sub>] complexes, Rodríguez-Jiménez found that in these complexes the HS state is favored when the Fe-NC-S angle is lower than 154°. <sup>14</sup> Large bending of thiocyanate ligand can increase the distortion of FeN<sub>6</sub> polyhedron and then favor the HS state. In the literature, four complexes with Fe-N-CS lower than 159° are reported to show SCO. In these complexes, the thiocyanate ligands are all in *trans* configuration. In polymorph **I-mBrA**, the angles around 158° at 300 K are close to the 154° value proposed by Rodríguez-Jimenez, and the compounds is SCO inactive in agreement with such value. However, in polymorph **II-mBrA** the Fe-NC-S angle is of 145° and we could expect a HS compound too, which is not the case. Indeed, despite the huge bending of the NCS group, the global distortion of the coordination sphere is weak ( $\theta < 200^\circ$  in **II-mBrA**), leading to the occurrence of SCO while it was not expected if we would have only looked at the Fe-NC-S angle.

If we look at the Br---Fe distances in both polymorphs at 300 K (Table III.6) we see that in polymorph **I-mBrA** the bromine are at 6.99 Å and 6.08 Å from Fe1 center and at 5.95 Å from Fe2 center. In polymorph **II-mBrA** where the iron site resembles to Fe2 of polymorph **I-mBrA**, the Br---Fe distance is of 5.97 Å, similarly to the Fe2 site in polymorph **I-mBrA**. If we compare these distances to the ones in complex **I-mFA** (around 5.65 Å in Fe1 that is SCO inactive and 6.27-6.53 Å in Fe2 that is SCO active), we can expect Fe2 in polymorphs **I-mBrA** and Fe1 in **II-mBrA** to be SCO inactive with the argument that the shorter the distance, the higher the steric strain, the higher the distortion, the more the HS state is stabilized. The occurrence of SCO in polymorph **II-mBrA** clearly invalidates this hypothesis. Moreover, the bigger Halogen---Fe distances in Fe1 site of polymorph **I-mBrA** that does not experience any SCO is opposite to the observation made in **I-mFA**. Moreover, if we look at the atomic radius of fluorine (0.64 Å) and bromine (1.14 Å) <sup>15</sup>, we see that the difference of 0.5 Å between both halogens is not recovered in the three compounds. Indeed, the mean variation from fluorine to bromine in these compounds is around 0.3 Å, possibly indicating a more constrained coordination sphere in the bromine derivatives. This is the case for polymorph **I-mBrA** but not for **II-mBrA**. We can see from the distortion parameters  $\Sigma$  and  $\theta$  that the SCO active sites have very similar values while the SCO inactive sites have also similar values, higher than for the SCO active sites. Therefore, the origin of SCO activity might come from an upper scale than just the coordination sphere.

*Part III – Promoting Distortion of the Coordination Polyhedron Using Polymorphism:  
Bromine Substitution of PM-zBrA Family*

For instance, the density of polymorph **I-mBrA** (1.606 g cm<sup>-3</sup>) is larger than 1.545 g cm<sup>-3</sup> in polymorph **II-mBrA**, which may indicate that the more dense packing in polymorph **I-mBrA** may restrict the molecular geometry and then block the HS state. We cannot really compare with the density of complex **I-mFA** (1.456 g cm<sup>-3</sup>) since the smaller fluorine group might intrinsically reduce the density.

**Table III.6.** Selected parameters in complexes **I-mBrA**, **II-mBrA** and **I-mFA** at 300 K.

Compound	Fe <sup>2+</sup> site	Fe---X / Å	SCO activity	Σ /°	Θ /°	Fe <sup>2+</sup> site	Fe---X / Å	SCO activity	Σ /°	Θ /°
<b>I-mFA</b>	Fe2	6.27 / 6.53	active	71	199	Fe1	5.65	inactive	92	231
<b>I-mBrA</b>	Fe1	6.08 / 6.99	inactive	94	254	Fe2	5.95	inactive	90	239
<b>II-mBrA</b>			-			Fe1	5.97	active	74	196

### III.4. Characterizations of four $[\text{Fe}(\text{PM-}p\text{BrA})_2(\text{NCS})_2]$ polymorphs

#### III.4.1. Polymorph $[\text{Fe}(\text{PM-}p\text{BrA})_2(\text{NCS})_2]$ -I: I- $p\text{BrA}$

- *Switching properties of I- $p\text{BrA}$*

Figure III.18 reports the thermal behavior of the  $\chi_{\text{MT}}$  product of polymorph I- $p\text{BrA}$ , recorded on an assembly of crystals. The  $\chi_{\text{MT}}$  value at 300 K of  $3.98 \text{ cm}^3 \text{ K mol}^{-1}$  agrees well with HS  $\text{Fe}^{2+}$  ion ( $g = 2.30$ ). Upon cooling, the  $\chi_{\text{MT}}$  product decreases rapidly below 175 K to reach  $0.07 \text{ cm}^3 \text{ K mol}^{-1}$  below 125 K which agrees with a purely LS state. Upon warming, the curve describes a hysteresis loop. This hysteresis is slightly temperature scan rate dependent (Figure III.18a). Extrapolating the evolution of the switching temperatures at infinitely slow scan rate leads to  $T_{1/2\downarrow} = 170 \text{ K}$  and  $T_{1/2\uparrow} = 181 \text{ K}$ , and an 11 K large hysteresis loop.

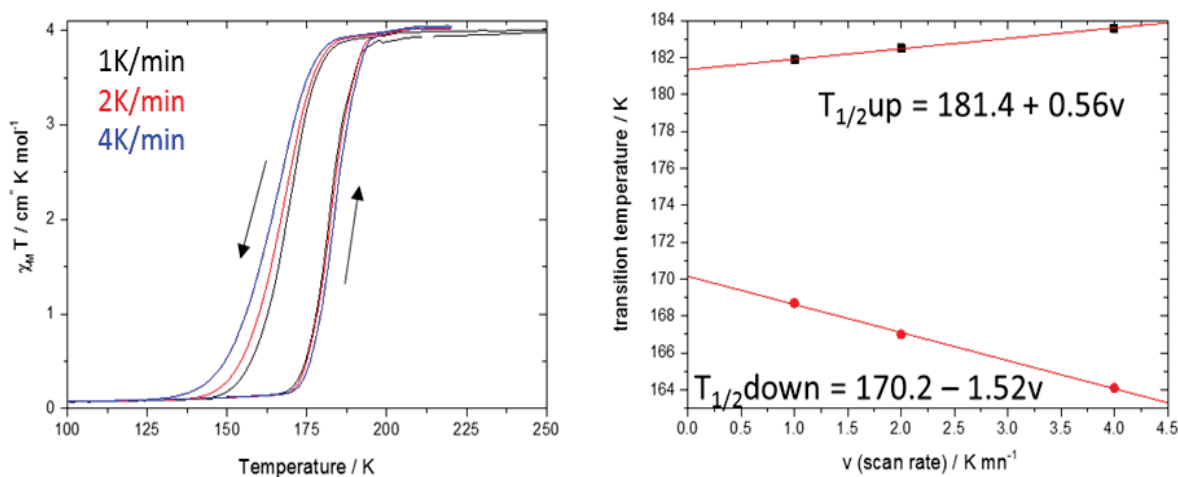


Figure III.18.  $\chi_{\text{MT}}$  as a function of the temperature for polymorph I- $p\text{BrA}$  at different scan rates (a), the evolution of the switching temperature  $T_{1/2}$  in warming and cooling modes as function of the temperature scan rate (b). The red right lines are the linear regression fits.

Differential Scanning Calorimetry (DSC) measurements have been performed to evidence the phase transition. Experimental details on DSC can be seen in Appendix 4. Figure III.19 reports two thermal cycles recorded at 4 K/min. Upon warming, only one peak is clearly evidenced, with no differences between the two cycles. Upon cooling, only one peak is observed, slightly influenced by the thermal cycling. The switching temperatures of the first cycle are 170 K and 180 K in cooling and warming modes, respectively. The variation of enthalpy ( $\Delta H = H_{HS} - H_{LS}$ ) and the entropy changes ( $\Delta S = S_{HS} - S_{LS}$ ) are  $9.4 \text{ kJ mol}^{-1}$  and  $49.1 \text{ J mol}^{-1} \text{ K}^{-1}$ , respectively, which are slightly lower than the typical values of iron-based SCO compounds ( $\Delta H$  :  $10\text{-}20 \text{ kJ mol}^{-1}$ ,  $\Delta S$  :  $50\text{-}80 \text{ J mol}^{-1} \text{ K}^{-1}$ )<sup>16</sup>

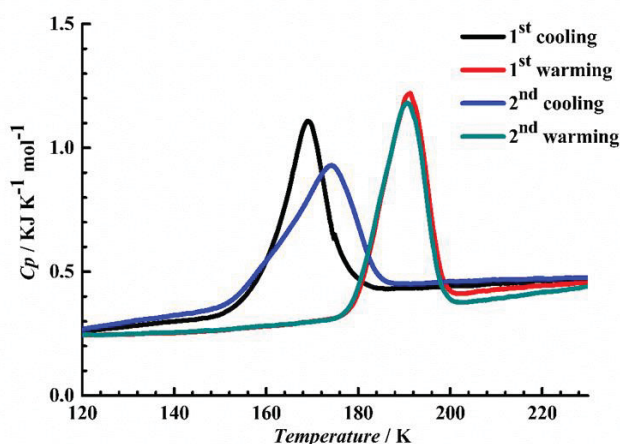
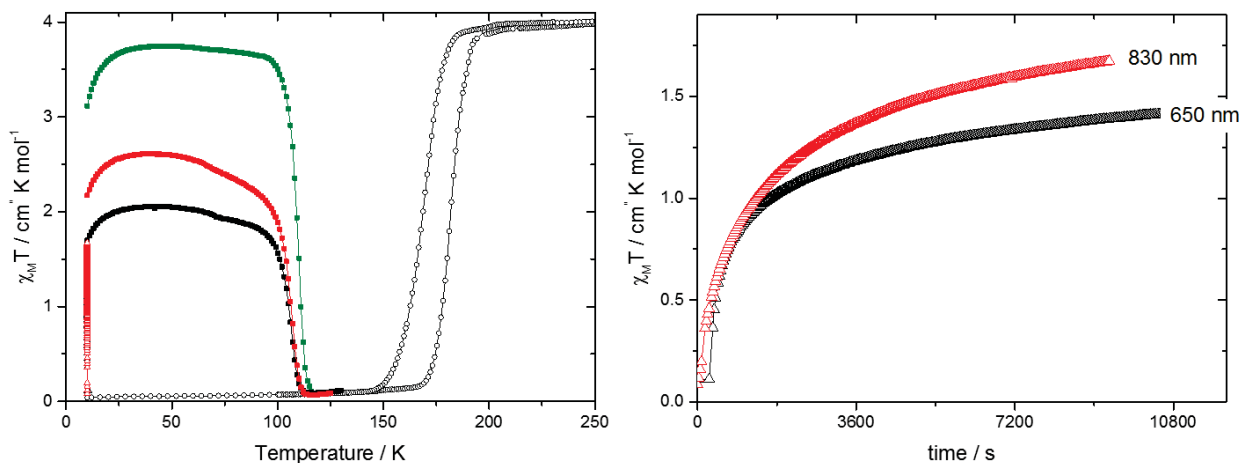


Figure III.19. DSC measurements of polymorph **I-pBrA** recorded at 4 K/min.

The HS state can be fully quenched at low temperature upon fast cooling. This thermally-induced excited spin-state trapping (TIESST) leads to the population of the Q-HS\* (Figure III.20a). Upon warming the thermally quenched state can be observed up to a  $T(\text{TIESST})$  value of 109 K. Light irradiation applied at 10 K in the LS state also allows to populate a metastable  $h\nu\text{-HS}^*$  state, at least partially. Indeed, a 830 nm irradiation allows 65 % of population (50 % at 650 nm) after 2h30 of irradiation (Figure III.20b). It is worth mentioning that this irradiation is slow, indicating a difficult light-induced process. The  $T(\text{LIESST})$  curves recorded at 0.4 K/min after irradiation leads to  $T(\text{LIESST})$  values of 107 K, very close to the  $T(\text{TIESST})$  value. Interestingly, **I-pBrA** shows the highest  $T(\text{LIESST})$  obtained so far of the PM-L family (Table I.1).<sup>17-18</sup> This characteristic represents a singular feature of this compound that we tried to understand from the crystallographic point of view.



**Figure III.20.** (left)  $\chi_M T$  as a function of temperature for polymorph **I-pBrA** showing the  $T(LIESST)$  curve ( $\blacksquare$ ), the LIESST effect under irradiation at 650 ( $\Delta$ ) and 830 nm ( $\triangle$ ) and the subsequent  $T(LIESST)$  curves ( $\blacksquare$  and  $\blacksquare$  after 650 and 830 nm irradiation respectively), recorded at 0.4 K/min. (Right).  $\chi_M T$  as a function of time at 10 K, under irradiation at 650 ( $\Delta$ ) and 830 nm ( $\triangle$ ) with around 5 mW/cm<sup>2</sup>.

- *Crystallographic study of I-pBrA*

Variable temperature single-crystal X-ray diffraction (SCXRD) was performed from 80 K to 350 K, including 80, 100, 120, 150, 170, 180, 200, 250 and 300. The thermally quenched Q-HS\* has been measured at 80 and 10 K, the latter was performed in collaboration with Dr. Sébastien Pillet in the University of Lorraine (Nancy, France). At all the measured temperatures **I-pBrA** crystallizes in the monoclinic system with the space group of  $P2_1/n$  (Table III.7).

In the asymmetric unit, all atoms sit on the general Wyckoff position (4e) and there are two crystallographically independent iron complexes in the asymmetric unit, which are labelled Fe1 and Fe2 (Figure III.21). The thiocyanate groups and PM-pBrA are in a *cis* configuration, where two pyridine rings are in *trans* form. At 300 K, the Fe-N-CS angles are 160.79° (Fe2-N-CS4), 175.85° (Fe2-N-CS3), 159.63° (Fe1-N-CS1), and 170.57° (Fe1-N-CS2) (Table III.8). It results in (SC)N---Fe---N(CS) angles in Fe1, and Fe2 of 94.4° and 96.5°, respectively, which are smaller than that in polymorph **II-mBrA**. The most salient difference between both molecules can be seen comparing  $\sigma_3$  values that probe the dihedral angle between the phenyl and pyridine rings within the same ligand. In Fe1, the  $\sigma_3$  values are of 75° and 52° while they are of 79° and 30° in Fe2. The geometry of the ligands are then clearly different, as illustrated by the large RMSD value of 0.650 Å in the superposition of molecules (Figure III.21d). The average <Fe-N> bond lengths are 2.183(5) Å and 2.178(6) Å in Fe1 and Fe2 entities at 300 K, respectively, in agreement with two HS Fe<sup>2+</sup> ions.

Part III – Promoting Distortion of the Coordination Polyhedron Using Polymorphism:  
Bromine Substitution of PM-zBrA Family

**Table III.7.** The crystal data and structure refinement data in polymorph **I-pBrA** at selected temperatures (full table with complementary temperatures in Appendix 5)

Empirical formula	C <sub>26</sub> H <sub>18</sub> Br <sub>2</sub> FeN <sub>6</sub> S <sub>2</sub>					
Formula weight / g mol <sup>-1</sup>	694.25					
Temperature / K	300	200	150	80	80	10
Radiation MoK $\alpha$ / Å	$\lambda=0.71073$					
Crystal size / mm <sup>3</sup>	0.20×0.10×0.10					
Crystal system	monoclinic					
Space group	P2 <sub>1</sub> /n					
<i>a</i> / Å	16.7235(7)	16.6521(3)	15.8370(6)	15.8078(8)	16.5266(5)	16.5140(4)
<i>b</i> / Å	21.3275(9)	21.2327(3)	21.0664(8)	20.9483(12)	21.0835(7)	20.9864(5)
<i>c</i> / Å	16.7294(7)	16.5891(3)	17.6888(7)	17.6727(10)	16.4474(5)	16.3611(5)
$\alpha$ / °	90					
$\beta$ / °	109.419(2)	109.0200(10)	109.710(2)	109.6700(15)	108.843(2)	108.785(3)
$\gamma$ / °	90					
Volume / Å <sup>3</sup>	5627.4(4)	5545.17(16)	5555.7(4)	5510.8(5)	5423.8(3)	5368.2(3)
Z-formula	8					
$\rho_{\text{calc}}$ / g cm <sup>-3</sup>	1.639	1.663	1.660	1.674	1.700	1.723
$\mu$ / mm <sup>-1</sup>	3.551	3.604	3.597	3.627	3.685	3.724
<i>F</i> (000)	2752	2752	2752	2752	2752	2752
2 $\theta$ range for data collection / °	2.984-52.744	4.628-50.09	3.866-56.34	2.994-55.112	4.246-52.744	3.268-54.206
Reflections collected	11404	9758	13364	12698	11087	9428
Independent Reflections(R <sub>int</sub> ,R <sub>sigma</sub> )	6078 (0.0687, 0.0827)	7807 (0.0209, 0.0299)	7689 (0.0597, 0.0786)	8823 (0.0617, 0.0457)	6126 (0.0689, 0.1184)	8599 (0.0352, 0.0260)
Goodness-of-fit on F <sup>2</sup>	1.012	1.029	1.026	1.063	0.978	1.069
Final R indexes [I>>=2 $\sigma$ (I)]	R <sub>1</sub> =0.0681 wR <sub>2</sub> =0.139	R <sub>1</sub> =0.0452 wR <sub>2</sub> =0.114	R <sub>1</sub> =0.0679 wR <sub>2</sub> =0.160	R <sub>1</sub> =0.0544 wR <sub>2</sub> =0.115	R <sub>1</sub> =0.0619 wR <sub>2</sub> =0.129	R <sub>1</sub> =0.0385 wR <sub>2</sub> =0.091
Final R indexes [all data]	R <sub>1</sub> =0.1546 wR <sub>2</sub> =0.1734	R <sub>1</sub> =0.0590 wR <sub>2</sub> =0.1228	R <sub>1</sub> =0.1303 wR <sub>2</sub> =0.2019	R <sub>1</sub> =0.0957 wR <sub>2</sub> =0.1379	R <sub>1</sub> =0.1364 wR <sub>2</sub> =0.1553	R <sub>1</sub> =0.0435 wR <sub>2</sub> =0.0934
Largest diff. peak/hole / e Å <sup>-3</sup>	0.89/-1.06	1.71/-1.47	1.79/-0.98	2.57/-1.18	2.39/-0.97	2.53/-0.98

$$R_1 = \frac{\sum ||F_o| - |F_c||}{\sum |F_o|}, wR_2 = \left[ \frac{\sum w(F_o^2 - F_c^2)^2}{\sum w(F_o^2)^2} \right]^{1/2}$$

At 80 K, all the coordination sphere parameters become very close in both sites (Table III.8). This is particularly the case for  $\sigma_3$ : 67° and 55° in Fe1 and 56° and 57° for Fe2. The bromophenyl rings are approximately perpendicular in both molecules. Therefore, both molecules become quite similar, with a RMSD value of 0.129 Å (Figure III.21e). A noticeable difference lies in the bending and orientation of the NCS<sup>-</sup> groups. The average <Fe-N> bond lengths are 1.953(5) Å and 1.955(5) Å at 80 K, corresponding to two LS molecules, in agreement with the magnetic measurements.

Part III – Promoting Distortion of the Coordination Polyhedron Using Polymorphism:  
Bromine Substitution of PM-zBrA Family

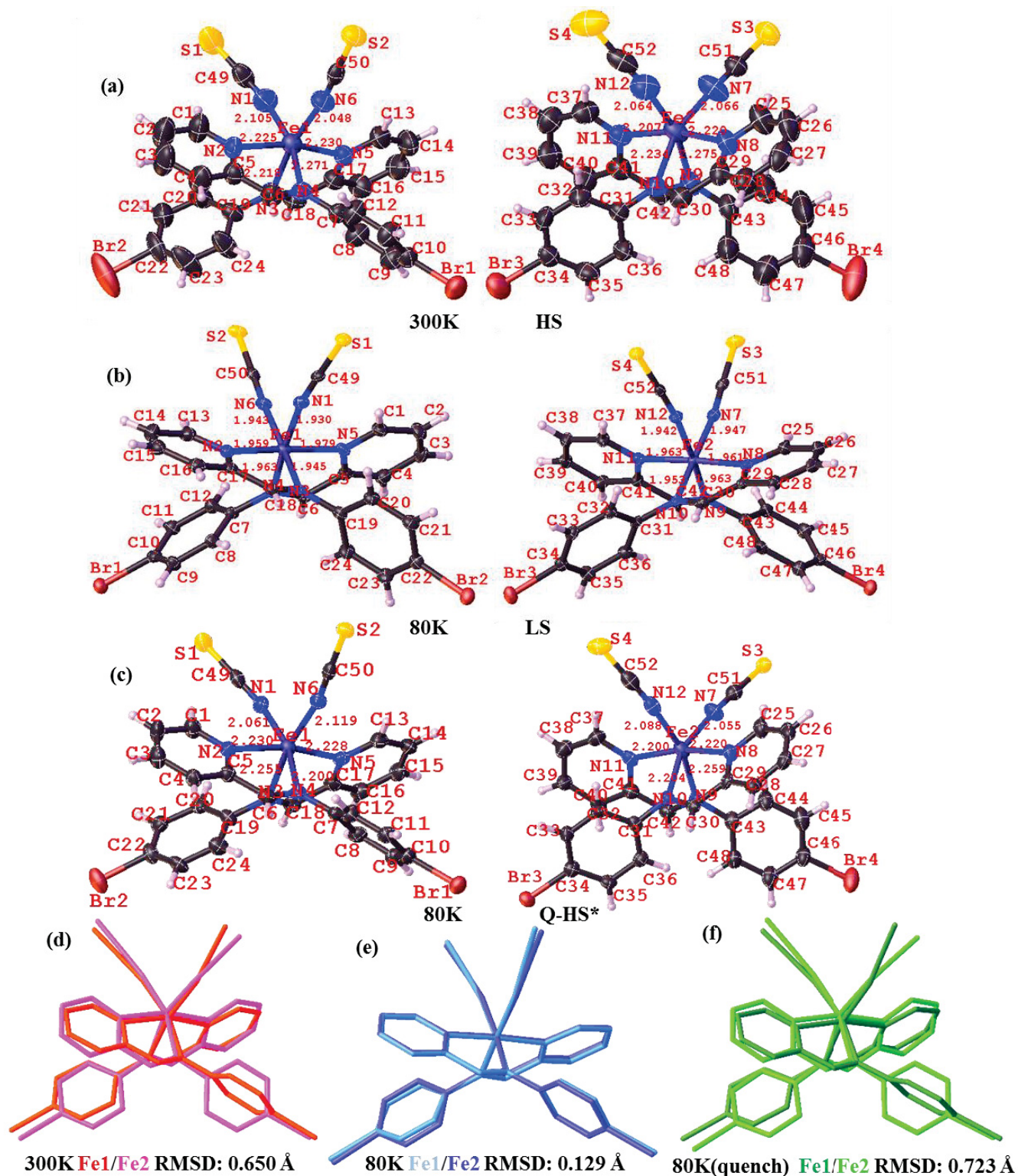


Figure III.21. The two independent molecules in the asymmetry unit at 300 K (a), 80 K (b), and 80 K in the Q-HS\* (c) of polymorph **I-pBrA**. Superpositions of Fe1 and Fe2 molecules at 300 K (d), 80 K (e), and 80 K in the Q-HS\* (f).

The thermally quenched structure was also determined at 80 K. The compound crystallizes in the same monoclinic space group  $P2_1/n$  with two molecules in the asymmetric unit (Table III.7 and Figure III.21c). The ligand conformations are very similar to that at 300 K with  $\sigma_3$  values of  $66^\circ$  and  $46^\circ$  for Fe1 and of  $79^\circ$  and  $22^\circ$  in Fe2 (Table III.8). The overlay of these two molecules is very similar to the one obtained at 300 K, with a RMSD value of 0.723 Å (Figure III.21f). The average  $\langle\text{Fe-N}\rangle$  bond lengths are 2.182(6) Å and 2.171(6) Å for Fe1 and Fe2 centers, respectively, indicating that the HS state can be fully quenched, in agreement with the magnetic measurements.

Table III.8. The coordination spheres parameters in polymorph I-pBrA at the selected temperature.

Temperature / K	300	300	80	80	80 <sub>quench</sub>	80 <sub>quench</sub>
Fe <sup>2+</sup> site	Fe1	Fe2	Fe1	Fe2	Fe1	Fe2
$\langle\text{Fe-N}\rangle / \text{Å}$	2.183(5)	2.178(6)	1.953(5)	1.955(5)	2.182(6)	2.171(6)
$\zeta / \text{Å}$	0.425	0.450	0.085	0.043	0.369	0.397
$\Sigma / ^\circ$	70.54	84.07	59.54	56.28	69.71	86.61
$\Theta / ^\circ$	265.41	269.23	167.56	159.26	263.00	281.43
Shape <sup>b</sup>	1.653	1.726	0.729	0.653	1.636	1.884
SC-N-Fe / $^\circ$	159.63 /	160.79 /	169.88 /	169.10 /	154.81 /	160.63 /
	170.57	175.85	172.95	170.28	168.79	174.92
(SC)N-Fe-N(CS) / $^\circ$	94.38	96.50	88.08	87.73	93.84	95.65
$\sigma_1 / ^\circ$	89.18	80.94	99.05	99.21	82.88	80.00
$\sigma_2 / ^\circ$	164.32	165.86	175.92	176.05	171.40	167.16
$\sigma_3 / ^\circ$	75.01 /	79.62 /	66.95 /	56.25 /	66.49 /	78.77 /
	52.67	30.26	55.49	57.20	45.96	22.46

$\sigma_1$ : N-Fe-N with N from imine;  $\sigma_2$ : N-Fe-N with N from pyridine;  $\sigma_3$ : dihedral angle of phenyl and pyridine in one ligand. <sup>a</sup> values obtained using the OctaDist program (<https://octadist.github.io>). <sup>b</sup> values obtained using the SHAPE program (ref.6)

In order to evidence the variation of the ligand geometries at SCO, the superposition of molecules are shown in Figure III.22. From HS to LS, the Fe1 molecule does not change too much (RMSD = 0.374 Å), except the change due to the contraction from the spin crossover. On the contrary, Fe2 experiences a huge change with a RMSD of 0.734 Å. In Fe2, SCO is accompanied by a motion of NCS<sup>-</sup> but overall by a huge rotation of the bromophenyl groups. This is evidenced by the evolution of the dihedral angle between the pyridine and bromophenyl groups of the same ligand,  $\sigma_3$ . In Fe1, from HS to LS,  $\sigma_3$  varies of  $-8^\circ$  and  $+2^\circ$  for the two ligands while in Fe2 site, it varies of  $-23^\circ$  and  $+27^\circ$  (Table III.8 and Figure III.22a). The latter corresponds to an impressive rotation of the ligand (Figure III.22).

*Part III – Promoting Distortion of the Coordination Polyhedron Using Polymorphism:  
Bromine Substitution of PM-zBrA Family*

In order to understand the structural variation during the thermal quenching effect, the comparison of the LS and Q-HS\* molecules are shown in **Figure III.22b** and between the HS and Q-HS\* in **Figure III.22c**. The resulting RMSD values for Fe1 and Fe2 are 0.397 Å and 0.788 Å, respectively from the LS/Q-HS\* overlay and 0.099 Å and 0.086 Å for Fe1 and Fe2 respectively from the HS/Q-HS\* overlay. We first clearly see the very same geometries for the HS and Q-HS\* states confirming the efficient thermal quenching of the HS state structure. The LS/Q-HS\* overlay gives values slightly bigger than the RMSD between HS and LS indicating a higher ligand modification in the Q-HS\* state. In Fe1, from Q-HS\* to LS,  $\sigma_3$  varies of  $0^\circ$  and  $+10^\circ$  for the two ligands while in Fe2 site, it varies of  $-22^\circ$  and  $+35^\circ$  (**Table III.8**). At the very same temperature of 80 K, therefore avoiding the effect of temperature on the structural motion, the differences between the Q-HS\* and LS state is enhanced compared to the 300K/80K comparison. Let us notice that this huge rotation of ligands in the crystalline state is reversible and reproducible. The energy cost associated to such rotation in the solid state might be too high at 10 K to promote a full LS  $\rightarrow$   $h\nu$ -HS\* photoswitching, explaining the incomplete LIESST process.

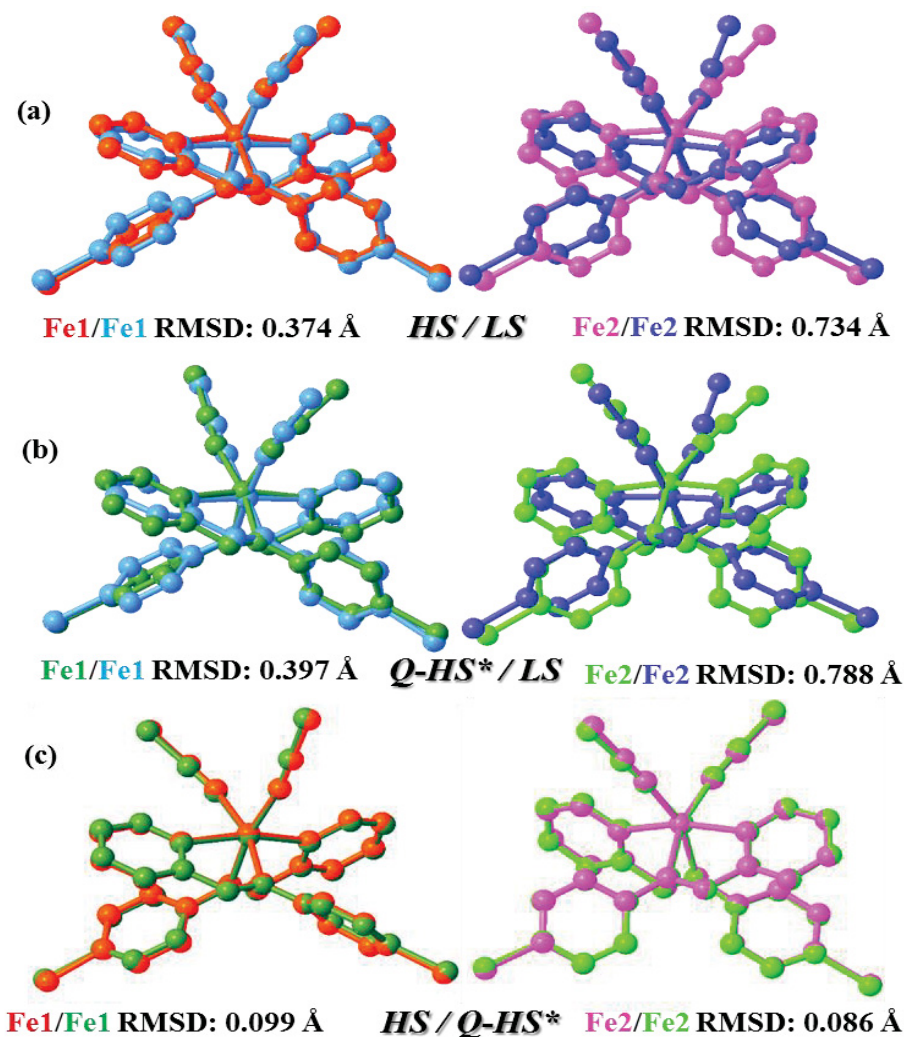
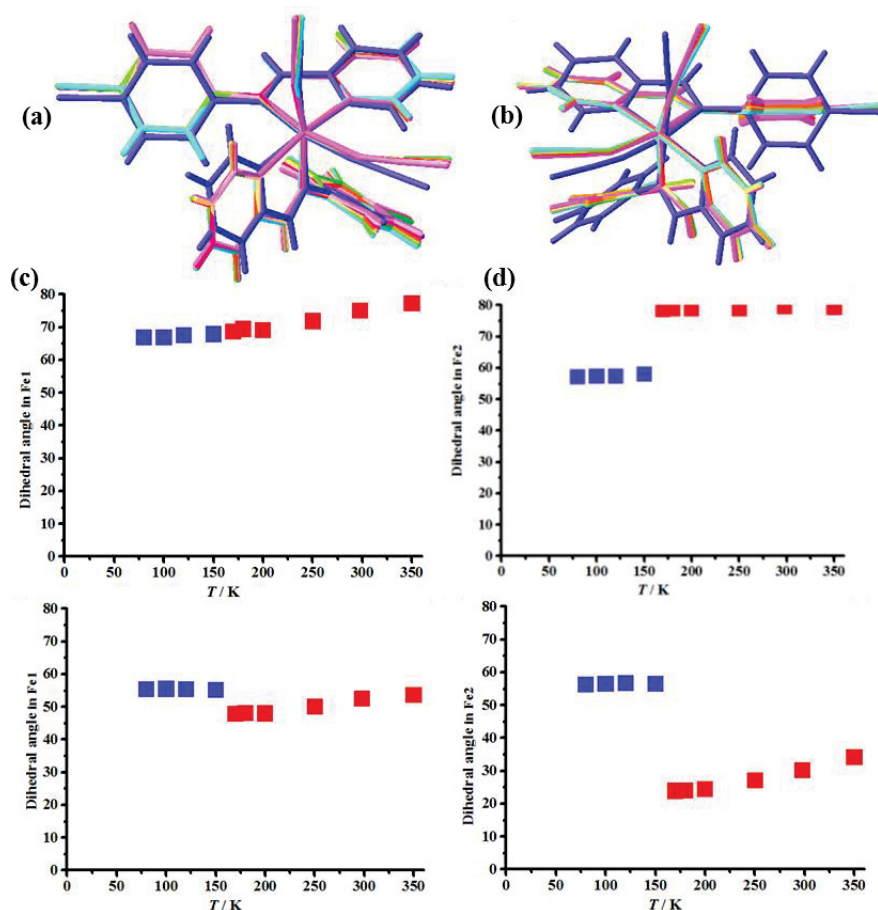


Figure III.22. Superposition of Fe1 and Fe2 between HS and LS (a), Q-HS\* and LS (b), Q-HS\* and HS (c) of polymorph **I-pBrA**.

In order to correlate this ligand rotation with the spin crossover and see if they are two concomitant phenomena, crystal structures were solved at 350, 300, 250, 200, 180, 170, 150, 120, 100, and 80 K. These structures were compared to the ones obtained at 80 K and 10 K in the thermally quenched Q-HS\* state. Figures III.23a and b show the superposition of all these molecules' structures for both Fe1 and Fe2 sites together with the thermal evolution of  $\sigma_3$  (Figures III.23c and d). From the overlay of Fe1 molecules, we can observe the motion of the NCS<sup>-</sup> groups at the spin crossover. The small change in  $\sigma_3$  ( $\delta\sigma_3 = 7^\circ$ ) is observed between the structures at 170 K (HS) and 150 K (LS) in Fe1. Similar observations can be made on Fe2 site with a bigger change in  $\sigma_3$  ( $\delta\sigma_3 = 33^\circ$ ) related to the rotation of phenyl ring at the SCO. Hence, it is reasonable to conclude the rotation and motion of ligands are concomitant with the SCO in polymorph **I-pBrA**.



**Figure III.23.** Superposition of Fe1(a) and Fe2 (b), and the dihedral angles of ligands ( $\sigma_3$ ) of Fe1 (c) and Fe2 (d) in polymorph **I-pBrA** at various temperature. The red and blue squares stand for HS and LS, respectively.

As a first insight to explain the high  $T(\text{LIESST})$  value for this compound, we followed in temperature the distortion parameters of the iron polyhedron (Figure III.24 and Table III.9). The thermal evolution of the  $\langle \text{Fe-N} \rangle$  distances, the bond distortion ( $\zeta$ ), and the trigonal distortion ( $\Theta$ ) in Fe1 and Fe2 are similar. However, the variation of the angular distortion ( $\Sigma$ ) is much bigger in Fe2N<sub>6</sub> than in Fe1N<sub>6</sub>. The variations of  $\langle \text{Fe-N} \rangle$ ,  $\zeta$ ,  $\Sigma$  and  $\Theta$  occur at the same temperature (temperature range of 20 K, Figure III.24), which may indicate that Fe1 and Fe2 undergo the SCO concomitantly, in agreement with the magnetic measurements which did not show any step in the spin crossover curve.

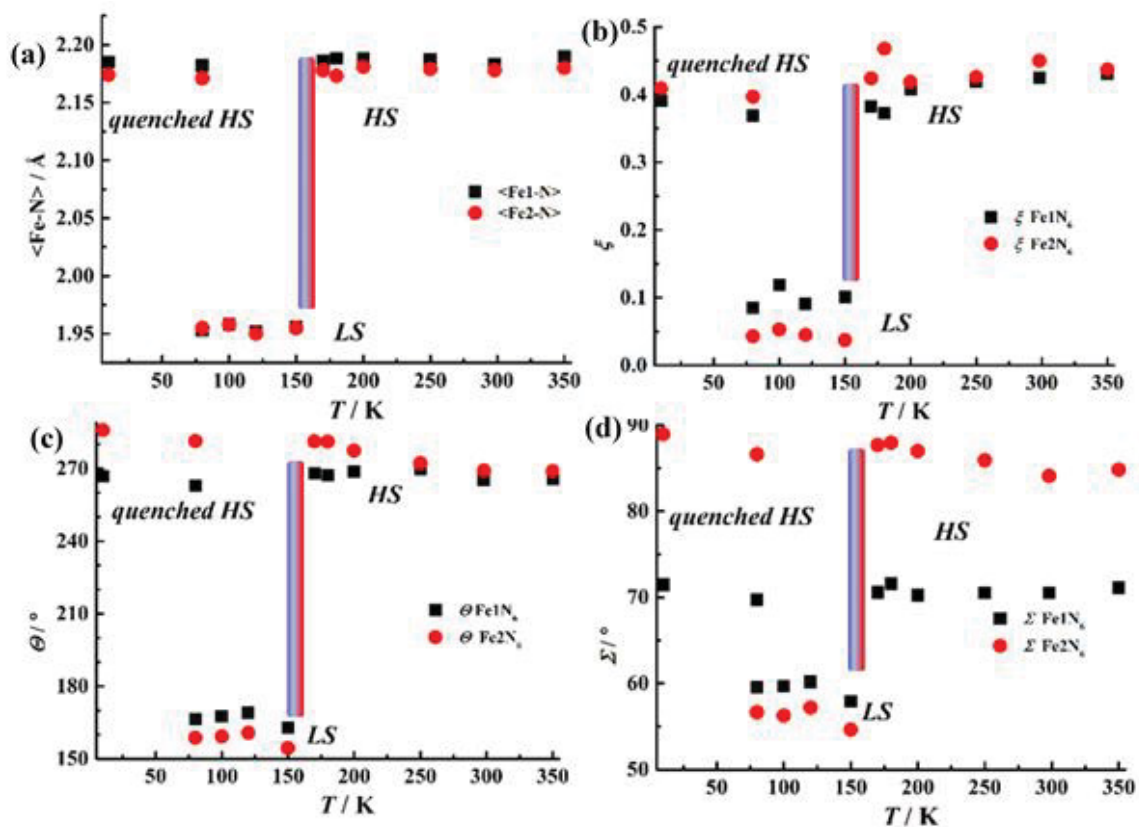


Figure III.24. Thermal variation of the distortion parameters of the coordination sphere of Fe1 (black squares) and Fe2 (red circles) entities in polymorph **I-pBrA**.

It is interesting to see that the values of  $\Theta(\text{Fe2})$  and  $\Sigma(\text{Fe2})$  in the Q-HS\* are slightly larger than that in the HS. Moreover,  $\Theta(\text{Fe2})$  increases slowly upon cooling (red sphere in Figures III.24c) while  $\Theta(\text{Fe1})$  and  $\Sigma(\text{Fe1})$  are nearly stable in both HS and Q-HS\* (black square in Figures III.24c, and d). Additionally, the value of  $\Sigma(\text{Fe1})$  is much smaller than  $\Sigma(\text{Fe2})$  in both HS and Q-HS\* by a factor 3. With such a difference, one might expect SCO and  $T(\text{LIESST})$  features to be stepped.<sup>19</sup> Obviously, it is not the case for polymorph **I-pBrA** and additionally, it somehow rules out the influence of  $\Sigma$  on the  $T(\text{LIESST})$  as already suspected.<sup>20</sup>

Thanks to the fact that the HS and Q-HS\* structures are similar and that we have access to the LS and Q-HS\* structures at the same temperature, 80 K, we can calculate the variation of the distortion parameters avoiding the effect of thermal contraction (Table III.9). One can immediately see that Fe2 experiences much bigger variations with a huge  $\Delta\Theta$  of  $122^\circ$ . However, the difference between Fe1 and Fe2 does not induce any step in the SCO features. Moreover, with a substitution in *para* position, we do not expect to exert *a priori* any steric strain on the coordination sphere and to increase the distortion. We have therefore explored the origin of these huge  $\Delta\Theta$  at a bigger scale within the crystal, starting by the intermolecular contacts.

Table III.9. Polyhedron distortion parameters of polymorph I-pBrA at various temperatures.

Temperature / K (spin state)	<Fe1-N> / Å	<Fe2-N> / Å	$\zeta$ / Å (Fe1N <sub>6</sub> )	$\zeta$ / Å (Fe2N <sub>6</sub> )	$\Sigma$ / ° (Fe1N <sub>6</sub> )	$\Sigma$ / ° (Fe2N <sub>6</sub> )	$\Theta$ / ° (Fe1N <sub>6</sub> )	$\Theta$ / ° (Fe2N <sub>6</sub> )
350 (HS)	2.190(5)	2.180(6)	0.431	0.437	71.11	84.83	265.56	268.96
300 (HS)	2.183(5)	2.178(6)	0.425	0.450	70.54	84.07	265.41	269.23
250 (HS)	2.187(4)	2.179(5)	0.419	0.426	70.54	85.90	269.82	272.25
200 (HS)	2.188(4)	2.181(4)	0.408	0.419	70.26	86.98	268.65	277.45
180 (HS)	2.188(7)	2.173(6)	0.373	0.468	71.59	87.94	267.19	281.13
170 (HS)	2.186(8)	2.178(8)	0.382	0.424	70.58	87.68	267.99	281.21
150 (LS)	1.956(6)	1.955(5)	0.101	0.037	57.89	54.63	162.73	154.39
120 (LS)	1.952(7)	1.950(7)	0.091	0.045	60.18	57.18	168.97	160.73
100 (LS)	1.958(6)	1.958(5)	0.119	0.053	59.69	56.28	167.56	159.26
80 (LS)	1.953(5)	1.955(5)	0.085	0.043	59.54	56.28	166.39	158.65
80 (Q-HS*)	2.182(6)	2.171(6)	0.369	0.397	69.71	86.61	263.00	281.43
10 (Q-HS*)	2.185(3)	2.174(3)	0.391	0.409	71.47	88.95	266.90	285.92
$\Delta(Q-HS^*-LS)$ at 80 K	0.229	0.216	0.284	0.354	10.17	29.96	96.61	122.78

The variation of ligand geometry can influence the intermolecular interactions and conversely, changes in intermolecular interactions can influence the ligand geometry.<sup>19,21</sup> We analyzed the intermolecular interactions using the fingerprint derived from the Hirshfeld surface in order to understand the origin of the rotation of the ligands and the high distortion of the coordination sphere.

Part III – Promoting Distortion of the Coordination Polyhedron Using Polymorphism:  
Bromine Substitution of PM-zBrA Family

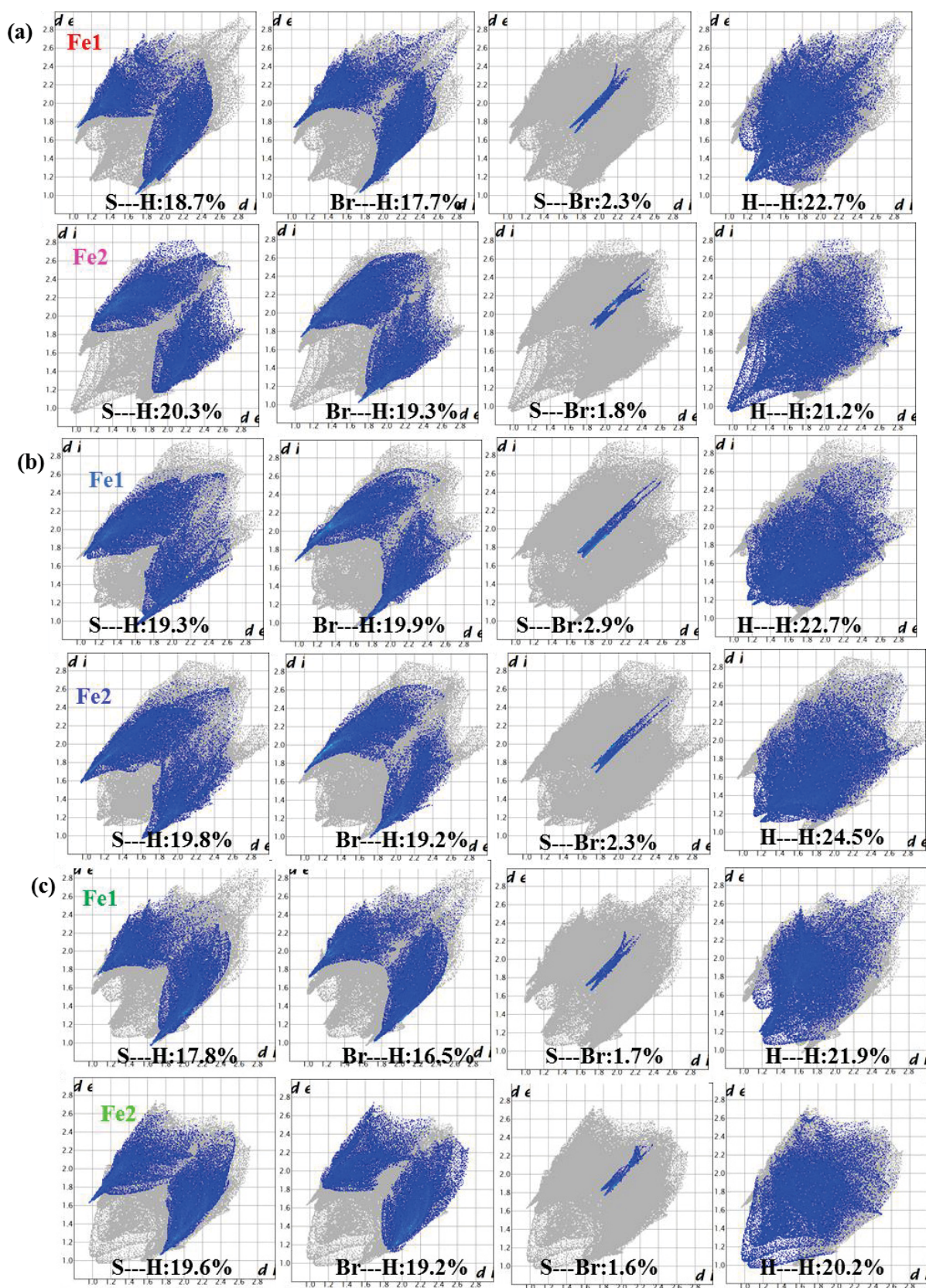


Figure III.25. The selected contacts in the fingerprints at 300 K (a), 80 K (b), and quenched 80 K (c) for polymorph I-pBrA, corresponding to the HS, LS, and Q-HS\* states.

Figure III.25a shows some selected contacts at 300 K. The shape of the fingerprints for Fe1 and Fe2 are different. Table III.10 gathers some selected distances as function of the temperature. The sharp head in fingerprint of Fe2 corresponds to short H---H contacts (H33---H45, 2.138 Å in Figure III.26). The ratio of the selected S---H and Br---H in Fe1 is lower than in Fe2 with distances of 2.887 Å (S2---H32), 2.911 Å (S2---H42), and 2.909 Å (Br2---H13) in Fe1. The slightly higher ratio of S---Br in Fe1 corresponds to the short S1---Br1 distance of 3.465 Å. Other short atom-atom contacts include S3---S3 (3.441 Å) and  $\pi_{\text{pyridine}}\cdots\pi_{\text{pyridine}}$  (3.978 Å), which can be evidenced in the Hirshfeld surface (Figure III.26). The fingerprints of the thermally quenched Q-HS\* state (Figure III.25c) are very similar to the ones at 300 K, with weak variations probably due to the thermal contraction (Table III.7).

Table III.10. Selected interatomic distances in polymorph I-pBrA at various temperatures.

<i>T</i> / K (spin state)	S1-Br1 / Å	S2-Br2 / Å	S3-Br3 / Å	S4-Br4 / Å	S3-S3 / Å	H45-H33 / Å	H48-H42 / Å	$\pi_{\text{py}}\cdots\pi_{\text{py}}$ / Å	Br2-C13H13 / Å Br2-H13-C13 / °	S2-H32 / Å S2-H32-C32 / °	S2-H42 / Å S2-H42-C42 / °
350 (HS)	3.465	3.685	3.763	4.264	3.441	2.144	2.253	4.048	3.731 / 143.05	2.887 / 146.16	2.911 / 158.15
300 (HS)	3.444	3.677	3.736	4.221	3.401	2.138	2.212	3.978	3.696 / 143.15	2.848 / 148.83	2.904 / 143.57
250 (HS)	3.430	3.704	3.720	4.237	3.377	2.153	2.179	3.923	3.685 / 143.70	2.82 / 150.73	2.875 / 145.11
200 (HS)	3.421	3.724	3.695	4.228	3.344	2.188	2.144	3.840	3.672 / 142.61	2.794 / 153.07	2.853 / 144.39
180 (HS)	3.418	3.719	3.684	4.217	3.332	2.163	2.143	3.835	3.67 / 140.95	2.779 / 152.22	2.861 / 143.02
170 (HS)	3.414	3.727	3.673	4.218	3.331	2.204	2.168	3.812	3.652 / 144.73	2.769 / 155.43	2.831 / 146.45
150 (LS)	3.476	3.496	3.643	3.496	3.637	2.787	2.541	5.281	3.634 / 151.69	2.979 / 133.70	3.108 / 106.41
120 (LS)	3.460	3.474	3.620	3.477	3.609	2.751	2.559	5.285	3.611 / 150.91	2.976 / 134.50	3.176 / 126.36
100 (LS)	3.451	3.477	3.612	3.477	3.606	2.784	2.565	5.303	3.641 / 151.85	2.966 / 133.80	3.173 / 127.22
80 (LS)	3.449	3.462	3.590	3.466	3.590	2.768	2.531	5.310	2.646 / 152.27	2.976 / 134.16	3.154 / 127.63
80 (Q-HS*)	3.398	3.750	3.622	4.225	3.297	2.181	2.131	3.738	3.652 / 141.56	2.747 / 158.71	2.813 / 144.29
10 (hv-HS*)	3.390	3.773	3.594	4.266	3.253	2.208	2.092	3.897	3.637 / 140.851	2.738 / 159.88	2.805 / 145.04

At 80 K, in the LS state (Figure III.25b), the shapes of the fingerprints for Fe1 and Fe2 become similar. Compared to 300 K, the short H---H distance below 2.4 Å disappears in Fe2. And the “wing” in the shape of Br---H and S---H become sharper, which means the S---H and Br---H distances become shorter. A noticeable change concerns the  $\pi_{\text{pyridine}}\cdots\pi_{\text{pyridine}}$  contact that increases from 3.978 Å to 5.310 Å.

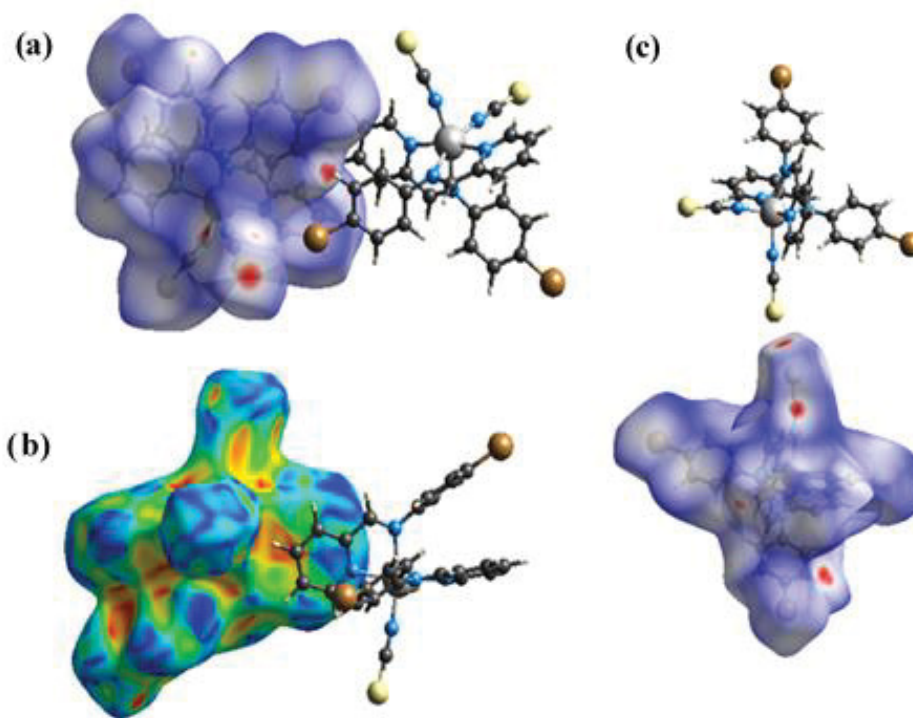


Figure III.26. The evidence for short H45---H33 (a), S3---S3 (b) contacts and  $\pi_{py} \cdots \pi_{py}$  interactions (c) in the Hirshfeld surface in polymorph **I-pBrA** at 300 K.

The variation of intermolecular interactions can influence the crystal packing. At 300 K, two Fe1 molecules are connected by S1---Br1 and S2---Br2 bonding while two Fe2 molecules are connected by H33---H45 and Br2---H13 contact along the *b* axis with  $2_1$  symmetry (Figure III.27a). Along the *b* axis, the Fe1 sites form a zig-zag chain with Fe1---Fe1 distance of 11.402 Å and Fe1-Fe1-Fe1 angle of 138.58°. Similarly, Fe2 sites form a zig-zag chain with Fe2---Fe2 distances of 11.219 Å and Fe2-Fe2-Fe2 angle of 143.78°. S---H contacts also link the Fe1 and Fe2 entities from two adjacent parallel chains (Figure III.27b). The Fe2 motifs can build a 2D network through S3---S3 and H33---H45 contacts (Figure III.27c). Moreover, the H33---H45 and  $\pi_{py} \cdots \pi_{py}$  can also texture the 2D network of Fe2 molecules at (10-1) plane (Figure III.28a). The inverted centers are located at the center of S3---S3 and  $\pi_{py} \cdots \pi_{py}$ . Finally, the crystal-packing can be viewed as Fe1 and Fe2 chains packing alternately along the *a* and *c* directions (Figure III.28b). Note that the arrangements of NCS<sup>-</sup> groups in Fe1 and Fe2 are very similar, toward the *a* direction.

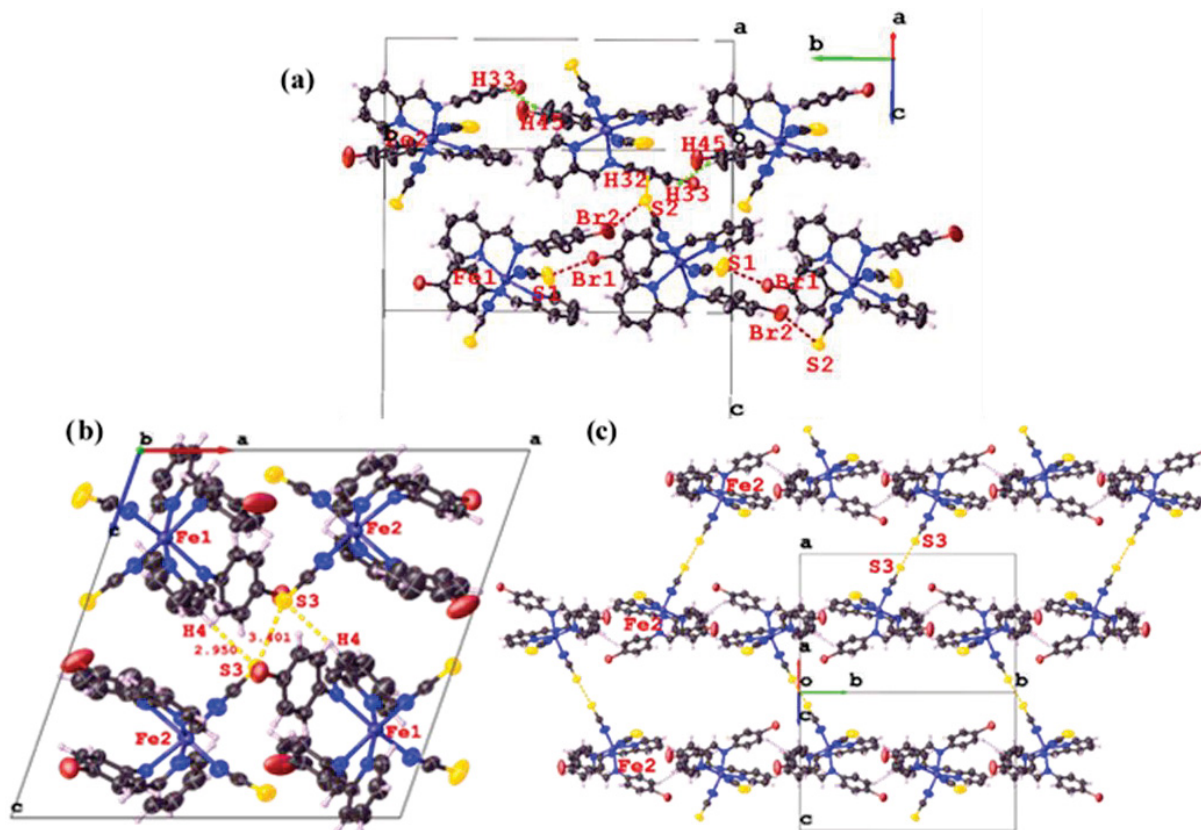


Figure III.27. The Fe1 and Fe2 packing along *b* direction (a), an inverted symmetry of four molecules (b), and the arrangement of Fe2 at (c) at (101) of polymorph **I-pBrA** at 300 K.

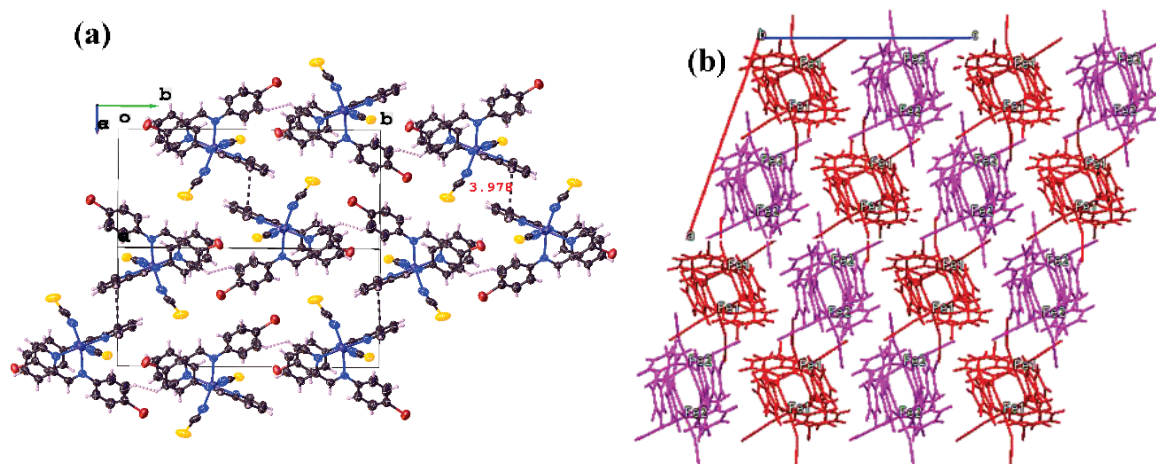


Figure III.28. The Fe2 packing at (10-1) by H---H and  $\pi_{py} \cdots \pi_{py}$  interactions (a) and 3D structure (b) of polymorph **I-pBrA** at 300 K.

When slowly cooled to 80 K, the network of Fe2 distends and appears less obvious due to the loss of S3---S3 and  $\pi_{py} \cdots \pi_{py}$  short contacts. (Figures III.29c and d). Due to the rotation of phenyl ring and atomic displacement of NCS<sup>-</sup> at SCO, the Fe2---Fe2 distance (10.712 Å) decreases and the Fe2-Fe2-Fe2 angle (155.83°) increases along the *b* direction, compared with 11.402 Å and 138.58° at 300 K. This leads to a more linear packing of Fe2 in LS state.

Part III – Promoting Distortion of the Coordination Polyhedron Using Polymorphism:  
Bromine Substitution of PM-zBrA Family

Regarding Fe1 at 80 K, it also become more linear along the *b* direction with the Fe1---Fe1 distance (10.746 Å) and the Fe1-Fe1-Fe1 angle (154.16°), compared with 11.219 Å and 143.78° at 300 K. Moreover, owing to the elongation of  $\pi_{py} \cdots \pi_{py}$  from 3.978 Å (300 K) to 5.310 Å (80 K), the corresponding Fe2---Fe2 distance increases from 9.131 Å to 9.607 Å. The overall packing therefore looks strongly modified from HS to LS, reflecting the modification of the intermolecular interactions itself in connection with the ligand rotation.

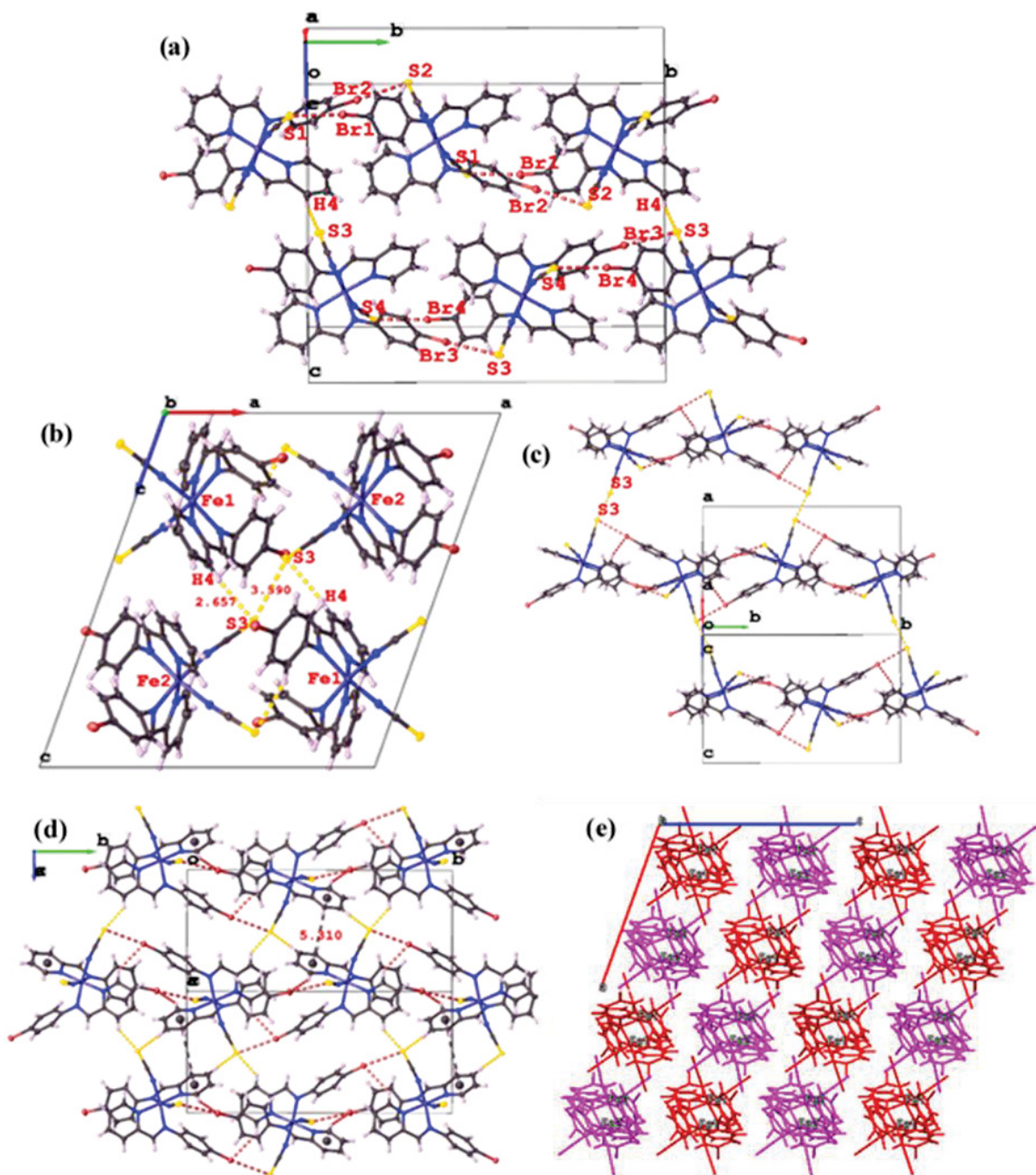


Figure III.29. The Fe1 and Fe2 packing along *b* direction (a), an inverted symmetry of four molecules (b), the arrangement of Fe2 at (101) (c), (10-1) (d), and crystal packing (e) of polymorph **I-pBrA** at 80 K.

*Part III – Promoting Distortion of the Coordination Polyhedron Using Polymorphism:  
Bromine Substitution of PM-zBrA Family*

At 80 K, in the Q-HS\*, the packing is similar to the 300 K one, though tiny differences. Along the *b* direction, the Fe2---Fe2 distance (10.101 Å) and the Fe2-Fe2-Fe2 angle (143.46°) decrease, compared with 11.032 Å and 145.95° at 300 K. This indicates slightly less linear Fe2 molecules sequences and a denser network of Fe2, based on shorter S---S and H---H contacts, which is consistent with the significant thermal contraction. Regarding Fe1 in the Q-HS\*, the Fe1---Fe1 distance (11.101 Å) and the Fe1-Fe1-Fe1 angle (143.467°) along the *b* direction are very similar to the one at at 300 K (11.219 Å and 143.78°). The modification of the packing noticed from HS to LS is still valid when comparing Q-HS\* to LS.

Thanks to this overview of the different intermolecular interactions at play in this compound, we can look at the driving force of the bromophenyl ring rotation. Regarding the Fe1 site, the H---H distances around the corresponding bromophenyl ring are larger than 2.3 Å and the variation of H---H upon SCO is smaller than 0.2 Å (Figure III.30a). Regarding the Fe2 site, there are very short H---H contacts with intramolecular H48---H42 of 2.212 Å and intermolecular H33-H45 of 2.138 Å at 300 K. In the high spin region from 300 K to 170 K, the intermolecular H33---H45 distance increases while the intramolecular H48---H42 distance decreases to become identical at 170 K. These short distances both increase dramatically from 170 K (HS) to 150 K (LS) with variation of H---H distance at SCO as large as 0.6 Å (Figure III.30b). The possible equal strength (distance) of both intra- and intermolecular H---H contacts at 170 K may leave the phenyl ring in an unstable state, where it may easily be perturbed by external stimuli. In all likelihood, the abrupt SCO triggers the rotation of the phenyl ring.

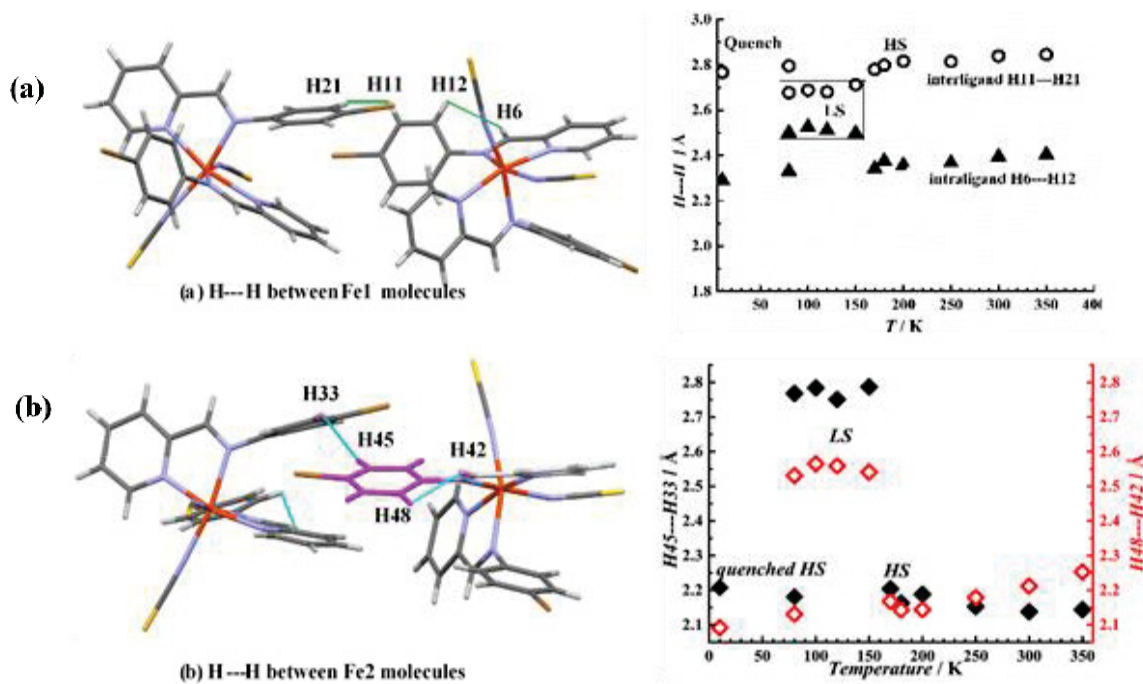


Figure III.30. Thermal dependence of the H---H distances around Fe1 (a) and Fe2 molecules (b) with values extracted from Table III.10 in polymorph I-pBrA.

- Unit-cell parameters as a function of temperature of I-pBrA

As a further consequence of all these rearrangements in the ligand conformation and atom-atom contacts the unit cell is strongly modified at SCO in a unique so far manner. Indeed, the unit-cell volume increases from HS to LS (Figure III.31): from 300 K to 170 K, the unit-cell volume decreases gradually due to thermal contraction while it increases abruptly from 170 K to 160 K at the SCO, this behavior being reversible upon warming. It is worth to mention that, to the best of our knowledge, it is the first time that the thermal SCO of a molecular complex corresponds to an increase of the unit-cell volume from HS to LS.<sup>19,22,23</sup> In the SCO temperature region, the increase of volume from HS to LS results in fact from the strong anisotropy of the unit-cell modifications. As shown in Figure III.32, when cooling from 150 K to 200 K, the value of  $a$  decreases by 4.40% while  $c$  and  $\beta$  increase by 6.55% and 0.83%. If the anisotropy of the unit-cell modifications due to the SCO is a usual fact, it may be the first time that a LS to HS conversion results in a negative expansion.<sup>19,22,23</sup> The latter amplitude is accurately determined by comparing the volumes of the HS and LS unit-cells at the same temperature, the HS one is obtained by thermal quenching and the LS one by slow cooling. At 80 K, the volumes of the Q-HS\* (5423.8(3) Å<sup>3</sup>) and LS (5510.8(5) Å<sup>3</sup>) unit-cells confirm an increase of 1.6 % from HS to LS (Table III.7) confirming this first observation of a unit-cell volume decrease from LS to HS (Q-HS\*).

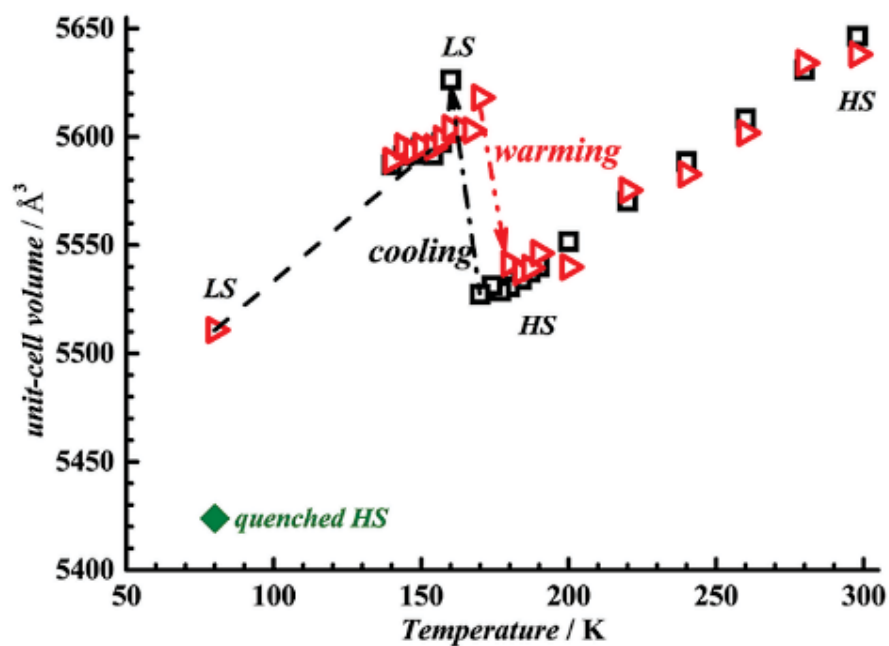


Figure III.31. Temperature dependence of the unit-cell volume in polymorph I-*p*BrA, determined by single-crystal X-ray diffraction.

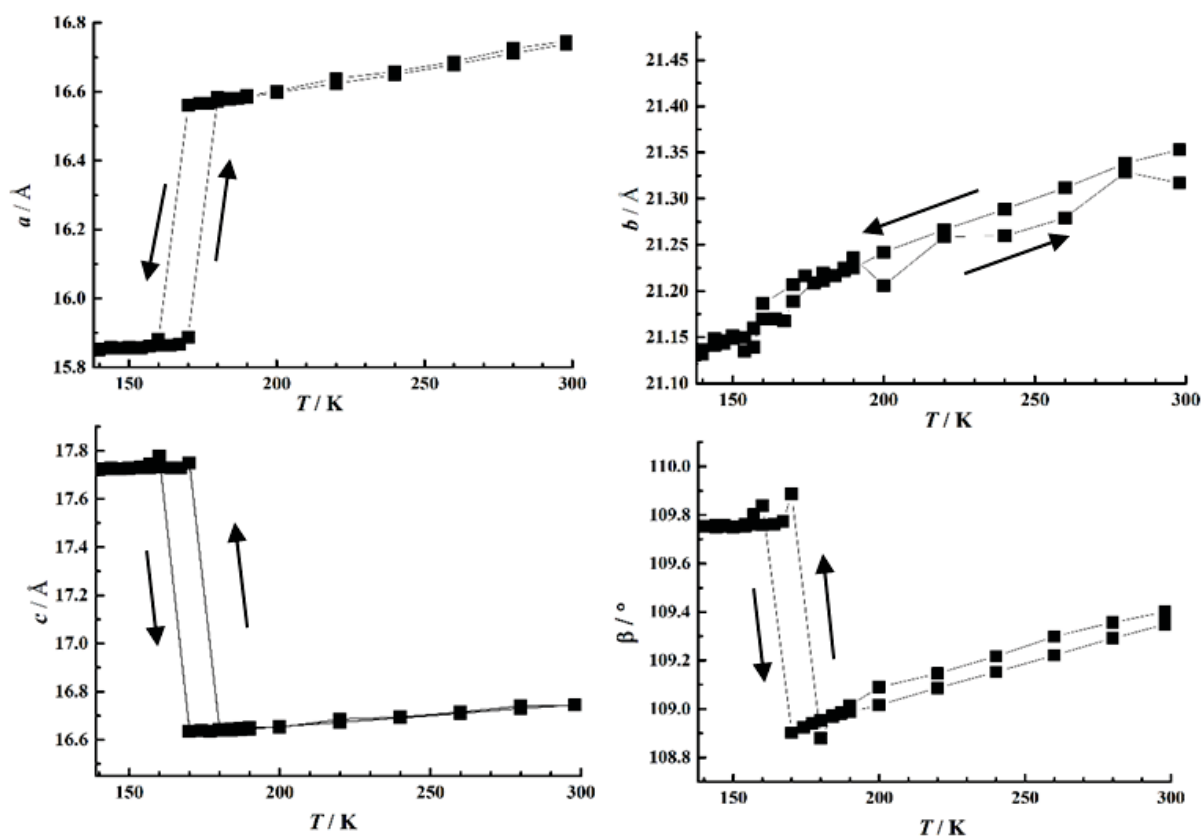


Figure III.32. Temperature dependence of the unit-cell parameters in polymorph I-*p*BrA, determined by SCXRD. The down (up) arrow means the cooling (warming) mode.

This anisotropic variation of the unit-cell at SCO is further evidenced in Figure III.33b that shows the superposition of the lattices in the Q-HS\* and LS states, both at 80 K. Owing to the motion of NCS<sup>-</sup> ligands, the S3---S3 contact increases by 0.35 Å, which leads to the expansion of *c* axis, (Figure III.33a). Simultaneously, the rotation and motion of ligands cause the molecular reorientation and rearrangement along [101], giving rise to the expansion of the distance between the adjacent pyridines of Fe2 molecules from 3.738 Å (80 K, Q-HS\*) to 5.310 Å (80 K, LS) (Figure III.33a). Hence, the expansion of lattice volume seems to be due to the synergistic effect between the rotation and motion of ligands, triggered by the SCO.

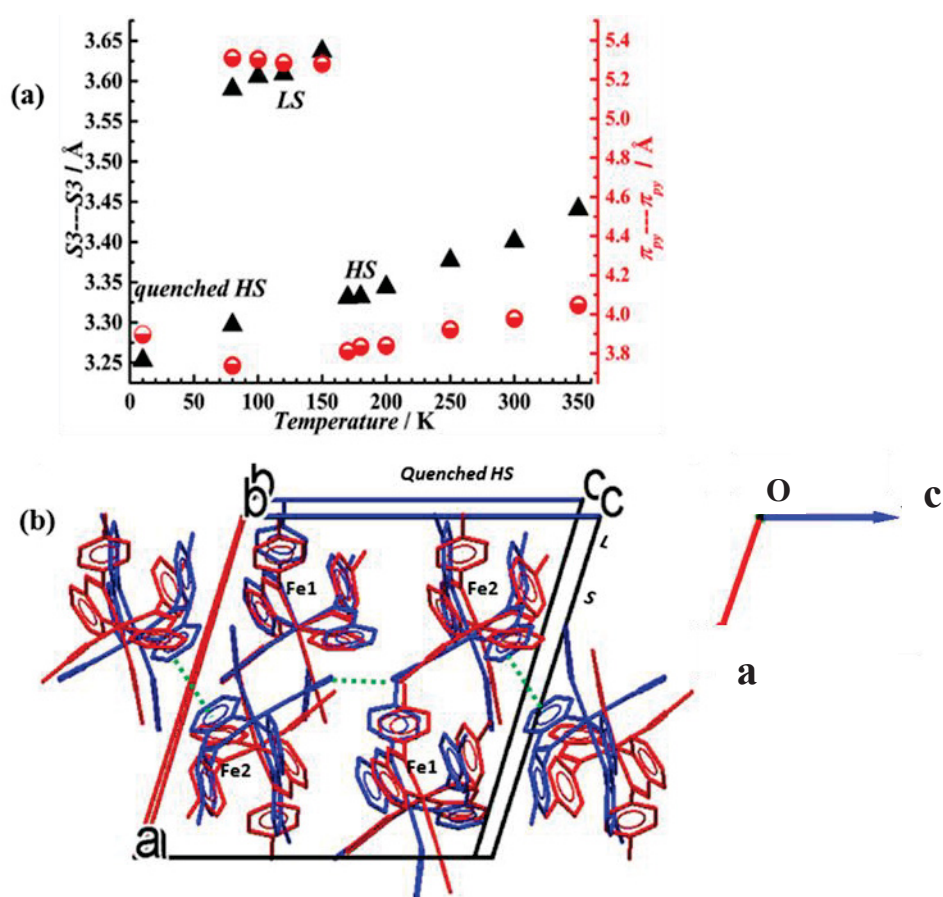


Figure III.33. Thermal variation of S---S and π<sub>py</sub>---π<sub>py</sub> distances around Fe2 molecules (a) and the structural overlay of the LS and Q-HS\* lattices (b) in polymorph I-pBrA.

- Powder X-Ray diffraction Photo-crystallography of I-pBrA

To have better insights on the photo-induced process from LS to *hν*-HS\*, photocrystallographic investigations were performed. However, the ease with which the HS is quenched below 80 K adds extra difficulties to perform the SCXRD photocrystallography study at very low temperature. For technical reasons, it is easier with PXR. Indeed, with our

collaborator Dr. Sébastien Pillet (University of Lorraine, Nancy, France), the low temperature region accessible was 10 to 80 K under a helium flux. This helium flux immediately quenches the HS state. The fact that  $T(\text{TIESST})$  is much higher than 80 K, prevent recording the  $h\nu$ -HS\* to LS relaxation and therefore the fully LS state at 10 K needed to further excite by light. Hence, the PXRD experiments at 15 K using light irradiation at 810 nm to convert from LS to  $h\nu$ -HS\*, were performed to explore the variation of unit-cell volume in the light-induced regime. The data were analyzed by the *Le Bail* method using Fullprof.<sup>24</sup> (Figure III.34a) and the results are gathered in Table III.11. Figure III.34b shows the peak index at 100 K and 300 K, where the main different peaks are (14-1) at  $2\theta = 18.05^\circ$  and (24-2) at  $2\theta = 21.3^\circ$  for LS, (320) at  $2\theta = 18.7^\circ$  and (32-3) at  $2\theta = 22.5^\circ$  for HS.

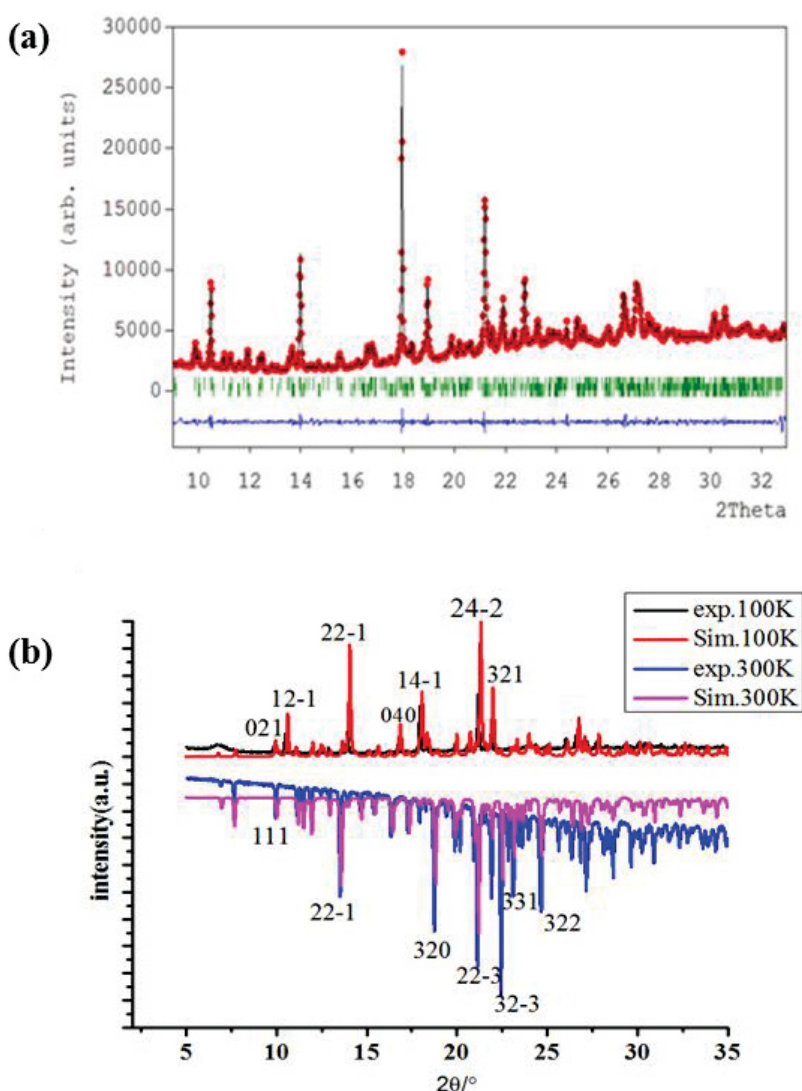


Figure III.34. Diffractogram of polymorph I-*p*BrA after 16 h of irradiation at 15K analyzed by *Le Bail* method (a) and the simulated from SCXRD data and experimental PXRD patterns with peak index at 300 K and 100 K (b).

Figure III.35a shows the thermal evolution of the diffraction patterns upon cooling. Above 190 K, it is fully HS with typical (320) at 18.7° and (32-3) at 22.5° peaks. Upon cooling below 180 K, peaks of the LS phase grow, with the typical (14-1) at 18.03° and (24-2) at 21.3° for example. Between 180 K and 160 K, the presence of peaks of both phases clearly shows that the transition occurs in domains, as often observed for first order phase transition.

Irradiation was applied at 15 K in the fully LS state, during 16 hours at 810nm. The diffractogram is shown in Figure III.34, with the presence of the (320) and (32-3) peaks typical of the HS state, together with the (14-1) and (24-2) peaks of the LS phase. The mixture of HS and LS peaks can be observed evidencing an incomplete photoswitching, similarly to the SQUID experiment. Figure III.35b shows the thermal evolution of the diffraction pattern upon warming after irradiation. Up to 90 K, both phases are still present but at 100 K, only the LS phase is observed. This value is slightly lower than the  $T(\text{LIESST})$  value, probably due to the long acquisition time needed to record the PXRD spectra.

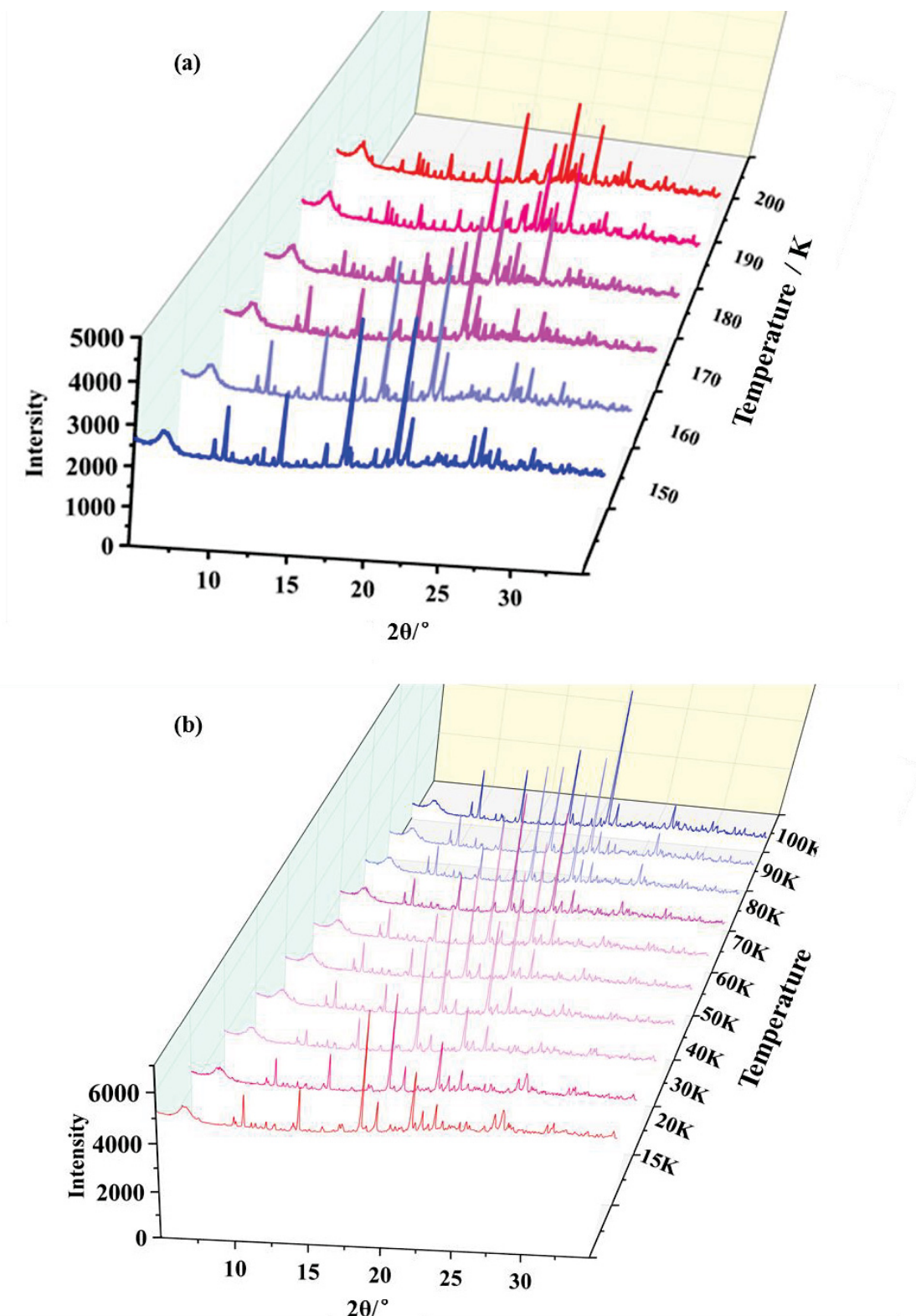


Figure III.35. Temperature dependence of the diffractograms in cooling model from 200K to 150K (a), and relaxation from  $h\nu$ -HS\* to LS (b) in polymorph **I-pBrA**, determined by PXRD.

**Table III.11.** The unit-cell parameters,  $R_p$  and  $wR_p$  values extracted from PXRD for polymorph **I-pBrA**. The data were analyzed by the *Le Bail* method using Fullprof software.

Temp /K	Spin State	$a/\text{Å}$	$b/\text{Å}$	$c/\text{Å}$	$\beta/^\circ$	Unit-cell volume / $\text{Å}^3$	$R_p$	$wR_p$
100	LS	15.82111	20.95809	17.7064	109.7222	5526.691	0.163	0.148
90	$h\nu$ -HS*	16.4653	21.0725	16.5736	108.7868	5447.383	0.151	0.151
90	LS	15.8291	20.9501	17.7196	109.6995	5532.248		
80	$h\nu$ -HS*	16.4596	21.0767	16.5699	108.7448	5443.438	0.155	0.158
80	LS	15.8290	20.9391	17.7171	109.6876	5528.617		
70	$h\nu$ -HS*	16.4356	21.0513	16.5562	108.6577	5427.263	0.138	0.139
70	LS	15.8128	20.9002	17.7088	109.7800	5507.263		
60	$h\nu$ -HS*	16.4353	21.0727	16.5569	108.6927	5431.767	0.163	0.149
60	LS	15.8232	20.8988	17.7161	109.7606	5513.514		
50	$h\nu$ -HS*	16.4230	21.0768	16.5409	108.7304	5422.310	0.140	0.148
50	LS	15.8113	20.8784	17.6921	109.7166	5497.989		
40	$h\nu$ -HS*	16.4120	21.0718	16.5312	108.7219	5414.498	0.138	0.153
40	LS	15.8129	20.8498	17.6966	109.7524	5491.215		
30	$h\nu$ -HS*	16.4093	21.0135	16.5341	108.7423	5398.928	0.157	0.162
30	LS	15.7872	20.8543	17.6838	109.6638	5482.512		
20	$h\nu$ -HS*	16.3989	21.0028	16.5305	108.7404	5391.653	0.144	0.150
20	LS	15.7956	20.8100	17.6833	109.6811	5473.028		
15	$h\nu$ -HS*	16.4008	20.9810	16.5225	108.7345	5385.246	0.102	0.101
15	LS	15.7995	20.8117	17.6858	109.7054	5474.798		
10	Q-HS*	16.5140(4)	20.9864(5)	16.3611(5)	108.785(3)	5368.2(3)	SC-XRD	

From these diffractograms, the unit cell parameters can be extracted using the Le Bail method.<sup>24</sup> (Table III.11). As seen in Figure III.36, the value of  $a$  decreases by 0.6 Å while  $c$  and  $\beta$  increases by 1.2 Å and 1.0° from 15 K ( $h\nu$ -HS\*) to 100 K (LS). This strongly anisotropic variation of unit-cell parameters during the  $h\nu$ -HS\* to LS relaxation process is quite similar to the one observed for the thermal SCO. So the increase of the unit-cell volume at the thermal SCO is also observed from  $h\nu$ -HS\* to LS as seen in Figure III.37. Considering the fact that the unit-cell parameters of  $h\nu$ -HS\* at 15 K are quite similar to the quenched one at 10 K, Q-HS\*, it could be reasonable to assume that  $h\nu$ -HS\* and Q-HS\* can have a similar crystal structure at 10 K. In this case, the same single-crystal to single-crystal transformation as the one observed from HS to LS may also occur from  $h\nu$ -HS\* to LS. In fact, the 75% of  $h\nu$ -HS\* at 10 K clearly witnesses the photo-driven rotation of the phenyl ring and the resulting unit-cell contraction from LS to  $h\nu$ -HS\* (expansion from  $h\nu$ -HS\* to LS relaxation), which is the reverse behavior of all other known so far SCO molecular compounds. The exotic and innovative character of this polymorph is highlighted again here.

Part III – Promoting Distortion of the Coordination Polyhedron Using Polymorphism:  
Bromine Substitution of PM-zBrA Family

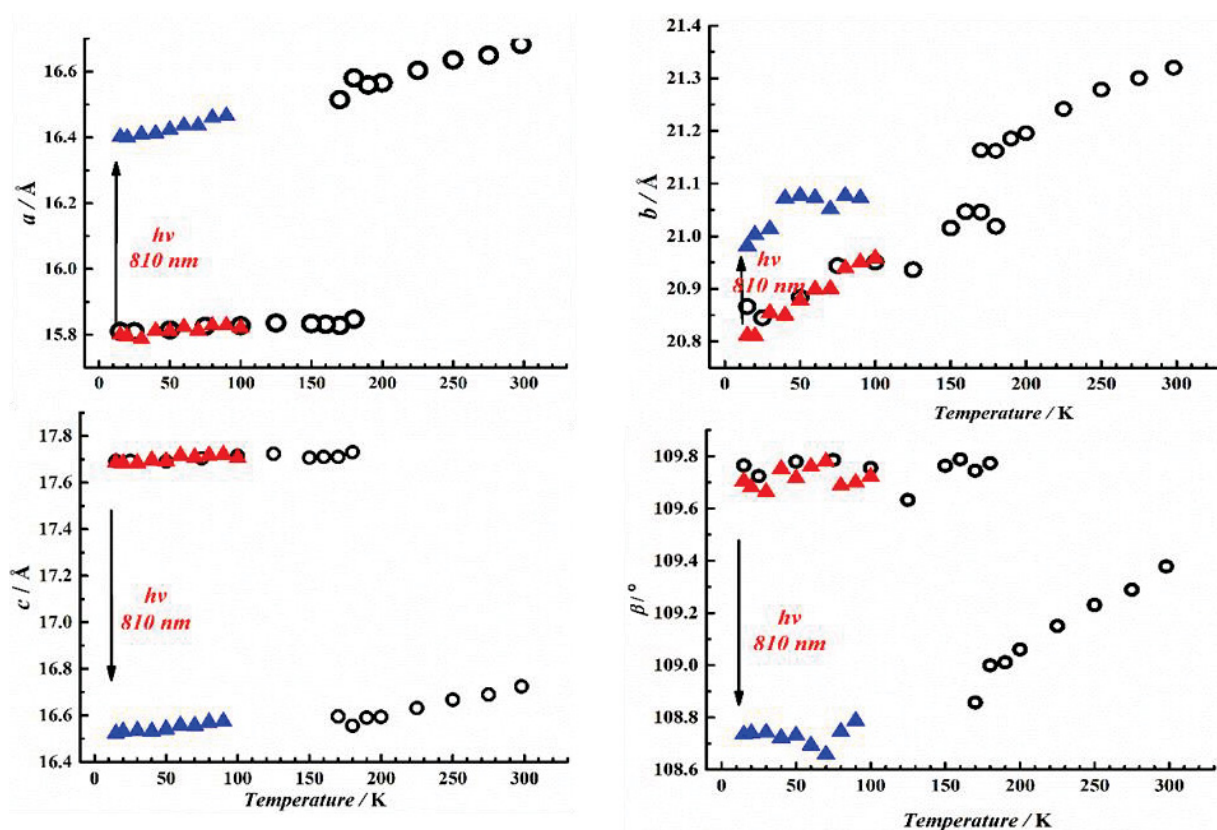


Figure III.36. Temperature dependence of the unit-cell parameters showing the thermal SCO (empty circles) as well as the photo-excitation from LS (red triangle) to  $h\nu$ -HS\* (blue triangle) in polymorph I-pBrA, determined by PXRD.

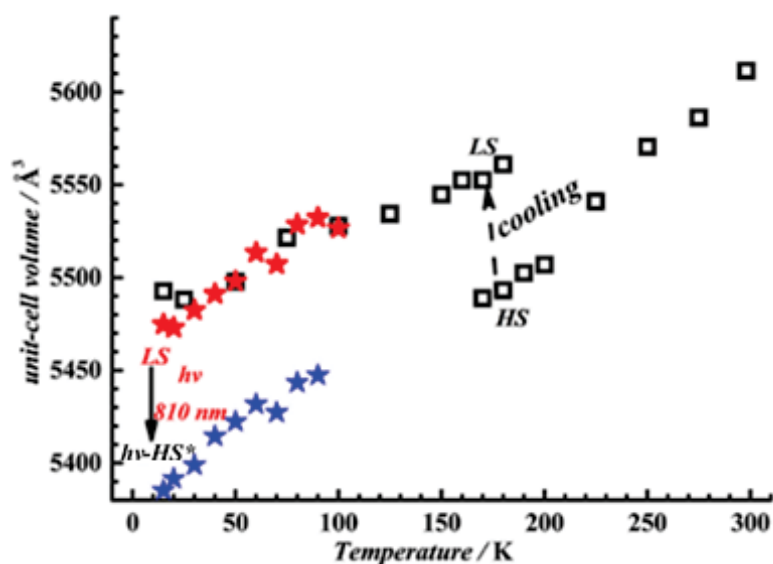


Figure III.37. Temperature dependence of the unit-cell parameters showing the thermal SCO (empty square) as well as the photo-excitation from LS (red star) to  $h\nu$ -HS\* (blue star) in polymorph I-pBrA, determined by PXRD.

- *The structure-properties relationship in I-pBrA*

**I-pBrA** presents four remarkable features as recalled below.

*A one step SCO with two very different Fe<sup>2+</sup> sites.* Basically, SCO in molecular complexes is greatly related to the crystallographically independent iron molecules in the asymmetry unit. Since differences in the coordination sphere geometry lead to differences in the ligand-field, it is consequently expected different spin crossover temperatures. Moreover, the environments around each iron sites can be very different leading to various cooperativity around each site. Here, despite the presence of two very different iron sites in polymorph **I-pBrA** and very different modifications of intra- and intermolecular interactions involving each site, only one step is observed in the SCO curve. There are few similar examples. For instance, [Fe(L<sup>H</sup><sup>iPr</sup>)<sub>2</sub>(NCS)<sub>2</sub>] (L<sup>H</sup><sup>iPr</sup> = N-2-pyridylmethylene-4-isopropylaniline) shows an abrupt spin-crossover (SCO) at T<sub>1/2</sub>↓ = 154 K on cooling and at T<sub>1/2</sub>↑ = 167 K on heating, with a 13 K thermal hysteresis, while two distinct molecules are observed.<sup>25</sup> Another example is found in a linear trinuclear triazole-based complex with the central site different from the two external sites of the linear trimeric unit. The three Fe<sup>2+</sup> centers undergo a very sharp SCO at 318 K, probably due to the strong ferro-elastic interactions between the three metal centers.<sup>26</sup>

On the contrary, dinuclear complex {[Fe(bt)(NCS)<sub>2</sub>]<sub>2</sub>(bpym)} with one crystallographic iron sites shows two-stepped SCO, due to antiferro-elastic interactions.<sup>27</sup> The type of SCO is related to the crystallographic sites but is determined by the antiferro-elastic and ferro-elastic interactions. So it is reasonable to assume that the ferro-elastic interactions exist between Fe1 and Fe2 in polymorph **I-pBrA**. Note that it is more common that one iron site breaks into more sites in multistep SCO complexes.<sup>28-30</sup>

*A huge reversible rotation of ligand from LS to HS\* as shown in the structure in HS, Q-HS\* and LS states:* one phenyl ring in Fe2 rotates by around 67° at SCO. Such an impressive rotation occurs in the solid state and was definitely demonstrated to be reversible. Rare but similar, though smaller, ligand rotations have been reported in some cases for SCO compounds but the concomitance of the rotation and the SCO was not fully demonstrated.<sup>25,31,32</sup> Based on the results of powder X-ray diffraction photo-crystallography (Table III.11), it is reasonable to speculate the same structure for *hv*-HS\* and Q-HS\*. Therefore, due to the ligand geometry change in Fe2 between the LS ground state and the photo-excited state, they can be viewed as photo-isomers. At 10 K, this huge rotation in solid needs a lot of energy, since it implies huge

*Part III – Promoting Distortion of the Coordination Polyhedron Using Polymorphism:  
Bromine Substitution of PM-zBrA Family*

changes in intermolecular interactions. It is then very difficult to promote this change at so low temperature and light irradiation leads to a mixture of  $h\nu$ -HS\* and LS in powder X-ray diffraction photo-crystallography and magnetic results. The presence of photo-isomers makes a link with Ligand-Driven Light-Induced Spin Change effect (LD-LISC) based on the promotion of a photo-isomerization of the ligand by light irradiation to tune the ligand field and the subsequent spin crossover features.<sup>33</sup>

*A strong distortion of the coordination sphere.* From LS (80 K) to the Q-HS\* state (80 K), the modification of the trigonal distortion ( $\Delta\theta$ ) is  $96.6^\circ$  and  $122.8^\circ$  for Fe1N<sub>6</sub> and Fe2N<sub>6</sub> octahedra, respectively. The trigonal distortion is suspected to be connected to the  $T(\text{LIESST})$  value (cf. **Part I.3**), the higher the distortion, the higher the  $T(\text{LIESST})$  temperature<sup>19-20</sup>. According to the empirical relationship between  $\Delta\theta$  and  $T(\text{LIESST})$  in the family with bidentate ligands, the  $T(\text{LIESST})$  is expected to be 110 K for this new complex (**Figure III.38**), which means the observed  $T(\text{LIESST})$  of 107 K from photomagnetic measurements fits here perfectly with the expected one from structural data. In other words, the high  $T(\text{LIESST})$  observed here mainly originates in the high trigonal distortion of the coordination sphere. However, as for the thermal SCO, while the two Fe<sup>2+</sup> sites have different distortion parameters, we do not see any clear step on the  $T(\text{TIESST})$  and  $T(\text{LIESST})$  curves. According to **Figure III.38**, we can expect a step around 70 K. We can guess the beginning of this step on the  $T(\text{LIESST})$  curve but clearly not on the  $T(\text{TIESST})$  curve. Another surprising aspect of this high value of the coordination sphere distortion is that the chemical substitution in *para* position of the phenyl group is not expected to bring any steric strain enhancing this distortion. This is strongly informing us on the intermolecular origin of this distortion, as discussed for polymorphs **I** and **II** in the [Fe(PM-BiA)<sub>2</sub>(NCS)<sub>2</sub>] system<sup>34-35</sup>. One may immediately correlate the strong ligand rotation in Fe2 to this high distortion. The fact that several polymorphs of this compound are available will allow us to discuss deeper in the next sections.

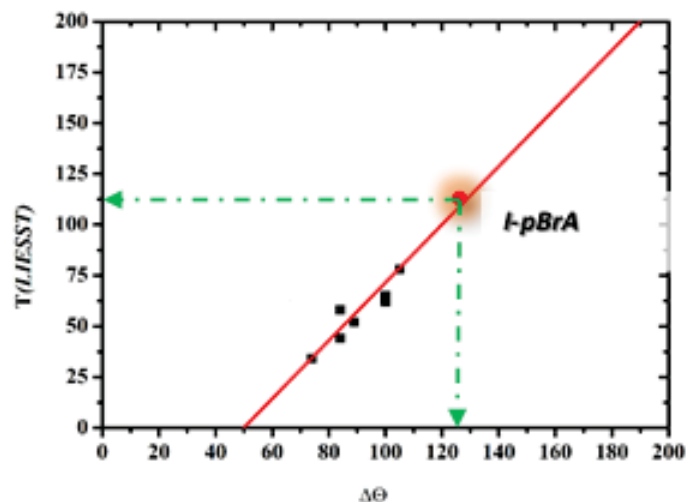


Figure III.38.  $T(\text{LIESST})$  vs  $\Delta\Theta$  in the  $[\text{Fe}(\text{PM-L})_2(\text{NCE})_2]$  family. The red sphere on the line represents for polymorph **I-pBrA**

If we check the position of **I-pBrA** on the  $T(\text{LIESST})$  vs  $T_{1/2}$  database<sup>17,36</sup>, (Figure III.39), we immediately see that this compound exhibits one of the highest  $T(\text{LIESST})$  reported so far. Moreover, it is the only bidentate ligand-based complex that lies on the  $T_0 = 150$  K line that corresponds to tridentate ligand-based complexes (Figure III.39). Compared to all the other members of the PM-L family, this compound is definitely very different. This observation illustrates that to go from one  $T_0$  line to another, the main parameter is most probably the distortion of the coordination sphere, as originally thought.<sup>20</sup>

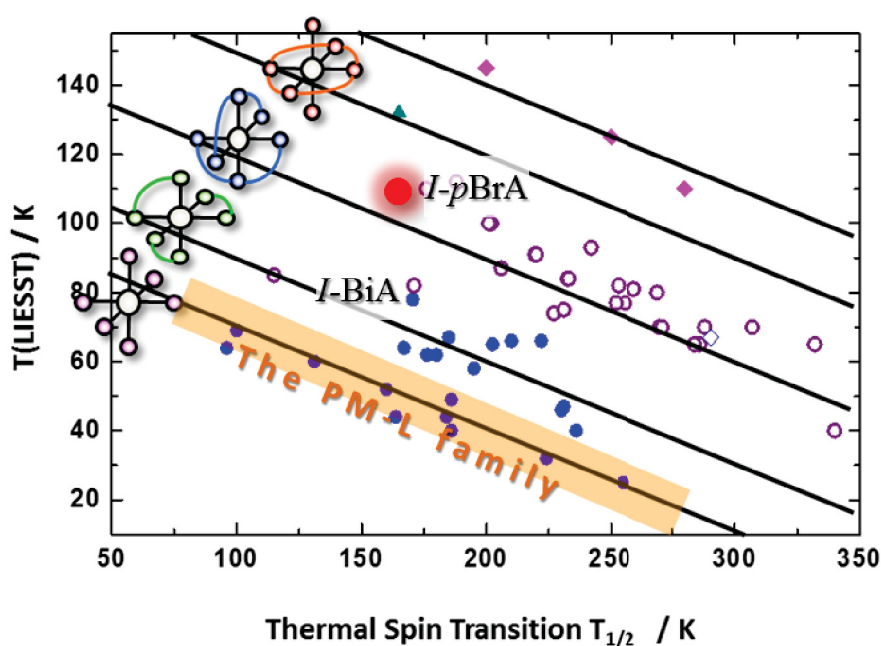


Figure III.39. The position of polymorph **I-pBrA** (red sphere) in the  $T(\text{LIESST})$  vs  $T_{1/2}$  database.

The negative expansion of unit-cell volume at SCO in polymorph **I-pBrA** is very unusual. Normally, the unit-cell volume decreases from HS to LS based on the natural breathing of FeN<sub>6</sub> polyhedron. The variation of volume of FeN<sub>6</sub> polyhedra from HS to LS are around 25%, which lead to a contraction of the unit-cell volume in the range 2-10%, as so far observed.<sup>23</sup> So the HS to LS expansion of unit-cell volume reported in polymorph **I-pBrA** is really exceptional. It most probably comes from the modification of atom-atom distances, including the S3---S3, H33---H45, and  $\pi_{py}$ --- $\pi_{py}$ . The reverse variation of unit-cell volume has been already suspected once but only in association to the LIESST effect.<sup>37</sup> It might also be related to the very small variation in density between the HS, LS and Q-HS\* states. It is therefore new for the thermal SCO and opens a new field of potentiality in term of applicative prospects.

In summary, **I-pBrA** shows some unique features. Firstly, it shows the highest  $T(TIESST)$  and  $T(LIESST)$  of the corresponding family of iron compounds, which greatly relates to the change in ligand conformation and distortion of FeN<sub>6</sub>. Secondly, this compound shows the unprecedented and reverse unit-cell volume expansion from HS (including Q-HS\* and  $h\nu$ -HS\*) to LS, which are fully demonstrated by SCXRD and PXRD.

#### **III.4.2. Polymorph [Fe(PM-pBrA)<sub>2</sub>(NCS)<sub>2</sub>]-II: II-pBrA**

- *Magnetic properties of II-pBrA*

Magnetic measurements were performed on VSM ([Appendix 3](#)). The powder sample (6.32 mg) was sealed in an aluminum capsule (33.84 mg) and the temperature was varied in the range from 150 K to 350 K at 1 K/min. As seen in [Figure III.40](#), the  $\chi_M T$  product at 350 K is 3.1 cm<sup>3</sup> K mol<sup>-1</sup>, indicating a HS state for the Fe<sup>2+</sup>. Upon cooling,  $\chi_M T$  gradually decreases to reach almost zero at 150 K, suggesting the diamagnetic LS ground state. Hence, polymorph **II-BrA** shows a gradual and complete spin crossover with  $T_{1/2} = 260$  K, without any indication of the appearance of steps. Furthermore, irradiating the sample in the SQUID magnetometer was unsuccessful and no LIESST could have been observed. Similarly, the HS state was not successfully thermally quenched at 10 K in the SQUID.

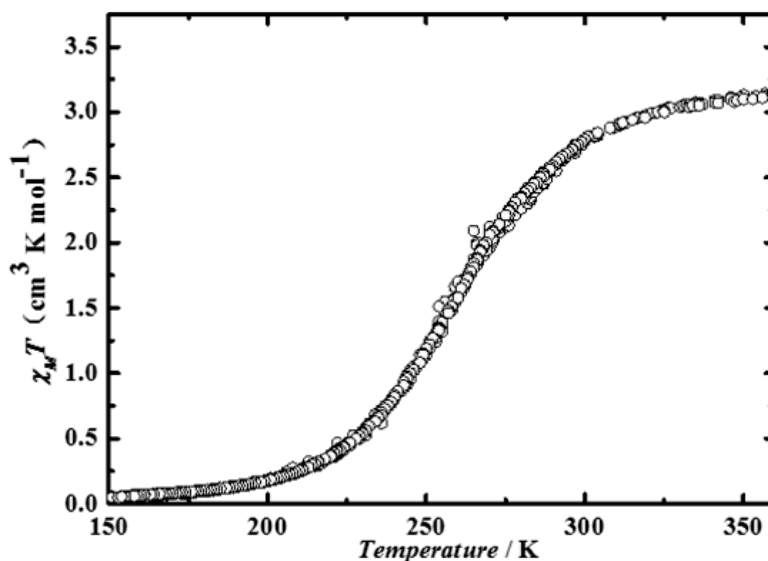


Figure III.40. Thermal dependence of the  $\chi_M T$  product of polymorph **II-pBrA**, recorded at 1 K/min under an applied magnetic field of 15 kOe.

- *Crystallographic study of II-pBrA*

SCXRD data were recorded at 10 K, 120, 200, 250, 300, 330, 350 K, and the structures were determined at each temperature. The data collection at 10 K was performed in collaboration with Dr Sébastien Pillet in the University of Lorraine (Nancy, France). The structure at 120 K was performed in collaboration with Dr. Brice Kauffmann in the Institut Européen de Chimie et Biologie (Bordeaux, France) using a copper source, since the X-ray diffractometer in the lab did not work at that time.

As seen in Table III.12, polymorph **II-pBrA** crystallizes at 350 K in the same space group as polymorph **I-pBrA**,  $P2_1/n$ , which remains at 120 K. However, it was impossible to thermally quench the Q-HS\* and only the LS state was observed at 10 K (as seen in Appendix 5). Similarly to **I-pBrA**, all atoms sit on the general Wyckoff position (4e) and there are two crystallographically independent molecules in the asymmetric unit (Figure III.41a). The average Fe-N bond lengths ( $\langle \text{Fe-N} \rangle$ ) are 2.140(5) Å and 2.144(7) Å at 350 K for Fe1 and Fe2 entities, which is slightly smaller than the typical value of HS in this family, which is possible due to the partial damage of crystal at high temperature. It is worth to mention that one phenyl ring in Fe2 molecules is disordered between two positions with the occupancy of 0.79/0.21. The dihedral angle of two disordered phenyl ring is 68°. That recalls the value of 67° observed for the rotation of the phenyl ring in **I-pBrA**. The Fe-N-CS angles are 171.22° and 165.47° in Fe1, and 170.50° and 172.71° in Fe2, suggesting the bending of NCS<sup>-</sup> groups. By the overlay

of Fe1 and Fe2 molecules, the main difference in Fe1 and Fe2 comes from the disordered phenyl ring with RMSD of 0.710 Å (Figure III.41c).

**Table III.12.** Crystal data and structure refinement data for polymorph **II-pBrA** at selected temperatures (full table with complementary temperatures in Appendix 5)

Empirical formula	C <sub>26</sub> H <sub>18</sub> Br <sub>2</sub> FeN <sub>6</sub> S <sub>2</sub>	
Formula weight / g mol <sup>-1</sup>	694.25	694.25
Temperature / K	350	120
Radiation MoKα / Å	λ = 0.71073	λ = 1.54184
Crystal size / mm <sup>3</sup>	0.18 × 0.12 × 0.06	
Crystal system	monoclinic	
Space group	P2 <sub>1</sub> /n	
<i>a</i> / Å	16.688(12)	16.3086(10)
<i>b</i> / Å	21.087(13)	20.7674(2)
<i>c</i> / Å	17.393(13)	16.8871(2)
<i>α</i> / °		90
<i>β</i> / °	107.342(19)	107.5110(10)
<i>γ</i> / °		90
Volume / Å <sup>3</sup>	5842(7)	5454.40(9)
Z-formula	8	
ρ <sub>calc</sub> / g cm <sup>-3</sup>	1.579	1.691
μ / mm <sup>-1</sup>	3.421	9.523
F(000)	2752.0	2752.0
2θ range for data collection / °	2.97 - 50.05	6.606 - 136.492
Index ranges	-19 ≤ h ≤ 19, -25 ≤ k ≤ 21, -20 ≤ l ≤ 20	-19 ≤ h ≤ 18, -25 ≤ k ≤ 24, -20 ≤ l ≤ 20
Reflections collected	107438	39776
Independent reflections	10 308 [R <sub>int</sub> = 0.0724, R <sub>sigma</sub> = 0.0547]	9 897 [R <sub>int</sub> = 0.0285, R <sub>sigma</sub> = 0.0196]
Data/restraints/parameters	10308/0/673	9897/0/667
Goodness-of-fit on F <sup>2</sup>	1.008	1.055
Final R indexes [I >= 2σ(I)]	R <sub>1</sub> = 0.0554, wR <sub>2</sub> = 0.1397	R <sub>1</sub> = 0.0351, wR <sub>2</sub> = 0.0956
Final R indexes [all data]	R <sub>1</sub> = 0.1440, wR <sub>2</sub> = 0.1822	R <sub>1</sub> = 0.0371, wR <sub>2</sub> = 0.0972
Largest diff. peak/hole / e Å <sup>-3</sup>	0.79/-0.60	1.15/-0.71

$$R_1 = \frac{\sum ||F_0| - |F_c||}{\sum |F_0|}, wR_2 = \left[ \frac{\sum w(F_0^2 - F_c^2)^2}{\sum w(F_0^2)^2} \right]^{1/2}$$

Part III – Promoting Distortion of the Coordination Polyhedron Using Polymorphism:  
Bromine Substitution of PM-zBrA Family

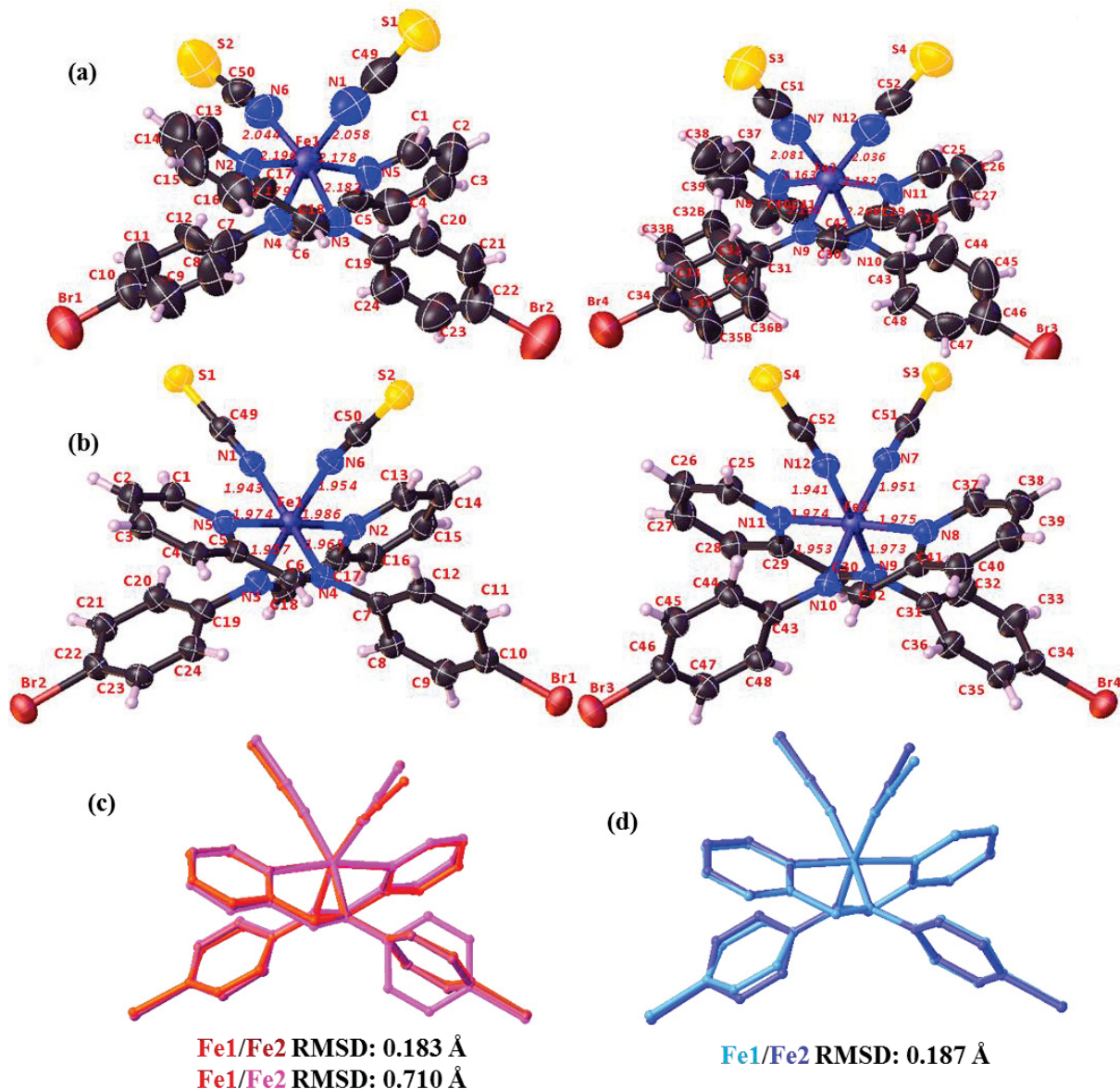


**Figure III.41.** The Fe1 and Fe2 molecules in the asymmetric unit at 350K (a), 120K (b), and their overlay at 350K (c) and 120K (d) of polymorph **II-pBrA**. The red and pink stand for molecules at 350 K while the blue and light blue stand for molecules at 120 K.

At 120 K, the  $\langle\text{Fe-N}\rangle$  values are 1.961(1) Å and 1.964(3) Å for Fe1 and Fe2, respectively, agreeing with the presence of LS states as shown by the magnetic measurements. Notice that there is no disorder in the fully LS Fe2 (**Figure III.41b**). The Fe-N-CS angles are 168.42° and 166.79° in Fe1, and 168.14° and 174.53° in Fe2, suggesting an increase of the bending of NCS<sup>-</sup> groups compare to 350 K. From the overlay of Fe1 and Fe2, the main differences in Fe1 and Fe2 result from the phenyl ring and NCS<sup>-</sup> with RMSD of 0.187 Å. The absence of disorder at low temperature leads the molecules to be very similar.

In order to check whether the order-disorder of the phenyl ring is coupled with the SCO, the structures at 200 K, 250 K, 300 K and 350 K were analyzed carefully, especially the dihedral angle and the ratio of the disordered phenyl rings. As seen in Table III.13, the disorder of phenyl ring exists only above 200 K. From 350 K to 300 K, the occupancy and the dihedral angle of disordered phenyl rings slightly change, while occupancy and the dihedral angle of disordered phenyl rings decrease a lot from 300 K to 250 K. Assuming that the dihedral angle at 350 K corresponds to the HS state, then the HS fraction can be calculated, labeled HS fraction1 in Table III.13. Actually, HS fraction can be also calculated based on the average  $\langle\text{Fe-N}\rangle$  distance, labeled as HS fraction2 in Table III.13. Figure III.42 reports the evolution of this calculated HS fraction from the dihedral angle as function of the temperature. One can clearly see that the evolution of the order-disorder of the phenyl ring correlates with the SCO curve in II-pBrA.

Table III.13. The summary of structural data of the disorder phenyl ring in II-pBrA.

Temperature / K	120	200	250	300	330	350
<i>C33a,C32a,C35a,C36a</i> <sup>1</sup>	1.0	1.0	0.630	0.810	0.792	0.790
<i>C33b,C32b,C35b,C36b</i> <sup>1</sup>	0.0	0.0	0.370	0.190	0.208	0.210
dihedral angle / °	0	0	22.19	56.6	64.42	68.44
HS fraction1 / % <sup>2</sup>	0	0	0.32	0.82	0.94	1
$\langle\text{Fe1-N}\rangle/\langle\text{Fe2-N}\rangle$ / Å	1.966 / 1.961	1.966 / 1.961	2.015 / 2.017	2.112 / 2.129	2.153 / 2.156	2.140 / 2.144
HS fraction2 / % <sup>3</sup>	0	0	0.26	0.78	0.95	0.89

<sup>1</sup>occupancy; <sup>2</sup> calculated from dihedral angle of disordered phenyl ring; <sup>3</sup> calculated from the  $\langle\text{Fe-N}\rangle$  distances.

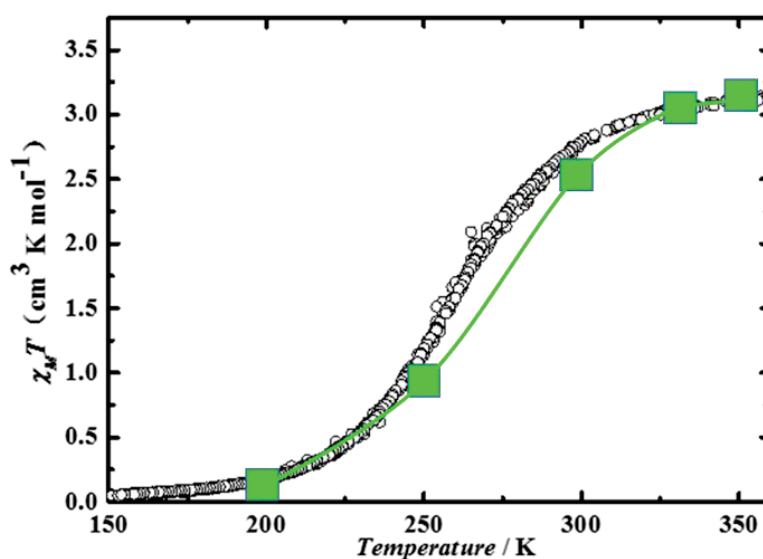


Figure III.42. Superposition of the experimental curve from magnetic measurements and the simulated one based on the dihedral angle of the disordered phenyl ring from SCXRD data (■) of polymorph II-pBrA.

Figure III.43 shows the superposition of the molecules in HS (350 K) and LS (120 K) and illustrates that the NCS<sup>-</sup> branches are slightly affected by the temperature. The temperature dependence of the molecular geometries (Table III.13 and Figure III.42) clearly evidences that in **II-pBrA** the rotation is acting concomitantly with the SCO and the whole variation of the molecular geometry appears here continuous, instead of being discontinuous in **I-pBrA**.

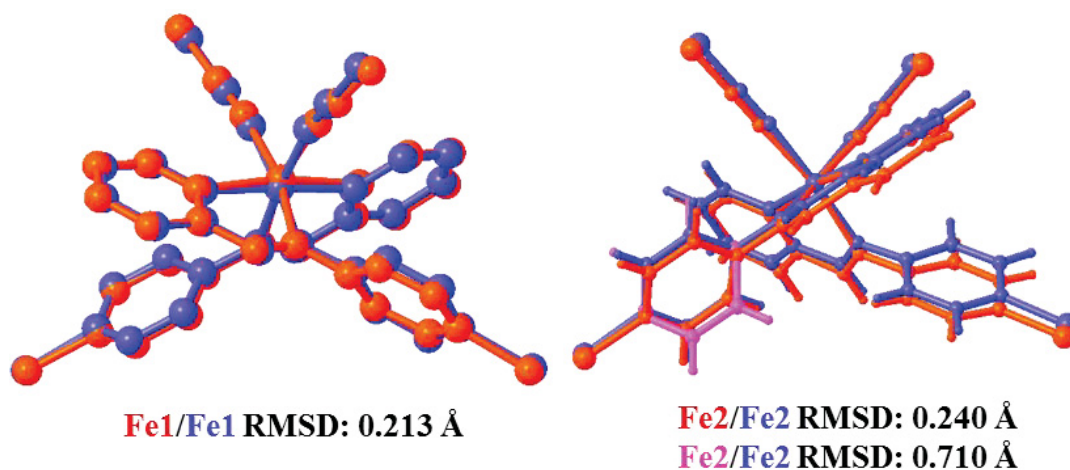


Figure III.43. The molecular overlay between 350K and 120K of polymorph **II-pBrA**.

SCXRD data allow to simulate to PXRD pattern at 300 K to compare with the experimental one (Figure III.44). One can clearly see the good agreement observed between both diffractograms indicating that the phase characterized by magnetic measurements corresponds to the crystalline phase studied in SCXRD.

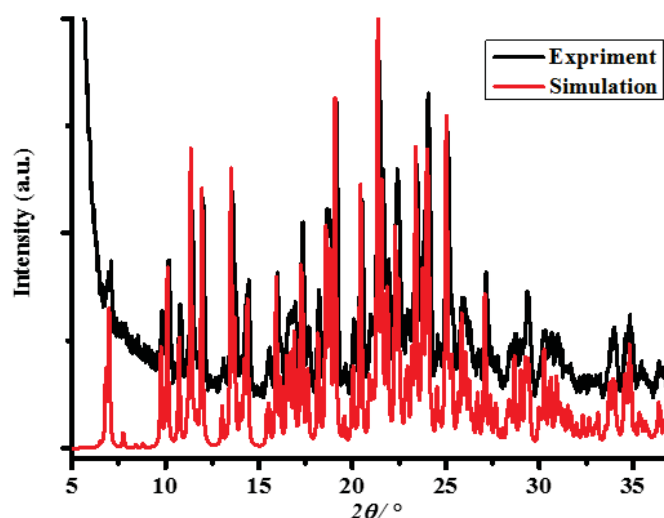


Figure III.44. Experimental (black) and simulated (red) from SCXRD data powder X-ray diffraction patterns of complex **II-pBrA**.

*Part III – Promoting Distortion of the Coordination Polyhedron Using Polymorphism:  
Bromine Substitution of PM-zBrA Family*

The variations of the angular and the trigonal distortions for Fe1N<sub>6</sub>/Fe2N<sub>6</sub> are 26/17° ( $\Delta\Sigma$ ) and 107/95° ( $\Delta\Theta$ ) from 350 K to 120 K, respectively (Table III.14). These values are slightly smaller than that in polymorph I-pBrA.

**Table III.14.** The coordination sphere parameters in polymorph II-pBrA.

Compound	II-pBrA			
	350		120	
Temperature / K	350	350	120	120
Fe <sup>2+</sup> site	Fe1	Fe2	Fe1	Fe2
<Fe-N> / Å	2.140	2.144	1.961	1.963
$\zeta$ / Å	0.354	0.339	0.076	0.071
$\Sigma$ / °	80	75	54	58
$\Theta$ / °	263	260	156	165
Shape <sup>b</sup>	1.726	1.613	0.633	0.717
SC-N-Fe / °	171.22 /	170.50 /	168.42 /	168.14 /
	165.47	172.71	166.79	174.53
(SC)N-Fe-N(CS) / °	95.79	95.67	90.49	89.49
$\sigma_1$ / °	92.93	92.27	97.68	97.26
$\sigma_2$ / °	169.56	167.75	176.17	176.26
$\sigma_3$ / °	52.86 /	64.40 /	57.84 /	68.14 /
	59.20	57.51 / 54.07	53.77	55.14

$\sigma_1$ :N-Fe-N with N from imine;  $\sigma_2$ :N-Fe-N with N from pyridine;  $\sigma_3$ ,dihedral angle of phenyl and pyridine in one ligand. <sup>a</sup> values obtained using the OctaDist program (<https://octadist.github.io>). <sup>b</sup> values obtained using the SHAPE program (ref. 6).

The disorder of ligand conformation can influence the intermolecular interactions. As shown in Figure III.45a, there are huge differences in the fingerprints between Fe1 and Fe2 at 350 K. The “corners” in the fingerprint of Fe2 separate very well, which is the H---H contacts (H45---H33b, 1.976 Å). The ratio of S---H and Br---H are almost equal in Fe1 and Fe2. The ratio of S---Br in Fe1 is higher than Fe2, which agrees with the observed contacts of S1---Br1 (3.629 Å), S2---Br2 (3.436 Å), S3---Br3 (3.897 Å) and S4---Br4 (3.826 Å). The difference in fingerprints between Fe1 and Fe2 at 120 K is very small (Figure III.45b). At 120 K, the ratio of selected contacts are similar except for S---Br. This may be due to the contacts of S1---Br1 (3.457 Å), S2---Br2 (3.364 Å), S3---Br3 (3.734 Å) and S4---Br4 (3.609 Å).

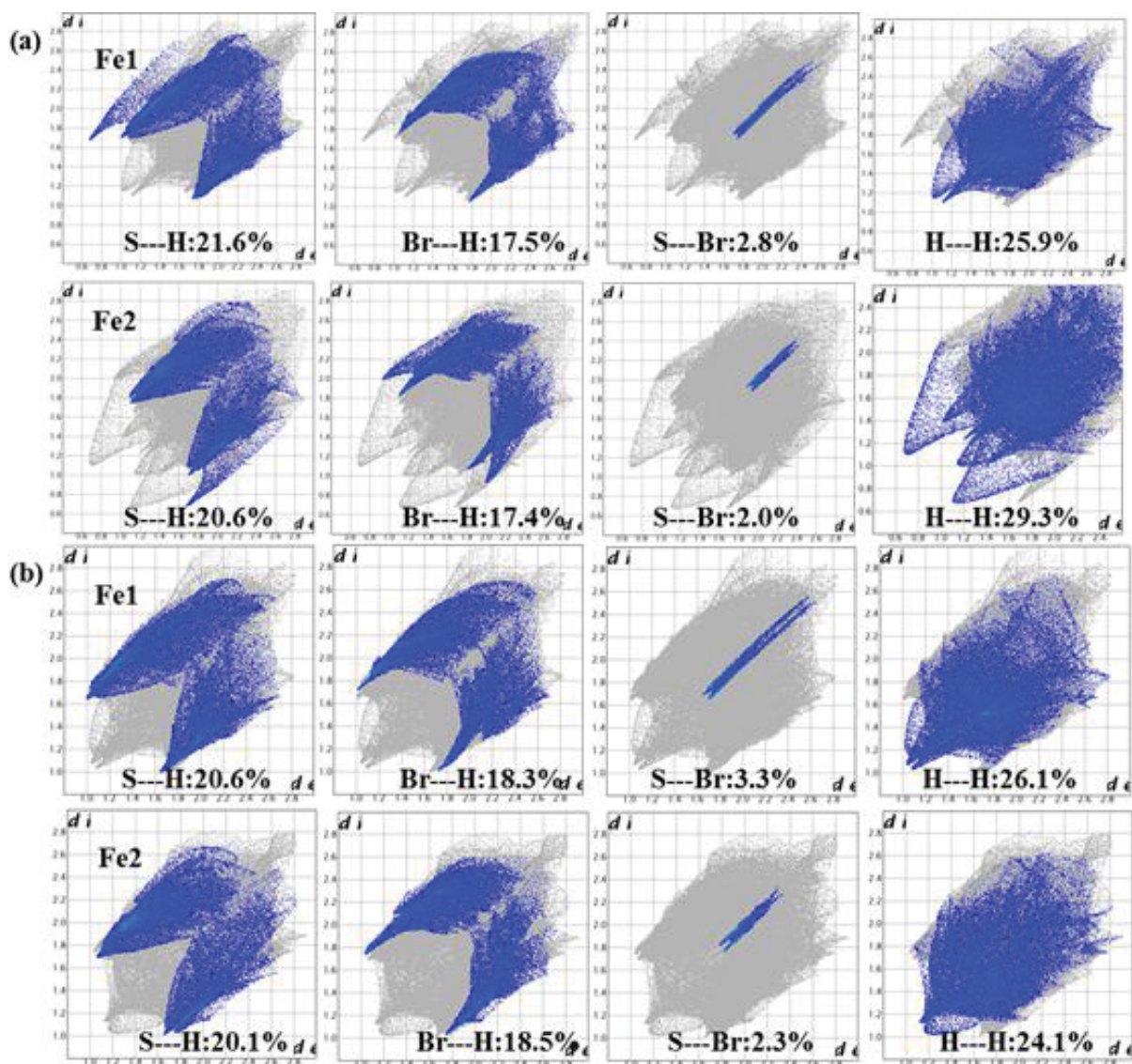


Figure III.45. Selected contacts at 350K (a) and 120K (b) for polymorph II-pBrA.

At 350 K, Fe1 molecules are connected by S1---Br1 and S2---Br2 bondings while Fe2 molecules are connected by H33b---H45 contact along the *b* axis with  $2_1$  symmetry (Figure III.46a). Along *b* axis, the Fe<sup>2+</sup> sites form a chain with Fe---Fe distances and Fe-Fe-Fe angles of 11.034 Å and 145.88° for Fe1 and 11.033 Å and 145.94° for Fe2, suggesting a zig-zag arrangement. The adjacent Fe1 and Fe2 are linked by S2---H28 (2.976 Å). Figure III.46b shows the S---H bonding between molecules, including S1---H4 (2.909 Å) between Fe1 molecules and S1---H36 (2.817 Å), S2---H36b (2.491 Å) of Fe2 molecules. Figure III.46c shows packing of four molecules at *ac* plane, where the inversion centers are located at the center of S3---S3. Thus, the crystal packing can be viewed as Fe1 and Fe2 chains packing alternately along the *a* and *c* directions with inversion symmetry (Figure III.46d). It seems II-pBrA has a similar packing mode as polymorph I-pBrA although they have different ligand conformation.

However, the orientation of molecules (especially the orientation of NCS<sup>-</sup> groups) are different, if we compare [Figure III.28b](#) and [Figure III.46d](#). The orientations of NCS<sup>-</sup> in polymorph **I-pBrA** is almost in the same direction while they are in the different directions of Fe1 and Fe2 in **II-pBrA**, which may result from the different interactions, especially the short contacts of S---S and  $\pi_{py} \cdots \pi_{py}$ .

At 120 K, Fe1 (Fe2) molecules are connected by S---Br bondings along *b* axis with  $2_1$  symmetry, owing to the loss of H---H short contact related to disorder of phenyl ring. Along *b* axis, the Fe---Fe distances and Fe-Fe-Fe angles are 10.729 Å and 150.84° for Fe1 zig-zag chain and 10.70 Å and 151.96° for Fe2 chain, suggesting Fe1 and Fe2 are more linear than 350 K. The adjacent Fe1 and Fe2 are linked by S---H bonding along the *a* and *c* directions. The molecular packing at 120 K is very similar to that at 300 K. The structural overlay in *bc* plane between 120 K and 350 K is shown in [Figure III.47b](#). Compared to structural overlay of polymorph **I-pBrA** ([Figure III.47a](#)), there is much less rearrangement of molecules in polymorph **II-pBrA**. It suggests that the order-disorder transition of the phenyl ring has less influence on the molecular rearrangement in polymorph **I-pBrA** than in polymorph **II-pBrA**.

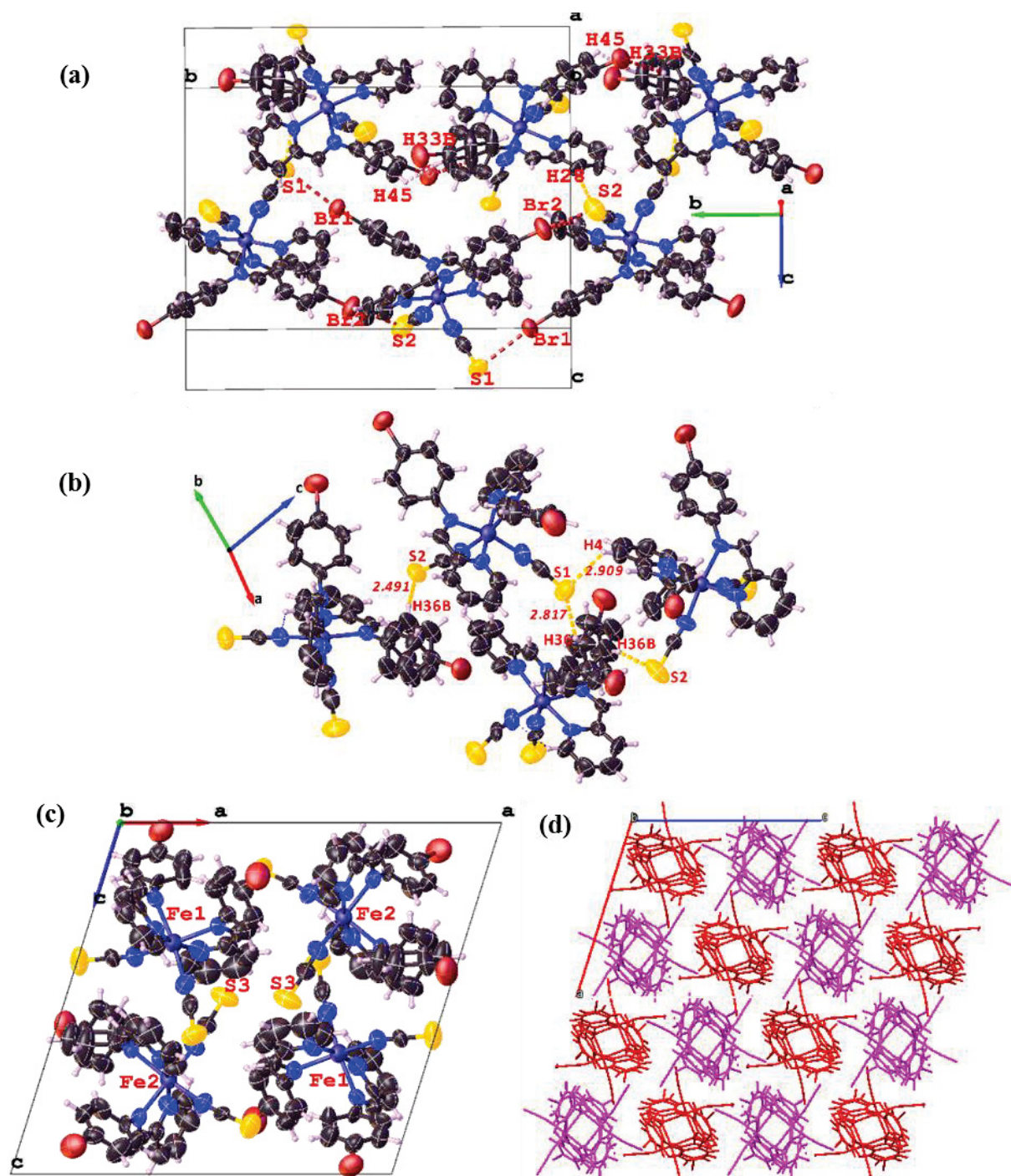


Figure III.46. The packing of Fe1 and Fe2 along *b* direction (a), the hydrogen bonding between Fe1 and Fe2 (b), an inverted cent of four molecules (c), 3D structure with Fe1 in red and Fe2 in pink at 350 K (d) of polymorph II-pBrA.

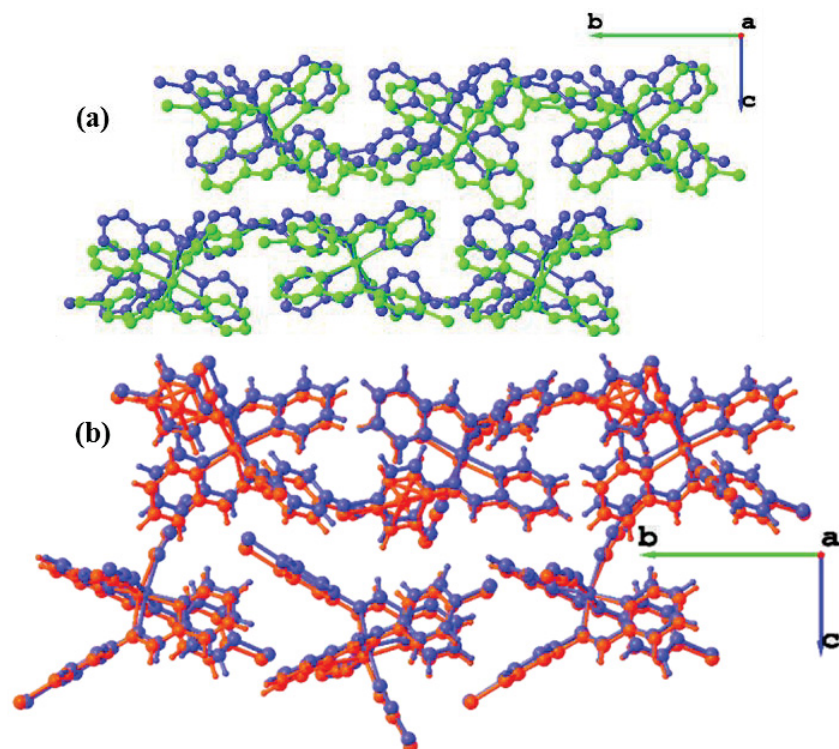


Figure III.47. The structural overlay at  $bc$  plane between HS (red, green) and LS (blue) of polymorphs **I-pBrA** (a) and **II-pBrA** (b).

- *Unit-cell parameters as a function of temperature of II-pBrA*

Figure III.48 reports the temperature dependence of the unit-cell parameters. It clearly shows a gradual decrease of  $a$ ,  $b$  and  $c$  values of 0.3 Å, 0.3 Å and 0.5 Å, respectively, from 350 K to 160 K. Only the  $\beta$  value increases of 0.5°. Concerning the unit-cell volume, it decreases upon cooling as a result of both the gradual spin crossover and the thermal contraction.

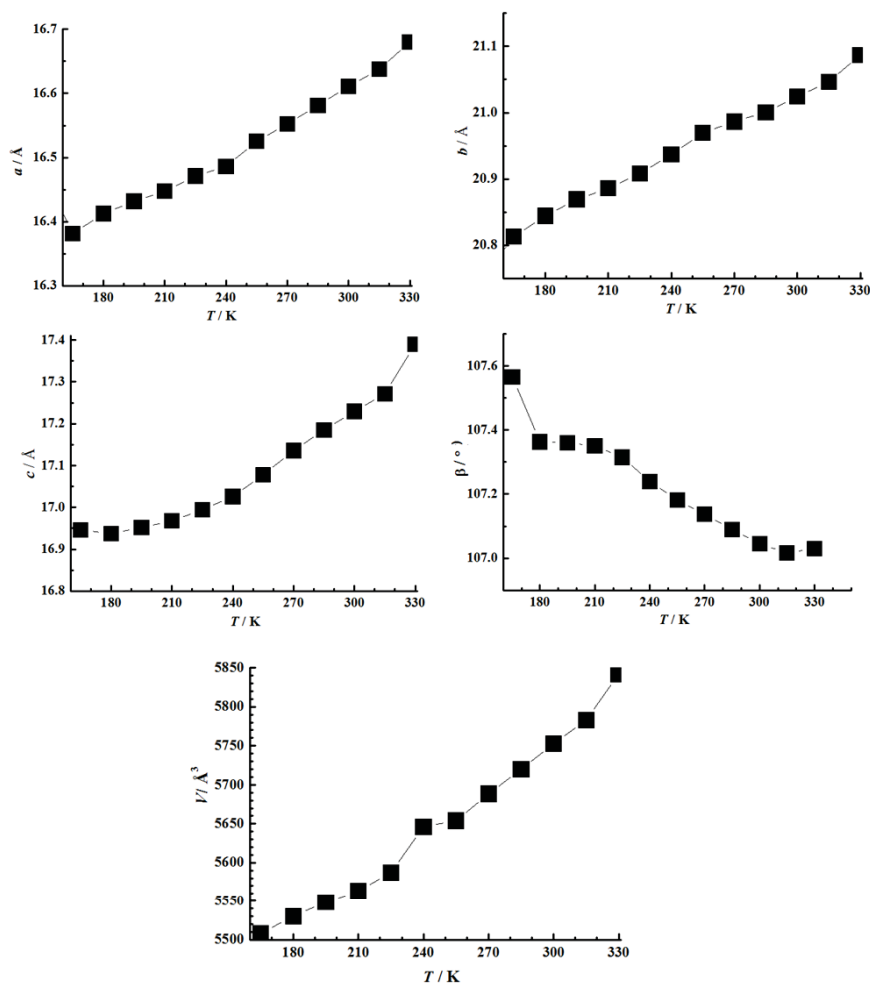


Figure III.48. Temperature dependence of the unit-cell parameters in polymorph **II-pBrA**, determined by SCXRD. The lines are only a guide for eyes.

- *Structure-properties relationship of II-pBrA*

According to the  $\Delta\theta$  values ( $107/95^\circ$  for  $\text{Fe}_1\text{N}_6/\text{Fe}_2\text{N}_6$ , compared to  $97/123^\circ$  in **I-pBrA**), the expected  $T(\text{LIESST})$  would be 65 K. However, there is no LIESST effect from the photo-magnetic measurements. Moreover, the thermal quenched structure at 10 K is fully LS, agreeing with the presence of a very short-lived metastable state. Several hypothesis can be made.

The absence of LIESST may be related to the continuous variation of ligand geometry. Based on the photocrystallography result of polymorph **I-pBrA**, the  $h\nu\text{-HS}^*$  has a similar structure as the thermally quenched Q- $\text{HS}^*$ . The energy provided by the presence of the abrupt ligand geometry variation upon  $\text{HS}^* \rightarrow \text{LS}$  relaxation, might contribute to increase the lifetime of this metastable state. In polymorph **II-pBrA**, the continuous variation of ligand geometry induces a much less additional energy that destabilizes the  $\text{HS}^*$  and increases its relaxation, preventing any observation.

Another explanation is based on the fact that we cannot be sure that the photo-induced  $h\nu$ -HS\* has the same disordered structure than the HS one. If the  $h\nu$ -HS\* state is not disordered the variation in the distortion parameters might be much smaller, strongly decreasing the lifetime of the metastable HS\* state.

Another hypothesis is that the model linking  $T(\text{LIESST})$  and  $\Delta\theta$  is not complete. Indeed, in polymorph **II-pBrA**, the coordination sphere parameters are very close from the FeI site in polymorph **I-pBrA** with  $\Delta\zeta = 0.278/0.268$  Å for both sites compared to  $\Delta\zeta = 0.284/0.354$  Å in polymorph **I-pBrA**. We can notice that, in addition to lower  $\Delta\theta$  values, one  $\Delta\zeta$  is also much lower. This parameter that measures the anisotropy of elongation has been highlighted during the study of polymorphs **I-BiA** and **II-BiA** of  $[\text{Fe}(\text{PM-BiA})_2(\text{NCS})_2]$  (cf. [Part I.3](#)).<sup>34-35</sup> It is therefore possible that the “simple” trigonal distortion parameter is not sufficient to describe and predict the  $T(\text{LIESST})$  behavior.

SCO coupled to order-disorder transition is very common<sup>38</sup> and the disorder can appear in ligand<sup>39-41</sup> and anion<sup>42-43</sup>. Usually, the disorder occurs at high temperature and the order at low temperature owing to the fact that high entropy and symmetry states are favored at high temperature.<sup>44</sup>

In summary, polymorph **II-pBrA** shows a gradual SCO coupled with an order-disorder transition. The corresponding modification of the intermolecular interactions and crystal packing is also continuous and polymorph **II-pBrA** shows the usual decrease of unit-cell volume from HS to LS.

### **III.4.3. Polymorph $[\text{Fe}(\text{PM-pBrA})_2(\text{NCS})_2]$ -III: **III-pBrA****

This polymorph was obtained in too small quantities to be able to perform any magnetic characterizations. Moreover, it was always obtained concomitantly with polymorph **I-pBrA** and the crystals have to be manually selected. Unfortunately, the crystals are very small and the ratio of polymorph **III-pBrA** is very low in the mixture. We therefore perform all our study on single crystals. Data were collected at 300, 220, 210, 205, 150, 90 K and at 10 K after a thermal quenching. The thermally quenched measurement at 10 K was performed in collaboration with Dr Sébastien PILLET (University of Lorraine, Nancy, France). Additionally to the structure refinement, the unit-cell parameters as function of temperature were also measured by SCXRD. [Table III.15](#) summarizes the experimental and structure refinement data at selected temperatures.

Table III.15. Crystal data and structure refinement data for polymorph III-pBrA at selected temperatures (full table with complementary temperatures in Appendix 5)

Empirical formula	C <sub>26</sub> H <sub>18</sub> N <sub>6</sub> S <sub>2</sub> FeBr <sub>2</sub>		
Formula weight / g mol <sup>-1</sup>	694.25		
Temperature / K	300	90	10 (thermally quenched)
Radiation MoK $\alpha$ / Å	$\lambda = 0.71073$		
Crystal size / mm <sup>3</sup>	0.26 × 0.22 × 0.14	0.28 × 0.24 × 0.14	0.22 × 0.24 × 0.20
Crystal system	triclinic		
Space group	P-1		
<i>a</i> / Å	9.9504(3)	10.3686(14)	9.8698(12)
<i>b</i> / Å	16.4925(5)	15.804(2)	16.0292(14)
<i>c</i> / Å	18.4995(6)	17.839(2)	18.2045(13)
$\alpha$ / °	102.6780(10)	98.998(3)	102.601(7)
$\beta$ / °	90.0430(10)	92.149(3)	90.214(8)
$\gamma$ / °	105.2950(10)	107.243(3)	104.530(9)
Volume / Å <sup>3</sup>	2851.42(15)	2746.5(6)	2715.6(5)
Z-formula	4		
$\rho_{\text{calc}}$ / g cm <sup>-3</sup>	1.617	1.679	1.698
$\mu$ / mm <sup>-1</sup>	3.504	3.638	3.680
F(000)	1376.0	1376.0	1376.0
2 $\theta$ range for data collection / °	3.838 - 53.59	2.74 - 50.05	3.916 - 50.054
Index ranges	-12 ≤ <i>h</i> ≤ 12, -20 ≤ <i>k</i> ≤ 20, -23 ≤ <i>l</i> ≤ 23	-11 ≤ <i>h</i> ≤ 12, -18 ≤ <i>k</i> ≤ 18, -21 ≤ <i>l</i> ≤ 21	-11 ≤ <i>h</i> ≤ 11, -19 ≤ <i>k</i> ≤ 16, -21 ≤ <i>l</i> ≤ 21
Reflections collected	86 509	42 764	20 752
Independent reflections	12 184 [R <sub>int</sub> = 0.0613, R <sub>sigma</sub> = 0.0563]	9 188 [R <sub>int</sub> = 0.1058, R <sub>sigma</sub> = 0.1410]	9 575 [R <sub>int</sub> = 0.1279, R <sub>sigma</sub> = 0.1929]
Data/restraints/parameters	12 184/0/667	9 188/0/661	9 575/0/587
Goodness-of-fit on F <sup>2</sup>	0.991	1.028	1.007
Final R indexes [I ≥ 2 $\sigma$ (I)]	R <sub>1</sub> = 0.0455, wR <sub>2</sub> = 0.0882	R <sub>1</sub> = 0.0582, wR <sub>2</sub> = 0.1030	R <sub>1</sub> = 0.1025, wR <sub>2</sub> = 0.2392
Final R indexes [all data]	R <sub>1</sub> = 0.1147, wR <sub>2</sub> = 0.1101	R <sub>1</sub> = 0.1495, wR <sub>2</sub> = 0.1325	R <sub>1</sub> = 0.1682, wR <sub>2</sub> = 0.2927
Largest diff. peak/hole / e Å <sup>-3</sup>	0.99/-0.67	0.84/-0.72	1.28/-1.74

$$R_1 = \frac{\sum ||F_0| - |F_C||}{\sum |F_0|}, wR_2 = \left[ \frac{\sum w(F_0^2 - F_C^2)^2}{\sum w(F_0^2)^2} \right]^{1/2}$$

- Crystallographic study of III-pBrA

Polymorph III-pBrA crystallizes in the triclinic system with the space group *P*-1 at 300 K and 150 K (Table III.15), which is a lower symmetry than *P*2<sub>1</sub>/*n* determined for polymorphs I-pBrA and II-pBrA. There are again two crystallographically independent molecules in the asymmetric unit with all atoms on the general Wyckoff position (2i) (Figure III.49). The thiocyanate groups and PM-pBrA ligands are in a *cis* configuration, where two pyridine rings are in *trans*, which is similar to other polymorphs.

Part III – Promoting Distortion of the Coordination Polyhedron Using Polymorphism:  
Bromine Substitution of PM-zBrA Family

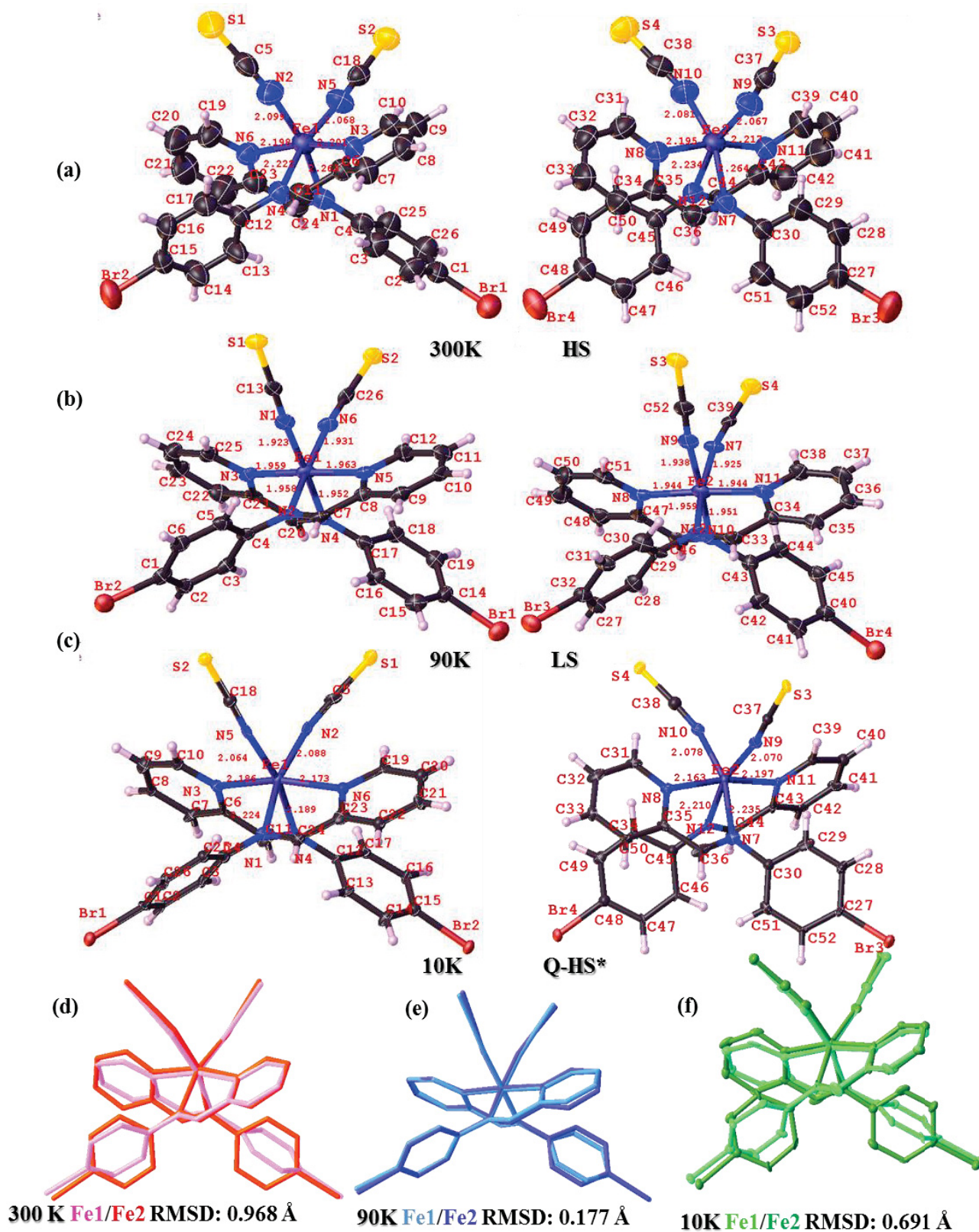


Figure III.49. The Fe1 and Fe2 molecules in the asymmetric unit and their superposition at 300 K (a, d), 90 K (b, e), the Q-HS\* at 10 K (c, f) of polymorph III-*p*BrA.

*Part III – Promoting Distortion of the Coordination Polyhedron Using Polymorphism:  
Bromine Substitution of PM-zBrA Family*

The first thing that should be notice is that Fe1 and Fe2 sites are rather different from each other and resemble to the corresponding ones in polymorph **I-pBrA**. The overlay of Fe1 and Fe2, exhibits a huge RMSD value of 0.968 Å (Figure III.49d). This is also illustrated by the difference in  $\sigma_3$ , the dihedral angle between the bromophenyl and the pyridine rings (Table III.16), in the two Fe<sup>2+</sup> sites. These differences in  $\sigma_3$  values,  $\delta\sigma_3$ , between the two ligands of the same molecule, are 15° and 38° for Fe1 and Fe2, respectively. This clearly indicates a stronger dissymmetry of the ligand geometry in Fe2. The average of the bond lengths,  $\langle\text{Fe-N}\rangle$ , are 2.176(6) Å and 2.177(6) Å in Fe1 and Fe2 entities at 300 K clearly indicating HS states for both sites.

At 90 K, both molecules tend toward similar geometries with a reduction of  $\delta\sigma_3$  to 2° in Fe1 and 9° in Fe2. This causes the decrease of the RMSD value to 0.177 Å. The differences that remain between the molecules are related to motion of NCS<sup>-</sup> groups as seen in the superposition of molecules (Figure III.49e) and in Table III.16. The averages of the bond lengths,  $\langle\text{Fe-N}\rangle$ , are 1.948(4) Å and 1.943(4) Å at 90 K, in Fe1 and Fe2, respectively, corresponding to full LS states.

**Table III.16.** The coordination sphere parameters in polymorph **III-pBrA**.

Compound	<b>III-pBrA</b>					
Temperature / K	300	300	90	90	10 <sub>quench</sub>	10 <sub>quench</sub>
Fe <sup>2+</sup> site	Fe1	Fe2	Fe1	Fe2	Fe1	Fe2
$\langle\text{Fe-N}\rangle$ / Å	2.176(6)	2.177(6)	1.948(4)	1.943(4)	2.154(5)	2.159(6)
$\zeta$ / Å	0.365	0.409	0.081	0.047	0.312	0.340
$\Sigma$ / °	70.68	83.77	57.82	53.80	65.40	81.50
$\Theta$ / °	258.77	257.88	163.41	159.49	250.62	259.97
Shape <sup>b</sup>	1.584	1.628	0.705	0.645	1.446	1.572
SC-N-Fe / °	157.78 /	170.68 /	173.51 /	171.01 /	154.32 /	170.07 /
	174.63	160.26	170.95	169.13	172.44	159.07
(SC)N-Fe-N(CS) / °	94.75	95.83	87.57	87.77	93.55	95.78
$\sigma_1$ / °	89.92	80.95	99.90	97.84	90.52	81.78
$\sigma_2$ / °	166.44	165.27	176.65	174.98	166.69	166.95
$\sigma_3$ / °	51.08 /	68.28 /	55.35 /	70.39 /	49.68 /	63.57 /
	65.57	30.75	53.10	61.71	58.63	29.73

$\sigma_1$ :N-Fe-N with N from imine;  $\sigma_2$ :N-Fe-Nwith N from pyridine;  $\sigma_3$ ,dihedral angle of phenyl and pyridine in one ligand. <sup>a</sup> values obtained using the OctaDist program (<https://octadist.github.io>). <sup>b</sup> values obtained using the SHAPE program (ref.6)

*Part III – Promoting Distortion of the Coordination Polyhedron Using Polymorphism:  
Bromine Substitution of PM-zBrA Family*

The thermally quenched Q-HS\* structure was also determined at 10 K. The compound crystallizes in the same space group *P*-1 with two molecules in the asymmetric units (Figure III.49f). The ligand conformation is very similar to that at 300 K with  $\delta\sigma$  of 9° and 34° for Fe1 and Fe2, respectively (Table III.16). The average bond lengths  $\langle\text{Fe-N}\rangle$ , are 2.154(5) Å and 2.159(6) Å for Fe1 and Fe2 centers, respectively, which indicates the HS state.

The superposition of the molecules at various temperatures are shown in Figure III.50. From the overlay of the Fe1 (Fe2) site in the HS and LS states, one can see the huge modifications of ligand conformation with RMSD of 0.385 Å and 0.906 Å for Fe1 and Fe2, respectively (Figure III.50a). The atomic displacements of NCS<sup>-</sup> contribute to the large value of RMSD in Fe1. For Fe2, in addition to the motion of NCS<sup>-</sup> there is also the huge motion of pyridine and phenyl rings, and the rotation of bromophenyl ring (Br3C<sub>6</sub>) by 67°. Similar differences can be seen from the overlay of the thermally quenched Q-HS\* and LS structures (Figure III.50b). The RMSD value for Fe1 and Fe2 are 0.393 Å and 0.949 Å, respectively, which are a little bigger than between HS and LS. In this case, the evolution of the dihedral angle of bromophenyl (Br3C<sub>6</sub>) rings in Fe2 leads to a rotation of 70°. Finally, the overlay of the HS and Q-HS\* structures show their similarity with RMSD value lower than 0.1 Å (Figure III.50c).

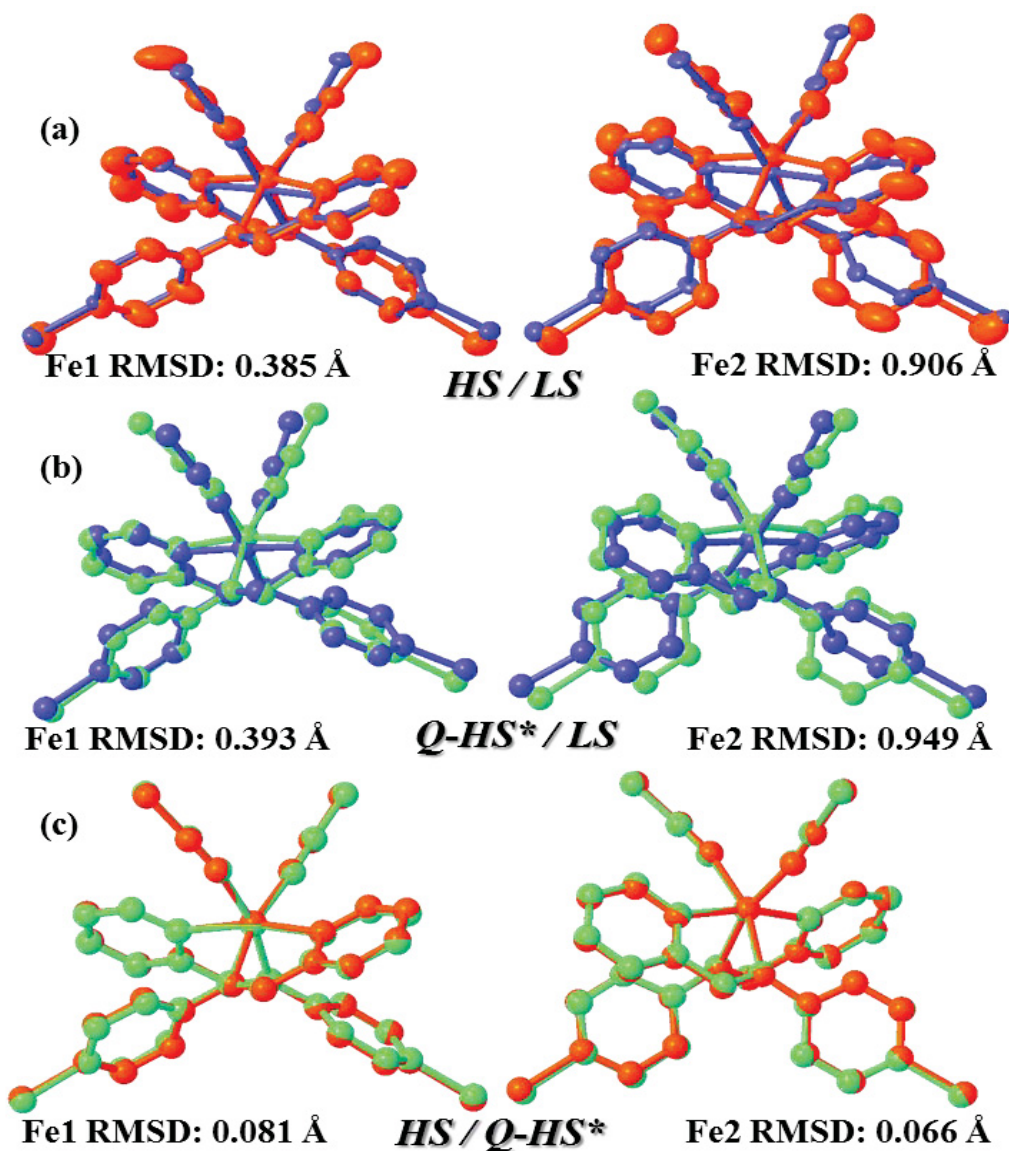


Figure III.50. The molecular overlay between 300 K (red) and 90 K (blue) (a), between 90 K and quenched 10 K (green) (b), and between 300 K and quenched 10K (c) of polymorph III-*pBrA*.

The distortion parameters of the iron polyhedron followed in temperature are shown in Figure III.51. The variation of  $\langle \text{Fe-N} \rangle$  distances, bond distortion ( $\zeta$ ), and trigonal distortion ( $\theta$ ) in Fe1 and Fe2 are very similar. On the contrary, the HS (Q-HS\*) values of  $\Sigma(\text{Fe1N}_6)$  being much smaller than  $\Sigma(\text{Fe2N}_6)$ , its variation upon SCO is weaker by a factor three. This is very similar to the observation made for polymorph I-*pBrA*. An abrupt decrease of all these parameters occurs between 210 K and 205 K, suggesting an abrupt SCO in polymorph III-*pBrA*. The fact that these variations occur at the same temperature (temperature range of 5 K), may indicate that Fe1 and Fe2 undergo the SCO concomitantly. Consequently, the switching temperature is around 205K, which is rather different from the 170 K for polymorph I-*pBrA*.

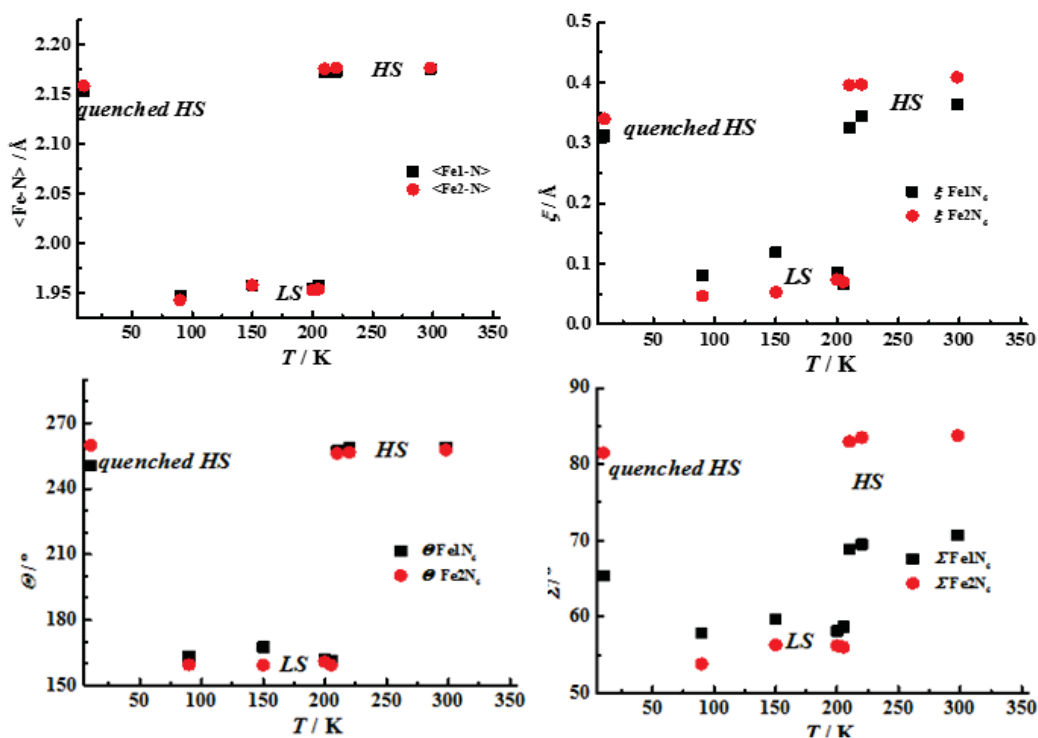


Figure III.51. Thermal variation of the distortion parameters of the coordination sphere of Fe1 (black squares) and Fe2 (red circles) entities in polymorph III-*p*BrA.

We have therefore a strong relationship with polymorph I-*p*BrA but with different switching temperatures. To account for the truthfulness of such polymorph despite the similarities of the Fe<sup>2+</sup> sites, we have to look at bigger scales probing the crystal packing and the intermolecular interactions.

The intermolecular interactions are analyzed by the fingerprints derived from the Hirshfeld surfaces. Figure III.52 shows the Hirshfeld surfaces at 300 K (HS), 90 K (LS) and 10 K (Q-HS\*), where the red spots are the positions of intermolecular interactions. Differences between HS and LS can be seen in the fingerprints.

At 300 K, the shape of fingerprints for Fe1 and Fe2 are similar and there are no short H---H contacts below 2.2 Å (Figure III.53a). The ratio of the selected S---H and Br---H contacts are similar in Fe1 and Fe2, due to the short distances of 2.750 Å (S2---H17), 2.888 Å (S3---H22), and 2.909 Å (Br2---H13). The almost equal ratio of S---Br corresponds to short distances of 3.724 Å (Br1---S4), 3.631 Å (S1---Br4), 3.562 Å (S1---Br3), and 3.553 Å (S3---Br2). Another short atom-atom contact includes S3---S3 (3.486 Å) that can be evidenced in the Hirshfeld surface (Figure III.52a). There is no π---π interaction which is an uncommon feature for PM-L family.<sup>22,45</sup>

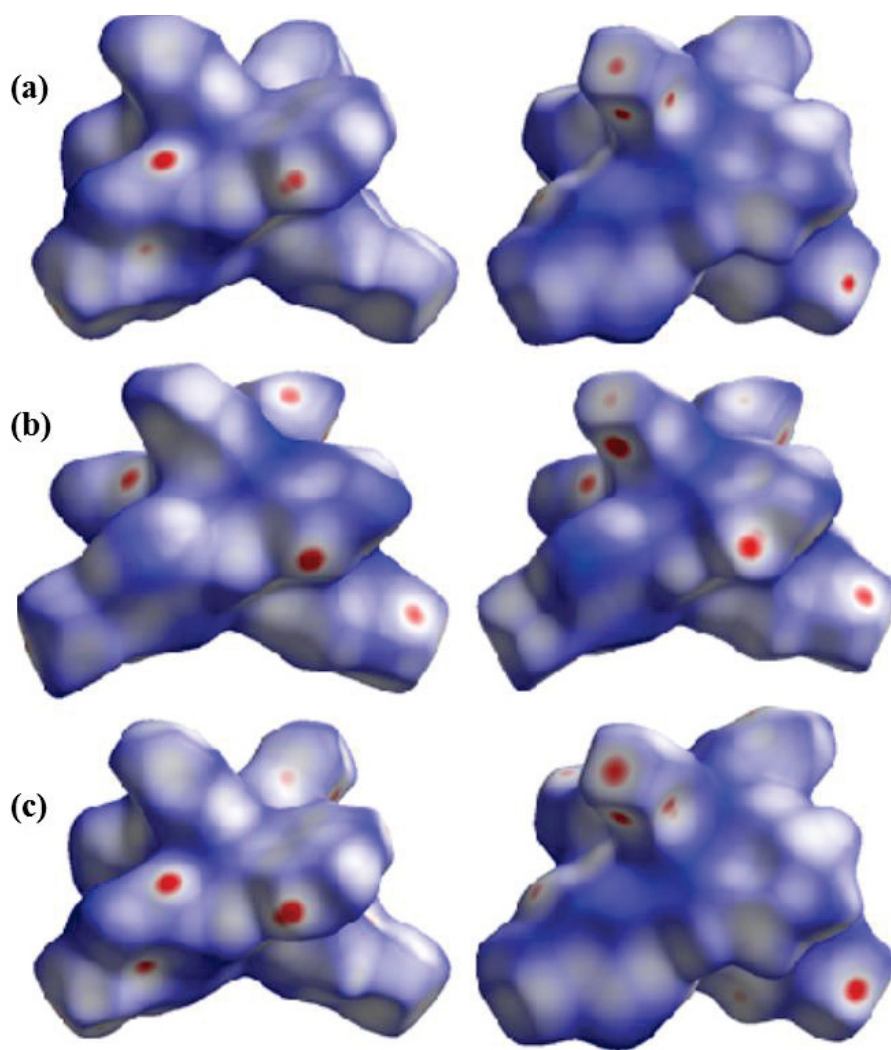


Figure III.52. The Hirshfeld surface at 300 K (a), 90 K (b) and quenched 10 K (c) of polymorph III- $\rho$ BrA.

In the fingerprint at 90 K (Figure III.53b), the shapes around Fe1 and Fe2 seem similar. The ratio of Br---H increases owing to short contacts of Br2---H51 (2.868 Å) and Br4---H25 (2.823 Å). The ratio of S---Br increases a little owing to the short distances of S---Br, including 3.459 Å (Br1---S4), 3.521 Å (S2---Br4), 3.454 Å (S1---Br3), and 3.488 Å (S3---Br2). The S3---S3 contact increases to 3.505 Å. For the thermally quenched Q-HS\* at 10 K (Figure III.53c), the shape of the fingerprints is very similar to that at 300 K and the ratio of selected interactions decrease a little. The S3---S3 contact is 3.340 Å.

Part III – Promoting Distortion of the Coordination Polyhedron Using Polymorphism:  
Bromine Substitution of PM-zBrA Family

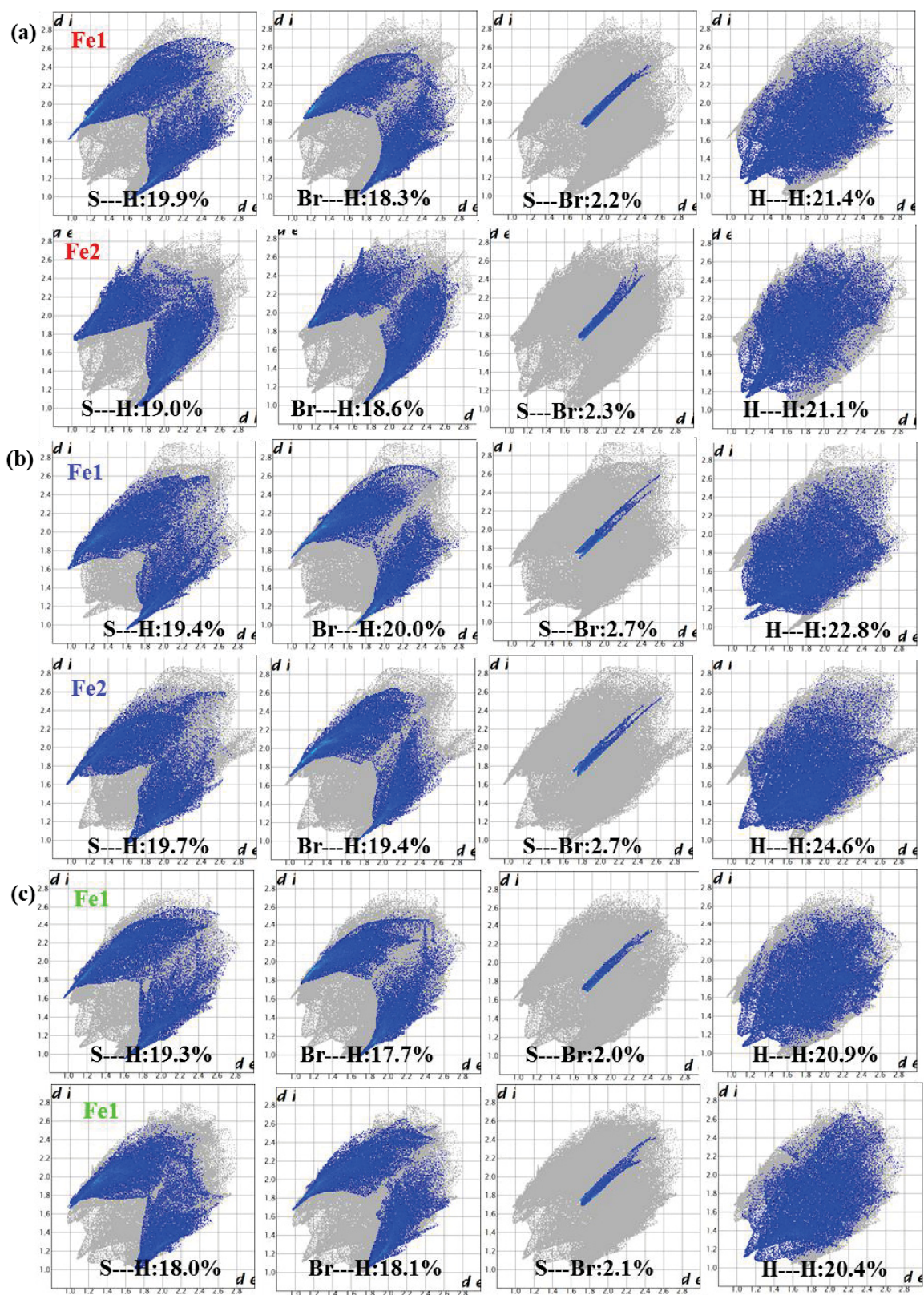


Figure III.53. Selected contacts in fingerprints at 300 K (a), 90 K (b) and 10 K Q-HS\* (c) of III-pBrA.

*Part III – Promoting Distortion of the Coordination Polyhedron Using Polymorphism:  
Bromine Substitution of PM-zBrA Family*

All these interactions drive the packing of the molecules. At 300 K, Fe1 and Fe2 molecules are connected alternately by S---Br and Br4---H25 bondings along [101] direction (Figure III.54a). This constitutes a major difference with **I-pBrA**: in **I-pBrA**, Fe1 sites (or Fe2 sites) are connected together along the *b* axis within Fe1---Fe1 (or Fe2---Fe2) zig-zag chains; in **III-pBrA** Fe1 sites are connected to Fe2 sites along [101] within zig-zag chains. Within these chains, the Fe1---Fe2 distances are 11.146 Å and 11.109 Å with a Fe2-Fe1-Fe2 angle of 141.32°. Along the *a* axis, the Fe1 molecules are linked by S2---H17 and molecules texture a layer at *ac* plane (Figure III.54c). The adjacent Fe1 and Fe2 link by S---Br and S3---H22 interactions. So the crystal packing can be viewed as layers packing along the *b* direction. It is noticed that the adjacent chains connected by S3---S3 forms a ribbon (Figure III.54b), which is also very different from the 2D network in **I-pBrA**. Due to the {Fe1Fe2} chain in **III-pBrA** and the same orientation of S3---S3 contacts, the 2D network of molecules constructed by S3---S3 and S---Br contacts is absent in **III-pBrA**. Actually, it is related to the symmetry breaking from **I-pBrA** to **III-pBrA**, where the two-fold axis is losing. The nearest Fe---Fe distance is 8.198 Å. The crystal packing of **III-pBrA** appears therefore completely different from **I-pBrA** and **II-pBrA**.

At 90 K, Fe1 and Fe2 are still connected alternately by S---Br and Br---H bondings along the [10-1] direction (Figure III.55a), where the distances between Fe1 and Fe2 are 10.573 Å and 10.885 Å with the Fe2-Fe1-Fe2 angle of 155.44°. Four adjacent molecules are connected by S1---H35 (2.678Å) and S3---H9 (2.688Å) with inversion symmetry. The 1D ribbon built by two zig-zag chains interconnected by S3---S3 contact (3.504Å) (Figure III.55b) is similar to that at 300 K. This is quite different from **I-pBrA**, where the huge modifications of S---S and  $\pi$ --- $\pi$  contacts at SCO lead to the expansion of sublattice of Fe2. The crystal packing remains the same at 90 K in **III-pBrA**, owing to the absence of the huge modifications of interactions (Figure III.55d). The nearest Fe---Fe distance slightly decreases to 7.871 Å.

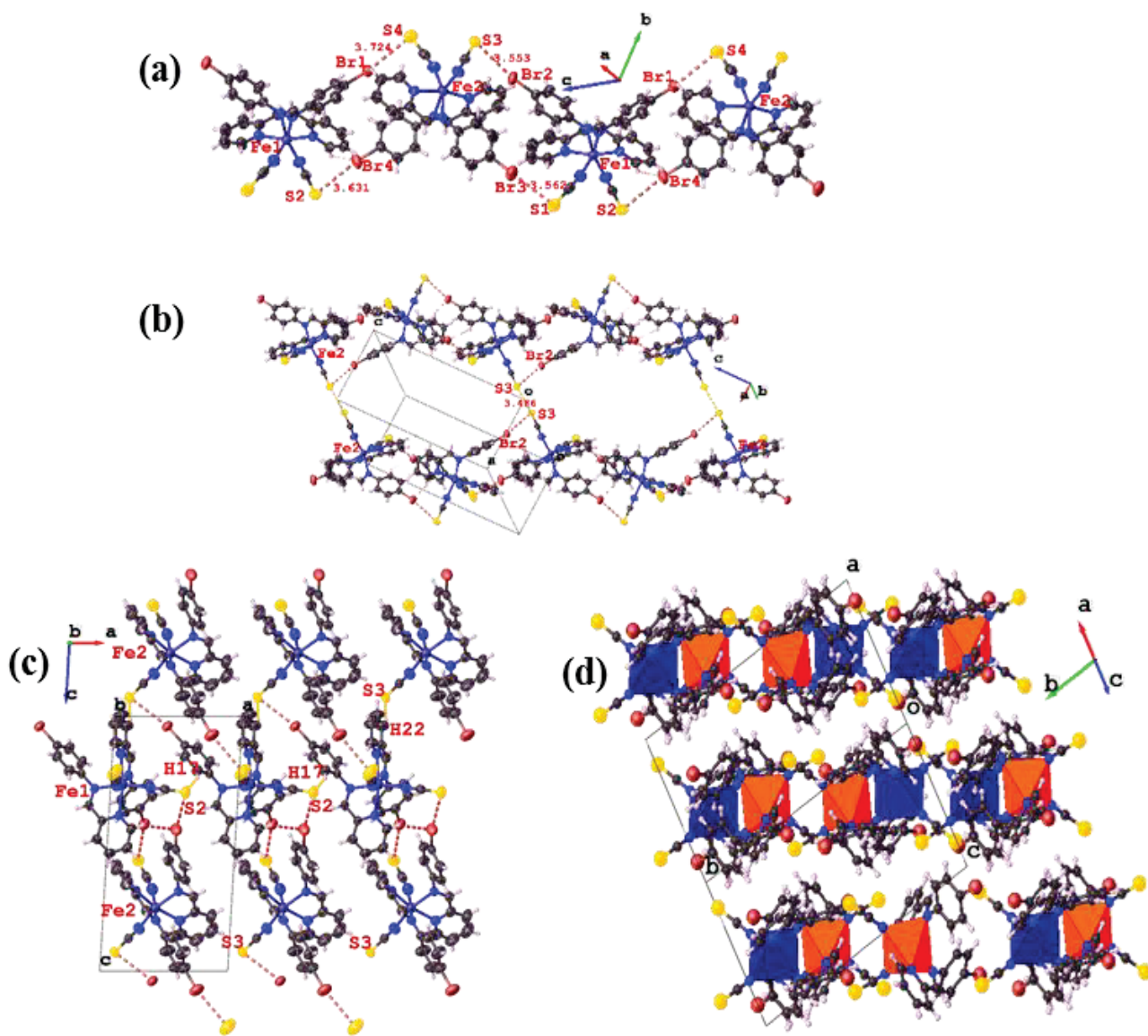
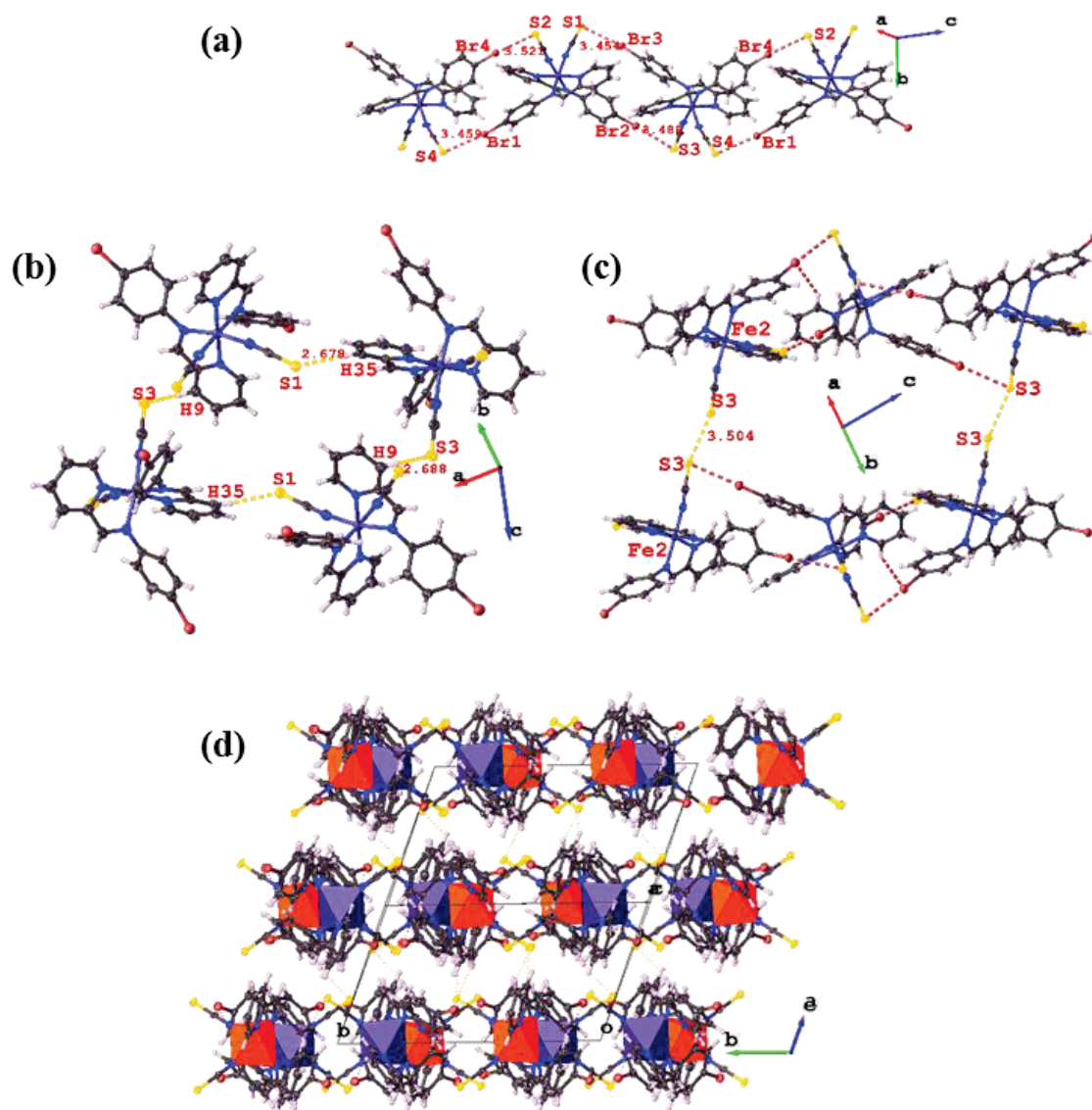


Figure III.54. The Fe1---Fe2 chain linked by S---Br (a), and 1D ribbon with two chains interconnected by S3---S3 (b), the 2D layer (c), molecular packing (d) of polymorph III-*p*BrA at 300 K. The red and blue polyhedra stand for Fe1 and Fe2, respectively.



**Figure III.55.** The chain of Fe1 and Fe2 linked by S---Br (a), the hydrogen bonding between Fe1 and Fe2 (b), 1D ribbon with two chains interconnected by S3---S3 (c), and molecular packing (d) of polymorph **III-pBrA** at 90 K. The red and blue polyhedra stand for Fe1 and Fe2 respectively.

For the quenched structure at 10 K, the crystal packing is similar to the one at 300 K (**Figure III.56**). The  $\{\text{Fe1Fe2}\}_\infty$  zig-zag chains are similar to that at 300 K with the same direction. Within the chains, the Fe1---Fe2 distances are 10.931 Å and 11.012 Å with Fe2-Fe1-Fe2 angle of 140.859°. The layer and ribbon are also similar to that at 300 K. So, the molecular packing is very similar between the thermally quenched at 10 K and 300 K. The single-crystal density at 10 K is larger than 300 K due to the thermal contraction.

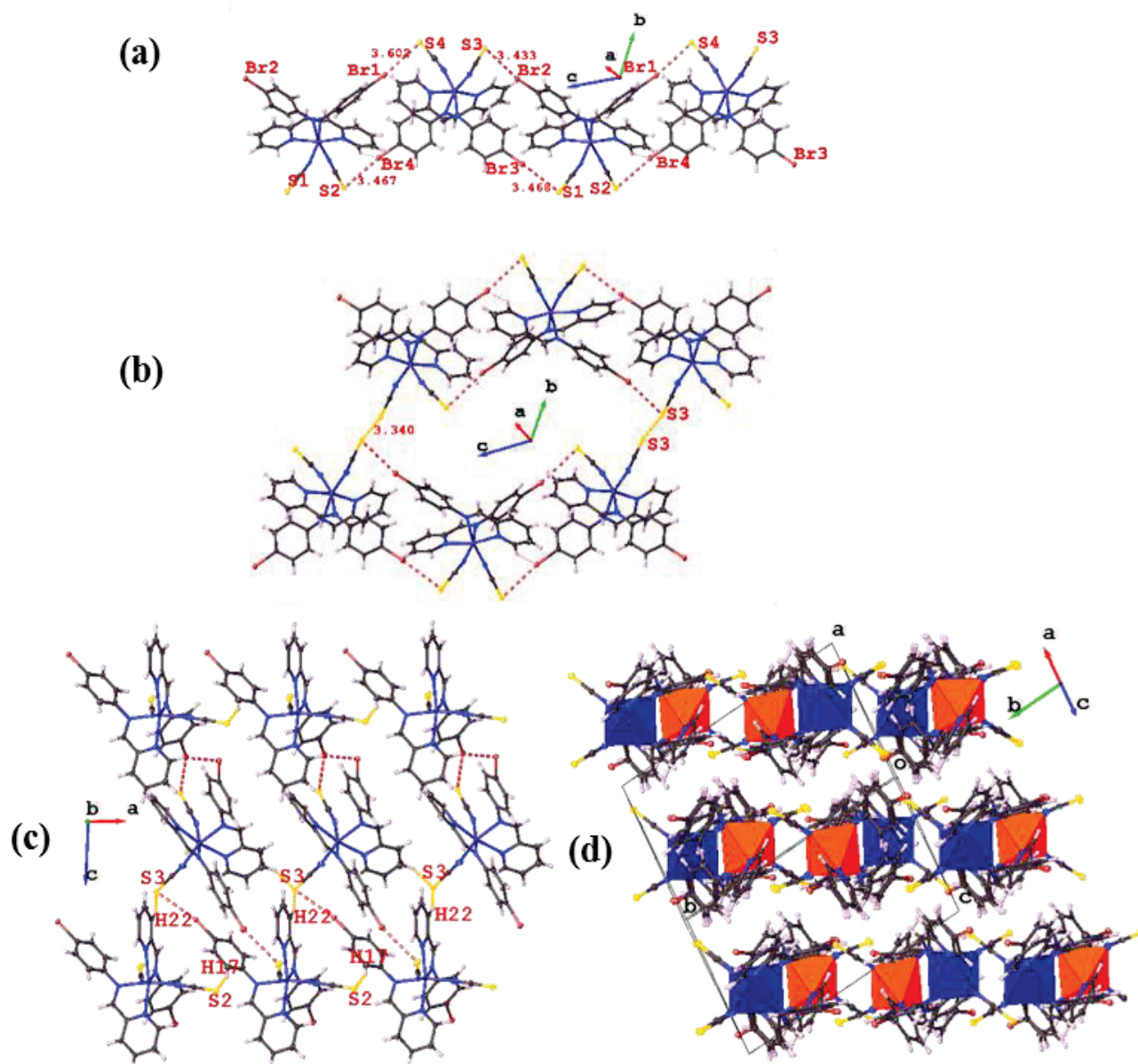


Figure III.56. The chain of Fe1 and Fe2 linked by S---Br (a), 1D ribbon with two chains interconnected by S3---S3 (b), the hydrogen bonding between Fe1 and Fe2 (c), molecular packing (d) of polymorph **III-pBrA** at the thermally quenched 10 K. The red and blue polyhedra stand for Fe1 and Fe2 respectively.

- *Unit-cell parameters as a function of temperature of III-pBrA*

In order to determine the SCO temperature more accurately we followed the thermal evolution of the unit-cell parameters with the idea of looking at the unit-cell volume variation to check whether it behaves similarly to polymorph **I-pBrA**, or not. As seen in Figure III.57, when cooling from 250 K to 180 K, the value of  $a$ ,  $\beta$  and  $\gamma$  increases by 0.5Å, 1.1° and 2.5° while  $c$ ,  $b$  and  $\alpha$  decreases by 0.45 Å, 0.35 Å and 3.2°. According to the Figure III.57, there is

Part III – Promoting Distortion of the Coordination Polyhedron Using Polymorphism:  
Bromine Substitution of PM-zBrA Family

no signal of two-stepped SCO. The unit-cell parameters evolve abruptly around 200 K with a hysteresis. The transition temperatures of SCO are  $T_{1/2\downarrow} = 198$  K and  $T_{1/2\uparrow} = 205$  K, which means a hysteresis width of 7 K in polymorph **III-pBrA**. This polymorph exhibits a similar thermal behavior than polymorph **I-pBrA** but at higher temperature ( $T_{1/2} = 170$  K for **I-pBrA**).

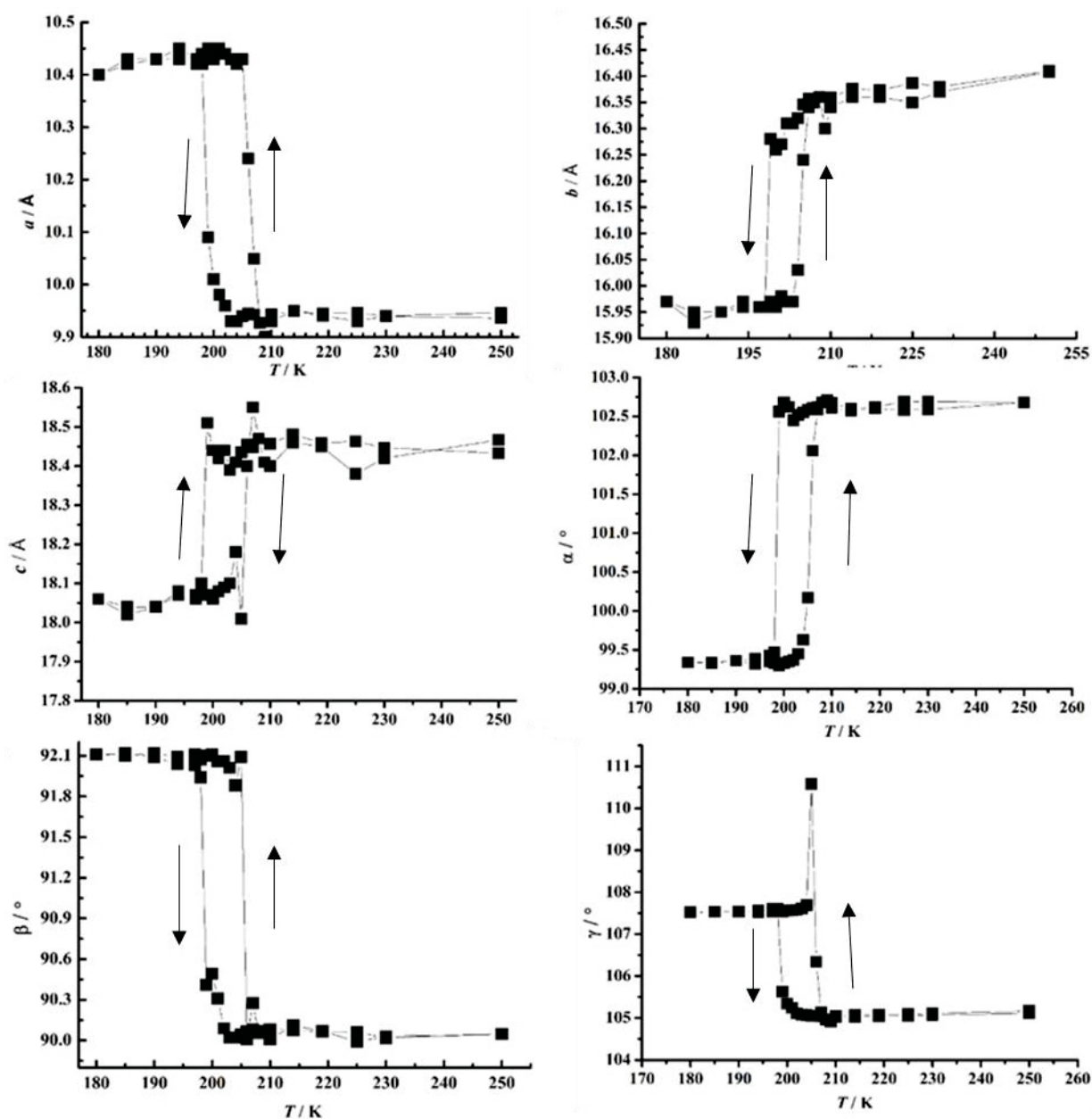
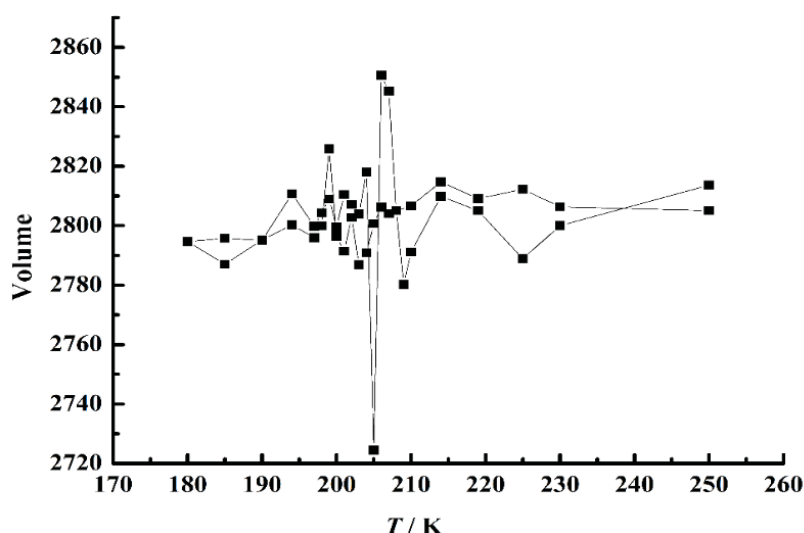


Figure III.57. Temperature dependence of the unit-cell parameters in polymorph **III-pBrA**, determined by SCXRD. The down (up) arrow means the cooling (warming) mode.

Despite the strongly anisotropic unit-cell modifications, the unusual negative expansion of unit-cell volume observed in **I-pBrA** at the SCO is not present in **III-pBrA**. As shown in [Figure III.58](#), the unit-cell volume of **III-pBrA** seems constant in cooling and warming mode, except for three peaks at 205 K, 207 K and 209 K during the SCO process. These three peaks at 205 K, 207 K and 209 K appear because these temperatures are in the range of SCO with a mixture of HS and LS structure, which leads to the unit-cell determination less precise. This behavior suggest the zero thermal expansion of unit-cell volume. This feature is also new in molecular SCO complexes. The anisotropy of the unit-cell modifications at SCO is very common but, to the best of our knowledge, it is the first time it results in a zero modification of the unit-cell volume. Thus, **I-pBrA** with the reverse volume expansion and **III-pBrA** with the zero expansion make a strong contribution of this compound to new opportunities of the SCO phenomenon in term of unit-cell volume changes.



**Figure III.58.** Temperature dependence of the unit-cell volume in polymorph **III-pBrA**, determined by SCXRD.

The value of  $T(\text{TIESST})$  was determined by following the unit-cell parameters from 10 K in the Q-HS\* to 72 K. According to the changes of the unit-cell parameters ([Table III.17](#)), the thermally quenched Q-HS\* is still observed at 70 K while the LS state is recovered at 72 K. Therefore, the Q-HS\* to LS relaxation temperature  $T(\text{TIESST})$  for polymorph **III-pBrA** is therefore around 70 K. This LS state obtained at 72 K can be cooled down again to 10 K, giving access to the LS unit-cell parameters, showing the reversibility and reproducibility of the

process. Note that the unit-cell parameters at 70 K is not precise because of the damage of crystal during increasing temperature from 10 K to 70 K.

**Table III.17.** Unit-cell parameters at various temperatures after thermal quenching in polymorph **III-pBrA**.

Temperature	$a / \text{Å}$	$b / \text{Å}$	$c / \text{Å}$	$V / \text{Å}^3$	Spin state
quench 10K	9.926(12)	16.134(18)	18.307(10)	2761(5)	Q-HS*
<b>increase to 70K</b>	<b>10.01(2)</b>	<b>16.22(3)</b>	<b>18.30(3)</b>	<b>2782(9)</b>	<b>Q-HS*</b>
quench 72K	10.394(16)	15.86(2)	17.80(2)	2760(7)	LS
relax 10 K	10.410(18)	15.79(4)	17.78(3)	2744(9)	LS

- *Structure-properties relationship of III-pBrA*

Compared to polymorph **I-pBrA**, the  $T(\text{TIESST})$  is much lower in polymorph **III-pBrA**. This might first come from the higher  $T_{1/2}$  temperature for polymorph **III-pBrA** that is expected to decrease the relaxation temperature  $T(\text{LIESST})$  (or  $T(\text{TIESST})$ ). Another explanation could be the lower values of  $\Delta\theta$ ,  $95^\circ/98^\circ$  in polymorph **III-pBrA** instead of  $97/123^\circ$  in polymorph **I-pBrA**, while the  $\Delta\zeta$  values are very similar ( $0.284/0.362 \text{ Å}$  in polymorph **III-pBrA**, against  $0.284/0.354$  in polymorph **I-pBrA**). According to [Figure III.38](#), the expected  $T(\text{LIESST})$  value for such  $\Delta\theta$  is around 70 K, which corresponds to the observed value of  $T(\text{TIESST})$ . Let us notice that these  $\Delta\theta$  in polymorph **III-pBrA** are similar to the ones in **II-pBrA**. It highlights again the surprising absence of  $T(\text{LIESST})$  in polymorph **II-pBrA**. Again, the explanation might come from the fact that the sole  $\Delta\theta$  is not enough to correlate with the lifetime of the metastable state. Indeed, in polymorph **II-pBrA**,  $\Delta\zeta$  are lower ( $0.278 \text{ Å} / 0.268 \text{ Å}$ ) than in polymorphs **I-pBrA** and **III-pBrA**. Regarding the position of polymorph **III-pBrA** on the  $T(\text{LIESST})$  vs  $T_{1/2}$  database<sup>17,36</sup>, it's lying on the  $T_0 = 120 \text{ K}$  (against  $150 \text{ K}$  for polymorph **I-pBrA**), close to polymorph **I-BiA** of the same family.

#### III.4.4. Polymorph $[\text{Fe}(\text{PM-pBrA})_2(\text{NCS})_2]$ -IV: IV-pBrA

- *Magnetic properties of IV-pBrA*

[Figure III.59a](#) reports the thermal behavior of the  $\chi_{MT}$  product of polymorph **IV-pBrA**. The  $\chi_{MT}$  value at 300 K of  $3.82 \text{ cm}^3 \text{ K mol}^{-1}$  agrees well with HS  $\text{Fe}^{2+}$  ion ( $g = 2.30$ ). Upon cooling, the  $\chi_{MT}$  product increases gradually till 15 K and then decreases to reach  $4.59 \text{ cm}^3 \text{ K mol}^{-1}$  at 10 K with a maximum  $\chi_{MT}$  of  $4.90 \text{ cm}^3 \text{ K mol}^{-1}$ . There is no SCO and the complex is fully HS

at all temperature range. Figure III.59b shows the  $1/\chi_M$  vs  $T$ . Above 100 K, the curve obeys the Curie-Weiss law very well and the Weiss temperature is around 19 K, suggesting the ferromagnetic-like interactions.

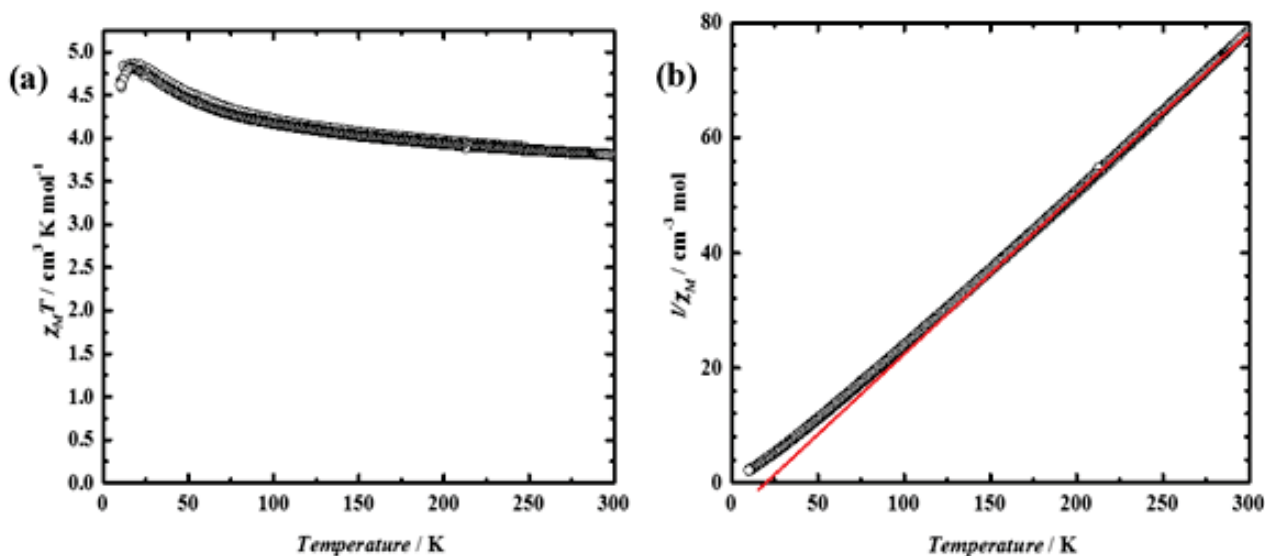


Figure III.59. Thermal dependence of the  $\chi_M T$  product of polymorph **IV-pBrA** (a) and the positive Weiss temperature in  $1/\chi_M$  vs  $T$  (b), recorded at 1 K/min under an applied magnetic field of 5 kOe.

- *Structure of polymorph IV-pBrA*

SCXRD data were recorded and crystal structures were solved at 300 K and 85 K. Since polymorph **IV-pBrA** does not exhibit SCO, the evolution of the unit-cell parameters as function of temperature was not measured.

As seen in Table III.18, polymorph **IV-pBrA** crystallizes in the same space group as polymorphs **I-pBrA** and **III-pBrA**,  $P2_1/n$ , at both 300 K and 85 K. Contrarily to the other polymorphs described before, however, there is only one  $\text{Fe}^{2+}$  site in the asymmetric unit (Figure III.60) with all atoms sitting on the general Wyckoff position (4e). The unit-cell parameters and volume appear thus quite different from other polymorphs. The average Fe-N bond lengths ( $\langle \text{Fe-N} \rangle$ ) are 2.174(6) Å and 2.168(7) Å at 300 K and 85 K, respectively, which are typical values for HS  $\text{Fe}^{2+}$ , agreeing with the absence of SCO. The Fe-N-CS angles are 156.25° and 155.33° at 300 K, suggesting an important bending of  $\text{NCS}^-$  groups. As already mentioned (Part. III.3.4), the bending of the  $\text{NCS}^-$  groups (lower than 152°) tend to favor the HS.<sup>14</sup> We are here at this limit. By the overlay of molecules at 300 K and 85 K, there is almost no difference with RMSD of 0.051 Å.

**Table III.18.** Crystal data and structure refinement data for polymorph **IV-pBrA**.

Empirical formula	C <sub>26</sub> H <sub>18</sub> Br <sub>2</sub> FeN <sub>6</sub> S <sub>2</sub>	
Formula weight / g mol <sup>-1</sup>	694.25	
Temperature / K	300	85
Radiation MoK $\alpha$ / Å	$\lambda = 0.71073$	
Crystal size / mm <sup>3</sup>	0.24 × 0.2 × 0.16	
Crystal system	monoclinic	
Space group	P2 <sub>1</sub> /n	
<i>a</i> / Å	9.83160(1)	9.7221(4)
<i>b</i> / Å	13.4637(2)	13.1922(6)
<i>c</i> / Å	21.5638(3)	21.4557(9)
$\alpha$ / °	90	90
$\beta$ / °	100.7442(8)	100.4530(10)
$\gamma$ / °	90	90
Volume / Å <sup>3</sup>	2804.35(6)	2706.2(2)
Z-formula	4	4
$\rho_{\text{calc}}$ / g cm <sup>-3</sup>	1.644	1.704
$\mu$ / mm <sup>-1</sup>	3.563	3.693
F(000)	1376.0	1376.0
2 $\theta$ range for data collection / °	6.052 - 54.994	3.642 - 55.072
Index ranges	-12 ≤ <i>h</i> ≤ 12, -17 ≤ <i>k</i> ≤ 17, -28 ≤ <i>l</i> ≤ 28	-10 ≤ <i>h</i> ≤ 12, -17 ≤ <i>k</i> ≤ 17, -27 ≤ <i>l</i> ≤ 27
Reflections collected	161654	43535
Independent reflections	6429 [R <sub>int</sub> = 0.0363, R <sub>sigma</sub> = 0.0139]	6247 [R <sub>int</sub> = 0.0255, R <sub>sigma</sub> = 0.0141]
Data/restraints/parameters	6429/0/334	6247/0/334
Goodness-of-fit on F <sup>2</sup>	1.149	1.043
Final R indexes [I ≥ 2 $\sigma$ (I)]	R <sub>1</sub> = 0.0448, wR <sub>2</sub> = 0.0908	R <sub>1</sub> = 0.0178, wR <sub>2</sub> = 0.0413
Final R indexes [all data]	R <sub>1</sub> = 0.0726, wR <sub>2</sub> = 0.1079	R <sub>1</sub> = 0.0205, wR <sub>2</sub> = 0.0424
Largest diff. peak/hole / e Å <sup>-3</sup>	0.85/-0.88	0.40/-0.31

$$R_1 = \frac{\sum ||F_0| - |F_C||}{\sum |F_0|}, wR_2 = \left[ \frac{\sum w(F_0^2 - F_C^2)^2}{\sum w(F_0^2)^2} \right]^{1/2}$$

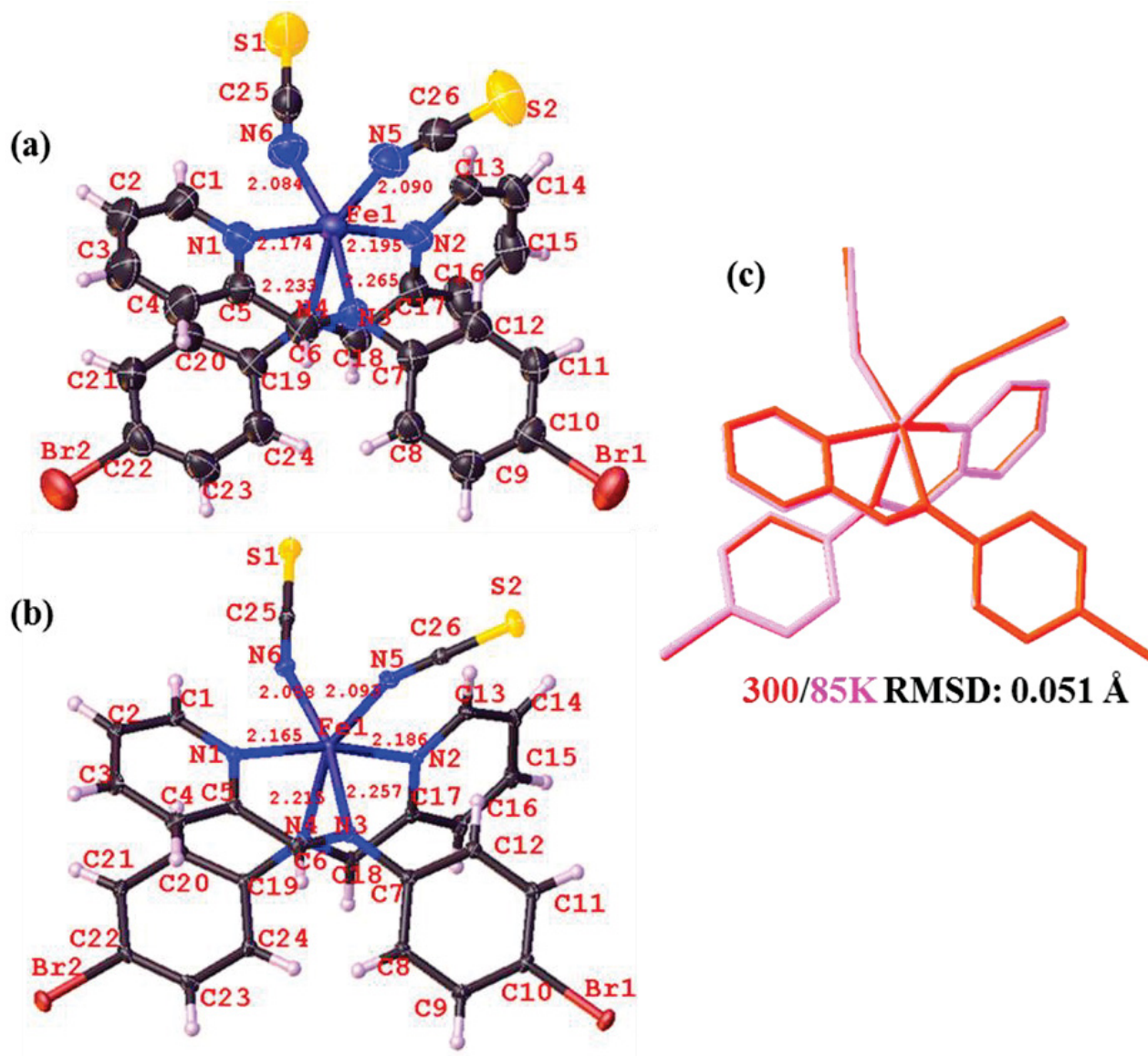


Figure III.60. The molecule in the asymmetric unit at 300 K (a), 85 K (b) and the molecular overlay between two temperatures (c) of polymorph IV-*p*BrA.

The ligand conformation in polymorph IV-*p*BrA is similar to Fe2 in polymorphs I-*p*BrA and III-*p*BrA with a difference  $\delta\sigma_3$  of  $38^\circ$  between the two ligands that remains constant upon cooling demonstrating the absence of ligand rotation. By the superposition of Fe site in polymorph IV-*p*BrA and Fe2 in polymorphs I-*p*BrA or III-*p*BrA (Figure III.61), the main difference results from the bending and orientation of NCS<sup>-</sup> groups. Another difference is the motion of pyridine ligand.

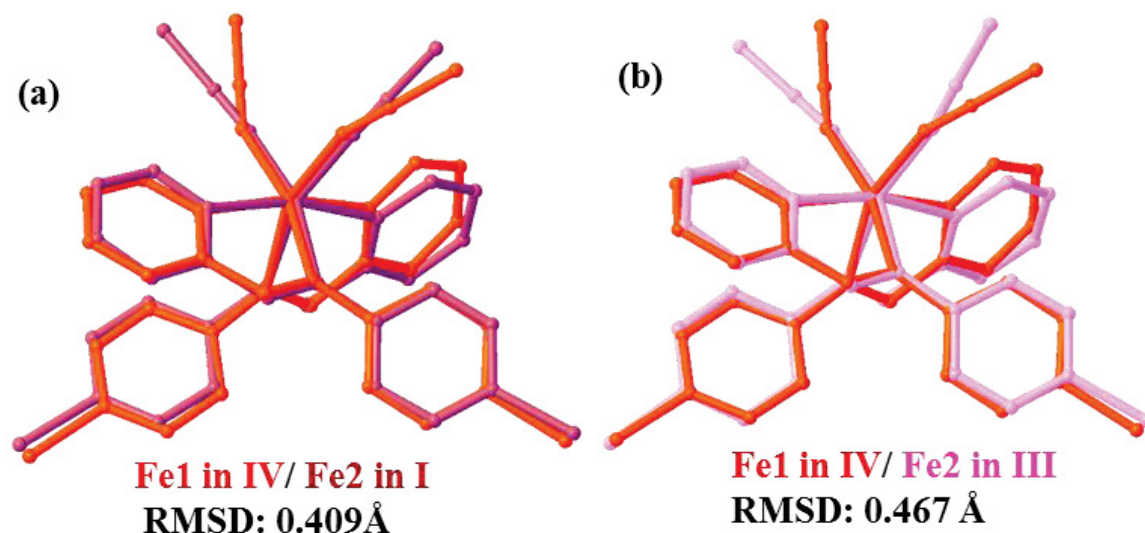


Figure III.61. The molecular overlay between polymorphs IV-*p*BrA and I-*p*BrA (a), and between polymorphs IV-*p*BrA and III-*p*BrA (b).

As shown in Table III.19, the bond distortion ( $\zeta$ ), angular distortion ( $\Sigma$ ), trigonal distortion angles ( $\theta$ ) and shape values in Fe1N<sub>6</sub> at 300 K and 85 K are very similar due to the same spin state and ligand conformation. It is noticed that the value of  $\theta$  in FeN<sub>6</sub> (288.9°) is larger than that in Fe2N<sub>6</sub> of polymorphs I-*p*BrA and III-*p*BrA, which indicates a strongly distorted coordination sphere in polymorph IV-*p*BrA again in favor of the HS state stabilization. This strong distortion in polymorph IV-*p*BrA mainly results from the bending of NCS<sup>-</sup> groups.

Table III.19. The coordination sphere parameters in polymorph IV-*p*BrA.

Compound	IV- <i>p</i> BrA	
Temperature / K	300	85
Fe <sup>2+</sup> site	Fe1	Fe1
<Fe-N> / Å	2.174(7)	2.168(6)
$\zeta$ / Å	0.346	0.311
$\Sigma$ / °	88.65	88.61
$\theta$ / °	288.95	291.35
Shape <sup>b</sup>	1.979	1.981
SC-N-Fe / °	156.25 / 155.33	154.56 / 153.65
(SC)N-Fe-N(CS) / °	97.09	96.59
$\sigma_1$ / °	79.73	79.61
$\sigma_2$ / °	166.89	167.08
$\sigma_3$ / °	71.10 / 33.10	71.12 / 32.2.

$\sigma_1$ :N-Fe-N with N from imine;  $\sigma_2$ :N-Fe-N with N from pyridine;  $\sigma_3$ ,dihedral angle of phenyl and pyridine in one ligand. <sup>a</sup> values obtained using the OctaDist program (<https://octadist.github.io>). <sup>b</sup> values obtained using the SHAPE program (ref 6).

Figure III.62 shows the fingerprints and Hirshfeld surfaces. There are no differences in the fingerprint shapes at 300 K and 85 K. (Figures III.62c and d). An important contribution to the intermolecular interactions comes from hydrogen bonding of S---H (S2---H6, 3.043 Å) and Br---H (S1---H4, 3.089 Å). Other interactions include the S2---Br2 (3.730 Å), H21-H4 (2.314 Å) and H14--- $\pi_{\text{phenyl}}$  (2.868 Å). The ratio of the selected S---H, Br---H, S---Br and H---H contacts are nearly the same, meaning weaker modification of intermolecular interactions from 300 K to 85 K. There is no short S---S contacts.

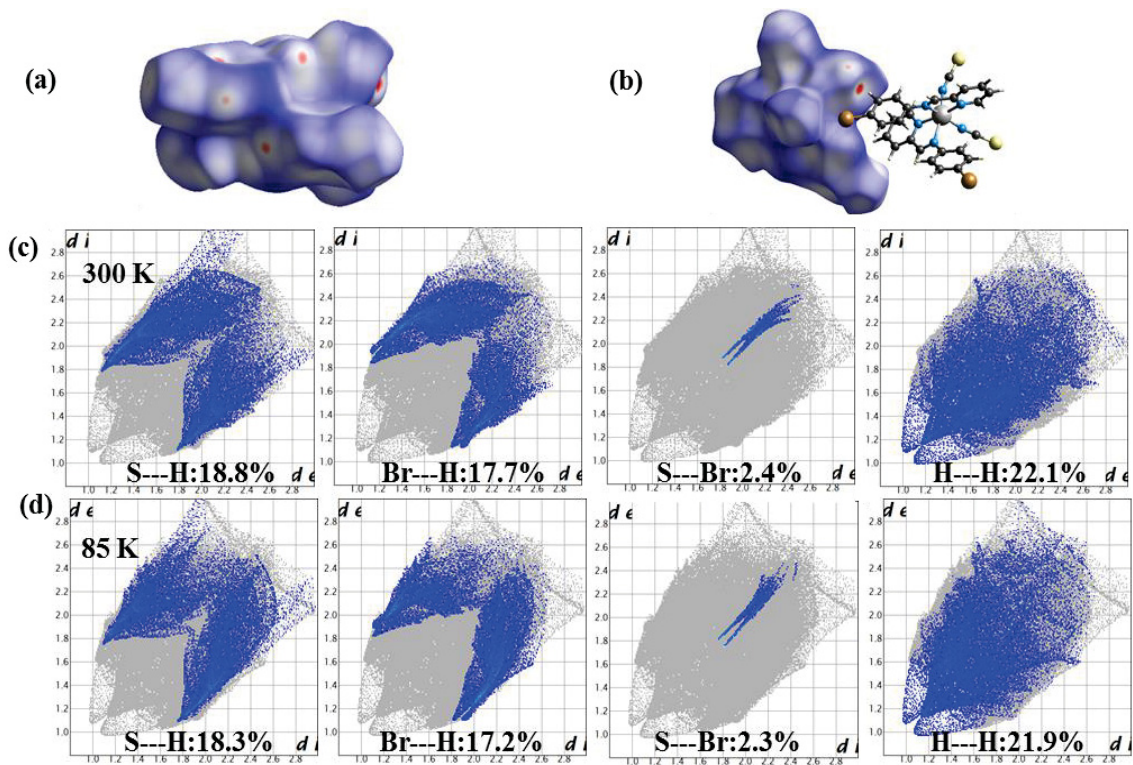


Figure III.62. The Hirshfeld surface at 300 K (a), 85 K (b), and the selected contacts in fingerprints at 300 K (c), 85 K (d) of polymorph IV-*p*BrA.

Figure III.63 shows the intermolecular interactions around Fe1. Along *b* direction, adjacent molecules are linked by S2---H6 bonding with  $2_1$  symmetry (Figure III.63a). The S2---Br2 and H21---H4 connect molecules along [101] direction. The shortest Fe---Fe distance is 7.757 Å, where the intermolecular interaction is H14--- $\pi_{\text{phenyl}}$  with distance 2.868 Å (Figure III.63b). The 2D packing of molecules at *ab* plane is shown in Figure III.63c, where the next-nearest Fe---Fe distance is 9.463 Å. The crystal packing can be viewed as Fe1 pseudo-layers alternating along *c* axis (Figure III.63d). The packing at 85 K is very similar to 300 K and there is no molecular rearrangement between 300 K and 85 K. So, polymorph IV-*p*BrA shows a high spin state without the variation of ligand conformation.

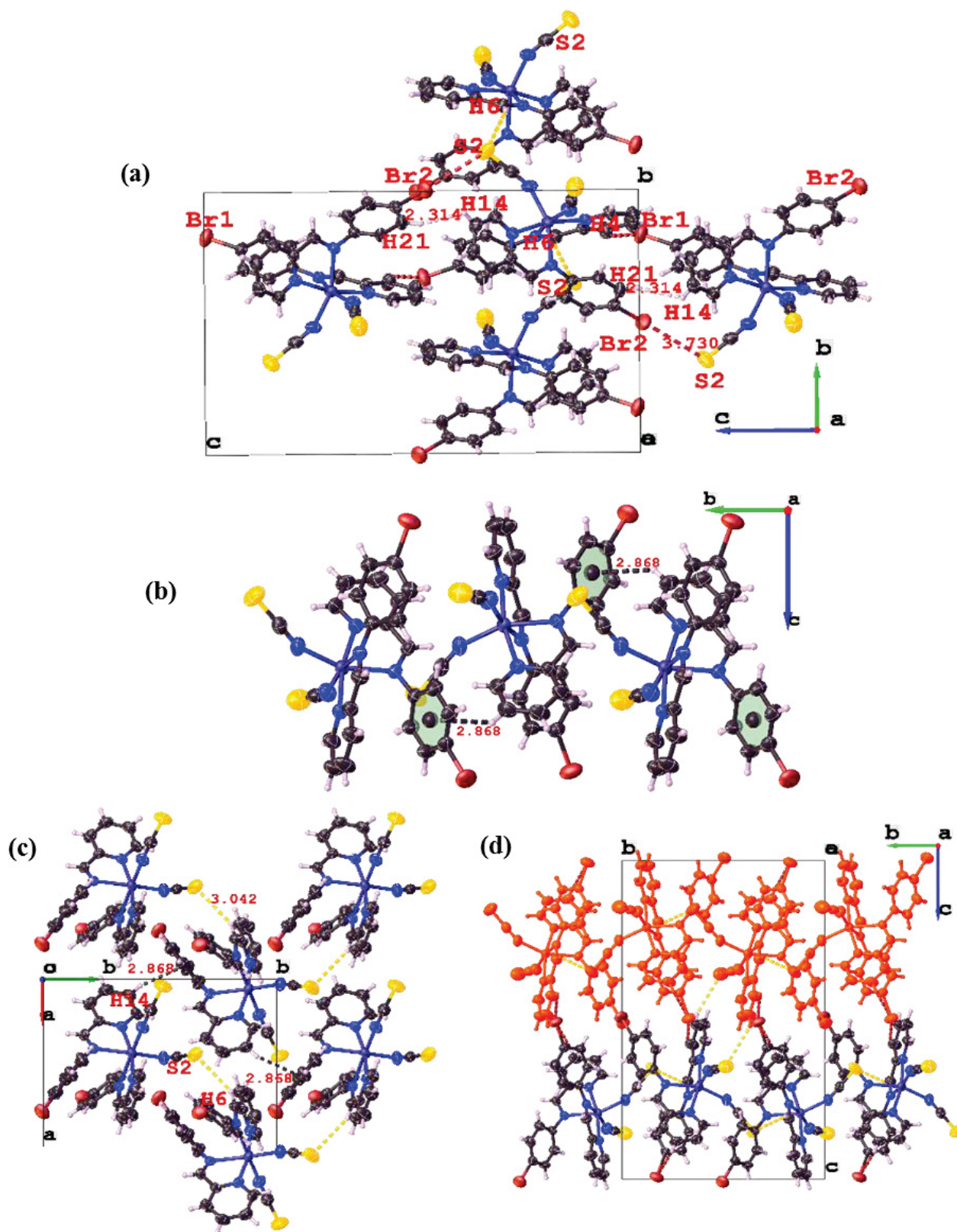


Figure III.63. The interaction around Fe1 at  $bc$  plane (a), the H--- $\pi$  interactions (b), the packing at  $ab$  plane (c), and crystal packing (d) of polymorph IV-*p*BrA at 300 K.

### III.4.5. Discussions on the four *p*BrA polymorphs

Regarding the number of polymorphs and what they allow in terms of comparison and understanding of the role of coordination sphere distortion on the metastable state lifetime, a detailed discussion will be done in Part IV, including all the other synthesized compounds. The discussion here is only focused on the general features of these four polymorphs. These polymorphs crystallize in the same  $P2_1/n$  space group except for polymorph III-*p*BrA in the low symmetry with the space group of  $P-1$ . Polymorphs I-*p*BrA, II-*p*BrA and III-*p*BrA exhibit two independent  $\text{Fe}^{2+}$  sites while polymorph IV-*p*BrA possesses only one  $\text{Fe}^{2+}$  site. From the different overlays IV/I and IV/III (Figure II.61), I/II (Figure II.64) and I/III (Figure II.65) one can clearly see that the Fe1 site is present in I, II and III. Concerning the Fe2 site it is common to all polymorphs (named Fe1 in IV). The RMSD values based on the molecular overlay of for I/II at HS (Fe1: 0.351 Å and Fe2: 0.539 Å) and LS (0.309 Å) is larger than 0.3 Å, indicating some differences in the NCS<sup>-</sup> bending and the ligand conformations (Figure II.64). In the LS state, the RMSD values for I/II become smaller and the small value of 0.191 Å for Fe2 suggests the similar molecular geometry between polymorphs I-*p*BrA and II-*p*BrA.

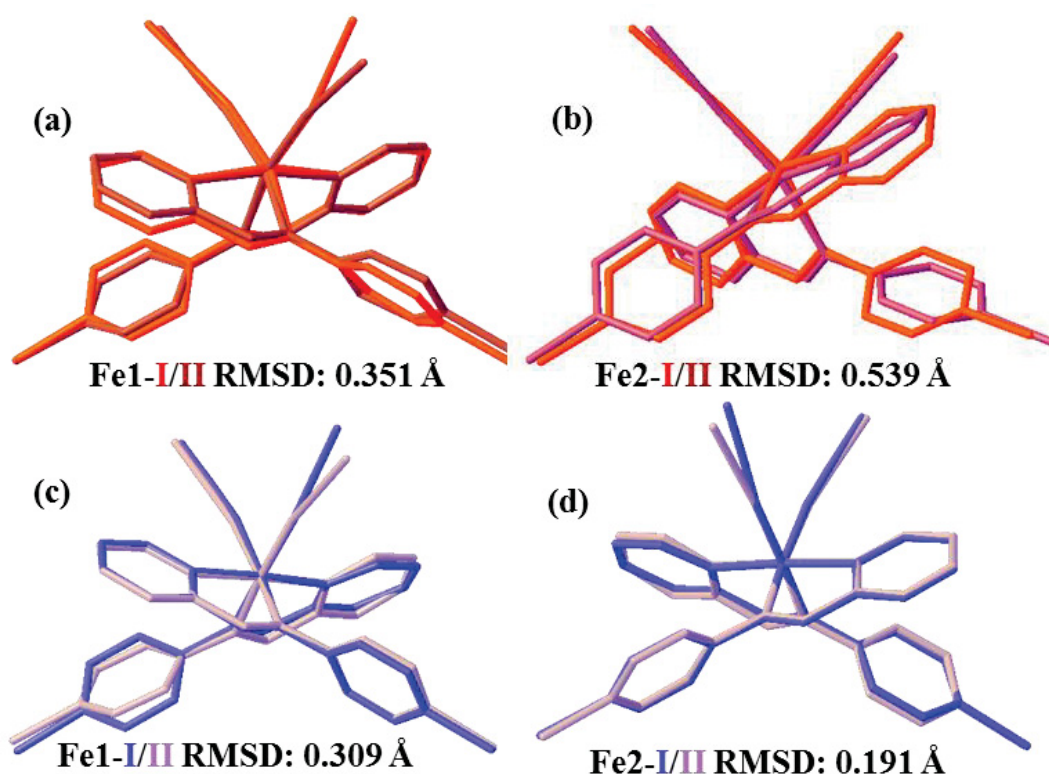
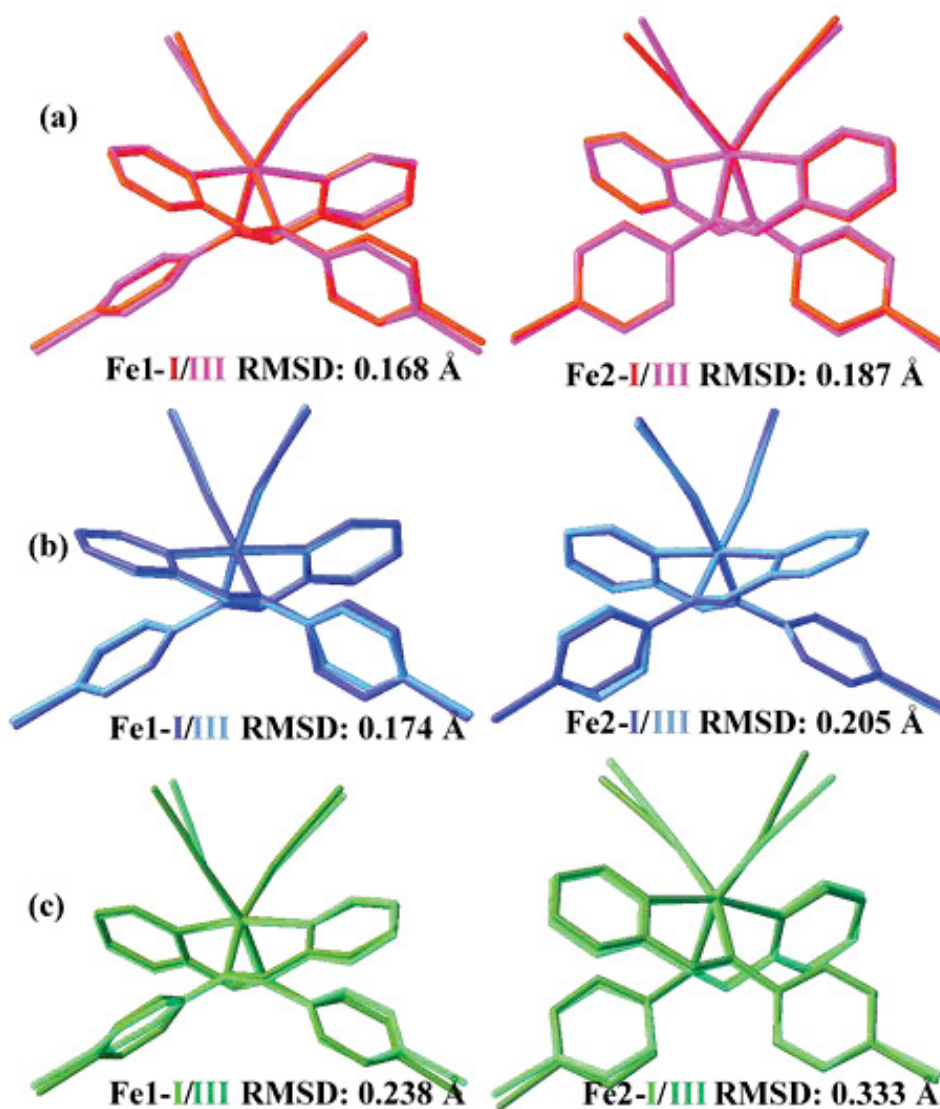


Figure II.64. Molecular overlay between I-*p*BrA and II-*p*BrA at HS of Fe1 (a) and Fe2 (b), and at LS of Fe1 (c) and Fe2 (d) with the RMSD values. One part of the disordered phenyl rings is omitted.

*Part III – Promoting Distortion of the Coordination Polyhedron Using Polymorphism:  
Bromine Substitution of PM-zBrA Family*

The RMSD values based on the molecular overlay of **I/III** in HS and LS states are below 0.21 Å, suggesting very similar complex geometries (**Figure II.65**). However, the high RMSD value of **I/III** in Q-HS\* suggests different molecular geometries at the metastable states, associated to the NCS<sup>-</sup> bending (**Figure II.65c**). This Fe2 site presents two ligands with two different conformations; one with a small dihedral angle  $\sigma_3$  between the pyridine and the bromophenyl rings and another one with a high  $\sigma_3$ . The ligand with the small dihedral angle tends to rotate upon cooling to have a similar geometry as the second ligand that does not rotate. This rotation is abrupt in polymorphs **I-pBrA** and **III-pBrA** but gradual in **II-pBrA** with a source of an order-disorder transition. Moreover, this rotation is concomitant to the occurrence of spin crossover in polymorphs **I-pBrA**, **II-pBrA** and **III-pBrA**.



**Figure II.65.** Molecular overlay between **I-pBrA** and **III-pBrA** at HS of Fe1 and Fe2 (a), at LS of Fe1 and Fe2 (b), and at Q-HS\* of Fe1 and Fe2 (c) with the RMSD values.

Figure III.66a shows the structural overlay of **I-pBrA** (pink) and **II-pBrA** (red) in *bc* plane. According to the superposition of Fe1 molecules, the position of the ligands and the orientation of the NCS<sup>-</sup> groups do not seem to change too much. However, for Fe2 molecules, there are huge differences. The orientation of NCS<sup>-</sup> in Fe1 is similar to Fe2 for **I-pBrA** with two NCS<sup>-</sup> opening towards the *a* direction (Figure III.28b), while the orientation of NCS<sup>-</sup> between Fe1 and Fe2 in **II-pBrA** are more or less perpendicular (Figure III.46d). Since the ligands and NCS<sup>-</sup> are in the *cis* conformation in both polymorphs, the different orientations of NCS<sup>-</sup> in Fe2 between two polymorphs can lead to different ligand orientations. These differences in Fe2 also can be seen clearly by the structural overlay of LS (Figure II.66b). So these two polymorphs show differences not only on the ligand conformation but also in the molecular packing mode.

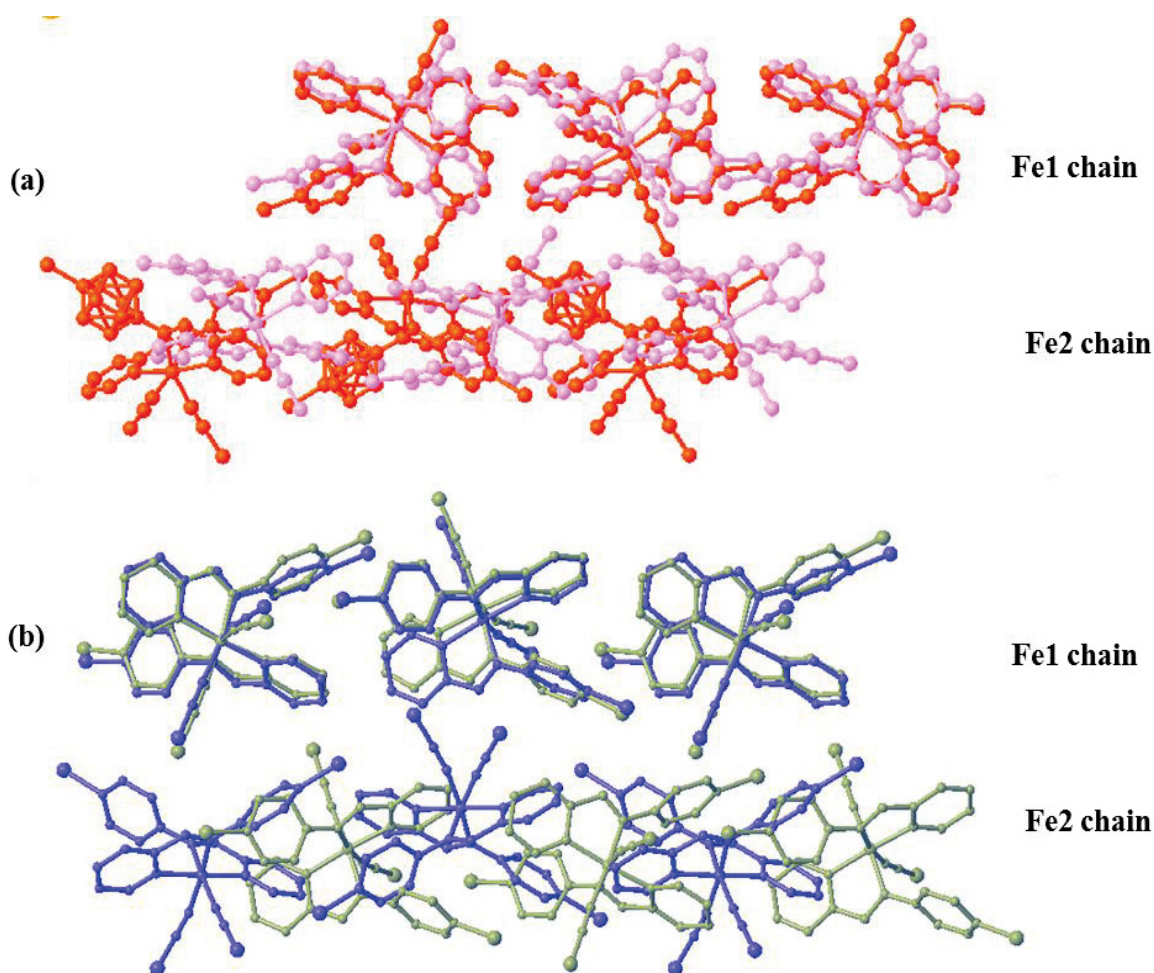


Figure II.66. Structural overlay between **I-pBrA** (pink and blue) and **II-pBrA** (red and green) at HS (a) and LS (b).

Concerning polymorphs **I-pBrA** and **III-pBrA**, their coordination environments are very different. The Fe<sup>2+</sup> molecules are arranged in zig-zag chains. In polymorphs **I-pBrA** and **II-pBrA** two chains are formed by Fe1 and Fe2, separately. In **III-pBrA**, only one chain is formed with alternation of Fe1 and Fe2 motifs. Concerning polymorph **IV-pBrA**, since there is only one Fe<sup>2+</sup> site, chains are formed by the same site, as in polymorphs **I-pBrA** and **II-pBrA**. Hence, **I-pBrA** and **III-pBrA** have the huge difference owing to the different lattice systems with the different space group.

Selected intermolecular interactions in the HS state are shown in **Table II.20**. For the sake of comparison, the structure of polymorphs **I-pBrA**, **III-pBrA** and **IV-pBrA** were used at 300 K and structure at 350 K was used for polymorph **II-pBrA** since it is not fully HS at 300 K. The S---Br bonding exists in four polymorphs. In polymorphs **I-pBrA** and **II-pBrA**, the distances of S---Br between Fe1 is much shorter than that between Fe2. Especially, the S---Br distances between Fe2 in polymorph **I-pBrA** can be as large as 4.221 Å. The interesting point in **I-pBrA** and **II-pBrA** is that the zig-zag chains of molecules linked by S---Br bondings along the b direction have a 2<sub>1</sub> axis. The short S---S contact appears in polymorph **I-pBrA**, and **III-pBrA** while it is absent in other two polymorphs, which may relate to the abrupt SCO. For example, Takahashi *et.al.* suggested the short S---S contacts play a key role in an abrupt spin transition in complex Fe(DPyDT)<sub>2</sub>(NCS)<sub>2</sub>·0.5CH<sub>3</sub>OH (DPyDT = di(2-pyridyl)methylidene-1,3-dithiol-2-ylidene).<sup>46</sup> Notice that, due to the lack of 2<sub>1</sub> axis in polymorph **III-pBrA**, the 2D network constructed by S3---S3 and S---Br in polymorph **I-pBrA** breaks into a 1D ribbon.

**Table II.20.** The shortest contacts between molecules in the HS state of four polymorphs.

Compound s	S---Br / Å	S---H / Å S-C-H / °	Br---H / Å Br-C-H / °	N---H / Å N-C-H / °	S3---S3 / Å	π---π / Å	H—H / Å
<b>I-pBrA</b>	3.444 / 3.677 3.736 / 4.221	2.848 / 148.83 2.904 / 143.57	2.909 / 143.15	3.013 / 148.8	3.441	3.978	2.212
<b>II-pBrA(*)</b>	3.433 / 3.632 3.823 / 3.899	2.499 / 152.28 2.840 / 137.82	2.952 / 141.55 3.023 / 127.09	2.940 / 152.34	4.366	-	1.957
<b>III-pBrA</b>	3.553 / 3.563 3.631 / 3.724	2.750 / 158.29 2.888 / 160.93	3.102 / 137.05	2.957 / 161.91	3.486	-	2.534
<b>IV-pBrA</b>	3.730	3.043 / 139.97 3.100 / 114.67	3.089 / 132.52	2.857 / 125.06 2.931 / 153.33	3.883	-	2.314

\*Data used at 350 K for **II-pBrA** and 300 K for others

*Part III – Promoting Distortion of the Coordination Polyhedron Using Polymorphism:  
Bromine Substitution of PM-zBrA Family*

The S---H bonding in polymorphs **II-pBrA** and **III-pBrA** are shorter than that in **I-pBrA**. The contacts of S---H in polymorph **IV-pBrA** are weakest. This corresponds to the observed result that S-H are important for the SCO occurrence in PM-L family.<sup>22,45</sup> The short H---H contacts occurs in polymorphs **I-pBrA** and **II-pBrA** and the shortest value of 1.957 Å is owing to the disorder of phenyl ring. The inter- and intramolecular H---H contacts play an important role for the rotation of phenyl ring in **I-pBrA**. The weak  $\pi$ --- $\pi$  contact only occurs in polymorph **I-pBrA**. Compared to other compounds in PM-L family<sup>22,45</sup>, the absence of  $\pi$ --- $\pi$  contact may be due to the occurrence of short contact of two phenyl rings forbidden by large atomic radius of Bromine at *para* position. The atom-atom contacts could be associated to the unique properties in polymorph **I-pBrA**, including H---H, S---S and  $\pi$ --- $\pi$ . Especially, the phase transition of phenyl rings in these polymorphs may result from the modification of H---H contacts at SCO.

Therefore, these four polymorphs differ from each other by the way the geometry of their ligands changes upon cooling and by their crystal packings. Additionally, upon spin crossover in **I-pBrA**, **II-pBrA** and **III-pBrA**, the intermolecular interactions change in different ways. These three polymorphs display one step SCO, despite the presence of two strongly different Fe<sup>2+</sup> sites. It's like the SCO of one site forces the second one to switch concomitantly. This has been already reported even if rather rarely<sup>25-26</sup> like in the [Fe(1-bpp)<sub>2</sub>]<sub>x</sub>[Co(terpy)<sub>2</sub>]<sub>1-x</sub>(BF<sub>4</sub>)<sub>2</sub> (1-bpp = 2,6-bis[pyrazol-1-yl]pyridine) solid solutions where the SCO on the iron site drives the SCO on the cobalt site.<sup>47-48</sup> This can be easily understood in compounds with strong cooperative interactions but it's more surprising in poorly cooperative compounds like in polymorph **II-pBrA**.

Polymorphism is very common in crystalline materials<sup>49-50</sup> and SCO materials with polymorphism have been deeply reviewed by Tao *et al.*<sup>51</sup> Since SCO phenomenon is a multiscale phenomenon from the coordination sphere to material, slight variations in one of these scale can change the magnetic properties greatly. Polymorphism provides platforms to compare and contrast the structures at all scales, which can help understanding the true structural-property relationship.

It is common that materials display two or three polymorphs with different magnetic behaviors. For example, two polymorphs have been observed in many compounds including [Fe(phen)<sub>2</sub>(NCS)<sub>2</sub>] (phen = phenanthroline)<sup>52</sup>, [Fe(bt)<sub>2</sub>(NCS)<sub>2</sub>] (bt = 2, 2'-bithiazoline)<sup>53</sup>, [Fe(PM-BiA)<sub>2</sub>(NCS)<sub>2</sub>]<sup>35</sup>, {Fe(abpt)<sub>2</sub>[N(CN)<sub>2</sub>]} (abpt = 4-amino-3,5-bis(pyridin-2-yl)-1,2,4-triazole)<sup>54</sup>, [Fe(abpt)<sub>2</sub>(tcnoet)<sub>2</sub>] (tcnoet = 1,1,3,3-tetracyano-2-ethoxypropenide anion)<sup>55</sup>,

*Part III – Promoting Distortion of the Coordination Polyhedron Using Polymorphism:  
Bromine Substitution of PM-zBrA Family*

[Fe{(pz)<sub>3</sub>CH}<sub>2</sub>](NO<sub>3</sub>)<sub>2</sub> ((pz)<sub>3</sub>CH = tris(pyrazol-1-yl)methane)<sup>56</sup>, {Fe[H<sub>2</sub>B(pz)<sub>2</sub>]<sub>2</sub>(phen)} (H<sub>2</sub>B(pz)<sub>2</sub> = dihydrobis(1-pyrazolyl)borate)<sup>57</sup>, Fe[(*p*-IC<sub>6</sub>H<sub>4</sub>)B(3-Mepz)<sub>3</sub>]<sub>2</sub> (((*p*-IC<sub>6</sub>H<sub>4</sub>)B(3-Mepz)<sub>3</sub> = (*p*-iodophenyl)tris(pyrazolyl)borate)<sup>58</sup>, [Fe(CNPh-bpp)<sub>2</sub>](BF<sub>4</sub>)<sub>2</sub> (4'- (4''-cyanophenyl)-1,2':6',1''-bispyrazolylpyridine)<sup>59</sup>, [Fe(Cl<sub>2</sub>bpp)<sub>2</sub>](BF<sub>4</sub>)<sub>2</sub> (2,6-bis (4-chloropyrazol-1-yl)pyridine)<sup>60</sup>, [Fe((pz)<sub>3</sub>CH)((3,5-Me<sub>2</sub>pz)<sub>3</sub>CH)](BF<sub>4</sub>)<sub>2</sub> (3,5-Me<sub>2</sub>pz = (3,5-dimethylpyrazolyl)methane)<sup>61</sup>, [Fe(Htrz)<sub>2</sub>(trz)](BF<sub>4</sub>) (Htrz = 1,2,4-1*H*-triazole)<sup>62</sup>, [Fe(NCS)<sub>2</sub>(cddt)]·2CH<sub>3</sub>OH (cddt = 2-chloro-4,6-bis(dipyrid-2-ylamino)-1,3,5-triazole)<sup>63</sup>, [Fe(NCS)<sub>2</sub>(bdpp)] (bdpp = 4,6-bis(2',2''-pyridyl)pyrazine)<sup>64</sup>, [Fe(abpt)<sub>2</sub>(NCSe)<sub>2</sub>]<sup>65</sup>, [(TPA)Fe(TCC)]PF<sub>6</sub> (TCC = 3,4,5,6-tetrachlorocatecholate dianion)<sup>66</sup>. Three polymorphs have been observed in some cases including [Fe(bpy)<sub>2</sub>(NCS)<sub>2</sub>] (bpy = 2,2'-bipyridine)<sup>67</sup>, *fac*-[Fe(dppa)<sub>2</sub>(NCS)<sub>2</sub>]<sup>68</sup>, [Fe(sal<sub>2</sub>-trien)][Ni(dmit)<sub>2</sub>] (sal<sub>2</sub>-trien = salicylaldehyde and triethylenetetramine, dmit = 2-thioxo-1,3-dithiole-4,5-dithiolate dianion)<sup>69</sup>, [Fe(PM-PeA)<sub>2</sub>(NCSe)<sub>2</sub>]<sup>70</sup>, [FeL<sub>2</sub>](BF<sub>4</sub>)<sub>2</sub> (L = 4-ethynyl-2,6-bis(pyrazol-1-yl)pyridine)<sup>71</sup>.

SCO materials with four polymorphs were only observed in very few compounds, [Fe(abpt)<sub>2</sub>(NCS)<sub>2</sub>]<sup>72</sup>, [Fe(tpa)(NCS)<sub>2</sub>] (tpa = tris(2-pyridylmethyl)amine)<sup>73</sup>. A long-lived photo-induced metastable state with *T*(LIESST) of 110 K is observed in polymorph D of [Fe(abpt)<sub>2</sub>(NCS)<sub>2</sub>], which is associated with the linkage isomerization between NCS<sup>-</sup> and SCN<sup>-</sup>.<sup>74</sup> Here, the observed polymorphism in PM-zBrA family suggests the flexibility of the ligand.

The variety of intermolecular interactions and the way they are changing along the SCO led to various behaviors of the unit-cell volume along the polymorphs (Figure II.67). A general feature for the spin crossover compounds is that from HS to LS, the volumes of the coordination sphere and of the unit-cell decrease. The unit-cell parameters can evolve anisotropically but, in general at the end, the unit-cell volume decreases. Here, it's the first time that polymorphs allow the observation of positive, zero and negative expansions of unit-cell volume at SCO.

The positive and negative expansions of unit-cell parameters can be observed in the temperature range of SCO, owing to the anisotropic variation of the coordination sphere at SCO. For example, a colossal NTE is driven by SCO in [Fe(bpac)(Au(CN)<sub>2</sub>)<sub>2</sub>]<sub>2</sub>·2EtOH (bpac=1,2-bis(4'-pyridyl)acetylene) with the flexible framework.<sup>75</sup> Accompanied with contraction of the coordination sphere at SCO, the unit-cell volume decreases from HS to LS. For example, unit-cell volume decreases by 80 Å<sup>3</sup> and 232 Å<sup>3</sup> in Fe(phen)<sub>2</sub>(NCS)<sub>2</sub><sup>76</sup>, and [Fe(Htrz)<sub>2</sub>(trz)](BF<sub>4</sub>)<sub>2</sub><sup>77</sup>, respectively. The unit-cell volume change about -1 to -10 % from HS to LS.<sup>22-23</sup> Here, the exotic behavior of the negative expansions of unit-cell volume from HS (including the *hν*-HS\* and Q-

HS) to LS in polymorph **I-pBrA** is unprecedented, which results from the molecular rearrangements at SCO associated to the variation of molecular geometries in space, especially the phenyl ring rotation. Moreover, the zero thermal expansion in polymorph **III-pBrA** can also be associated to the rotation of phenyl ring.

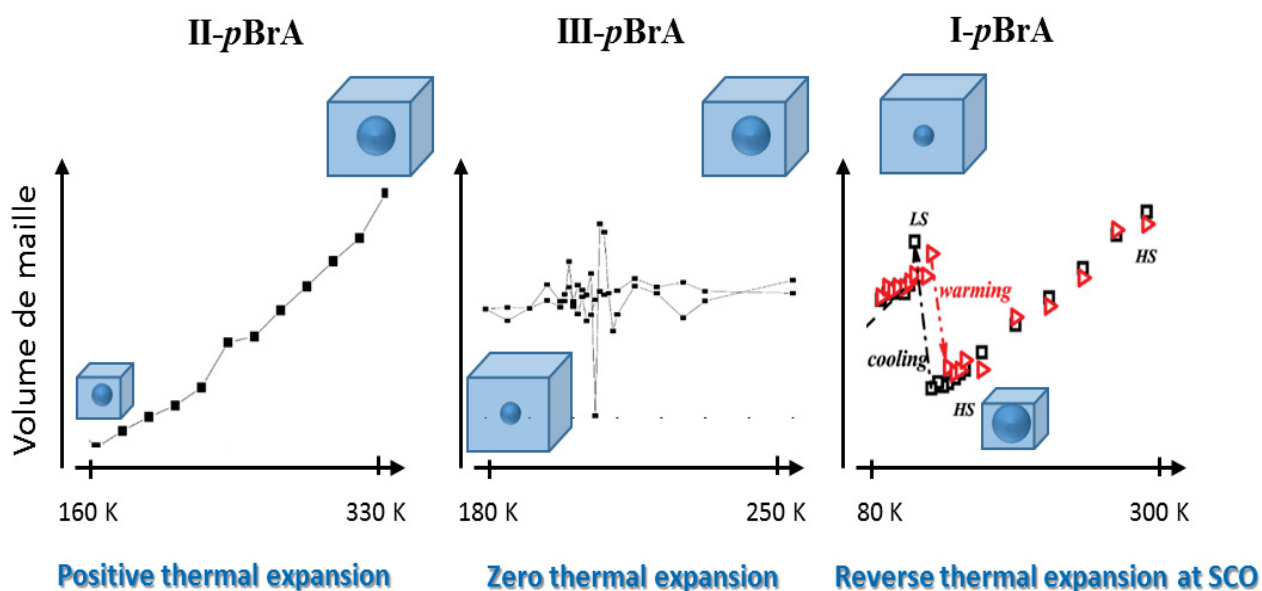


Figure II.67. Variety of unit-cell volume dependences on temperature for polymorphs **I-pBrA**, **II-pBrA** and **III-pBrA**.

Geometrically flexible networks in compounds will facilitate the negative thermal expansion (NTE).<sup>78</sup> The NTE effect in  $ZrW_2O_8$ -type solids can be well explained by the rotations of rigid polyhedra units in rigid unit modes. Structural flexibility is a key factor for NTE effect.  $[Cu_3(btc)_2]$  ( $btc=1,3,5$ -benzene-tricarboxylate), a metal–organic framework that consists of dicopper tetracarboxylate “paddlewheels” and aromatic ring motifs shows the large negative thermal expansion.<sup>79</sup> Here, in polymorphs **I-pBrA** and **III-pBrA**, the conformation changes of ligands (variation of  $\sigma_3$ ) at SCO indicates the flexibility of ligands and the networks constructed by the short contacts of S---Br and S---S may be also flexible. Hence, the unusual global volume variations in these two polymorphs may provide interesting clues for the design of materials with NTE effect.

*Part III – Promoting Distortion of the Coordination Polyhedron Using Polymorphism:  
Bromine Substitution of PM-zBrA Family*

As often observed for polymorphism, the behaviors of the four polymorphs are strongly different (Table III.21). **I-pBrA** and **III-pBrA** show abrupt and hysteretic SCO at different temperatures, correlated to ligand rotation, while polymorph **II-pBrA** experiences a gradual SCO together with an order-disorder transition and polymorph **IV-pBrA** remains HS. Regarding the population of the HS\* metastable state it was only possible to observe it in polymorphs **I-pBrA** and **III-pBrA**. Indeed, the HS\* was accessible efficiently using thermal quenching for both polymorphs. However, light irradiation was only possible on polymorph **I-pBrA** (there was not enough compound of **III-pBrA** to make any measurement) and it was shown to be only 65 % efficient. The main hypothesis to explain the difficulty to obtain the light-induced phase is that at 10 K, the energy needed to promote the rotation of the ligand is too high. Therefore, the photoswitching is slow and not totally efficient. This has already been reported on other compounds such as the  $[\text{Fe}(\text{3-bpp})_2][\text{Au}(\text{CN})_2]_2$  that experiences a twinning and reconstructive phase transition in temperature that is almost impossible to induce by light (another phase is partially obtained).<sup>80</sup>

**Table III.21.** Summary of relevant parameters for the  $[\text{Fe}(\text{PM-zBrA})_2(\text{NCS})_2]$  compounds.

<i>Compounds</i>	<i>SCO</i>	$T_{1/2} / \text{K}$	$T(\text{LIESST}) / T(\text{TIESST}) / \text{K}$	<i>Space Group</i>
<b>I-oBrA</b>	Gradual	220	50	
<b>I-mBrA</b>	Fully HS	-	-	$C2/c \leftrightarrow P2_1/c$
<b>II-mBrA</b>	Gradual	163	no	$C2/c$
<b>I-pBrA</b>	Abrupt	170 / 181	107 / 109	$P2_1/n$
<b>II-pBrA</b>	Gradual	260	no	$P2_1/n$
<b>III-pBrA*</b>	Abrupt	198 / 205	- / 70	$P-1$
<b>IV-pBrA</b>	Fully HS	-	-	$P2_1/n$

\* data for **III-pBrA** are coming from the SCXRD results.

Concerning the  $T(\text{LIESST})$  or  $T(\text{TIESST})$  values, we can only discuss **I-pBrA** and **III-pBrA** on the  $T(\text{LIESST})$  vs  $T_{1/2}$  database<sup>36</sup> (Figure II.68). As already mentioned, polymorph **I-pBrA** falls on the  $T_0 = 150$  K line while polymorph **III-pBrA** falls on  $T_0 = 120$  K line. Having a bidentate ligand-based complex on the  $T_0$  line gathering most of the tridentate-based compounds is remarkable. It makes polymorph **I-pBrA** the compound with the highest  $T(\text{LIESST})$  of the “bidentate” family and one of the highest among SCO compounds.<sup>17-18</sup>. Concerning polymorph **III-pBrA**, it lies on the same line than **I-S-BiA**, a compound belonging to the PM-L family. Therefore, these two polymorphs are remarkable since they do not fit the  $T_0 = 100$  K line where all the other compounds of this family lie.<sup>36</sup> More details on this aspect will be discussed in Part IV.

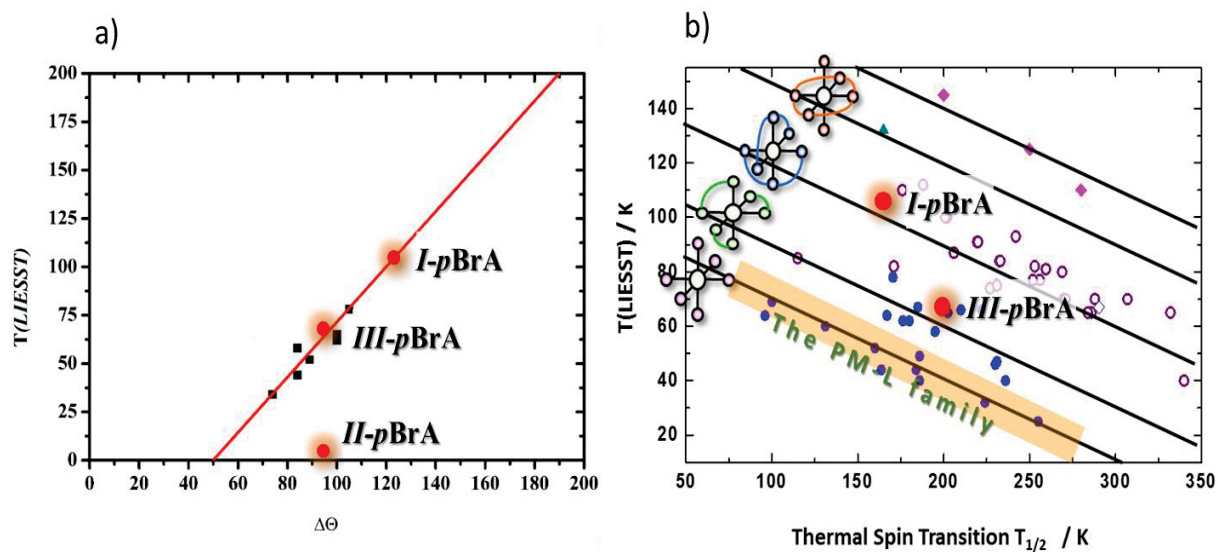


Figure II.68. The highlight of position of polymorphs (red sphere) in the  $T(\text{LIESST})$  vs  $\Delta\Theta$  in the  $[\text{Fe}(\text{PM-L})_2(\text{NCS})_2]$  family (a) and the database of  $T(\text{LIESST})$  vs  $T_{1/2}$  (b).

### III.5. Conclusion

In conclusion, we have explored the functionalization of the N-(2'-pyridylmethylne)-aniline ligand by bromo groups in *ortho*, *meta* and *para* positions in this section. With these ligands we have synthesized seven new compounds, including: complex **I-oBrA**, polymorphs **I-mBrA** and **II-mBrA**, polymorphs **I-pBrA**, **II-pBrA**, **III-pBrA** and **IV-pBrA**. The driving idea was to study the steric strain induced on the coordination sphere by this various substitutions with the expectation of changing the coordination sphere distortion. Unfortunately, the complex with ligands substituted in *ortho* did not crystallize preventing crystallographic investigations, despite a SCO at 220 K and a  $T(\text{LIESST})$  value at 50 K. The characteristics of the spin crossover and the  $T(\text{LIESST})$  temperatures are reported in [Table III.21](#).

Polymorphs in this family revealed a wide variety of behaviors with order-disorder transition coupled to SCO (**II-pBrA**), abrupt and hysteretic transitions (**I-pBrA**, **III-pBrA**), gradual SCO (**II-mBrA**) and even the absence of any spin change (**IV-pBrA**, **I-mBrA**). In polymorph **I-pBrA** a great  $T(\text{LIESST})$  value of 107 K was recorded, one of the highest reported and associated with a huge distortion of the coordination sphere. From the multiscale description of the structures of each compound, some crucial clues to understand the observed properties were highlighted, as it will be deeply discussed in part IV.

Polymorphs **I-pBrA** and **III-pBrA** display the thermal induced the excited spin state trapping effect with  $T(\text{TIESST})$  at 109 K and around 70 K, respectively. Considering the same space group and the similar ligand conformation between the HS and Q-HS\*, the relaxation from the Q-HS\* to LS really corresponds to the rotation of phenyl ring. Polymorphs **II-pBrA** shows the order-disorder transition of phenyl ring coupling with SCO while LIESST and TIESST effects are absent. Generally, the dynamics of molecular geometry at SCO, including the motion of ligands, the rotation of ligand, the order-disorder transition, the other conformational changes, can affect the thermally quenching effect. Our results provide a platform to explore the molecular dynamics at thermal quenching.

Moreover, two crystallographically independent iron sites in polymorphs **I-pBrA**, **II-pBrA** and **III-pBrA** exhibit one step thermal SCO. This is not due to the cooperativity because **II-pBrA** shows a gradual SCO. Since SCO is concomitant with the transition of ligands in these

*Part III – Promoting Distortion of the Coordination Polyhedron Using Polymorphism:  
Bromine Substitution of PM-zBrA Family*

polymorphs, spin state of one iron site might be driven and dominated by the other one associated to the transition of ligands.

Last but important, unique thermal expansion phenomena were recorded. Indeed, polymorph **I-pBrA** shows a negative expansion of the lattice at SCO and **III-pBrA** seems to do not exhibit any unit-cell volume change at the SCO. Therefore, it should be taken into account that the volume modification associated to the SCO can be negative, zero or positive depending on the compound but independently of the sense of the conversion (HS to LS or LS to HS). The negative and zero expansion of unit-cell volume can open new avenues in the possible application of the SCO phenomenon.

## Bibliography

- [1] P. Harding, D. J. Harding, N. Soponrat, K. Tinpun, S. Samuadnuan, H. Adams, *Aust. J. Chem.*, 2010, **63**, 75.
- [2] N. Diko, S. J. Zamisa, H. B. Friedrich, M. L. Shozi, *Z. Kristallogr. New Cryst. Struct.*, 2019, **234**, 1069.
- [3] O. V. Dolomanov, L. J. Bourhis, R. J. Gildea, J. A. K. Howard, H. Puschmann, *J. Appl. Crystallogr.*, 2009, **42**, 339.
- [4] M. A. Spackman, D. Jayatilaka, *Cryst. Eng. Comm.*, 2009, **11**, 19.
- [5] D. Jayatilaka, S. K. Wolff, D. J. Grimwood, J. J. McKinnon, M. A. Spackman, *Acta Cryst.*, 2006. **A62**, s90.
- [6] M. Llunell, D. Casanova, J. Cirera, M. Alemany, S. Alvarez, SHAPE, v. 2.0, University of Barcelona, Barcelona, Spain, 2010.
- [7] M. A. Halcrow, *Chem. Soc. Rev.*, 2011, **40**, 4119.
- [8] E. Tailleux, M. Marchivie, N. Daro, G. Chastanet, P. Guionneau, *Chem. Commun.*, 2017, **53**, 4763.
- [9] M. Shatruk, H. Phan, B. A. Chrisostomo, A. Suleimenova, *Coordi. Chem. Rev.*, 2015, **62-73**, 289.
- [10] S. Lakhloufi, P. Guionneau, M. H. Lemée-Cailleau, P. Rosa, J. F. Létard, *Phys. Rev. B*, 2010, **82**, 132104
- [11] A. Kaiba, H. J. Shepherd, D. Fedouai, P. Rosa, A. E. Goeta, N. Rebbani, J. F. Létard, P. Guionneau, *Dalton Trans.*, 2010, **39**, 2910.
- [12] H. J. Shepherd, P. Rosa, I. A. Fallis, P. Guionneau, J. A. K. Howard, A. E. Goeta, *J. Phys. Chem. Solids*, 2012, **73**, 193.
- [13] S. Lakhloufi, M. H. Lemée-Cailleau, G. Chastanet, P. Rosa, N. Daro, P. Guionneau, *Phys. Chem. Chem. Phys.*, 2016, **18**, 28307.
- [14] Rodríguez-Jiménez S, Brooker S, *Inorg Chem.*, 2017, **56**, 13697.
- [15] J. C. Slater, *J. Chem. Phys.*, 1964, **41**, 3199.
- [16] P. Gütllich, A. B. Gaspar, Y. Garcia, *J. Org. Chem.*, 2013, **9**, 342.
- [17] G. Chastanet, C. Desplanches, C. Balde, P. Rosa, M. Marchivie, P. Guionneau, *Chem. Sq.*, 2018, **2**, 2.
- [18] G. Chastanet, M. Lorenc, R. Bertoni, C. Desplanches, *C. R. Chim.*, 2018, **21**, 1075-1094.
- [19] P. Guionneau. *Dalton. Trans.*, 2014, **14**, 382.
- [20] M. Marchivie, P. Guionneau, J. F. Létard, D. Chasseau, *Acta Cryst.*, 2005, **B61**, 25.

*Part III – Promoting Distortion of the Coordination Polyhedron Using Polymorphism:  
Bromine Substitution of PM-zBrA Family*

- [21] D. Rosario-Amorin, P. Dechambenoit, A. Bentaleb, M. Rouzières, C. Mathonière, R. Clérac, *J. Am. Chem. Soc.*, 2018, **140**, 98.
- [22] P. Guionneau, M. Marchivie, G. Bravic, J.-F. Létard, D. Chasseau, *Top. Curr. Chem.*, 2004, **234**, 97.
- [23] E. Collet, P. Guionneau, *C. R. Chim.*, 2018, **21**, 1133.
- [24] A. LeBail, *Powder Diffraction*, 2005, **20**, 316.
- [25] N. Mochida, A. Kimura, T. Ishida, *Magnetochemistry*, 2015, **1**, 17.
- [26] N. Pittala, F. Thetiot, C. Charles, S. Triki, K. Boukheddaden, G. Chastanet, M. Marchivie, *Chem. Commun.*, 2017, **53**, 8356.
- [27] E. Trzop, M. Buron-Le Cointe, H Cailleau, L. Toupet, G. Molnar, A. Bousseksou, A. B. Gaspar, J. A. Real, E. Collet, *J. Appl. Cryst.*, 2007, **40**, 158.
- [28] D. Chernyshov, M. Hostettler, K. W. Törnroos, H.-B. Bürgi, *Angew. Chem. Int. Ed.*, 2003, **42**, 3825.
- [29] A. Lennartson, A. D. Bond, S. Piligkos, C. J. McKenzie, *Angew. Chem. Int. Ed.*, 2012, **51**, 11049.
- [30] N. Bréfuel, H. Watanabe, L. Toupet, J. Come, N. Matsumoto, E. Collet, K. Tanaka, J. P. Tuchagues, *Angew. Chem. Int. Ed.*, 2009, **48**, 9304.
- [31] C. Bartual-Murgui, R. Diego, S. Vela, S. J. Teat, O. Roubeau, G. Aromí, *Inorg. Chem.*, 2018, **57**, 11019.
- [32] J. Sánchez Costa, S. Rodríguez-Jiménez, G. A. Craig, B. Barth, C. M. Beavers, S. J. Teat, G. Aromí, *J. Am. Chem. Soc.*, 2014, **136**, 3869.
- [33] B. Brachňáková, I. Šalitraš, *Chem. Pap.*, **72**, 773.
- [34] M. Buron-Le Cointe, J. Hébert, C. Baldé, N. Moisan, L. Toupet, P. Guionneau, J. F. Létard, E. Freysz, H. Cailleau, E. Collet, *Phys. Rev. B*, 2012, **85**, 064114.
- [35] J. F. Létard, G. Chastanet, O. Nguyen, S. Marcén, M. Marchivie, P. Guionneau, D. Chasseau, P. Gülich, *Monatsh. Chem.*, 2003, **134**, 165.
- [36] J. F. Létard, *J. Mater. Chem.*, 2006, **16**, 2550.
- [37] R. Kulmaczewski, E. Trzop, L. J. Kershaw Cook, E. Collet, G. Chastanet, M. A. Halcrow, *Chem. Commun.*, 2017, **53**, 13268.
- [38] M. Shatruk, *Coord. Chem. Rev.*, 2015, **289**, 62.
- [39] G. S. Matouzenko, D. Luneau, G. Molnar, N. Ould-Moussa, S. Zein, S. A. Borshch, A. Bousseksou, F. Averseng, *Eur. J. Inorg. Chem.*, 2006, 2671.
- [40] A. Kashiro, K. Some, Y. Kobayashi, T. Ishida, *Inorg. Chem.*, 2019, **58**, 7672.

*Part III – Promoting Distortion of the Coordination Polyhedron Using Polymorphism:  
Bromine Substitution of PM-zBrA Family*

- [41] T. M. Ross, B. Moubaraki, K. S. Wallwork, S. R. Batten, K. S. Murray, *Dalton Trans.*, 2011, **40**, 10147.
- [42] G. A. Craig, J. Sánchez Costa, O. Roubeau, S. J. Teat, G. Aromí, *Chem. Eur. J.*, 2011, **17**, 3120.
- [43] M. Seredyuk, M. C. Muñoz, M. Castro, T. Romero-Morcillo, A. B. Gaspar, J. A. Real, *Chem. Eur. J.*, 2013, **19**, 6591.
- [44] D. Zhang, E. Trzop, F. J. Valverde-Muñoz, L. Piñeiro-López, M. C. Muñoz, E. Collet, J. A. Real, *Cryst. Growth Des.*, 2017, **17**, 2736.
- [45] P. Guionneau, J. F. Létard, D. S. Yufit, D. Chasseau, G. Bravic, A. E. Goeta, J. A. K. Howard, O. Kahn, *J. Mater. Chem.*, 1999, **9**, 985.
- [46] K. Takahashi, T. Kawakami, Z. Z. Gu, Y. Einaga, A. Fujishima, O. Sato. *Chem Commun.*, 2003, **18**, 2374.
- [47] G. Chastanet, C. A. Tovee, G. Hyett, M. A. Halcrow, J. F. Létard, *Dalton Trans.*, 2012, **41**, 4896.
- [48] S. V. Tumanov, S. L. Veber, S. Greatorex, M. A Halcrow, M. V Fedin, *Inorg. Chem.*, 2018, **57**, 8709.
- [49] *Polymorphism in pharmaceutical solids*, Ed. H. G. Brittain, 2016, CRC Press.
- [50] L. Yu, *Acc. Chem. Res.*, 2010, **43**, 1257.
- [51] J. Tao, R. J. Wei, R. B. Huang, L. S. Zheng, *Chem. Soc. Rev.*, 2012, **41**, 703.
- [52] E. König, K. Madeja, *Inorg. Chem.*, 1967, **6**, 48.
- [53] A. Galet, A. B. Gaspar, M. C. Muñoz, G. Levchenko, J. A. Real, *Inorg. Chem.*, 2006, **45**, 9670.
- [54] S. Pillet, C. Lecomte, C. F. Sheu, Y. C. Lin, I. J. Hsu, Y. Wang, *J. Phys. C*, 2005, **21**, 221.
- [55] G. Dupouy, M. Marchivie, S. Triki, J. Sala-Pala, J. Y. Salaün, C. J. Gómez-García, P. Guionneau, *Inorg. Chem.*, 2008, **47**, 8921.
- [56] P. A. Anderson, T. Astley, M. A. Hitchman, F. R. Keene, B. Moubaraki, K. S. Murray, B. W. Skelton, E. R. T. Tiekink, H. Toftlund, A. H. White, *Dalton Trans.*, 2000, **20**, 3505.
- [57] A. L. Thompson, A. E. Goeta, J. A. Real, A. Galet, M. C. Muñoz, *Chem. Commun.*, 2004, **12**, 1390.
- [58] D. L. Reger, J. R. Gardinier, M. D. Smith, A. M. Shahin, G. J. Long, L. Rebbouh, F. Grandjean, *Inorg. Chem.*, 2005, **44**, 1852.
- [59] C. Rajadurai, Z. Qu, O. Fuhr, B. Gopalan, R. Kruk, M. Ghafari, M. Ruben, *Dalton Trans.*, 2007, 3531.

*Part III – Promoting Distortion of the Coordination Polyhedron Using Polymorphism:  
Bromine Substitution of PM-zBrA Family*

- [60] R. Pritchard, H. Lazar, S. A. Barrett, C. A. Kilner, S. Asthana, C. Carbonera, J. F. Létard, M. A. Halcrow, *Dalton Trans.*, 2009, **33**, 6656.
- [61] B. Moubaraki, B. A. Leita, G. J. Halder, S. R. Battern, P. Jensen, J. P. Smith, J. D. Cashion, C. J. Kepert, J. F. Létard, K. S. Murray, *Dalton Trans.*, 2007, **39**, 4413.
- [62] J. Krober, J. P. Audiére, R. Claude, E. Codjovi, O. Kahn, J. G. Haasnoot, F. Grolière, C. Jay, A. Bousseksou, J. Linarés, F. Varret, A. Gonthiervassal, *Chem. Mater.*, 1994, **6**, 1404.
- [63] S. M. Neville, B. A. Leita, D. A. Offermann, M. B. Duriska, B. Moubaraki, K. W. Chapman, G. J. Halder, K. S. Murray, *Eur. J. Inorg. Chem.*, 2007, 1073.
- [64] S. M. Neville, B. A. Leita, G. J. Halder, C. J. Kepert, B. Moubaraki, J. F. Létard, K. S. Murray, *Chem. Eur. J.*, 2008, **14**, 10123.
- [65] H. E. Mason, M. L. Hamilton, J. A. K. Howard, H. A. Sparkes, *New J. Chem.*, 2018, **42**, 18028.
- [66] E. Collet, M. L. Boillot, J. Hebert, N. Moisan, M. Servol, M. Lorenc, L. Toupet, B. L. Cointe, A. Tissot, J. Sainton, *Acta Cryst.*, 2009, **B65**, 474.
- [67] S. Zein, G. S. Matouzenko, S. A. Borshch, *J. Phys. Chem. A*, 2005, **109**, 8568.
- [68] G. S. Matouzenko, A. Bousseksou, S. Lecocq, P. J. van Koningsbruggen, M. Perrin, O. Kahn, A. Collet, *Inorg. Chem.*, 1997, **36**, 5869.
- [69] C. Faulmann, P. Szilágyi, K. Jacob, J. Chahine, L. Valade, *New J. Chem.*, 2009, **33**, 1268.
- [70] E. Tailleur, M. Marchivie, P. Negrier, D. Denux, S. Massip, D. Mondieig, G. Chastanet, P. Guionneau, *Cryst. Eng. Comm.*, 2019, **21**, 6246.
- [71] I. Šalitroš, O. Fuhr, A. Eichhöfer, R. Kruk, J. Pavlik, L. Dlháň, R. Boča, M. Ruben *Dalton Trans.*, 2012, **41**, 5163.
- [72] C. F. Sheu, S. M. Chen, S. C. Wang, G. H. Lee, Y. H. Liu, Y. Wang, *Chem. Commun.*, 2009, **48**, 7512.
- [73] R. J. Wei, B. Li, J. Tao, R. B. Huang, L. S. Zheng, Z. P. Zheng, *Inorg. Chem.*, 2011, **50**, 1170.
- [74] C. F. Sheu, C. H. Shih, K. Sugimoto, B. M. Cheng, M. Takata, Y. Wang, *Chem. Commun.*, 2012, **48**, 5715.
- [75] B. R. Mullaney, L. Goux-Capes, D. J. Price, G. Chastanet, J. F. Létard, C. J. Kepert. *Nat. Commun.*, 2017, **8**, 1053.
- [76] V. Legrand, S. Pillet, H. P. Weber, M. Souhassou, J. F. Létard, P. Guionneau, C. Lecomte, *J. Appl. Cryst.*, 2007, **40**, 1076.
- [77] A. Grosjean, P. Négrier, P. Bordet, C. Etrillard, D. Mondieig, S. Pechev, E. Lebraud J. F. Létard, P. Guionneau, *Eur. J. Inorg. Chem.*, 2013, 796.

*Part III – Promoting Distortion of the Coordination Polyhedron Using Polymorphism:  
Bromine Substitution of PM-zBrA Family*

- [78] W. Miller, C. W. Smith, D. S. Mackenzie, K. E. Evans, *J. Mater. Sci.*, 2009, **44**, 5441.
- [79] Y. Wu, A. Kobayashi, G. J. Halder, V. K. Peterson, K. W. Chapman, N. Lock, P. D. Southon, C. J. Kepert, *Angew. Chem. Int. Ed.*, 2008, **47**, 8929.
- [80] A. Djemel, O. Stefanczyk, M. Marchivie, E. Trzop, E. Collet, C. Desplanches, R. Delimi, G. Chastanet. *Chem. Eur. J.*, 2018, **24**, 1, 4760.

**Part IV – T(LIESST): A Close and Comprehensive View**

<b>IV.1. Introduction.....</b>	<b>197</b>
<b>IV.2. T(LIESST) and the coordination sphere .....</b>	<b>198</b>
IV.2.1. Comparison of the [Fe(PM-zXA) <sub>2</sub> (NCS) <sub>2</sub> ] compounds.....	198
IV.2.2. Comparison with the whole PM-L family.....	202
IV.2.3. New solvatomorphs based on [Fe(PM-pFA) <sub>2</sub> (NCE) <sub>2</sub> ] and [Fe(PM-pBrA) <sub>2</sub> (NCE) <sub>2</sub> ] .....	205
IV.2.4. Comparison with SCO complexes based on bidentate ligands .....	211
<b>IV.3. Lifetime of the metastable HS* state – a multiscale view .....</b>	<b>216</b>
<b>Bibliography .....</b>	<b>223</b>

## IV.1. Introduction

In **Parts II** and **III** of the manuscript, we have explored the functionalization of the N-(2'-pyridylmethylne)-aniline ligand by fluoro and bromo groups in *ortho*, *meta* and *para* positions. With these ligands we have synthesized ten new compounds: complexes **I-oFA**, **I-mFA** and **I-pFA**, with the fluorine and complex **I-oBrA**, polymorphs **I-mBrA** and **II-mBrA**, and polymorphs **I-pBrA**, **II-pBrA**, **III-pBrA** and **IV-pBrA** with the bromine ligands. The driving idea was to study the steric strain induced on the coordination sphere by these various substitutions with the expectation of changing the coordination sphere distortion. Unfortunately, the complexes with ligands substituted in *ortho* did not crystallize preventing crystallographic investigations. The origin of polymorphism and the differences between them has been deeply investigated and described and the respective parts. Here, these ten compounds will be compared with the other members of the PM-L family with a focus on the coordination sphere scale to see if any correlation with the *T(LIESST)* can be confirmed or evidenced.

Then, novel solvatomorphs  $[\text{Fe}(\text{PM-}p\text{XA})_2(\text{NCE})_2] \cdot S$  ( $E = \text{S}$  and  $\text{Se}$ ,  $S = \text{Solvent}$ ,  $X = \text{F}$  and  $\text{Br}$ ) will be introduced, though not fully described since there are still under investigation.

These results will be compared to the literature, especially the one focused on SCO complexes based on at least one bidentate ligand. This will give more impact on the correlation, if any. This discussion will be performed, separating compounds with structural transition at the SCO (phase transition, symmetry breaking, order-disorder...) from compounds without. This should allow to discuss separately the effect of crystal packing change upon SCO on the photo-induced  $h\nu\text{-HS}^*$  state lifetime.

Finally, a comprehensive discussion on the *T(LIESST)* and the lifetime of the photo-induced state using a multi-scale view will be presented, similarly to the thermal SCO. This description will be strengthened using data from the literature to tend toward a complete overview.

All this part should allow to draw new trends in the chemical design of SCO with enhanced lifetime of the  $h\nu\text{-HS}^*$  metastable state.

## IV.2. *T(LIESST)* and the coordination sphere

### IV.2.1. Comparison of the $[\text{Fe}(\text{PM-}z\text{XA})_2(\text{NCS})_2]$ compounds

Table IV.1 summarizes relevant information for the following discussion on the ten new compounds: complexes **I-oFA**, **I-mFA** and **I-pFA** with the fluorine substitution, and complex **I-oBrA**, polymorphs **I-mBrA** and **II-mBrA**, and polymorphs **I-pBrA**, **II-pBrA**, **III-pBrA** and **IV-pBrA** with the bromo-substituted ligands. The structure of **I-oFA** and **I-oBrA** are unknown due to the absence of single-crystal samples.

Table IV.1. Summary of relevant parameters for the 10 compounds described in part II and III.

	<i>SCO</i>	$T_{1/2}$ /K	$T(\text{LIESST})$ / $T(\text{TIESST})$ /K	Space Group (HS and LS)	$\Delta\zeta$ /Å	$\Delta\theta$ /Å	$\Delta S$	comment
<b>I-oFA</b>	Gradual	215	55 / -	unknown structure				
<b>I-mFA</b>	Gradual & incomplete	215	32 / -	C2/c	0.017(Fe1) / 0.262(Fe2)	-6(Fe1) / 66(Fe2)	0.067(Fe1) / 0.59(Fe2)	Fe1 SCO active; Fe2, HS;
<b>I-pFA</b>	Gradual 2 steps	100( $T_{1/2}$ ) /140( $T_{2/2}$ )	55/57	R-3	0.181(Fe1) / 0.335(Fe2)	57(Fe1) / 62(Fe2)	0.79(Fe1) / 0.68(Fe2)	R-3 and nanoporous
<b>I-oBrA</b>	Gradual	220	55 / -	unknown structure				
<b>I-mBrA</b>	Fully HS	-	-	C2/c ↔ $P2_1/c$	-	-	-	phase transition without SCO
<b>II-mBrA</b>	Gradual	163	no	C2/c	0.276	40	0.46	
<b>I-pBrA</b>	Abrupt & hysteresis	170( $T_{1/2}\downarrow$ ) /181( $T_{1/2}\uparrow$ )	107 / 109	$P2_1/n$	0.28(Fe1) / 0.35(Fe2)	95(Fe1) / 122(Fe2)	0.91(Fe1) / 1.23(Fe2)	rotation of phenyl ring and reverse volume expansion
<b>II-pBrA</b>	Gradual	260	no	$P2_1/n$	0.28(Fe1) / 0.27(Fe2)	107(Fe1) / 95(Fe2)	0.89(Fe1) / 1.09(Fe2)	order- disorder of phenyl ring
<b>III- pBrA*</b>	Abrupt & hysteresis	198( $T_{1/2}\downarrow$ )/2 05( $T_{1/2}\uparrow$ )	- / 70	$P-1$	0.28(Fe1) / 0.36(Fe2)	95(Fe1) / 98(Fe2)	0.92(Fe1) / 0.96(Fe2)	rotation of phenyl ring
<b>IV-pBrA</b>	Fully HS	-	-	$P2_1/n$	-	-	-	-

\* Data for **III-pBrA** coming from the SCXRD results, the other ones from magnetic data

From this table we can first report the  $[T_{1/2}, T(\text{LIESST})]$  couples on the corresponding  $T(\text{LIESST})$  database (Figure IV.1).<sup>1</sup> Compounds **I-mFA** and **I-pFA** fall on the  $T_0 = 100$  K line, **I-oFA**, **I-oBrA** and **III-pBrA** are lying on the  $T_0 = 120$  K and **I-pBrA** fits above the  $T_0 = 150$  K. If the hypothesis on influence of an increasing trigonal distortion to increase  $T_0$ , we can therefore expect the following evolution in  $\Delta\theta$ : **I-mFA**  $\approx$  **I-pFA** < **I-oFA**  $\approx$  **I-oBrA** < **III-pBrA** < **I-pBrA**. Unfortunately the crystal structure of **I-oFA** and **I-oBrA** are unknown and therefore their trigonal distortion are not accessible. According to the values reported in Table IV.1, this trend is observed. Therefore, we can expect a higher variation of the trigonal distortion in complex **I-oFA** than in **I-mFA** and **I-pFA**. It could mean that the strategy of promoting the steric strain by adding substituents close to the coordination sphere is successful.

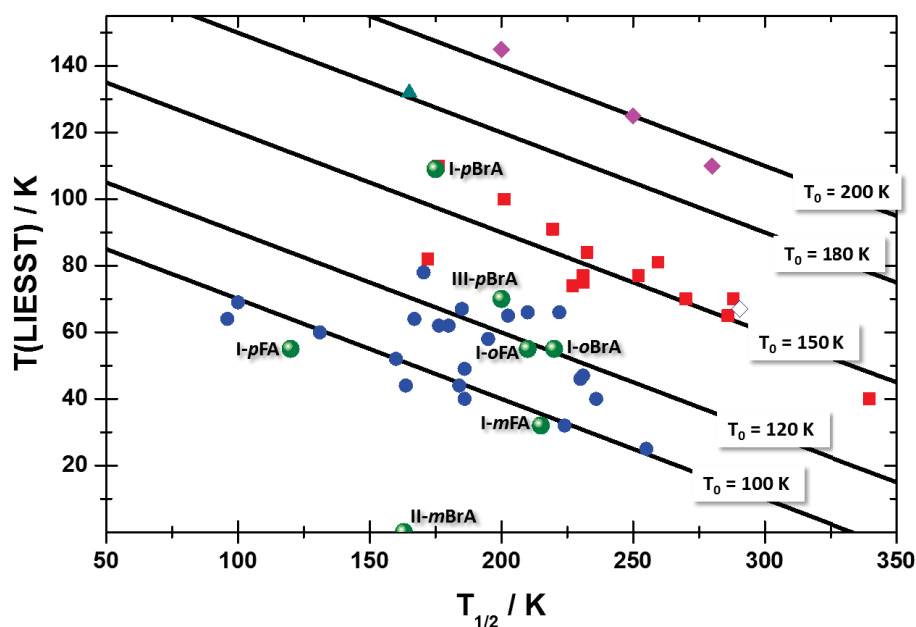


Figure IV.1. The positions of the new compounds obtained in this work (green spheres) and described in parts II-III in the  $T(\text{LIESST})$  vs  $T_{1/2}$  database.

As mentioned before (Part II.3.2), in complex **I-mFA**, the pyridine rings are in *cis* configuration in Fe2 site and in *trans* configuration in Fe1 site. This *cis* ion displays a spin crossover. The other site exhibiting a usual *trans* conformation of the pyridine rings remains HS at low temperature. As already noticed for the SCO inactive site Fe1, the fluorine groups are at 5.654 Å and 5.650 Å from the  $\text{Fe}^{2+}$  center. For the SCO active Fe2 site, the fluorine groups are at 6.526 Å and 6.273 Å from the  $\text{Fe}^{2+}$  center, almost 1 Å farther than in Fe1. Therefore, even in *meta* position the fluorine atoms may exert a steric strain on the coordination, in that case preventing the SCO to occur. This could explain the expected higher distortion observed

in the *ortho*-substituted compounds. This conclusion is strengthened by the fact that polymorph **II-*m*BrA** with  $\Delta\theta = 40^\circ$  exhibits a fast relaxation of the  $h\nu\text{-HS}^*$  that prevents any observation of  $T(\text{LIESST})$ . However, it is also weakened by the fact that **II-*p*BrA**  $\Delta\theta \sim 100^\circ$  does not exhibit any efficient LIESST effect. Moreover, as already discussed on [Table III.6 \(Part III\)](#), this correlation of the Br---Fe distances with the occurrence of SCO and the  $\Delta\theta$  is not so obvious.

Let us focus our attention on the four polymorphs of ***p*BrA**. Firstly, polymorph **IV-*p*BrA** has the biggest angular and trigonal distortions, in agreement with the stabilization of the HS state in this polymorph and the absence of any SCO. Secondly, despite the presence of two distinct sites in polymorph **I-*p*BrA**, they both behave simultaneously, as if the most distorted site drives the spin crossover of the other site. Thirdly, polymorphs **I-*p*BrA**, **II-*p*BrA** and **III-*p*BrA** show similar  $\Delta\Sigma$  values, ruling out its influence on  $T_{1/2}$  and  $T(\text{LIESST})$ . The variation of bond-length is weaker in polymorph **II-*p*BrA**, probably because the fully HS state above 330 K is difficult to obtain *via* single crystal X-Ray diffraction. From [Table IV.1](#), we clearly see that the highest  $\Delta\theta$  is of the same order in polymorphs **II-*p*BrA** and **III-*p*BrA** that is around  $100^\circ \pm 5^\circ$ , while it is around  $120^\circ$  in polymorph **I-*p*BrA**. We should therefore expect similar  $T(\text{LIESST})$  values for polymorphs **II-*p*BrA** and **III-*p*BrA**. However, for polymorph **II-*p*BrA** we were not able to observe the metastable  $\text{HS}^*$  state and therefore to record any  $T(\text{LIESST})$ . Two hypothesis can be proposed to explain this result.

The first possibility is that for polymorphs **I-*p*BrA** and **III-*p*BrA**, the metastable states  $\text{HS}^*$  correspond to the HS states observed at room temperature, with the ligand rotation along the  $\text{HS}^*$  to LS relaxation. In polymorph **II-*p*BrA**, it is possible that at low temperature, the  $h\nu\text{-HS}^*$  is not similar to the HS state at high temperature and does not present any disorder. Therefore, it is possible that the  $\Delta\theta$  obtained from the thermal spin crossover does not correspond to the true  $\Delta\theta$  between the non-disordered  $h\nu\text{-HS}^*$  and the LS states. Then, it leads to a difficult comparison of this compound with the others. The second possible explanation is that  $\Delta\theta$  is not the unique parameter to correlate with the  $T(\text{LIESST})$ . Indeed, in **II-*p*BrA** both  $\Delta\theta$  and  $\Delta\zeta$  are smaller than in **I-*p*BrA** while in **III-*p*BrA** only  $\Delta\theta$  is smaller ([Table IV.1](#)). This  $\Delta\zeta$  was the parameter supposed to be responsible of the difference in behavior between polymorphs **I-S-BiA** and **II-S-BiA** of  $[\text{Fe}(\text{PM-BiA})_2(\text{NCS})_2]$ .<sup>2</sup>

Figure IV.2 reports the  $T(\text{LIESST})$  as function of both  $\Delta\theta$  and  $\Delta\zeta$  in a 3D plot for **I-mFA**, **I-pFA**, **I-pBrA** and **III-pBrA**. It appears clearly that the highest  $T(\text{LIESST})$  are found for high values of both  $\Delta\theta$  and  $\Delta\zeta$ . However, with values of  $\Delta\theta = 107^\circ$  and  $\Delta\zeta = 0.28 \text{ \AA}$ , we could expect  $T(\text{LIESST})$  above 50 K for **II-pBrA** while we did not observe anything. Therefore, the hypothesis that the  $\Delta\theta$  obtained from the thermal SCO is much bigger than the  $\Delta\theta$  between LS and  $h\nu\text{-HS}^*$  might be right. Without the photo-induced structure, it remains a hypothesis.

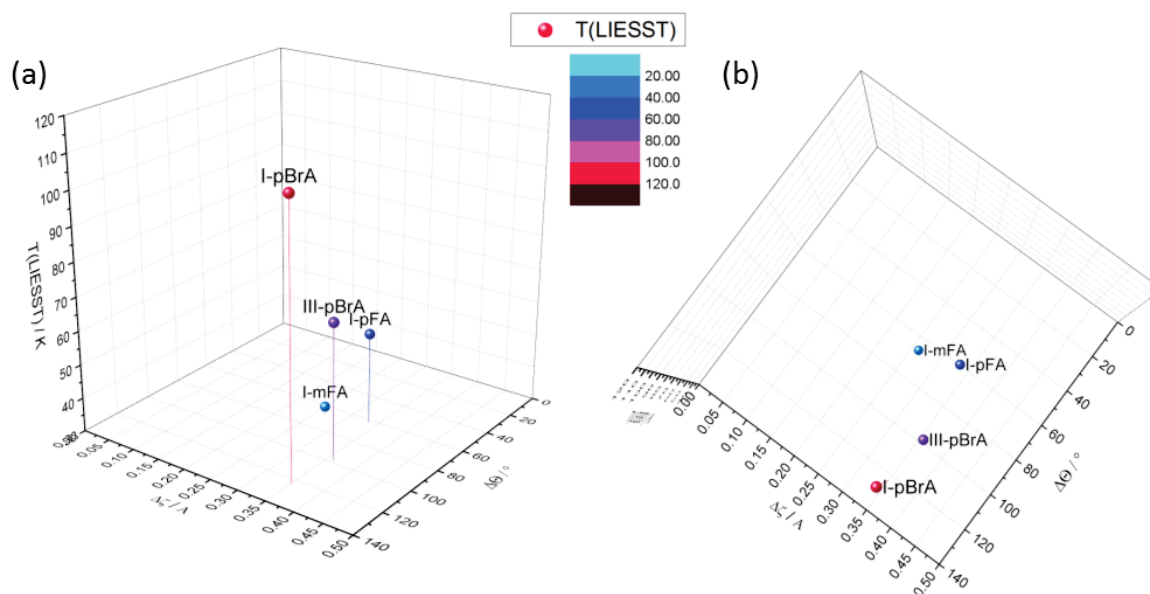


Figure IV.2.  $T(\text{LIESST})/T(\text{TIESST})$  as function of  $\Delta\theta$  and  $\Delta\zeta$  for the four compounds reported in Table IV.1 in a 3D view (a) and in projection on the  $(\Delta\theta, \Delta\zeta)$  plane (b).

It is surprising to reach such high values of coordination sphere distortion with chemical substitution in *para* position of the phenyl group that is far from the coordination sphere. This is strongly informing us on the intermolecular origin of this distortion, as discussed for polymorphs **I-S-BiA** and **II-S-BiA**.<sup>2</sup> The immediate correlation of the strong ligand rotation in Fe2 site in polymorph **I-pBrA** responsible of this high distortion is ruled out by the presence of the same rotation in **III-pBrA** but without the same effect on the distortion, even if the values in polymorph **III-pBrA** remain high. Indeed, the rotation of the bromophenyl ring in both polymorphs is around  $68^\circ$ . However, more than the rotation, one has to look at the motion of the whole ligand which can be probed through the dihedral angle between the pyridine and the bromophenyl,  $\sigma_3$ . In polymorph **I-pBrA**, the  $|\Delta\sigma_3|$  of the two ligands in Fe2 site are  $22^\circ$  and  $35^\circ$  while in polymorph **III-pBrA** they are of  $2^\circ$  and  $31^\circ$ . There is clearly a higher motion of ligands in **I-pBrA** than in **III-pBrA** that might be responsible of the higher trigonal distortion in polymorph **I-pBrA**. This might come from the difference in the crystal packing and intermolecular interactions as discussed above.

In addition, polymorphism on this new compounds allow to evidence that  $\Delta\theta$  is not the unique parameter to correlate with the  $T(\text{LIESST})$  and that  $\Delta\zeta$  has to be taken into account. However, this aspect has to be confronted with first the other members of the PM-L family then complexes based on bidentate ligands.

### IV.2.2. Comparison with the whole PM-L family

Table IV.2 summarizes some parameters of importance to be compared, of the whole  $[\text{Fe}(\text{PM-L})_2(\text{NCE})_2]$  ( $E = \text{S}$  and  $\text{Se}$ ). In the original paper from Marchivie *et al.*, a linear relationship between  $T(\text{LIESST})$  and  $\Delta\theta$  was observed (black squares on Figure IV.3a).<sup>3</sup> On the contrary no correlation can be observed with  $\Delta\zeta$  (Figure IV.3b).

**Table IV.2.** Summary of the SCO characteristics of the  $[\text{Fe}(\text{PM-L})_2(\text{NCE})_2]$  ( $E = \text{S}$  and  $\text{Se}$ ).

Compound	SCO	$T_{1/2}$ /K	$T(\text{LIESST})$ /K	Space Group HS/LS	$\Delta\zeta$ /Å	$\Delta\theta$ /°	$\Delta S$	comment	Ref.
<i>I</i> - $[\text{Fe}(\text{PM-BiA})_2(\text{NCS})_2]$	Hysteresis	168( $T_{1/2\downarrow}$ ) / 173( $T_{1/2\uparrow}$ )	78	Pccn	0.46	110	1.15		4
<i>II</i> - $[\text{Fe}(\text{PM-BiA})_2(\text{NCS})_2]$	Gradual	190	34	$P2_1/c$	0.33	76	0.76		4
$[\text{Fe}(\text{PM-NEA})_2(\text{NCS})_2]$	Gradual	210	58	$P2_1/c$	0.29	84	0.74		5
<i>I</i> - $[\text{Fe}(\text{PM-TheA})_2(\text{NCS})_2]$	Gradual	208	no	Pccn	0.17	83	0.76		6
$[\text{Fe}(\text{PM-PEA})_2(\text{NCS})_2]$	Hysteresis	188( $T_{1/2\downarrow}$ ) / 228( $T_{1/2\uparrow}$ )	64	$P2_1/c \leftrightarrow \text{Pccn}$	0.50	72	0.92	Sym. break.	4
<i>I</i> - $[\text{Fe}(\text{PM-PEA})_2(\text{NCSe})_2]$	Hysteresis	266( $T_{1/2\downarrow}$ ) / 307( $T_{1/2\uparrow}$ )	no	$P2_1/c \leftrightarrow \text{Pccn}$	0.28	45	0.66	Sym. break.	7
<i>II</i> - $[\text{Fe}(\text{PM-PEA})_2(\text{NCSe})_2]$	Gradual	245	no	$P2_1/c$	0.12	36	0.38		8
$[\text{Fe}(\text{PM-AzA})_2(\text{NCS})_2]$	Gradual	189	46	$P2_1/c$	0.32	87	0.82		4, 9
$[\text{Fe}(\text{PM-FIA})_2(\text{NCS})_2]$	Gradual	165	64	-	-	-	-	No data	10
$[\text{Fe}(\text{PM-FIA})_2(\text{NCSe})_2]$	Gradual	236	35	-	-	-	-	No data	10

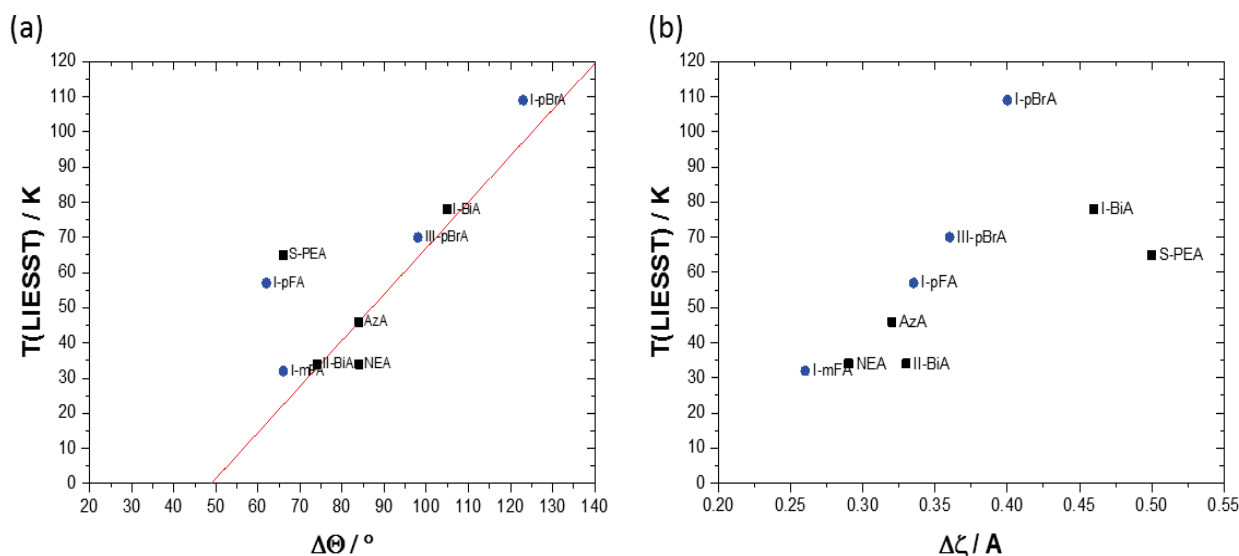


**Figure IV.3.**  $T(\text{LIESST})$  as function of  $\Delta\Theta$  (a) and  $\Delta\zeta$  (b) for the PM-L family. Black square and blue sphere represent the compounds reported in Table IV.2 and Table IV.1, respectively.

Compound **S-PEA** from the PM-L family, recorded after the first study, does not lay on the original line.<sup>11</sup> This probably comes from the presence of structural phase transition upon SCO that introduces an additional network energy to overcome during the relaxation process or that leads to a  $\text{HS}^*$  different from the HS whose  $\Theta$  value is used for the calculation of  $\Delta\Theta$ .

On this graph, the compounds obtained during this PhD work and discussed in Parts II and III are introduced (blue circles on Figure IV.3). They all fit closely with the original linear trend of  $T(\text{LIESST})$  vs  $\Delta\Theta$ , except **I-pFA**. It has to be noticed that this compound exhibits a disorder of the solvent molecule (cf. Part II.3.3). As for compound **II-pBrA** with an order-disorder of the phenyl ring, the  $\Delta\Theta$  calculated from the thermal SCO might be overestimated compare to the true  $\Delta\Theta$  between the  $h\nu\text{-HS}^*$  and LS states. Therefore, the two compounds that do not lie on the line are those with some structural features that prevent calculation of a reliable  $\Delta\Theta$  value. Contrarily to the other PM-L compounds, **I-mFA**, **I-pFA**, **III-pBrA** and **I-pBrA** seem to align along a given  $T(\text{LIESST})$  vs  $\Delta\zeta$  line. However, no clear trend can be seen if we account for all the compounds.

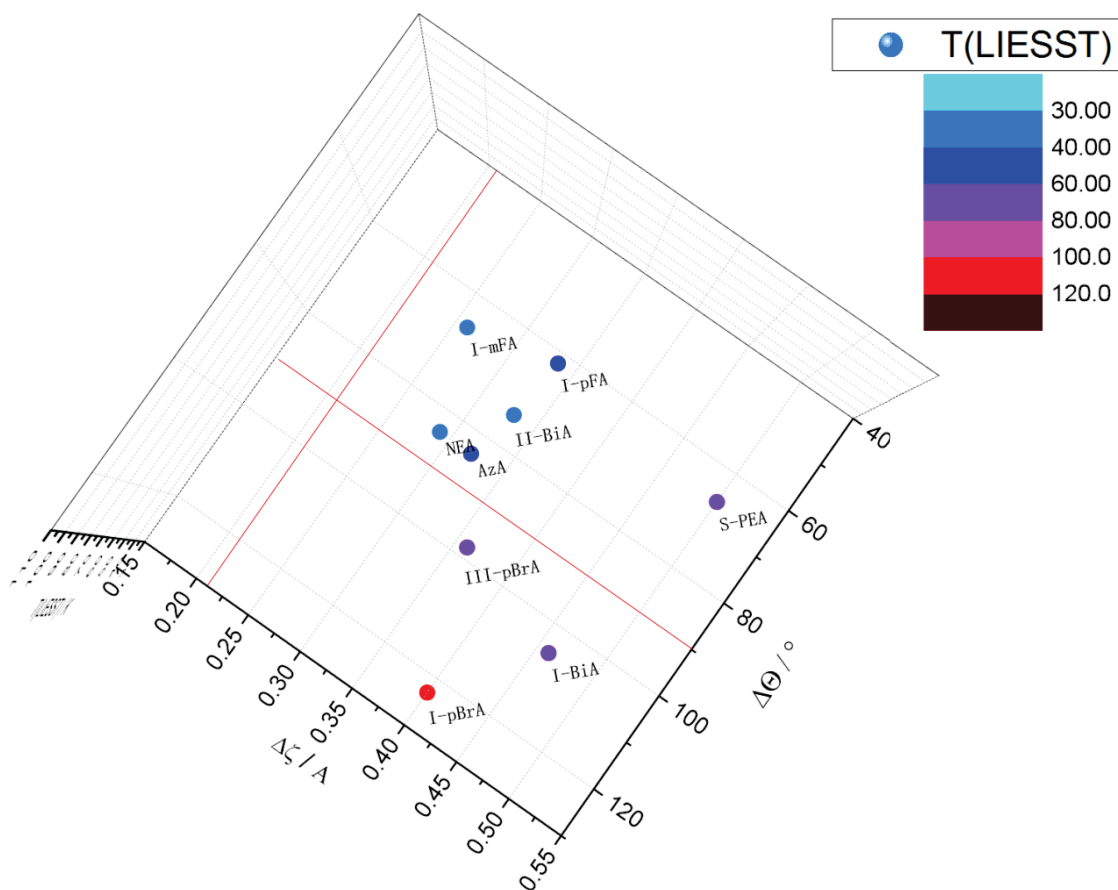


**Figure IV.4.** Projection on the  $(\Delta\Theta, \Delta\zeta)$  plane of the  $T(\text{LIESST})$  values. The red lines stand for the average  $\Delta\Theta$  ( $90^\circ$ ) and  $\Delta\zeta$  ( $0.21 \text{ \AA}$ ) values.

Concerning the 3D plot of  $T(\text{LIESST}) = f(\Delta\Theta, \Delta\zeta)$  (Figure IV.4) we can notice that the highest  $T(\text{LIESST})$  are for compounds exhibiting both high  $\Delta\Theta$  and  $\Delta\zeta$  values. At first glance, to have high  $T(\text{LIESST})$  one should have these two distortion parameters above average. **S-PEA** is out of this area, probably because it experiences a crystallographic phase transition that can affect the measured  $\Delta\Theta$  value, or add an additional energy to overcome during the relaxation process. This is also the case for **I-pFA**.

Concerning the variation of the Shape parameter between the HS and LS states (Figure IV.5), it seems there is a linear relationship. The value of the Shape parameter, indicates the deviation from the ideal octahedron ( $O_h$ ) to a trigonal prismatic structure ( $D_{3h}$ ). The higher the Shape value, the higher this deviation. Although, it takes part of a global description of symmetries (bonds and angles), Shape has the same trend than with the trigonal distortion (see Part I.1.2). Compared the Figures IV.3a with IV.5, a better linear relationship in Figure IV.5 may also indicates both bond and trigonal distortion are important in a certain extent.

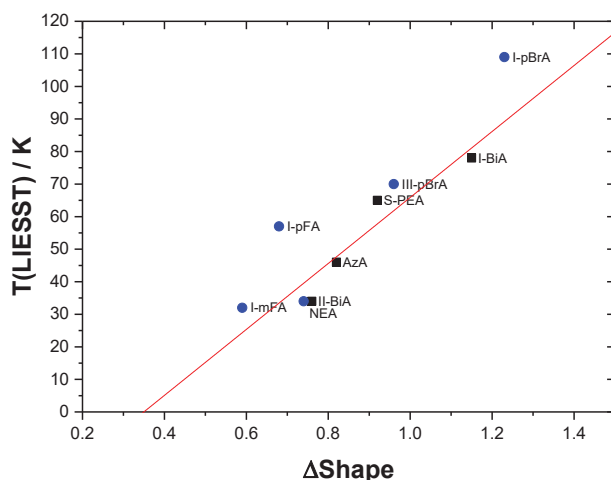


Figure IV.5.  $T(\text{LIESST})$  as function of  $\Delta\text{shape}$  for the PM-L family. Black square and blue sphere represent the compounds reported in Table IV.2 and Table IV.1, respectively.

#### IV.2.3. New solvatomorphs based on $[\text{Fe}(\text{PM-}p\text{FA})_2(\text{NCE})_2]$ and $[\text{Fe}(\text{PM-}p\text{BrA})_2(\text{NCE})_2]$

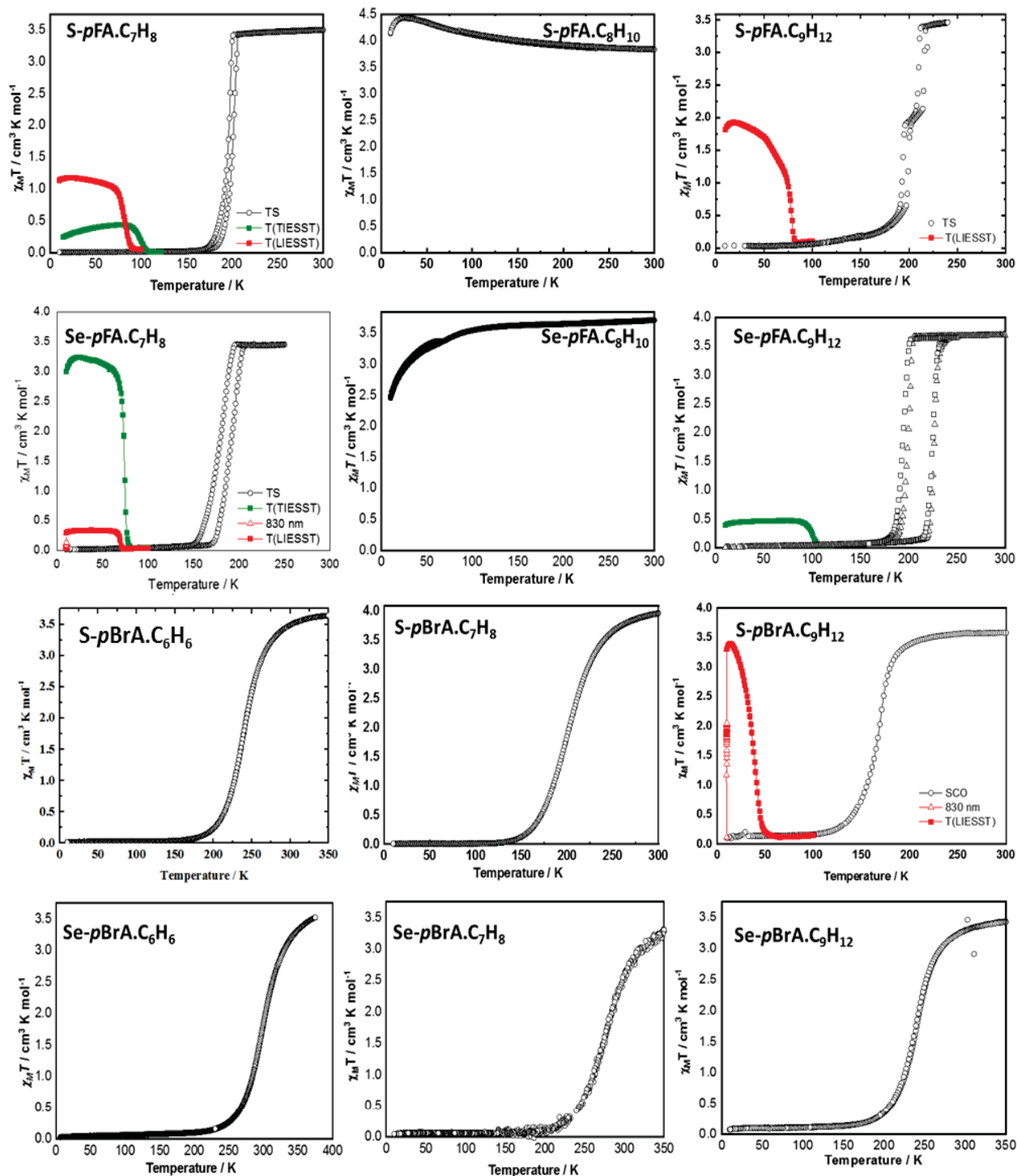
As discussed above, S-PEA, for example, experiences a structural phase transition together with the spin crossover that does not fit the  $T(\text{LIESST})$  vs  $\Delta\theta$  trend. We suppose it's coming from the occurrence of the phase transition that introduces an additional energy barrier or because the  $h\nu\text{-HS}^*$  is different from the HS one, leading to a pseudo value of  $\Delta\theta$  from  $h\nu\text{-HS}^*$  to LS. During the PhD work, many other compounds were synthesized by introducing various solvents in the structure. The idea was, for a given ligand, to regulate the intermolecular interaction and see how it influences the distortion of the coordination sphere. This work, done for “bpp” compounds for example, generally allows to move along one  $T_0$  line of the  $T(\text{LIESST})$  vs  $T_{1/2}$  database.<sup>12-13</sup> Since the  $p\text{FA}$  and  $p\text{BrA}$ -based compounds seem to be very sensitive to the environment we expected to move not only along one  $T_0$  line but also to move from one line to another. This would strongly favor the idea that  $T(\text{LIESST})$ , as for S-PEA, is influenced by the molecular packing, *i.e.* intermolecular contacts.

Table IV.3 and Figure IV.6 summarize various compounds  $[\text{Fe}(\text{PM-}p\text{XA})_2(\text{NCE})_2] \cdot S$  ( $E = \text{S}$  and  $\text{Se}$ ,  $S = \text{Solvent}$ ,  $X = \text{F}$  and  $\text{Br}$ ) and their characteristics further obtained along this work. The synthesis and single-crystal structure data can be seen in Appendix 6 and 7. Unfortunately, these compounds were not fully characterized due to very peculiar behaviors that deserve long and detailed analysis. Moreover, not all the LIESST measurements were performed on these samples due to restriction time.

Table IV.3. Summary of the SCO characteristics of new compounds in the family of [Fe(PM-*p*XA)<sub>2</sub>(NCE)<sub>2</sub>].*S* (E = S and Se, *S* = Solvent, X = F and Br) additionally obtained in this work.

	SCO	$T_{1/2}$ /K 170( $T_{1/2\downarrow}$ ) / 181( $T_{1/2\uparrow}$ )	$T(\text{LIESST}) /$ $T(\text{TIESST})$ /K	Space Group (HS/LS)	$\Delta\zeta$ /Å	$\Delta\theta$ /°	$\Delta S$	comment
<i>S-pFA.C<sub>6</sub>H<sub>6</sub></i>	SCO			$P2_1/c \leftrightarrow C2/c$	0.29	62	0.71	Not enough sample for SQUID
<i>S-pFA.C<sub>7</sub>H<sub>8</sub></i>	hysteresis	194( $T_{1/2\downarrow}$ ) / 210( $T_{1/2\uparrow}$ )	82 / 100	$C2/c \leftrightarrow P-1$ Q-HS*: $P-1$	0.36(Fe1) / 0.37(Fe2) / 0.36(Fe3)	178(Fe1) / 178(Fe2) / 179(Fe3)	1.78(Fe1) / 1.79(Fe2) / 1.78(Fe3)	Twinning
<i>S-pFA.C<sub>8</sub>H<sub>10</sub></i>	HS	-	-	-	-	-	-	-
<i>S-pFA.C<sub>9</sub>H<sub>12</sub></i>	2-step hysteresis	Step 1: 210/215 Step 2: 194/199	Step 1: 58 / - Step 2: 79/-	Step 1: $P-1 \leftrightarrow P-1$ Step 2: $P-1 \leftrightarrow C2/c$	0.33	105	1.06	Order-disorder of solvent
<i>Se-pFA.C<sub>6</sub>H<sub>6</sub></i>	-	-	-	-	-	-	-	Not synthesized
<i>Se-pFA.C<sub>7</sub>H<sub>8</sub></i>	hysteresis	176( $T_{1/2\downarrow}$ ) / 191( $T_{1/2\uparrow}$ )	70 / 74	$C2/c \leftrightarrow C2/c$ Q-HS*: $P-1$	0.28	179	1.71	Twinning
<i>Se-pFA.C<sub>8</sub>H<sub>10</sub></i>	HS	-	-	-	-	-	-	-
<i>Se-pFA.C<sub>9</sub>H<sub>12</sub></i>	hysteresis	194( $T_{1/2\downarrow}$ ) / 226( $T_{1/2\uparrow}$ )	- / 100	$C2/c$	0.35	151	1.5	Rotation of solvent
<i>S-pBrA.C<sub>6</sub>H<sub>6</sub></i>	gradual	255		$C2/c$	0.34	69	0.76	-
<i>S-pBrA.C<sub>7</sub>H<sub>8</sub></i>	gradual	200		$C2/c$	0.32	82	0.91	Disorder of solvent
<i>S-pBrA.C<sub>8</sub>H<sub>10</sub></i>	-	-	-	-	-	-	-	didn't try
<i>S-pBrA.C<sub>9</sub>H<sub>12</sub></i>	gradual	170	40/-	$C2/c$	0.34	100	1.12	Disorder of solvent
<i>Se-pBrA.C<sub>6</sub>H<sub>6</sub></i>	gradual	297		$C2/c$				-
<i>Se-pBrA.C<sub>7</sub>H<sub>8</sub></i>	gradual	278		$C2/c$	0.20	59	0.55	Disorder of solvent
<i>Se-pBrA.C<sub>8</sub>H<sub>10</sub></i>	-	-	-	-	-	-	-	didn't try
<i>Se-pBrA.C<sub>9</sub>H<sub>12</sub></i>	gradual	238	0 / 0	$C2/c$	0.27	97	1.0	Disorder of solvent

As a general observation (Figure IV.6), all the solvatomorphs made with the *p*-BrA ligand exhibit gradual spin crossover and the solvent entities are disordered in the HS and LS states. On the contrary, *p*-FA-based compounds present a wide variety of behaviors, with HS compounds (*S-pFA.C<sub>8</sub>H<sub>10</sub>* and *Se-pFA.C<sub>8</sub>H<sub>10</sub>*), symmetry breaking with order-disorder transition (*S-pFA.C<sub>9</sub>H<sub>12</sub>*), rotation of methyl in mesitylene (*Se-pFA.C<sub>9</sub>H<sub>12</sub>*) or twinning (*S-pFA.C<sub>7</sub>H<sub>8</sub>* and *Se-pFA.C<sub>7</sub>H<sub>8</sub>*). Moreover, most of the switching phenomena occur with hysteresis.



**Figure IV.6.** Thermal dependence of the  $\chi_M T$  product of the new compounds in the family of  $[\text{Fe}(\text{PM-}p\text{XA})_2(\text{NCE})_2].S$  ( $E = \text{S}$  and  $\text{Se}$ ,  $S = \text{Solvent}$ ,  $X = \text{F}$  and  $\text{Br}$ ), recorded at 0.4 K/min (in settle mode), before irradiation ( $\blacksquare$ ), under irradiation ( $\blacktriangle$ ), after irradiation in the dark ( $\blacksquare$ ), and the thermal quenching ( $\blacksquare$ ) measurements.

If we have a closer look at **S-*p*FA.C<sub>7</sub>H<sub>8</sub>**, we can see that the HS state can be partially thermally quenched (~15%) at low temperature (Figure IV.6). Upon warming, this Q-HS\* can be observed up to a *T*(TIESST) value of 101 K. Light irradiation applied at 10 K in the LS state also allows to populate this HS\* state, at least partially. Indeed, a 650 nm irradiation allows 50 % of population after 12 hours of irradiation. It is worth mentioning that this irradiation is very slow, indicating a very difficult light-excited process. The *T*(LIESST) curve recorded at 0.4 K/min after irradiation leads to *T*(LIESST) value of 82 K, 20 K lower than the *T*(TIESST) value. This indicates that the structures of the Q-HS\* and *hν*-HS\* states are different.

**S-*p*FA.C<sub>7</sub>H<sub>8</sub>** shows an abrupt SCO with symmetry breaking going from *C2/c* at 300 K to *P-1* at 135 K with an increase of the unit cells parameters. One Fe<sup>2+</sup> crystallographic site and one solvent site in the asymmetric unit at 300 K break into three iron sites and three toluene molecules at 135 K. Moreover, the disordered solvent at 300 K splits in two ordered and one disordered solvent molecules. This symmetry change is accompanied by a reversible twinning of the crystal. In collaboration with Dr. Sébastien Pillet in the University of Lorraine (Nancy, France), the structure of Q-HS\* at 10 K was determined by SCXRD. As shown in Figure IV.7a, the twinning in the Q-HS\* can be demonstrated by the appearance of twin domains that disappear upon warming to 300 K, suggesting a reversible behavior. Therefore a tentative phase diagram can be proposed (Figure IV.7b): From HS to LS the materials moves from *C2/c* to *P-1*. This LS *P-1* phase might be photo-switched into the possible *C2/c* *hν*-HS\*, identical to the HS phase, that relaxes at 82 K. Therefore, the very long photo-switching time needed to induce 50 % of conversion at 10 K might come from the energy needed to erase this twinning. The relaxation upon warming might allow to recover the twinned LS state. The Q-HS\* however seems to be in the *P-1* state, in the twinned state as the initial LS state, the relaxation then occurs between two twinned states. The reasons why the relaxations temperatures are different is not clear and without crystal structures of the *hν*-HS\* and Q-HS\*, it is difficult to conclude.

Nevertheless, this compound clearly shows that the *hν*-HS\* and Q-HS\* might be different, illustrating the fact that the calculation of the distortion parameters using HS and LS values at different temperatures instead of the LS and *hν*-HS\* or Q-HS\* at the same temperature might lead to wrong interpretation and bias any tentative correlation.

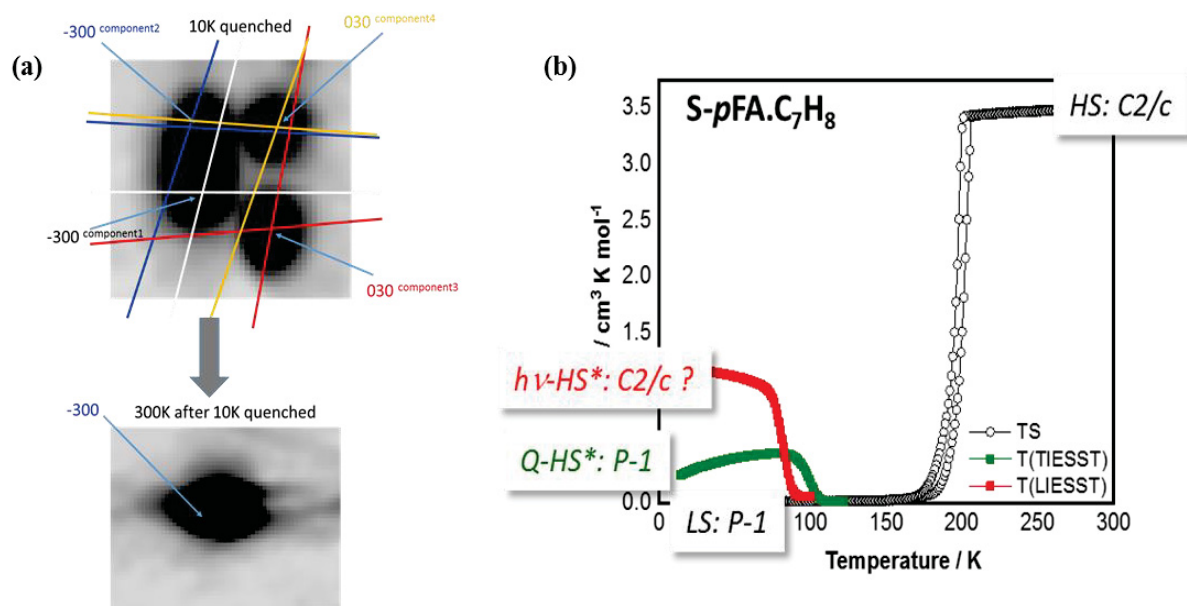


**Figure IV.7.** The reversible symmetry breaking with twin domains in the Q-HS\* at 10 K (a) and a tentative phase diagram of the symmetry breaking at the SCO (b) in compound **S-pFA.C<sub>7</sub>H<sub>8</sub>**

Figures IV.8 and IV.9 report these new compounds on the  $T(\text{LIESST}) = f(\Delta\theta)$ ,  $f(\Delta\zeta)$ ,  $f(\Delta\text{Shape})$  and  $f(\Delta\theta, \Delta\zeta)$  graphs. None of these new compounds are aligned with the other members of the PM-L family. This is particularly the case of **S-pFA.C<sub>7</sub>H<sub>8</sub>** and **Se-pFA.C<sub>7</sub>H<sub>8</sub>** that both exhibit very high  $\Delta\theta$  with  $T(\text{TIESST})$  of 100 K, 70 K below the expected values if there were aligned with the other compounds. Even the Shape parameter that was quite correlating with the previous PM-L compounds fail to present a reliable trend. Compounds **Se-pFA.C<sub>9</sub>H<sub>12</sub>**, **S-pFA.C<sub>7</sub>H<sub>8</sub>** and **Se-pFA.C<sub>7</sub>H<sub>8</sub>** are far away from the red line, suggesting the solvent disorder can influence  $T(\text{LIESST})/T(\text{TIESST})$ . Despite this absence of direct correlation of  $T(\text{LIESST})$  (or  $T(\text{TIESST})$ ) with one structural parameter, Figures IV.9 clearly emphasize that the highest  $T(\text{LIESST})$  are found when both  $\Delta\theta$  and  $\Delta\zeta$  are high and above their respective average values.

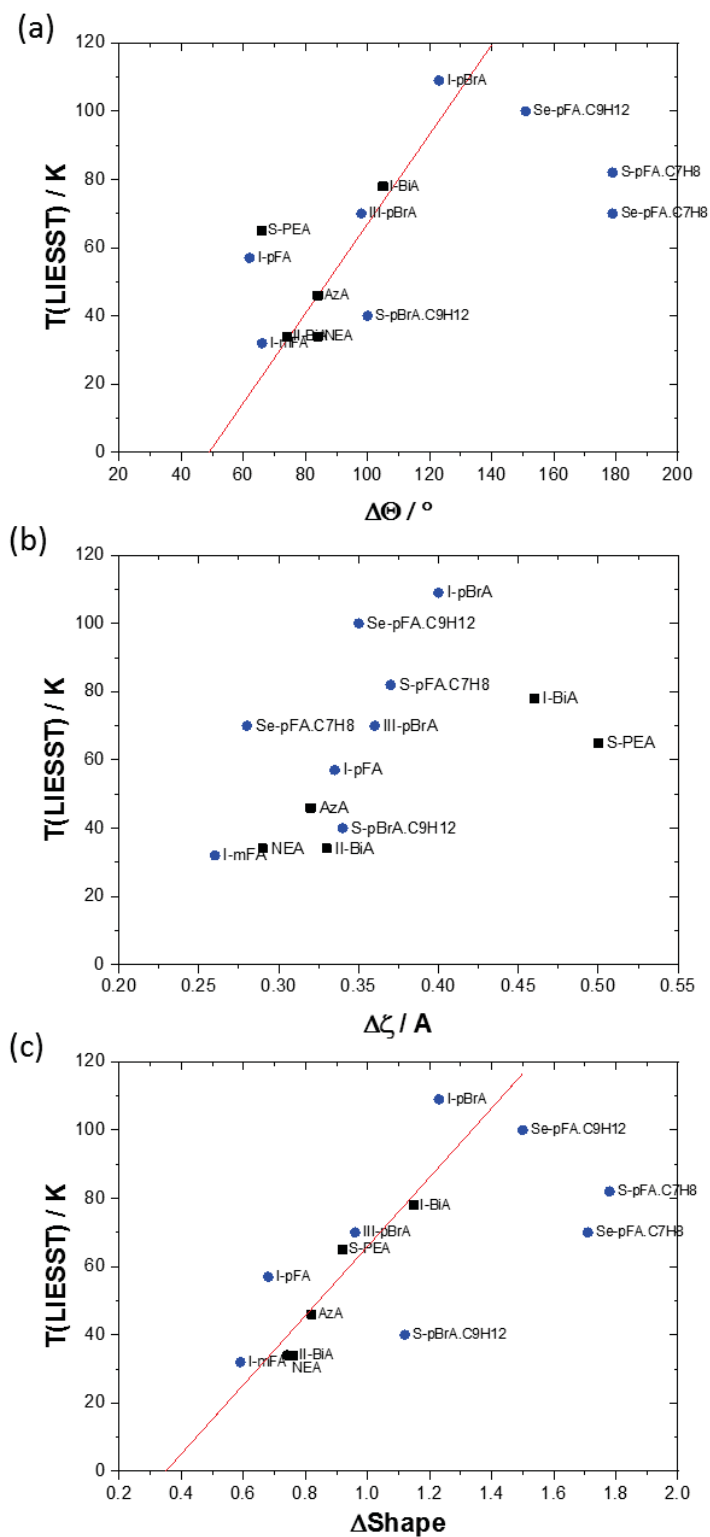
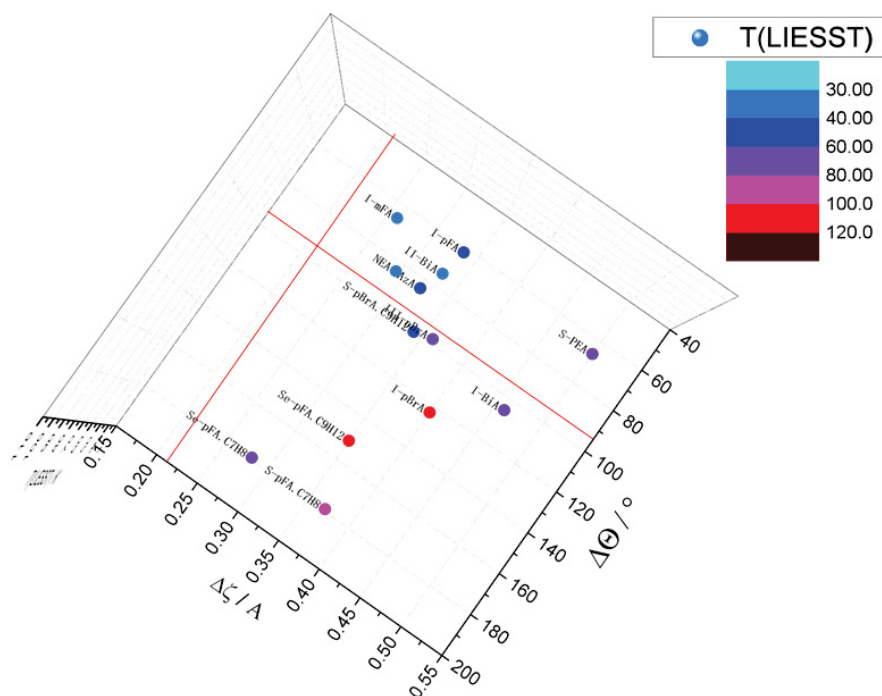


Figure IV.8.  $T(\text{LIESST})$  as function of  $\Delta\Theta$  (a),  $\Delta\zeta$  (b) and  $\Delta\text{Shape}$  (c) for the PM-L family. Blue sphere represent for the compounds reported in Table IV.1 and Table IV.3.



**Figure IV.9.**  $T(\text{LIESST})$  as function of  $\Delta\theta$  and  $\Delta\zeta$  for the whole new PM-L family. The red lines stand for the average  $\Delta\theta$  ( $95^\circ$ ) and  $\Delta\zeta$  ( $0.21 \text{ \AA}$ ) values.

The new compounds additionally obtained in this work clearly show that, even if the coordination sphere distortion parameters are prone to give high  $T(\text{LIESST})$ , symmetry changes (order-disorder, twinning, symmetry breaking) can strongly affect the lifetime of the photo-induced state. This is true as soon as we only discuss the variation of these structural parameters between the HS and LS phases. Without more photo-induced crystal structures we cannot totally exclude that the estimation of the distortion parameters is not accurate in such compounds experiencing significant packing modifications.

#### IV.2.4. Comparison with SCO complexes based on bidentate ligands

We have extended our comparison to other SCO complexes based on bidentate ligands. [Table IV.4](#) summarizes the compounds studied, as well as compounds obtained during this PhD work, separating those experiencing some drastic changes in the crystal packing. We removed compounds with poor LIESST effect or with  $T(\text{LIESST})$  too close to the hysteresis loop and consequently more sensitive to dynamical effects.<sup>31-32</sup> From these 32 compounds the average  $\Delta\theta$  and  $\Delta\zeta$  values can be calculated at  $115^\circ$  and  $0.21 \text{ \AA}$ , respectively.

**Table IV.4.** Overview of some geometrical characteristics of the coordination sphere and  $T(\text{LIESST})$  for selected compounds based on bidentate ligands. The selection is made through the literature and this work on the efficiency of  $T(\text{LIESST})$ , see text for details.

label	Compounds	$\Delta\zeta$ / Å	$\Delta\theta$ / °	$\Delta S$	$T(\text{LIESST})$ / K	comment	Ref.
<i>Without symmetry change</i>							
1	$I\text{-}[\text{Fe}(\text{PM-BiA})_2(\text{NCS})_2]$	0.46	110	1.15	78		4
2	$II\text{-}[\text{Fe}(\text{PM-BiA})_2(\text{NCS})_2]$	0.33	76	0.76	34		4
3	$[\text{Fe}(\text{PM-AzA})_2(\text{NCS})_2]$	0.32	87	0.82	46		4,9
4	$[\text{Fe}(\text{PM-NEA})_2(\text{NCS})_2]$	0.29	84	0.74	58		5
5	$[\text{Fe}(\text{phen})_2(\text{NCS})_2]$	0.255	100	0.96	62		14
6	$[\text{Fe}(\text{phen})_2(\text{NCSe})_2]$	0.156	123	1.06	40		15
7	$I\text{-}p\text{BrA}$	0.4	123	1.23	109		This work
8	$III\text{-}p\text{BrA}$	0.36	98	0.96	70		This work
9	$I\text{-}m\text{FA}$	0.26	66	0.59	32		This work
10	$[\text{Fe}(\text{H}_2\text{B}(\text{pz})_2\text{bpy})]$	0.01	123	0.43	52		16
11	$[\text{FeL}^1_3]\text{ClO}_4$	0.163	73	0.8	48		17
12	$trans\text{-}[\text{Fe}(\text{Cladpat})_2(\text{NCS})_2]$	0.165	65	0.27	30		18
13	$[\text{Fe}(\text{abpt})_2(\text{NCSe})_2]$	0.05	78.1	0.54	32		19
14	$C\text{-}[\text{Fe}(\text{abpt})_2(\text{NCS})_2]$	0.03	92.5	0.61	54		20
15	$D\text{-}[\text{Fe}(\text{abpt})_2(\text{NCS})_2]$	0.001	83	0.48	36		21
16	$trans\text{-}[\text{Fe}(\text{Fc-tzpy})_2(\text{NCSe})_2] \cdot \text{CHCl}_3$	0.051	85.8	0.55	39		22
17	$A\text{-}trans\text{-}[\text{Fe}(\text{tzpy})_2(\text{NCS})_2]$	0.09	95	0.7	54		23
18	$[\text{FeL}^2_2(\text{NCSe})_2]$	0.07	89	0.66	50		24
19	$[\text{Fe}(\text{L}^3)_2(\text{NCS})_2]$	0.08	89.6	0.65	40		25
20	$[\text{Fe}(\text{DPyDT})_2(\text{NCS})_2] \cdot 0.5\text{CH}_3\text{O}$	0.142	74.3	0.45	66		26
21	$[\text{Fe}(\text{tap})_2(\text{NCS})_2]\text{CH}_3\text{CN}$	0.29	99.8	0.76	52		27
<i>With symmetry change</i>							
22	$II\text{-}[\text{Fe}(\text{PM-PEA})_2(\text{NCS})_2]$	0.5	72	0.92	65	Phase transition	4
23	$[\text{Fe}(\text{pic})_3]\text{Cl}_2 \cdot \text{EtOH}$	0.02	130	1.71	45		28
24	$[\text{Fe}(\text{pic})_3]\text{Cl}_2 \cdot \text{MeOH}$	0.009	117.6	1.526	50		29
25	$trans\text{-}[\text{Fe}(\text{L}^4\text{F})_2(\text{NCS})_2] \cdot 2\text{CH}_3\text{CN}$	0.24	64	0.31	58		30
26	$[\text{Fe}(\text{H}_2\text{B}(\text{pz})_2)_2\text{phen}]$	0.006	39.4	0.32	44		16
27	$D'\text{-}[\text{Fe}(\text{abpt})_2(\text{NCS})_2]$	0.108	49	0.29	108	Photo-isomerization	21
28	$I\text{-}p\text{FA}$	0.355	62	0.68	55		This work
29	$S\text{-}p\text{FA} \cdot \text{C}_7\text{H}_8$	0.37	179	1.78	82	Twinning	This work
30	$\text{Se}\text{-}p\text{FA} \cdot \text{C}_7\text{H}_8$	0.28	179	1.71	70	Twinning	This work
31	$\text{Se}\text{-}p\text{FA} \cdot \text{C}_9\text{H}_{12}$	0.35	151	1.5	100	Solvent rotation	This work
32	$S\text{-}p\text{BrA} \cdot \text{C}_9\text{H}_{12}$	0.34	100	1.12	40	Solvent disorder	This work

Figure IV.10 shows the evolution of  $T(\text{LIESST})$  as function of  $\Delta\theta$ ,  $\Delta\zeta$  and  $\Delta\text{Shape}$ . One can clearly see that none of the compounds experiencing a structural rearrangement upon SCO fits the linear trend proposed by Marchivie *et al.* of  $T(\text{LIESST})$  vs  $\Delta\theta$ .<sup>3</sup> This is also the case for the other parameters. If we consider only the compounds without any structural rearrangement upon SCO (compounds **1** to **21**), most of them are aligned along the  $T(\text{LIESST})$  vs  $\Delta\theta$  line. Only  $[\text{Fe}(\text{phen})_2(\text{NCSe})_2]$  (**6**)<sup>15</sup>,  $[\text{Fe}(\text{H}_2\text{B}(\text{pz})_2)_2\text{bpy}]$  (**10**)<sup>16</sup> and  $[\text{Fe}(\text{DPyDT})_2(\text{NCS})_2]0.5\text{CH}_3\text{O}$  (**20**)<sup>26</sup> are clearly misaligned. A deeper look at these compounds might help to understand this fact. Regarding the evolution of  $T(\text{LIESST})$  as function of  $\Delta\text{Shape}$ , more compounds are misaligned compare to the trend found in Figure IV.7. It indicates that the Shape parameter and  $\Delta\theta$  are not strictly equivalent. When Shape account for all the modifications,  $\Delta\theta$  only focus on one aspect, giving more insight on the molecular geometry. Finally, concerning  $\Delta\zeta$ , the cloud of points prevent any tentative of correlation.

If we look at the  $T(\text{LIESST}) = f(\Delta\theta, \Delta\zeta)$  (Figure IV.11), we can still observe that the highest  $T(\text{LIESST})$  are for compounds with both high values of  $\Delta\theta$  and  $\Delta\zeta$ . This is confirmed statistically even if we account for the compounds that experience structural rearrangement upon SCO. There are however some noticeable exceptions.

The  $[\text{Fe}(\text{pic})_3]\text{Cl}_2 \cdot \text{EtOH}$  (**23**) for instance exhibits a high  $\Delta\theta$  value of  $130^\circ$  and we could expect a  $T(\text{LIESST})$  around 100 K while it is only of 45 K.<sup>28</sup> This might correspond to the very weak  $\Delta\zeta$  of  $0.02 \text{ \AA}$  that “compensates” the huge trigonal distortion. It is not clear if the weak  $\Delta\zeta$  comes from the structural rearrangement reported in this compound. Polymorph D of the  $[\text{Fe}(\text{abpt})_2(\text{NCS})_2]$  compound (**27**) exhibits an unexpectedly high  $T(\text{LIESST})$  of 108 K regarding the weak  $\Delta\theta$  ( $49^\circ$ ) and  $\Delta\zeta$  ( $0.10 \text{ \AA}$ ) values.<sup>21</sup> When irradiation is long enough, the  $\text{NCS}^-$  changes into  $\text{SCN}^-$ , leading the  $\text{FeN}_6$  coordination sphere to a  $\text{FeN}_5\text{S}$  octahedron. This high  $T(\text{LIESST})$  value with such low parameters might come from the additional energy needed to promote the thermal-isomerization during the  $\text{HS}^*$  to LS relaxation process. Finally,  $[\text{Fe}(\text{H}_2\text{B}(\text{pz})_2)_2\text{phen}]$  (**26**) presents a high  $T(\text{LIESST})$  regarding the weak  $\Delta\theta$  ( $39^\circ$ ) and  $\Delta\zeta$  ( $0.006 \text{ \AA}$ ) values. This might come from the fact that the  $h\nu\text{-HS}^*$  corresponds to a polymorph of the HS state.<sup>16</sup> The  $\Delta\theta$  calculated between the LS and the  $h\nu\text{-HS}^*$  ( $51^\circ$ ) is greater than the one calculated from HS and LS states. It is however not enough to bring the compound into the “high  $T(\text{LIESST})$ ” region in Figure IV.11.

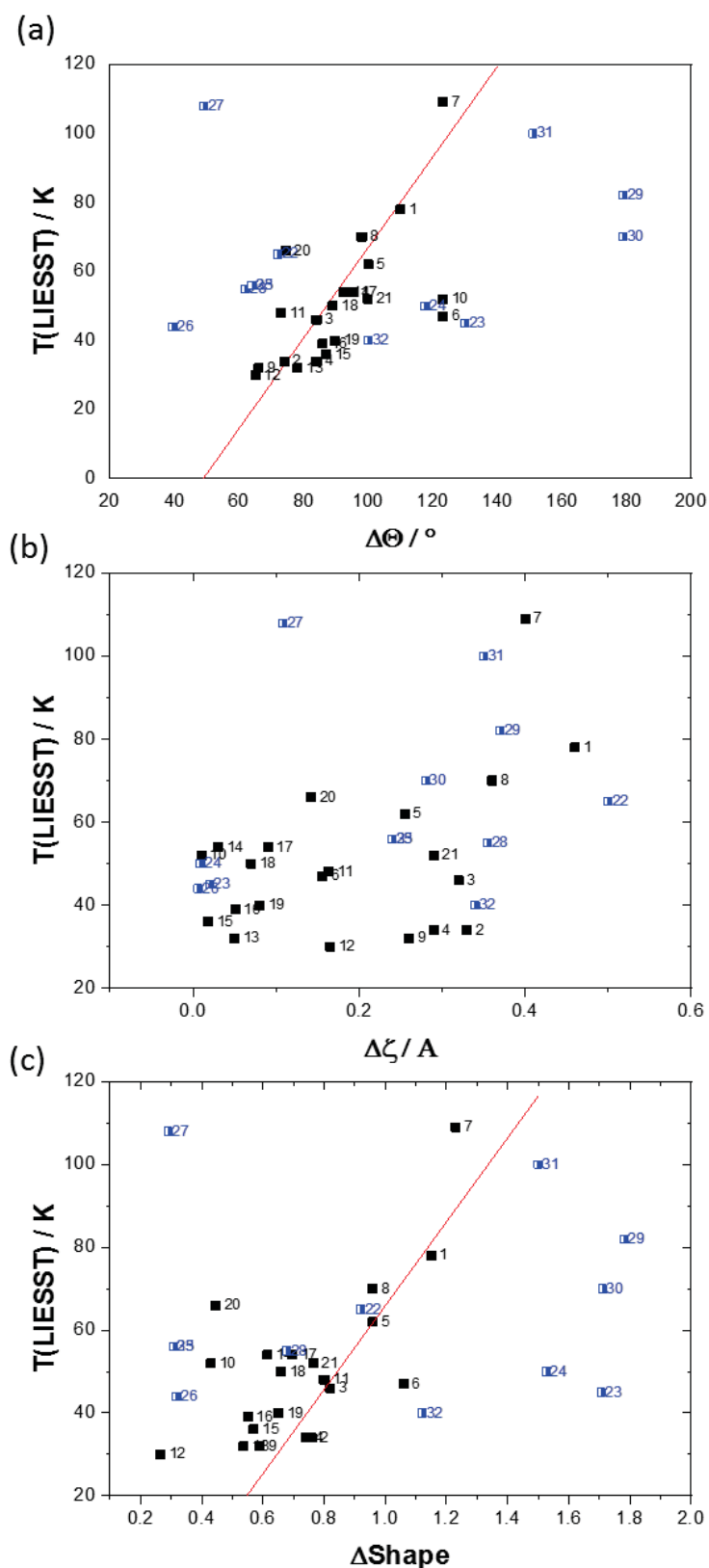
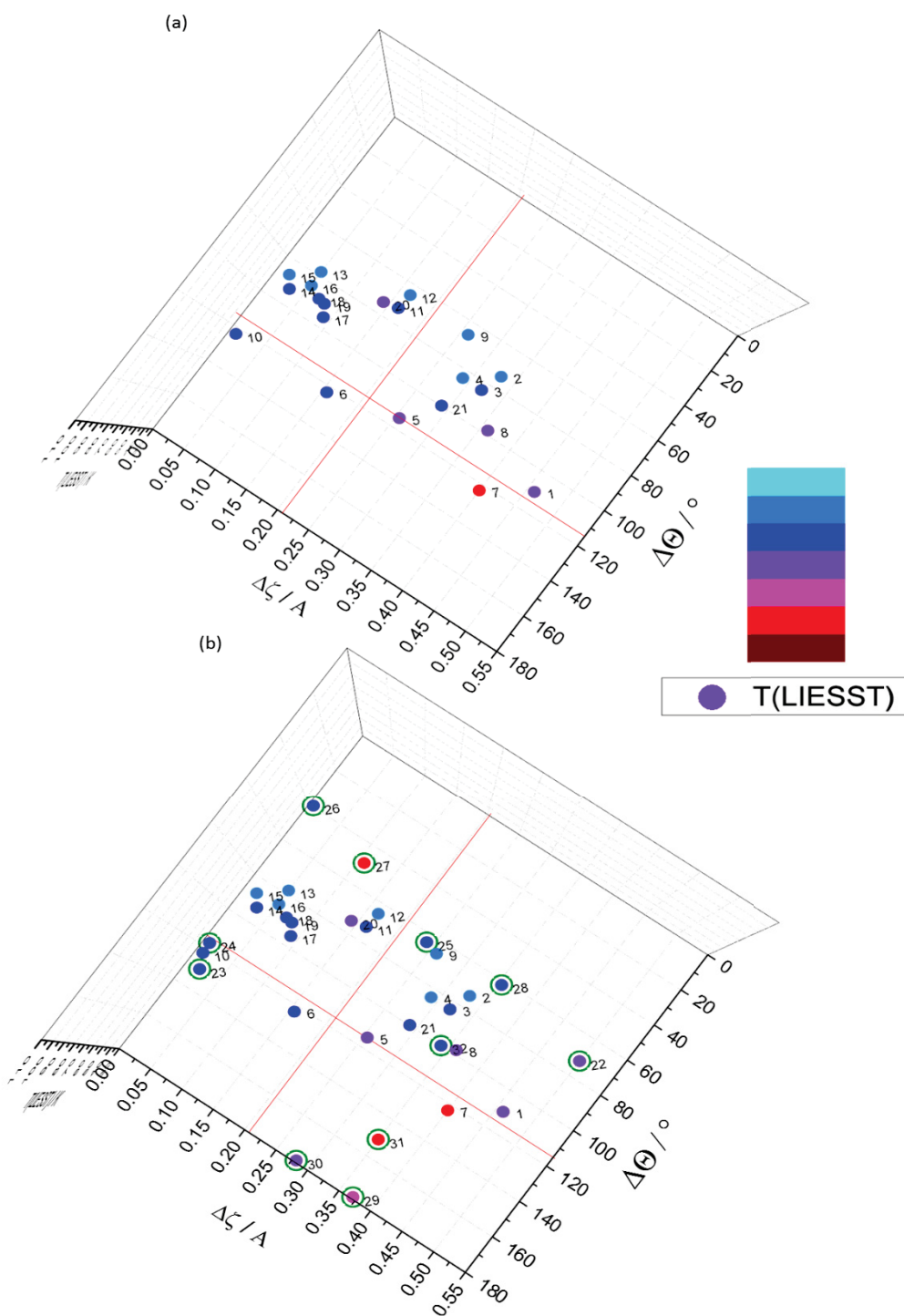


Figure IV.10.  $T(\text{LIESST})$  as function of  $\Delta\Theta$  (a),  $\Delta\zeta$  (b) and  $\Delta\text{Shape}$  (c). The half-filled blue squares correspond to compound experiencing significant structural rearrangement upon SCO. The labels correspond to the compounds listed in Table IV.4.



**Figure IV.11.**  $T(\text{LIESST})$  as function of  $\Delta\Theta$  and  $\Delta\zeta$  for compounds without any structural rearrangement at SCO (a) and including compounds experiencing structural rearrangement upon SCO (green circles in b). The red lines stand for the average  $\Delta\Theta$  ( $115^\circ$ ) and  $\Delta\zeta$  ( $0.21 \text{ \AA}$ ) values.

The detailed analysis of the influent parameters on lifetime of the  $h\nu\text{-HS}^*$  metastable state allows us to draw a general picture for this lifetime, as a mirror of the multiscale view of the thermal spin crossover, as proposed in the following chapter.

### **IV.3. Lifetime of the metastable HS\* state – a multiscale view**

From the above analysis of data, including other information from the literature, we can discuss more accurately what influences  $T(\text{LIESST})$  and more precisely the lifetime of the photo-induced state. This lifetime has been deeply studied by Andreas Hauser in the 80's and 90's.<sup>33-35</sup> As already introduced in [Part I.2](#), the inverse energy gap law links  $T_{1/2}$  to the relaxation rate at  $T \rightarrow 0 \text{ K}$ .<sup>33</sup> In a classical 2D view of the vibrational potential wells, it corresponds to a variation of the activation energy through a vertical displacement of the potential wells. The higher  $T_{1/2}$ , to lower the activation energy, the faster the relaxation. In addition, Hauser described that the higher the horizontal displacement of the potential wells (that is the higher the average elongation of bond lengths), the higher the activation energy, the slower the relaxation.<sup>34</sup> As mentioned in [Part I.2](#), this view has been shown to be no more valid, or at least not sufficient to describe some behaviors. Finally, Hauser deeply investigated the influence of cooperativity on the relaxation features, that is the isothermal evolution of the HS\* fraction as function of time.<sup>35</sup> He showed that cooperative interactions lead to self-accelerated relaxation (see [Part I.2.2](#)). While cooperativity and  $T_{1/2}$  are thermodynamic parameters that account for the collective behavior of SCO, only the average elongation of bond lengths is a molecular parameter, related to the coordination sphere. For a given elongation of bond lengths, cooperativity can influence the lifetime. This is a first indication that the lifetime of the photo-induced state is sensitive not only to the coordination sphere but also to its environment within the crystal: everything being equal, an increase of the sole cooperativity parameters fastens the relaxation.

Later on, the introduction of the trigonal distortion evolution at SCO,  $\Delta\theta$ , and the supposed effect of denticity on the  $T(\text{LIESST})$ , brought the attention on the coordination sphere as a key scale to control the lifetime of the photo-induced state and the increase of  $T(\text{LIESST})$ .<sup>3,36,37</sup> This PhD work is based on this assumption, with a focus on coordination sphere distortion to go toward a 2-parameters (at least) description of the HS\* lifetime. Along this work, compared to about 30 bidentate-based complexes from the literature, a much more complicated view has been evidenced that is detailed below as a multiscale view.

- Coordination sphere scale

The breathing of the coordination sphere is anisotropic, the HS state being bigger and more distorted. This includes both the angular distortion that measures the angular deviation of the coordination sphere to a perfect octahedron,  $\Sigma$  and  $\Theta$ , and anisotropy of bond lengths,  $\zeta$ , that measures the deviation of these bond lengths from the average value  $\langle \text{Fe-L} \rangle$ . More than a given value, it is their variations upon spin crossover that seem to be relevant as influent parameters on the lifetime of  $h\nu\text{-HS}^*$ . This is particularly the case for  $\Delta\Theta$  and  $\Delta\zeta$  as discussed in Part IV.2. Figure IV.11b has evidenced that compounds with the highest  $T(\text{LIESST})$  values are those exhibiting the highest  $\Delta\Theta$  and  $\Delta\zeta$ . This implies that upon SCO, the coordination sphere has to be both distorted and elongated, as schematized in Figure IV.12. From the chemical point of view, promoting both distortion and elongation is not trivial. All this analysis on the relevant parameters on the lifetime of the photo-induced state deeply changes the perspectives in terms of chemical design of long-lived metastable state in SCO compounds.

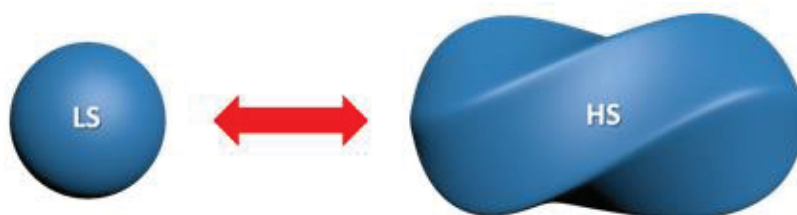


Figure IV.12. Schematic picture of the anisotropic variation of the coordination sphere at SCO, including distortion and elongation.

This kind of picture might explain why compounds with Fe-L bond breaking upon SCO exhibit high  $T(\text{LIESST})$ . Indeed, bond breaking tend to favor elongated geometries. There are two reported situations of bond break. The first case is the change of coordination number and the second case is the photo-induced linkage isomerization. A rare example of change in coordination number upon SCO was reported on the complex  $[\text{FeL}(\text{CN})_2] \cdot \text{H}_2\text{O}$  ( $\text{L} = [2,13\text{-dimethyl-6,9-dioxa-3,12,18-triazabicyclo}[12.3.1]\text{octadeca-1(18),2,12,14,16-pentaene}]$ ) where the coordination metal environment changes from a hexa-coordinate LS state to a hepta-coordinate  $\text{HS}^*$  state owing to the photo-induced Fe-O bonding.<sup>38</sup> Another example involves Fe-N bond break in an analog of the previous compound  $[\text{Fe}(\text{LN}_5)(\text{CN})_2] \cdot \text{MeOH}$  ( $\text{LN}_5 = 2,13\text{-dimethyl-3,6,9,12,18-pentaazabicyclo}[12.3.1]\text{octadeca-1(18),2,12,-14,16-pentaene}$ ).<sup>39-40</sup> The photo-induced linkage isomerization was reported in polymorph D of  $\text{trans-}[\text{Fe}(\text{abpt})_2(\text{NCS})_2]$  ( $\text{abpt} = 4\text{-amino-3,5-bis(pyridin-2-yl)-1,2,4-triazole}$ ). When irradiation is long enough, the  $\text{NCS}^-$  changes into  $\text{SCN}^-$ , leading the  $\text{FeN}_6$  coordination sphere to a  $\text{FeN}_5\text{S}$  octahedron. For

short irradiation, no changes in the coordination geometry are observed and  $T(\text{LIESST}) = 36 \text{ K}$  while for the  $\text{FeN}_5\text{S}$  situation  $T(\text{LIESST})$  rises at  $108 \text{ K}$ .<sup>21</sup> This high  $T(\text{LIESST})$  is associated to weak  $\Delta\theta$  ( $49^\circ$ ) and  $\Delta\zeta$  ( $0.10 \text{ \AA}$ ). This unexpectedly high  $T(\text{LIESST})$  value with such low parameters might come from the additional energy needed to promote the thermal-isomerization.

This also agrees with the recent study made on tripodal ligands-based complexes, showing that, at least thermal spin crossover, occurs along a coupled breathing/torsion reaction coordinate, moving the complex from octahedral LS state to trigonal prismatic HS state.<sup>41</sup>

This analysis, unfortunately has some drawbacks. The main one is that, in most cases the  $\Delta\theta$  and  $\Delta\zeta$  values are calculated using the HS and LS values, at different temperatures, instead of the LS and HS\* values at the same temperature. This is particularly important when dealing with symmetry changes in the materials. Indeed, as discussed above, compounds with symmetry changes are more prone to stand out of the trend. This is particularly the case of  $[\text{Fe}(\text{PM-PEA})_2(\text{NCS})_2]$ ,  $[\text{Fe}(\text{pic})_3]\text{Cl}_2 \cdot \text{EtOH}$  or **S-*p*FA.C7H8** and **Se-*p*FA.C7H8** as discussed above. For these compounds, nothing insures that the  $\text{LS} \leftrightarrow \text{HS}^*$  and the  $\text{LS} \leftrightarrow \text{HS}$  transition have the same structural changes. Therefore, using the  $\Delta\theta$  and  $\Delta\zeta$  values calculated from the  $\text{LS} \leftrightarrow \text{HS}$  transition might be wrong, explaining why these compounds do not fit the trend.

This latter aspect points out the fact that the lifetime of the  $\text{HS}^*$  state might be influenced by other aspects than just the coordination sphere geometry and the cooperativity. Indeed, cooperativity does not necessarily implies symmetry changes. Therefore, looking at upper scales of the materials and their influence on the  $\text{HS}^*$  lifetime is important.

- Conformational change

When studying the structural movies of thermal spin crossover, clear motions of ligands have been observed. In this current work, **I-*p*BrA** and **III-*p*BrA** clearly show a rotation of the bromophenyl rings, both upon  $\text{LS} \leftrightarrow \text{HS}^*$  and  $\text{LS} \leftrightarrow \text{HS}$  transitions. However, despite similar rotation, its impact on the coordination sphere and  $T(\text{LIESST})$  (on  $T(\text{TIESST})$  more precisely) is different since **I-*p*BrA** shows a  $T(\text{TIESST})$  of  $107 \text{ K}$  and **III-*p*BrA** of  $70 \text{ K}$ . The same effect does not gives the same result in that case. This effect can be related to LD-LISC phenomenon (Ligand-Driven Light-Induced Spin Change) where a change in ligand conformation, triggered by light, changes the ligand field and the subsequent SCO properties.<sup>42</sup> However, in the present compounds, the change in conformation is not decorrelated from the SCO and it is therefore difficult to disentangle both effects.

In the literature, two different thermal spin transitions have been observed in compound  $[\text{Fe}(\text{n-Bu-im})_3\text{tren}](\text{PF}_6)_2$   $[(\text{n-Bu-im})_3(\text{tren}) = \text{n-butylimidazoltris(2-ethylamino)amine}]$  depending on the sweeping rate of the temperature.<sup>43</sup> Two different low spin structures are obtained upon fast cooling at 4 K/min or slow cooling at 0.1 K/min, labeled LS1 and LS2, respectively. Irradiation from the LS2 state leads to a  $T(\text{LIESST})$  around 50 K while irradiating from LS1 leads to a  $T(\text{LIESST})$  of 80 K. Delgado *et al.* found that an irradiation from LS1 at 10 K leads to a short-lived  $h\nu\text{-HS}^*$  while irradiating at 80 K leads to a long-lived  $h\nu\text{-HS}^*$  state, with a relaxation 40 times slower than that recorded at 80 K but obtained from irradiation at 10 K. The structures of  $h\nu\text{-HS}^*$  states were obtained by irradiation at 10 K and 80 K using synchrotron single-crystal X-ray diffraction. The difference in lifetime was attributed to the promotion of a disorder in conformation of the butyl chains of the ligand when irradiating at 80 K while this disorder is not observed under irradiation at 10 K.

- Intermolecular interactions

Since both the volume of the molecule and the ligand conformation can change upon SCO, the intermolecular interactions can be strongly affected. Reversely, as we have described in **I-*pBrA*** and **III-*pBrA***, short intermolecular H---H interactions might drive ligand conformation changes. Therefore, there could be subtle feedback effects. Such feedback effect might be viewed as cooperativity.

Sometimes, changes in intermolecular interactions are driven by solvent reorganization. In compound **Se-*pFA.C<sub>9</sub>H<sub>12</sub>*** ( $[\text{Fe}(\text{PM-}i\text{pFA})_2(\text{NCSe})_2].\text{C}_9\text{H}_{12}$ ) the methyl group of the mesitylene solvent rotates by 30° from HS to LS. It is not clear yet if the 32 K large hysteresis that is observed nor if the recorded  $T(\text{LIESST})$  and  $T(\text{TIESST})$  around 100 K, are driven by this conformational change. Up to now, the crystal structures of the Q- $\text{HS}^*$  and  $h\nu\text{-HS}^*$  are not determined. Regarding the  $\Delta\theta$  value of 151°, one may expect much higher  $T(\text{LIESST})$ , so probably, the conformational change of mesitylene affects the lifetime of the  $\text{HS}^*$ . In the compound  $[\text{FeL}_2][\text{BF}_4]_2 \cdot \text{MeCN}$  with  $\text{L} = 4\text{-}\{\text{isopropylsulfanyl}\}\text{-}2,6\text{-di}\{\text{pyrazol-1-yl}\}\text{-pyridine}$ , a reorientation of the linear acetonitrile was reported to contribute to a temperature-dependent lattice activation barrier to the spin-transition associated to a higher  $T(\text{LIESST})$  compared to other solvatomorphs.<sup>44</sup>

Obviously, such changes in intermolecular interactions might change cooperativity. Another approach to tune the cooperativity is the metal dilution. By substituting the Fe<sup>2+</sup> ion by SCO-inactive cation, the cooperativity pathways are cut and some internal pressure is exert. The bigger the SCO-inactive ion, the higher the “negative” internal pressure, the more the HS state is stabilized. Solid solutions are generally made with, Ni<sup>2+</sup>, Co<sup>2+</sup>, Zn<sup>2+</sup>, Mn<sup>2+</sup>, and Cd<sup>2+</sup> in order of increasing ionic radius. For a given amount of non-SCO active metal, the bigger the ion the more  $T_{1/2}$  is decreased.<sup>45</sup> The effect of metal dilution on  $T(\text{LIESST})$  has been studied on several compounds and especially on [Fe<sub>x</sub>M<sub>1-x</sub>(phen)<sub>2</sub>(NCS)<sub>2</sub>] with phen = 1,10-phenanthroline (M = Ni<sup>2+</sup>, Zn<sup>2+</sup>, Mn<sup>2+</sup> and Cd<sup>2+</sup>).<sup>46</sup> It was reported that substitution of Fe<sup>2+</sup> ions by Ni<sup>2+</sup> ions induces a decrease of  $T(\text{LIESST})$  while with Zn<sup>2+</sup>, no change in  $T(\text{LIESST})$  was observed and for Cd<sup>2+</sup> a 40 K increase of  $T(\text{LIESST})$  was noticed.<sup>47</sup> This effect was also reported on relaxation kinetics.<sup>48</sup> These studies and others clearly show that these solid solutions do not follow the “inverse energy gap law” nor the  $T(\text{LIESST})$  vs  $T_{1/2}$  trend, indicating that  $T(\text{LIESST})$  is indeed dependent on parameters external to the coordination sphere.<sup>49</sup>

- Molecular rearrangement and symmetry breaking

Several kinds of structural rearrangements may occur and influence the lifetime of the photo-induced state.

As we have seen in **I-pFA**, and in various solvatomorphs, some disordered crystallization solvent molecule create different intermolecular interaction networks around the various Fe<sup>2+</sup> sites there are interacting with. However, in the temperature range of study, no clear ordering of solvent was observed. However, in the literature, several compounds are reported to experience order-disorder of solvent or counter-ion upon SCO, but studies of the metastable HS\* state in these system remains rare.<sup>50</sup> Let us note that the order-disorder hysteretic behaviour in the tridentate ligand-based complex [Fe(H<sub>4</sub>L)<sub>2</sub>] [ClO<sub>4</sub>]<sub>2</sub>·H<sub>2</sub>O·2(CH<sub>3</sub>)<sub>2</sub>CO is supposed to be responsible of the high  $T(\text{LIESST})$  value of 104 K.<sup>51</sup>

In **S-pFA.C<sub>9</sub>H<sub>12</sub>** a symmetry breaking has been observed leading to a two-step character of the SCO. The  $h\nu$ -HS\*, even if incompletely populated, exhibits a two-step  $T(\text{LIESST})$  curve, without clear influence of the symmetry breaking on its lifetime. Symmetry breaking due to elastic competition is increasingly reported in the last ten years, especially on 2D and 3D coordination polymers like the Hoffman-like structures.<sup>52-54</sup> Subtle effects might be observed with some regime change in the relaxation rate but without information on the  $h\nu$ -HS\* structure

it is often difficult to discuss in detail.<sup>55</sup> In compound  $[\text{FeH}_2\text{L}^{2-\text{Me}}][\text{ClO}_4]_2$ , symmetry breaking occurs at around 120 K, which leads to two different LS phases and two iron sites appear at 100 K with the doubling of  $a$  value.<sup>56</sup> The relaxation from  $h\nu\text{-HS}^*$  to LS occurs through an intermediate LS high-symmetry phase, which suggests dynamical separation of spin and lattice degrees of freedom in the relaxation process from the photo-induced state.<sup>57</sup> In the  $\{\text{Fe}[\text{H}_2\text{B}(\text{pz})_2]_2\text{L}\}$  family symmetry breaking only occurs with  $\text{L} = \text{phen}$  (compound 26 of Table IV.4) leading to a different and lower  $T(\text{LIESST})$  of 44 K than with  $\text{L} = \text{bpy}$  without symmetry breaking ( $T(\text{LIESST}) = 52$  K).<sup>16</sup> Symmetry breaking from  $h\nu\text{-HS}^*$  to LS also occurs in other compounds, including polymorph C of *trans*- $[\text{Fe}(\text{abpt})_2(\text{NCS})_2]$ <sup>20</sup>,  $[\text{FeH}_2\text{L}^{2-\text{Me}}][\text{XF}_6]_2$  ( $\text{L} = \text{bis}\{[(2\text{-methylimidazol-4-yl)methylidene]-3\text{-aminopropyl}\}\text{ethylenediamine}$ ,  $\text{X} = \text{P}$  and  $\text{As}$ )<sup>58-</sup><sup>59</sup>,  $[\text{FeL}_{\text{eq}}(\text{bppa})] \cdot \text{MeOH}$  ( $\text{L}_{\text{eq}} = \{3,3'\text{-}[1,2\text{-phenylenebis(iminomethylidene)]bis(2,4-pentanedionato)(2-)-N,N',O2,O2'}\}$ ,  $\text{bppa} = 1,3\text{-bis(4-pyridyl)propane}$ )<sup>60</sup>.

At upper scale, some twinning may happen, as observed in **S-pFA.C7H8**. The occurrence of light-induced twinning remains rather rare in the literature. Compound  $[\text{Fe}(3\text{-bpp})_2][\text{Au}(\text{CN})_2]_2$  shows a two steps thermal hysteresis of 45 K, accompanied by a reversible reconstructive structural transition and twinning. The low conversion of LIESST as well as unexpected  $T(\text{LIESST})$  values are attributed to the high energy cost of this twinning that requires huge motion of molecules.<sup>61</sup> An unpublished results from Triki *et al.* has shown the reversible photo-induced twinning that leads to a competition of long-range and short-range interactions during the relaxation process.<sup>62</sup>

The number of structures in the  $\text{HS}^*$  state remains relatively rare yet to afford a clear picture of the influence of such structural rearrangement on the lifetime of the  $\text{HS}^*$  state.

- Nanoscale

Finally, to complete the multiscale view of  $T(\text{LIESST})$ , we have to mention the few studies made on nanoparticles. A first report was made by Neville *et al.* on nanoparticles of  $[\text{Fe}(\text{NCS})_2(\text{bpe})_2]$ . It was shown that, down to 80 nm, the  $T(\text{LIESST})$  temperature does not change.<sup>63</sup> However, a recent report shows relatively opposite observations. Reducing the size of  $[\text{Fe}(\text{pz})\text{Pt}(\text{CN})_4]$  particles induces a drastic lowering of the relaxation rate after photo-excitation.<sup>64</sup> Up to now, this nanoscale is poorly explored in terms of lifetime of the photo-induced state, as well as the coherent domain scale still unexplored.

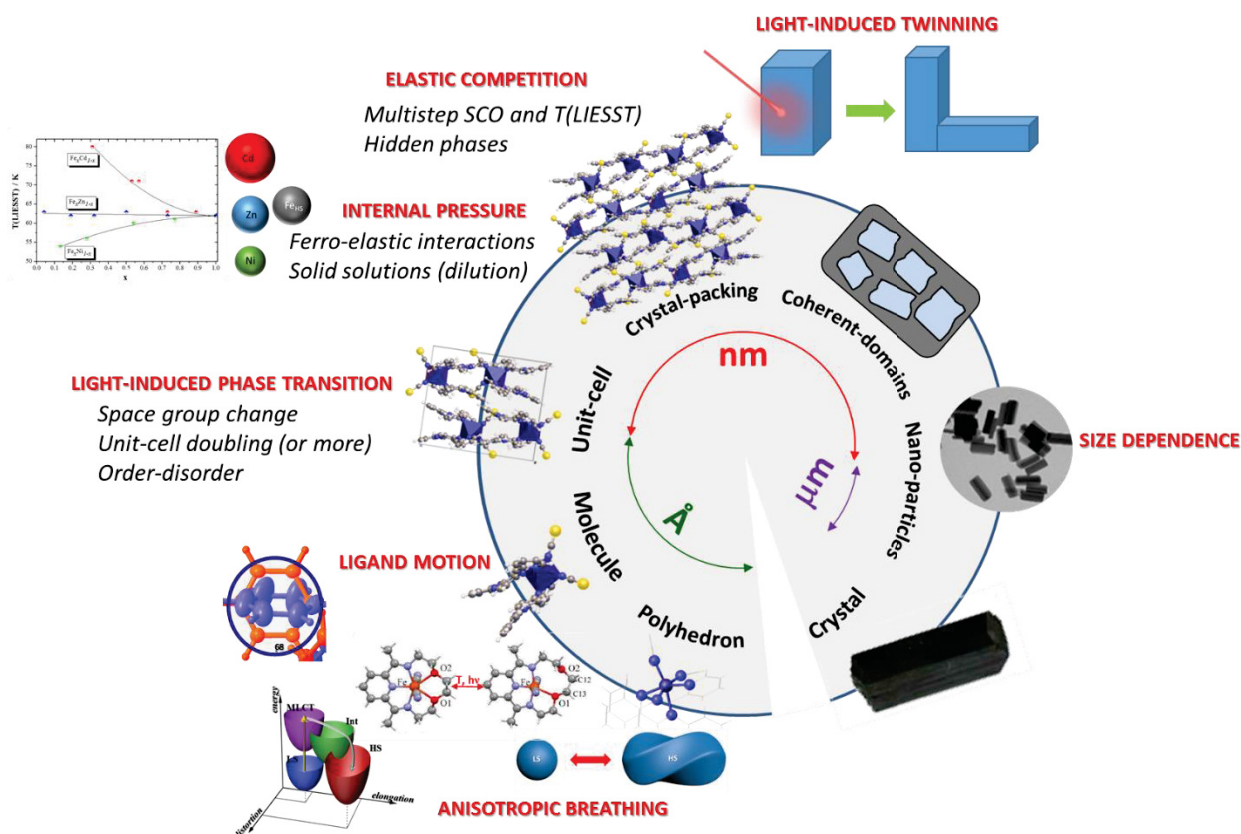


Figure IV.13. Multiscale view of the relaxation temperature of  $T(\text{LIESST})$  showing events or features linked to  $T(\text{LIESST})$ . Adapted from ref. 64.

In summary, the energy barrier from  $h\nu\text{-HS}^*$  to LS associated to the relaxation temperature can be influenced by the anisotropic distortion of the coordination sphere, the variation of ligand conformation, the modification of interactions, the molecular rearrangement as well as symmetry breaking. In other words, the relaxation from  $h\nu\text{-HS}^*$  to LS can also be viewed as a multiscale process as shown in Figure IV.13, similar to the multiscale view of thermal SCO.<sup>65</sup>

The important impact of such view is that it emphasizes the few amount of photo-induced structures to evidence the real modifications upon light-irradiation and relaxation. Moreover, it clearly shows that, even if everything seems to be controlled at the coordination sphere level, all the chemical design of this sphere might be maximized or minimized by all the other physical scales. In forthcoming research, the target will be to make the synergy between coordination sphere, ligand conformation and symmetry breaking during the LIESST process to reach the maximum of relaxation temperature.

## Bibliography

- [1] J. F. Létard, *J. Mater. Chem.*, 2006, **16**, 2550.
- [2] M. Buron-Le Cointe, J. Hébert, C. Baldé, N. Moisan, L. Toupet, P. Guionneau, J. F. Létard, E. Freysz, H. Cailleau, E. Collet, *Phys. Rev. B.*, 2012, **85**, 064114.
- [3] M. Marchivie, P. Guionneau, J. F. Létard, D. Chasseau, *Acta Cryst.*, 2005, **B61**, 25.
- [4] P. Guionneau, J. F. Létard, D. S. Yufit, D. Chasseau, G. Bravic, A. E. Goeta, J. A. K. Howard, O. Kahn, *J. Mater. Chem.*, 1999, **9**, 985.
- [5] J. F. Létard, J. M. Kollmansberger, C. Carbonera, M. Marchivie, P. Guionneau, *C. R. Chim.*, 2008, **11**, 1155.
- [6] T. Boonprab, S. J. Lee, S. G. Telfer, K. S. Murray, W. Phonsri, G. Chastanet, E. Collet, E. Trzop, G. N. L. Jameson, P. Harding, D. J. Harding, *Angew. Chem. Int. Ed.*, 2019, **58**, 11811.
- [7] E. Tailleur, M. Marchivie, N. Daro, G. Chastanet, P. Guionneau, *Chem. Commun.*, 2017, **53**, 4763.
- [8] E. Tailleur, M. Marchivie, P. Negrier, D. Denux, S. Massip, Denise Mondieig, G. Chastanet, P. Guionneau, *Cryst. Eng. Comm.*, 2019, **21**, 6246.
- [9] S. Lakhroufi, M. H. Lemee-Cailleau, G. Chastanet, P. Rosa, N. Daro, P. Guionneau, *Phys. Chem. Chem. Phys.*, 2016, **18**, 28307.
- [10] L. Capes, J. F. Létard, O. Kahn, *Chem. Eur. J.*, 2000, **6**, 2246.
- [11] N. Paradis, F. Le Gac, P. Guionneau, Largeteau, A., D. S. Yufit, P. Rosa, J. F. Létard, G. Chastanet, *Magnetochemistry*, 2016, **2**, 15.
- [12] L. J. Kershaw Cook, R. Kulmaczewski, O. Cespedes, M. A. Halcrow, *Chem. Eur. J.*, 2016, **22**, 1789.
- [13] R. Kulmaczewski, E. Trzop, L. J. Kershaw Cook, E. Collet, G. Chastanet, M. A. Halcrow, *Chem. Commun.*, 2017, **53**, 13268.
- [14] B. Gallois, J. A. Real, C. Hauw, J. Zarembowitch, *Inorg. Chem.*, 1990, **29**, 1152.
- [15] E. J. MacLean, C. M. McGrath, C. J. O'Connor, C. Sangregorio, J. M. Seddon, E. Sinn, F. E. Sowrey, S. J. Teat, A. E. Terry, G. B. Vaughan, N. A. Young, *Chem. Eur. J.*, 2003, **9**, 5314.
- [16] A. L. Thompson, A. E. Goeta, J. A. Real, A. Galet, M. Carmen Munoz, *Chem. Commun.*, 2004, **12**, 1390.

- [17] J. R. Thompson, R. J. Archer, C. S. Hawes, A. Ferguson, A. Wattiaux, C. Mathonière, R. Clérac, P. E. Kruger. *Dalton Trans.*, 2012, **41**, 12720.
- [18] N. Wannarit, O. Roubeau, S. Youngme, P. Gamez, *Eur J. Inorg. Chem.*, 2013, 730.
- [19] H. E. Mason, M. L. Hamilton, J. A. Howard, H. A. Sparkes, *New J. Chem.*, 2018, **42**, 18028.
- [20] C. H. Shih, C. F. Sheu, K. Kato, K. Sugimoto, J. Kim, Y. Wang, M. Takata. *Dalton Trans.*, 2010, **39**, 9794.
- [21] C. F. Sheu, C. H. Shih, K. Sugimoto, B. M. Cheng, M. Takata, Y. Wang, *Chem. Commun.*, 2012, **48**, 5715.
- [22] T. Romero-Morcillo, F. J. Valverde-Muñoz, L. Piñeiro-López, *Dalton Trans.*, 2015, **44**, 18911.
- [23] C. F. Sheu, K. Chen, S. M. Chen, Y. S. Wen, G. H. Lee, J. M. Chen, J. F. Lee, B. M. Cheng, H. S. Sheu, N. Yasuda, Y. Ozawa, K. Toriumi, Y. Wang. *Chem. Eur. J.*, 2009, **15**, 2384.
- [24] J. L. Wang, Q. Liu, X. J. Lv, R. L. Wang, C. Y. Duan, T. Liu, *Dalton Trans.*, 2016, **45**, 18552.
- [25] J. L. Wang, Q. Liu, Y. S. Meng, X. Liu, H. Zheng, Q. Shi, C. Y. Duan, T. Liu, *Chem. Sci.*, 2018, **9**, 2892.
- [26] K. Takahashi, T. Kawakami, Z. Z. Gu, Y. Einaga, A. Fujishima, O. Sato, *Chem. Commun.*, 2003, **18**, 2374.
- [27] J. A. Real, M. C. Munoz, E. Andres, T. Granier, B. Gallois, *Inorg. Chem.*, 1994, **33**, 3587.
- [28] M. Mikami, M. Konno, Y. Saito, *Acta Cryst. B*, 1980, **36**, 275.
- [29] B. A. Katz, C. E. Strouse, *J. Am. Chem. Soc.*, 1979, **101**, 6214.
- [30] N. Wannarit, O. Roubeau, S. Youngme, S. J. Teat, P. Gamez. *Dalton Trans.*, 2013, **42**, 7120.
- [31] F. Varret, K. Boukheddaden, G. Chastanet, N. Paradis, J. F. Létard, *Eur. J. Inorg. Chem.*, 2013, **5-6**, 763.
- [32] M. A. Halcrow, *Chem. Soc. Rev.*, 2011, **40**, 4119.
- [33] R. H. Herber, L. M. Casson, *Inorg. Chem.*, 1986, **25**, 847.
- [34] A. Hauser, *Coord. Chem. Rev.*, 1991, **111**, 275.
- [35] A. Hauser, *Chem. Phys. Lett.*, 1992, **192**, 65.
- [36] P. Guionneau. *Dalton. Trans.*, 2014, **14**, 382.
- [37] J. F. Létard, *J. Mater. Chem.*, 2006, **16**, 2550.
- [38] P. Guionneau, F. Le Gac, A. Kaiba, J. S. Costa, D. Chasseau, J. F. Létard, *Chem. Commun.*, 2007, **36**, 3723.

- [39] S. Zerdane, E. Collet, X. Dong, S. F. Matar, H. F. Wang, C. Desplanches, G. Chastanet, M. Chollet, J. M. Glowina, H. T. Lemke, M. Lorenc, M. Cammarata, *Chem. Eur. J.*, 2018, **24**, 5064.
- [40] D. Aguila, P. Dechambenoit, M. Rouzières, C. Mathonière, R. Clérac, *Chem. Commun.*, 2017, **53**, 11588.
- [41] P. Stock, E. Deck, S. Hohnstein, J. Korzekwa, K. Meyer, F. W. Heinemann, F. Breher, G. Hörner, *Inorg Chem.*, 2016, **55**, 5254.
- [42] B. Rosner, M. Milek, A. Witt, B. Gobaut, P. Torelli, R. H. Fink, M. M. Khusniyarov, *Angew. Chem. Int. Ed.*, 2015, **54**, 12976.
- [43] T. Delgado, A. Tissot, L. Guénée, A. Hauser, F. J. Valverde-Muñoz, M. Seredyuk, J. A. Real, S. Pillet, E. E. Bendeif, C. Besnard, *J Am Chem Soc.*, 2018, **140**, 12870.
- [44] R. Kulmaczewski, E. Trzop, E. Collet, S. Vela, M. A. Halcrow, *J. Mater. Chem. C*, 2020, **8**, 8420.
- [45] P. Ganguli, P. Gütllich, E. W. Müller, *Inorg. Chem.*, 1982, **21**, 3429.
- [46] C. Baldé, C. Desplanches, A. Wattiaux, P. Guionneau, P. Gütllich, J. F. Létard, *Dalton Trans.*, 2008, **20**, 2702.
- [47] M. S. Sylla, C. Baldé, N. Daro, C. Desplanches, M. Marchivie, G. Chastanet, *Eur. J. Inorg. Chem.*, 2018, 297.
- [48] S. Schenker, A. Hauser, W Wang, I. Y. Chan, *Chem. Phys. Lett.*, 1998, **297**, 281.
- [49] N. Paradis, G. Chastanet, J. F. Létard, *Eur. J. Inorg. Chem.*, 2012, 3618.
- [50] M. Shatruk, H. Phan, B. A. Chrisostomo, A. Suleimenova, *Coord. Chem. Rev.*, 2015, **289**, 62.
- [51] G. A. Craig, J. S. Costa, O. Roubeau, S. J. Teat, G. Aromí, *Chem. Eur. J.*, 2011, **17**, 3120.
- [52] E. Collet, P. Guionneau, *C. R. Chim.*, 2018, **21**, 1133.
- [53] M. C. Munoz, J. A. Real, *Coord. Chem. Rev.*, 2011, **255**, 2068.
- [54] V. Rubio-Giménez, S. Tatay, C. Martí-Gastaldo, *Chem. Soc. Rev.*, 2020, **49**, 5601.
- [55] G. Chastanet, N. Sciortino, S. Neville, C. Kepert, *Eur. J. Inorg. Chem.*, 2018, 314.
- [56] H. Watanabe, N. Bréfuel, E. Collet, L. Toupet, K. Tanaka, J. P. Tuchagues, *Eur. J. Inorg. Chem.*, 2013, 710.
- [57] H. Watanabe, N. Bréfuel, S. Mouri, J. P. Tuchagues, E. Collet, K. Tanaka, *Eur. Phys. Lett.*, 2011, **96**, 17004.
- [58] N. Bréfuel, H. Watanabe, L. Toupet, J. Come, N. Matsumoto, E. Collet, K. Tanaka, J. P. Tuchagues, *Angew. Chem. Int. Ed.*, 2009, **48**, 9304.

- [59] N. Bréfuel, E. Collet, H. Watanabe, M. Kojima, N. Matsumoto, L. Toupet, K. Tanaka, J. P Tuchagues, *Chem. Eur. J.*, 2010, **16**, 14060.
- [60] C. Baldé, W. Bauer, E. Kaps, S. Neville, C. Desplanches, G. Chastanet, B. Weber, J. F. Létard, *Eur. J. Inorg. Chem.*, 2013, 2744.
- [61] A. Djemel , O. Stefanczyk, M. Marchivie , E. Trzop, E. Collet, C. Desplanches, R. Delimi, G. Chastanet, *Chem. Eur. J.*, 2018, **24**,14760.
- [62] K. Deniel, S. Pillet, M. Marchivie, K. Boukheddaden, G. Chastanet, S. Triki, unpublished.
- [63] S. M. Neville, C. Etrillard, S. Asthana, J. F. Létard, *Eur. J. Inorg. Chem.*, 2010, 282.
- [64] T. Delgado, C. Enachescu, A. Tissot, A. Hauser, L. Guénée, C. Besnard, *J. Mater. Chem. C*, 2018, **6**, 12698.
- [65] P. Guionneau, M. Marchivie, G. Chastanet, *Chem. Eur. J.*, 10.1002/chem.202002699.

## **General Conclusions and Perspectives**



The study of this thesis was devoted to the fundamental understanding of the lifetime of the photo-induced state LIESST effect. The target was to attempt to establish reliable structure-properties relationships to evidence the chemical parameters to play with in order to reach high relaxation temperature  $T(\text{LIESST})$ . This work was based on previous results from the literature presenting the distortion of the coordination sphere as a crucial parameter to account for. However, it was not clearly evidenced if it was an angular distortion or an anisotropy of elongation. Moreover, polymorphism might induce very different features of this coordination sphere distortion. Therefore, we explore these aspects through the synthesis of new complexes.

To increase the distortion of the coordination sphere, different chemical strategies were attempted, including steric strain at molecular scale, polymorphism and solvent effect at supramolecular level. New ligands and complexes were then prepared, belonging to the “PM-L family”  $[\text{Fe}(\text{PM-L})_2(\text{NCE})_2]$  where PM-L is a bidentate Schiff base ligand formed by the condensation of pyridine carbaldehyde with a substituted aniline. These ligands were designed to promote steric strain close to the coordination polyhedron thanks to halogen substitution on the aniline group. Structures and (photo)magnetic properties were analysed in the multiscale view, from the coordination polyhedron to the crystal packing, through the analysis of the intermolecular interactions. Ten new compounds were synthesized and deeply investigated. Thirteen solvatomorphs were also obtained but not fully characterized yet.

All these new compounds from the  $[\text{Fe}(\text{PM-L})_2(\text{NCE})_2].\text{S}$  family, were compared with the other members of this family already known for many years, but also with compounds from the literature based on bidentate ligands. This work allow exotic and significant clues can be drawn.

- ***Both trigonal distortion and anisotropic elongation are relevant parameters towards high  $T(\text{LIESST})$ .*** Indeed, we demonstrated that the trigonal distortion, thought to be responsible of the increase of the  $h\nu\text{-HS}^*$  lifetime, is most probably not sufficient to increase  $T(\text{LIESST})$ . The coordination sphere seems to be both distorted and anisotropically elongated to stabilize this  $\text{HS}^*$  state.  $T(\text{LIESST})$  up to 107 K was evidenced on this new compound with both high trigonal distortion and anisotropic elongation. Several compounds stand above the usual trend for this family, showing that the strategy to promote steric strain close to the coordination sphere was successful, at least partially. From the comparison of more than thirty compounds we also evidenced that, whatever the chemical design made on the coordination sphere, **the upper scales can strongly come into play and perturb the coordination sphere scale.** Indeed, crystal packing and intermolecular interactions can maximize or minimize the effect of

the coordination sphere distortion on the  $T(\text{LIESST})$ . This led to the multiscale view of the  $T(\text{LIESST})$ .

- ***The multiscale view of  $T(\text{LIESST})$*** . The study of polymorphism and compounds with symmetry changes during the spin crossover provided crucial information. The anisotropic breathing of the coordination sphere can strongly affect the motion of ligands, the intermolecular interactions and the crystal packing. As a feedback, all the scale of the material can act as a perturbation on the lower scale. This perturbation can add an additional energy to overcome during the  $h\nu\text{-HS}^*$  to LS relaxation process, therefore enhancing the initial coordination polyhedron distortion or, on the contrary, it can provide additional relaxation pathways that minimize the effect of coordination sphere distortion. Therefore, thinking about increase  $T(\text{LIESST})$ , not only starts **on the design of the coordination sphere but also on accounting for all the physical scales**. These modifications can be the source of exotic behaviours.
- ***Unique thermal expansion of unit-cell volume phenomena*** has been evidenced. Polymorph **I-pBrA** shows a reverse expansion of the lattice volume, *i.e.* an expansion from HS to LS, and polymorph **III-pBrA** exhibits a zero expansion of the unit-cell volume change at the SCO. Spin switch in polymorphs **I-pBrA** to **III-pBrA** are coupled to strong motion of ligands. Therefore, it should be taken into account that the ***volume modification associated to the SCO can be negative, zero or positive*** depending on the compound but independently of the sense of the conversion (HS to LS or LS to HS). Incidentally, this clearly put in light that the investigation of SCO materials requires a detailed analysis of the unit-cell parameters as function of the temperature, far beyond the sole HS and LS crystal structures. Overall, this result opens new perspectives, even for applicative targets, since we clearly evidence here, probably for the first time, that the volume of the sample does not necessarily decrease from HS to LS, but can on the contrary increase, depending on the compound and even on the polymorph.

These conclusions are giving important information for the design of high  $T(\text{LIESST})$  materials. Regarding the coordination sphere scale, a useful chemical strategy will play not only on the trigonal distortion but also on the elongation of the polyhedron.

- The trigonal distortion is linked to the anisotropic coordination sphere hidden in the shape of a molecule. The steric strain, as a useful method, can promote the trigonal distortion of the coordination sphere. The rigidity and flexibility of ligand must be

considered when introducing the steric hindrance. The steric strain in molecular structure may be destroyed owing to the conformational change of ligand. Moreover, the molecular anisotropy and shape are mainly determined by the type of ligands, but also related to the intermolecular interactions. The subtle influence of interactions in polymorphs or solvatomorphs can also regulate the trigonal distortion.

- The anisotropic elongation of the coordination sphere seems more complicated than trigonal distortion to chemically design. One can link the elongation of metal-ligand bond length to the *Jahn-Teller* effect. Metal ions like  $Mn^{3+}$  can be a good candidate. Working on heteroleptic compounds and inducing steric strain through one ligand substitution could help to locally break the symmetry of the molecule and favor some elongation directions. Finally, considering complexes with spin switching associated to the coordination change, such as the coordination/decoordination in macrocyclic complexes, might be a fruitful strategy to follow. Indeed, creating or removing a metal-ligand bond upon thermal stimulus could strongly enhanced the anisotropic elongation of the coordination sphere. Systems exhibiting such behaviors are compounds with very high  $T(LIESST)$  around 130 K.

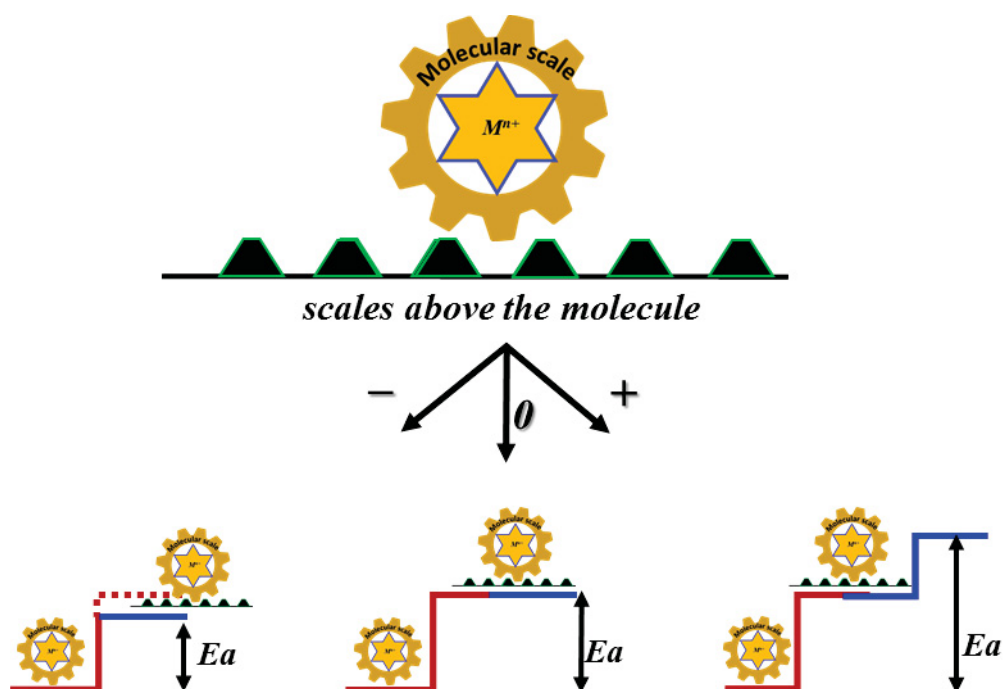
As we have discussed,  $T(LIESST)$  is however not only determined by the coordination sphere scale. One has to account for the upper scales. However, controlling intermolecular interactions in the three directions of space around a strongly unsymmetrical complexes is highly challenging. This is even more challenging when thinking that this scales can help or not the stabilization of the  $h\nu$ -HS\* state. Intuitively, if molecular rearrangements increase the density of vibrational states and phonons, one may expect the  $h\nu$ -HS\* to LS relaxation to be favored. On the contrary very abrupt changes associated with symmetry breakings, with strong energy differences in the LS and HS crystal packings, might favor the  $h\nu$ -HS\* and high  $T(LIESST)$ . A recent work was focused on the calculation of the lattice energy evidencing that cooperative spin crossover are associated to high energy changes of this energy from HS to LS.<sup>1</sup> Such difference in lattice energy should be taken into account while discussing the lifetime of the  $h\nu$ -HS\* state in the solid state. Several strategies might be proposed.

- Molecular reorganization, caused by the conformational change or the order-disorder transition of ligands, can strongly influence the modification of intra- and intermolecular interactions. If flexible ligands are introduced, able to change of conformation, this might introduce more phonon and can disfavor the  $h\nu$ -HS\* state. Therefore, flexible

ligands should be associated with the promotion of strong intermolecular contacts in order to propagate the change to the whole packing and induce a strong energy difference.

- Symmetry breaking can regulate the lattice energy and then affect the energy barrier from  $h\nu$ -HS\* to LS. However, promoting such symmetry breaking is challenging. Again flexible ligands may help to provide antiferro-elastic directions in the network leading to elastic competition. This might be “easier” in 3D networks in which only one or two directions are tunable. However, this should be associated to the coordination sphere distortion too. Highly deformable networks should be considered to both promote high coordination sphere anisotropic distortion and symmetry changes. Unfortunately, at this level of investigation, knowing if these symmetry changes will stabilize or destabilize the  $h\nu$ -HS\* state is difficult. Generalizing the investigations on the calculations of lattice energy could provide in the future more insights.

A very schematic view can be that every structural change (trigonal distortion, elongation, change of conformation, symmetry changes, twinning...) is a step in the activation energy stair-like pathway. Each step can increase the energy barrier and stabilize the  $h\nu$ -HS\* state (Scheme 1). However, sometimes another path comes to life and the energy is split and the activation energy is not increased (Scheme 1). Moreover, the counterpart is that a network that needs high energy to be deformed won't allow to reach the  $h\nu$ -HS\* using light at low temperature. One has to balance all these scales and to make them act in a synergetic way in order that deformation of the coordination sphere is not absorbed by the crystal packing but instead enhanced.



**Scheme 1.** Scheme of the relationship at and above the molecular scales. The variation of scales above the molecule in the solid state can destabilize or stabilize the  $h\nu$ -HS\* state, leading to decrease and increase the activation energy associated to the ultimate relaxation temperature  $T(\text{LIESST})$ , respectively.

Another interesting aspect of the multiscale view of  $T(\text{LIESST})$  is that it evidences some missing parts. Indeed, no investigations on the fatigability of the light-induced and relaxation processes have been made. Information on the coherent domain scale are missing. This would be very interesting for any application involving light-induced process in order to estimate the lifetime of the whole device in terms of cycles. Moreover, very few studies are dealing with nanoparticles, and they currently are contradictory. Again, since thin films or nanoparticles are envisioned in electronic devices, one has to investigate such aspects in the future.

This work has therefore provided new perspectives in terms of chemical design of switchable compounds exhibiting long-lived photo-induced states.

Reference:

- [1] M. G. Reeves, E. Tailleur, P. A. Wood, M. Marchivie, G. Chastanet, P. Guionneau, S. Parsons, *Chem.Sci.*, accepted.



## **Appendix**



## Appendix 1 - Hirshfeld surface and Fingerprint

The Hirshfeld surface of a molecule in a crystal is constructed by partitioning space in the crystal into regions where the electron distribution of a sum of spherical atoms for the molecule dominates the corresponding sum over the crystal. It is defined by the weight function (**eq. 1**), the sum of spherical atom electron densities from the molecule of interest (the promolecule) divided by the same sum for the crystal (the procrystal).  $\rho_i(r)$  is a spherically-averaged atomic electron density centred on nucleus A, and the promolecule and procrystal are sums over the atoms belonging to the molecule and to the crystal, respectively. The Hirshfeld surface is then defined in a crystal as that region around a molecule where  $w(r) \geq 0.5$ . That is, the region where the promolecule contribution to the procrystal electron density exceeds that from all other molecules in the crystal.

$$wA(r) = \frac{\sum_{i \in \text{molecule}} \rho_i^{\text{at}}(r)}{\sum_{i \in \text{crystal}} \rho_i^{\text{at}}(r)} \quad \text{eq.1}$$

The useful property to map onto the surface is the distance from the surface to the nearest nucleus external to the surface, which we call  $d_e$ . This property provides an immediate picture of the nature of intermolecular contacts in the crystal. In a similar fashion, we can define  $d_i$ , the distance from the surface to the nearest nucleus internal to the surface (**Table 1**). The value of  $d_{\text{norm}}$  (**eq.2**) is a normalized contact distance that informs the shortest contacts (red area on the surface) or the the longest ones (blue area on the surface). Derived from the Hirshfeld surface, the 2D plot of  $d_i$  vs  $d_e$  provides a visual summary of the frequency of each combination of  $d_e$  and  $d_i$  across the surface of a molecule. So they not only indicate which intermolecular interactions are present, but also the relative area of the surface corresponding to each kind of interaction. Quantitative comparisons between contributions to crystal packing from various types of intermolecular contacts can be done based on Hirshfeld surfaces and fingerprints.

$$d_{\text{norm}} = \frac{d_i - r_i^{\text{vdW}}}{r_i^{\text{vdW}}} + \frac{d_e - r_e^{\text{vdW}}}{r_e^{\text{vdW}}} \quad \text{eq.2}$$

## Appendix

The shape index of Hirshfeld surface is defined in terms of principle curvatures  $k_1$  and  $k_2$  (eq.3). The maps of shape index on the Hirshfeld surface can be used to identify complementary hollows (red) and bumps (blue) where two molecular surfaces touch one another. These patterns of red and blue triangles on the shape index surface are diagnostic for close C/C interplanar contacts.

$$S = \frac{2}{\pi} \tan^{-1} \frac{k_1+k_2}{k_1-k_2} \quad \text{eq.3}$$

Table 1. Summary of various functions of distance and curvature mapped on Hirshfeld surfaces.

Function	Symbol and definition	Mapping range
distance from the surface to the nearest nucleus external to the surface	$d_e$	red through green to blue
distance from the surface to the nearest nucleus internal to the surface	$d_i$	red through green to blue
curvatures	C	-4 to +4
normalized contact distance	$d_{norm}$	red through white to blue
Shape index, in terms of principle curvatures $k_1$ and $k_2$	S	-1 to +1

[1] M. A. Spackman, D. Jayatilaka, *Cryst. Eng. Comm.*, 2009, **11**, 19-32.

[2] M. A. Spackman, J. J. McKinnon, *Cryst. Eng. Comm.*, 2002, **4**, 378-392.

[3] J. J. McKinnon, M. A. Spackman, A. S. Mitchell, *Acta. Cryst. B*, 2004, **60**, 627-668.

[4] J. J. McKinnon, D. Jayatilaka, M. A. Spackman, *Chem. Commun.*, 2007, **37**, 373814-3816.

## Appendix 2 - Single-crystal and Powder X-ray Diffraction Experiments.

Single-crystal X-ray diffraction (SCXRD): The variable temperature structural determinations all along the thermal SCO were performed on a Kappa Nonius-Brüker diffractometer ( $\lambda = 0.71071 \text{ \AA}$ ) or Bruker Apex II diffractometer ( $\lambda = 0.71071 \text{ \AA}$ ) equipped with an Oxford Cryosystem nitrogen cryostat.

Collaborating with Dr. Sébastien Pillet in the University of Lorraine (Nancy, France), the thermally quenched states at 10 K were collected with an Oxford Diffraction SuperNova diffractometer equipped with an Atlas CCD detector, using a helium openflow cryosystem.

Absorption corrections, data reduction and unit cell refinements were performed using the SADABS and SAINT programs.<sup>1-3</sup> The structures were solved and refined using weighted full-matrix least-squares on  $F^2$  in olex2.<sup>1-3</sup> The constraint code AFIX / EADP were used when refining the disorder of phenyl ring in  $\text{II-[Fe(PM-}i>p\text{BrA)}_2(\text{NCS})_2]$  and  $[\text{Fe(PM-}i>p\text{FA)}_2(\text{NCS})_2] \cdot \text{sol}$ . The atomic occupancy was refined freely in compounds  $[\text{Fe(PM-}i>p\text{FA)}_2(\text{NCS})_2] \cdot \text{CHCl}_3$ .

Powder X-ray diffractograms were acquired using a PANalytical X'Pert 3 Powder ( $\text{CuK}\alpha$ , X'Celerator detector). The crystals were crushed firstly and then transfer to the sample holder carefully, using a blade to make the surface smooth. The conditions of PXRD measurements are shown in [Table 2](#).

Photocrystallography of Powder X-Ray Diffraction was performed using a Panalytical X'Pert Pro diffractometer with monochromatized  $\text{CuK}\alpha 1$  radiation ( $\lambda = 1.54060 \text{ \AA}$ ) and a closed cycle He cryostat in the 15 K - 300 K temperature range, collaborating with Dr. Sébastien Pillet in the University of Lorraine. The sample was irradiated at 15 K with a LED (810 nm, 50  $\text{mW/cm}^2$ ) for 16 hours. Measurements were done from 5 to 42 ° with step of 0.02° and data were analyzed in the Fullprof software.<sup>4</sup>

Table 2. Experimental conditions of PXRD measurements.

<i>Compounds</i>	<i>Sample No.</i>	<i>2θ range / °</i>	<i>Time / min</i>
<i>[Fe(PM-oFA)<sub>2</sub>(NCS)<sub>2</sub>]</i>	PGWG130D	8-80	34
<i>[Fe(PM-mFA)<sub>2</sub>(NCS)<sub>2</sub>]</i>	PGWG130G	5-80	90
<i>[Fe(PM-pFA)<sub>2</sub>(NCS)<sub>2</sub>]·0.47CHCl<sub>3</sub></i>	PGWG128E	3-80	93
<i>[Fe(PM-oBrA)<sub>2</sub>(NCS)<sub>2</sub>]</i>	PGWG130E	4-38	113
<i>I-[Fe(PM-mBrA)<sub>2</sub>(NCS)<sub>2</sub>]</i>	PGWG32O	8-80	34
<i>II-[Fe(PM-mBrA)<sub>2</sub>(NCS)<sub>2</sub>]</i>	PGWG128I	8-80	34
<i>I-[Fe(PM-pBrA)<sub>2</sub>(NCS)<sub>2</sub>]</i>	PGWG79B	4-38	113
<i>II-[Fe(PM-pBrA)<sub>2</sub>(NCS)<sub>2</sub>]</i>	PGWG51	4-38	113

- [1] G. M. Sheldrick, SADABS Version 2.03, Bruker Analytical X-Ray Systems, Madison, WI, USA, 2000.
- [2] O. V. Dolomanov, L. J. Bourhis, R. J. Gildea, J. A. K. Howard, H. Puschmann, *J. Appl. Crystallogr.*, 2009, **42**, 339-341.
- [3] G. M. Sheldrick, *Acta Crystallogr. Sect. C: Struct. Chem.*, 2015, **71(1)**, 3-8.
- [4] Rodriguez-Carvajal, *J Phys. B*, 1993, **192**, 55-69.

## Appendix 3 - Magnetic and Photo-magnetic Measurements

Magnetic measurements were performed on the MPMS-5S Quantum Design SQUID magnetometer. The crystal or powder samples around 10 mg were carefully weighted and sealed in the film of polyethylene.

Magnetic measurements of polymorph II-[Fe(PM-*p*BrA)<sub>2</sub>(NCS)<sub>2</sub>] was performed on EZ7 Microsense Vibrating Sample Magnetometer. Powder sample (6.32 mg) was sealed in aluminum foil and pasted on quartz rods.

Photomagnetic measurements were performed on the same SQUID as above coupled with a set of laser diodes *via* an optical fiber to the magnetometer cavity. The powder samples were prepared as thin layers and irradiated at 10 K. The detailed conditions for magnetic and photomagnetic measurements are reported in Table 3.

Table 3. Magnetic and photomagnetic measurements conditions.

<i>Compounds</i>	<i>Sample No.</i>	<i>Weight(m g)</i>	<i>External field(Oe)</i>	<i>Scan rate(K/min)</i>	<i>Wavelength (nm) / time (min)</i>	<i>Scan rate(K/min)</i>
<i>[Fe(PM-oFA)<sub>2</sub>(NCS)<sub>2</sub>]</i>	PGWG130D	7.80	10000	1.0	830nm / 60min	0.4
<i>[Fe(PM-mFA)<sub>2</sub>(NCS)<sub>2</sub>]</i>	PGWG130G	1.20	20000	0.4	830nm / 160min	0.4
<i>[Fe(PM-pFA)<sub>2</sub>(NCS)<sub>2</sub>]·nCHCl<sub>3</sub></i>	PGWG128E	8.17	10000	0.5	830nm / 60min	0.4
<i>[Fe(PM-oBrA)<sub>2</sub>(NCS)<sub>2</sub>]</i>	PGWG130E	13.26	20000	1.0	830nm / 60min	0.4
<i>I-[Fe(PM-mBrA)<sub>2</sub>(NCS)<sub>2</sub>]</i>	PGWG32O	1.65	10000	1.0	-	-
<i>II-[Fe(PM-mBrA)<sub>2</sub>(NCS)<sub>2</sub>]</i>	PGWG128I	12.01	10000	1.0	830nm / 60min	0.4
<i>I-[Fe(PM-pBrA)<sub>2</sub>(NCS)<sub>2</sub>]</i>	PGWG30O	1.35	20000	0.4	830nm / 160min	0.4
<i>II-[Fe(PM-pBrA)<sub>2</sub>(NCS)<sub>2</sub>]*</i>	PGWG51	6.32	15000	1.0	830nm / 60min	0.4
<i>IV-[Fe(PM-pBrA)<sub>2</sub>(NCS)<sub>2</sub>]</i>	PGWG79C	22.15	5000	2.0		

\*Measurement performed on EZ7 Microsense Vibrating Sample Magnetometer.

## Appendix 4 - Elemental Analysis and Differential Scanning Calorimetry Measurements

**Element Analysis:** Elemental analysis were performed on the Thermo Fischer Scientific equipped with a sample changer. Samples were precisely weighted on Microbalance Mettler MX5 and sealed in aluminum foil to compress into a small square. As seen in Table 4, the values of elements are different for one sample measured at two times. It was not obvious to obtain something relevant, maybe because of the presence of F and Br that are influencing the measurements and datatratements.

**Differential Scanning Calorimetry (DSC):** DSC measurements were performed on a power compensated DSC 8000 PERKIN ELMER equipped with a CLN<sub>2</sub> liquid nitrogen cooling system. Crystals of I-[Fe(PM-*p*BrA)<sub>2</sub>(NCS)<sub>2</sub>] were pressed manually in a conventional aluminum crucible with special care in order to insure the most stable mechanical behavior despite the large volume change during the transition (volume change which is the most difficult to contain as it is positive during cooling). Three consecutive cycles were measured on the 20 mg sample under helium at 4 °C.min<sup>-1</sup> from -30 °C to -160 °C and Capacity (*C<sub>p</sub>*) were obtained by three curves method with a sapphire as standard.

*Appendix*

Table 4. Elemental analysis results at different measurements.

<i>formula</i>	<i>Sample No.</i>	<i>C / %</i>	<i>H / %</i>	<i>N / %</i>	
<i>[Fe(PM-oFA)<sub>2</sub>(NCS)<sub>2</sub>]</i>	PGWG130D	48.66	3.31	12.63	experiment
		54.55	3.17	14.68	calculation
<i>[Fe(PM-pFA)<sub>2</sub>(NCS)<sub>2</sub>]·0.47CHCl<sub>3</sub></i>	PGWG128E	52.37	3.08	13.42	experiment
		50.62	2.96	13.38	calculation
<i>[Fe(PM-oBrA)<sub>2</sub>(NCS)<sub>2</sub>]</i>	PGWG130E	48.56	3.29	12.96	first measurement
		52.32	2.93	13.14	second measurement
		44.98	2.61	12.11	calculation
<i>I-[Fe(PM-mBrA)<sub>2</sub>(NCS)<sub>2</sub>]</i>	PGWG32O	44.49	2.48	11.46	experiment
		44.98	2.61	12.11	calculation
<i>II-[Fe(PM-mBrA)<sub>2</sub>(NCS)<sub>2</sub>]</i>	PGWG128I	0.26	1.43	0.44	first measurement
		0.11	1.63	0.63	second measurement
		44.98	2.61	12.11	calculation
<i>I-[Fe(PM-pBrA)<sub>2</sub>(NCS)<sub>2</sub>]</i>	PGWG30O	44.31	2.62	12.23	first measurement
		44.93	2.57	11.79	second measurement
		44.98	2.61	12.11	calculation
<i>II-[Fe(PM-pBrA)<sub>2</sub>(NCS)<sub>2</sub>]</i>	PGWG51	56.11	3.70	15.45	first measurement
		44.97	2.45	11.85	second measurement
		44.98	2.61	12.11	calculation
<i>IV-[Fe(PM-pBrA)<sub>2</sub>(NCS)<sub>2</sub>]</i>	PGWG79C	44.41	2.80	11.17	experiment
		44.98	2.61	12.11	calculation

## Appendix 5 - Crystallographic Data for Polymorphs [Fe(PM-*p*BrA)<sub>2</sub>(NCS)<sub>2</sub>].

**Table 5.** Crystal data and structure refinement data for polymorph I-[Fe(PM-*p*BrA)<sub>2</sub>(NCS)<sub>2</sub>].

Empirical formula	C <sub>26</sub> H <sub>18</sub> Br <sub>2</sub> FeN <sub>6</sub> S <sub>2</sub>				
Formula weight / g mol <sup>-1</sup>	694.25				
Temperature / K	350	250	180	170	100
Radiation MoK $\alpha$ / $\text{\AA}$	$\lambda = 0.71073$				
Crystal size / mm <sup>3</sup>	0.2 $\times$ 0.1 $\times$ 0.1				
Crystal system	monoclinic				
Space group	<i>P</i> 2 <sub>1</sub> / <i>n</i>				
<i>a</i> / $\text{\AA}$	16.8011(4)	16.7009(3)	16.6098(15)	16.6046(15)	15.8230(6)
<i>b</i> / $\text{\AA}$	21.3926(3)	21.2963(3)	21.1736(16)	21.1608(16)	21.0048(7)
<i>c</i> / $\text{\AA}$	16.8227(4)	16.6548(3)	16.5520(13)	16.5325(13)	17.6823(7)
$\alpha$ / $^\circ$	90	90	90	90	90
$\beta$ / $^\circ$	109.54	109.1890(10)	109.065(4)	108.988(4)	109.72
$\gamma$ / $^\circ$	90	90	90	90	90
Volume / $\text{\AA}^3$	5698.3(2)	5594.45(17)	5501.9(8)	5492.9(8)	5532.3(4)
Z-formula	8	8	8	8	8
$\rho_{\text{calc}}$ / g cm <sup>-3</sup>	1.618	1.649	1.676	1.679	1.667
$\mu$ / mm <sup>-1</sup>	3.507	3.572	3.632	3.638	3.612
F(000)	2752.0	2752.0	2752.0	2752.0	2752.0
2 $\theta$ range for data collection / $^\circ$	4.596 - 50.032	4.616 - 50.094	4.234 - 50.054	4.232 - 50.054	4.746 - 50.008
Index ranges	-19 $\leq$ h $\leq$ 19, -25 $\leq$ k $\leq$ 25, -20 $\leq$ l $\leq$ 20	-19 $\leq$ h $\leq$ 19, -25 $\leq$ k $\leq$ 25, -19 $\leq$ l $\leq$ 19	-16 $\leq$ h $\leq$ 19, -25 $\leq$ k $\leq$ 25, -19 $\leq$ l $\leq$ 19	-16 $\leq$ h $\leq$ 19, -25 $\leq$ k $\leq$ 25, -19 $\leq$ l $\leq$ 19	-18 $\leq$ h $\leq$ 18, -24 $\leq$ k $\leq$ 24, -21 $\leq$ l $\leq$ 21
Reflections collected	19491	19170	33236	33169	17992
Independent reflections	10011 [R <sub>int</sub> = 0.0279, R <sub>sigma</sub> = 0.0397]	9854 [R <sub>int</sub> = 0.0232, R <sub>sigma</sub> = 0.0328]	9667 [R <sub>int</sub> = 0.1729, R <sub>sigma</sub> = 0.1654]	9657 [R <sub>int</sub> = 0.1676, R <sub>sigma</sub> = 0.1585]	9551 [R <sub>int</sub> = 0.0416, R <sub>sigma</sub> = 0.0528]
Data/restraints/parameters	10011/0/661	9854/0/667	9667/0/667	9657/0/667	9551/0/667
Goodness-of-fit on F <sup>2</sup>	1.033	1.031	0.949	0.955	1.057
Final R indexes [I $\geq$ 2 $\sigma$ (I)]	R <sub>1</sub> = 0.0547, wR <sub>2</sub> = 0.1441	R <sub>1</sub> = 0.0492, wR <sub>2</sub> = 0.1245	R <sub>1</sub> = 0.0692, wR <sub>2</sub> = 0.1264	R <sub>1</sub> = 0.0677, wR <sub>2</sub> = 0.1225	R <sub>1</sub> = 0.0542, wR <sub>2</sub> = 0.1237
Final R indexes [all data]	R <sub>1</sub> = 0.0967, wR <sub>2</sub> = 0.1677	R <sub>1</sub> = 0.0695, wR <sub>2</sub> = 0.1377	R <sub>1</sub> = 0.2017, wR <sub>2</sub> = 0.1653	R <sub>1</sub> = 0.1912, wR <sub>2</sub> = 0.1600	R <sub>1</sub> = 0.0838, wR <sub>2</sub> = 0.1419
Largest diff. peak/hole / e $\text{\AA}^{-3}$	0.88/-0.78	1.47/-1.34	0.76/-0.58	0.88/-0.61	1.63/-0.77

$$R_1 = \frac{\sum ||F_0| - |F_C||}{\sum |F_0|}, wR_2 = \left[ \frac{\sum w(F_0^2 - F_C^2)^2}{\sum w(F_0^2)^2} \right]^{1/2}$$

Table 6. Crystal data and structure refinement data for polymorph II-[Fe(PM-*p*BrA)<sub>2</sub>(NCS)<sub>2</sub>].

Empirical formula	C <sub>26</sub> H <sub>18</sub> Br <sub>2</sub> FeN <sub>6</sub> S <sub>2</sub>			
Formula weight / g mol <sup>-1</sup>	694.25			
Temperature / K	330	300	250	10
Radiation MoK $\alpha$ / Å	$\lambda = 0.71073$			
Crystal size / mm <sup>3</sup>	0.18 × 0.12 × 0.06			
Crystal system	monoclinic			
Space group	P2 <sub>1</sub> /n			
<i>a</i> / Å	16.688(12)	16.5583(5)	16.4370(7)	16.1982(8)
<i>b</i> / Å	21.087(13)	20.9993(6)	20.9170(9)	20.6684(10)
<i>c</i> / Å	17.393(13)	17.2361(6)	17.0599(8)	16.8258(10)
$\alpha$ / °	90	90	90	90
$\beta$ / °	107.342(19)	107.1025(9)	107.3862(14)	107.492(6)
$\gamma$ / °	90	90	90	90
Volume / Å <sup>3</sup>	5842(7)	5728.2(3)	5597.4(4)	5372.6(5)
Z-formula	8			
$\rho_{\text{calc}}$ / g cm <sup>-3</sup>	1.579	1.610	1.648	1.717
$\mu$ / mm <sup>-1</sup>	3.421	3.489	3.570	3.720
F(000)	2752.0	2752.0	2752.0	2752.0
2 $\theta$ range for data collection / °	2.97 - 50.05	2.998 - 54.354	3.02 - 51.362	3.64 - 52.744
Index ranges	-19 ≤ <i>h</i> ≤ 19, -25 ≤ <i>k</i> ≤ 21, -20 ≤ <i>l</i> ≤ 20	-21 ≤ <i>h</i> ≤ 21, -26 ≤ <i>k</i> ≤ 26, -22 ≤ <i>l</i> ≤ 22	-20 ≤ <i>h</i> ≤ 20, -22 ≤ <i>k</i> ≤ 25, -20 ≤ <i>l</i> ≤ 20	-20 ≤ <i>h</i> ≤ 20, -25 ≤ <i>k</i> ≤ 18, -19 ≤ <i>l</i> ≤ 21
Reflections collected	107438	72498	80083	37342
Independent reflections	10308 [R <sub>int</sub> = 0.0724, R <sub>sigma</sub> = 0.0547]	12711 [R <sub>int</sub> = 0.0627, R <sub>sigma</sub> = 0.0671]	10628 [R <sub>int</sub> = 0.0615, R <sub>sigma</sub> = 0.0481]	10883 [R <sub>int</sub> = 0.0653, R <sub>sigma</sub> = 0.0717]
Data/restraints/parameters	10308/0/673	12711/0/656	10628/0/656	10883/0/667
Goodness-of-fit on F <sup>2</sup>	1.008	1.005	1.001	1.035
Final R indexes [I ≥ 2 $\sigma$ (I)]	R <sub>1</sub> = 0.0554, wR <sub>2</sub> = 0.1397	R <sub>1</sub> = 0.0671, wR <sub>2</sub> = 0.1447	R <sub>1</sub> = 0.0472, wR <sub>2</sub> = 0.1050	R <sub>1</sub> = 0.0489, wR <sub>2</sub> = 0.1109
Final R indexes [all data]	R <sub>1</sub> = 0.1440, wR <sub>2</sub> = 0.1822	R <sub>1</sub> = 0.1559, wR <sub>2</sub> = 0.1798	R <sub>1</sub> = 0.1039, wR <sub>2</sub> = 0.1291	R <sub>1</sub> = 0.0757, wR <sub>2</sub> = 0.1265
Largest diff. peak/hole / e Å <sup>-3</sup>	0.79/-0.60	1.05/-0.58	1.09/-0.47	2.31/-0.98

$$R_1 = \frac{\sum ||F_0| - |F_C||}{\sum |F_0|}, wR_2 = \left[ \frac{\sum w(F_0^2 - F_C^2)^2}{\sum w(F_0^2)^2} \right]^{1/2}$$

Table 7. Crystal data and structure refinement data for polymorph III-[Fe(PM-*p*BrA)<sub>2</sub>(NCS)<sub>2</sub>].

Empirical formula	C <sub>26</sub> H <sub>18</sub> N <sub>6</sub> S <sub>2</sub> FeBr <sub>2</sub>		
Formula weight / g mol <sup>-1</sup>	694.25		
Temperature / K	220	210	150
Radiation MoK $\alpha$ / Å	$\lambda = 0.71073$		
Crystal size / mm <sup>3</sup>	0.28 × 0.24 × 0.14		
Crystal system	triclinic		
Space group	<i>P</i> -1		
<i>a</i> / Å	9.9422(4)	9.9447(7)	10.4005(6)
<i>b</i> / Å	16.3778(6)	16.3647(12)	15.8356(9)
<i>c</i> / Å	18.4452(6)	18.4366(14)	17.8941(10)
$\alpha$ / °	102.7020(10)	102.720(2)	99.009(2)
$\beta$ / °	90.0740(10)	90.089(2)	92.205(2)
$\gamma$ / °	105.0720(10)	105.015(2)	107.245(2)
Volume / Å <sup>3</sup>	2823.71(18)	2821.4(4)	2768.6(3)
Z-formula	4	4	4
$\rho_{\text{calc}}$ / g cm <sup>-3</sup>	1.633	1.634	1.666
$\mu$ / mm <sup>-1</sup>	3.539	3.542	3.609
F(000)	1376.0	1376.0	1376.0
2 $\theta$ range for data collection / °	2.644 - 53.464	2.268 - 50.052	2.314 - 49.826
Index ranges	-12 ≤ <i>h</i> ≤ 12, -20 ≤ <i>k</i> ≤ 20, -21 ≤ <i>l</i> ≤ 23	-11 ≤ <i>h</i> ≤ 11, -19 ≤ <i>k</i> ≤ 19, -21 ≤ <i>l</i> ≤ 21	-12 ≤ <i>h</i> ≤ 12, -18 ≤ <i>k</i> ≤ 18, -16 ≤ <i>l</i> ≤ 21
Reflections collected	56481	46044	53684
Independent reflections	12010 [R <sub>int</sub> = 0.0315, R <sub>sigma</sub> = 0.0288]	9830 [R <sub>int</sub> = 0.0465, R <sub>sigma</sub> = 0.0565]	9552 [R <sub>int</sub> = 0.0517, R <sub>sigma</sub> = 0.0523]
Data/restraints/parameters	12010/0/667	9830/0/667	9552/0/667
Goodness-of-fit on F <sup>2</sup>	1.059	1.136	1.056
Final R indexes [ <i>I</i> > 2 $\sigma$ ( <i>I</i> )]	R <sub>1</sub> = 0.0378, wR <sub>2</sub> = 0.0804	R <sub>1</sub> = 0.0635, wR <sub>2</sub> = 0.1167	R <sub>1</sub> = 0.0380, wR <sub>2</sub> = 0.0665
Final R indexes [all data]	R <sub>1</sub> = 0.0646, wR <sub>2</sub> = 0.0939	R <sub>1</sub> = 0.1177, wR <sub>2</sub> = 0.1451	R <sub>1</sub> = 0.0756, wR <sub>2</sub> = 0.0787
Largest diff. peak/hole / e Å <sup>-3</sup>	1.40/-0.95	1.01/-0.77	0.56/-0.39

$$R_1 = \frac{\sum ||F_0| - |F_C||}{\sum |F_0|}, wR_2 = [\frac{\sum w(F_0^2 - F_C^2)^2}{\sum w(F_0^2)^2}]^{1/2}$$

## Appendix 6 - Synthesis and Crystallographic Data for [Fe(PM-*p*FA)<sub>2</sub>(NCS)<sub>2</sub>].S

- Synthesis of [Fe(PM-*p*FA)<sub>2</sub>(NCS)<sub>2</sub>].S

When 2 ml of Fe(NCS)<sub>2</sub> methanolic solution (0.1mmol Fe<sup>2+</sup>) are added dropwise into 2 ml mesitylene containing 0.2 mmol of ligand, dark flake crystals are formed after one week at 25 °C, leading to the black bulk crystals of [Fe(PM-*p*FA)<sub>2</sub>(NCS)<sub>2</sub>].C<sub>9</sub>H<sub>12</sub>. Compounds [Fe(PM-*p*FA)<sub>2</sub>(NCS)<sub>2</sub>].C<sub>6</sub>H<sub>6</sub>, [Fe(PM-*p*FA)<sub>2</sub>(NCS)<sub>2</sub>].C<sub>7</sub>H<sub>8</sub> and [Fe(PM-*p*FA)<sub>2</sub>(NCS)<sub>2</sub>].C<sub>8</sub>H<sub>10</sub> were prepared by changing the solvents.

- Synthesis of [Fe(PM-*p*FA)<sub>2</sub>(NCSe)<sub>2</sub>].S

A first step consisted in preparing the Fe(NCSe)<sub>2</sub> reactant. 1 mmol of FeSO<sub>4</sub>.7H<sub>2</sub>O and 2 mmol of KNCSe were dissolved in 20 ml of methanol each, in presence of few ascorbic acid. After stirring 2 hours, the resulting solution is filtered under nitrogen atmosphere to remove the K<sub>2</sub>SO<sub>4</sub> formed during the reaction.

When 2 ml of Fe(NCSe)<sub>2</sub> methanolic solution (0.1mmol Fe<sup>2+</sup>) are added dropwise into 2 ml mesitylene containing 0.2 mmol of ligand, dark flake crystals are formed after one week at 25 °C, leading to the black bulk crystals of [Fe(PM-*p*FA)<sub>2</sub>(NCSe)<sub>2</sub>].C<sub>9</sub>H<sub>12</sub>. Compounds [Fe(PM-*p*FA)<sub>2</sub>(NCSe)<sub>2</sub>].C<sub>7</sub>H<sub>8</sub> and [Fe(PM-*p*FA)<sub>2</sub>(NCSe)<sub>2</sub>].C<sub>8</sub>H<sub>10</sub> were prepared by changing the solvents.

**Table 8.** Crystal data and structure refinement data for **[Fe(PM-*p*FA)<sub>2</sub>(NCS)<sub>2</sub>].C<sub>9</sub>H<sub>12</sub>.**

Empirical formula	C <sub>35</sub> H <sub>30</sub> F <sub>2</sub> FeN <sub>6</sub> S <sub>2</sub>	C <sub>35</sub> H <sub>30</sub> F <sub>2</sub> FeN <sub>6</sub> S <sub>2</sub>	C <sub>35</sub> H <sub>30</sub> F <sub>2</sub> FeN <sub>6</sub> S <sub>2</sub>	C <sub>35</sub> H <sub>30</sub> F <sub>2</sub> FeN <sub>6</sub> S <sub>2</sub>
Formula weight / g mol <sup>-1</sup>	692.62	692.62	692.62	692.62
Temperature / K	220	202(cooling)	150	210(warming)
Radiation MoK $\alpha$ / Å	$\lambda = 0.71073$			
Crystal size / mm <sup>3</sup>	0.26 × 0.24 × 0.08			
Crystal system	triclinic	triclinic	monoclinic	triclinic
Space group	<i>P</i> -1	<i>P</i> -1	<i>C</i> 2/ <i>c</i>	<i>P</i> -1
<i>a</i> / Å	9.5921(4)	9.6370(4)	10.8700(11)	9.6289(6)
<i>b</i> / Å	9.8949(5)	9.7960(5)	15.9764(16)	9.7910(6)
<i>c</i> / Å	20.0929(9)	39.011(2)	19.1126(19)	39.026(2)
$\alpha$ / °	86.2986(14)	87.1983(17)	90	87.141(3)
$\beta$ / °	78.7771(13)	85.617(2)	94.892(3)	85.594(3)
$\gamma$ / °	67.5557(13)	68.1210(18)	90	68.099(2)
Volume / Å <sup>3</sup>	1728.81(14)	3406.7(3)	3307.1(6)	3402.7(4)
Z-formula	2	4	4	4
$\rho_{\text{calc}}$ / g cm <sup>-3</sup>	1.331	1.350	1.391	1.352
$\mu$ / mm <sup>-1</sup>	0.601	0.610	0.628	0.611
F(000)	716.0	1432.0	1432.0	1432.0
2 $\theta$ range for data collection / °	4.454 - 57.4	2.094 - 50.054	4.278 - 52.744	2.094 - 50.052
Index ranges	-12 ≤ <i>h</i> ≤ 12, -12 ≤ <i>k</i> ≤ 13, -27 ≤ <i>l</i> ≤ 27	-11 ≤ <i>h</i> ≤ 11, -11 ≤ <i>k</i> ≤ 11, -46 ≤ <i>l</i> ≤ 46	-13 ≤ <i>h</i> ≤ 12, -19 ≤ <i>k</i> ≤ 19, -23 ≤ <i>l</i> ≤ 23	-11 ≤ <i>h</i> ≤ 11, -11 ≤ <i>k</i> ≤ 11, -46 ≤ <i>l</i> ≤ 46
Reflections collected	33384 8840	14985 9427	16983 3328	46821 11238
Independent reflections	R <sub>int</sub> = 0.0258, R <sub>sigma</sub> = 0.0235	R <sub>int</sub> = 0.0309, R <sub>sigma</sub> = 0.0671]	R <sub>int</sub> = 0.0339, R <sub>sigma</sub> = 0.0240	R <sub>int</sub> = 0.0322, R <sub>sigma</sub> = 0.0368
Data/restraints/parameters	8840/0/418	9427/0/823	3328/0/212	11238/0/835
Goodness-of-fit on F <sup>2</sup>	1.102	0.813	1.150	1.206
Final R indexes [ <i>I</i> ≥ 2 $\sigma$ ( <i>I</i> )]	R <sub>1</sub> = 0.0529, wR <sub>2</sub> = 0.1009	R <sub>1</sub> = 0.0451, wR <sub>2</sub> = 0.1149	R <sub>1</sub> = 0.0478, wR <sub>2</sub> = 0.1032	R <sub>1</sub> = 0.0872, wR <sub>2</sub> = 0.1839
Final R indexes [all data]	R <sub>1</sub> = 0.0675, wR <sub>2</sub> = 0.1097	R <sub>1</sub> = 0.0885, wR <sub>2</sub> = 0.1402	R <sub>1</sub> = 0.0576, wR <sub>2</sub> = 0.1083	R <sub>1</sub> = 0.1031, wR <sub>2</sub> = 0.1894
Largest diff. peak/hole / e Å <sup>-3</sup>	0.70/-0.73	0.26/-0.42	0.92/-0.52	0.55/-1.25

$$R_1 = \frac{\sum ||F_o| - |F_c||}{\sum |F_o|}, wR_2 = \left[ \frac{\sum w(F_o^2 - F_c^2)^2}{\sum w(F_o^2)^2} \right]^{1/2}$$

**Table 9.** Crystal data and structure refinement data for **[Fe(PM-*p*FA)<sub>2</sub>(NCS)<sub>2</sub>].C<sub>7</sub>H<sub>8</sub>**.

Empirical formula	C <sub>33</sub> H <sub>26</sub> F <sub>2</sub> FeN <sub>6</sub> S <sub>2</sub>		
Formula weight / g mol <sup>-1</sup>	664.57	664.57	664.57
Temperature / K	300	135	10 <sub>quench</sub>
Radiation MoK $\alpha$ / Å		$\lambda = 0.71073$	
Crystal size / mm <sup>3</sup>	0.26 × 0.14 × 0.16	0.26 × 0.14 × 0.16	0.18 × 0.16 × 0.16
Crystal system	monoclinic	triclinic	triclinic
Space group	<i>C2/c</i>	<i>P</i> -1	<i>P</i> -1
<i>a</i> / Å	11.1780(3)	10.772(3)	8.7866(6)
<i>b</i> / Å	15.2583(3)	19.4813(12)	9.6806(6)
<i>c</i> / Å	19.5577(4)	23.026(3)	19.0021(12)
$\alpha$ / °	90	88.089(7)	95.928(5)
$\beta$ / °	100.5900(10)	76.506(18)	96.333(5)
$\gamma$ / °	90	81.870(14)	104.928(5)
Volume / Å <sup>3</sup>	3278.89(13)	4651.4(15)	1537.56(18)
Z-formula	4	6	2
$\rho_{\text{calc}}$ / g cm <sup>-3</sup>	1.344	1.423	1.435
$\mu$ / mm <sup>-1</sup>	0.631	0.667	0.673
F(000)	1364.0	2052.0	684.0
2 $\theta$ range for data collection / °	4.74 - 53.464	6.12 - 54.998	4.354 - 59.592
Index ranges	-13 ≤ <i>h</i> ≤ 14, -19 ≤ <i>k</i> ≤ 19, -24 ≤ <i>l</i> ≤ 24	-13 ≤ <i>h</i> ≤ 13, -24 ≤ <i>k</i> ≤ 25, -29 ≤ <i>l</i> ≤ 29	-12 ≤ <i>h</i> ≤ 12, -11 ≤ <i>k</i> ≤ 13, -26 ≤ <i>l</i> ≤ 23
Reflections collected	8998	62278	19188
Independent reflections	3392 [R <sub>int</sub> = 0.0250, R <sub>sigma</sub> = 0.0241]	20777 [R <sub>int</sub> = 0.0360, R <sub>sigma</sub> = 0.0425]	7407 [R <sub>int</sub> = 0.0694, R <sub>sigma</sub> = 0.0731]
Data/restraints/parameters	3392/5/186	20777/0/1214	7407/0/397
Goodness-of-fit on F <sup>2</sup>	1.064	1.030	1.166
Final R indexes [ <i>I</i> ≥ 2 $\sigma$ ( <i>I</i> )]	R <sub>1</sub> = 0.0592, wR <sub>2</sub> = 0.1943	R <sub>1</sub> = 0.0514, wR <sub>2</sub> = 0.1242	R <sub>1</sub> = 0.1071, wR <sub>2</sub> = 0.2977
Final R indexes [all data]	R <sub>1</sub> = 0.0725, wR <sub>2</sub> = 0.2193	R <sub>1</sub> = 0.0946, wR <sub>2</sub> = 0.1535	R <sub>1</sub> = 0.1213, wR <sub>2</sub> = 0.3088
Largest diff. peak/hole / e Å <sup>-3</sup>	0.55/-0.48	1.56/-0.90	3.88/-1.51

$$R_1 = \frac{\sum ||F_0| - |F_c||}{\sum |F_0|}, wR_2 = [\frac{\sum w(F_0^2 - F_c^2)^2}{\sum w(F_0^2)^2}]^{1/2}$$

**Table 10.** Crystal data and structure refinement data for **[Fe(PM-*p*FA)<sub>2</sub>(NCS)<sub>2</sub>].C<sub>6</sub>H<sub>6</sub>**.

Empirical formula	C <sub>32</sub> H <sub>24</sub> F <sub>2</sub> FeN <sub>6</sub> S <sub>2</sub>	C <sub>32</sub> H <sub>24</sub> F <sub>2</sub> FeN <sub>6</sub> S <sub>2</sub>
Formula weight / g mol <sup>-1</sup>	650.57	650.54
Temperature / K	300	150.0
Radiation MoK $\alpha$ / Å	$\lambda = 0.71073$	
Crystal size / mm <sup>3</sup>	0.22 × 0.08 × 0.06	
Crystal system	monoclinic	
Space group	<i>P</i> 2 <sub>1</sub> / <i>c</i>	<i>C</i> 2/ <i>c</i>
<i>a</i> / Å	10.8040(3)	10.5722(6)
<i>b</i> / Å	15.2976(5)	14.9941(6)
<i>c</i> / Å	21.9104(5)	19.4743(10)
$\alpha$ / °	90	90
$\beta$ / °	98.457(2)	99.609(2)
$\gamma$ / °	90	90
Volume / Å <sup>3</sup>	3581.87(17)	3043.8(3)
Z-formula	4	4
$\rho_{\text{calc}}$ / g cm <sup>-3</sup>	1.206	1.420
$\mu$ / mm <sup>-1</sup>	0.577	0.678
F(000)	1288.0	1336.0
2 $\theta$ range for data collection / °	3.258 - 52.744	4.76 - 61.306
Index ranges	-13 ≤ <i>h</i> ≤ 13, -19 ≤ <i>k</i> ≤ 18, -25 ≤ <i>l</i> ≤ 27	-15 ≤ <i>h</i> ≤ 15, -20 ≤ <i>k</i> ≤ 21, -27 ≤ <i>l</i> ≤ 27
Reflections collected	19212	41142
Independent reflections	6759 [R <sub>int</sub> = 0.0339, R <sub>sigma</sub> = 0.0363]	4677 [R <sub>int</sub> = 0.0672, R <sub>sigma</sub> = 0.0228]
Data/restraints/parameters	6759/0/388	4677/1/198
Goodness-of-fit on F <sup>2</sup>	1.019	1.124
Final R indexes [ <i>I</i> ≥ 2 $\sigma$ ( <i>I</i> )]	R <sub>1</sub> = 0.0580, wR <sub>2</sub> = 0.1930	R <sub>1</sub> = 0.0439, wR <sub>2</sub> = 0.0993
Final R indexes [all data]	R <sub>1</sub> = 0.1003, wR <sub>2</sub> = 0.2391	R <sub>1</sub> = 0.0497, wR <sub>2</sub> = 0.1049
Largest diff. peak/hole / e Å <sup>-3</sup>	0.83/-0.70	0.70/-0.53

$$R_1 = \frac{\sum ||F_0| - |F_C||}{\sum |F_0|}, wR_2 = \left[ \frac{\sum w(F_0^2 - F_C^2)^2}{\sum w(F_0^2)^2} \right]^{1/2}$$

**Table 11.** Crystal data and structure refinement data for **[Fe(PM-*p*FA)<sub>2</sub>(NCS)<sub>2</sub>].C<sub>8</sub>H<sub>10</sub>**.

Empirical formula	C <sub>34</sub> H <sub>28</sub> F <sub>2</sub> FeN <sub>6</sub> S <sub>2</sub>	C <sub>34</sub> H <sub>28</sub> F <sub>2</sub> FeN <sub>6</sub> S <sub>2</sub>
Formula weight / g mol <sup>-1</sup>	678.59	678.59
Temperature / K	250	100
Radiation MoK $\alpha$ / Å	$\lambda = 0.71073$	
Crystal size / mm <sup>3</sup>	0.26 × 0.2 × 0.16	
Crystal system	monoclinic	
Space group	C2/c	
<i>a</i> / Å	11.1696(3)	10.9579(3)
<i>b</i> / Å	15.2835(3)	15.1016(3)
<i>c</i> / Å	19.7038(5)	19.7131(4)
$\alpha$ / °	90	90
$\beta$ / °	100.0280(10)	100.1230(10)
$\gamma$ / °	90	90
Volume / Å <sup>3</sup>	3312.26(14)	3211.38(13)
Z-formula	4	4
$\rho_{\text{calc}}$ / g cm <sup>-3</sup>	1.361	1.404
$\mu$ / mm <sup>-1</sup>	0.626	0.646
F(000)	1400.0	1400.0
2 $\theta$ range for data collection / °	4.198 - 54.972	4.198 - 55.004
Index ranges	-14 ≤ <i>h</i> ≤ 14, -19 ≤ <i>k</i> ≤ 19, -25 ≤ <i>l</i> ≤ 25	-14 ≤ <i>h</i> ≤ 14, -19 ≤ <i>k</i> ≤ 19, -25 ≤ <i>l</i> ≤ 25
Reflections collected	7392	7176
Independent reflections	3808 [R <sub>int</sub> = 0.0155, R <sub>sigma</sub> = 0.0262]	3698 [R <sub>int</sub> = 0.0135, R <sub>sigma</sub> = 0.0230]
Data/restraints/parameters	3808/2/207	3698/0/191
Goodness-of-fit on F <sup>2</sup>	1.088	1.151
Final R indexes [ <i>I</i> ≥ 2 $\sigma$ ( <i>I</i> )]	R <sub>1</sub> = 0.0784, wR <sub>2</sub> = 0.1774	R <sub>1</sub> = 0.0673, wR <sub>2</sub> = 0.1820
Final R indexes [all data]	R <sub>1</sub> = 0.1152, wR <sub>2</sub> = 0.2310	R <sub>1</sub> = 0.0852, wR <sub>2</sub> = 0.2210
Largest diff. peak/hole / e Å <sup>-3</sup>	1.56/-1.10	1.84/-1.10

$$R_1 = \frac{\sum ||F_0| - |F_c||}{\sum |F_0|}, wR_2 = [\frac{\sum w(F_0^2 - F_c^2)^2}{\sum w(F_0^2)^2}]^{1/2}$$

**Table 12.** Crystal data and structure refinement data for  $[\text{Fe}(\text{PM-}p\text{FA})_2(\text{NCSe})_2] \cdot \text{C}_9\text{H}_{12}$ .

Empirical formula	$\text{C}_{35}\text{H}_{30}\text{F}_2\text{FeN}_6\text{Se}_2$	$\text{C}_{35}\text{H}_{30}\text{F}_2\text{FeN}_6\text{Se}_2$
Formula weight / $\text{g mol}^{-1}$	786.42	786.42
Temperature / K	300	120
Radiation $\text{MoK}\alpha$ / $\text{\AA}$	$\lambda = 0.71073$	
Crystal size / $\text{mm}^3$	$0.30 \times 0.26 \times 0.24$	
Crystal system	monoclinic	
Space group	$C2/c$	
$a$ / $\text{\AA}$	10.9515(1)	10.9564(4)
$b$ / $\text{\AA}$	16.4673(3)	16.0929(9)
$c$ / $\text{\AA}$	20.0501(1)	19.4083(3)
$\alpha$ / $^\circ$	90	90
$\beta$ / $^\circ$	102.179(9)	94.996(6)
$\gamma$ / $^\circ$	90	90
Volume / $\text{\AA}^3$	3534.5(2)	3409.1(2)
Z-formula	4	4
$\rho_{\text{calc}}$ / $\text{g cm}^{-3}$	1.478	1.532
$\mu$ / $\text{mm}^{-1}$	2.530	2.623
F(000)	1576.0	1576.0
$2\theta$ range for data collection / $^\circ$	6.464 - 52.738	6.392 - 54.994
Index ranges	$-13 \leq h \leq 13, -19 \leq k \leq 20, -24 \leq l \leq 25$	$-14 \leq h \leq 13, -20 \leq k \leq 20, -24 \leq l \leq 25$
Reflections collected	9665	21064
Independent reflections	3558 [ $R_{\text{int}} = 0.0290, R_{\text{sigma}} = 0.0352$ ]	3904 [ $R_{\text{int}} = 0.0766, R_{\text{sigma}} = 0.0482$ ]
Data/restraints/parameters	3558/0/211	3904/0/212
Goodness-of-fit on $F^2$	1.110	1.243
Final R indexes [ $I \geq 2\sigma(I)$ ]	$R_1 = 0.0528, wR_2 = 0.1309$	$R_1 = 0.0730, wR_2 = 0.1847$
Final R indexes [all data]	$R_1 = 0.0767, wR_2 = 0.1460$	$R_1 = 0.0901, wR_2 = 0.1975$
Largest diff. peak/hole / $\text{e \AA}^{-3}$	0.84/-1.08	1.30/-1.35

$$R_1 = \frac{\sum ||F_0| - |F_c||}{\sum |F_0|}, wR_2 = \left[ \frac{\sum w(F_0^2 - F_c^2)^2}{\sum w(F_0^2)^2} \right]^{1/2}$$

**Table 13.** Crystal data and structure refinement data for **[Fe(PM-*p*FA)<sub>2</sub>(NCSe)<sub>2</sub>].C<sub>7</sub>H<sub>8</sub>**.

Empirical formula	C <sub>33</sub> H <sub>25</sub> F <sub>2</sub> FeN <sub>6</sub> Se <sub>2</sub>		
Formula weight / g mol <sup>-1</sup>	757.36	757.36	757.36
Temperature / K	300	100	10 <sub>quench</sub>
Radiation MoK $\alpha$ / Å	$\lambda = 0.71073$		
Crystal size / mm <sup>3</sup>	0.18 × 0.16 × 0.12		0.16 × 0.14 × 0.10
Crystal system	monoclinic		triclinic
Space group	C2/c		<i>P</i> -1
<i>a</i> / Å	11.294(3)	10.7551(8)	8.9676(10)
<i>b</i> / Å	15.333(4)	15.2338(10)	9.6849(9)
<i>c</i> / Å	19.556(4)	19.6837(17)	19.0647(10)
$\alpha$ / °	90	90	95.533(6)
$\beta$ / °	100.786(8)	98.346(4)	96.642(7)
$\gamma$ / °	90	90	105.266(9)
Volume / Å <sup>3</sup>	3327.0(14)	3190.8(4)	1572.7(3)
Z-formula	4	4	2
$\rho_{\text{calc}}$ / g cm <sup>-3</sup>	1.512	1.577	1.601
$\mu$ / mm <sup>-1</sup>	2.684	2.799	2.839
F(000)	1508.0	1508.0	756.0
2 $\theta$ range for data collection / °	4.24 - 51.362	4.182 - 55.116	4.34 - 66.128
Index ranges	-13 ≤ <i>h</i> ≤ 12, -18 ≤ <i>k</i> ≤ 18, -23 ≤ <i>l</i> ≤ 23	-13 ≤ <i>h</i> ≤ 13, -18 ≤ <i>k</i> ≤ 19, -24 ≤ <i>l</i> ≤ 25	-13 ≤ <i>h</i> ≤ 7, -11 ≤ <i>k</i> ≤ 14, -26 ≤ <i>l</i> ≤ 27
Reflections collected	19031	34920	18072
Independent reflections	3078 [R <sub>int</sub> = 0.0530, R <sub>sigma</sub> = 0.0373]	3675 [R <sub>int</sub> = 0.0494, R <sub>sigma</sub> = 0.0271]	10337 [R <sub>int</sub> = 0.0827, R <sub>sigma</sub> = 0.1177]
Data/restraints/parameters	3078/3/206	3675/4/186	10337/0/397
Goodness-of-fit on F <sup>2</sup>	1.134	1.101	1.090
Final R indexes [ <i>I</i> ≥ 2 $\sigma$ ( <i>I</i> )]	R <sub>1</sub> = 0.0778, wR <sub>2</sub> = 0.2179	R <sub>1</sub> = 0.0757, wR <sub>2</sub> = 0.1628	R <sub>1</sub> = 0.1532, wR <sub>2</sub> = 0.4248
Final R indexes [all data]	R <sub>1</sub> = 0.1104, wR <sub>2</sub> = 0.2420	R <sub>1</sub> = 0.1035, wR <sub>2</sub> = 0.1837	R <sub>1</sub> = 0.1887, wR <sub>2</sub> = 0.4544
Largest diff. peak/hole / e Å <sup>-3</sup>	0.84/-1.13	2.17/-2.47	6.80/-2.70

$$R_1 = \frac{\sum ||F_0| - |F_C||}{\sum |F_0|}, wR_2 = \left[ \frac{\sum w(F_0^2 - F_C^2)^2}{\sum w(F_0^2)^2} \right]^{1/2}$$

**Table 14.** Crystal data and structure refinement data for **[Fe(PM-*p*FA)<sub>2</sub>(NCSe)<sub>2</sub>].C<sub>8</sub>H<sub>10</sub>**.

Empirical formula	C <sub>34</sub> H <sub>28</sub> F <sub>2</sub> FeN <sub>6</sub> Se <sub>2</sub>	C <sub>34</sub> H <sub>28</sub> F <sub>2</sub> FeN <sub>6</sub> Se <sub>2</sub>
Formula weight / g mol <sup>-1</sup>	772.39	772.39
Temperature / K	300	100
Radiation MoK $\alpha$ / Å	$\lambda = 0.71073$	
Crystal size / mm <sup>3</sup>	0.22 × 0.2 × 0.18	
Crystal system	monoclinic	
Space group	C2/c	
<i>a</i> / Å	11.3126(4)	11.0470(3)
<i>b</i> / Å	15.3944(7)	15.1094(5)
<i>c</i> / Å	19.8473(5)	19.8405(7)
$\alpha$ / °	90	90
$\beta$ / °	100.5330(2)	100.8010(17)
$\gamma$ / °	90	90
Volume / Å <sup>3</sup>	3398.2(2)	3252.98(18)
Z-formula	4	4
$\rho_{\text{calc}}$ / g cm <sup>-3</sup>	1.510	1.577
$\mu$ / mm <sup>-1</sup>	2.630	2.747
F(000)	1544.0	1544.0
2 $\theta$ range for data collection / °	6.592 - 55.06	4.18 - 55.164
Index ranges	-14 ≤ <i>h</i> ≤ 14, -19 ≤ <i>k</i> ≤ 18, -25 ≤ <i>l</i> ≤ 25	-14 ≤ <i>h</i> ≤ 14, -19 ≤ <i>k</i> ≤ 19, -25 ≤ <i>l</i> ≤ 25
Reflections collected	6896	7381
Independent reflections	3896 [R <sub>int</sub> = 0.0182, R <sub>sigma</sub> = 0.0323]	3767 [R <sub>int</sub> = 0.0354, R <sub>sigma</sub> = 0.0577]
Data/restraints/parameters	3896/0/190	3767/0/206
Goodness-of-fit on F <sup>2</sup>	1.104	1.078
Final R indexes [I ≥ 2 $\sigma$ (I)]	R <sub>1</sub> = 0.0517, wR <sub>2</sub> = 0.1566	R <sub>1</sub> = 0.0453, wR <sub>2</sub> = 0.1185
Final R indexes [all data]	R <sub>1</sub> = 0.0855, wR <sub>2</sub> = 0.1736	R <sub>1</sub> = 0.0947, wR <sub>2</sub> = 0.1991
Largest diff. peak/hole / e Å <sup>-3</sup>	0.98/-0.56	1.10/-1.03

$$R_1 = \frac{\sum ||F_0| - |F_C||}{\sum |F_0|}, wR_2 = \left[ \frac{\sum w(F_0^2 - F_C^2)^2}{\sum w(F_0^2)^2} \right]^{1/2}$$

## Appendix 7 - Synthesis and Crystallographic Data for [Fe(PM-*p*BrA)<sub>2</sub>(NCE)<sub>2</sub>].S

- Synthesis of [Fe(PM-*p*BrA)<sub>2</sub>(NCE)<sub>2</sub>].S (E = S and Se)

When 2 ml of Fe(NCS)<sub>2</sub> (Fe(NCSe)<sub>2</sub>) methanolic solution (0.1 mmol Fe<sup>2+</sup>) are added dropwise into 2 ml mesitylene / benzene / toluene containing 0.2 mmol of ligand, dark flake crystals are formed after one week at 25 °C, leading to the black bulk crystals of compounds [Fe(PM-*p*BrA)<sub>2</sub>(NCE)<sub>2</sub>].C<sub>9</sub>H<sub>12</sub> / [Fe(PM-*p*BrA)<sub>2</sub>(NCE)<sub>2</sub>].C<sub>6</sub>H<sub>6</sub> / [Fe(PM-*p*BrA)<sub>2</sub>(NCE)<sub>2</sub>].C<sub>7</sub>H<sub>8</sub>, respectively.

**Table III.15.** Crystal data and structure refinement data for **S-pBrA.C<sub>9</sub>H<sub>12</sub>**.

Empirical formula	C <sub>35</sub> H <sub>30</sub> Br <sub>2</sub> FeN <sub>6</sub> S <sub>2</sub>	C <sub>35</sub> H <sub>30</sub> Br <sub>2</sub> FeN <sub>6</sub> S <sub>2</sub>	C <sub>35</sub> H <sub>30</sub> Br <sub>2</sub> FeN <sub>6</sub> S <sub>2</sub>	C <sub>35</sub> H <sub>30</sub> Br <sub>2</sub> FeN <sub>6</sub> S <sub>2</sub>
Formula weight / g mol <sup>-1</sup>	814.44	814.44	814.44	814.44
Temperature / K	300	120	10 ( <i>hν</i> -HS*)	10
Radiation MoK $\alpha$ / Å			$\lambda = 0.71073$	
Crystal size / mm <sup>3</sup>	0.28 × 0.24 × 0.18			0.24 × 0.22 × 0.16
Crystal system			monoclinic	
Space group			C2/c	
<i>a</i> / Å	10.7938(5)	10.5394(4)	10.5303(10)	10.5072(7)
<i>b</i> / Å	16.6292(2)	16.5336(6)	16.6057(13)	16.4822(16)
<i>c</i> / Å	20.1262(4)	19.4755(8)	19.543(2)	19.4710(14)
$\alpha$ / °	90	90	90	90
$\beta$ / °	90.953(3)	94.8340(10)	94.301(10)	94.724(7)
$\gamma$ / °	90	90	90	90
Volume / Å <sup>3</sup>	3612.00(19)	3381.6(2)	3407.8(6)	3360.6(5)
Z-formula	4	4	4	4
$\rho_{\text{calc}}$ / g cm <sup>-3</sup>	1.498	1.600	1.587	1.610
$\mu$ / mm <sup>-1</sup>	2.779	2.968	2.945	2.987
F(000)	1640.0	1640.0	1640.0	1640.0
2 $\theta$ range for data collection / °	6.012 - 55	4.198 - 54.406	4.18 - 57.4	4.198 - 57.388
Index ranges	-14 ≤ <i>h</i> ≤ 13, -21 ≤ <i>k</i> ≤ 21, -26 ≤ <i>l</i> ≤ 21	-11 ≤ <i>h</i> ≤ 13, -21 ≤ <i>k</i> ≤ 21, -24 ≤ <i>l</i> ≤ 22	-14 ≤ <i>h</i> ≤ 13, -22 ≤ <i>k</i> ≤ 21, -20 ≤ <i>l</i> ≤ 26	-14 ≤ <i>h</i> ≤ 14, -22 ≤ <i>k</i> ≤ 15, -26 ≤ <i>l</i> ≤ 23
Reflections collected	18251	17649	11238	17392
Independent reflections	4136 [R <sub>int</sub> = 0.0346, R <sub>sigma</sub> = 0.0308]	3771 [R <sub>int</sub> = 0.0181, R <sub>sigma</sub> = 0.0147]	4408 [R <sub>int</sub> = 0.1192, R <sub>sigma</sub> = 0.1222]	4337 [R <sub>int</sub> = 0.0644, R <sub>sigma</sub> = 0.0533]
Data/restraints/parameters	4136/0/211	3771/0/211	4408/0/198	4337/0/211
Goodness-of-fit on F <sup>2</sup>	1.049	0.911	1.084	1.096
Final R indexes [ <i>I</i> >= 2 $\sigma$ ( <i>I</i> )]	R <sub>1</sub> = 0.0362, wR <sub>2</sub> = 0.0836	R <sub>1</sub> = 0.0250, wR <sub>2</sub> = 0.0963	R <sub>1</sub> = 0.1100, wR <sub>2</sub> = 0.2510	R <sub>1</sub> = 0.0462, wR <sub>2</sub> = 0.1021
Final R indexes [all data]	R <sub>1</sub> = 0.0574, wR <sub>2</sub> = 0.0930	R <sub>1</sub> = 0.0299, wR <sub>2</sub> = 0.1040	R <sub>1</sub> = 0.1381, wR <sub>2</sub> = 0.2711	R <sub>1</sub> = 0.0563, wR <sub>2</sub> = 0.1071
Largest diff. peak/hole / e Å <sup>-3</sup>	0.28/-0.62	0.41/-0.49	3.22/-2.82	1.30/-1.14

$$R_1 = \frac{\sum ||F_0| - |F_C||}{\sum |F_0|}, wR_2 = \left[ \frac{\sum w(F_0^2 - F_C^2)^2}{\sum w(F_0^2)^2} \right]^{1/2}$$

**Table III.16.** Crystal data and structure refinement data for and **S-*p*BrA.C<sub>6</sub>H<sub>6</sub>** and **S-*p*BrA.C<sub>7</sub>H<sub>8</sub>**.

Empirical formula	C <sub>32</sub> H <sub>24</sub> Br <sub>2</sub> FeN <sub>6</sub> S <sub>2</sub>	C <sub>32</sub> H <sub>24</sub> Br <sub>2</sub> FeN <sub>6</sub> S <sub>2</sub>	C <sub>33</sub> H <sub>26</sub> Br <sub>2</sub> FeN <sub>6</sub> S <sub>2</sub>	C <sub>33</sub> H <sub>26</sub> Br <sub>2</sub> FeN <sub>6</sub> S <sub>2</sub>
Formula weight / g mol <sup>-1</sup>	772.36	772.36	786.39	786.39
Temperature / K	300	100	300	120
Radiation MoK $\alpha$ / Å	$\lambda = 0.71073$			
Crystal size / mm <sup>3</sup>	0.28 × 0.24 × 0.2		0.26 × 0.2 × 0.16	
Crystal system	monoclinic			
Space group	C2/c			
<i>a</i> / Å	10.7312(4)	10.4745(2)	10.6754(5)	10.4480(3)
<i>b</i> / Å	15.9483(3)	15.5975(3)	16.2571(5)	15.9476(3)
<i>c</i> / Å	20.1701(3)	19.7065(3)	20.2526(7)	19.8220(5)
$\alpha$ / °	90	90	90	90
$\beta$ / °	97.734(4)	99.0719(12)	95.6283(16)	97.9181(16)
$\gamma$ / °	90	90	90	90
Volume / Å <sup>3</sup>	3420.60(15)	3179.30(10)	3497.9(2)	3271.25(13)
Z-formula	4	4	4	4
$\rho_{\text{calc}}$ / g cm <sup>-3</sup>	1.500	1.614	1.664	1.597
$\mu$ / mm <sup>-1</sup>	2.930	3.152	2.876	3.065
F(000)	1544.0	1544.0	1768.0	1576.0
2 $\theta$ range for data collection / °	6.536 - 52.74	7.88 - 52.708	4.58 - 50.054	4.15 - 50.05
Index ranges	-13 ≤ <i>h</i> ≤ 13, -19 ≤ <i>k</i> ≤ 19, -23 ≤ <i>l</i> ≤ 25	-13 ≤ <i>h</i> ≤ 13, -19 ≤ <i>k</i> ≤ 19, -24 ≤ <i>l</i> ≤ 24	-12 ≤ <i>h</i> ≤ 12, -19 ≤ <i>k</i> ≤ 19, -24 ≤ <i>l</i> ≤ 24	-12 ≤ <i>h</i> ≤ 12, -18 ≤ <i>k</i> ≤ 18, -23 ≤ <i>l</i> ≤ 23
Reflections collected	12976	6222	34542	25089
Independent reflections	3464 [R <sub>int</sub> = 0.0383, R <sub>sigma</sub> = 0.0356]	3233 [R <sub>int</sub> = 0.0128, R <sub>sigma</sub> = 0.0235]	3077 [R <sub>int</sub> = 0.0341, R <sub>sigma</sub> = 0.0160]	2889 [R <sub>int</sub> = 0.0234, R <sub>sigma</sub> = 0.0112]
Data/restraints/parameters	3464/0/195	3233/0/195	3077/0/189	2889/0/186
Goodness-of-fit on F <sup>2</sup>	1.077	1.046	1.060	1.050
Final R indexes [ <i>I</i> ≥ 2 $\sigma$ ( <i>I</i> )]	R <sub>1</sub> = 0.0386, wR <sub>2</sub> = 0.0984	R <sub>1</sub> = 0.0200, wR <sub>2</sub> = 0.0451	R <sub>1</sub> = 0.0527, wR <sub>2</sub> = 0.1438	R <sub>1</sub> = 0.0457, wR <sub>2</sub> = 0.1165
Final R indexes [all data]	R <sub>1</sub> = 0.0567, wR <sub>2</sub> = 0.1109	R <sub>1</sub> = 0.0247, wR <sub>2</sub> = 0.0468	R <sub>1</sub> = 0.0660, wR <sub>2</sub> = 0.1561	R <sub>1</sub> = 0.0486, wR <sub>2</sub> = 0.1194
Largest diff. peak/hole / e Å <sup>-3</sup>	0.46/-0.69	0.40/-0.43	0.68/-0.72	2.33/-1.71

$$R_1 = \frac{\sum ||F_0| - |F_c||}{\sum |F_0|}, wR_2 = \left[ \frac{\sum w(F_0^2 - F_c^2)^2}{\sum w(F_0^2)^2} \right]^{1/2}$$

**Table III.17.** Crystal data and structure refinement data for **Se-pBrA.C<sub>9</sub>H<sub>12</sub>**, **S-pBrA.C<sub>7</sub>H<sub>8</sub>** and **S-pBrA.C<sub>6</sub>H<sub>6</sub>**.

Empirical formula	C <sub>35</sub> H <sub>30</sub> Br <sub>2</sub> FeN <sub>6</sub> Se <sub>2</sub>	C <sub>35</sub> H <sub>30</sub> Br <sub>2</sub> FeN <sub>6</sub> Se <sub>2</sub>	C <sub>33</sub> H <sub>26</sub> Br <sub>2</sub> FeN <sub>6</sub> Se <sub>2</sub>	C <sub>33</sub> H <sub>26</sub> Br <sub>2</sub> FeN <sub>6</sub> Se <sub>2</sub>	C <sub>32</sub> H <sub>24</sub> Br <sub>2</sub> FeN <sub>6</sub> Se <sub>2</sub>
Formula weight / g mol <sup>-1</sup>	908.24	908.24	880.18	880.18	866.16
Temperature / K	300	120	300	150	300
Radiation MoK $\alpha$ / Å			$\lambda = 0.71073$		
Crystal size / mm <sup>3</sup>	0.32 × 0.28 × 0.24		0.22 × 0.2 × 0.18		0.22 × 0.2 × 0.16
Crystal system			monoclinic		
Space group			C2/c		
<i>a</i> / Å	10.8789(9)	10.60210(10)	10.7370(3)	10.5500(2)	10.7075(3)
<i>b</i> / Å	16.7652(2)	16.6497(7)	16.3479(3)	16.0549(3)	16.0486(4)
<i>c</i> / Å	20.3013(3)	19.7938(8)	20.4336(5)	20.1587(4)	20.2715(5)
$\alpha$ / °	90	90	90.01	90	90
$\beta$ / °	91.348(8)	95.420(2)	97.1951(11)	98.8580(10)	99.2720(10)
$\gamma$ / °	90	90	89.99	90	90
Volume / Å <sup>3</sup>	3701.7(3)	3478.4(2)	3558.41(15)	3373.74(11)	3437.95(15)
Z-formula	4	4	4	4	4
$\rho_{\text{calc}}$ / g cm <sup>-3</sup>	1.630	1.734	1.641	1.731	1.673
$\mu$ / mm <sup>-1</sup>	4.565	4.858	4.746	5.006	4.911
F(000)	1784.0	1784.0	1716.0	1716.0	1688.0
2 $\theta$ range for data collection / °	7.428 - 52.732	6.404 - 54.99	4.018 - 54.972	5.074 - 55.054	4.072 - 55.198
Index ranges	-13 ≤ <i>h</i> ≤ 13, -20 ≤ <i>k</i> ≤ 20, -21 ≤ <i>l</i> ≤ 25	-13 ≤ <i>h</i> ≤ 13, -21 ≤ <i>k</i> ≤ 21, -25 ≤ <i>l</i> ≤ 25	-13 ≤ <i>h</i> ≤ 13, -21 ≤ <i>k</i> ≤ 21, -26 ≤ <i>l</i> ≤ 25	-13 ≤ <i>h</i> ≤ 13, -20 ≤ <i>k</i> ≤ 20, -26 ≤ <i>l</i> ≤ 25	-13 ≤ <i>h</i> ≤ 13, -20 ≤ <i>k</i> ≤ 18, -26 ≤ <i>l</i> ≤ 26
Reflections collected	16973	27027	11951	13708	31359
Independent reflections	3774 [R <sub>int</sub> = 0.0476, R <sub>sigma</sub> = 0.0402]	3997 [R <sub>int</sub> = 0.0441, R <sub>sigma</sub> = 0.0290]	4090 [R <sub>int</sub> = 0.0270, R <sub>sigma</sub> = 0.0303]	3877 [R <sub>int</sub> = 0.0372, R <sub>sigma</sub> = 0.0293]	3972 [R <sub>int</sub> = 0.0385, R <sub>sigma</sub> = 0.0208]
Data/restraints/parameters	3774/0/208	3997/0/212	4090/0/192	3877/0/206	3972/0/195
Goodness-of-fit on F <sup>2</sup>	1.032	1.069	1.055	1.058	1.089
Final R indexes [I ≥ 2 $\sigma$ (I)]	R <sub>1</sub> = 0.0378, wR <sub>2</sub> = 0.0811	R <sub>1</sub> = 0.0306, wR <sub>2</sub> = 0.0790	R <sub>1</sub> = 0.0483, wR <sub>2</sub> = 0.1699	R <sub>1</sub> = 0.0312, wR <sub>2</sub> = 0.0764	R <sub>1</sub> = 0.0349, wR <sub>2</sub> = 0.0740
Final R indexes [all data]	R <sub>1</sub> = 0.0696, wR <sub>2</sub> = 0.0933	R <sub>1</sub> = 0.0395, wR <sub>2</sub> = 0.0856	R <sub>1</sub> = 0.0833, wR <sub>2</sub> = 0.2127	R <sub>1</sub> = 0.0381, wR <sub>2</sub> = 0.0806	R <sub>1</sub> = 0.0511, wR <sub>2</sub> = 0.0814
Largest diff. peak/hole / e Å <sup>-3</sup>	0.81/-0.94	0.58/-1.01	0.91/-0.92	1.42/-1.08	0.75/-0.55

$$R_1 = \frac{\sum ||F_0| - |F_C||}{\sum |F_0|}, wR_2 = \left[ \frac{\sum w(F_0^2 - F_C^2)^2}{\sum w(F_0^2)^2} \right]^{1/2}$$

## Appendix 8 - List of Publications

1 S. Lakhroufi, E. Tailleux, **W. B. Guo**, F. Le Gac, M. Marchivie, M.-H. Lemée-Cailleau, G. Chastanet, P. Guionneau, *Mosaicity of spin-crossover crystals*. *Crystals*, 2018, **8**, 363. Doi.org/10.3390/cryst8090363.

2 **W. B. Guo**, N. Daro, S. Pillet, M. Marchivie, E. E. Bendeif, E. Tailleux, K. Chainok, D. Denux, G. Chastanet, P. Guionneau. *Unprecedented Reverse Volume Expansion in Spin-Transition Crystals*. *Chem. Eur. J.*, 2020, **26**, 12927. Doi.org/10.1002/chem.202001821.



*Résumé*

***Résumé***

## *Résumé*

## Nouveaux composés à conversion de spin et polymorphisme pour une approche multi-échelle vers les hautes $T$ (LIESST)

Le phénomène à conversion de spin (CS) est de plus en plus envisagé pour intégrer des dispositifs de l'électronique moléculaire, comme unité de traitement des données, capteur, actionneurs et/ou pigments intelligents.<sup>1</sup> Cela concerne des complexes métalliques dont la configuration électronique dépend du champ de ligand. Pour des complexes à base d'ions  $Fe^{2+}$ , ces configurations sont soit BS (bas spin,  $S = 0$ ) soit HS (haut spin,  $S = 2$ ). Pour des champs de ligands moyens, l'application d'un stimulus extérieur peut permettre de passer d'une configuration électronique à l'autre. On parle alors de conversion de spin (CS).

La lumière, est l'un des stimuli externes importants. Tout d'abord, la lumière peut être utilisée pour induire une photo-réaction sur le ligand qui affectera le champ du ligand et l'état du spin. Ceci concerne l'effet LD-LISC (Ligand-Driven Light-Induced Spin Change) et l'effet LD-CISSS (Light-Driven-Coordination-Induced Spin State Switching).<sup>2</sup> Ensuite, la lumière peut être utilisée pour apporter de l'énergie et chauffer l'échantillon, favorisant l'effet photothermique.<sup>3</sup> La lumière peut également être réglée pour exciter et peupler des états impliquant le centre métallique. Grâce à la population d'états excités, un état métastable ( $h\nu$ -HS\*) peut être piégé à basse température. Cet effet est appelé Light-Induced Excited Spin-State Trapping (LIESST).<sup>4</sup> Cependant, cet état métastable a tendance à relaxer vers l'état state BS. la température de relaxation ( $h\nu$ -HS\* $\rightarrow$ LS) qui mesure la température limite à laquelle l'état photo-induit est effacé en quelques minutes, appelée  $T$ (LIESST), est généralement inférieure à 50 K, ce qui restreint fortement son application. Il est encore très difficile d'établir les relations structure-propriétés correspondant au processus LIESST, bien que cette approche soit cruciale pour découvrir des matériaux photocommutables avec des températures de relaxation élevées. La compréhension fondamentale de la durée de vie de l'état photo-induit doit encore être approfondie avant toute conception rationnelle d'un matériau efficace.

Plusieurs tentatives de corrélations structure-propriétés ont été effectuées dans le passé de façon à déterminer quels étaient les paramètres structuraux importants sur le maintien de l'état photo-induit à haute température. La déformation de la sphère de coordination lors que la conversion de spin semble un élément important. En effet, l'état HS est plus gros et distordu que l'état BS. Favoriser cette distorsion de la sphère de coordination semble accroître la durée de vie de l'état photo-induit. Plus précisément, c'est la distorsion trigonale ( $\Delta\theta$ ) du polyèdre de

## Résumé

coordination qui semble favoriser de hautes  $T(\text{LIESST})$ .<sup>5,6</sup> Cependant, sur la base d'études photocrystallographiques de deux polymorphes du complexe  $[\text{Fe}(\text{PM-BiA})_2(\text{NCS})_2]$  ( $\text{PM-BiA} = \text{N-2'-pyridylméthylène-4-(aminobiphényle)}$ ), l'anisotropie de l'élongation de la liaison métal-ligand ( $\Delta\zeta$ ) a été identifiée comme un facteur important.<sup>7</sup> Le rôle de la distorsion de la sphère de coordination dans la durée de vie du  $h\nu\text{-HS}^*$  implique qu'une représentation de la spectroscopie des niveaux vibrationnels en fonction de l'élongation de la liaison métal-ligand n'est plus suffisante. Il faut utiliser une vision tridimensionnelle, allant d'une respiration isotrope de la sphère de coordination vers une respiration anisotrope (Figure R1).<sup>8</sup>

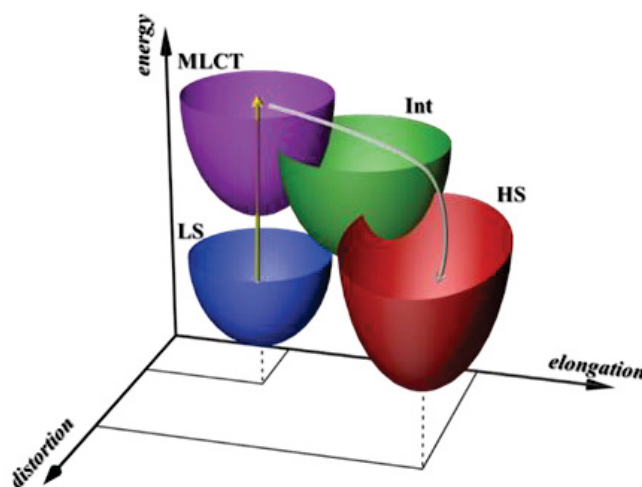


Figure R1. Vue tridimensionnelle des puits de potentiel BS (bleu) et HS (rouge) dans le modèle de respiration anisotrope de la sphère de coordination. Figure adaptée de la référence 8.

L'objectif de ce travail de thèse est de comprendre comment augmenter la température  $T(\text{LIESST})$  vers une plage de température de la vie quotidienne. Pour cela nous avons choisi de promouvoir, par conception de ligands adaptés, la distorsion angulaire de la sphère de coordination. Pour cela nous avons choisi deux stratégies basées sur la chimie : i) jouer à l'échelle moléculaire *via* des contraintes stériques produites par des ligands substitués par des halogènes et ii) étudier l'effet des contraintes intermoléculaires par le polymorphisme. La partie I présente quelques connaissances fondamentales sur le TS et les parties II et III sont consacrées à la synthèse, à la cristallographie et aux études (photo)magnétiques de nouveaux composés moléculaires, y compris les nombreux polymorphes, de la famille  $[\text{Fe}(\text{PM-zBrA})_2(\text{NCS})_2]$ . De nouveaux complexes ont été synthétisés en utilisant les ligands fonctionnalisés de  $\text{PM-zXA}$  ( $z = o, m, p, X = \text{F}$  et  $\text{Br}$ ).

Dans la **Partie II**, trois composés de la famille  $[\text{Fe}(\text{PM-}z\text{FA})_2(\text{NCS})_2]$  avec du fluor en positions *para*, *mé*ta, et *ortho* ont été présentés. Des études structurales et photomagnétiques révèlent que la distorsion angulaire de la sphère de coordination augmente de la position *para* à *ortho* sans pour autant augmenter de façon claire la température de relaxation  $T(\text{LIESST})$  qui est inférieure à 60 K. De plus, la variation de la distorsion trigonale  $\Delta\theta$  est faible pouvant expliquer les faibles valeurs de  $T(\text{LIESST})$ . Le complexe  $[\text{Fe}(\text{PM-}m\text{FA})_2(\text{NCS})_2]$  présente une conversion de spin incomplète d'un seul ion  $\text{Fe}^{2+}$  sur les deux cristallographiquement présents. L'examen des distances Fe---F montre que la distance la petite dans  $\text{Fe1N}_6$  conduit à une forte distorsion qui favorise l'état HS tandis que la distance la plus grande dans  $\text{Fe2N}_6$  conduit à une faible distorsion en faveur de la conversion de spin. Cela démontre que les contraintes stériques peuvent augmenter la distorsion à l'échelle de la sphère de coordination.

La **Partie III** concerne la synthèse et les caractérisations du complexe  $[\text{Fe}(\text{PM-}o\text{BrA})_2(\text{NCS})_2]$  pour lequel nous n'avons malheureusement pas la structure, de deux polymorphes du  $[\text{Fe}(\text{PM-}m\text{BrA})_2(\text{NCS})_2]$  et de quatre polymorphes du  $[\text{Fe}(\text{PM-}p\text{BrA})_2(\text{NCS})_2]$ . Ces sept nouveaux composés ont été analysés selon une approche multi-échelle pour montrer comment la distorsion et les interactions intermoléculaires s'influencent mutuellement. Une attention particulière a été portée aux différents polymorphes du complexe  $[\text{Fe}(\text{PM-}p\text{BrA})_2(\text{NCS})_2]$ . De plus, l'état HS\* métastable peut être obtenu par effet LIESST et par trempe thermique, donnant lieu à des températures de relaxation élevées de 109 K et 70 K. Les études structurales révèlent une rotation énorme du cycle phényle dans trois des polymorphes. Cette rotation est concomitante à la conversion de spin et provient de fortes contraintes dans les interactions intermoléculaires. Le polymorphe I-*p*BrA présente conversion de spin abrupte avec hystérèse thermique autour de 175 K et un  $T(\text{LIESST})$  de 109 K. Le  $T(\text{LIESST})$  à 109 K dans ce polymorphe est la valeur la plus élevée de la famille PM-L, ce qui peut s'expliquer par la grande valeur de  $\Delta\theta$  et  $\Delta\zeta$ . Le polymorphe II-*p*BrA présente une conversion de spin graduelle mais pas d'effet LIESST. Le polymorphe III-*p*BrA présente transition abrupte avec un  $T_{1/2}$  autour de 200 K. La variation de la distorsion ( $\Delta\theta$ ,  $\Delta\zeta$ ) est plus faible que celle du I-*p*BrA, ce qui conduit à une petite valeur de  $T(\text{LIESST})$  autour de 70 K. Alors que la rotation des ligands se fait de façon abrupte dans les polymorphes I-*p*BrA et III-*p*BrA, elle est graduelle et combinée à une conversion ordre-désordre du cycle phényle dans II-*p*BrA. Le polymorphe IV-*p*BrA présente un HS complet avec une très grande distorsion trigonale. Cette rotation des ligands ainsi que la modification que cela entraîne sur les interactions intermoléculaires conduit à des comportements inhabituels au niveau des expansions thermiques des mailles cristallines. Ainsi,

le polymorphe I-*p*BrA présente une expansion volumique inverse sans précédent à la transition de spin. A lieu de l'habituelle diminution du volume de maille lors de la conversion HS → BS une augmentation de presque 2% du volume de maille est observée à la transition de spin (Figure R2). Cette première est entièrement démontrée par des expériences de diffraction des rayons X sur monocristal et sur poudre. Le composé III-*p*BrA quant à lui ne montre aucune variation volumique de la maille cristalline à la transition ce qui constitue également un fait inhabituel.

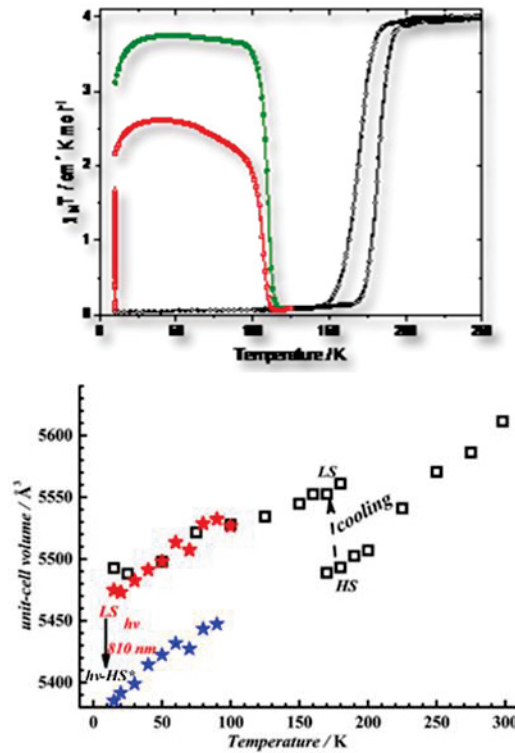


Figure R2. Dépendance thermique du produit  $\chi_M T$  du polymorphe I-*p*BrA (haut) montrant les courbes de relaxation après trempe thermique (■), pendant l'irradiation à 830 nm (Δ) et la courbe (■), enregistrées à 0.4 K/min. Dépendance thermique de volume de maille cristalline (bas) montrant la conversion thermo-induite (□) ainsi que la photo-excitation depuis l'état BS (étoile rouge) vers l'état  $h\nu$ -HS\* (étoile bleue).

L'absence de  $T(\text{LIESST})$  dans II-*p*BrA indique que  $\Delta\Theta$  n'est probablement pas le seul paramètre à corrélérer avec le  $T(\text{LIESST})$  et qu'il faut également tenir compte de  $\Delta\zeta$ . Cette hypothèse a été confrontée à l'examen de treize nouveaux composés obtenus en faisant varier le solvant de cristallisation pour obtenir des solvatomorphes ainsi qu'à une vingtaine de composés de la littérature formés à partir de ligand bidentes. Cet examen constitue la [Partie IV](#).

## Résumé

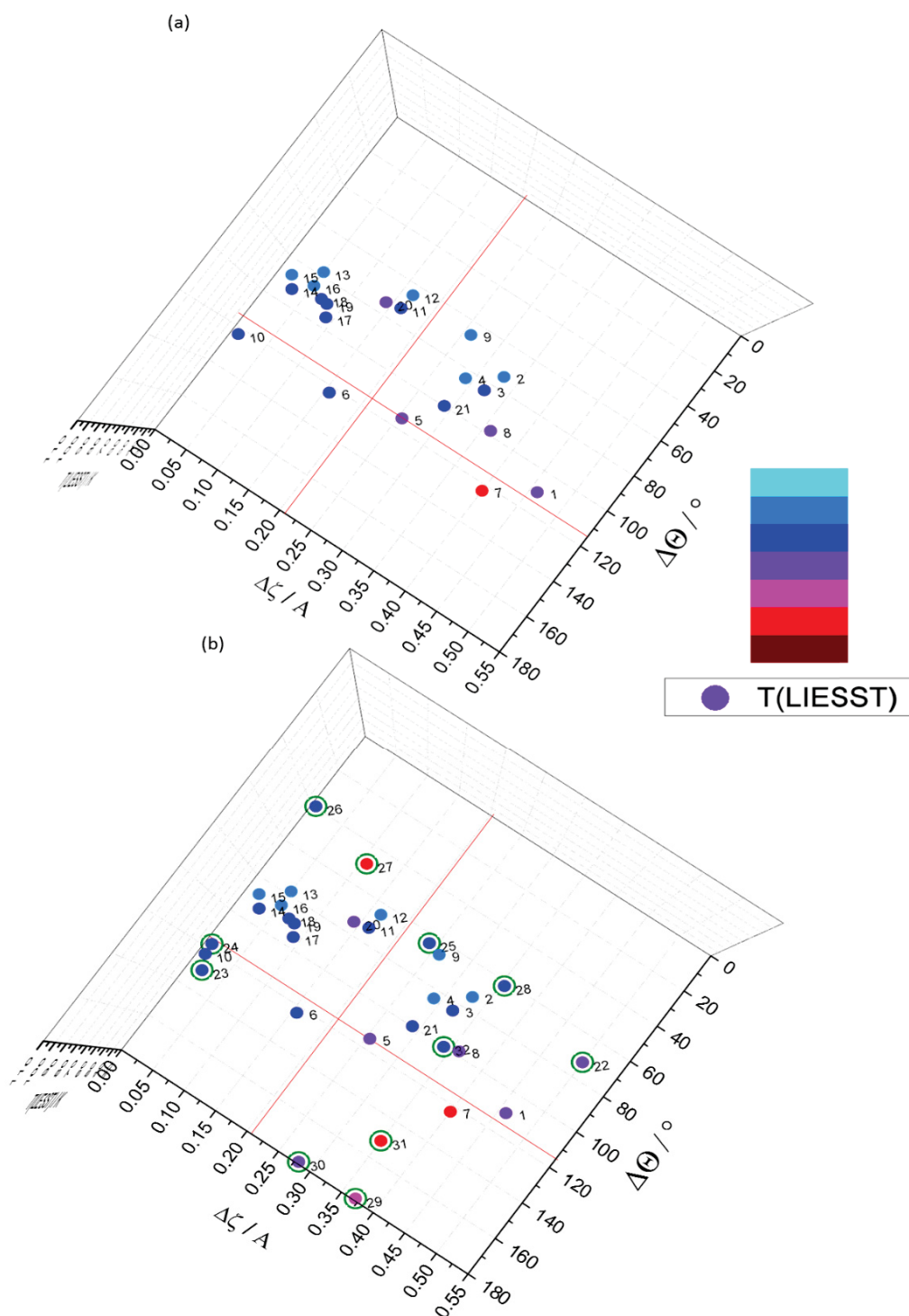


Figure R3.  $T(\text{LIESST})$  en fonction de  $\Delta\theta$  and  $\Delta\zeta$  pour les composés ne présentant pas de changements structuraux (a) et ceux avec changements structuraux cerclés de vert (b). Les lignes rouges représentent les valeurs moyennes de  $\Delta\theta$  (115°) et  $\Delta\zeta$  (0.21 Å).

Cette discussion détaillée démontre deux points importants.

Le premier est que pour s'assurer des valeurs de  $T(\text{LIESST})$  élevées, il faut combiner des hautes valeurs de  $\Delta\Theta$  et  $\Delta\zeta$ . En effet, la [Figure R3a](#) démontre clairement que les hautes  $T(\text{LIESST})$  sont obtenues pour des composés présentant une forte distorsion trigonale et une forte anisotropie d'élongation. Cela implique une nouvelle façon d'envisager la chimie des ligands et des complexes de coordination qui devront promouvoir à la fois une grande distorsion angulaire et une forte anisotropie de l'élongation.

Le second point important est que la durée de vie de l'état photo-induit est impliquée dans un processus multi-échelle. En effet, les composés présentant des changements structuraux notables (ordre-désordre, brisure de symétrie, macles...) ne suivent pas cette règle des hautes valeurs de  $\Delta\Theta$  et  $\Delta\zeta$  ([Figure R3b](#)). Cela implique que la  $T(\text{LIESST})$  peut être influencée par toutes les échelles du matériau : la distorsion anisotrope de la sphère de coordination, la variation de la conformation du ligand, la modification des interactions, le réarrangement moléculaire ainsi que la brisure de symétrie. Toutes ces modifications structurales peuvent renforcer ou affaiblir l'influence de la respiration anisotrope de la sphère de coordination sur la durée de vie de l'état métastable. Il y a donc une forte intrication entre l'influence de la respiration de la sphère de coordination sur les échelles supérieures et, en retour, une influence des échelles supérieures sur la sphère de coordination. Là encore, d'un point de la synthèse, les défis sont nombreux pour que le réseau cristallin ne vienne pas perturber négativement une chimie spécifique sur la sphère de coordination.

En conclusion, les vingt-trois nouveaux composés de ce travail offrent un large panel de comportements innovants, comme par exemple des expansions volumiques négatives ou nulles à la transition de spin et l'absence de transition à plusieurs étapes malgré des sites métalliques indépendants à l'intérieur du cristal. De plus des températures de relaxation élevées ont été obtenues et comparées à la littérature permettant de dégager une vision multi-échelle de la  $T(\text{LIESST})$ . Cela permet d'envisager de nouvelles voies de conception de matériaux commutables vers une température de relaxation  $T(\text{LIESST})$  élevée. Ces travaux élargissent considérablement la richesse des perspectives basées sur la conversion de spin.

## References:

- [1] a) *Spin-Crossover Materials Properties and Applications*, ed. M. A. Halcrow, John Wiley & Sons, 2013; b) *Spin Crossover in Transition Metal Compounds I–III*, ed. P. Gütllich, H. A. Goodwin, *Top. Curr. Chem.*, 2004, vol. 233; c) K. S. Kumar, M. Ruben, *Coord. Chem. Rev.*, 2017, **346**, 176; d) K. Ridier, A. C. Bas, Y. Zhang, L. Routaboul, L. Salmon, G. Molnár, C. Bergaud, A. Bousseksou, *Nat. Commun.*, 2020, **11**, 3611; e) T. Mallah, M. Cavallini, *C. R. Chim.*, 2018, **21**, 1270; f) A. Bousseksou, G. Molnár, L. Salmon, W. Nicolazzi, *Chem Soc Rev.*, 2011, **40**, 3313; g) J. Linares, E. Codjovi, Y. Garcia, *Sensors*, 2012, **12**, 4479; h) G. Aromí, L. A. Barrios, O. Roubeau, P. Gamez, *Coord. Chem. Rev.*, 2011, **255**, 485; i) S. Brooker, *Chem. Soc. Rev.*, 2015, **44**, 2880.
- [2] a) M. L. Boillot, J. Zarembowitch, A. Sour, *Top. Curr. Chem.*, 2004, **234**, 261; 17) B. Rosner, M. Milek, A. Witt, B. Gobaut, P. Torelli, R. H. Fink, M. M. Khusniyarov, *Angew. Chem. Int. Ed.*, 2015, **54**, 12976; b) S. Venkataramani, U. Jana, M. Dommaschk, F. D. Sonnichsen, F. Tuczek, R. Herges, *Science*, 2011, **331**, 445.
- [3] E. Freysz, S. Montant, S. Létard, J. L. Létard, *Chem. Phys. Lett.*, 2004, **394**, 318.
- [4] S. Decurtins, P. Gütllich, C. P. Kohler, H. Spiering, A. Hauser, *Chem. Phys. Lett.*, 1984, **105**, 1.
- [5] M. Marchivie, P. Guionneau, J. F. Létard, D. Chasseau, *Acta Cryst.*, 2005, **B61**, 25.
- [6] J. F. Létard, *J. Mater. Chem.*, 2006, **16**, 2550-2559.
- [7] a) M. Buron-Le Cointe, J. Hébert, C. Baldé, N. Moisan, L. Toupet, P. Guionneau, J. F. Létard, E. Freysz, H. Cailleau, E. Collet, *Phys. Rev. B.*, 2012, **85**, 064114.; b) J. F. Létard, G. Chastanet, O. Nguyen, S. Marcén, M. Marchivie, P. Guionneau, D. Chasseau, P. Gütllich, *Monatsh. Chem.*, 2003, **134**, 165; c) K. Ichiyangi, J. Hebert, L. Toupet, H. Cailleau, P. Guionneau, J. F. Létard, E. Collet *Phys. Rev B*, 2006, **73**, 060408.
- [8] a) R. Bertoni, M. Cammarata, M. Lorenc, S. F. Matar, J. F. Létard, H. T. Lemke, E. Collet, *Acc. Chem. Res.*, 2015, **48**, 774; b) S. Hayami, K. Hiki, T. Kawahara, Y. Maeda, D. Urakami, K. Inoue, M. Ohama, S. Kawata, O. Sato, *Chem. Eur. J.* 2009, **15**, 3497.

## *Résumé*

## Nouveaux composés à conversion de spin et polymorphisme pour une approche multi-échelle vers les hautes $T$ (LIESST)

L'effet LIESST (Light-Induced Excited Spin-State Trapping) apparaît comme l'un des phénomènes les plus prometteurs et les plus excitants pour les dispositifs applicatifs basés sur les complexes à transition de spin (TS). Cependant, la compréhension fondamentale du LIESST doit encore être approfondie avant toute conception rationnelle. Par exemple, il est encore très difficile d'établir les relations structure-propriétés, bien que cette approche soit cruciale pour découvrir des matériaux à TS ayant une température de relaxation  $T$ (LIESST) élevée. L'objectif de ce travail est donc de comprendre comment augmenter la valeur de  $T$ (LIESST) vers une plage de température de la vie quotidienne. Nous avons choisi de l'atteindre en tentant d'augmenter la distorsion de la sphère de coordination du métal par deux stratégies basées sur la chimie : *i*) influencer à l'échelle moléculaire via des contraintes stériques induites par des ligands halogénés et *ii*) moduler la contrainte moléculaire *via* du polymorphisme. La partie *I* présente quelques aspects fondamentaux et les parties *II* et *III* sont consacrées à la synthèse, à la cristallographie et aux études (photo)magnétiques des nouveaux composés moléculaires, y compris des polymorphes, de la famille  $[\text{Fe}(\text{PM-L})_2(\text{NCX})_2]$ . Ces nouveaux composés offrent tout d'abord un large éventail de comportements innovants, comme par exemple des expansions volumiques négatives ou nulles à la TS et l'absence de transition à plusieurs étapes malgré des sites métalliques indépendants au sein du cristal. Ces travaux élargissent considérablement la richesse des perspectives du phénomène de TS. De plus, l'examen approfondi des paramètres pertinents pour l'obtention d'un  $T$ (LIESST) élevé, tel que discutés dans la partie *IV*, apporte de nouvelles caractéristiques et prouve définitivement que toutes les échelles physiques doivent être prises en compte, ce qui conduit à proposer un concept multi-échelle de l'effet LIESST.

*Mots clés:* conversion de spin, magnétisme, cristallographie, effet LIESST, complexes moléculaires, transition de phase, fer, halogènes, polymorphisme.

---

## New spin-crossover compounds including polymorphism for a multiscale approach towards high $T$ (LIESST)

The Light-Induced Excited Spin-State Trapping effect (LIESST) appears as one of the most promising and exciting phenomena for applicative devices based on Spin-CrossOver (SCO) complexes. However, the fundamental understanding of the LIESST effect must be yet deeply completed prior to any rational design of any efficient material. For instance, it is still a great challenge to establish the structure-properties relationships corresponding to the LIESST process, though this approach is crucial to discover SCO materials with a high relaxation temperature  $T$ (LIESST). The target of this work is therefore to understand how to increase  $T$ (LIESST) towards a daily-life temperature range. We choose to reach this goal by increasing the distortion of the metal coordination sphere through two chemistry-based strategies: *i*) playing at the molecular scale via steric strains produced by halogen-substituted ligands and *ii*) controlling the molecular stress through polymorphism. *Part I* displays some fundamental knowledge on SCO and *Part II* and *III* are devoted to the synthesis, crystallography and (photo)magnetic studies of new molecular compounds, including polymorphs, of the  $[\text{Fe}(\text{PM-L})_2(\text{NCX})_2]$  family. First these new compounds offer a large panel of innovative behaviours, such as, for instance, negative or zero volume expansions at the SCO and the absence of multi-step transition despite independent metal sites within the crystal. This work enlarges significantly the richness of the SCO based perspectives. Second, the deep examination of the relevant parameters to high  $T$ (LIESST) as discussed in *Part IV* brings new features and, overall, definitively proves that all physical scales must be taken into account, leading to a multiscale concept of the LIESST effect.

*Keywords:* spin-crossover, magnetism, crystallography, Light-Induced Excited Spin-State Trapping (LIESST), molecular complexes, phase transition, iron, halogen, polymorphism.

**Unité de recherche**

ICMCB, UMR 5026, 87 avenue du Dr Albert Schweitzer 3600 Pessac

